UNIVERSITY OF SOUTHAMPTON
FACULTY OF ENGINEERING, SCIENCE AND MATHEMATICS
SCHOOL OF ELECTRONICS AND COMPUTER SCIENCE
Southampton SO17 1BJ
United Kingdom

Low-Complexity Near-Optimum Detection Techniques for Non-cooperative and Cooperative MIMO Systems

by

Li Wang
B.Eng., M.Sc.

A Doctoral thesis submitted in partial fulfilment of the requirements for the award of Doctor of Philosophy at the University of Southampton

January 2010

SUPERVISOR:
Professor Lajos Hanzo
M.Sc., Ph.D, FREng, DSc, FIEEE, FIET
Chair of Telecommunications
School of Electronics and Computer Science

Dedicated to my family

UNIVERSITY OF SOUTHAMPTON

ABSTRACT

FACULTY OF ENGINEERING AND APPLIED SCIENCE
DEPARTMENT OF ELECTRONICS AND COMPUTER SCIENCE

A thesis submitted in partial fulfilment of the
requirements for the award of Doctor of Philosophy

Low-Complexity Near-Optimum Detection Techniques for Non-cooperative and Cooperative MIMO Systems

by Li Wang

In this thesis, firstly we introduce various reduced-complexity near-optimum Sphere Detection (SD) algorithms, including the well-known depth-first SD, the *K*-best SD as well as the recently proposed Optimized Hierarchy Reduced Search Algorithm (OHRSA), followed by comparative studies of their applications, characteristics, performance and complexity in the context of uncoded non-cooperative Multiple-Input Multiple-Output (MIMO) systems using coherent detection. Particular attention is devoted to Spatial Division Multiple Accessing (SDMA) aided Orthogonal Frequency Division Multiplexing (OFDM) systems, which are considered to constitute a promising candidate for next-generation mobile communications.

It is widely recognized that the conventional List SD (LSD) employed in channel-coded iterative detection aided systems may still impose a potentially excessive complexity, especially when it is applied to high-throughput scenarios employing high-order modulation schemes and/or supporting a high number of transmit antennas/users. Hence, in this treatise three complexity-reduction schemes are devised specifically for LSD-aided iterative receivers in the context of high-throughput channel-coded SDMA/OFDM systems in order to maintain a near-optimum performance at a reduced complexity. Explicitly, based on the exploitation of the soft-bit-information fed back by the channel decoder, the iterative center-shifting and *Apriori*-LLR-Threshold (ALT) schemes are contrived, which are capable of achieving a significant complexity reduction. Additionally, a powerful three-stage serially concatenated scheme is created by intrinsically amalgamating our proposed center-shifting-assisted SD with the decoder of a Unity-Rate-Code (URC). For the sake of achieving a near-capacity performance, Irregular Convolutional Codes (IrCCs) are used as the outer code for the proposed iterative center-shifting SD aided three-stage system.

In order to attain extra coding gains along with transmit diversity gains for Multi-User MIMO (MU-MIMO) systems, where each user is equipped with multiple antennas, we contrive a multi-layer tree-search based *K*-best SD scheme, which allows us to apply the Sphere Packing (SP) aided Space-Time Block Coding (STBC) scheme to the MU-MIMO scenarios, where a near Maximum-a-Posteriori (MAP) performance is achieved at a low complexity.

An alternative means of achieving transmit diversity while circumventing the cost and size constraints of implementing multiple antennas on a pocket-sized mobile device is cooperative diversity, which relies on antenna-sharing amongst multiple cooperating single-antenna-aided users. We design a realistic cooperative system, which operates without assuming the knowledge of the Channel State Information (CSI) at transceivers by employing differentially encoded modulation at the trans-

mitter and non-coherent detection at the receiver. Furthermore, a new Multiple-Symbol Differential Sphere Detection (MSDSD) is contrived in order to render the cooperative system employing either the Differential Amplify-and-Forward (DAF) or the Differential Decode-and-Forward (DDF) protocol more robust to the detrimental channel-envelope fluctuations of high-velocity mobility environments. Additionally, for the sake of achieving the best possible performance, a resource-optimized hybrid relaying scheme is proposed for exploiting the complementarity of the DAF- and DDF-aided systems.

Finally, we investigate the benefits of introducing cooperative mechanisms into wireless networks from a pure channel capacity perspective and from the practical perspective of approaching the Discrete-input Continuous-output Memoryless Channel (DCMC) capacity of the cooperative network with the aid of our proposed Irregular Distributed Hybrid Concatenated Differential (Ir-DHCD) coding scheme.

Acknowledgements

Numerous people have supported me during my graduate research in diverse ways, without whom the completion of this thesis would be impossible. Only a few words here could not adequately capture all my appreciation.

I would like to take this opportunity to express my deepest gratitude to my supervisor Prof. Lajos Hanzo, for his exceptional supervision, insightful guidance and overall for his supreme friendship. He has helped me reach milestones that I never imagined, and prepared me to reach many more. His utmost kindness and encouragement have greatly benefited me; especially his generous investment of time and energy deserve my utmost acknowledgement. He has left an indelible mark.

Many thanks also to my colleagues and the staff of the Communications Group for the useful discussions and comments throughout my research. I thank my colleague Dr. Soon Xin Ng, Dr. Jos Akhtman and Dr. Lei Xu for their generous support during the initial stage of my research. Many thanks to Dr. C. Y. Wei, Dr. L. L. Yang, Prof. S. Chen, Dr. R. Maunder and L. K. Kong for fruitful discussions as well as for their friendship.

As always, I would express my sincere appreciation to my dear parents Xiaonan Zhang and Jingyi Wang for their love, unconditional support as well as for their cultivation, without whom I would not have reached where I am. I also feel extremely lucky to live in a big family, where my dearest ones have given me their endless love since the day I came to this world and have always been a great source of support and motivation. Many, many thanks to my dear aunt Prof. L. Wang and my grandfather Prof. J. W. Wang. Special thanks to my grandmother Prof. X. D. Jian, whose face and voice are being missed by me so much.

Last but not least, my most tender and sincere thanks to my beloved girlfriend Manna Xiong. Her love, support and care gave me the courage and internal peace to face up to the various challenges of life.

List of Publications

Journal Papers:

[**1**] **Li Wang**, Lei Xu, Sheng Chen and Lajos Hanzo, "Generic Iterative Search-Center-Shifting *K*-Best Sphere Detection for Rank-Deficient SDM-OFDM Systems", Electronics Letters, Vol. 44, No. 8, April 2008.

[**2**] **Li Wang**, Lei Xu, Sheng Chen and Lajos Hanzo, "Three-Stage Irregular Convolutional Coded Iterative Center-Shifting *K*-Best Sphere Detection for Soft-Decision SDMA-OFDM", IEEE Transactions on Vehicular Technology, Vol. 58, pp. 2103-2109, May 2009.

[**3**] **Li Wang**, Osamah Alamri and Lajos Hanzo, "Sphere Packing Modulation in the SDMA Uplink Using *K*-Best Sphere Detection", IEEE Signal Processing Letters, Vol. 16, pp. 291-294, April 2009.

[**4**] **Li Wang** and Lajos Hanzo, "The Amplify-and-Forward Cooperative Uplink Using Multiple-Symbol Differential Sphere-Detection", IEEE Signal Processing Letters, Vol. 16, pp. 913-916, October 2009.

[**5**] **Li Wang** and Lajos Hanzo, "The Resource-Optimized Differentially Modulated Hybrid AF/DF Cooperative Cellular Uplink Using Multiple-Symbol Differential Sphere Detection", IEEE Signal Processing Letters, Vol. 16, pp. 965-968, November 2009.

[**6**] Chun-Yi Wei, **Li Wang**, Lajos Hanzo, "Iterative Irregular Sphere Detection in High-Rate Downlink SDMA Systems", IEEE Transactions on Vehicular Technology, Vol. 58, pp. 3855-3861, September 2009.

Conference Papers:

[**1**] **Li Wang**, Lei Xu, Sheng Chen and Lajos Hanzo, "Three-Stage Serially Concatenated Codes and Iterative Center-Shifting *K*-Best Sphere Detection for SDM-OFDM: An EXIT Chart Aided Perspective", in Proceedings of IEEE Wireless Communications and Networking Conference (WCNC'08), pp. 611-615, March, 2008.

[**2**] **Li Wang**, Lei Xu, Sheng Chen and Lajos Hanzo, "MMSE Soft-Interference-Cancellation Aided Iterative Center-Shifting *K*-Best Sphere Detection for MIMO Channels", in Proceedings of IEEE International Conference on Communications (ICC'08), pp. 3819 - 3823, May 2008.

[**3**] **Li Wang**, Lei Xu, Sheng Chen and Lajos Hanzo, "Apriori-LLR-Threshold-Assisted *K*-Best Sphere Detection for MIMO Channels", in Proceedings of IEEE Vehicular Technology Conference (VTC'08 Spring), pp. 867 - 871, May 2008.

[**4**] **Li Wang**, Lei Xu, Sheng Chen and Lajos Hanzo, "Channel Coded Iterative Center-Shifting *K*-Best Sphere Detection for Rank-Deficient Systems", in Proceedings of IEEE Vehicular Technology Conference 2008 (VTC'08 Fall), pp. 1-5, September 2008.

[**5**] **Li Wang**, Osamah Alamri and Lajos Hanzo, "*K*-Best Sphere Detection for the Sphere Packing Modulation Aided SDMA/OFDM Uplink", in Proceedings of IEEE Global Telecommunications Conference (GLOBECOM'08), pp. 1-5, November 2008.

[**6**] **Li Wang** and Lajos Hanzo, "Multiple-Symbol Differential Sphere Detection for the Amplify-and-Forward Cooperative Uplink", to appear in Proceedings of IEEE Vehicular Technology Conference (VTC'09 Fall), September 2009.

[**7**] **Li Wang** and Lajos Hanzo, "The Resource-Optimized Differentially Modulated Hybrid AF/DF Cooperative Cellular Uplink", to appear in Proceedings of IEEE Global Telecommunications Conference (GLOBECOM'09), November 2009.

[**8**] **Li Wang**, Lingkun Kong, Soon Xin Ng and Lajos Hanzo, "To Cooperate or Not: A Capacity Perspective", in IEEE Vehicular Technology Conference (VTC 2010 Spring), May 2010.

[**9**] **Li Wang**, Lingkun Kong, Soon Xin Ng and Lajos Hanzo, "A Near-Capacity Differentially Encoded Non-Coherent Adaptive Multiple-Symbol-Detection Aided Three-Stage Coded Scheme", in IEEE Vehicular Technology Conference (VTC 2010 Spring), May 2010.

[**10**] Chun-Yi Wei, **Li Wang**, and Lajos Hanzo, "A Novel Reduced-Complexity Irregular Sphere Detection Aided Iterative Downlink SDMA Systems Using Linear Dispersion Codes", submitted to IEEE Vehicular Technology Conference (VTC 2010 Spring), May 2010.

Contents

List of Symbols

General notation

- The superscript * is used to indicate complex conjugation. Therefore, a^* represents the complex conjugate of the variable a.
- The superscript ^{T} is used to indicate matrix transpose operation. Therefore, $\mathbf{A}^T$ represents the transpose of the matrix $\mathbf{A}$.
- The superscript ^{H} is used to indicate complex conjugate transpose operation. Therefore, $\mathbf{A}^H$ represents the complex conjugate transpose of the matrix $\mathbf{A}$.
- The notation b_i represents the ith entry of the column vector $\mathbf{b}$.
- The notation $\overrightarrow{b_i}$ represents the ith entry of the row vector $\overrightarrow{\mathbf{b}}$.
- The notation $a_{i,j}$ represents the entry located in the ith row and jth column of the matrix $\mathbf{A}$.
- The notation $*$ denotes the convolutional process. Therefore, $a * b$ represents the convolution between variables a and b.
- The notation $\hat{x}$ represents the estimate of x.
- The notation $\check{x}$ represents the trial candidate of x.
- The notation $X(f)$ is the Fourier Transform of $x(t)$.

Special symbols

- **Matrices and vectors** :

$\mathbf{H}$	The Channel State Information (CSI) matrix
$\mathbf{W}$	The AWGN noise (CSI) matrix
$\mathbf{S}_n$	The nth transmitted space-time signal matrix
$\mathbf{I}_n$	The $(n \times n)$-element identity matrix
$\mathbf{s}$	The signal column vector transmitted from a Mobile Station
$\mathbf{y}$	The received signal column vector at the Base Station
$\mathbf{w}$	The Additive White Gaussian Noise column vector at the Base Station
$\hat{\mathbf{c}}$	The search center of hyper-sphere search space employed by the sphere detection (SD)

- **Variables** :

U	The number of users within a system
M	The number of transmit antenna elements employed at a terminal
N	The number of receive antenna elements employed at a terminal
M_c	The modulation constellation size
$\mathcal{M}_c$	The set of modulation constellation points
C	The search radius of the hypersphere, in which the sphere detector (SD) carries out the search for the solution
$\mathcal{C}_i$	The decoupled search center for $\check{s}_i$
$\mathcal{D}_i$	The accumulated Partial Euclidean Distance (PED) between $\check{\mathbf{s}}_i = [\check{s}_i\ \check{s}_{i+1}\ \cdots\ \check{s}_U]$ and the center $\hat{\mathbf{c}}_i = [\hat{c}_i\ \hat{c}_{i+1}\ \cdots\ \hat{c}_U]$ of the hyper-sphere search space
K	The number of candidates having the lowest accumulated Partial Euclidean Distances (PEDs) retained at each tree search level by the K-best SD
T_b	The length of the correlated-envelope block-fading intervals
η	The bandwidth efficiency in bit/sec/Hz
$\mathcal{L}$	Transmittedc MIMO-symbol candidate list generated by the LSD
$\mathcal{N}_{cand}$	The size of the candidate list $\mathcal{L}$ generated by the LSD
L_f	The transmission frame length
M_r	The number of available cooperating MSs within a cell
f_d	The normalized Doppler frequency

- **Mathematical operations** :

$\sum$	Sum operation
$\otimes$	Kronecker product
$log[\cdot]$	Logarithm operation
$\max(\cdot)$	The maximum value of a matrix/vector
$\min(\cdot)$	The minimum value of a matrix/vector
$vec(\cdot)$	Vertical stacking of the columns of a matrix
$row(\cdot)$	Vertical stacking of the rows of a matrix
$tr(\cdot)$	Trace operation of a matrix
$QR(\cdot)$	The QR-decomposition of a square matrix
$det(\cdot)$	The determinant operation

$p(\cdot)$	The probability density function
$\|\|\cdot\|\|^2$	The second order norm
$\Re\{\cdot\}$	Real part of a complex value
$\Im\{\cdot\}$	Imaginary part of a complex value
$E\{\cdot\}$	Expectation of a random variable
$\mathbf{A}^H$	Matrix/vector Hermitian adjoint
$\mathbf{A}^{-1}$	Matrix inverse
$\mathbf{A}^T$	Matrix/vector transpose
$\mathbf{A}^*$	Matrix/vector/variable Complex conjugate

- **Symbols** :

$\mathbb{R}^n$	n-dimensional real-valued Euclidean space
$\mathbb{C}^n$	n-dimensional complex-valued Euclidean space
Π	Interleaver
Π^{-1}	Deinterleaver
E_{total}	The total power of a sphere packing symbol

Chapter 1

Introduction

The main goals in developing next-generation wireless communication systems are to increase the achievable transmission capacity and to enhance the attainable spectral efficiency at an affordable complexity. Thus, a system designer aims for:

- *Data rate maximization* in order to support flawless multi-media transmissions;
- *Error probability minization*;
- *Signal processing complexity minimization* under the above-mentioned two constraints.

1.1 OFDM Technique

When aiming for high data rates, the bandwidth occupied by the transmitted signal in conventional Single-Carrier (SC) communication systems often significantly exceeds the coherent bandwidth [1,2] of the wireless channel, resulting in a frequency-selective wireless propagation medium. In the context of the SC transmission, complex equalization techniques have to be employed at the receiver in order to mitigate the channel-induced Inter-Symbol-Interference (ISI). Orthogonal Frequency-Division Multiplexing (OFDM) [3], which belongs to the family of Multi-Carrier (MC) transmission schemes, has become the predominant transmission technique in broadcasting and in the Third-Generation Partnership Projects Long Term Evolution (3GPP-LTE). The prime benefit of OFDM is that the original frequency-selective wideband channel may be viewed as a set of parallel narrow-band channels created by the OFDM scheme. Thus, a high data rate may be achieved without using complex equalization techniques at the receiver.

1.1.1 Principle of OFDM

In practice it is rare that a pure Line-Of-Sight (LOS) path exists between the Mobile Station (MS) and the Base Station (BS), owing to the multipath propagation effects imposed by surrounding objects, such as buildings, trees, hills, cars and the like. Consequently, different copies of the transmitted signals experiencing random amplitude attenuation and phase rotation arrive at the receiver

with different time delay. If the *maximum time delay spread* is higher than the symbol duration, which means that some delayed copies of the previous transmitted symbol are received within the current symbol duration, ISI is imposed, hence the channel is referred to as time dispersive or frequency selective. Again, OFDM systems [3] were designed to counteract these channel-induced distortions. Over the years the OFDM technique has drawn wide research interests as a benefit of its merits, although during its early evolution, its application has been mostly limited to the military field as a result of its implementation complexity [3].

OFDM is a combination of a modulation and multiplexing technique [4]. *Modulation* may be interpreted as a method of mapping the data signal to the carrier's amplitude, phase, frequency or their combinations, while *multiplexing* conventionally refers to a scheme of sharing the bandwidth amongst independent data channels of different users. To some extent, OFDM and conventional Frequency Division Multiplexing (FDM) are similar. Orthogonality of the sub-carriers constitutes an important underlying concept in OFDM, which will be briefly reviewed as follows.

Let us assume that all the sub-carriers are sine or cosine waves, which are expressed in the form of $\sin 2\pi k f_0 t$, where k is an integer. Then for a pair of subcarriers we have:

$$f(t) = \sin 2\pi k f_0 t \cdot \sin 2\pi l f_0 t, \tag{1.1}$$

where l is also an integer not equal to k and the integral of this product yields:

$$\begin{aligned}
\int_0^{2\pi} f(t)dt &= \int_0^{2\pi} \sin 2\pi k f_0 t dt \cdot \sin 2\pi l f_0 t dt \\
&= \int_0^{2\pi} \frac{1}{2}\cos 2\pi(k-l) f_0 t dt - \int_0^{2\pi} \frac{1}{2}\cos 2\pi(k+l) f_0 t dt \qquad (1.2)\\
&= 0 - 0 \qquad (1.3)\\
&= 0 \qquad (1.4)
\end{aligned}$$

If $k = l$, the above integral yields π. Consequently, if a number of correlators corresponding to the sub-carrier waveforms are employed at the receiver, each signal stream carried by the corresponding sub-carrier can be recovered without interference from the other sub-carriers, owing to their orthogonality as demonstrated above. Thus, OFDM systems are capable of simultaneously transmitting a number of parallel sub-carriers without interference from each other.

1.1.2 Implementations of OFDM [3] [4]

1.1.2.1 Original Implementation of OFDM

Based on the aforementioned basic philosophy, OFDM constitutes a multi-carrier transmission technique, which divides the available bandwidth into parallel carriers, each of which is modulated by a low-rate data stream, as shown in Figure 1.1. The original serial data stream is split into K parallel channels after being passed through a Serial-to-Parallel (S/P) convertor, which is not shown in the figure to avoid obfuscating details. Given a fixed total data rate, the data rate of each sub-channel becomes a fraction of $1/K$ of the original serial data rate v, i.e. we have v/K. Subsequently, these K sub-streams are mapped to a bank of modulators, modulating the corresponding K sub-carriers $\triangle f, 2\triangle f, ..., K\triangle f$. At the receiver, the same bank of modulators is employed in order

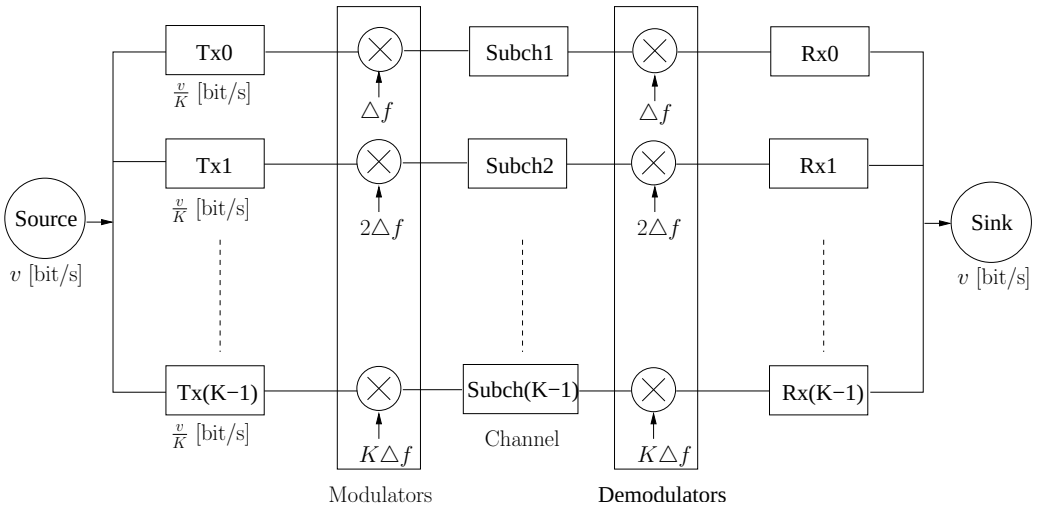

Figure 1.1: Block diagram of the orthogonal parallel modem: it consists of a bank of *K* modulators and a bank of *K* demodulators at the transmitter and receiver, respectively. The serial-to-parallel convertor at its input and the parallel-to-serial convertor at its output are omitted.

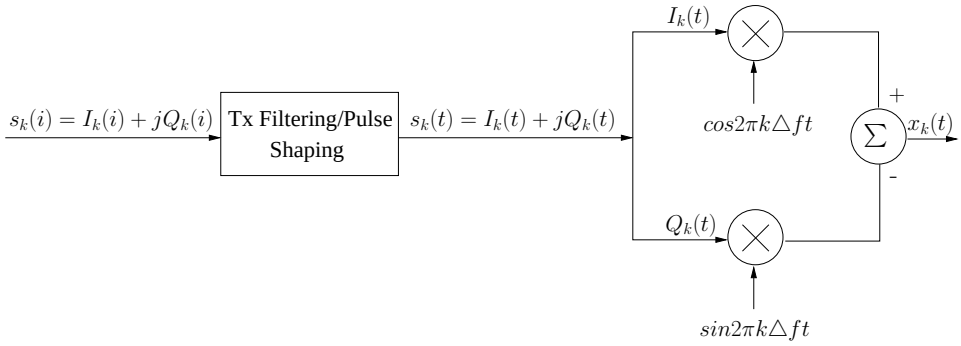

Figure 1.2: Typcial QAM modulator schematic. This represents one of the *K* modulators in the modulator bank at the transmitter of Figure 1.1.

to recover each sub-stream. It is clear that the difference between the adjacent sub-carriers is $\triangle f$ in this case, thus, the total bandwidth *W* of the *K* modulated carriers is $K\triangle f$.

A disadvantage of the OFDM implementation shown in Figure 1.1 is its potentially high implementational complexity as a result of employing *K* individual modulators and transmit filters at the transmitter as well as *K* demodulators and receive filters at the receiver. This limited the employment of OFDM to military applications until it was discovered that the OFDM technique can be conveniently implemented with the aid of the Discrete Fourier Transform (DFT) or the Fast Fourier Transform (FFT) [3, 5]. The latter is used, when the number of sub-carriers is high. This reduced-complexity implementation of OFDM will be discussed in the next section.

1.1.2.2 OFDM Implementations by DFT/FFT [3]

Based on the simplified block diagram of OFDM modem shown in Figure 1.1, a typical Quadrature Amplitude Modulation (QAM) schematic is shown in Figure 1.2, which represents one of the *K* modulators (denoted by a multiplier in Figure 1.1) in the modulator bank of the transmitter, in order to analyze the modulation process mathematically, before highlighting the reason why OFDM

can be implemented by the DFT. In Figure 1.2, $s_k(t) = I_k(t) + jQ_k(t)$ denotes the baseband waveform in the kth parallel path after a S/P convertor at the transmitter. Assuming that at the transmitter rectangular pulse shaping is carried out, the pulse-shaped signal $s_k(t)$ at the input of the kth modulator can be interpreted as the rectangular function $m_T(t-iT) = rect\frac{t-iT}{T}$ weighted by the complex QAM symbol $s_k(i) = I_k(i) + jQ_k(i)$. Consequently, the baseband signal waveform can be written as:

$$s_k(t) = \sum_{i=-\infty}^{\infty} s_k(i) m_T(t-iT), \tag{1.5}$$

where i is the signalling interval index and T is the symbol duration. Then the quadrature components $I_k(t)$ and $Q_k(t)$ are split into two streams and are multiplied by the quadrature carriers $\cos(2\pi k \triangle f t)$ and $\sin(2\pi k \triangle f t)$, respectively. This operation yields modulated signal $x_k(t)$ in the passband in the form of:

$$\begin{aligned} x_k(t) &= I_k(t)\cos(2\pi k \triangle f t) - Q_k(t)\sin(2\pi k \triangle f t) & (1.6)\\ &= \gamma_k(t)\cos(2\pi k \triangle f t + \psi_n), & (1.7) \end{aligned}$$

where the amplitude of the kth output of the bank of modulators is given by

$$\gamma_k(t) = \sqrt{I_k^2(t) + Q_k^2(t)} \tag{1.8}$$

and its phase by

$$\psi_k(t) = \tan^{-1}(\frac{-Q_k(t)}{I_k(t)}), \quad k = 0,\ 1,\ 2,\ \cdots,\ K-1. \tag{1.9}$$

The signal at the transmit antenna is denoted by $x(t)$, which can be formulated as the superposition of all the K sub-carrier signals, yielding:

$$x(t) = \sum_{k=0}^{K-1} x_k(t). \tag{1.10}$$

Eq.(1.6) can be equivalently expressed as:

$$x_k(t) = \Re\{s_k(t) e^{j2\pi k \triangle f t}\}, \tag{1.11}$$

where $\Re\{\bullet\}$ represents the real value of $\bullet$. By substituting Eq.(1.5) into Eq.(1.11), we arrive at:

$$x_k(t) = \Re\{\sum_{i=-\infty}^{\infty} s_k(i) m_T(t-iT) e^{j2\pi k \triangle f t}\}. \tag{1.12}$$

Then substituting Eq.(1.12) into Eq.(1.10), we have:

$$x(t) = \sum_{k=0}^{K-1} \Re\{\sum_{i=-\infty}^{\infty} s_k(i) m_T(t-iT) e^{j2\pi k \triangle f t}\}. \tag{1.13}$$

Without loss of generality, we only consider the signalling interval $i = 0$, thus we have the modulated signal for the signalling interval $i = 0$ as:

$$x_{i=0}(t) = \sum_{k=0}^{K-1} \Re\{s_k(0) m_T(t) e^{j2\pi k \triangle f t}\}. \tag{1.14}$$

For notational convenience, we drop the signalling interval index i, and bear in mind that the modulated signal is confined to the interval $|t| < \frac{T}{2}$ for $i = 0$, where the OFDM symbol duration T is defined as

$$T \triangleq \frac{1}{\triangle f}. \tag{1.15}$$

Consequently, we arrive at a simplified formalism for the modulated signal in signalling interval $i = 0$ as:

$$x(t) = \sum_{k=0}^{K-1} \Re\{s_k e^{j2\pi k \triangle f t}\}. \tag{1.16}$$

Then we take the $\Re$ part with the aid of the complex conjugate operation as follows:

$$\begin{aligned} x(t) &= \sum_{k=0}^{K-1} \frac{1}{2}\{s_k e^{j2\pi k \triangle f t} + s_k^* e^{-j2\pi k \triangle f t}\} && (1.17) \\ &= \sum_{k=-(K-1)}^{K-1} \frac{1}{2} s_k e^{j2\pi k \triangle f t}, && (1.18) \end{aligned}$$

where for $k = 0, 1, ..., K-1$ we have $s_{-k} = s_k^*$, $s_0 = 0$. Furthermore, we introduce the Fourier coefficient F_k, which is defined as:

$$F_k = \begin{cases} \frac{1}{2} s_k & \text{if } 1 \leq k \leq K-1, \\ \frac{1}{2} s_k^* & \text{if } -(K-1) \leq k \leq -1, \\ 0 & \text{if } k = 0. \end{cases} \tag{1.19}$$

Then we can represent the modulated signal $x(t)$ as:

$$x(t) = \sum_{k=-(K-1)}^{K-1} F_k e^{j2\pi k \triangle f t}. \tag{1.20}$$

Until now the modulated signal $x(t)$ was assumed to be continuous function of time within the signalling interval $k = 0$, which has a very similar form to the Inverse Discrete Fourier Transform (IDFT) [5]. For the sake of arriving at a discrete-time expression for $x(t)$, the sampling frequency f_s is introduced, which is at least twice the overall bandwidth $B = (K-1)\triangle f$ according to the Nyquist criterion [3, 6], hence we have:

$$f_s \geq 2(K-1)\triangle f. \tag{1.21}$$

Thus, the sampling interval T_s can be expressed as:

$$T_s = \frac{1}{f_s} \leq \frac{1}{2(K-1)\triangle f}. \tag{1.22}$$

Upon introducing the discrete time $t = \imath T_s$, leading to the discrete time expression of Eq.(1.20), we have:

$$\begin{aligned} x(\imath T_s) &= \sum_{k=-(K-1)}^{K-1} F_k e^{j2\pi k \triangle f \imath T_s} && (1.23) \\ &= \sum_{k=-(K-1)}^{K-1} F_k e^{j\frac{2\pi}{Q} k\imath}, \ \imath = 0...Q-1, && (1.24) \end{aligned}$$

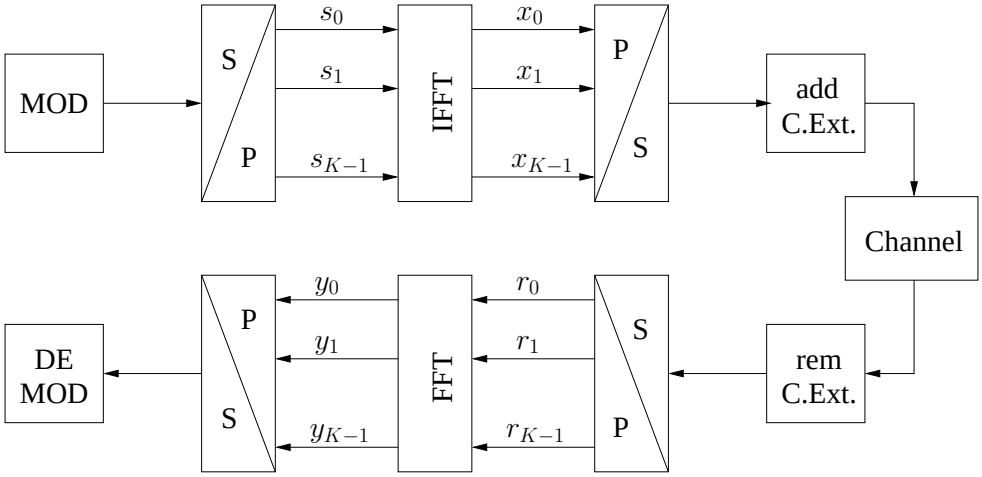

Figure 1.3: Simplified Schematic of OFDM Transmitter and Receiver by the Employment of IFFT/FFT

where

$$Q = \frac{f_s}{\triangle f} \geq 2(K-1). \tag{1.25}$$

Furthermore, by exploiting the conjugate complex symmetry of the spectrum, Eq. (1.24) can be reformulated as:

$$x(\iota T_s) = \sum_{k=0}^{Q} F_k e^{j\frac{2\pi}{Q}k\iota},\ \iota = 0...Q-1, \tag{1.26}$$

where

$$F_k = \begin{cases} F_{k-Q} = F^*_{Q-k} & \text{if } (\frac{Q}{2}+1) \leq k \leq Q-1, \\ 0 & \text{if } K-1 < k \leq \frac{Q}{2}. \end{cases} \tag{1.27}$$

Observe that Eq.(1.26) represents the standard IDFT expression that can be computed by the Inverse Fast Fourier Transform (IFFT) if Q is an integer power of 2. According to the properties of the IDFT, $x(t)$ can be represented by its T_s-spaced samples if and only if $x(t)$ is assumed to be periodic and bandlimited to $2(K-1)\triangle f$. In other words, in order to get a bandlimited frequency domain representation of $x(t)$, it has to expand from $-\infty$ to ∞ in the time domain. Therefore, the modulated signal $x(t)$ derived by IFFT has to be quasi-periodically extended at least for the duration of the channel's memory before transmission through the channel. Consequently, instead of employing a bank of K individual modulators and demodulators at transmitter and receiver respectively, as seen in Figure 1.1, the implementational complexity can be reduced by employing the IFFT/FFT, when the number of sub-carrier is high. The simplified schematic of the OFDM system implemented using the IFFT and FFT is shown in Figure 1.3, where we assume that the QAM symbols before being passed through the IFFT block represent frequency domain signals, denoted by s_0, s_1, ... , s_{N-1}, whereas the modulated signal at the output of the block IFFT denoted by x_0, x_1, ... , x_{N-1}, may be regarded as time domain signals. Similarly, the assumption applies at the receiver end, where r_0, r_1, ... , r_{N-1}, and y_0, y_1, ... , y_{N-1} represent the received time domain signals and demodulated frequency domain signals, respectively.

1.2 MIMO Techniques

The limitation of classic modulation/transmission schemes is that their capacity obeys the Shannon-Hartley law, which only increases the achievable throughput logarithmically with the transmit power. By contrast, Multiple-Input Multiple-Output (MIMO) techniques have a capacity, which is linearly dependent on $\min\{M, N\}$, i.e. on the number of transmit and receive antennas. Hence, provided that any extra power is assigned to additional antennas, their capacity is linearly dependent on the transmit power. Therefore, the most significant technical breakthrough is the emergence of multifunctional MIMOs [7]. The research of MIMO systems was inspired by the pioneering work of Foschini [8,9] and Telatar [10], who demonstrated that the capacity of MIMO systems increases linearly with $m = \min(M, N)$, where M and N are the number of antenna elements employed at the transmitter and the receiver, respectively. The basic philosophy of MIMOs is centered around *space-time* signal processing, where the natural time-dimension is complemented by the 'spatial' dimension created by the employment of multiple spatially distributed antennas [11]. Depending on the specific configuration of the MIMO elements, MIMO techniques may be classified into the following categories [3, 11]:

- Beamforming [12, 13]: When each element of the antenna array is spaced by half of the wave-length, an angularly selective radiation pattern of the antenna array can be created by constructively superimposing the appropriately phased signals in the direction of the desired MSs and creating a null in the direction of the interfering MSs. Beamforming will perform better in LOS environments than in those scenarios, where the multipath components are angularly dispersed.

- Spatial Division Multiplexing/Spatial Division Multiple Access (SDM/SDMA) [3, 14–16]: The user-specific or antenna-specific Channel Impulse Responses (CIRs) are used to differentiate a number of parallel streams. The separability of the MIMO streams relies on having sufficiently different CIRs, which may be ensured in the presence of rich multipath propagation conditions and that of well-separated antennas (at least ten times the wave-length).

- Space-Time Coding (STC) [17–20]: In contrast to spatial-multiplexing-oriented MIMOs, e.g. SDM/SDMA, the STC schemes may be regarded as spatial-diversity-oriented MIMO techniques aiming for mitigating the effects of multipath propagation, by transmitting multiple copies of the data from multiple antennas, in order to improve the reliability of the wireless link.

Hence, the benefits of MIMO systems can be exploited either to enhance the robustness of the system by achieving a diversity gain or to increase the data rate with the aid of attaining a multiplexing gain. The various trade-offs between multiplexing and diversity have been investigated, for example, in [7, 21, 22].

1.3 Combination of MIMO and OFDM Techniques [23, 24]

Based on our brief review of OFDM and MIMO techniques in Sections 1.1 and 1.2, respectively, we may argue that multiple-antenna-assisted MIMO-OFDM has become one of the most promising

candidates when addressing the two major challenges faced by the next-generation communication systems, namely the limited availability of spectral resources and the impairments induced by the wideband propagation channel. In this section, the MIMO-OFDM transmission model is reviewed, which will be used as our fundamental system model employed throughout this treatise.

For the sake of simplicity, a baseband MIMO-OFDM transmission scheme using M co-located or distributed transmit antennas and N receive antennas for communicating over a frequency-selective wideband channel is considered. The continuous-time CIR of the spatial subchannel between the mth transmit antenna and the nth receive antenna can be expressed as [2, 25]:

$$g_{nm}(\tau,t) = \sum_{l=1}^{L_g} g_{nm}^{(l)}(t)\gamma(\tau-\tau_l),\ 1 \le m \le M,\ 1 \le n \le N, \tag{1.28}$$

where the L_g resolvable multipath components are described by their complex coefficients $g_{nm}^{(l)}(t)$ and excess delays τ_l, $1 \le l \le L_g$. Speficially, τ_{L_g} denotes the *maximum delay spread* of the channel. Moreover, the signalling pulse $\gamma(t)$ describes the pulse shaping action of the transmitter as well as of the matched filter at the receiver. Under the assumption that the coefficients $g_{nm}^{(l)}(t)$ remain constant within an OFDM symbol duration of $T = 1/\triangle f$ as defined in Eq. (1.15) and the guard interval T_g introduced by the Cyclic Prefix (CP) to avoid ISI among the consecutive OFDM symbols, the low-pass equivalent discrete time-domain CIR of Eq. (1.28) can be simplified for a single OFDM symbol's transmission by omitting the time index t, yielding:

$$g_{nm}[\iota] = \sum_{l=1}^{L_g} g_{nm}^{(l)}\gamma(\iota T_s-\tau_l),\ 1 \le m \le M,\ 1 \le n \le N, \tag{1.29}$$

where T_s was defined in Eq. (1.22) as the sampling interval. Let us stipulate two additional standard assumptions in order to guarantee that the freqeuncy-selective fading channel is indeed decoupled into a set of parallel frequency-flat fading channels [26]: 1) The frequency-domain representation of the signalling pulse $\gamma(t)$ is flat in the frequency range of interest, namely, we have $|\mathcal{F}\{\gamma(t)\}|$=constant. 2) The length of the inserted CP is higher than that of the discrete-time baseband CIR, so that we can avoid the ISI between the OFDM symbols, namely, we have $T_g > \tau_{L_g}$.

On the other hand, the low-pass equivalent discrete time-domain OFDM symbols transmitted from the mth antenna corresponding to its passband counterpart of Eq. (1.26) can be written as:

$$x_m[\iota] = \sum_{k=0}^{K-1} s_{m,k} e^{j2\pi k \triangle f \iota T_s},\ \iota = 1, 2, \cdots, K. \tag{1.30}$$

Hence, the signal launched from the mth transmit antenna and recovered at the nth receive antenna, namely r_{nm}, can be computed as the time-domain convolution of the transmitted signal of Eq. (1.30) and the CIR of Eq. (1.29), yielding:

$$r_{nm}[\iota] = [x_m * g_{nm}](\iota) \tag{1.31}$$

$$= \sum_{i=0}^{T_f/T_s-1} x_m[i] \cdot g_m[\iota - i]. \tag{1.32}$$

Then the CP of length T_g is discarded, which is chosen to be long enough to ensure that all significant CIR components which would cause distortion die down during T_g. Hence, the receiver

views the convolutions with the linear channel's CIR as cyclic, provided that accurate symbol synchronization is guaranteed. Consequently, this time domain convolution is equivalent to the corresponding frequency domain scalar multiplication [3,23,24], leading to the following representation of the received signal in the frequency domain:

$$\mathrm{FFT}\{r_{nm}\} = \mathrm{FFT}\{x_m\} \cdot \mathrm{FFT}\{g_{nm}\}. \tag{1.33}$$

More specifically, since the K subcarriers are mutually orthogonal, the frequency-domain representation of the signal received by the nth antenna can be written on a per-subcarrier basis as:

$$y_{n,k} = \sum_{m=1}^{M} s_{m,k} h_{nm,k}, \quad (k = 0, 1, \cdots, K-1), \tag{1.34}$$

where we have:

$$h_{nm,k} = \sum_{l=1}^{L_g} g_{nm}^{(l)} \mathrm{e}^{-j2\pi k \triangle f \tau_l}. \tag{1.35}$$

In other words, the MIMO-aided signal processing can be carried out independently for each of the K subcarriers. Consequently, the subcarrier index k may be omitted without any ambiguity, and the MIMO model derived for each subcarrier can be expressed as:

$$\mathbf{y} = \mathbf{H}\mathbf{s} + \mathbf{w}, \tag{1.36}$$

where the received signal column vector $\mathbf{y}$, the transmitted signal column vector $\mathbf{s}$ and the noise column vector $\mathbf{w}$ can be written, respectively, as:

$$\mathbf{y} = [y_1\ y_2\ \cdots\ y_N]^T, \tag{1.37}$$

$$\mathbf{s} = [s_1\ s_2\ \cdots\ s_M]^T, \tag{1.38}$$

and

$$\mathbf{w} = [w_1\ w_2\ \cdots\ w_N]^T. \tag{1.39}$$

The corresponding Frequency-Domain Channel Transfer Factor (FDCTF) matrix $\mathbf{H}$ of each subcarrier may be expressed as:

$$\mathbf{H} = \begin{bmatrix} h_{11} & h_{12} & \cdots & h_{1M} \\ h_{21} & h_{22} & \cdots & h_{2M} \\ \vdots & \vdots & \ddots & \vdots \\ h_{N1} & h_{N2} & \cdots & h_{NM} \end{bmatrix}. \tag{1.40}$$

1.4 Low-Complexity Near-Optimum Detection Techniques

As discussed in Section 1.3, since the wideband channel can be decoupled into a set of parallel narrow-band subchannels with the aid of the OFDM technique, the MIMO-aided signal processing can be carried out on a per-subcarrier basis. In other words, the conventional MIMO detection schemes may be directly employed by the MIMO-OFDM system after the IFFT/FFT-based processing, which transforms the received time-domain signal of Eq. (1.32) into the frequency-domain

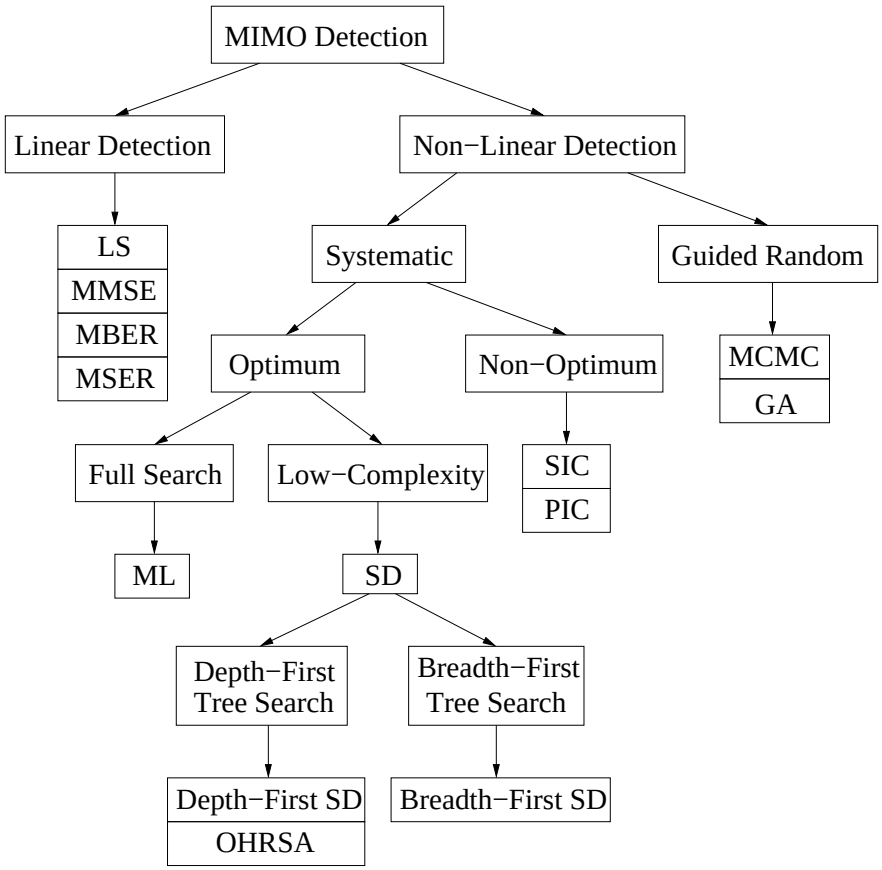

Figure 1.4: The classification of narrow-band MIMO detection techniques.

signal of Eq. (1.34). The classification of narrow-band MIMO detection techniques is portrayed in Figure 1.4. First of all, we distinguish between linear and non-linear detection schemes. In general, the achievable performance of the latter family is superior to that of the former class, which is achieved at the cost of a potentially higher complexity. The most well-known linear MIMO detectors are the Least Square (LS) detector as well as the Minimum Mean Squared Error (MMSE) detector, which are discoursed in a number of text books, such as [3, 6]. The MMSE detector is optimum in terms of minimizing the Mean Squared Error (MSE) of a linear detector by taking the effect of the noise into account. By contrast, the LS detection approach directly multiplies the inverse of the CIR matrix in Eq. (1.40) by the received signal in order to obtain the estimate of the transmitted signal, which might potentially enhance the noise component of Eq. (1.39), thus resulting in a relatively modest performance in comparison to its MMSE counterpart. A Soft-Input Soft-Output (SISO) MMSE detector has also been designed in [27], which can be employed by channel-coded iterative detection assisted systems. In contrast to the minimization of MSE in the MMSE detector, novel linear detectors were also designed to directly minimize the Bit Error Rate (BER) in [28–32]. The corresponding linear detectors were referred to as Minimum BER (MBER) detectors, since they are optimum in terms of minimizing the BER. Since it is challenging to design MBER detectors for higher-order QAM, Minimum Symbol Error Rate (MSER) detectors designed for higher-order QAM have been proposed in [33], which were further developed in [34].

The performance achieved by the family of linear detector is typically regarded as satisfactory in a MIMO system, where the number of transmit antennas is no higher than that of the receive

antennas. However, their performance is often unacceptable, when the former exceeds the latter, rendering the overall MIMO system rank-deficient. In rank-deficient scenarios, the family of non-linear detectors has to be employed. As shown in Figure 1.4, the set of non-linear detectors may be further divided into two categories, depending on the search strategies employed, namely, whether a systematic or a guided random search strategy is utilized. In the former class, a set of detectors, which is capable of achieving an enhanced performance while exhibiting a relatively low computational complexity is constitued by the family of interference cancellation based algorithms [35]. The well-known Vertical Bell LAbs Layered Space Time (V-BLAST) scheme, operating based on Serial Interference Cancellation (SIC), was introduced by Foschini [8]. Recently, a more powerful SISO V-BLAST algorithm has been proposed by Lee *et al.* [36] as well as by Kim and Kim [37] in order to significantly benefit from the channel-coded iterative detection mechanism employed. In contrast to SIC, Parallel Interference Cancellation (PIC) has been investigated in [3, 38–40]. Although the complexity imposed by the interference cancellation based detection may remain affordable, the achievable performance is still sub-optimum, which is expected to degrade owing to error propagation.

[41] Demen *et. al.* 1999	The first paper to extend the original SD to a GSD, which is capable of operating in rank-deficient systems.
[42] Yang *et. al.* 2005	An improved generalized hard-output SD is introduced, which is designed for rank-deficient MIMO systems. The high-complexity detection process is divided into two detection stages, which significantly reduced the complexity.
[43] Cui and Tellambura 2005	For constant modulus constellations, the ML cost metric of the rank-deficient system using N transmit antennas and M receive antennas ($N > M$) is modified so that the equivalent Grammian becomes equal to N. The resultant GSD algorithm has significantly lower complexity than previous algorithms.
[44] Akhtman *et. al.* 2007	Based on the modified Grammian matrix of [43], an optimized hierachical search structure is introduced to the GSD in order to further reduce its complexity.

Table 1.1: Major contributions addressing the design of generalized sphere detection.

The classic non-linear Maximum-Likelihood (ML) detector [45] finds the ML solution by examining all the legitimate MIMO symbol candidates, which is regarded to be optimum in terms of the achievable performance. However, the full-search-based ML detector may impose an excessive computational complexity, especially in high-throughput systems either invoking high-order modulation schemes or employing a large number of transmit antennas, potentially preventing its application in practical scenarios. Fortunately, inspired by the Sphere Detection (SD) algorithm introduced by Porst and Finke [46], Vitelko and Boutros have applied the original SD algorithm to communication systems in [47] in order to approach the ML performance at a complexity, which avoids the exponentially increasing complexity of the ML search as a function of the number of unknowns. Hence the design of SDs opened up a whole new research area. At the early stages, Brunel and Boutros [48] as well as Hassibi and Vikalo [49] considered systems, where the number of transmit antennas was no higher than that of the receive antennas. Thus, in order to render the SD applicable to rank-deficient systems, where the number of the transmit antennas exceeds that of the receive antennas, researchers embarked on contriving so-called Generalized Sphere Detection (GSD) schemes [41, 42, 44, 50]. Table 1.1 summarizes the major contributions addressing the GSD along with their short description. Furthermore, for the sake of approaching the channel capacity at a low complexity, the SISO SD algorithm was extended by Hochwald and ten Brink in [51], where a list of the best hypothesized transmitted MIMO symbol candidates was generated

and used as the most likely representatives of the entire lattice, when computing the soft bit information. This SD family was termed as the class of List Sphere Decoders (LSD). However, in order to achieve a good performance, the list size has to remain sufficiently large, since the above-mentioned LSD does not take into account the effect of the *a priori* soft bit information during the candidate list generation process. Hence, for the sake of reducing the complexity imposed by the original LSD, Vikalo *et al.* [52] devised an enhanced LSD, which takes the *a priori* soft bit information delivered by the channel decoder into account during the candidate list generation process. Furthermore, a SD has been proposed by Pauli *et al.* in [53, 54], which is capable of detecting Differential Phase Shift Keying (DPSK) modulated sigals. Table 1.2 provides the major contributions addressing the design of the differential SD.

[53] Lampe *et. al.* 2005	The first paper to introduce the SD algorithm to mitigate the complexity of ML multiple-symbol differential detection (ML-MSDD) of [55, 56].
[57] Pauli and Lampe 2005	The first contribution to extend the MSDSD to detect the differential space-time modulation.
[54] Pauli *et. al.* 2006	A soft-decision-aided MSDSD is devised, which can be employed in iterative detection assisted receivers.
[58] Pauli and Lampe 2007	Complexity of the MSDSD is intensively investigated in the paper.
[25] Pauli *et. al.* 2008	2-D observation window technique is contrived for the MSDSD employed in the MIMO-OFDM system using differential space-frequency modulation.

Table 1.2: Major contributions addressing the design of differential sphere detection.

As observed in Figure 1.4, the SD technique can be further divided into two sub-groups, depending on the specifics of the tree search employed, namely, whether the depth-first tree search or the breadth-first tree search is used, which will be contrasted in Chapter 2. Note that all the previously mentioned SD algorithms carry out a depth-first tree search. Similarly, the recently conceived Optimized-Hierarchy-Reduced-Search-Algorithm (OHRSA) [44, 59] also belongs to the depth-first category. The breadth-first SD is also referred to as the K-best SD [60, 61], which has a convenient implementation and an SNR-independent computational complexity.

In contrast to the above-mentioned family of systematic detection based techniques, the other category of non-linear detection schemes relies on guided random strategies, as seen in Figure 1.4. Members of this detector family are for example Markov Chain Monte Carlo (MCMC) detection [72–74] as well as the class of Genetic Algorithm (GA) [75] aided schemes. MCMC techniques have been shown to exhibit a low complexity, especially in the low-SNR region. In Table 1.3 we have provided a number of relevant references for MIMO detection, including their description.

1.5 Novel Contributions and Outline

1.5.1 Novel Contributions

Part I: Non-Cooperative MIMO-OFDM Scenario: In the previous sections we highlighted the benefits of combining the OFDM and MIMO techniques. Based on the above-mentioned background, high-efficiency MIMO-OFDM systems have been designed, with an emphasis on the development of advanced yet low-complexity near-capacity detection techniques. Specifically, we designed new SDs for low-complexity near-ML detection for high-throughput bandwidth-efficient

[62] Thoen *et. al.* 2003	A LS MIMO detector is introduced and its performance is investigated when applied in a SDMA OFDM system.
[27] Wang and Poor 1999	In this paper conventional MMSE detection is extended to SISO MMSE detection, which may be employed in iterative receivers.
[29] Chen *et. al.* 2005	Presents a MBER beamformer designed for BPSK and 4QAM signals as well as for static channel conditions.
[63] Gesbert 2003	The author presented a robust MBER MIMO detector, which can be constructed using a closed-form expression, provided that certain channel conditions are fulfilled.
[8] Foschini 1996	The first low complexity V-BLAST receiver designed for MIMO based systems is proposed.
[64] Lee *et. al.* 2006	The original V-BLAST technique is extended to a SISO algorithm and is employed in an OFDM system. For the scenarios considered the proposed V-BLAST detector approaches the ML performance.
[47] Viterbo and Boutros 1999	First paper, which applied the SD proposed in [46] to the detection of received signals. This contribution inspired a whole new research area.
[41] Damen *et. al.* 2000	In this paper the original SD is extended to a GSD, which is capable of operating in rank-deficient systems.
[51] Hochwald and ten Brink 2003	The authors propose a List Sphere Decoder (LSD), which is capable of processing soft information and compare the attainable performance of their LSD to the channel capacity bound, which is also derived in the paper.
[52] Vikalo *et. al.* 2004	A SISO SD is proposed, which is employed in an iterative system using different convolutional codes as well as Low-Density Parity-Check (LDPC) [65] codes.
[66] Yang *et. al.* 2005	An improved generalized hard-output SD is introduced, which is designed for rank-deficient MIMO systems. The high-complexity detection process is divided into two detection stages, which significantly reduced the complexity.
[60] Guo and Nilsson 2006	A SD algorithm based on K-best Schnorr-Euchner (KSE) decoding is proposed, which is capable of providing both hard as well as soft outputs. Furthermore, hardware based performance results are presented.
[67] Wang and Giannakis 2006	The original SD algorithm is extended to an exact Max-Log detector, which is employed in an iterative system.
[68] Santiago Mozos and Fernandez-Getino Garcia 2006	Extends the SD using real-valued signals to a SD considering complex-valued signals, which is capable of detecting arbitrary modulation constellations. The performance of the proposed SD is investigated in the context of MC-CDMA.
[69] Zhu *et. al.* 2005	In this paper MCMC aided MIMO detection is proposed and the performance is compared to that of SD algorithms. The results suggest that MCMC aided detection is capable of outperforming SD at a similar computational cost.
[70] Boroujeny *et. al.* 2006	MCMC based MIMO detection is discussed and the benefits of different methods used for generating soft-information are presented. These methods include taking the empirical average as well as using importance sampling.
[71] Aggarwal and Wang 2007	Presents a MCMC based detector optimized for MIMO systems employing higher-order QAM signals. In order to reduce the computational complexity of the proposed system, the received signal space is partitioned into subspaces, each of which is optimized independently.

Table 1.3: Selection of narrowband MIMO detection contributions.

communication systems.

Contribution 1 **[76–79]**: We designed low-complexity SDs for channel-coded high-throughput systems using high-order modulation and/or large number of transmit antennas, where the SD has to generate soft information for every transmitted bit. This requires the observation of a high number of hypotheses about the transmitted MIMO symbol, resulting in a potentially excessive complexity. To be specific, two major complexity-reduction schemes were devised for iterative detection aided channel coded systems with the aid of EXtrinsic Information Transfer (EXIT) chart analysis. More specifically, we designed a generic SD scheme termed as the *center-shifting* SD and the *apriori-LLR-threshold* (ALT) aided SD scheme. The former one substantially reduces the detection complexity by decomposing it into two stages, namely the generic iterative search-center-update phase and the reduced-complexity search around it. By contrast, the latter is capable of achieving a more flexible compromise between the performance and the complexity by expoiting the *a priori* LLRs provided by the outer channel decoder.

Contribution 2 **[80–83]**: A generalized multi-layer tree search was proposed for SD for the sake of carrying out Maximum-a-Posteriori (MAP) detection at a significantly reduced complexity in a multi-dimensional modulated system, such as for example a sphere packing (SP) scheme. Moreover, the iterative decoding convergence of the conventional two-stage system, where the channel encoder/decoder and the modulator/detector are employed at the transmitter/receiver, were improved by incorporating a Unity-Rate-Code (URC) having an infinite impulse response, which improves the efficiency of extrinsic information exchange.

Part II: Cooperative MIMO-OFDM Scenario: The above-mentioned multiple co-located antenna aided diversity techniques are capable of mitigating the deleterious effects of fading, hence improving the end-to-end system performance. However, it is often impractical for the mobile to employ a large number of antennas for the sake of achieving a diversity gain due to its limited size. Furthermore, owing to the limited separation of the antenna elements, they rarely experience independent fading, which limits the achievable diversity gain and may be further compromised by the detrimental effects of the shadow fading, imposing further signal correlation amongst the antennas in each other's vicinity. Fortunately, in multi-user wireless systems cooperating mobiles may share their antennas in order to achieve uplink transmit diversity by formig a Virtual Antenna Array (VAA) in a distributed fashion. Thus, so-called cooperative diversity relying on the cooperation among multiple terminals may be achieved. On the other hand, the employment of coherent detection becomes less practical in such scenarios, since the required channel estimation may impose both an excessive complexity and a high pilot overhead, especially in mobile environments associated with relatively rapidly fluctuating channel conditions. Therefore, in the second part of our work, we investigate the distributed MIMO or user-cooperation aided OFDM system, where differentially encoded transmission was employed combined with non-coherent detection schemes, which requires no channel state information (CSI) at the receiver.

Contribution 3 **[84, 85]**: The classic Maximum-Likelihood Multiple-Symbol Differential Detection (ML-MSDD) technique is capable of eliminating some of the power-loss experienced by low-complexity non-coherent transmissions, when compared to their high-complexity coherent-detection-aided counterparts. We further developed this technique for user-cooperative communication and invoked a low-complexity SD algorithm for the sake of making the system robust to

time-selective environments at an affordable complexity, leading to multiple-symbol based differential sphere detection (MSDSD) assisted user-cooperative communication.

Contribution 4 **[86, 87]**: Since the transmit power allocaton and the cooperating user selection play a vital role in achieving the best possible performance, we proposed novel Cooperating-User-Selection (CUS) schemes and Adaptive Power Control (APC) schemes for both Differental-Amplify-and-Forward (DAF) and Differential-Decode-and-Forward (DDF) aided cooperative systems. It was demonstrated that they are capable of significantly improving the achievable performance as well as reducing the detection complexity at the destination BS. Furthermore, in order to exploit the complementarity of the above-mentioned two types of cooperative systems, we proposed a more flexible resource-optimized adaptive hybrid cooperation-aided system, yielding a further improved performance.

Contribution 5 **[88]**: It is widely recognized that DDF-aided cooperative transmission schemes are capable of providing a superior performance compared to classic direct transmissions employing differential detection, where no channel coding is used. However, the cooperative diversity gains promised by the cooperative system are actually achieved at the cost of suffering a significant so-called multiplexing loss compared to direct transmissions, which is imposed by the half-duplex communications of practical transceivers. Moreover, the cooperative diversity gains achieved become modest in practical channel coded scenarios, where the interleaving and channel coding gains tend to dominate. Therefore, when a cooperative wireless communication system is designed to approach the maximum achievable spectral efficiency by taking the cooperation-induced multiplexing loss into account, it is not obvious, whether or not the relay-aided system becomes superior to its direct-transmission based counterpart, especially, when advanced channel coding techniques are employed. Hence in this thesis the capacity of the single-relay-assisted DDF based cooperative system was studied in comparison to that of its direct-transmission based counterpart in order to resolve the above-mentioned dilemma.

Contribution 6 **[89]**: Based on the above-mentioned capacity evaluation of the DDF-aided cooperative system, we proposed a practical framework of designing a cooperative system, which is capable of performing close to the corresponding network's non-coherent Discrete-input Continuous-output Memoryless Channel (DCMC) capacity. Using our low-complexity near-capacity design criterion, a novel Irregular Distributed Hybrid Concatenated Differential (Ir-DHCD) coding scheme is proposed for the DDF-aided cooperative system employing our capacity-achieving low-complexity adaptive-window-aided SISO iterative MSDSD scheme.

1.5.2 Outline

In this section we provide an overview of the remainder of this thesis.

- **Chapter 2:** The main objective of this chapter is to systematically review the fundamentals of the SD, which is considered to be one of the most promising low-complexity near-optimum detection techniques at the time of writing. Furthermore, we address the SD-related complexity reduction issues. Specifically, the principle of the Hard-Input Hard-Output (HIHO) SD is reviewed first in the context of both the depth-first and breadth-first tree search based sce-

narios, along with that of the GSD, which is applicable to challenging rank-deficient MIMO scenarios. A comprehensive comparative study of the complexity reduction schemes devised for different types of SDs, namely, the conventional depth-first SD, the *K*-best SD and the novel OHRSA detector, is carried out by analyzing their conceptual similarities and differences. Finally, their achievable performance and the complexity imposed by the various types of SDs are investigated in comparison to each other.

- **Chapter 3:** The fundamentals of the LSD scheme are studied at the beginning of this chapter in the context of an iterative detection aided channel coded MIMO-OFDM system. A potentially excessive complexity may be imposed by the conventional LSD, since it has to generate soft information for every transmitted bit, which requires the observation of a high number of hypotheses about the transmitted MIMO symbol. Based on the above-mentioned complexity issue, we contrive a generic center-shifting SD scheme and the so-called *apriori*-LLR-threshold assisted SD scheme with the aid of EXIT chart analysis, both of which are capable of effectively reducing the potentially high complexity imposed by the SD-aided iterative receiver. Moreover, we combine the above-mentioned schemes in the interest of further reducing the complexity imposed. In addition, for the sake of enhancing the achievable iterative detetion gains and hence improving the bandwidth efficiency, a Unity-Rate Code (URC) assisted three-stage serially concatenated transceiver employing the so-called Irregular Convolutional Codes (IrCCs) is devised. Finally, the benefits of the proposed center-shifting SD scheme are also investigated in the context of the above-mentioned three-stage iterative receiver.

- **Chapter 4:** In this chapter we extend the employment of the turbo-detected Sphere Packing (SP) aided Space-Time Block Coding (STBC) scheme to Multi-User MIMO (MU-MIMO) scenarios, because SP was demonstrated to be capable of providing useful performance improvements over conventionally-modulated orthogonal design based STBC schemes in the context of Single-User MIMO (SU-MIMO) systems. For the sake of achieving a near-MAP performance, while imposing a moderate complexity, we specifically design the *K*-best SD scheme for supporting the operation of the SP-modulated system, since the conventional SD cannot be directly applied to such a system. Consequently, when relying on our SD, a significant performance gain can be achieved by the SP-modulated system over its conventionally-modulated counterpart in the context of MU-MIMO systems.

- **Chapter 5:** The principle of the MSDSD is first reviewed, which has been recently proposed for mitigating the time-selective-channel-induced performance loss suffered by classic direct transmission schemes employing the Conventional Differential Detection (CDD) scheme. Then, we specifically design the MSDSD for both the Differential Amplify-and-Forward (DAF) and Differential Decode-and-Forward (DDF) assisted cooperative systems based on the multi-dimensional tree search proposed in Chapter 4, which is capable of achieving a significant performance gain for transmission over time-selective channels induced by the relative mobility amongst the cooperating transceivers.

- **Chapter 6:** In this chapter the theoretical BER performance of both the DAF- and DDF-aided cooperative cellular uplinks are investigated. Then, based on the minimum BER criterion, we design efficient Cooperating-User-Selection (CUS) and Adaptive-Power-Control (APC)

schemes for the above-mentioned two types of differentially modulated cooperative systems, while requiring no Channel State Information (CSI) at the receiver. Moreover, we investigate the Cooperative-Protocol-Selection (CPS) of the uplink system in conjunction with a beneficial CUS as well as the APA scheme in order to further improve the achievable end-to-end performance, leading to a resource-optimized hybrid cooperative system. Hence, a number of cooperating MSs may be adaptively selected from the available MS candidate pool and the cooperative protocol employed by a specific cooperating MS may also be adaptively selected in the interest of achieving the best possible BER performance.

- **Chapter 7:** The DDF-aided cooperative system's DCMC capacity is investigated in comparison to that of its classic direct-transmission based counterpart in order to answer the grave fundamental question, whether it is worth introducing cooperative mechanisms into the development of wireless networks, such as the cellular voice and data networks. Then, we propose a practical framework of designing a cooperative system, which is capable of performing close to the network's corresponding non-coherent DCMC capacity. Based on our low-complexity near-capacity design criterion, a novel Irregular Distributed Hybrid Concatenated Differential (Ir-DHCD) coding scheme is contrived for the DDF cooperative system employing our proposed capacity-achieving low-complexity adaptive-window-aided SISO iterative MSDSD scheme.

- **Chapter 8:** The main findings are summarized and suggestions for future research are presented.

Chapter 2

Reduced-Complexity Sphere Detection for Uncoded MIMO-OFDM Systems

2.1 Introduction

2.1.1 System Model

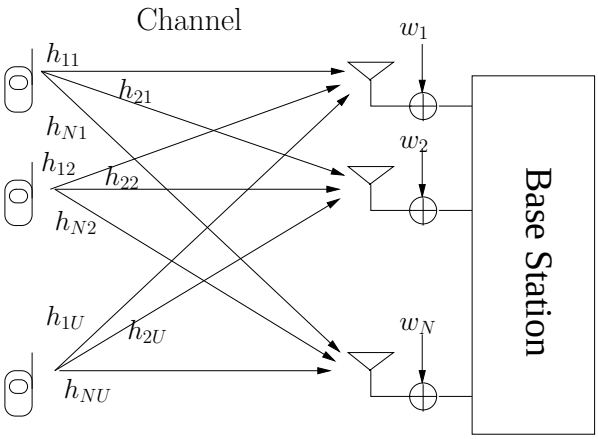

Figure 2.1: Schematic of an SDMA uplink MIMO channel scenario.

In Figure 2.1 a SDMA/OFDM Uplink (UL) transmission scenario is portrayed, where each of the U users is equipped with a single transmit antenna, while the BS has N receive antenna elements. Based on our discourse on MIMO-OFDM in Section 1.3, for each subcarrier the link between each pair of transmit and receiver antennas may be characterized with the aid of a unique user-specific FDCTF, which was described by Eq. (1.35) and is denoted as h_{nu} in Figure 2.1. The subscripts of h, i.e. u and n, represent the user and receive antenna element index at the BS, respectively. For example, the FDCTF or the spatial signature of the uth user can be expressed as a column vector:

$$\mathbf{h}_u = [h_{1u}, h_{2u}, ..., h_{Nu}]^T, \tag{2.1}$$

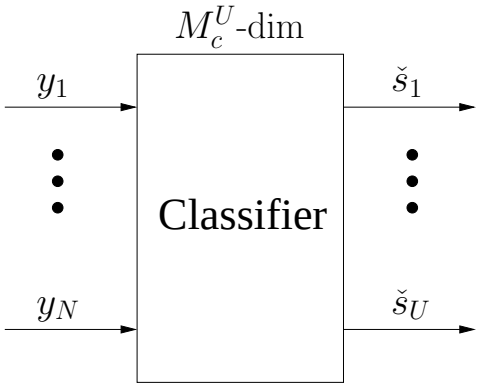

Figure 2.2: Representation of the optimum ML detector

with $u \in 1, ..., U$. If the transmitted signal of the uth user is denoted by s_u and the received signal plus the Additive White Gaussian Noise (AWGN) at the nth receive antenna element is represented by y_n and w_n, respectively, the entire SDMA/OFDM system can be described on a per-subcarrier-basis by a matrix equation written as:

$$\mathbf{y} = \mathbf{H}\mathbf{s} + \mathbf{w}, \tag{2.2}$$

where the received signal's column vector is $\mathbf{y} \in \mathbb{C}^{N\times 1}$, the transmitted signal's column vector is $\mathbf{s} \in \mathbb{C}^{U\times 1}$, and the noise's column vector is $\mathbf{w} \in \mathbb{C}^{N\times 1}$, which are given by the following equations, respectively:

$$\mathbf{y} = [y_1, y_2, ..., y_N]^T, \tag{2.3}$$

$$\mathbf{s} = [s_1, s_2, ..., s_U]^T, \tag{2.4}$$

$$\mathbf{w} = [w_1, w_2, ..., w_N]^T. \tag{2.5}$$

The FDCTF matrix $\mathbf{H} \in \mathbb{C}^{N\times U}$ is constituted by the U number of user-specific CTF vectors defined by Eq. (2.1), with $\mathbf{h}_u \in \mathbb{C}^{N\times 1}$, where $u = 1, 2, ..., U$. Explicitly, the FDCTF matrix $\mathbf{H}$ can be expressed as:

$$\mathbf{H} = [\mathbf{h}_1\ \mathbf{h}_2\ ...\ \mathbf{h}_U], \tag{2.6}$$

where each column represents a user's unique spatial signature. Here, we assume that the FDCTF H_{nu} between user $u \in 1, 2, ..., U$ and receive antenna element $n \in 1, 2, ..., N$ are independent, stationary, complex-valued Gaussian distributed processes with a zero-mean and a unit variance [3]. Furthermore, both the transmitted signal of each of the U users and the AWGN noise encountered at each of the N antenna elements exhibit a zero-mean and a variance of $2\sigma_s^2$ and $2\sigma_w^2$, respectively.

2.1.2 Maximum Likelihood Detection

The Maximum-Likelihood (ML) detector jointly detects the U different users' complex symbols that are most likely to have been transmitted. The stylized schematic of the ML detector is shown in Figure 2.2, where M_c is the constellation size of a specific modulation scheme. Observe that the received signal's column vector $\mathbf{y}$ of Eq. (2.2) possesses an U-dimensional multi-variate complex

Gaussian distribution, with a vector of mean values of $\mathbf{Hs}$ and a covariance matrix given by $\mathbf{R_w} \in \mathbb{C}^{N\times N}$. The latter is given by:

$$\mathbf{R_n} = E\{\mathbf{ww}^H\} \tag{2.7}$$
$$= 2\sigma_w^2\mathbf{I}, \tag{2.8}$$

under the assumption that the noise contribution added at each receive antenna element are uncorrelated. Consequently, the *a priori* probability function of the received signal vector $\mathbf{y}$ is equivalent to the complex Gaussian distribution function, which can be written as [3]:

$$P(\mathbf{y}|\mathbf{s},\mathbf{H}) = f(\mathbf{y}|\mathbf{s},\mathbf{H}) = \frac{1}{\pi^N|\mathbf{R_w}|}exp(-(\mathbf{y}-\mathbf{Hs})^H\mathbf{R_w}^{-1}(\mathbf{y}-\mathbf{Hs})) \tag{2.9}$$
$$= \frac{1}{(2\sigma_w^2\pi)^N}exp(-\frac{1}{2\sigma_w^2}||\mathbf{y}-\mathbf{Hs}||^2). \tag{2.10}$$

On the other hand, the basic idea behind the ML detector is to maximize the *a posteriori* probability $P(\check{\mathbf{s}}|\mathbf{y},\mathbf{H})$, where the candidate vector $\check{\mathbf{s}} \in \mathbb{C}^{U\times 1}$ is an element of the set M_c^U of trial vectors, which was transmitted over the channel characterised by the channel matrix $\mathbf{H} \in \mathbb{C}^{N\times U}$, and under the condition that the received signal vector is $\mathbf{y}$. Importantly, the relationship between the *a posteriori* probability and the *a priori* probability can be formulated with the aid of Bayes' theorem [3] as follows:

$$P(\check{\mathbf{s}}|\mathbf{y},\mathbf{H}) = P(\mathbf{y}|\check{\mathbf{s}},\mathbf{H})\frac{P(\check{\mathbf{s}})}{P(\mathbf{y})}, \tag{2.11}$$

where $P(\check{\mathbf{s}}) = \frac{1}{M_c^U}$ is a constant, since it is assumed that all symbol vector probabilities are identical. Furthermore, since all probabilities have to sum to unity, we have:

$$\sum_{\check{\mathbf{s}}\in M_c^U} P(\check{\mathbf{s}}|\mathbf{y},\mathbf{H}) = 1. \tag{2.12}$$

Additionally, the total probability $P(\mathbf{y})$ can be expressed by:

$$P(\mathbf{y}) = \sum_{\hat{\mathbf{s}}\in M_c^U} P(\mathbf{y}|\check{\mathbf{s}},\mathbf{H})P(\check{\mathbf{s}}), \tag{2.13}$$

which is also a constant. Consequently, we have:

$$\frac{P(\check{\mathbf{s}})}{P(\mathbf{y})} = const., \tag{2.14}$$

which leads to the conclusion that for the ML detector, the problem of finding the optimum solution $\hat{\mathbf{s}}_{\mathbf{ML}}$, which maximizes the *a posteriori* probability of $P(\check{\mathbf{s}}|\mathbf{y},\mathbf{H})$ is equivalent to maximizing the *a priori* probability of $P(\mathbf{y}|\check{\mathbf{s}},\mathbf{H})$. Hence, according to Eq.(2.10), the problem is also equivalent to minimizing the Euclidean distance metric $||\mathbf{y}-\mathbf{H}\check{\mathbf{s}}||^2$, i.e. we have:

$$\hat{\mathbf{s}}_{ML} = arg\min_{\check{\mathbf{s}}\in M_c^U} ||\mathbf{y}-\mathbf{H}\check{\mathbf{s}}||^2. \tag{2.15}$$

The ML detector is capable of achieving the optimum BER performance by jointly detecting all the U different users' symbols at the cost of a potentially excessive computational complexity, which depends on the size of the modulation constellation and/or the number of users supported by the system, since the ML detector evaluates the Euclidean distance metric of Eq. (2.15) for all the possible transmitted symbol vectors. For example, if a SDMA/OFDM system employs 16-QAM and supports $U = 8$ users, a full-search of 2^{32} possibilities will be encountered in order to find the optimum solution, imposing an excessive computational complexity.

2.1.3 Chapter Contributions and Outline

The motivation of finding a low complexity solution while achieving a near-ML performance has driven researchers to develop new algorithms. Recently, inspired by the Sphere Detection (SD) algorithm originally introduced by Porst and Finke [46] to efficiently calculate a vector of short length in a lattice, Vitelko and Boutros have applied the original SD algorithm in communication systems [47] in order to approach the ML performance at a complexity, which is polynomially, rather than exponentially dependent on the number of unknowns, which opened up a whole new research area. Different types of SDs and complexity reduction schemes have been proposed, for example in [90–93] for the depth-first SD. By contrast, the schemes proposed in [60,61,94,95] were designed for the breadth-first SD. As a benefit of the superior performance of the SD algorithm, it will serve as a key mechanism to reduce the complexity of diverse MIMO-OFDM scenarios throughout this treatise. Hence, for the sake of further developing the SD algorithm and applying it to various problems, a comprehensive understanding of the SD's operating principle is a vital prerequisite. Thus, the main objective of this chapter is to review the fundamentals of both the depth-first as well as of the breadth-first tree search based SDs and to carry out in-depth comparative studies in terms of their corresponding complexity reduction schemes as well as their achievable performance. More specifically, the main contributions of this chapter are as follows:

- *Compare and analyze the most influential complexity reduction schemes proposed in the literature for the conventional depth-first SD, the breadth-first SD as well as for the recently proposed OHRSA detector, which may be regarded as an advanced extension of the depth-first SD.*
- *Extend the performance versus complexity studies of the above-mentioned SD algorithms to challenging rank-deficient MIMO scenarios.*

The outline of this chapter is as follows. In Section 2.2 the SD fundamentals are reviewed, followed by a discourse on GSDs, which are capable of operating in rank-deficient MIMO systems. The most influential complexity reduction schemes proposed for the depth-first and breadth-first SDs are discussed in Sections 2.3.1 and 2.3.2, respectively. Then, Section 2.3.3 introduces the recently proposed OHRSA detector and analyzes both its hierarchical search structure as well as its optimization strategies in comparison to the complexity-reduction schemes of its conventional SD counterparts. The achievable BER performance versus complexity imposed by the above-mentioned SDs is characterized in Section 2.4 for both full-rank and rank-deficient MIMO systems. Finally, our concluding remarks are provided in Section 2.5.

2.2 Principle of Sphere Detection

2.2.1 Transformation of the Maximum-Likelihood Metric

As discoursed in Section 2.1.2, the ML solution for a SDMA system of Eq. 2.2 can be written as:

$$\hat{\mathbf{s}}_{ML} = arg \min_{\check{\mathbf{s}} \in \mathcal{M}_c^U} ||\mathbf{y} - \mathbf{H}\check{\mathbf{s}}||^2, \tag{2.16}$$

where $\mathcal{M}_c$ is the set of M_c legitimate symbol points in the modulation constellation and U is the number of users supported by the system. Thus, a potentially excessive-complexity search is likely to be encountered, depending on the value of M_c and/or U, which prevents the application of the full-search-based ML detectors in most practical high-throughput scenarios. Fortunately, Eq. (2.16) can be extended as [51]:

$$\hat{\mathbf{s}}_{ML} = arg \min_{\check{\mathbf{s}} \in \mathcal{M}_c^U} \left\{ (\check{\mathbf{s}} - \hat{\mathbf{c}})^H \mathbf{H}^H \mathbf{H} (\check{\mathbf{s}} - \hat{\mathbf{c}}) + \underbrace{\mathbf{y}^H (\mathbf{I} - \mathbf{H}(\mathbf{H}^H \mathbf{H})^{-1} \mathbf{H}^H) \mathbf{y}}_{\varphi} \right\}, \tag{2.17}$$

where

$$\hat{\mathbf{c}} = (\mathbf{H}^H \mathbf{H})^{-1} \mathbf{H}^H \mathbf{y} \tag{2.18}$$

which is the unconstrained ML estimate of $\mathbf{s}$ or the LS solution of Eq.(2.2). Importantly, the value of φ in Eq. (2.17) is independent of the argument $\check{\mathbf{s}}$, when minimizing the Objective Function (OF) of Eq. (2.16). Hence, the trial candiate $\check{\mathbf{s}}$ minizing $||\mathbf{y} - \mathbf{H}\check{\mathbf{s}}||^2$ also minimizes $(\check{\mathbf{s}} - \hat{\mathbf{c}})^H \mathbf{H}^H \mathbf{H} (\check{\mathbf{s}} - \hat{\mathbf{c}})$, Thus, we have:

$$\hat{\mathbf{s}}_{ML} = arg \min_{\check{\mathbf{s}} \in \mathcal{M}_c^U} (\check{\mathbf{s}} - \hat{\mathbf{c}})^H \mathbf{H}^H \mathbf{H} (\check{\mathbf{s}} - \hat{\mathbf{c}}). \tag{2.19}$$

In fact, the well-known Sphere Detection (SD) algorithm was derived from the mathematical problem of finding the shortest vector in a lattice, which was originally described in [96] and refined in [46]. Even when exploiting the above-mentioned simplifications, finding the ML solution $\hat{\mathbf{s}}$ still has to be carried out on an exhaustive search basis for the entire M_c^U number of legitimate transmitted signal vector combinations.

Therefore, in the following sections, two different types of SD algorithms will be introduced and compared, which are capable of significantly reducing the associated search complexity, namely the original SD algorithm of [47] which is also referred to as a *Depth-First SD* and the *K-Best SD* of [61], which can be regarded as a *Breadth-First SD*.

2.2.2 Depth-First Tree Search [47]

For the depth-first SD scheme, a search-radius C is set in order to limit the search range. Specifically, we limit the search according to:

$$(\check{\mathbf{s}} - \hat{\mathbf{c}})^H \mathbf{H}^H \mathbf{H} (\check{\mathbf{s}} - \hat{\mathbf{c}}) \leq C, \tag{2.20}$$

where C is the Initial Search Radius (ISR), which has to be sufficiently high in order to contain the ML solution of Eq. (2.16). Let

$$\mathbf{G} = \mathbf{H}^H \mathbf{H}, \tag{2.21}$$

which is a $(U \times U)$ Grammian matrix [47]. Thus, we can obtain the $(U \times U)$ upper-triangular matrix $\mathbf{U}$, which satisfies $\mathbf{U}^H \mathbf{U} = \mathbf{H}^H \mathbf{H}$ with the aid of, for example, the ubiquitous Cholesky factorization [47]. Thus, the entries of the upper-triangular matrix $\mathbf{U}$ are denoted by $u_{i,j}$, satisfying $u_{i,j} = 0$ if $i > j$ for $i, j = 1, 2, ..., U$. Furthermore, the entries on the diagonal of $\mathbf{U}$ are denoted by $u_{i,i}$, which are assumed to be of positive real value without loss of generality [51]. Consequently,

bearing in mind that the matrix $\mathbf{U}$ is upper-triangular, we can rewrite Eq. (2.20) as:

$$\begin{aligned}(\check{\mathbf{s}}-\hat{\mathbf{c}})^H\mathbf{H}^H\mathbf{H}(\check{\mathbf{s}}-\hat{\mathbf{c}}) &= (\check{\mathbf{s}}-\hat{\mathbf{c}})^H\mathbf{U}^H\mathbf{U}(\check{\mathbf{s}}-\hat{\mathbf{c}}), &(2.22)\\ &= \sum_{i=1}^{U}\left|\sum_{j=i}^{U}u_{i,j}(\check{s}_j-\hat{c}_j)\right|^2, &(2.23)\\ &= \sum_{i=1}^{U}\left|u_{i,i}\,(\check{s}_i-\hat{c}_i)+\sum_{j=i+1}^{U}u_{i,j}(\check{s}_j-\hat{c}_j)\right|^2 \le C. &(2.24)\end{aligned}$$

Hence, we can recursively calculate the bound for each $\check{s}_i$ value with the aid of Eq. (2.24), if we start from $i = U$. Specifically, in the light of Eq. (2.24), we can enumerate legitimate values for $\check{s}_U$ based on the following derived criterion as:

$$|\check{s}_U-\hat{c}_U| \le \frac{\sqrt{C}}{u_{U,U}}. \tag{2.25}$$

Then, as indicated by Eq. (2.25), after choosing a legitimate symbol value for $\check{s}_U$ around $\hat{c}_U$ within a radius of $\frac{\sqrt{C}}{u_{U,U}}$, we can continue to choose a trial legitimate value for $\check{s}_{U-1}$ sastifying the criterion derived from Eq. (2.24), which can be expressed as:

$$|u_{U-1,U-1}\,(\check{s}_{U-1}-\hat{c}_{U-1})+u_{U-1,U}(\check{s}_U-\hat{c}_U)|^2+|u_{U,U}(\check{s}_U-\hat{c}_U)|^2 \le C, \tag{2.26}$$

or equivalently:

$$\left|\check{s}_{U-1}-\left(\hat{c}_{U-1}-\frac{u_{U-1,U}}{u_{U-1,U-1}}\xi_U\right)\right| \le \frac{\sqrt{C-|u_{U,U}\xi_U|^2}}{u_{U-1,U-1}}, \tag{2.27}$$

where

$$\xi_i \triangleq \check{s}_i-\hat{c}_i. \tag{2.28}$$

Now a trial value can be chosen for s_{U-1} around $\left(\hat{c}_{U-1}-\frac{u_{U-1,U}}{u_{U-1,U-1}}\xi_U\right)$ within a radius of $\frac{\sqrt{C-|u_{U,U}\xi_U|^2}}{u_{U-1,U-1}}$ in the light of Eq. (2.27). The recursive process continues by choosing a trial candiate for s_{U-2} based on its corresponding criterion. Following the rationale of Eq. (2.24), the decoupled search space for the ith component $\check{s}_i$ can be evaluated by:

$$|\check{s}_i-\mathcal{C}_i| \le \frac{\sqrt{C-\mathcal{D}_{i+1}}}{u_{i,i}}, \tag{2.29}$$

where

$$\mathcal{C}_i \triangleq \left(\hat{c}_i-\sum_{j=i+1}^{U}\frac{u_{i,j}}{u_{i,i}}\xi_j\right) \tag{2.30}$$

and

$$\mathcal{D}_i \triangleq \left|\sum_{l=i}^{U}\sum_{j=l}^{U}u_{l,j}\xi_j\right|^2, \tag{2.31}$$

are defined as the decoupled search center for $\check{s}_i$ and the accumulated Partial Euclidean Distance (PED) between $\check{\mathbf{s}}_i = [\check{s}_i\ \check{s}_{i+1}\ \cdots\ \check{s}_U]$ and the center $\hat{\mathbf{c}}_i = [\hat{c}_i\ \hat{c}_{i+1}\ \cdots\ \hat{c}_U]$ of the hyper-sphere, respectively. Thus, this recursive process can be continued, until i reaches 1. Then the search radius C is updated by calculating the Euclidean distance between the newly obtained signal point $\check{\mathbf{s}}$ and the center $\hat{\mathbf{c}}$ of the hyper-sphere, namely, the unconstrained ML solution. Equivalently, we have:

$$C = \mathcal{D}_1. \tag{2.32}$$

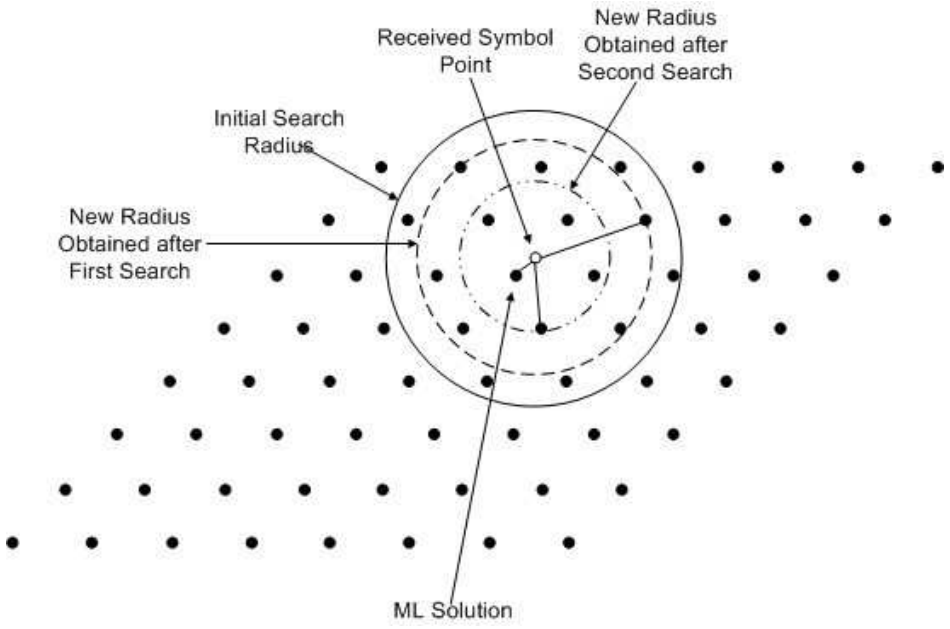

Figure 2.3: Geometric representation of the SD algorithm

Following that a new search is carried out within a smaller compound confined by the newly obtained search radius. The search then proceeds in the same way, until no more legitimate signal points can be found in the increasingly reduced search space. Consequently, the last found legitimate signal point $\check{\mathbf{s}}$ is regarded as the ML solution.

To elaborate a little further, the search radius $\frac{\sqrt{C-\mathcal{D}_{i+1}}}{u_{i,i}}$ for $\check{s}_i$ in Eq. (2.29) provides the information on how large is the remaining search space that has to be scoured for identifying s_i. Moreover, in the light of Eqs. (2.30) and (2.31), the relationship between the decouple search center for $\check{s}_i$ and its corresponding accumulated PED for $\check{\mathbf{s}}_i$ can be expressed as:

$$\mathcal{D}_i = \mathcal{D}_{i+1} + u_{i,i} \left| \check{s}_i - \mathcal{C}_i \right|^2, \tag{2.33}$$

which indicates that given a specific $\mathcal{D}_{i+1}$, the value of $\mathcal{D}_i$ only depends on the tentative choice for the current s_i value.

Intuitively, an astutely selected ISR C can substantially speed up the search process, since the employment of a small radius excludes a high proportion of the low-probability lattice points at the very beginning. However, the radius must not be set too small either, since that would jeopardise finding the ML solution of Eq. (2.16). Hence, the appropriate choice of the ISR is a key factor in determining both the performance and the complexity imposed by the sphere detector discussed in this chapter. In practice, the ISR C has to be set according to the noise variance σ_w^2, more explicitly, according to the SNR encountered, which is achieved by obeying [51]:

$$C^2 = 2\sigma_w^2 JN - \mathbf{y}^T(\mathbf{I} - \mathbf{H}(\mathbf{H}^T\mathbf{H})^{-1}\mathbf{H}^T)\mathbf{y}, \tag{2.34}$$

for the sake of ensuring that the probability of detection failure becomes negligible [47], where N is the number of receive antenna elements, while $J \geq 1$ is a parameter appropriately selected to ensure that the detector will indeed capture the true transmitted signal-vector $\mathbf{s}$.

The SD algorithm can be interpreted as a geometric problem, which is shown in Figure 2.3, where the depth-first SD is applied to a one-dimensional case, namely to a single-user system, for

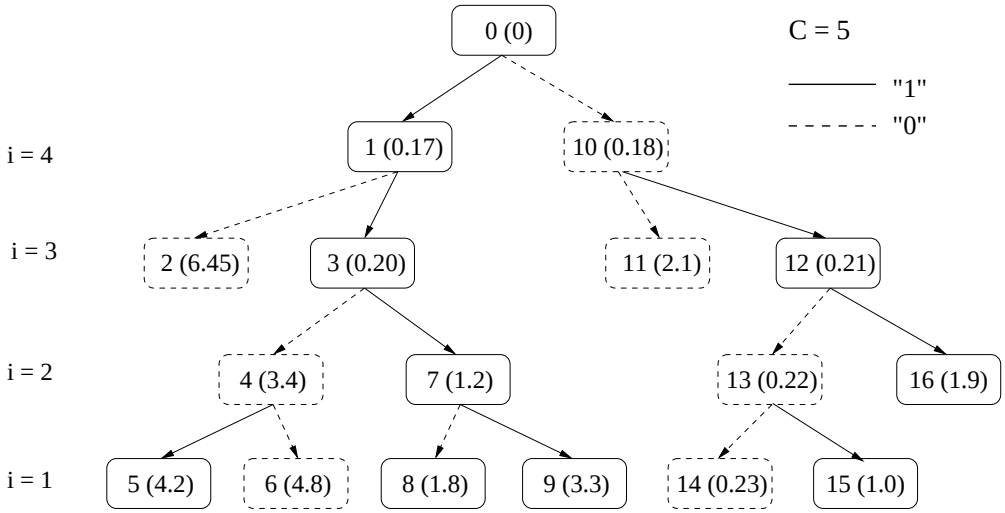

Figure 2.4: Illustration of the depth-first SD algorithm with the aid of the classic tree searching: The figure in ( ) indicates the PED of a specific node for the trial point in the modulated constellation; while the number outside represents the order in which the points are visited. Finally, the ML solution of 0100 is found by choosing the tree leaf having the minimum Euclidean distance of 0.23 and backtracking to the level $i = 4$.

the sake of convenience. In the example shown in Figure 2.3, the employment of 64-QAM was assumed. At the receiver, the shape of the constellation is assumed to be distorted to a diamond-shape instead of the original square-shape, due to the routinely encountered multipath channel-induced phase rotation and magnitude attenuation. Instead of carrying out a full search over the entire 64-point constellation, as the ML detection would in order to find the statistically optimum solution, the sphere detector initializes the search radius depending on the estimated SNR, which confines the search area to the outer-most circle centred at the reconstructed received symbol point $\mathbf{y}_{reconstr} = \mathbf{H}\hat{\mathbf{c}}$, where $\hat{\mathbf{c}}$ is the unconstraint ML solution. As seen from Figure 2.3, the search area is significantly reduced in comparison to the ML detector. It is indeed intuitive that only the trial lattice points in the immediate neighbourhood of the received point are worth examining. Inside the search area confined by the radius, all the symbols are deemed to be the tentative candidates for the transmitted symbol. Now the core operation of the sphere detection algorithm is activated: Specifically, a new radius is calculated by measuring the distance between the candidate and the reconstructed received symbol point $\mathbf{y}_{reconstr}$, which should be no higher than the original radius. Then another arbitrary symbol point is chosen from the newly obtained search area as the trial transmitted point. Again, the search radius is updated with the value of the distance between the newly obtained trial point and the reconstructed received symbol point $\mathbf{y}_{reconstr}$. These operations continue, until the detector finds the specific legitimate constellation point, which is nearest to $\mathbf{y}_{reconstr}$. At the end of the search, we assume that the last trial point that was found is the ML solution. In the example shown in Figure 2.3, the detector reaches the optimum ML solution after two radius updates. Hence, only three trial points are examined in terms of their Euclidean distance with respect to the reconstructed received symbol point $\mathbf{y}_{reconstr}$. Therefore, the potentially full search carried out by the ML detector is avoided by the sphere detector.

A better way of illustrating the depth-first SD algorithm's philosophy, when it is applied to multi-dimensional scenarios, namely to multi-user systems, is constituted by the search tree exam-

ple provided for the scenario of the (4×4) BPSK modulated SDMA/OFDM system characterized in Figure 2.4. Before we further elaborate on the original depth-first SD with the aid of the search tree of Figure 2.4, it is important to note that the SD detector earmarks a legitimate symbol point as the tentative decision for $\check{s}_i$ only if the resultant $\mathcal{D}_i$ of Eq. (2.33) is no higher than the search radius C, implying that the earmarked symbol point for $\check{s}_i$ is located inside the circle of Eq. (2.29) centered at $\mathcal{C}_i$. Otherwise, this point is not earmarked. As shown in Figure 2.4, the depth-first SD commences its search procedure using an ISR of $C = 5$ from the top level $(i = 4)$. For each tree node, the number within the bracket denotes the corresponding accumulated PED of that node, while the number outside the bracket indicates the order in which the node is visited. The broken line represents a binary zero, whereas the continuous line denotes a binary one. As we can see in Figure 2.4, the search is carried out from the left to the right, but in both downward and upward directions along the tree. Specifically, there are two scenarios that may be encountered during the tree search portrayed in Figure 2.4. Firstly, the search may reach a leaf node at the bottom, i.e. the lowest level corresponding to s_1 in Figure 2.4. The other possible scenario is that the detector cannot find any point inside the circle of Eq. (2.29) for the ith element s_i, or equivalently, the accumulated PEDs of all the candidates for s_i are higher than the current search radius C. In the first case, once the search reaches a leaf node, for example, at its fifth step the detector reaches a tree leaf having an Euclidean distance of 4.2 as shown in Figure 2.4, which is smaller than the current search radius of $C = 5$, then the detector starts the search process again with the reduced radius $C = 4.2$. In the second case, the detector must have made at least one erroneous tentative point selection for the previous $(U - i)$ lattice coordinates. In this scenario, the detector goes back to the $(i+1)$th search tree level and selects another tentative point for s_{i+1} within the circle formulated by Eq. (2.29), and proceeds downwards along the tree again to try and find a legitimate decision for s_i. If all the available tentative points for s_{i+1} fail to lead to a legitimate decison, the search backtracks to s_{i+2} with the same objective, and so on. For example, at the ninth step seen in Figure 2.4, the detector is unable to find a legitimate point within the new smaller hyper-sphere having the radius of 1.8, which was obtained at the previous step, hence the search backtracks to level $i = 4$, since no more available candidates can be found within corresponding search area for s_2, and s_3. In the end, after visiting a total of 15 tree nodes and leaves in Figure 2.4, the SD chooses the tree leaf having a minimum Euclidean distance of 0.23 and backtracks to the level $i = 4$ to yield the final ML solution $\hat{\mathbf{s}}_{ML}$.

2.2.3 Breadth-First Tree Search [61]

Based on our discussions on the depth-first SD algorithm in Section 2.2.2, we can observe that the tree search is carried out in a depth-first manner, with the goal of reaching a leaf node for the sake of ensuring that the newly calculated Euclidean distance allows us to rapidly shrink the search-hyper-sphere. However, as we will see in Section 2.2.5, the computational complexity of the depth-first SD depends very much on the ISR C of Eq 2.34, and the appropriate choice of C constitutes a design challenge. Therefore, another tree search scheme was proposed to circumvent this problem based on the idea of searching the tree in a *breadth-first* manner by limiting the number of tree-nodes to be expanded to K, where K denotes the maximum number of nodes having the K lowest accumulated PEDs at every level of the tree. Hence, the computational complexity of the

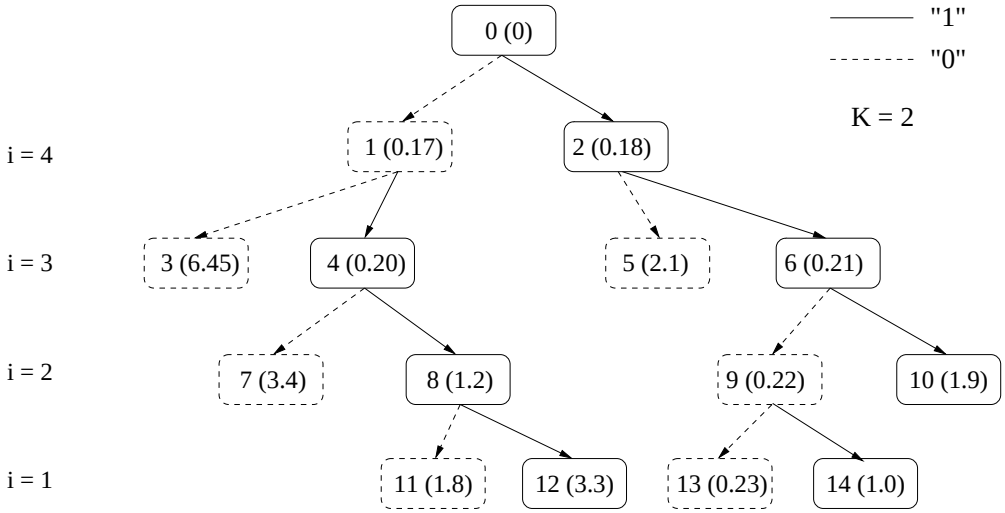

Figure 2.5: Illustration of breadth-first SD algorithm by the corresponding tree searching: The figure in ( ) indicates the PED of a specific node for the trial point in the modulated constellation; while the number outside represents the order in which the points are visited. Finally, the ML solution of 0100 is found by choosing the tree leaf having the minimum Euclidean distance of 0.23 and backtracking to the level $i = 4$.

tree search is reduced, while circumventing the problem of finding an appropriate choice of the ISR. More importantly, a SNR-independent computational complexity is expected and the search is guaranteed to be carried out in the downward direction along the tree.

The search tree of the K-best SD algorithm using $K = 2$ is shown in Figure 2.5, which was applied to the same example of Figure 2.4, where the depth-first SD algorithm was employed. Since we use $K = 2$, following the evaluation of the PEDs of all nodes at a certain level, only the two nodes having the lowest PEDs are expanded or pursued further at each level. Consequently, the detector successfully finds the ML solution with a high probability, which has an Euclidean distance of $\mathcal{D}_1 = 0.23$ in Figure 2.5 with respect to the center $\hat{\mathbf{c}}$ of the search-hyper-sphere. Comparing the two expanded search trees portrayed in Figure 2.4 and Figure 2.5, we can see that a higher complexity reduction was achieved by the K-best SD detector. However, we cannot simply conclude that the K-best SD is always better than its depth-first counterpart, since upon reducing the ISR of the latter, a higher complexity reduction may be expected to be attained. On the other hand, if K is set to an excessively low value, such as $K = 1$ for example, the K-best SD becomes unable to find the true ML solution due to the fact that the detector discontinues the search along the true ML branch as early as the 4th level in Figure 2.5 by choosing to expand and pursue a node having a PED of 0.17. Therefore, the K-best SD does not necessarily arrive at the ML solution, while the depth-first SD does. More discussions on the comparison of these two SDs in terms of achievable performance and imposed complexity will be carried out based on the simulation results in Sectioins 2.2.5 and 2.4.

2.2.4 Generalized Sphere Detection (GSD) for Rank-Deficient Systems

Our discussions in the previous sections implied the assumption that the number of users U, or the number of the transmit antennas M is no more than that of the receive antennas N, i.e. we have $U \leq N$ and $M \leq N$. However, this is not always the case in practice, for example, when SD detection is implemented in a typical down-link of an SDM/OFDM system, where the number of antenna elements employed by the BS exceeds that used at the MS. In this scenario the channel-matrix $\mathbf{H}$ of Eq. (2.6) becomes non-invertible and hence the system is referred to as rank-deficient, where the SDs discussed in Section 2.2 fail to work. Recall that the SD applied in a MIMO system, where the number of transmit antennas M is no higher than the number of receive antennas N, i.e. we have $M \leq N$, the QR decompostion or the Cholesky factorization has to be invoked for decomposing the Grammian matrix $\mathbf{G} = \mathbf{H}^T\mathbf{H}$ in order to obtain the upper-triangular matrix $\mathbf{U}$ having a rank of M, which is identical to the length of the transmitted MIMO symbol vector $\mathbf{s}$. However, for rank-deficient systems the rank of the matrix $\mathbf{H}$ is lower than the number of transmitted symbols to be estimated, which in turn results in zero elements along the diagonal of the upper-triangular matrix $\mathbf{U}$. Recall the decoupled search space of Eq. (2.29) for the ith component $\check{s}_i$ in SD, which is written here:

$$|\check{s}_i - \mathcal{C}_i| \leq \frac{\sqrt{\mathcal{C} - \mathcal{D}_{i+1}}}{u_{i,i}}, \tag{2.35}$$

that all the diagonal elements $u_{i,i}$ have to be non-zero integers. Similarly, the Cholesky decompostion will also fail since the matrix $\mathbf{G} = \mathbf{H}^T\mathbf{H}$ is no longer positive definite. Hence two different techniques of circumventing this problem will be briefly introduced in Sections 2.2.4.1 and 2.2.4.2.

2.2.4.1 Generalized Sphere Detection [41]

After examining the resultant upper-triangular matrix $\mathbf{U}$ evaluated by the QR decomposition in the context of a rank-deficient system where we have $M > N$, it may be readily shown that the diagonal elements in the first N rows of the $(M \times M)$ matrix $\mathbf{U}$ are non-zero, while the diagonal elements in the remaining $(M - N)$ rows are zero. Hence, if $\mathbf{U}$ is partitioned so that the first N rows and the remaining $(M - N)$ rows are seperated, we can use the resultant $(N \times M)$ matrix that has non-zero diagonal elements for SD detection of the first N transmitted symbols based on one of the $M_c^{(M-N)}$ possible combinations of the remaining $(M - N)$ symbols. Essentially, this GSD algorithm [41] can be considered as the combination of the SD for the first N number of transmitted symbols in $\mathbf{s}$ and the full ML detection of the remaining $(M - N)$ symbols, which is a conceptually straightforward method that eliminates the problem of having zero diagonal elements in the upper-triangular matrix $\mathbf{U}$ of a rank-deficient MIMO system. The SD scheme invoked in the GSD can be any of the SDs discussed in Sections 2.2.2 and 2.2.3.

Due to the fact that only N symbols are detected by using low-complexity SD, while all possible $M_c^{(M-N)}$ combinations of the remaining $(M - N)$ symbols have to be tested by the ML detector, the complexity of this GSD scheme is expected to be high, especially when the number of the transmit antennas is significantly higher than that of the receive antennas, namely, when we have $M >> N$. More quantitatively, the resultant complexity is an exponential function of $(M - N)$ [50], potentially preventing its practical application. Thus, our forthcoming disucssions will be focused on the design of more efficient SDs applicable to rank-deficient systems.

2.2.4.2 Generalized Sphere Detection Using Modified Grammian Matrix [50]

In Section 2.2.4.1, a particular partitioning of the matrix $\mathbf{U}$ is conducted in order to circumvent the problem of having zero diagonal elements. In this section, a different GSD scheme will be discussed, which carries out the Cholesky factorization of a modified Grammian matrix $\tilde{\mathbf{G}}$ in order to obtain an upper-triangular $\mathbf{U}$ having non-zero diagonal element. The basic idea behind the GSD algorithm of [50] is that under the assumption of using constant modulus modulation scheme, such as BPSK and QPSK, which implies that every elements in the signal vector $\check{\mathbf{s}}$ has a constant modulus, the product $\alpha\check{s}_i^*\check{s}_i$ becomes a constant value of α under the assumption of a unity transmit power. Consequently, we have an equivalent ML solution for the corresponding SD formulated as [50]:

$$\begin{aligned}\hat{\mathbf{s}}_{ML} &= arg\min_{\check{\mathbf{s}}\in\mathcal{M}_c^M}\{||\mathbf{y}-\mathbf{H}\check{\mathbf{s}}||_2^2+\alpha\check{\mathbf{s}}^H\check{\mathbf{s}}\}, &(2.36)\\ &= arg\min_{\check{\mathbf{s}}\in\mathcal{M}_c^M}\{(\check{\mathbf{s}}-\hat{\mathbf{c}})^H(\mathbf{H}^H\mathbf{H}+\alpha\mathbf{I})(\check{\mathbf{s}}-\hat{\mathbf{c}})\\ &+ \underbrace{\mathbf{y}^H(\mathbf{I}-\mathbf{H}(\mathbf{H}^H\mathbf{H}+\alpha^2\mathbf{I})^{-1}\mathbf{H}^H)\mathbf{y}}_{\varphi}\}, &(2.37)\end{aligned}$$

where

$$\hat{\mathbf{c}} = (\underbrace{\mathbf{H}^H\mathbf{H}+\alpha\mathbf{I}}_{\triangleq\tilde{\mathbf{G}}})^{-1}\mathbf{H}^H\mathbf{y}, \tag{2.38}$$

and $\mathbf{I}$ represents an identity matrix. Normally, α is set to be the noise variance $2\sigma_w^2$, namely, we arrive at:

$$\hat{\mathbf{c}} = (\mathbf{H}^H\mathbf{H}+2\sigma_w^2\mathbf{I})^{-1}\mathbf{H}^H\mathbf{y}, \tag{2.39}$$

which is the MMSE solution of Eq. (2.2).

Since the last term denoted by φ portion of Eq. (2.37) is independent of the value of $\check{\mathbf{s}}$, Eq. (2.37) can be simplified as:

$$\hat{\mathbf{s}}_{ML} = arg\min_{\check{\mathbf{s}}\in\mathcal{M}_c^M}\left\{(\check{\mathbf{s}}-\hat{\mathbf{c}})^H\tilde{\mathbf{G}}(\check{\mathbf{s}}-\hat{\mathbf{c}})\right\}. \tag{2.40}$$

Furthermore, the modified Grammian matrix, $\tilde{\mathbf{G}}$, is always Hermitian and positive definite in contrast to the original Grammian matrix $\mathbf{G}=\mathbf{H}^H\mathbf{H}$. Hence, the modified Grammian matrix $\tilde{\mathbf{G}}$ can be Cholesky factorized in order to attain an upper-triangular matrix $\mathbf{U}$ having non-zero diagonal element, regardless of the rank of the matrix $\mathbf{H}$, namely, we have $\tilde{\mathbf{G}}=\mathbf{U}^H\mathbf{U}$. Consequently, the metric of the GSD can be expressed as:

$$\hat{\mathbf{s}}_{ML} = arg\min_{\check{\mathbf{s}}\in\mathcal{M}_c^M}||\mathbf{U}(\check{\mathbf{s}}-\hat{\mathbf{c}})||^2, \tag{2.41}$$

which is in an identical form of Eq. (2.22) for the full-rank scenario. Finally, due to the fact that all diagonal elements in $\mathbf{U}$ are now non-zero, the standard SD tree search algorithm of Sections 2.2.2 and 2.2.3 can be applied to Eq. (2.41).

2.2.5 Simulation Results

In this section, the achievable performance versus the complexity imposed by the SD is discussed and analyzed in comparison to conventional ML detection based on our simulation results. The

System Parameters	Choice
System	SDMA/OFDM
Uplink/Downlink	Uplink
Number of Sub-Carriers	128
CIR Model	3-tap frequency-selective channel
CIR Tap Fading	OFDM symbol invariant
Channel estimation	ideal
Transmit Antennas per User	1
Initial Squared Search Radius	SNR-Based

Table 2.1: Summary of system parameters

system parameters used in all of our simulations throughout the chapter are shown in Table 2.1. Note that the power delay profile of the 3-path frequency-selective channel is given by $P(\tau) = \sum_{k=0}^{2} P(\tau_k)\delta(t - k\tau)$, where τ is the delay spread and we have $P(\tau_k) = [0.5\ 0.3\ 0.2]$ for $k = 0,\ 1,\ 2$. It is assumed that each user has a single transmit antenna and perfect FD/CHTF estimation is available in all the simulations. The ISR of the depth-first SD was adjusted according to the SNR level [51]. Specifically, we used the setting of $C = 2\sigma_w^2 JN$, where the parameter J was chosen to satisfy $J \geq 1$, while N is the number of receive antennas.

- **BER Performance and Computational Complexity Versus SNR**
  Both the BER performance achieved and the computational complexity imposed by the ML as well as by the aformentioned two types of SD algorithms are shown in Figure 2.6 for the fully-loaded (4×4)-antenna SDMA/OFDM scenario, where 16-QAM transmissions were employed. The BER curves of both the depth-first SD and the K-best SD ($K = 16$) virtually coincide with that of the ML detector. The y-axis on the right quantifies the algorithm's complexity expressed in terms of the number of real-valued additions and multiplications versus E_b/N_o, as shown by the broken line. As seen from Figure 2.6, both SD algorithms are capable of approaching the ML performance at a significantly lower complexity compared to the ML detector. More importantly, upon comparing the depth-first SD and the K-best SD detectors, we found that the former, which carries out the tree search in a depth-first manner, exhibits an E_b/N_o-dependent complexity. Specifically, the higher the received signal power, the lower the computational complexity imposed. Since the complexity of the depth-first SD is variable, it is less suitable for real-time implementation [61]. This phenomenon can be explained as follows. When the signal $\mathbf{y}$ is received at a higher SNR, the ML solution is typically closer to search center $\hat{\mathbf{c}}$ of the hyper-sphere search space, which is either obtained by the LS algorithm of Eq. (2.18) or by the MMSE algorithm of Eq. (2.39). Hence the ISR can be set to a smaller value, in order to avoid a time-consuming search within a large hyper-sphere. Therefore, in our simulations, the ISR C was set according to the noise level, as mentioned previously. On the other hand, the K-best SD detector exhibits a constant computational complexity, since its complexity depends only on the maximum number of nodes K to be considered for each search tree level, on the modulation scheme used and

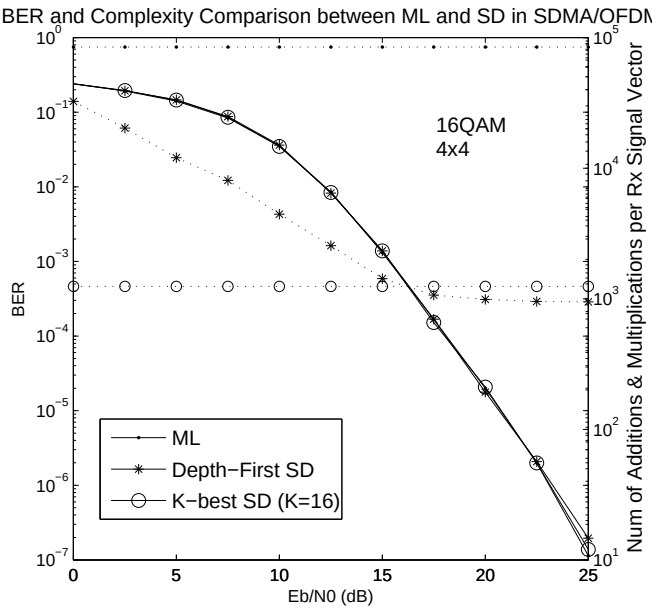

Figure 2.6: Comparison of the ML and SD algorithm: The y-axis on the left quantifies the BER performance of the ML and SD algorithms using continuous lines, while the right y-axis quantifies the complexity versus the E_b/N_o, which is plotted using broken lines. All system parameters were summarised in Table 2.1.

on the number of transmit antennas employed. Hence, when all these parameters are fixed, the complexity of the K-best SD remains constant. It is observed from Figure 2.6 that the complexity imposed by the K-best SD is significantly lower than that imposed by its depth-first counterpart, when the SNR is low, while the former becomes slightly higher than the latter when the SNR encountered is high.

- **Complexity Versus the Number of Transmit Antennas or Users**

  Figure 2.7 portrays the complexity of both the ML and that of the SDs versus the number of users U in the scenario of a fully-loaded 4-QAM SDMA/OFDM system. Observe in Figure 2.7 that the ML detector's complexity increases exponentially with U, which is independent of the value of the SNR, since the ML detector jointly detects the U number of users, imposing a potentially excessive computational complexity of M_c^U Euclidean distance metric evaluations between all possible tentative transmitted signal vectors $\check{\mathbf{s}}$ and the received signal vector $\mathbf{y}$. As shown in Figure 2.7, a significant complexity gain is achieved by both types of SDs over the ML detector, which further escalates as the number of transmit antennas increases. Again, the complexity of the depth-first SD is dependent on the SNR, while the K-best SD exhibits an SNR-independent comlpexity, as observed in Figure 2.7. According to [97], the order of SD complexity in the context of an m-dimensinal lattice is at most $O(m^{4.5})$ at low SNRs, while $O(m^3)$ at high SNRs. Again, we can observe from Figure 2.7 that the K-best SD ($K = 16$) exhibits a significantly lower complexity than its depth-first counterpart at an SNR of 4dB, while it exhibits a complexity slightly higher, when the SNR is 20dB.

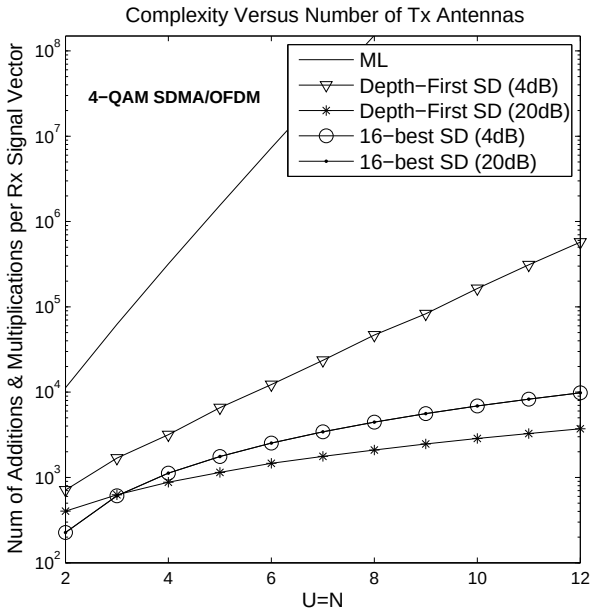

Figure 2.7: Complexity versus the number of transmit antennas. All system parameters were summarised in Table 2.1.

- **Effects of K on the BER Performance and the Complexity of K-best SD**

  Figure 2.8 reveals the effects of the parameter K on both the achievable BER performance and the computational complexity of the K-best SD detector. Observe in Figure 2.8 that K has to be set to at least 16 for the SD to approach the ML detector's performance. However, setting K to be lower than that would reduce the computational complexity imposed, as the broken line representing the complexity versus E_b/N_o trends indicates, which is achieved at the cost of a BER performance degradation. The same conclusion can be drawn from Figure 2.8 as deduced from Figure 2.6 earlier, namely that the complexity of the K-best SD algorithm is independent of the received signal power. Thus, for a given scenario, the trade-off between the achievable BER performance and the computational complexity imposed is effectively controlled by the choice of K.

- **Effects of the ISR on the Complexity of Depth-First SD**

  From our previous results shown in Figure 2.6 we infer that the complexity of the SD may vary as the received signal's SNR changes. Essentially, the complexity of the SD is dependent on the specific choice of the ISR C that confines the search area, which in turn determines the efficiency of the search. Figure 2.9 offers an insight into the dependence of the SD's complexity on the ISR C. The associated complexity increases significantly as C is increased. Therefore, a judicious choice of the ISR plays a vital role in determining both the performance and the complexity of the SD scheme. If it is set too small, the resultant initial search space may not contain the ML solution. On the other hand, it should not be set too higher, otherwise a near-exhaustive search may be encountered.

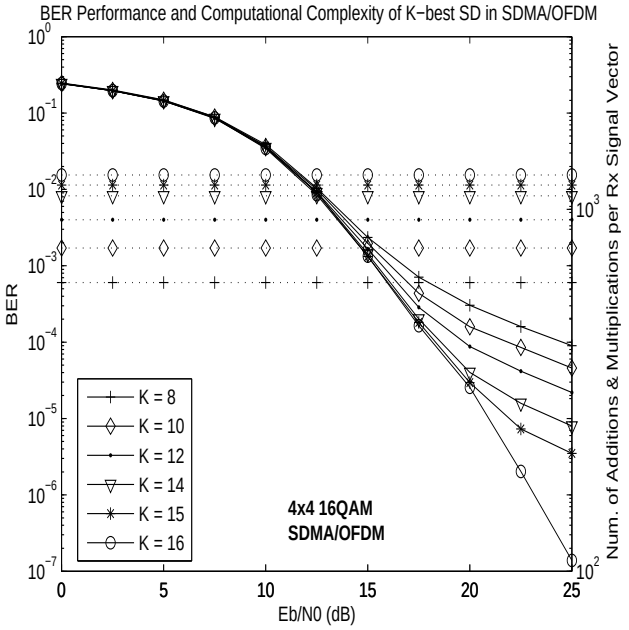

Figure 2.8: Effects of K on the BER performance and complexity of K-best SD: The y-axis on the right represents the scale for the broken lines, indicating the complexity versus E_b/N_o trends, while the y-axis on the left indicates the continuous lines showing the BER performance versus E_b/N_o. All system parameters were summarised in Table 2.1.

2.3 Complexity-Reduction Schemes for SD

2.3.1 Complexity-Reduction Schemes for Depth-First SD

2.3.1.1 Initial-Search-Radius Selection Optimization [93]

From our previous discussions based on the simulation results of Figure 2.9, we know that the choice of the ISR is crucial as regards to the performance of the depth-first SD detector. Hence, the key of further reducing the associated complexity is to optimize the ISR selection. All our simulations characterized so far we have employed an experimentally motivated ISR scheme, where the ISR C is defined as $C = 2\sigma_w^2 JN$, where the parameter J is chosen to satisfy $J \geq 1$, while N represents the number of receive antennas. However, this ISR scheme is suboptimal, since it is unable to guarantee that there is always at least one legitimate signal point within the initial hyper-sphere, potentially leading to a decoding failure. The failure may require a second tentative decoding using a larger ISR and hence wastes valuable computational resources. Two other ISR selection schemes are investigated in this section, namely, the MMSE-based ISR selection and a hybid scheme, which is constituted by a contribution of the previous two schemes.

- **MMSE-Based ISR Selection Scheme**
  The idea behind this ISR selection scheme is appealingly simple. In order to guarantee successful decoding, the ISR is set to the Euclidean distance between the received signal point $\mathbf{y}$ and the MMSE solution based reconstructed recieved signal $\mathbf{y}_{mmse}$, which can be

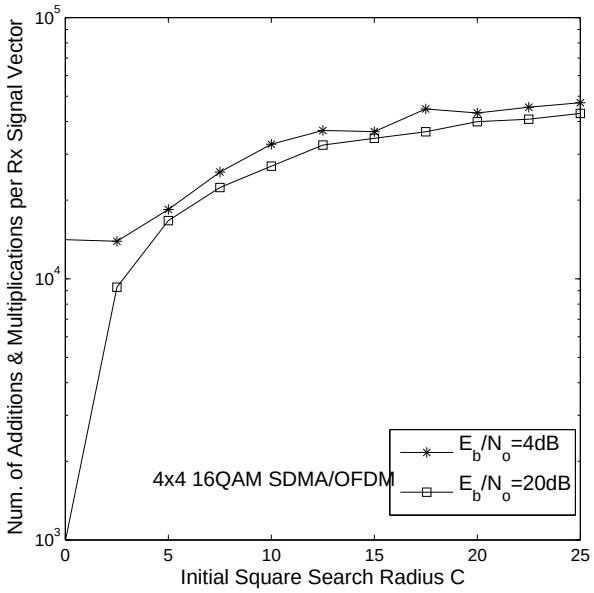

Figure 2.9: The complexity of depth-first SD versus ISR. All system parameters were summarised in Table 2.1.

expressed as [93]:

$$\hat{\mathbf{y}}_{mmse} = \mathbf{H}\hat{\mathbf{s}}_{mmse}, \tag{2.42}$$

where $\hat{\mathbf{s}}_{mmse}$ is the hard-decision based MMSE solution, which can be written as:

$$\hat{\mathbf{s}}_{mmse} = (\mathbf{H}^H\mathbf{H} + 2\sigma_w^2\mathbf{I})^{-1}\mathbf{H}^H\mathbf{y}. \tag{2.43}$$

As expected, the ISR C can be formulated as:

$$C = \|\mathbf{y} - \mathbf{y}_{mmse}\|^2. \tag{2.44}$$

- **Hybrid ISR Selection Scheme**

  The hybrid ISR selection scheme obtains its ISR based on the combination of the above-mentioned experimentally adjusted and the MMSE-based solution. Specifically, we assume that C_1 and C_2 are the ISR calculated by the aformentioned two ISR schemes, respectively. In order to achieve a reduced complexity, the hybrid ISR scheme opts for the smaller of the two, namely, for:

$$C = \min(C_1, C_2). \tag{2.45}$$

Our comparison of the three previously discussed ISR schemes is provided in Figure 2.10, which suggests that the hybrid ISR scheme achieves the lowest complexity over the entire SNR range of our interest. However, it suffers from the same problem of potential decoding failure, as the pure experimentally adjusted ISR scheme. On the other hand, the MMSE-based ISR is the most reliable one in terms of guaranteeing successful sphere decoding [93]. In terms of complexity, the MMSE-based scheme outperforms the experimentally motivated arrangement at low SNRs, while imposing a higher complexity at high SNRs.

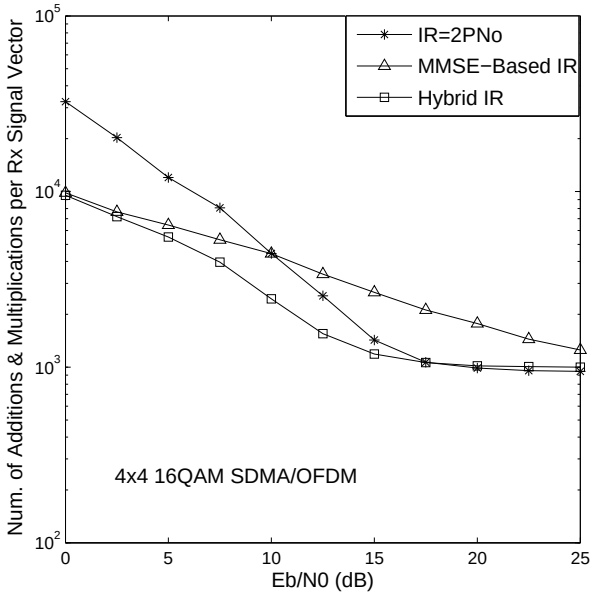

Figure 2.10: Comparison of different ISR selection schemes for depth-first SD. All system parameters were summarised in Table 2.1.

2.3.1.2 Optimal Detection Ordering [98]

In the context of a SDMA system supporting U transmitted data streams, the original SD algorithm of [99] commences the detection of symbols from the Uth signal component to the first one, without considering any specifically beneficial detection order. However, if we expand the ML error formula of Eq. (2.24), we can arrive at:

$$Err_{ml} = \sum_{i=1}^{U} \left| u_{ii}(\check{s}_i - \hat{c}_i) + \sum_{j=i+1}^{U} u_{ij}(\check{s}_j - \hat{c}_j) \right|^2, \tag{2.46}$$

$$= |u_{U,U}\xi_U|^2 + |u_{U-1,U-1}\xi_{U-1} + u_{U-1,U}\xi_U|^2 \tag{2.47}$$

$$+ |u_{U-2,U-2}\xi_{U-2} + u_{U-2,U-1}\xi_{U-1} + u_{U-2,U}\xi_U|^2 + ..., \tag{2.48}$$

where we have $\xi_i = \check{s}_i - \hat{c}_i$. Then we can observe in Eq. (2.48) that the transmitted symbol $\check{s}_U$ appears U times in the above summation, $\check{s}_{U-1}$ appears $(U-1)$ times,... and $\check{s}_1$ appears only once. Based on this observation, we infer that the correct detection probability of the first detected symbol $\check{s}_U$ has an impact on all of the following $(U-1)$ detection steps, while the weight of $\check{s}_{U-1}$ is somewhat lower, since it has an impact only on the next $(U-2)$ steps, etc. In other words, the highest quality signal in terms of SNR should be detected first. This philosophy is the essence of the detection ordering technique, which is a key advance applied for example in the context of the V-BLAST system [16].

Under the assumption that each transmitted stream has an identical transmit power and that each signal experiences the same amount of noise after passing through the channel, the received signal s_m of the mth transmitted signal component can be written as:

$$y_u = \sum_{n=1}^{N} h_{nu} \cdot s_u, \tag{2.49}$$

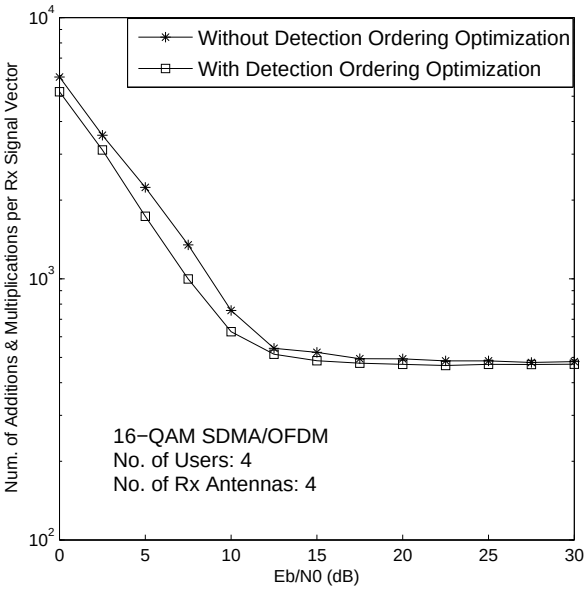

Figure 2.11: The computational complexity benefit of detection order optimization for depth-first SD. All system parameters were summarised in Table 2.1.

where the noise term is omitted here for convenience and h_{nu} represents the FD/CHTF between the uth user and the nth receive antenna, while $\mathbf{h}_u$ is the uth column of the FD/CHTF matrix $\mathbf{H}$. Hence, we can see that the SNR of the uth signal component is proportional to the norm of its corresponding column $\mathbf{h}_u$ in the FD/CHTF matrix $\mathbf{H}$. Bearing in mind the above-mentioned rationale of detection ordering, the norm of the column vector $\mathbf{h}_u$, $(u = 1, 2, \cdots, U)$ is ordered as:

$$||\mathbf{h}_1|| \leq ||\mathbf{h}_2|| \leq ... \leq ||\mathbf{h}_U||. \tag{2.50}$$

Consequently, when the sphere detector is applied to this reordered FD/CHTF matrix $\mathbf{H}$, the detection of $\check{\mathbf{s}}$ proceeds in a descending order of the channel SNR, which may be estimated with the aid of frequency-domain pilots. After finding the ML solution, the resultant vector $\hat{\mathbf{s}}$ of modulated symbols has to be reordered again, according to the symbol-positions of the original sequence. The complexity reduction facilitated by the most beneficial detection ordering scheme is revealed in Figure 2.11.

2.3.1.3 Search Algorithm Optimization

2.3.1.3.1 Sorted SD (SSD)

Although the depth-first SD scheme [47] of Section 2.2.2 is capable of approaching the ML performance at a significantly reduced complexity, it does not operate efficiently at every search step. In fact, the search commences from the surface of the sphere towards the centre. The search carried out in this order does not take into account the definition of the ML solution, which is defined by that specific valid lattice point, which is closest to the centre $\hat{\mathbf{c}}$ of the search sphere [90]. Therefore, the SD follows a zigzag-shaped search trajectory from the surface of the sphere towards its centre $\hat{\mathbf{c}}$ as the search for the ML solution proceeds, which is not as efficient as it could be.

Thus, modifications can be introduced in the search order of the SD algorithm in order to reduce its complexity further. Bearing in mind the aforementioned definition of the ML solution, the modified SD should commence its search near the centre of the sphere. Consequently, a reduced-complexity SD was proposed in [90], where the elements in the candidate set $\mathcal{B}_i$ for the ith signal component $\check{s}_i$ are first sorted in ascending order according to the metric:

$$|\check{s}_i - \mathcal{C}_i|, \tag{2.51}$$

in which $\mathcal{C}_i$ given by Eq. (2.30) decoupled center of the search area of Eq. (2.29) for $\check{s}_i$. Essentially, upon sorting the legitimate candidates for $\check{s}_i$ according to their distance from the decoupled search center $\mathcal{C}_i$ of Eq. (2.30), the modified algorithm commences its search from the most promising lattice point. Thus, the SD complexity is expected to be significantly reduced by the rapid reduced search radius. We refer to this modified SD scheme as the Sorted Sphere Detection (SSD) algorithm which is expected to exhibit a reduced complexity.

2.3.1.3.2 Sorted SD Using Updated-Bounds

Another SD method operating on the basis of SSD was proposed in [90], which is capable of achieving an even lower complexity. Specifically, when a new candidate lattice point is found within the search hyper-sphere, in addition to updating the search radius, the following three modifications are introduced:

[**1**] The decouple search areas of Eq. (2.29) recorded for all candidate basis sets $\mathcal{B}_i$, $(i = 1, 2, \cdots U)$ are also updated immediately with the aid of the most recently obtained lattice point;

[**2**] The next round of search is carried out commencing from $\check{s}_1$, instead of $\check{s}_U$;

[**3**] The new search for $\check{s}_i$ is carried out without going back to start from the first component in the newly obtained smaller candidate set $\mathcal{B}_i$.

Note that the immediate update of the decouple search area of Eq. (2.29) for each tree search level actually eliminates some of the search candidates at the rightmost end of the sorted set $\mathcal{B}_i$ with its leftmost end unchanged [90]. This facilitates the above-mentioned third action, which in turn allows the SD to avoid searching candidates already identified during the last round of the search. Finally, we refer to this modified SD scheme as the Updated-Bound-Aided Sorted SD (SSD-UB).

2.3.1.3.3 Sorted SD Using Termination-Threshold

A more intutive approach that retains most of the benefits of the SSD reduces the complexity further by introducing a search-termination threshold t [98] for informing the SD to curtail the search, when the ML error term of Eq. (2.19) becomes lower than t, where the ML error refers to the newly obtained squared search radius of Eq. (2.32). This procedure aims for avoiding testing all possible tentative ML solution points one by one, which is time consuming. Recall that the SSD reorders the components in the ith basis set $\mathcal{B}_i$, which contains all the tentative points within the search hyper-sphere for the ith signal component $\check{s}_i$, in an ascending order according to the metric given by Eq. (2.51). Therefore, the point considered first in the set $\mathcal{B}_i$ is the most promising

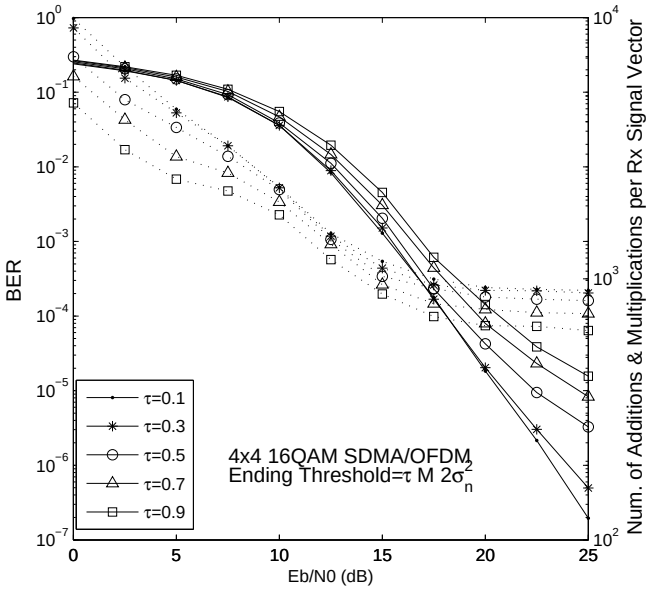

Figure 2.12: BER performance and computational complexity of termination-threshold-aided SSD. The y-axis on the left quantifies the BER performance of the ML and SD algorithms using continuous lines, while the right y-axis quantifies the complexity versus the E_b/N_0, which is plotted using broken lines. All system parameters were summarised in Table 2.1.

one. Thus with the aid of the termination threshold t, the search procedure may be curtailed, provided that the newly obtained lattice point is sufficiently close to the received signal. Hence, the appropriate choice of the termination threshold is the key point for ensuring the efficiency of this reduced-complexity SD. Specifically, if the termination threshold t is set too small, it does not have any effects, since it is unlikely that the ML error would be smaller than t. On the other hand, if t is too large, the search for the ML solution may be curtailed when it tests a non-ML point, whose distance from the received symbol point is less than t. In this scenario, the complexity imposed can be further reduced at the cost of a performance degradation. A judicious choice of the termination threshold t is given by [98]:

$$t = \tau \cdot U \cdot 2\sigma_w^2, \tag{2.52}$$

where U is the number of users, σ_w^2 is the noise level and τ is a parameter typically set to 0.1, 0.3, etc. Consequently, the termination threshold should be set proportional to the number of transmit antennas as well as to the noise power. In this treatise, we refer to this reduced-complexity SD as the Termination-Threshold-Aided Sorted SD (SSD-TT). As shown in Figure 2.12, there is a trade-off between the achievable performance and the complexity imposed by the SD, which is controlled by the appropriate choice of the termination threshold.

Let us now compare the search algorithm optimization schemes discussed in this section in Figure 2.13. Our comparisons are carried out in the scenarios of both (8×8)-element 4QAM and (4×4)-element 16QAM SDMA/OFDM systems, which have an identical throughput of 16bits/symbol. In both cases, the updated-bound-assisted SD detector achieves a significantly lower computational complexity than the termination-threshold-assisted arrangement, rendering it a more effective complexity-reduction scheme. The termination-threshold assisted scheme is capable of attaining

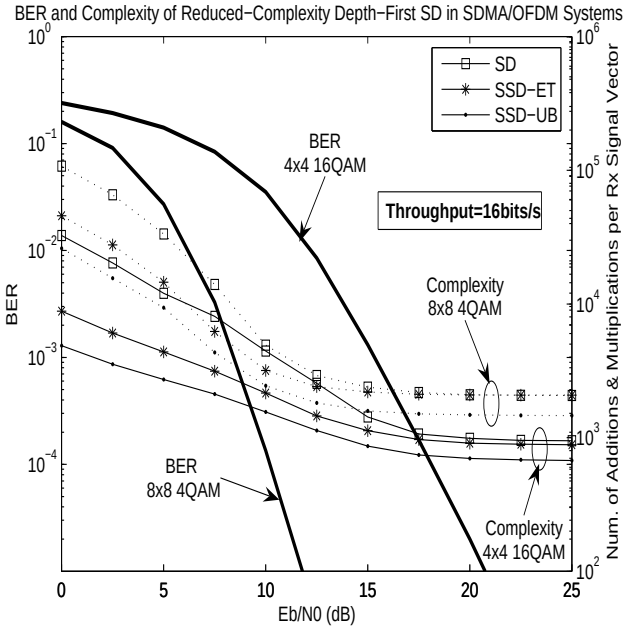

Figure 2.13: BER performance and computational complexity of reduced-complexity depth-first SDs. The y-axis on the left quantifies the BER performance of the ML and SD algorithms using continuous lines, while the right y-axis quantifies the complexity versus the E_b/N_o, which is plotted using broken lines. All system parameters were summarised in Table 2.1.

an evident complexity reduction, when the SNR is relatively low, while imposing only a slightly lower complexity than the original SD detector of [99] when the SNR is in excess of 17.5dB. On the other hand, when comparing two different SDMA/OFDM systems, we found that the (8×8)-antenna 4QAM system substantially outperforms the (4×4)-element 16QAM system in terms of the achievable BER, as a benefit of its higher diversity gain and its lower-density modulation constellation, while imposing an acceptable computational complexity. More specifically, for a given target BER of 10^{-5}, we have an SNR gain of about 9dB if the (8×8)-antenna 4QAM scheme is employed, rather than the (4×4)-element 16QAM arrangement. This is achieved at the cost of less than three times increased computational complexity, as quantified in terms of the number of real-valued additions and multiplications per received signal vector, when the updated-bound-assisted scheme is employed.

In addition to their reduced complexity, the search algorithm optimization schemes discussed in this section have a further benefit of rendering the complexity of the SD less sensitive to the specific choice of the ISR, which can be observed from Figure 2.14.

2.3.2 Complexity-Reduction Schemes for K-Best SD

2.3.2.1 Optimal Detection Ordering

Having discussed various complexity reduction schemes designed for the depth-first SD detector, let us now consider a range of complexity reduction schemes applicable to the K-best SD. The detection ordering optimization scheme introduced in Section 2.3.1.2, which is capable of effectively

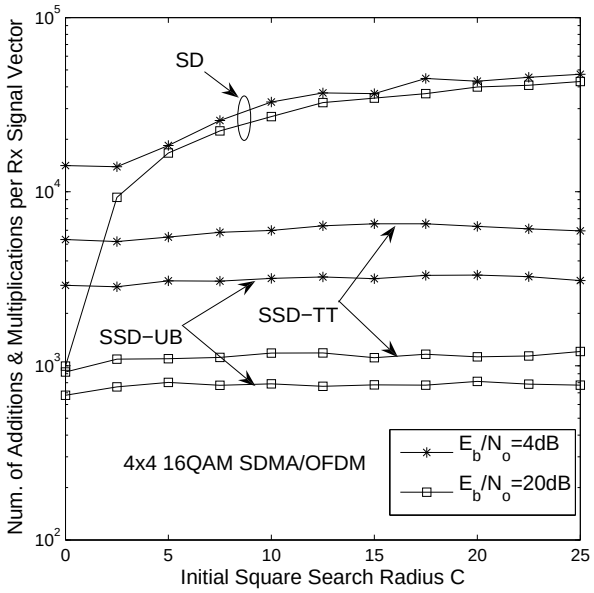

Figure 2.14: Complexity versus the square ISR of reduced-complexity depth-first SDs. All system parameters were summarised in Table 2.1.

reducing the complexity of the depth-first SD, was found suitable also for the K-best SD, which achieved a similar performance to that shown in Figure 2.11. For a rudimentary introduction to this scheme, please refer to Section 2.3.1.2.

2.3.2.2 Search-Radius-Aided K-Best SD

It becomes explicit based on the portrayal of the K-best SD in Sections 2.2.3 and 2.2.5, that its computational complexity is controlled by the parameter K, for a certain modulation scheme and a certain number of transmit antennas or users. This is in contrast to its depth-first counterpart, which achieves a low complexity, despite approaching the ML performance with the aid of the rapid shrinking the original search radius. Intuitively, if we can introduce a search radius for the employment in the K-best SD, its complexity can be further reduced by discarding the unlikely ML candidate nodes which are located outside the sphere confined by the search radius, hence reducing the number of tentative nodes at each level. Consequently, since the partial Euclidean distances evaluated for some of the nodes exceed the radius, there may be less than K nodes that have to be considered for each level, resulting in an additional complexity reduction. In contrast to the gradually reduced radius of the depth-first SD algorithm, the radius used for the K-best SD remains unchanged during the entire search process, since it carries out the tree search in the downwards direction only and the search is ceased, whenever it reaches tree leaf level, namely the lowest level of the tree exemplified in Figure 2.5. Hence, exactly the same search radius selection problem is encountered by the K-best SD, as faced by the depth-first SD. In order to avoid having no lattice points inside the sphere, which in turn results in a repeated search using an increased radius, the radius selection schemes used for the K-best SD should guarantee that at least one lattice point is located in the search sphere. In this report, two radius selection schemes for K-best SD will be examined, namely the *LS-Criterion-Based* and the *MMSE-Criterion-Based* radius calculation

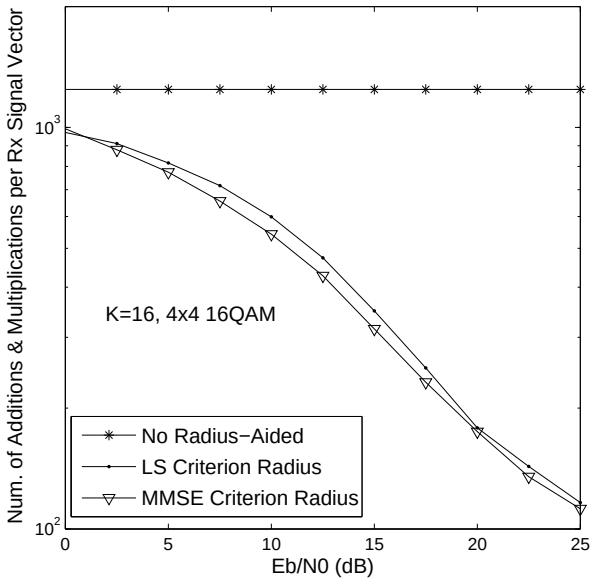

Figure 2.15: Complexity versus SNR of the radius-based K-best SD

schemes, while the latter was already discussed in the context of depth-first SD in Section 2.3.1.1.

In Figure 2.15 we characterize these two radius-based K-best SDs and the original K-best SD of Secction 2.2.3 [61], where we find that a significantly lower complexity can be achieved by both of the radius-based K-best SDs, compared to the original K-best SD of [61]. Hence, the radius-based K-best SD no longer exhibits an SNR-independent complexity as characterized in Figure 2.15, because a higher complexity reduction can be attained when the SNR increases. On the other hand, the complexity of the MMSE-criterion-based radius scheme of Section 2.3.1.1 is evidently lower than that of the LS-criterion-based radius scheme, due to the fact that the former scheme is expected to operate using a smaller search radius, which is capable of reducing the number of nodes at each level that would be expanded.

2.3.2.3 Complexity-Reduction Parameter δ for Low SNRs

Although the complexity of K-best SD can be significantly reduced by introducing a search radius, it still exhibits a relatively high complexity when the SNR is low, as we can observe from Figure 2.15. Intuitively, when the noise level is high, i.e. at low SNRs, investing excessive detection efforts in terms of a large search space becomes futile. This will become more explicit by considering the ML detector, which has a high computational complexity and yet, hardly achieves any performance gain in comparison to the MMSE detector, for example, when the SNR is low. In order to mitigate the problem, we introduce a complexity-reduction parameter δ, which allows us to reduce the complexity of the K-best SD, when the SNR is low. A similar parameter γ was employed in the OHRSA detector of [59] in order to control its complexity, which will be discussed in Section 2.3.3.

The parameter δ is used as follows. When the SNR corresponding to the currently detected ith signal component is lower than δ, namely we have $\frac{\|\mathbf{h}_i\|^2}{\sigma_w^2} < \delta$, only the tentative constellation point

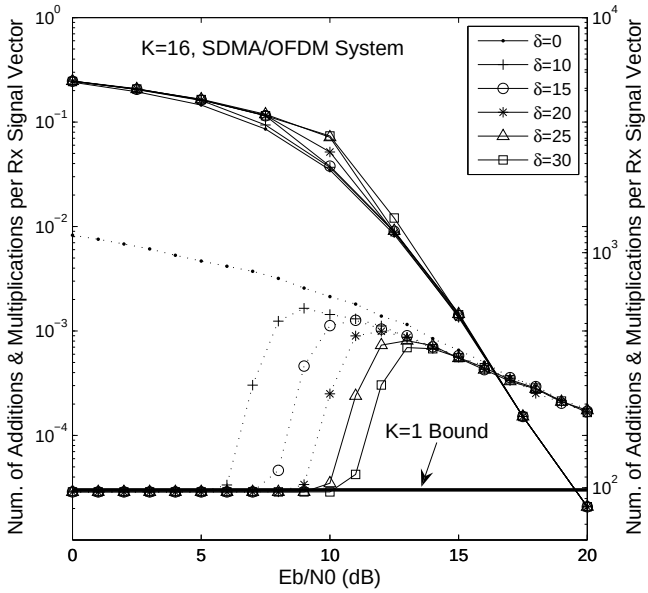

Figure 2.16: Effect of Parameter δ on the BER and complexity of K-best SD detector. the continuous lines scaled on the y-axis on the left represent the BER performance, while the broken lines scaled on the y-axis on the right show the corresponding complexity.

yielding the smallest value of $|s_i - \mathcal{C}_i|$ is considered, rather than testing all the original K candidates. Moreover, due to the employment of the detection ordering optimization scheme of Section 2.3.1.2, the SNRs associated with the signal components about to be detected, i.e. $\check{s}_{i-1}$, $\check{s}_{i-2}$, $\cdots$, $\check{s}_1$, will also be lower than δ. Thus, only a single tentative point will be enumerated, which in fact represents the final decision for the corresponding signal components.

Consequently, the complexity associated with a low SNR is significantly reduced at the cost of a modest BER performance degradation, provided that we choose the value of δ appropriately, as observed in Figure 2.16. Specifically, if δ is chosen to be 10 for the K-best SD ($K = 16$) in the scenario of a (4×4)-antenna 16QAM SDMA/OFDM system, the corresponding BER curve is almost the same as the ML curve, but the corresponding complexity curve indicates a significantly lower complexity, which coincides with the $K = 1$ complexity bound for the SNR range spanning from 0dB to 6dB. In other words, with the aid of δ, the original computationally demanding low-SNR range imposes a computational complexity associated with the case of $K = 1$.

2.3.3 Optimized Hierarchy Reduced Search Algorithm [44] - An Advanced Extension of SD

2.3.3.1 Hierarchical Search Structure

Recently, another advanced tree search detection method, referred to as the Optimized Hierarchy Reduced Search Algorithm (OHRSA), was proposed in [44] as an extention of the conventional depth-first SD, which is capable of further reducing the detection complexity. Since its preprocessing stage actually employs exactly the same strategy as the GSD discussed in Section 2.2.4.2,

the OHRSA may also be readily applied to rank-deficient MIMO systems, where the number of transmit antennas or users exceeds that of the receive antennas. Hence, the emphasis of this section will be put on its search philosophy.

In order to enable the OHRSA detector to handle rank-deficient scenarios, the Grammiam matrix $\tilde{\mathbf{G}}$ of Eq. (2.38) is employed, which can be Cholesky factorized to obtain the upper-triangular matrix $\mathbf{U}$. Thus, the OF of the OHRSA may be formulated in a similar manner to the conventional SDs by rewriting Eq. (2.24) based on the fact that the diagonal elements u_{ii} are positive real values [44]:

$$J(\check{\mathbf{s}}) = \sum_{i=1}^{U} \left| u_{i,i}(\check{s}_i - \hat{c}_i) + \sum_{j=i+1}^{M} u_{i,j}(\check{s}_j - \hat{c}_j) \right|^2, \tag{2.53}$$

$$= \sum_{i=1}^{U} \left| \sum_{j=i}^{U} u_{i,j}(\check{s}_j - \hat{c}_j) \right|^2, \tag{2.54}$$

$$= \sum_{i=1}^{U} \phi_i(\check{\mathbf{s}}_i), \tag{2.55}$$

where the Sub-Cost Function (SCF) $\phi_i(\check{\mathbf{s}}_i)$ can be written as:

$$\phi_i(\check{\mathbf{s}}_i) = \left| \sum_{j=i}^{U} u_{i,j}(\check{s}_j - \hat{c}_j) \right|^2, \tag{2.56}$$

$$= \left| u_{i,i}(\check{s}_i - \hat{c}_i) + \sum_{j=i+1}^{U} u_{i,j}(\check{s}_j - \hat{c}_j) \right|^2, \tag{2.57}$$

$$= |u_{i,i}(\check{s}_i - \hat{c}_i) + a_i|^2, \tag{2.58}$$

where

$$a_i \triangleq \sum_{j=i+1}^{U} u_{i,j}(\check{s}_j - \hat{x}_j), \tag{2.59}$$

which is a complex-valued scalar, which is independent of the ith element $\check{s}_i$ of the *a priori* candidate signal vector $\check{\mathbf{s}}$.

Furthermore, according to [44], the so-called Cumulative Sub-Cost Function (CSCF) $J_i(\check{\mathbf{s}}_\mathbf{i})$ is defined recursively as:

$$J_U(\check{\mathbf{s}}_U) = \phi_U(\check{\mathbf{s}}_U) = |u_{U,U}(\check{s}_U - \hat{c}_U)|^2 \tag{2.60}$$

$$J_i(\check{\mathbf{s}}_i) = \sum_{i}^{U} \phi_i(\check{\mathbf{s}}_i), \tag{2.61}$$

$$= \sum_{j=i+1}^{U} \phi_j(\check{\mathbf{s}}_j) + \phi_i(\check{\mathbf{s}}_i), \tag{2.62}$$

$$= J_{i+1}(\check{\mathbf{s}}_{i+1}) + \phi_i(\check{\mathbf{s}}_i), \quad i = 1, ..., U-1, \tag{2.63}$$

where $\check{\mathbf{s}}_i$ is defined as the candidate subvector, which is given by: $\check{\mathbf{s}}_i = [\check{s}_i, ..., \check{s}_U]$. According to Eq. (2.63), a recursive search can be carried out starting from the calculation of $J_M(\check{\mathbf{s}}_M)$. At the ith recursive step, a tentative candidate $\check{s}_i$ is selected from the set of M_c possible hypothesises for the transmitted signal s_i associated with the ith user. Then, based on the value of the tentative

candidate $\check{s}_i$, $J_i(\check{\mathbf{s}}_i)$ is evaluated, which depends only on the tentative values of $\check{s}_j$, where we have $j = i,\ i+1,...,\ U$. The recursive calculation of the SCF $J_i(\check{\mathbf{s}})$ proceeds until i reaches 1. The resultant OF of $J(\check{\mathbf{s}})$ is equal to the value of the CSC function $J_1(\check{\mathbf{s}}_i)$, namely we have:

$$J(\check{\mathbf{s}}) = J_1(\check{\mathbf{s}}_1), \tag{2.64}$$

which can be derived from Eq. (2.55) and Eq. (2.63). Hence, a recursive search process may be formulated on the basis of Eq. (2.63) for testing all legitimate tentative signal vectors $\check{\mathbf{s}}$ and then the value of its corresponding OF $J(\check{\mathbf{s}})$ is stored. Then i is reset to U, and according to Eq. (2.63) a new recursive process is commenced from the calculation of $J_U(\check{\mathbf{s}}_U)$. Finally, after an exhaustive computation of all the M_c^U number of values for $J(\check{\mathbf{s}})$ corresponding to all possible hypothesised signal vectors $\check{\mathbf{s}}$, the ML solution is guaranteed to be found as the one associated with the lowest value of $J(\check{\mathbf{s}})$. The recursive hierarchical search formulated in Eq. (2.63), is in fact also carried out in conventional depth-first sphere detection algorithms of Section 2.2.2, but with a significantly small search space (i.e. within the search hyper-sphere) given by the search radius, which is updated once a hypothesised signal vector $\check{\mathbf{s}}$ is obtained. Essentially, the recursive hierarchical search discussed so far in this section is the same as the full search technique employed in conventional ML detectors, which exhibits a potentially excessive complexity, if a high-throughput modulation scheme is employed or a high number of users are supported by the system. Instead of introducing a search radius to confine the search area of the SD, the OHRSA invokes several optimisation rules on the basis of exploiting the properties of the CSCF $J_i(\check{\mathbf{s}}_\mathbf{i})$ of Eq. (2.63). Note that the SCF ϕ_i given by Eq. (2.56) is always positive, therefore, the value of the CSCF $J_i(\check{\mathbf{s}}_\mathbf{i})$ monotonically increases, as the hierarchical search continues. Specifically, we have:

$$J(\check{\mathbf{s}}) = J_1(\check{\mathbf{s}}_1) > J_2(\check{\mathbf{s}}_2) > \ \cdots > J_M(\check{s}_M) > 0. \tag{2.65}$$

The hierarchical search structure combined with the property given by Eq. (2.65) allow the search process to achieve a significant complexity reduction, which will be considered in the next section in comparison to the complexity-reduction techniques discussed for the depth-first SD in Section 2.3.1, since the OHRSA detector also falls into the category of the depth-first SDs.

2.3.3.2 Optimization Strategies for the OHRSA Versus Complexity-Reduction Techniques for the Depth-First SD

In Section 2.3.3.1 we argued that the conventional depth-first SD of Section 2.2.2 and the OHRSA algorithms share the same recursive hierarchical search structure. Given the aim of decreasing the number of OF evaluations required for finding the ML solution, the optimization strategy of OHRSA will be contrasted to the complexity-reduction techniques of SD in our following discourse.

2.3.3.2.1 Best-First Detection Strategy

This strategy is identical to the detection order optimization technique discussed in Section 2.3.1.2 for the depth-first SD. Briefly, the best-first detection strategy entails detecting the received signal in a descending order according to their received signal quality expressed in terms of the SNR

encountered, which is proportional to the norm of its corresponding column vector in the channel transfer function matrix $\mathbf{H}$ of Eq. (2.6). The corresponding mathematical proof was provided in Section 2.3.1.2, which will not be restated here.

2.3.3.2.2 Sorting Criterion

Recall that in the SSD technique of Section 2.3.1.3 the elements in the resultant tentative candidate set $\mathcal{B}_i$ delimited by the decoupled search area of Eq. (2.29) for the specific signal component $\check{s}_i$ are sorted in an ascending order according to their distance from the decoupled search center $\mathcal{C}_i$ of Eq. (2.30). The rationale of this was based on the idea that the ML solution is likely to be located near the center of the decoupled search area. Thus the SD becomes capable of promptly findng the ML solution, avoiding a 'zigzagging' search from the surface of the sphere to the ML solution, which is closest to the center $\hat{\mathbf{c}}$ of the hyper-sphere.

The rationale of the SSD of Section 2.3.1.3.1 can be transplanted into OHRSA, despite the fact that their mathematical sorting criteria are quite different from each other. To expound a little further, for OHRSA, there is no need for the concept of a search radius and corresponding search sphere, which is the basic difference between OHRSA and the conventional SD of Section 2.2.2. However, bearing in mind the definition of the ML solution and the specific property of the OHRSA formulated in Eq. (2.65), another scheme capable of achieving the same objective of avoiding futile search steps may be devised. Specifically, in the context of OHRSA, the ML solution $\mathbf{s}_{ML}$, can be interpreted as the tentative signal vector $\check{\mathbf{s}}$ whose corresponding OF $J(\check{\mathbf{s}})$ is the smallest one. On the other hand, the CSCF of Eq. (2.63) is increased cumulatively, as the recursive search proceeds from $\check{s}_U$ to $\check{s}_1$ and hence we arrive at the final value of the OF $J(\check{\mathbf{s}})$ formulated in Eq. (2.65) which is repeated here for convenience:

$$J(\check{\mathbf{s}}) = J_1(\check{\mathbf{s}}_1) > J_2(\check{\mathbf{s}}_2) > \cdots > J_U(\check{\mathbf{s}}_U) > 0. \tag{2.66}$$

Let us now rewrite Eq. (2.63) as follows:

$$J_i(\check{\mathbf{s}}_i) = J_{i+1}(\check{\mathbf{s}}_{i+1}) + \phi_i(\check{\mathbf{s}}_i),\ i = 1, ..., U-1. \tag{2.67}$$

Based on the above two equations, it is intuitive that in order to arrive at the lowest possible OF value $J(\check{\mathbf{s}})$ after a single cycle of the recursive search loop is completed, the increment $\phi_i(\check{\mathbf{s}}_i)$ seen in Eq. (2.67) should be as small as possible at each recursive step. If we denote the set of M_c number of tentative candidate values of the transmitted signal component s_i at each recursive step $i = U, ..., 1$ as $\{\tilde{s}_m\}_{m=1,...,M_c} \in \mathcal{M}_c$, the set of potential candidates $\{\tilde{s}_m\}_{m=1,...,M_c}$ should be tested in an ascending order according to their corresponding value of $\phi_i(\check{\mathbf{s}}_i) = \phi_i(\tilde{s}_m, \check{\mathbf{s}}_{i+1})$, as formulated in Eq. (2.56). As a consequence, we have:

$$\phi_i(\tilde{s}_1, \check{\mathbf{s}}_{i+1}) < \cdots < \phi_i(\tilde{s}_m, \check{\mathbf{s}}_{i+1}) < \cdots < \phi_i(\tilde{s}_U, \check{\mathbf{s}}_{i+1}), \tag{2.68}$$

where according to Eq. (2.58) we have:

$$\phi_i(\tilde{s}_m, \check{\mathbf{s}}_{i+1}) \quad = \quad |u_{i,i}(\tilde{s}_m - \check{c}_i) + a_i|^2. \tag{2.69}$$

Therefore, with the aid of this sorting criterion, the more likely for ML solution candidates are tested earlier.

2.3.3.2.3 Local Termination-Threshold

In contrast to the sorting technique employed in the conventional SD algorithms of Sections 2.3.1 and 2.3.2, the computational complexity of the OHRSA can only be further reduced if it is combined with other surrogate techniques, since no radius-reduction is used to confine the search area. As an example, a local Termination Threshold (TT) can be introduced for controlling the operation of the OHRSA, for example to curtail operation based on the OF value computed at the current level search. Recall that the *global* TT technique of Section 2.3.1.3, instructs the SD to curtail its search and output the most recently found signal vector $\check{\mathbf{s}}$ as the ML solution, when the Euclidean distance between the newly obtained signal vector and the search center $\hat{\mathbf{c}}$ is equal to or smaller than the preset termination threshold. The TT technique used in the OHRSA algorithm is a *local* one, which is invoked to curtail the current recursive search loop instead of discontinuing the search all together. Therefore, the local TT employed in the OHRSA is reminiscent of the search bound formulated in Eq. (2.29) for depth-first SD algorithm, which confines the decoupled search area for a specific signal component $\check{s}_i$.

The local TT of the OHRSA may be formulated as:

$$J_{min} = \min\{J_{min},\ J(\check{\mathbf{s}})\}, \tag{2.70}$$

which is updated every time when a new OF value $J(\check{\mathbf{s}})$ is obtained and hence the recursive search reaches the decision for deciding upon signal component $\check{s}_1$. Therefore, with the aid of the sorting criterion of Eq. (2.68), the search loop is discontinued at ith recursive search step aiming for deciding upon the signal component $\check{s}_i$, whenever the search satisfies $J_i(\tilde{s}_m, \check{\mathbf{s}}_{i+1}) > J_{min}$. And the search steps back to $(i+1)$th detection step, where another tentative candidate $\tilde{s}_m$ is chosen for $\check{s}_{i+1}$. By constrast, if the most recently obtained $J_{i+1}(\tilde{s}_m, \check{\mathbf{s}}_{i+2}) < J_{min}$, then the algorithm returns to the ith detection step. In the worst case scenario, when the detection loop returns to $i = M$ and all the potential candidates for $\check{s}_M$ have been tested, but the algorithm still fails to find a new search path to reach $J_1(\tilde{s}_m, \check{\mathbf{s}}_2)$, the detector outputs the currently available tentative signal vector $\check{\mathbf{s}}$, whose corresponding OF $J(\check{\mathbf{s}})$ has the minimum value, as the ML solution.

2.3.3.2.4 Performance Evaluation

In Figure 2.17 both the BER performance achieved and the complexity imposed by the OHRSA detector is portrayed in conjunction with different complexity reduction parameter values γ. As argued in Section 2.3.2.3, the appropriate SNR-dependent choice of the complexity reduction parameter allows us to avoid the computationally demanding and yet inefficient detection of the specific signal components, which have their signal energy well below the noise floor [59]. Following from our previous discussion on the parameter δ employed by the K-best SD in Section 2.3.2.3, recall that δ has a similar role to that of the parameter γ in the context of the OHRSA detector. Suffice to state here that the introduction of the parameter γ reduces the complexity of the OHRSA at low SNRs as we can see from results of Figure 2.17, which is achieved at the cost of a slight BER performance degradation. By comparing Figures 2.17 and 2.16 we found that the BER performance degradation suffered by the OHRSA detector occurs in an SNR range, which is different from that of the K-best SD detector of Section 2.3.2.3. More specifically, the BER performance degradation of the OHRSA detector takes place in the SNR range associated with the highest complexity reduction, i.e. in the low-SNR range. By constrast, the performance degradation of the K-best SD

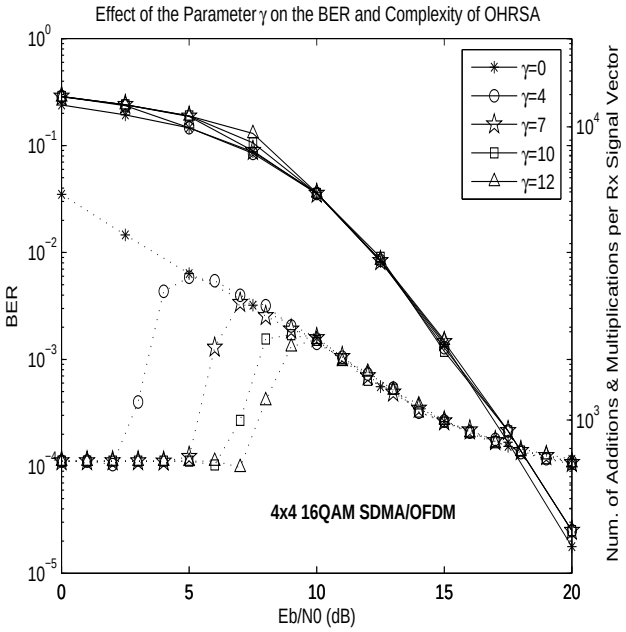

Figure 2.17: BER and complexity of the OHRSA detector: the real lines together with the left y-axis show the BER trends versus the SNR, while the broken lines with the aid of the right y-axis exhibit the complexity trend versus the SNR.

becomes most pronounced in the moderate SNR range.

2.4 Comparison of the Depth-First, K-Best and OHRSA Detectors

2.4.1 Full-Rank Systems

In this section, we compare the depth-first and *K*-best SDs of Sections 2.2.2 and 2.2.3 and the OHRSA detector of Section 2.3.3, which can be regarded as an advanced extension of the depth-first SD in the specified scenario of full-rank systems. Figures 2.18(a) and 2.18(b) show both the BER performance and the computational complexity of these three detectors in the scenarios of (4×4) 16QAM and (8×8) 4QAM SDMA/OFDM systems, respectively. Both systems had an effective throughput of $4 \cdot 4 = 16$ and $8 \cdot 2 = 16$ bit/symbol. By choosing an appropriate K and δ value for the *K*-best SD of Section 2.2.3, it was ensured in Figure 2.18 that it was capable of maintaining a near-ML BER performance, while exhibiting the lowest complexity of the three in both scenarios. When comparing our identical-throughput of 16bits/symbol systems, the one which employs an antenna arrangement of (4×4)-elements and the 16QAM scheme has a significantly worse BER performance at a commensurately reduced complexity.

2.4.2 Rank-Deficient Systems

In this section, we compare the three types of SDs in terms of their BER performance and computaional complexity in the context of rank-deficient 4QAM SDMA/OFDM systems in conjunction

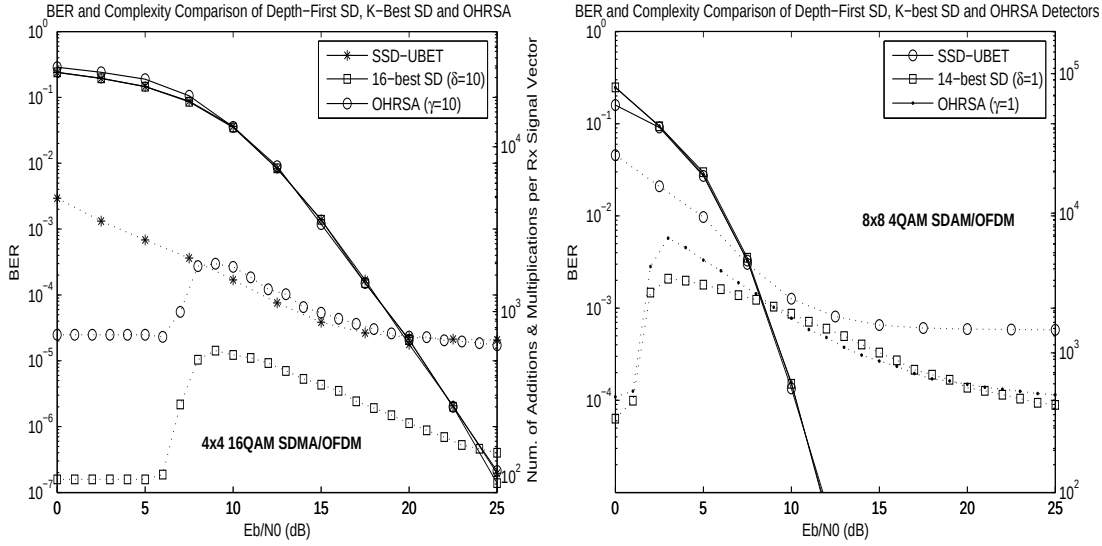

(a) 4×4 16QAM SDMA/OFDM System (b) 8×8 4QAM SDMA/OFDM System

Figure 2.18: BER and complexity comparison of depth-first SD, K-best SD and OHRSA detectors: the continuous lines scaled on the left y-axis show the BER trends versus the SNR, while the broken lines scaled on the right y-axis exhibit the complexity trends versus the SNR. All the remaining system parameters wrere summarized in Table 2.1

with different antenna arrangements. In Figure 2.19 the BER curves associated with the depth-first SD, the K-best SD, and the OHRSA detectors are portrayed, demonstrating that all of them achieves a near ML performance in the different rank-deficient scenarios considered. However, unlike the other two detectors, the K-best SD does not guarantee a ML performance without an appropriate choice of K. More specifically, setting $K = 32$, which ensures that the K-best SD does exhibit a ML BER performance in a (8×5)-element system, does not necessarily guarantee a ML performance if the rank-deficient system becomes more asymmetrical in terms of having an excessive number of transmitters. For example, for an antenna arrangement of (8×4)-elements, we can see this phenomenon in Figure 2.19. In other words, more computational efforts are required for approaching the ML performance as the difference between the number of transmit and receive antennas increases. This will be become more explicit by considering Figure 2.20.

To expound a little further, Figure 2.20 compares the complexity of these three detectors in both (8×4)-element and (8×7)-element 4QAM systems. We observe that all of these detectors exhibit a significantly lower complexity in the context of the latter system than in the former one, since in the latter, the number of receive antennas increases to approaches that of the transmit antennas, making the system less rank-deficient. In these 4QAM scenarios, we found that the OHRSA detector has the lowest computational complexity, while the depth-first SD and the K-best SD typically exhibit a similar complexity, although their specific relationship depends on the SNR encountered. An interesting observation from Figure 2.20 is that instead of decreasing, the complexity of the OHRSA detector increases as the SNR increases in the high-SNR region, namely in the SNR range spanning from 12 to 25dB. The reason behind this phenomenon can be explained

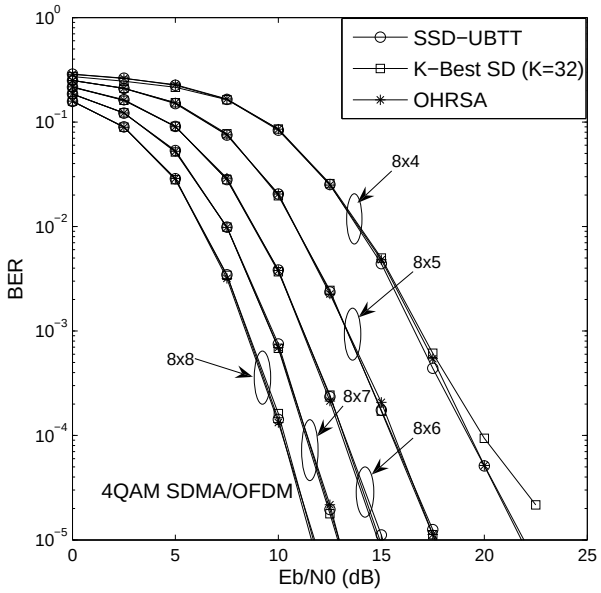

Figure 2.19: The BER performance comparison of the depth-first SD, the K-best SD and the OHRSA detectors in rank-deficient systems. All the remaining system parameters wrere summarized in Table 2.1

as follows. In the heavily loaded system, the interference between the different antenna elements becomes much more significant, while in the high-SNR region, i.e. the noise variance becomes low and hence a well-shaped decision lattice is created, which suggests that the OHRSA requires a sufficiently high complexity budget in order to approach the ML solution. Furthermore, owing to the specific search strategy of the OHRSA detector of Section 2.3.3, an erroneous decision is more likely to be made at the higher level of the search tree. Therefore, instead of decreasing, the complexity of the OHRSA detector increases as the SNR increases in the high-SNR region.

2.5 Chapter Conclusions

In this chapter, one of the most promising low-complexity near-ML detector, i.e. the SD, has been investigated. Specifically, the derivation of the SD's objective function from the conventional ML metric was performed in Section 2.2.1, followed by a discourse on the SD's tree search process in Sections 2.2.2 and 2.2.3. More particularly, depending on whether the tree search was carried out in both the downward and upward directions of Figure 2.4 or solely in the downward direction of Figure 2.5, SDs were classified into two categories, namely, the family of depth-first and breadth-first SDs. The search space of the former, which is a hyper-sphere initially confined by the ISR C of Figure 2.3, rapidly shrinks upon regularly updating the search radius, as soon as the depth-first tree search reaches a leaf node. In contrast to the former, the breadth-first SD or the so-called K-best SD confined the search space by introducing a parameter K, which indicates the number of best candiates retained for each search tree level, rather than employing a search radius C. Hence, it was found in Figures 2.6 and 2.9 of Section 2.2.5 that the complexity imposed by the depth-first SD may vary depending on the received SNR and on the choice of the ISR C, whereas the K-best SD may

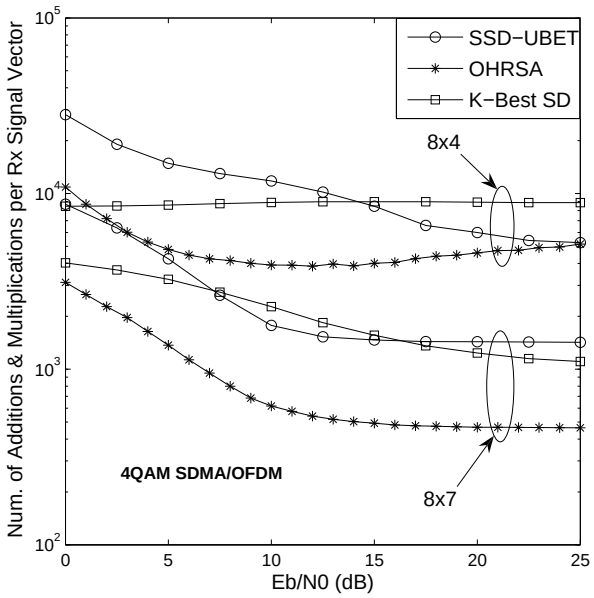

Figure 2.20: The complexity comparison of the depth-first SD, *K*-best SD and the OHRSA detectors in rank-deficient systems: the complexity curve corresponding to the *K*-best SD in the scenario of (8×4) antenna arrangement is obtained by setting $K = 32$, whereas under the antenna arrangement of (8×7)-element, we set $K = 18$, since *K* is expected to have a larger value, as the rank-deficient system becomes more asymmetrical in terms of having an excessive number of transmitters, in order to maintain a near ML BER performance. All the remaining system parameters wrere summarized in Table 2.1

exhibit a constant complexity, regardless of the received SNR. As to the achievable performance, both types of SDs are capable of attaining the exact ML performance, provided that the ISR C of Figure 2.3 derived for the depth-first SD or the parameter K for the breadth-first SD is chosen to be sufficiently high. Additionally, due to the SNR-independent computational complexity, the *K*-best SD is more suitable for real-time applications and it may be readily implemented in a pipelined fashion.

In the scenario of rank-deficient MIMO systems, where the number of the transmit antennas M is higher than that of the receive antennas N, the Grammian matrix $\mathbf{G}$ of Eq. (2.21) has $(M - N)$ zero diagonal-elements. Hence, Cholesky factorisation of $\mathbf{G}$ cannot be directly applied, thus the conventional SD has to be modified in order to apply it in rank-deficient situations, which results in the so-called GSD of Section 2.2.4. Two SD methods have been introduced in Section 2.2.4 for handling the challenging rank-deficient scenarios. Essentially, the first scheme of Section 2.2.4.1 may be regarded as the combination of the standard SD for the first N transmitted symbols and ML detection for the remaining $(M - N)$ symbols, since only the diagonal elements of the last $(M - N)$ rows of the Grammian matrix $\mathbf{G}$ are zero. The other technique of Section 2.2.4.2 dealing with the problem of having $(M - N)$ zero diagonal elements in the matrix $\mathbf{G}$ is to generate a modified Grammian matrix $\tilde{\mathbf{G}}$, which becomes $\mathbf{G} + \alpha\mathbf{I}$, where a judicious choice of the parameter α is required in order to achieve a sufficiently low computational complexity. As detailed in Section 2.2.4.2, the parameter α is chosen to be the noise variance $2\sigma_w^2$. Thus, the GSD commences

its search for the ML solution within a search space centered around the MMSE solution, rather than the LS solution of the conventional SD.

The OHRSA detector, which was developed as an extension of the GSD detector of Section 2.2.4 was introduced in Section 2.3.3. It was studied in comparison to the most influential complexity reduction schemes invoked for the SDs, which were detailed in Sections 2.3.1 and 2.3.2. More specifically, the OHRSA invokes exactly the same preprocessing operations as the GSD, which were shown in to be capable of dealing with rank-deficient scenario in Section 2.2.4.2, where the number of transmit antennas is higher than that of the receive antennas. Furthermore, a comprehensive discussion on the search techniques used by the OHRSA algorithm was provided in Section 2.3.3 in comparison to the classic SDs. Essentially, both the OHRSA and the SD rely on a hierarchical search structure, and they both rely on identical ML metric equations. On the other hand, although the search strategy of OHRSA is quite different from that of the conventional SD, their basic philosophy may be deemed as bing reminiscent of each other.

Simulation results have been provided in Section 2.4 to investigate the achievable performance versus the complexity imposed by the OHRSA detector in comparison to those of several reduced-complexity SDs. It was shown in Figure 2.19 that all these low-complexity near-ML detectors are capable of approaching the ML performance. As to the complexity, the OHRSA detector does not always exhibit a lower complexity than its classic counterparts. For example, observed in Figure 2.20 that in a rank-deficient system using 4-QAM the OHRSA detector may indeed impose a significantly lower complexity compared to the conventional SDs. However, it was demonstrated in Figure 2.18 that when 16-QAM or even higher throughput modulation schemes are employed, or when the number of the transmit antennas is not higher than that of the receive antennas, the complexity of the OHRSA detector may in fact becomes higher than that of its conventional SD counterparts. On the other hand, recall from Figure 2.18 that the K-best SD, which is assisted by the complexity-reduction techniques of Section 2.3.2, exhibits a modest complexity in comparison to the depth-first SD.

Chapter 3

Reduced-Complexity Iterative Sphere Detection for Channel Coded MIMO-OFDM Systems

3.1 Introduction

The radio spectrum is a scarce resource. Therefore, one of the most important objectives in the design of future communications systems is the efficient exploitation of the available spectrum, in order to accommodate the ever-increasing traffic demands. Any effort to achieve bandwidth-efficient transmissions over hostile wireless channels typically requires advanced channel coding. Powerful turbo codes were introduced by Berrou in [100, 101] in the context of iteratively decoding two parallel concatenated convolutional codes. His work has later been extended to serially concatenated codes [102] and then found its way gradually into iterative detector designs, such as for example iterative multi-user detectors [103]. Despite their modest complexity, iterative detection and decoding mechanisms are capable of approaching the capacity limits for transmission over wireless MIMO channels.

3.1.1 Iterative Detection and Decoding Fundamentals

3.1.1.1 System Model

Before introducing the channel coding blocks in our MIMO system model, let us briefly review the mathematical model of a SDMA system supporting U users and having N receive antennas at the BS, which is formulated as:

$$\mathbf{y} = \mathbf{H}\mathbf{s} + \mathbf{n}, \tag{3.1}$$

where $\mathbf{y}$, $\mathbf{H}$, $\mathbf{s}$, $\mathbf{n}$ are the $(N \times 1)$-element received signal column vector, the $(N \times U)$-element FDCTF matrix, the $(U \times 1)$-element transmitted signal column vector, and the $(N \times 1)$-element

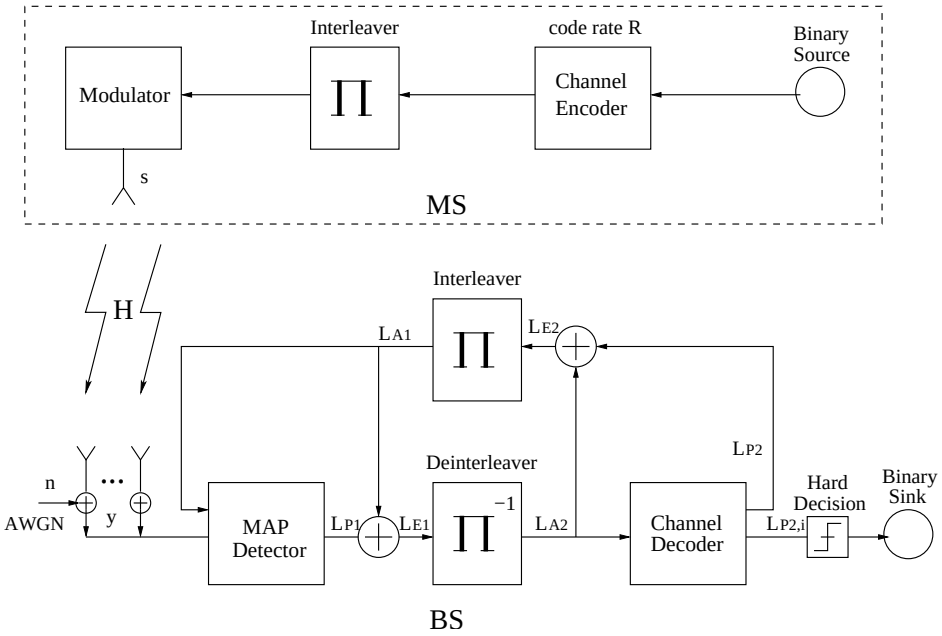

Figure 3.1: Schematic diagram of iterative detection and decoding

AWGN column vector, respectively. Each element s_m of the transmitted signal vector $\mathbf{s}$ can be further represented as $s_u = \text{map}(x^u),\ u = 1, 2, ..., U$, where $\text{map}(\cdot)$ represents a specific bit-to-symbol mapping scheme and $x^{<u>}$ is a $(\log_2 M_c \times 1)$ block of raw bits. In other words, each element of the transmitted signal vector $\mathbf{s}$, i.e. a constellation symbol, contains $\log_2 M_c$ number of information bits.

When no channel encoder is employed at the transmitter, the estimates of the transmitted signal $\mathbf{s}$ can be obtained by the low-complexity near-ML detectors of Chapter 2. Note that all the low-complexity near-ML SDs we encountered so far in Chapter 2 are HIHO detectors.

Thanks to the employment of channel coding, the SNR required for achieving a desirable BER may be further reduced. Hence in Figure 3.1 a MIMO system employing a channel encoder and an iterative receiver is portrayed. The interleaver and deinterleaver pair seen at the receiver side of Figure 3.1 divides the receiver into two parts, namely, the inner MAP detector and the outer decoder. Note that in Figure 3.1, the subscript '1' denotes variables associated with the inner detector, while the subscript '2' represents variables associated with the outer channel decoder. It was detailed throughout [104] and [105] that the iterative exchange of extrinsic information between these serially concatenated receiver blocks results in substantial performance improvements. In this treatise we assume familiarity with the classic turbo detection principles [104]. Natually, the inner MIMO detector has to be capable of processing the soft-bit information provided by the soft-output channel decoder. On the other hand, the outer channel decoder also has to be capable of processing the soft reliability information provided by the soft-output inner MIMO detector. The resultant soft bit information is iteratively exchanged between the inner MIMO detector and the outer channel decoder.

3.1.1.2 MAP Bit Detection

In contrast to the conventional HIHO detector, which outputs hard symbol decisions, and hence results in hard bit decisions also at the output of the demodulator, the inner MIMO detector of Figure 3.1 has to be capable of providing soft bit reliability information for further processing by the outer channel decoder. The advantage of providing soft bit information is that the channel decoder benefits from exploiting the reliability information provided by the detector and returns to the detector its improved-confidence soft-information in the interest of iteratively improving the resultant *A Posteriori* Probability (APP). Hence, the probability of bit errors is minimized. This SISO scheme may be referred to as a MAP detector. Conventionally, the APP is quantified in terms of the Log-Likelihood Ratio (LLR) as [104]:

$$L_D(x_k|\mathbf{y}) = \ln \frac{P[x_k = +1|\mathbf{y}]}{P[x_k = -1|\mathbf{y}]}, \tag{3.2}$$

where $\mathbf{y}$ is the received symbol vector, and x_k, $k = 0, 1, ..., U \cdot \log_2 M_c - 1$ is the kth element of the corresponding transmitted bit vector $\mathbf{x}$. Since the bits in the vector $\mathbf{x}$ have been channel encoded and scrambled by the interleaver, we may assume that the bits of the vector $\mathbf{x}$ are statistically independent of each other. With the aid of Bayes' theorem, the LLRs of Eq.(3.2) can be rewritten as [51] [106]:

$$\begin{aligned} L_D(x_k|\mathbf{y}) &= \ln \frac{p(\mathbf{y}|x_k = +1)P[x_k = +1]/p(\mathbf{y})}{p(\mathbf{y}|x_k = -1)P[x_k = -1]/p(\mathbf{y})} && (3.3)\\ &= \ln \frac{P[x_k = +1]}{P[x_k = -1]} + \ln \frac{p(\mathbf{y}|x_k = +1)}{p(\mathbf{y}|x_k = -1)} && (3.4)\\ &= L_A(x_k) + \underbrace{\ln \frac{\sum_{\mathbf{x}\in\mathbb{X}_{k,+1}} p(\mathbf{y}|\mathbf{x}) \cdot \exp \sum_{j\in\mathbb{J}_{k,x}} L_A(x_j)}{\sum_{\mathbf{x}\in\mathbb{X}_{k,-1}} p(\mathbf{y}|\mathbf{x}) \cdot \exp \sum_{j\in\mathbb{J}_{k,x}} L_A(x_j)}}_{L_E(x_k|\mathbf{y})}, && (3.5) \end{aligned}$$

where $\mathbb{X}_{k,+1}$ represents the set of $\frac{M_c^U}{2}$ number of legitimate transmitted bit vectors $\mathbf{x}$ associated with $x_k = +1$, and similarly, $\mathbb{X}_{k,-1}$ is defined as the set corresponding to $x_k = -1$. Specifically, we have:

$$\mathbb{X}_{k,+1} = \{\mathbf{x}|x_k = +1\}, \mathbb{X}_{k,-1} = \{\mathbf{x}|x_k = -1\}. \tag{3.6}$$

Note here that the value of $x_k = -1$ represents a logical value of 0, while $x_k = 1$ represents a logical value of 1. Furthermore $\mathbb{J}_{k,\mathbf{x}}$ is the set of indices j, which is defined as:

$$\mathbb{J}_{k,\mathbf{x}} = \{j|j = 0, 1, ..., U \cdot \log_2 M_c - 1, j \neq k\}. \tag{3.7}$$

The *a priori* LLR value L_A defined for the jth bit is given by [104]:

$$L_A(x_j) = \ln \frac{P[x_j = +1]}{P[x_j = -1]}. \tag{3.8}$$

According to [51], following a number of manipulations, the *a posteriori* LLR value can be expressed with the aid of the *a priori* LLRs as:

$$L_D(x_k|\mathbf{y}) = L_A(x_k) + \underbrace{\ln \frac{\sum_{\mathbf{x}\in\mathbb{X}_{k,+1}} p(\mathbf{y}|\mathbf{x}) \cdot \exp(\frac{1}{2}\mathbf{x}_{[k]}^T \cdot \mathbf{L}_{A,[k]})}{\sum_{\mathbf{x}\in\mathbb{X}_{k,-1}} p(\mathbf{y}|\mathbf{x}) \cdot \exp(\frac{1}{2}\mathbf{x}_{[k]}^T \cdot \mathbf{L}_{A,[k]})}}_{L_E(x_k|\mathbf{y})}, \tag{3.9}$$

where the subscript $[k]$ denotes the exclusion of the kth element of a vector. Hence, $\mathbf{x}_{[k]}$ represents a specific sub-vector of the bit vector $\mathbf{x}$ obtained by omitting the kth component and retaining the rest of them. Similarly, $\mathbf{L}_{A,[k]}$ represents the specific sub-vector of the *a priori* LLR vector $\mathbf{L}_A$ obtained by excluding the kth element, where $\mathbf{L}_A$ is the vector containing the *a priori* LLR value of all the bits in $\mathbf{x}$.

Observe from Eq.(3.9) that the *a posteriori* LLR is equal to the sum of the *a priori* LLR and the so-called *extrinsic* LLR, which is the second component in the equation. Note that although the above derivation of the soft reliability information is valid for the bit vector $\mathbf{x}_1$ which is associated with the inner MIMO detector, the subscript '1' is omitted, since Eq.(3.9) also holds for the bit vector $\mathbf{x}_2$ associated with the outer channel code. Assuming that an AWGN channel is encountered, the conditional probability of receiving the MIMO output signal $\mathbf{y}$, provided that $\mathbf{x}$ was transmitted , namely $p(\mathbf{y}|\mathbf{x})$, can be computed as:

$$p(\mathbf{y}|\mathbf{s} = map(\mathbf{x})) = \frac{\exp[-\frac{1}{2\sigma_w^2} \cdot ||\mathbf{y} - \mathbf{H}\mathbf{s}||^2]}{(2\pi\sigma_w^2)^N}, \tag{3.10}$$

where the denominator is a constant when the noise variance $2\sigma_w^2$ is constant, hence it can be omitted in the calculation of the LLR values. In order to reduce the computational complexity imposed, the *Jacobian logarithm* [104] may be employed to approximate the *extrinsic* LLRs as follows:

$$\begin{aligned} jac\ln(a_1, a_2) &= \ln(e^{a_1} + e^{a_2}), & (3.11)\\ &= \max(a_1, a_2) + \ln(1 + e^{-|a_1 - a_2|}), & (3.12) \end{aligned}$$

where the second term may be omitted in order to further approximate the original log value, since $\ln(1 + e^{-|a_1 - a_2|})$ can be regarded as a refinement of the coarse approximation provided by the maximum. Consequently, when using the above-mentioned Jacobian approximation, the extrinsic LLR, i.e. the second term of Eq.(3.9) can be rewritten as:

$$\begin{aligned} L_e(x_k|\mathbf{y}) = \frac{1}{2} \max_{\mathbf{x} \in \mathbb{X}_{k,+1}} \{-\frac{1}{\sigma_w^2}||\mathbf{y} - \mathbf{H}\mathbf{s}||^2 + \mathbf{x}_{[k]}^T \cdot \mathbf{L}_{A,[k]}\} \\ - \frac{1}{2} \max_{\mathbf{x} \in \mathbb{X}_{k,-1}} \{-\frac{1}{\sigma_w^2}||\mathbf{y} - \mathbf{H}\mathbf{s}||^2 + \mathbf{x}_{[k]}^T \cdot \mathbf{L}_{A,[k]}\}, \end{aligned} \tag{3.13}$$

which represents the information exchanged between the inner MIMO detector and the outer channel decoder, as seen in Figure 3.1.

3.1.2 Chapter Contributions and Outline

Even with the aid of the Jacobian approximation of Eq. (3.12), the calculation of the *extrinsic* LLR value using Eq. (3.13) may still impose an excessive computational complexity, depending on the number of users U and on the constellation size M_c of the modulation scheme employed, since a brute-force full-search has to be carried out by the MAP detector in order to find the joint maximimum of the two terms of Eq. (3.13). From our discourse on the SD scheme provided in Section 2.2 as well as in the light of the corresponding complexity reduction techniques of Section 2.3, we may argue that the HIHO SD constitutes a computationally efficient solution to

the ML detection problem in uncoded MIMO systems. For the sake of approaching the channel capacity at a low complexity, the SISO SD algorithm was contrived by Hochwald and ten Brink in [51], where a list of the best hypothesized transmitted MIMO symbol candidates was generated, which was representative of the entire lattice in computing the soft bit information, resulting in the concept of the LSD of Section 3.2.1. However, in order to achieve a good performance, when the LSD is employed in an iterative detection aided channel coded system, the list size has to remain sufficiently large, resulting in a potentially excessive complexity. Hence, for the sake of further reducing the complexity imposed by the LSD of Section 3.2.1, we proposed various solutions to the problem of how to maintain a near-MAP performance with the aid of a small candidate list size. More specifically, the novel contributions of this chapter are as follows:

- *Our discovery is that in contrast to the conventional SD, it is plausible to set the search center of the SD to a point which is typically closer to the real ML solution than the conventional LS or MMSE solution. Commencing the search from a more accurate search center may be considered as a process of search-complexity reduction.*

- *A generic center-shifting SD scheme is proposed for channel coded iterative receivers based on the above-mentioned perception, which substantially reduces the detection complexity by decomposing it into two stages, namely the iterative search-center-update phase and the reduced-complexity search around it. Three search-center-update algorithms are devised in order to iteratively shift the search center to a point closer to the true ML point with the aid of the soft-bit-information delivered by the outer channel decoder.*

- *We propose a novel complexity-reduction scheme, referred to as the Apriori-LLR-Threshold (ALT) based technique for the LSD, which is also based on the exploitation of the soft-bit-information, namely, the a priori LLRs provided by the outer channel decoder in the context of iterative detection aided channel coded systems.*

- *We significantly improve the performance of the conventional two-stage SD-aided turbo receiver by intrinsically amalgamating our proposed center-shifting-assisted SD with the decoder of a Unity-Rate-Code (URC) having an Infinite Impulse Response (IIR), both of which are embedded in a channel-coded SDMA/OFDM transceiver, hence creating a powerful three-stage serially concatenated scheme. Moreover, for the sake of achieving a near-capacity performance, Irregular Convolutional Codes (IrCCs) are used as the outer code for the proposed iterative center-shifting SD aided three-stage system.*

- *The convergence characteristics of the proposed schemes are visualized and analyzed with the aid of EXIT charts. Furthermore, performance versus complexity comparsions are carried out amongst the above-mentioned novel schemes.*

The remainder of this chapter is organized as follows. The fundamentals of the conventional LSD are briefly reviewed in Section 3.2.1, followed by a discussion on the center-shifting theory in the context of the SD in Section 3.2.2, which partitions the SD into two parts, i.e. the search-center-update phase and the search around it. Then, three search-center-update algorithms are contrived in Section 3.2.3 in order to iteratively update the search center to a point, which is expected to be increasingly closer to the true ML MIMO symbol point. This search-center-update

is achieved by exploiting the soft-bit-information delivered of the outer channel decoder in the iterative receiver. The ALT based SD scheme is devised in Section 3.3 in the interest of achieving a complexity reduction, which also relies on the exploitation of the soft-bit-information gleaned from the outer channel decoder, but in a different manner in comparison to the center-shifting SD scheme of Section 3.2. In Section 3.4 we demonstrate that the iterative decoding convergence of the conventional two-stage system may be improved by constructing a three-stage system with the aid of the URC encoder/decoder pair of Figure 3.37. Furthermore, IrCCs are employed as the outer code for the proposed iterative center-shifting SD aided three-stage system for the sake of achieving a near-capacity performance. Finally, we summarize the findings of this chapter and provide our concluding remarks in Section 3.5.

3.2 Channel Coded Iterative Center-Shifting SD

3.2.1 Generation of the Candidate List

3.2.1.1 List Generation and Extrinsic LLR Calculation

The inner MIMO detector seen in Figure 3.1 is chosen to be one of the SDs detailed in Chapter 2, in order to approach the MAP performance, while avoiding a potentially excessive computational complexity, which is likely to be encountered by the employment of the conventional MAP detector. However, when calculating the soft information generated by the HIHO SD of Section 2.2, finding the ML solution of $\hat{\mathbf{s}}_{\mathbf{ML}} = arg\min_{\check{\mathbf{s}}\in M_c^U} ||\mathbf{y}-\mathbf{H}\mathbf{s}||^2$ does not necessarily solve the problem of maximizing the two terms in Eq.(3.13), because here the search for $\mathbf{s}_{ML} = arg\min_{\check{\mathbf{s}}\in M_c^U} ||\mathbf{y}-\mathbf{H}\mathbf{s}||^2$ in each term is carried out in the bit-domain having $x_k = 1$ or $x_k = -1$, rather than in the original MIMO-symbol domain in the scenario of HIHO SD. Therefore, conventional SDs cannot be directly employed in the iterative detection scheme shown in Figure 3.1, because the ML solution $\mathbf{s}_{ML}$ provides us with a single hard-decision based MIMO symbol value, rather than the required bit-based soft information. Fortunately, based on the idea that although the MIMO bit vector for maximizing the two terms in Eq.(3.13) is not necessarily the ML MIMO-symbol solution $\mathbf{s}_{ML}$, the bit-vector is typically located near the ML MIMO-symbol solution $\mathbf{s}_{ML}$. Hence, finding the MIMO bit-vector which maximizes the two terms of Eq.(3.13) does not require the full search of the entire lattice. Similarly to the conventional SD, the search can be carried out in a significantly smaller hyper-sphere containing the ML solution $\mathbf{s}_{ML}$, but instead of simply finding the ML solution, the SD has to output a list $\mathcal{L}$, which contains the ML solution as well as its neighbours, which might constitute the MIMO bit-vector maximizing the two terms of Eq.(3.13) with a high probability. Finally, by doing the substraction between the two obtained values of the OFs corresponding to the two terms of Eq.(3.13), we can get the *extrinsic* LLR required.

Based on the above discussions, simple modifications of the conventional depth-first SD of Section 2.2.2 may be carried out by appropriately modifying: (1) the search radius update strategy; (2) modifying output stack for storing the aforementioned list $\mathcal{L}$. As to the search radius, it has to be constant all the time during the search regardless whether a new signal point was found. However, this does not mean that there is no need for calculating the Euclidean distance between the newly

obtained signal point and the received signal point, because their distance is used as the metric controlling the update of the output stack. Again, the output stack was introduced for storing the aforementioned list $\mathcal{L}$. Let us assume that the size of $\mathcal{L}$ is preset to be $\mathcal{N}_{cand}$. When a new signal point is found inside the sphere, two possible actions may be taken: 1). the newly obtained signal point is added directly to the output stack $\mathcal{L}$, provided that it is not full; 2). if the stack is already full, the new signal point is compared to the element having the largest distance from the received signal point, and replaces it if the new signal point has a smaller distance. Consequently, the resultant list $\mathcal{L}$ contains the ML solution as well as $(\mathcal{N}_{cand}-1)$ number of candidates which are close to the former. According to [107], during the generation of the candidate list $\mathcal{L}$, the search radius can only be reduced to the value of the maximum distance metric found in the list $\mathcal{L}$, if the output stack is full. Based on this intuition, if there are more signal vectors having $x_k = 1$, the resultant soft reliability information indicates with a high probability that the kth bit is a logical one. On the other hand, if there are more signal vectors having $x_k = -1$, a reasonable decision can be made implying that the kth bit is a logical zero. Hence, we can finally rewrite Eq.(3.13) for the list sphere detector as:

$$L_e(x_k|\mathbf{y}) \approx \frac{1}{2}\max_{\mathbf{x}\in\mathcal{L}\cap\mathbb{X}_{k,+1}}\{-\frac{1}{\sigma_w^2}||\mathbf{y}-\mathbf{Hs}||^2+\mathbf{x}_{[k]}^T\cdot\mathbf{L}_{A,[k]}\} - \frac{1}{2}\max_{\mathbf{x}\in\mathcal{L}\cap\mathbb{X}_{k,-1}}\{-\frac{1}{\sigma_w^2}||\mathbf{y}-\mathbf{Hs}||^2+\mathbf{x}_{[k]}^T\cdot\mathbf{L}_{A,[k]}\} \tag{3.14}$$

The above approximation becomes an equality, when the output stack $\mathcal{L}$ contains the entire lattice, i.e. we have $\mathcal{N}_{cand} = M_c^U$. However, as mentioned before, the maximizer of both two terms of Eq.(3.14) is located near the ML solution, hence the size of the list $\mathcal{L}$ required to achieve a desired performance is typically far smaller than M_c^U.

As to the application of the K-Best SD of Section 2.2.3 in our channel coded system, the list generation is more straightforward than for its depth-first counterpart discussed previously in this section. Specifically, instead of generating a single signal vector after the breadth-first tree search, which is expected to be the near-ML solution, the K-Best SD retains $\mathcal{N}_{cand}$ number of the best tree leaf candidates having the lowest accumulated Euclidean distances from the received signal point $\mathbf{y}$. Eventually, after backtracking from these tree leaves, $\mathcal{N}_{cand}$ number of signal vectors can be generated, constituting the list $\mathcal{L}$.

3.2.1.2 Computational Complexity of List SDs

Let us now quantify the computational complexity of both the soft-output LSD and the exact MAP detectors in terms of the number of OF evaluations, which corresponds to the two terms in Eq.(3.14). As mentioned previously, the approximation in Eq.(3.14) becomes an equality, when $\mathcal{L}$ represents the entire search space, constituted by $\mathcal{N}_{cand} = M_c^U = 2^{U\cdot BPS}$ number of OF evaluations, where BPS is the number of bits per symbol. Therefore, the complexity of the exact MAP detector can be calculated as the total number of OF evalutions given by:

$$\mathcal{C}_{MAP} = U\cdot BPS\cdot 2^{(U\cdot BPS)}. \tag{3.15}$$

Clearly, the complexity grows exponentially with the product of the number of users U and the number of bits per symbol BPS. Let us consider an 8-user 4QAM SDMA system as an example.

It corresponds to a complexity of $\mathcal{C}_{MAP} = 1,048,576$ OF evaluations, which is excessive. If a 16QAM scheme is employed, the complexity is increased to $1.3744 \cdot 10^{11}$ OF evaluations, which is implementationally infeasible.

As to the computational complexity imposed by the LSD of Section 3.2.1.1, it may be significantly reduced by generating a list of candidates having a length of $\mathcal{N}_{cand}$, where we have $2^{U \cdot BPS} \geq \mathcal{N}_{cand} \geq 1$, since the corresponding complexity can be expressed as:

$$\mathcal{C}_{MAP} = U \cdot BPS \cdot \mathcal{N}_{cand}. \tag{3.16}$$

Consequently, the complexity has become linearly proportional to the length of the list $\mathcal{L}$. In the following sections, we can observe that the value of $\mathcal{N}_{cand}$ can be set to a small fraction of $2^{U \cdot BPS}$, especially when a high-throughput modulation scheme, e.g. 64QAM, is employed and/or a high number of users are supported by the system.

3.2.1.3 Simulation Results and 2D-EXIT Chart Analysis

Our forthcoming EXIT chart analysis and Monte Carlo simulations, if not stated otherwise, will be carried out in the scenario of (8×4)-element rank-deficient 4QAM SDMA/OFDM systems, under the simplifying assumptions that perfect channel estimation is available at the BS and that the channel is time-invariant. Note that the power delay profile of the 3-path frequency-selective channel considered is given by $P(\tau) = \sum_{k=0}^{2} P(\tau_k)\delta(t - k\tau)$, where τ is the delay spread and we have $P(\tau_k) = [0.5\ 0.3\ 0.2]$ for $k = 0,\ 1,\ 2$. We employ a constraint-length $K_c = 3$, half-rate Recursive Systematic Convolutional (RSC) code RSC(2,1,3) having the octally represented generator polynomials of (6/13). The length of the interleaver between the channel encoder and the modulator/mapper is $10,240$ bits. It is reasonable to set the length of the list to be the same as the parameter K of the K-best SD, which represents the maximum number of candidates to be retained at each search tree level. Our system parameters are summarized in Table 3.1.

Figure 3.2 depicts the EXIT functions of both the K-Best LSD and of the outer convolutional decoder. Observe in Figure 3.2 that the EXIT curve corresponding to the SD, which we refer to as the inner decoder, intersects that of the outer decoder before reaching the convergence point of $[I_A(MUD) = 1, I_E(MUD) = 1]$. Therefore, regardless of the number of iterations invoked and the length of the interleaver, residual errors may persist at this specific SNR$=$ 8dB. More importantly, as seen in Figure 3.2, the shape of the EXIT curve of the inner decoder depends significantly on the size of the list $\mathcal{N}_{cand}$ employed, which is equal to K in all forthcoming simulations. Specifically, having a longer list leads to a steeper and hence more beneficial slop of the EXIT curve. In other words, the EXIT curves of the inner decoder and the outer decoder will intersect at a higher $[I_A, I_E]$ value, when the list is extended. The phenomenon that the inner decoder's EXIT curve may even decay as the *a priori* information fed back by the outer decoder increases can be explained by the fact that the inner and outer decoders exchange flawed information owing to a shortage of candidate solutions, more particularly owing to the absence of the ML solution in the candidate list, which is not long enough. Consequently, the maximum achievable iteration gain may be significantly reduced, when employing a very small list, althought as expected the overall computational complexity imposed by the soft-bit-information calculation is substantially reduced. Furthermore, we can infer from Figure 3.2, that the BER performances corresponding to different

System Parameters	Choice
System	SDMA/OFDM
Number of Sub-Carriers	128
Uplink/Downlink	Uplink
Modulation	4QAM
Number of Users/Transmit Antenna	8
Number of Receive Antennas	4
Transmit Antennas per User	1
Block Length	10240 bits
CIR Model	$P(\tau_k) = [0.5\ 0.3\ 0.2]$, for $k = 0,\ 1,\ 2$
CIR Tap Fading	OFDM symbol invariant
Channel Estimation	Ideal
Detector/MAP	K-Best List-SD
List Length $\mathcal{N}_{cand}$	$=K$
Channel Encoder	RSC(2,1,3)
	Generator Polynomials (6/13)
	Code Termination (Off)
No. of Iterations (Variable)	Iterations terminate as soon as the resultant trajectory line reaches the convergence point

Table 3.1: Summary of system parameters for the K-best SD aided coded SDMA/OFDM system

list sizes do not dramatically differ from each other at low SNRs, when the open tunnel between the EXIT curves of the inner and outer decoders closes at low $[I_A, I_E]$ values. This is because all inner EXIT curves corresponding to different list sizes have similar $[I_A, I_E]$ starting points for a given SNR. On the other hand, a higher iteration gain can be ahieved by a longer list at high SNRs. These inferences can be verified by the BER results depicted in Figure 3.3.

Figure 3.3 compares the achievable BER performances of the K-best LSD aided iterative detector having different list sizes in the scenario of the (8×4) rank-deficient SDMA/OFDM system. It can be seen that compared to the uncoded system a signifcant performance gain is achieved by employing the channel encoder/decoder. Moreover, the attainable performance can be further improved by invoking the iterative detection scheme of Figure 3.1 which exchanges soft information between the inner decoder, i.e. the soft-output K-best SD and the convolutional decoder. The difference between the attainable iteration gains exhibited by the inner decoder using different list sizes remains insignificant until the SNR increases to about 5dB, which is also the convergence threshold of the inner decoder having the list length of $K = 128$. The convergence threshold associated with the list length of $K = 32$, on the other hand, is about 7dB. In other words, useful iteration gain can only be observed for relatively high SNRs, provided that a sufficiently high list length is employed. Hence, the BER performance suffers from having an insufficiently long list size. On the other hand, the computational complexity imposed and the memory required by the LSD may be substantially reduced with the aid of iterative detection, as quantified in Table 3.2.

More explicitly, Table 3.2 shows the trade-off between the SNR required and the computational complexity imposed by the K-best LSD/MAP detector at the target BER of 10^{-5}. Note that we

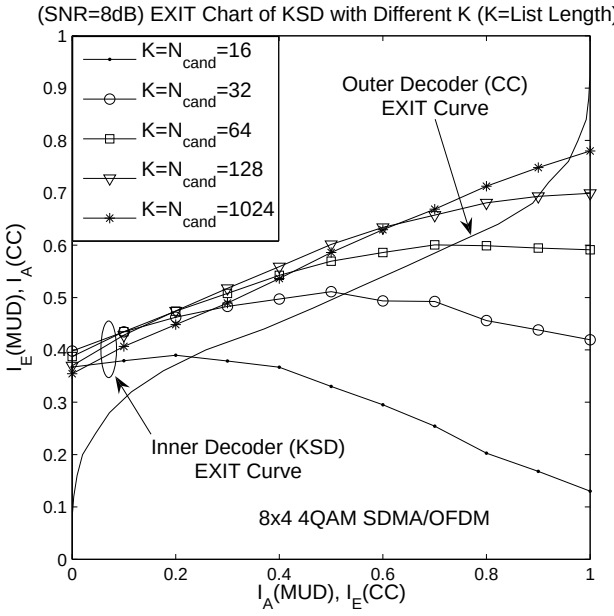

Figure 3.2: 2D-EXIT chart of the *K*-Best SD using different list lengths in the scenario of an (8×4)-antenna 4QAM SDMA/OFDM System at SNR=8 dB. All other system parameters are listed in Table 3.1.

quantify the computational complexity of the list generation in the *K*-best LSD in terms of the total number of PED evaluations according to Eq.(2.31) in Section 2.2.2, whereas we calculate the complexity of the soft information generation at the output of the *K*-best LSD/MAP detector using Eq.(3.16) in terms of the total number of OF evaluations corresponding to the two terms of Eq. (3.14).

Therefore, we can observe from both Figure 3.3 and Table 3.2 that in order to achieve a near-MAP BER performance, we have to set both K and the list size $\mathcal{N}_{cand}$ to at least 1024. In other words, for a given target BER of 10^{-5}, to achieve a performance gain of 3 dB over the system where both K and $\mathcal{N}_{cand}$ are set to 32 in the scenario of an (8×4)-element over-loaded 4-QAM SDM/OFDM system, substantial computational and memory investments have to be made, which requires nearly 19 times more PED evaluations per channel use for the candidate list generation, 32 times more OF evaluations per channel use for the LLR calculation and 32 times more memory requirements per channel use. Although the computational complexity imposed is only a small fraction of that required by the EXACT MAP detector (which requires, for example, more than 10^6 OF evaluations for the LLR calculation in this particular scenario), it is still substantially higher than desirable, especially in heavily rank-deficient systems.

3.2.2 Center-Shifting Theory for SDs

Recall from Sections 2.2 the philosophy of various types of SD is that of finding the ML solution, which minimizes the ML error term of Eq.(2.16), which is then transformed into the problem of finding the specific MIMO symbol, which minimizes the first term of Eq.(2.17) or the first term of

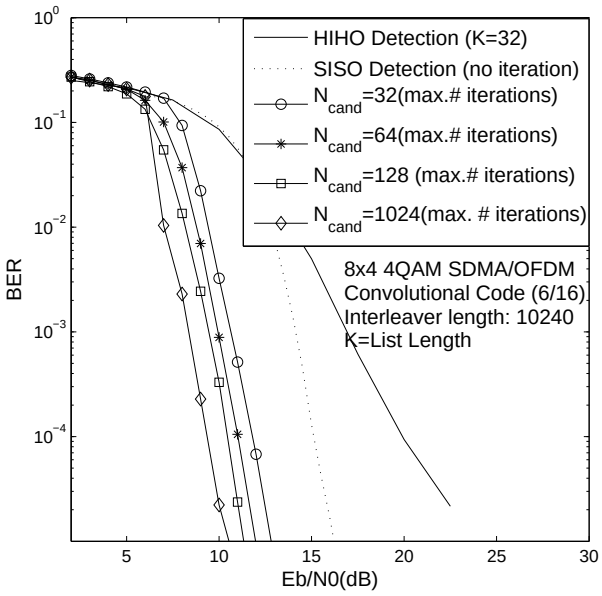

Figure 3.3: The achievable BER performance of the conventional K-Best SD aided iterative detection in the scenario of (8×4)-antenna 4QAM SDMA/OFDM system with different K: In all cases, the maximum iteration gain has been achieved.

Eq.(2.37). More explicitly, according to Eq.(2.19) we have:

$$\hat{\mathbf{s}}_{ML} = arg \min_{\check{\mathbf{s}} \in M_c^U} (\check{\mathbf{s}} - \hat{\mathbf{c}})^H \mathbf{H}^H \mathbf{H} (\check{\mathbf{s}} - \hat{\mathbf{c}}), \tag{3.17}$$

where $\hat{\mathbf{c}} = (\mathbf{H}^H\mathbf{H})^{-1}\mathbf{H}^H\mathbf{y}$ is the unconstrained ML estimate of $\mathbf{s}$, i.e. the LS solution. In addition, according to Eq.(2.40) we arrive at:

$$\hat{\mathbf{s}}_{ML} = arg \min_{\check{\mathbf{s}} \in M_c^U} (\check{\mathbf{s}} - \hat{\mathbf{c}})^H (\mathbf{H}^H\mathbf{H} + 2\sigma_w^2\mathbf{I}) (\check{\mathbf{s}} - \hat{\mathbf{c}}), \tag{3.18}$$

where $2\sigma_w^2$ represents the nosie variance and hence $\hat{\mathbf{c}} = (\mathbf{H}^H\mathbf{H} + 2\sigma_w^2\mathbf{I})\mathbf{H}^H\mathbf{y}$ corresponds to the MMSE solution.

(8×4) **4-QAM SDMA/OFDM Rank-Deficient System**					
BER	**List (=K)**	**Memory**	**SNR(dB)**	**SD Compl.**	**MAP Compl.**
10^{-5}	32	256	14	724	1024 (2 iter.)
	64	512	13.2	1364	2048 (2 iter.)
	128	1024	11.2	2388	4096 (2 iter.)
	1024	8196	10.5	13652	32768 (2 iter.)

Table 3.2: Simulation results of the conventional K-Best LSD aided iterative detection in the scenario of (8×4)-element 4-QAM rank-deficient SDMA/OFDM system as depicted in Figure 3.1: Note that the computational complexity of the list generation by the LSD is calculated in terms of the total number of PED evaluations, while that of the soft information generation by the List SD/MAP detector is computed using Eq.(3.16) in terms of the total number of OF evaluations corresponding to the two terms in Eq.(3.14).

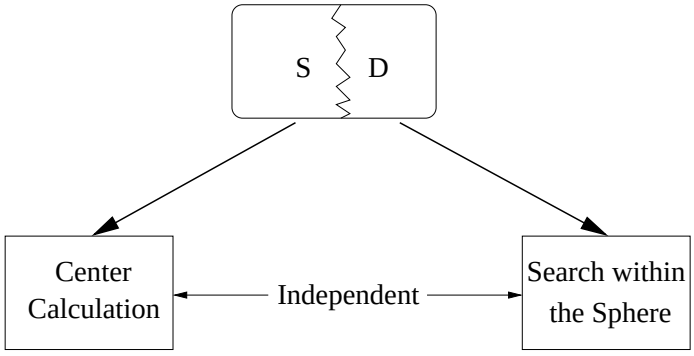

Figure 3.4: Independent SD blocks: the search center calculation and the search.

Therefore, when using SD, the ML solution can be found by creating a reduced-size search-hyper-sphere centered around the LS solution or the MMSE solution and then reducing the search radius when possible. During our investigations of SD, we suggested the plausible idea of setting the search center to a MIMO signal constellation point, which is typically closer to the real ML solution than the conventional LS or MMSE solution. To some extent, extending the search from a more accurate search center can be considered as a process of search-complexity reduction. In fact, the computational complexity reduction achieved by the MMSE-based center over the LS-aided one was quantified in Figure 2.15 in Section 2.3.2. Hence, it is plausible that the closer the search center is located to the real ML solution, the lower the computational complexity, which has been verified by all of our simulations in the context of the SD aided uncoded SDMA/OFDM systems considered.

Consequently, the SD can be split into two independent functional blocks, namely, the center calculation or center update block and the SD's hyper-sphere search block, as shown in Figure 3.4. Hence, the search can be carried out independently of the search center calculation. Thus, the search center can be obtained by arbitrary detection schemes, not only by the conventional LS or MMSE detection scheme. This observation turns the SD into a high-flexiblility detector, which can be readily combined with other well-established linear or non-linear detectors. As a result, the total computational complexity imposed by the SD is constituted by that of the detector which provides the search center for consecutive search operation of Figure 3.4. In other words, the affordable computational complexity can be flexibly split between the center calculation phase and the search phase of Figure 3.4. The simple schematic of Figure 3.4 is further detailed in Figure 3.5, where the triangularization of the channel matrix $\mathbf{H}$ and the PED calculation previously detailed in Section 2.2 is portrayed more explicitly. It is also plausible that an improved performance versus complexity trade-off emerges as the search-center calculation is regularly updated, before further triangularization and PED calculation is carried out as seen in Figure 3.5.

3.2.3 Center-Shifting K-Best SD Aided Iterative Receiver Architetures

The novel idea of center-shifting, which was proposed in the context of an uncoded system in Section 3.2.2 has the benefit of less memory requirements imposed by the K-Best SD, since K can be set a small value. However, the overall computational complexity reduction may still remain modest if the iterative scheme shown in Figure 3.5 is employed, since a fraction of the original computational

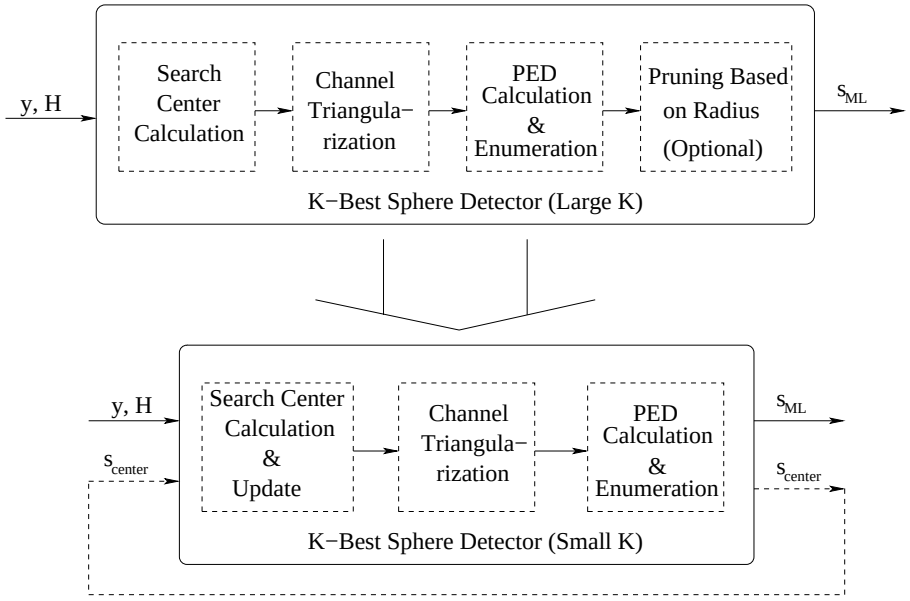

Figure 3.5: The structure of the iterative K-Best SD using center-shifting scheme: The search center of the SD can be set to a more accurate center than the original LS or MMSE solution to allow using small K for the sake of reducing the computational complexity required by each iteration, while maintaining the performance. A benefit of this is that the memory requirements can be largely reduced, although the overall computational complexity remains almost the same as proved by our simulations.

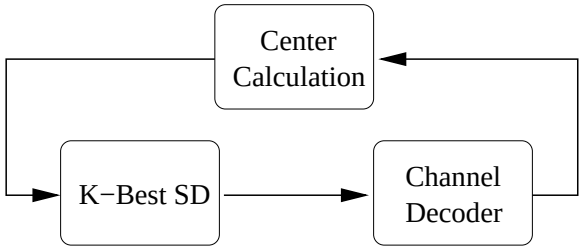

Figure 3.6: Center-shifting-aided K-Best SD in coded system

complexity imposed by the search process is in fact transferred to the center calculation phase. Hence, the overal computational complexity may remain similar to that of the non-iterative SD.

On the other hand, the center-shifting scheme applied for the K-Best SD is expected to become significantly more powerful if it is employed in the scenario of the iterative detection aided channel coded system of Figure 3.6, since the process of obtaining a more accurate search center is further aided by the channel decoder, which substantially contributes towards the total error-correction capability of the iterative receiver. Beneficially, no additional computational complexity is imposed by calculating the search center based on the output of the channel decoder. Note that although the SD process is repeated according to the number of iterations, the overall computational complexity imposed by the iterative receiver may be substantially reduced while maintaining a high BER performance, since K and N_{cand} can be set to substantially lower values when combined with the center-shifting scheme than that required without it.

In our forthcoming discourse on the center-shifting K-Best SD aided iterative reciever, first

(4×4) 16-QAM SDMA/OFDM Full-Rank System				
SNR(dB)	**K**	**No. of Iteration**	**BER**	**Complexity**
20	16	None	$1.481 \times 10^{-}5$	2048
	8	1	0.0188	2048
	4	2	0.0069	8192
	2	4	0.0063	16384
	1	16	0.0001	1230

Table 3.3: Performance versus complexity characterization of self-iterative K-Best SD in full-rank 16QAM systems

(8×4) 4-QAM SDMA/OFDM Rank-Deficient System				
SNR(dB)	**K**	**No. of Iteration**	**BER**	**Complexity**
16	8	1 (upper)	0.15078	2048
		4 (upper)	0.0188	2048
		4(upper), 3(both)	0.0069	8192
	8	6(upper)	0.0063	16384

Table 3.4: Performance versus complexity characterization of iterative K-Best SD in rank-deficient systems

of all, we prospose three different receiver architectures employing different center-calculation schemes. Then we will opt for using the best of the three center-calculation schemes in a Unity-Rate-Code (URC) assisted three-stage iterative receiver in Section 3.4. More explicitly, the schematic of Figure 3.1 is extended in Figure 3.37 of Section 3.4 with a URC decoder. Accordingly, the receiver incorperates the URC's decoder, as seen in Figure 3.37. **During our EXIT-chart-assisted receiver design, our aim is to construct a low-complexity near-MAP detector, which is capable of supporting high-throughput modulation schemes operating in heavily rank-deficient systems.**

3.2.3.1 Direct-Hard-Decision-Center-Update-Based Two-Stage Iterative Architecture

3.2.3.1.1 Receiver Architecture and EXIT-Chart-Aided Analysis

Our first proposed center-calculation scheme is the Direct-Hard-Decsion-Center-Shifting (DHDC) scheme portrayed in Figure 3.7, which calculates the search center for the forthcoming detection iteration by imposing hard decisions on the interleaved *a posteriori* LLRs at the output of the channel decoder. Then it remodulates the resultant bit streams of all the SDMA users, in order to generate the mapped symbol matrix, where each column corresponds to the most-recently obtained search center.

The main purpose of invoking the center-shifting scheme for the K-Best SD in the context of the iterative detection aided system of Figure 3.1 is to increase the maximum attainable iterative gain, while maintaining an affordable complexity. The list size $\mathcal{N}_{cand}$ is equal to the number of tentative MIMO symbol candidates retained at each tree search level, which is set to the lowest possible value in order to reduce the computational complexity imposed. Naturally, additional

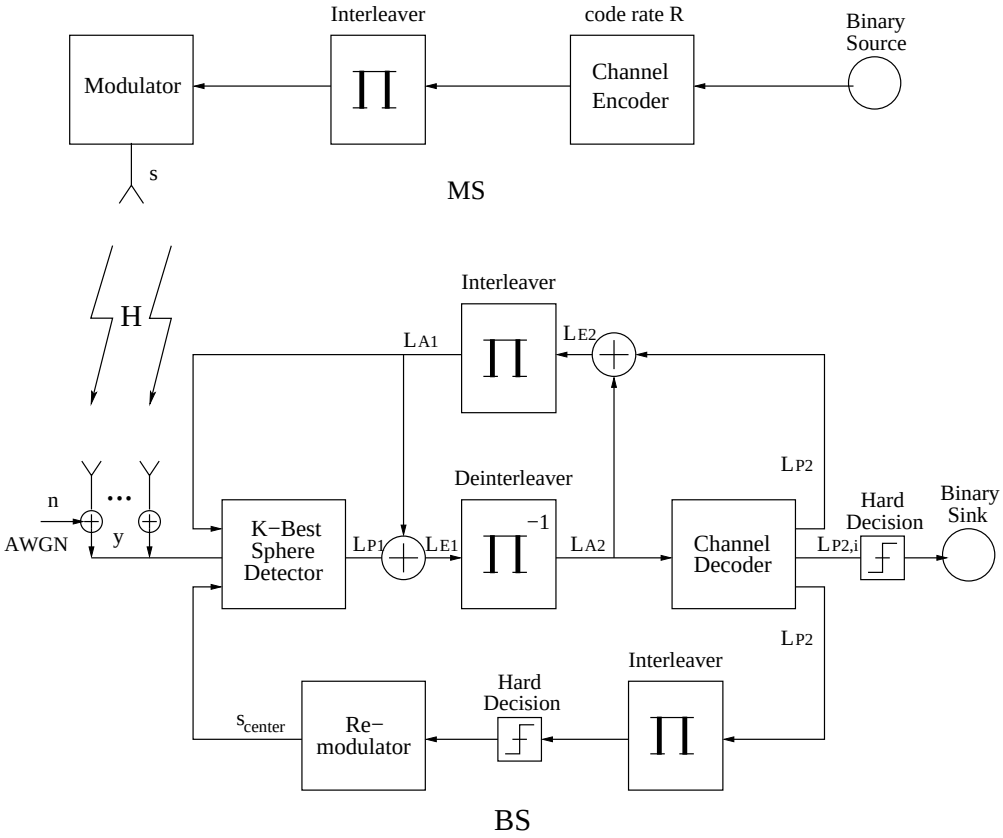

Figure 3.7: DHDC assisted K-best SD-aided iterative detection scheme

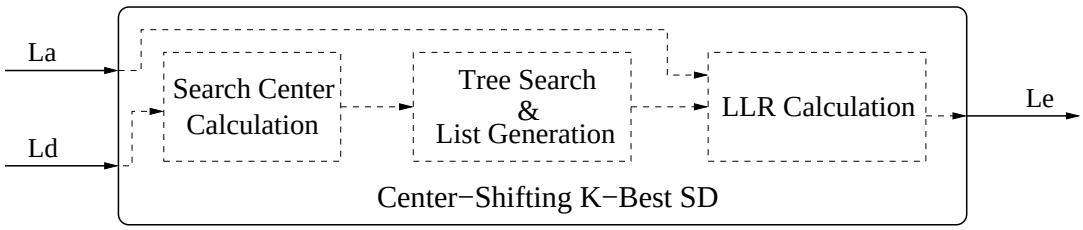

Figure 3.8: Structure of the center-shifting K-Best SD: a two-input one-output block

computational efforts are imposed by the SD based on the updated search center since after a certain number of iterations the candidate list used for the LLR calculation is regenerated. But again, as a whole, the total memory requirements of the K-Best SD and the overall computational complexity imposed by the list generation and the LLR calculation of the K-Best SD is expected to be substantially reduced with the aid of the iterative information exchange between the center-shifting scheme and the channel decoder. In order to investigate the benefits of invoking the center-shifting scheme, EXIT charts are used to analyze the modified SD block, which has two inputs and one output, as shown in Figure 3.8. The center-calculation phase portrayed in Figure 3.4 is transplanted into the SD block of Figure 3.8. The two inputs seen in Figure 3.8 are the *a priori* LLRs and the interleaved *a posteriori* LLRs provided by the channel decoder, whereas the output is the resultant *extrinsic* LLR. As a consequence, we have to employ the 3D-EXIT chart first and then project it to two dimensions, in order to obtain the 2D-EXIT chart of the iterative receiver, as it will be detailed in the context of Figure 3.9.

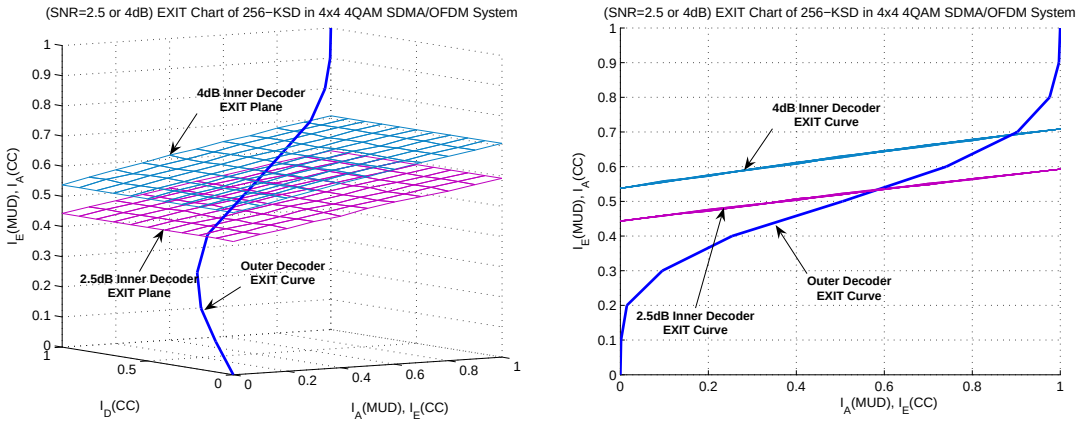

(a) 3D-EXIT Chart Analysis.

(b) (Projection) 2D-EXIT Chart Analysis.

Figure 3.9: EXIT chart analysis of the DHDC based K-best SD aided iterative receiver: Since K is set to 256 in (4×4) 4QAM system, the K-best SD is in fact the exact ML detector. All other system parameters are listed in Table 3.1.

More explicitly, Figure 3.9 depicts the 3D-EXIT chart of the DHDC-aided K-Best SD iterative receiver, where $K = 256$ is used in our (4×4)-element 4QAM SDM/OFDM system. Since the total number of MIMO symbols is $4^4 = 256$, the SD is actually the exact MAP detector, which computes the LLRs by conducting the totally $M \cdot BPS \cdot \mathcal{N}_{cand} = 4 \cdot 2 \cdot 256 = 2048$ OF evaluations, which correspond to the evaluations of the two terms in Eq.(3.14). We evaluate the *extrinsic* Mutual Information (MI), I_E, at the output of the SD, which is quantified on the vertical axis of Figure 3.9(a), after providing the SD with the two inputs required, which correspond to the *a priori* LLRs and the *a posteriori* LLRs gleaned from the channel decoder, respectively. The MI associated with the two inputs, namely I_A and I_D, are quantified on the two abscissa axes, namely on the x-axis and y-axis, respectively. The two parallel EXIT planes of the inner decoder, i.e. the K-Best SD, recorded for different SNRs in Figure 3.9(a) indicate that the *extrinsic* outputing I_E is acctually independent of the input I_D, implying that the DHDC scheme is unable to glean any benefits for the exact MAP detector. This is not unexpected, since the inner EXIT curve seen in Figure 3.9(b), which was obtained by projecting on the 3D-EXIT chart of Figure 3.9(a) to the 2D-EXIT chart on the plane given by the two axes, which quantify the *extrinsic* MI and the *a priori* MI at the the output and input of the MUD, i.e. the SD, respectively, does not encounter the problem of going down as the input MI I_A increases as shown in Figure 3.2 of Section 3.2.1.3. Thus, it depends only on the SNR of the received signal and the *a priori* LLRs. Therefore, we can infer that when the list size is sufficiently high, the EXIT curve of the inner decoder is proportional to the input *a priori* LLRs, whereas the DHDC scheme provides hardly any performance improvement, since it fails to provide an itertive gain.

However, if we reduce the list size $\mathcal{N}_{cand}$ of the SD to a relatively small value, the output *extrinsic* LLRs are no longer independent of the input I_D LLRs, based on which the iterative detection aided DHDC scheme of Figure 3.7 updates the search center of the K-Best SD as seen in Figure 3.10, where the inner and outer EXIT surfaces are depicted for the $K = \mathcal{N}_{cand} = 32$ and

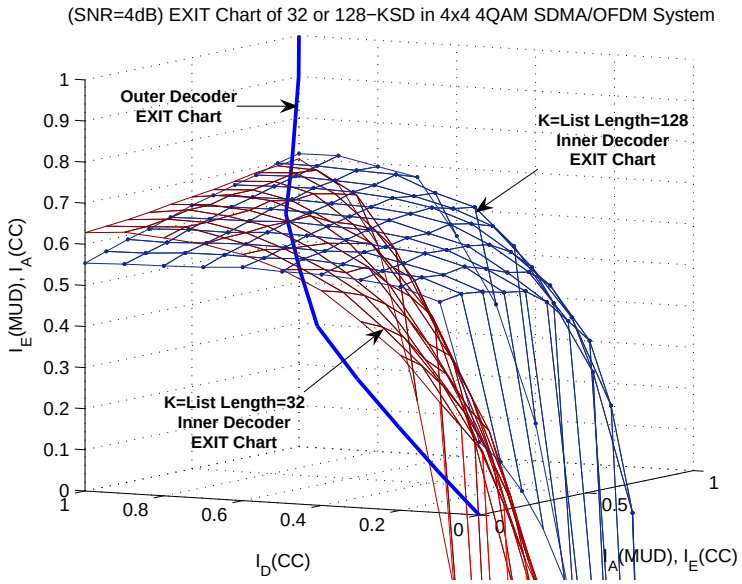

Figure 3.10: 3D-EXIT chart analysis of the DHDC aided K-best SD using $K = 32$ or 128 in the (4×4)-element 4QAM SDMA/OFDM system operating at SNR=4 dB. All other system parameters are listed in Table 3.1.

$K = \mathcal{N}_{cand} = 128$, respectively. More specifically, we can observe from Figure 3.10 that for a given input *a priori* MI I_A, the output *extrinsic* MI I_E is proportional to the input *a posteriori* MI I_D. On the other hand, the relationship between the output I_E and the input I_A represented by the corresponding LLR in Figure 3.8 is quite different, when the other input I_D is fixed. More explicitly, when I_D is not high enough, because the search center is insufficiently accurate, the output I_E seen in Figure 3.10 may not be proportional to the input I_A. However, when the I_D is sufficient high, since the SD carries out detection using an accurate center, which is close to the ML solution, the output I_E is expected to increase proportionally, as the input I_A approaches unity, even for a small value of $\mathcal{N}_{cand}$. In fact, the observations based on Figure 3.10 coincide with the simulation results shown in Figure 3.2, where the EXIT curve of the K-Best SD starts to decrease, despite having increasing value of I_A, when K and $\mathcal{N}_{cand}$ are insufficiently high. In this scenario, having small K and $\mathcal{N}_{cand}$ values may yield a candidate list, which may not contain the ML solution with a high probability, which in turn leads to the flawed information exchanged between the inner decoder and the outer decoder during iterative detection. Consequently, instead of increasing the iterative gain, using more iterations results in a reduced output I_E value for the K-Best SD. However, as a benefit of the center-shifting scheme, we can improve the resultant candidate list without increasing K and $\mathcal{N}_{cand}$, by simply updating the search center to a more accurate one. Hence, the quality of the output soft bit information, i.e. L_E, is improved without increasing the list size $\mathcal{N}_{cand}$ or K. Finally, based on the above discussions, we summarise the aforementioned relationships in Figure 3.11.

Due to the fact that the two inputs of the K-Best SD shown in Figure 3.8, namely, the *a priori* LLRs and the *a posteriori* LLRs are not perfectly independent, whereas the 3D-EXIT chart of Figure 3.10 was obtained by providing the K-Best SD two perfectly independent inputs Gaussian-distributed LLR, it is anticipated that the actual decoding trajectory will deviate from the EXIT-chart predictions. As a result, the iterative detector may not be able to achieve an infinitesimally low BER at the same channel SNR, where the EXIT-chart analysis exhibited a marginally open

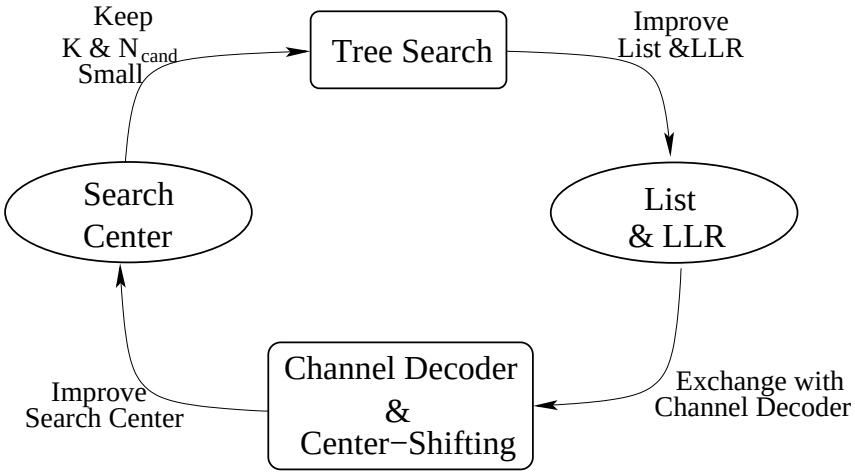

Figure 3.11: Relationship between the search center and the resultant *extrinsic* LLRs when the center-shifting scheme is invoked and K and $\mathcal{N}_{cand}$ are fixed to a relatively small value.

tunnel.

3.2.3.1.2 Simulation Results

Let us now characterize the achievable performance of the DHDC aided K-Best SD iterative receiver in the scenario of an (8×4)-element rank-deficient 4-QAM SDMA/OFDM system. Since the values of K and $\mathcal{N}_{cand}$ were set relatively low, we know from the EXIT chart of Figure 3.2 and the BER curve of Figure 3.3, that the conventional K-Best SD iterative receiver dispensing with center-shifting suffers from a performance degradation compared to the more complex system using $K = \mathcal{N}_{cand} = 1024$. Therefore, it is beneficial to switch off the DHDC scheme of Section 3.2.3.1 during the first a few iterations. However, when the maximum attainable iterative gain is achieved with the DHDC scheme being switched off, the DHDC scheme is activated again in order to update the search center of the K-Best SD. This center-update action may be expected to create a wider EXIT tunnel between the EXIT curves of the inner and outer decoder, potentially facilitating an easier passage of the decoding trajectary through the tunnel. Our system parameters are summarized in Table 3.5.

Figure 3.12 reveals the BER performance improvement brought about by the DHDC-aided K-Best SD iterative receiver over that of the conventional SD iterative receiver using no center-shifting in the scenario of an (8×4)-element rank-deficient SDM/OFDM system. The BER curves of the iterative receiver correspond to a variable number of iterations, which were enabled to iterate until perceivable iterative gains were achieved. Specifically, within the SNR range of 6 - 13 dB, where useful performance improvements can be observed, a maximum performance gain of 2 dB can be achieved by the DHDC scheme over the system using no center-shifting, if we fix the values of K and $\mathcal{N}_{cand}$ to 64. By contrast, a slightly lower performance gain of about 1.5 dB can be attained, if K and $\mathcal{N}_{cand}$ are set to 32, and hence the complexity is reduced by about a factor of four. It is worth emphasizing that the DHDC-aided system associated with $K = \mathcal{N}_{cand} = 64$ is capable of achieving a near-MAP performance, which can only be attained by setting K and $\mathcal{N}_{cand}$ to at least 1024 for the system using non-center-shifting in the heavily rank-deficient scenario considered. Hence, the memory required by the K-Best SD was significantly reduced.

System Parameters	Choice
System	SDMA/OFDM
Number of Sub-Carriers	128
Uplink/Downlink	Uplink
Modulation	4QAM
Number of Users/Transmit Antennas	8
Number of Receive Antennas	4
Transmit Antennas per User	1
Block Length	10240
CIR Model	3-path frequency-selective channel
CIR Tap Fading	OFDM symbol invariant
Channel Estimation	Ideal
Detector/MAP	Center-Shifting-Aided K-Best List-SD
List Length $\mathcal{N}_{cand}$	$= K = 128$
Channel Encoder	RSC(2,1,3)
	Generator Polynomials (6/13)
	Code Termination (Off)
Iteration Mode	Once no more iterative gain can be achieved by the conventional iterative receiver, the center-shifting function is switched on

Table 3.5: Summary of system parameters for the *K*-Best SD aided coded SDM/OFDM System

More importantly, the associated computational complexity is also expected to be substantially reduced, if we consider $SNR = 8$ dB in Figure 3.13, where the corresponding EXIT chart is portrayed. Figure 3.13(a) depicts the 3D EXIT chart of the DHDC-aided *K*-Best SD iterative receiver in the scenario of an (8×4)-element rank-deficient system. Since the function of DHDC center-shifting scheme is only switched on when the maximum iterative gain of the scheme using no center-shifting is achieved, i.e., when the resultant trajectory reaches the crossing point of the EXIT curves of the inner and the outer decoder, the stair-case-shaped decoding trajectory follows exactly the same path as with the DHDC scheme disabled, until it reaches the intersection. Then, with the aid of the increasingly accurate search center provided by the DHDC center-shifting scheme, the decoding trajectory continues to evolve through the tunnel of Figure 3.13(a) between the 3D-EXIT surface of the inner decoder and the EXIT curve of the outer decoder, both of which are obtained by considering the *a posteriori* LLR values. The resultant additional iterative gain brought about by the DHDC scheme may be more explicitly observed if we refer to the projection of the 3D-EXIT chart depicted in Figure 3.13(b). As we can observe, the maximum MI measured at the output of the channel decoder of the iterative receiver using no center-shifting is about $I_E = 0.85$ after four iterations exchanging *extrinsic* information between the inner and outer decoder. By contrast, the maximum achievable MI approaches about $I_E = 0.95$ with the aid of the DHDC scheme when activating three additional iterations, hence resulting in a further reduced BER.

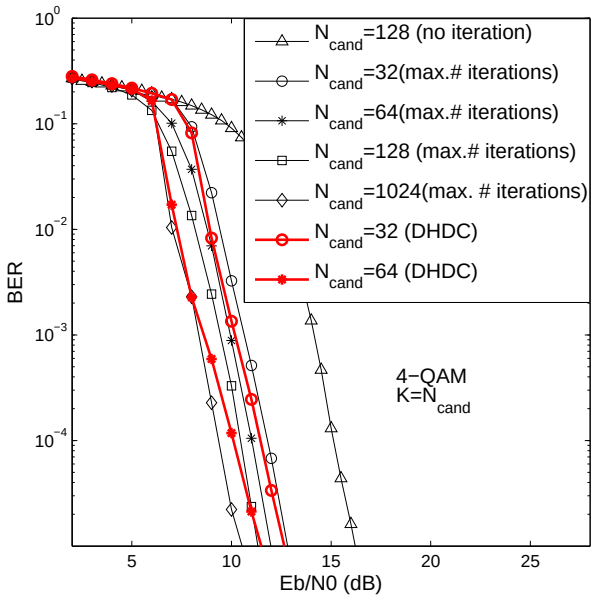

Figure 3.12: BER performance improvement brought about by the DHDC scheme in the context of an (8×4)-element rank-deficient SDM/OFDM system: significant BER performance improvement can be achieved by the employment of the DHDC scheme. All other system parameters are listed in Table 3.1.

3.2.3.2 Two-Stage Iterative Architecture Using a Direct Soft Decision Center-Update

In Section 3.2.3.1 we updated the search center of the SD by making hard decisions at the output of the channel decoder when generating the *a posteriori* LLRs. Given this simple center-update strategy, the center-shifting scheme was capable of achieving evident performance gains as we can see in Figure 3.12 of Section 3.2.3.1.2. However, the attainable performance improvements are expected to be increased by exploiting the slightly more sophisticated center-calculation technique of the Direct-Soft-Decision-Center-Shifting (DSDC) scheme, to be introduced in our forthcoming discourse. These further improvements are expected, because the action of subjecting the LLRs to hard decisions discards the useful soft information contained in the LLRs, which indicates how reliable our estimate of the most recently obtained center is. Consequently, in DSDC scheme we calculate the soft-LLRs of the symbols based on the interleaved soft-bit-information. Then the SD carries out the detection again with this newly obtained search center during the next iteration.

3.2.3.2.1 Soft-Symbol Calculation

Since the *a posteriori* soft-bit-information delivered from the channel decoder to the SD is defined to be the logarithm of the bit-probability ratios of its two legitimate values [104], namely of $+1$ and -1, given the received signal vector $\mathbf{y}$, formulated in Eq.(3.2). For convenience, we rewrite Eq.(3.2) as follows:

$$L(x_k|\mathbf{y}) = \ln \frac{P[x_k = +1|\mathbf{y}]}{P[x_k = -1|\mathbf{y}]}. \tag{3.19}$$

Therefore, bearing in mind that we have $P[x_k = +1|\mathbf{y}] = 1 - P[x_k = -1|\mathbf{y}]$, and taking the exponent of both sides in Eq.(3.19), it is possible to derive the probability that $x_k = +1$ or

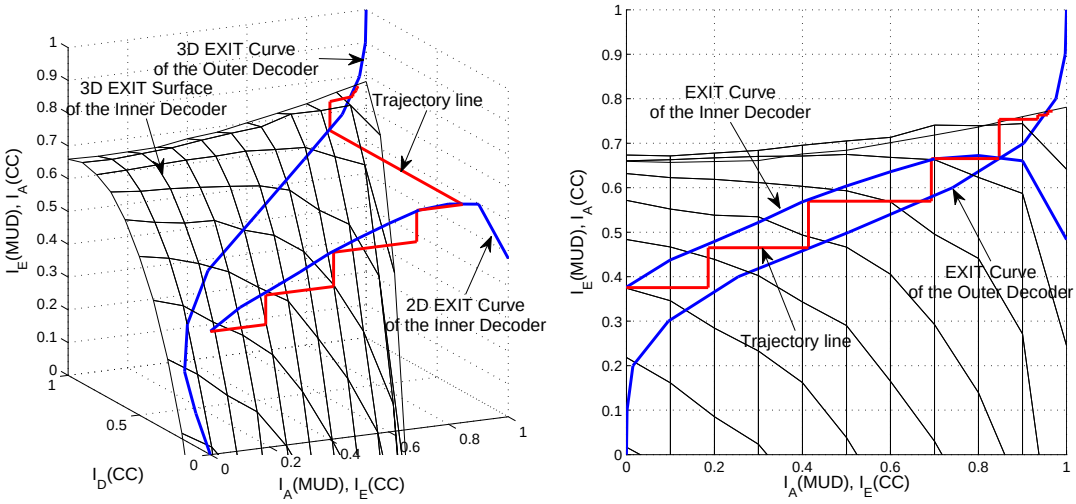

(a) 3D-EXIT Chart Analysis.

(b) (Projection) 2D-EXIT Chart Analysis.

Figure 3.13: EXIT Chart Analysis of Direct-Hard-Decision-Center-Shifting K-Best SD Aided Iterative Receiver In the Scenario of (8×4) Rank-Deficient 4-QAM SDMA/OFDM System. (SNR=8 dB, $K = \mathcal{N}_{cand} = 128$). All other system parameters are listed in Table 3.1.

$x_k = -1$ was transmitted in terms of their LLRs as follows:

$$e^{L(x_k|\mathbf{y})} = \frac{P[x_k = +1|\mathbf{y}]}{1 - P[x_k = +1|\mathbf{y}]}. \tag{3.20}$$

From Eq.(3.20) we arrive at:

$$\begin{aligned} P[x_k = +1|\mathbf{y}] &= \frac{e^{L(x_k|\mathbf{y})}}{1 + e^{L(x_k|\mathbf{y})}} \\ &= \frac{1}{1 + e^{-L(x_k|\mathbf{y})}}. \end{aligned} \tag{3.21}$$

Similarly, we have:

$$P[x_k = -1|\mathbf{y}] = \frac{1}{1 + e^{+L(x_k|\mathbf{y})}}. \tag{3.22}$$

In the following, we consider 4-QAM as an example to briefly discuss the soft-symbol calculation process with the aid of the LLR-to-probability conversion formula of Eq.(3.21) and Eq.(3.22). The symbol alphabet of the 4-QAM scheme is shown in Table 3.6, which indicates that a 4-QAM symbol is constituted of two bits, the first of which determines the imaginary part of the symbol, while the second controls the real part. Specifically, given the probabilities of two successive bits which constitute a 4-QAM symbol, from their two legitimate values of $+1$ and -1, we can calculate the jth user's soft-symbol, s_j, as follows:

$$\begin{aligned} s_j =& [\Re(s_j);\ \Im(s_j)], \\ =& [P[x_{j,2} = -1|\mathbf{y}] \cdot (+1) + P[x_{j,2} = +1|\mathbf{y}] \cdot (-1); \\ & P[x_{j,1} = -1|\mathbf{y}] \cdot (+1) + P[x_{j,1} = +1|\mathbf{y}] \cdot (-1)]/\sqrt{2}, \end{aligned} \tag{3.23}$$

4-QAM Symbol Alphabets Over The Complex Numbers				
j	1	2	3	4
$x_{j,1}\ x_{j,2}$	00	01	10	11
s_j	$(+1+i)/\sqrt{2}$	$(-1+i)/\sqrt{2}$	$(+1-i)/\sqrt{2}$	$(-1-i)/\sqrt{2}$

Table 3.6: 4-QAM symbol alphabets over the complex numbers (i denotes $\sqrt{-1}$)

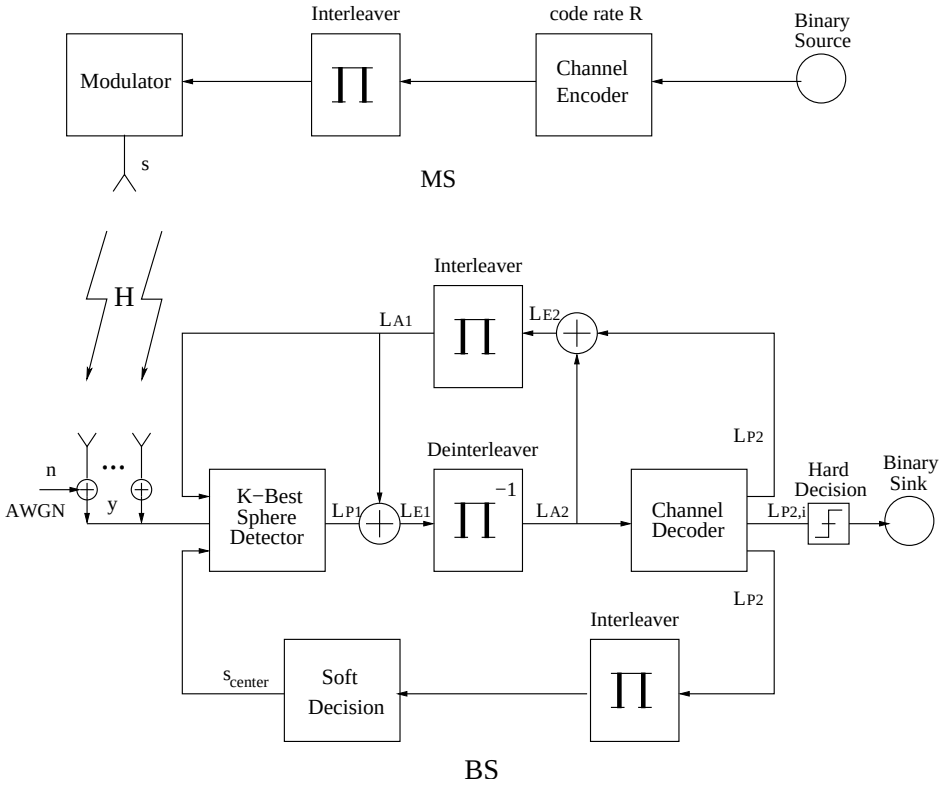

Figure 3.14: Direct-soft-decision-center-shifting K-best SD-aided iterative detection scheme

where we assumed that the 2 bits are independent of each other, which is not entirely true owing to their correlation imposed by the Gray mapping to the 4QAM symbols. The probabilities $P[x_{j,k} = \pm 1|\mathbf{y}]$ can be calculated from Eq.(3.21) and Eq.(3.22) based on the *a posteriori* LLR values received from the outer channel decoder.

3.2.3.2.2 Receiver Architecture and EXIT-Chart-Aided Analysis

Based on the idea of retaining the soft-bit-information contained in the *a posteriori* LLRs, we propose the iterative DSDC-aided K-Best SD receiver portrayed in Figure 3.14, where the soft-decision block substitutes the hard-decision and re-modulation functionality of the DHDC-aided iterative receiver shown in Figure 3.7. The scheme of Figure 3.14 provides a soft search center for the K-Best SD and based on the soft centers the SD is expected to generate a better candidate list for the following LLR calculation, which is then delivered to the outer channel decoder. Although the soft center calculation imposes a slightly higher computational complexity than its hard-decision based counterpart, the iterative DSDC-aided K-Best SD receiver is capable of attaining a higher performance gain over the conventional iterative receiver, as observed throughout our forthcoming EXIT chart analysis and BER results.

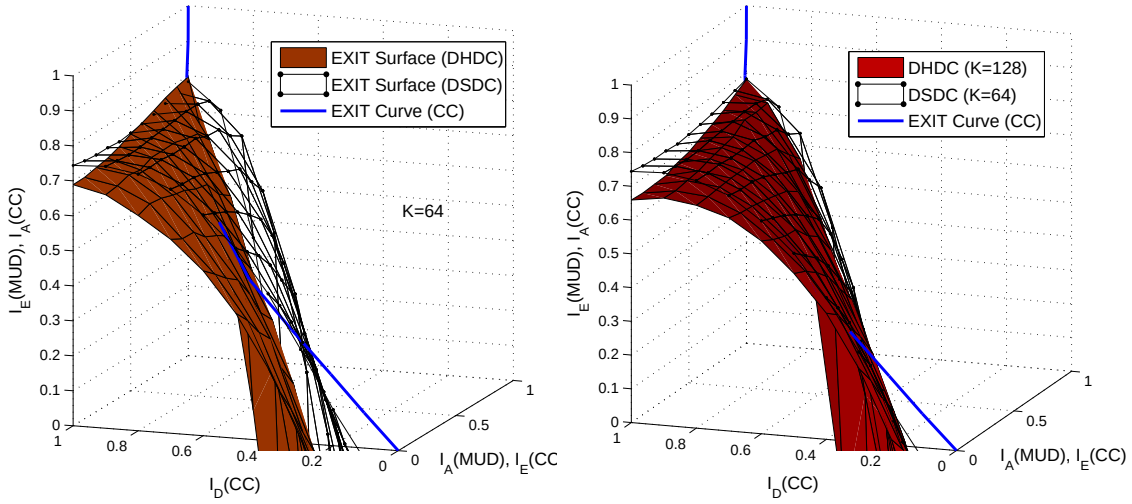

(a) In the Scenario of K-Best SD ($K = 64$)

(b) DHDC-Aided K-Best SD ($K = 128$) & DSDC-Aided K-Best SD ($K = 64$)

Figure 3.15: EXIT chart comparison of the DHDC and the DSDC center-shifting scheme in the scenario of 4-QAM (8×4)-element SDMA/OFDM System at SNR=8 dB. All other system parameters are listed in Table 3.1.

Figure 3.15 compares the 3D-EXIT charts of the DHDC-aided and DSDC-aided iterative receivers, at SNR=8 dB in the scenario of an (8×4)-element rank-deficient SDMA/OFDM system. We can observe in Figure 3.15(a), that the DSDC scheme's EXIT surface is distinctly higher than that of the DHDC-aided SD at the same values of K or N_{cand} ($K = N_{cand} = 64$ in this case). Thus, for a given number of iterations, a higher iterative gain is expected. On the other hand, since the tunnel between the EXIT surface of the SD and the EXIT curve of the outer convolutional channel decoder opens at a lower $[I_A, I_E]$ point, when the DSDC scheme is invoked instead of the DHDC arrangement, the center-shifting scheme may provide performance benefits at lower SNRs. Specifically, when the SNR is too low, the EXIT surface of the SD may still be beneath the EXIT curve of the outer decoder, even though the center-shifting scheme was switched on after the maximum attainable iterative gain has been achieved by the iterative receiver dispensing with center-shifting. Therefore, the higher the corresponding EXIT surface, the better the achievable performance of the center-shifting scheme. We can observe in Figure 3.15(b) that the EXIT surface of the DSDC-aided receiver is still slightly higher for $K = 64$ than that of the DHDC-aided one using $K = 128$ and hence potentially doubling the associated complexity. In other words, the computational complexity imposed by the SD can be substantially reduced with the aid of the DSDC scheme, without sacrificing the attainable iterative gain.

3.2.3.2.3 Simulation Results

Figure 3.16 depicts the BER curves of the DSDC-aided K-best SD iterative receiver in comparison to those of the conventional iterative receiver dispensing with center-shifting and the DHDC-aided iterative receiver in the scenario of an (8×4)-element rank-deficient 4QAM SDMA/OFDM

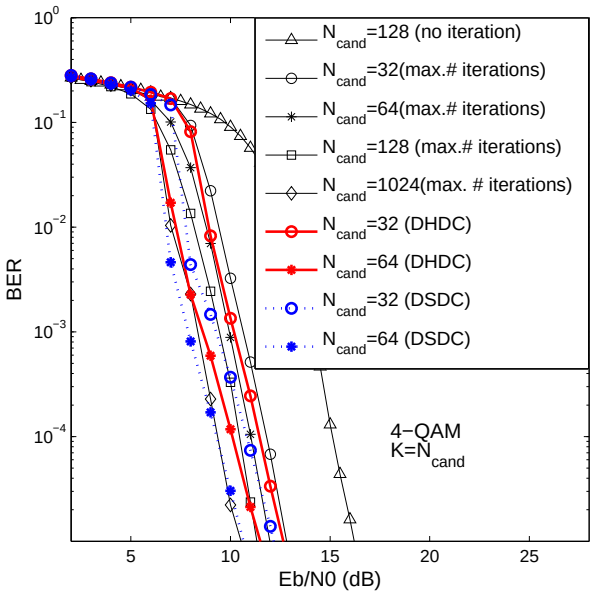

Figure 3.16: BER performance improvements provided by the DSDC scheme in the context of an (8×4)-element Rank-Deficient SDMA/OFDM System: Compared to the DHDC-aided receiver, the DSDC-aided K-Best SD iterative receiver is capable of achieving a better BER performance at a slightly higher computational complexity imposed by the search center calculation process. All other system parameters are listed in Table 3.1.

system. The system parameters used and the iteration mode control remain the same as listed in Table 3.5, except that the center-shifting scheme is changed to the DSDC. As seen in Figure 3.16, a better BER performance can be achieved in both scenarios, where $K = N_{cand} = 32$ and $K = N_{cand} = 64$ were employed by the DSDC-aided iterative receiver than that by the DHDC-aided one. These observations confirm our discussions based on the EXIT chart analysis of Figure 3.15. Remarkably, by having list-length of $K = N_{cand} = 64$, the DSDC-aided receiver outperforms the conventional iterative receiver using no center-shifting having a high complexity associated with a list size of $K = N_{cand} = 1024$. This remarkable performance improvement is achieved, while simultaneously approaching the performance of the exact MAP detector, which may be implementationally infeasible, especially in such a heavily rank-deficient system. The additional iterative gain attained by the DSDC scheme can be observed from the EXIT charts plotted in Figure 3.17. More specifically, since the value of K and N_{cand} are as low as 64, no additional iterative gains can be achieved by the system using the DHDC scheme beyond a few iterations. By contrast, as soon as the DSDC scheme is activated, a substantially higher iteration gain is attained.

3.2.3.3 Two-Stage Iterative Architecture Using an Iterative SIC-MMSE-Aided Center-Update

As evidenced by our simulation results shown in Figure 3.16, upon exploiting the soft-bit information contained in the *a posteriori* LLRs gtleaned from the channel decoder, the DSDC center-shifting scheme brings about a higher performance gain than its hard-decision based counterpart, i.e. the DHDC scheme. In order to further exploit the soft information so that the K-best SD iter-

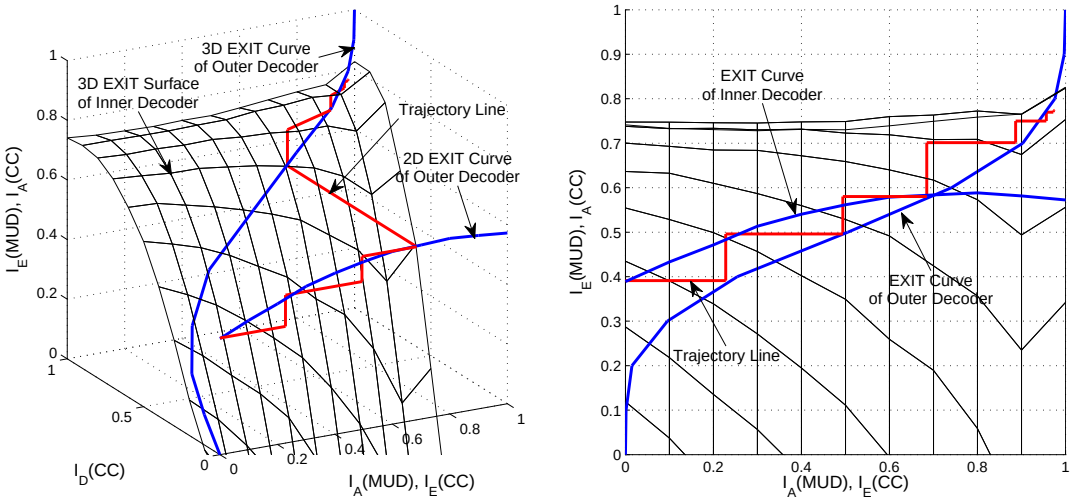

(a) 3D-EXIT Chart Analysis.

(b) (Projection) 2D-EXIT Chart Analysis.

Figure 3.17: EXIT chart analysis of the DSDC based K-best SD aided iterative receiver in the scenario of (8×4)-element rank-deficient 4-QAM SDMA/OFDM System. (SNR=8 dB, $K = \mathcal{N}_{cand} = 64$). All other system parameters are listed in Table 3.1.

ative receiver benefits more substantially from the center-shifting scheme at the cost of a slightly higher computational complexity, we take advantage of the iterative Soft Interference Cancellation aided MMSE (SIC-MMSE) [108] [109] algorithm in order to generate the search center for the SD.

3.2.3.3.1 Soft Interference Cancellation Aided MMSE Algorithm [108] [109]

As discussed in Section 3.2.3.2, given the *a posteriori* LLRs, we can calculate the corresponding soft symbol for a specific modulation scheme, i.e. 4QAM, using Eq.(3.21), Eq.(3.22) and Eq.(3.23). Similarly, given the *a priori* LLRs, we can also define the jth user's soft symbol, more precisely, the mean of the jth user's symbol as [108]:

$$\bar{s}_j = E[s_j] = \sum_{q} s_j^{(q)} \cdot P[s_j = s_j^{(q)}], \tag{3.24}$$

where q is the number of points in the modulation constellation, e.g. $q = 4$ for 4QAM or QPSK, while $s_j^{(q)}$ represents the qth legitimate value of the symbol s_j. Consequently, for 4-QAM, we arrive at:

$$\begin{aligned} \bar{s}_j =& (\Re(s_j);\ \Im(s_j)), \\ =& [P[x_{j,2} = -1] \cdot (+1) + P[x_{j,2} = +1] \cdot (-1); \\ & P[x_{j,1} = -1] \cdot (+1) + P[x_{j,1} = +1] \cdot (-1)]/\sqrt{2}, \end{aligned} \tag{3.25}$$

where $P[x_k = \pm 1]$ can be computed according to [104]:

$$\begin{aligned} P[x_k = +1] &= \frac{e^{L(x_k)}}{1 + e^{L(x_k)}} \\ &= \frac{1}{1 + e^{-L(x_k)}}. \end{aligned} \tag{3.26}$$

and

$$P[x_k = -1] = \frac{1}{1 + e^{+L(x_k)}}, \tag{3.27}$$

respectively. On the other hand, we define the covariance of the jth user's symbol as [108] [110]:

$$\begin{aligned} v_j =& Cov[s_j, s_j], \\ =& E[s_j s_j^*] - E[\bar{s}_j]E[\bar{s}_j^*], \qquad (3.28) \\ =& 1 - |\bar{s}_j|^2, \qquad (3.29) \end{aligned}$$

for constant-modulus modulation schemes, such as BPSC, QPSK and 4-QAM.

The estimated symbol of the jth user generated by the MMSE algorithm can be expressed with the aid of the SIC principle as [108] [109]:

$$\hat{s}_j = \bar{s}_j + v_j \mathbf{w}_j^H (\mathbf{y} - \mathbf{H}\bar{\mathbf{s}}), \tag{3.30}$$

where the jth column of the MMSE weight matrix $\mathbf{W}_{MMSE}$ can be expressed as [108] [109]:

$$\mathbf{w}_{j,MMSE} = (\mathbf{HVH}^H + 2\sigma_w^2 \mathbf{I}_P)^{-1} \mathbf{h}_j, \tag{3.31}$$

where $\mathbf{I}_P$ represents the $(P \times P)$-element identity matrix and $\mathbf{V} = diag[v_1, v_2, \cdots, v_J]$.

As we may notice that for the first iteration, the *a priori* LLRs gleaned from the outer decoder are not available, i.e. we have $L_A(CC) = 0$, which in turn leads to $\bar{s}_j = 0$ and $v_j = 1, j = 1, 2, \cdots, J$. In the sequel, the resultant search center computed in Eq.(3.30) is actually the conventional MMSE solution, where Eq.(3.30) converges to the non-SIC-aided MMSE algorithm expressed as:

$$\check{s}_j = \mathbf{w}_j^H \mathbf{y}, \tag{3.32}$$

where

$$\mathbf{w}_{j,MMSE} = (\mathbf{HH}^H + 2\sigma_n^2 \mathbf{I}_P)^{-1} \mathbf{h}_j. \tag{3.33}$$

However, the SIC-MMSE starts to take effect from the second iteration onward, which is expected to provide a more accurate search center for the SD than both the previously investigated DHDC and DSDC schemes, since in addition to retaining the soft bit information during the soft symbol generation, it carries out the soft interference cancellation at each iteration.

3.2.3.3.2 Receiver Architecture and EXIT-Chart Analysis

In this section we investigate the SIC-MMSE-aided iterative center-shifting K-best SD receiver depicted in Figure 3.18, where the *a posteriori*-LLR feedback based DHDC and DSDC schemes are replaced by the SIC-MMSE-aided search center calculation, which is carried out based on the *a priori* LLRs gleaned from the channel decoder. Therefore, as portrayed in Figure 3.19, we may consider the modified SD as a single input component fed with the *a priori* LLRs, and producing a single output, namely the *extrinsic* LLRs, which contains both the center-calculation part and the original SD part. Then the EXIT chart used to analyze the system becomes two dimensional.

The benefits of the SIC-MMSE-aided center-shifting scheme become clearer, if we refer to the EXIT charts obtained in the (8×4)-element rank-deficient scenario of 4-QAM SDMA/OFDM system as seen in Figure 3.20. Recall from Figure 3.2 that the inner decoder's EXIT curve decayed

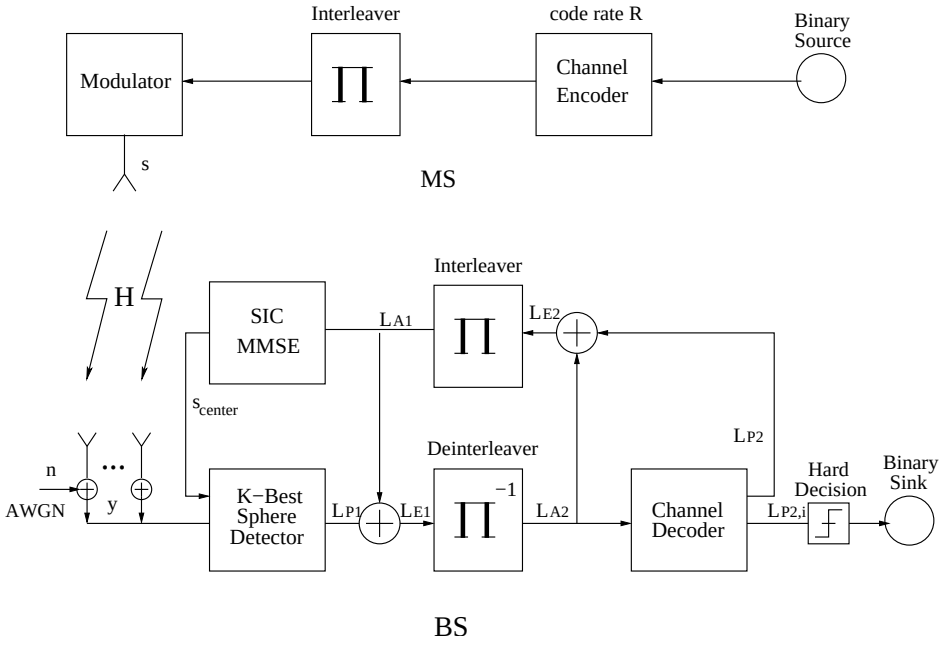

Figure 3.18: SIC-MMSE-aided center-shifting K-best SD scheme

Figure 3.19: Structure of the SIC-MMSE-aided center-shifting K-best SD: a single-input single-output block

upon increasing the *a priori* information owing to the flawed information exchange between the inner and outer decoders, which was caused by the employment of an insufficiently large candidate list size N_{cand} and by the number of candidates K retained at each search level. The comparisons in Figure 3.20(a) indicate that this problem was effectively solved by the application of the SIC-MMSE-aided center-shifting scheme. More explicitly, when using the SIC-MMSE scheme, the inner decoder's EXIT curve no longer decays, when the *a priori* MI increases, even when using a limited list size of $K = N_{cand} = 16$. On the other hand, as shown in Figure 3.20(b), when K and N_{cand} are increased to 128 and 1024 for the K-best SD using no center-shifting, both of the resultant inner decoder's EXIT curves increase. As expected the EXIT curve corresponding to $K = N_{cand} = 1024$ reaches a higher end point than that associated with $K = N_{cand} = 128$. However, as a benefit of the SIC-MMSE center-shifting scheme, the EXIT curve of the inner decoder may arrive at an even higher end point, despite using smaller K and N_{cand} values than that of the SD dispensing with center-shifting and high values of K and N_{cand}, such as 1024. Hence, we can infer from the above observations that the SIC-MMSE-aided receiver is capable of achieving a near-MAP BER performance conjunction with small values of K and N_{cand}.

3.2.3.3.3 Simulation Results

Both subfigures of Figure 3.21 show a significant performance gain, which was facilitated by

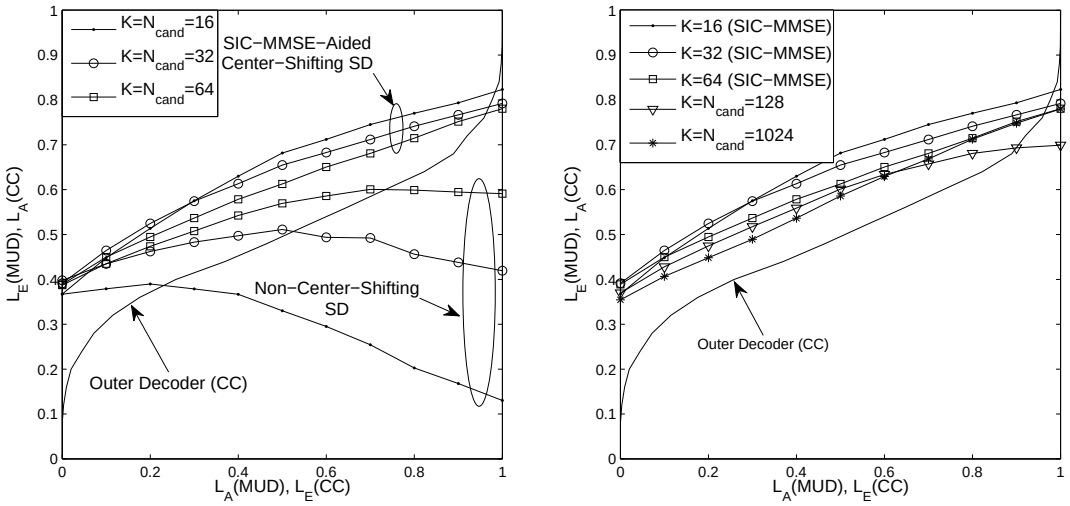

(a) (b)

Figure 3.20: EXIT chart comparison of SIC-MMSE-aided center-shifting and the non-center-shifting K-best SD iterative receiver in the scenario of (8×4)-element rank-deficient 4-QAM SDMA/OFDM system at SNR=8 dB. All other system parameters are listed in Table 3.1.

the SIC-MMSE-aided center-shifting K-best SD iterative receiver. Specifically, as seen in Figure 3.20(a), the SIC-MMSE-aided center-shifting K-best SD is capable of approaching almost the same iterative gain by setting $K = 16$, as iterative SD using no center-shifting does in conjunction with $K = 1024$, at a BER of 10^{-5}. Hence, both the associated memory requirements and the computational complexity imposed are substantially reduced. Explicitly, for a fixed value of K, such as for example $K = 32$ and for the same target BER of 10^{-5}, we can observe that the iterative gain over the non-iterative receiver was doubled by the SIC-MMSE-aided center-shifting scheme, when compared to that achieved by the iterative SD using no center-shifting, corresponding to about 6dB.

On the other hand, in Figure 3.21(b) we compare the achievable performance of the three proposed center-shifting schemes, namely, the DHDC, the DSDC and the SIC-MMSE, in the context of K-best SD in the scenario of an (8×4)-element rank-deficient SDMA/OFDM system. We classify the center-shifting schemes into two categories, namely the hard-decision based methods, such as the DHDC scheme, and the soft-decision based techniques, which include the two other center-shifting schemes, exploiting the soft-bit information that arrives at the SD from the outer channel decoder. As argued before, the better the soft information is exploited by the center-shifting scheme, the higher the achievable performance improvement or the higher the attainable complexity-reduction facilitated by the SISO SD-aided iterative receiver. As seen in Figure 3.21(b), performance gains of about 2.5 dB and 2 dB are attained by the SIC-MMSE center-shifting scheme over the DHDC and the DSDC schemes at the cost of a slightly higher computational complexity, respectively, at the target BER of 10^{-5}. Therefore, the SIC-MMSE-aided center-shifting scheme significantly outperforms the other two by invoking the idea of SIC.

We quantify the achievable performance gain and the complexity-reduction facilitated by the

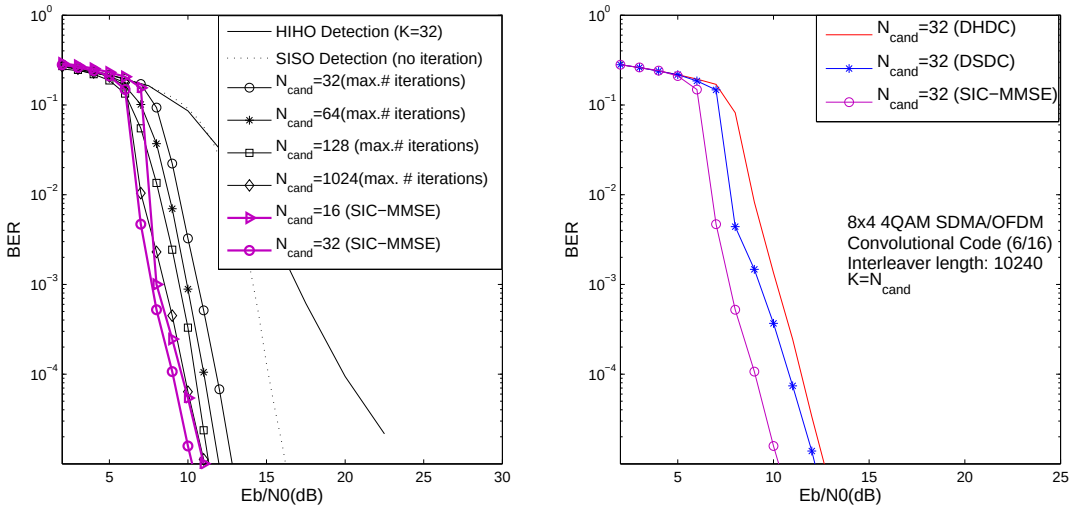

(a) Performance Gain

(b) BER Performance Comparison of the DHDC, the DSDC, and the SIC-MMSE Center-Shifting Schemes

Figure 3.21: BER performance of the SIC-MMSE-aided center-shifting K-best SD iterative receiver. All other system parameters are listed in Table 3.1.

SIC-MMSE-aided center-shifting scheme in Table 3.7, in comparison to the conventional non-center-shifting SD-aided iterative receiver. Again, we view the SD module as being constituted by two serially concatenated parts, namely the SD and the MAP decoder, which are responsible for carrying out the list-generation and the soft-bit information calculation, respectively. Table 3.7 quantifies the computational complexity imposed by the SD section in terms of the total number of PED evaluations, and that associated with the MAP part in terms of the total number of OF evaluations corresponding to the two terms in Eq.(3.14). Thus, as explicitly indicated in Table 3.7, in order to achieve a near-MAP performance, i.e. to achieve a BER of 10^{-5} at an SNR below 11 dB in the context of an (8×4)-element rank-deficient SDMA/OFDM system, we have to use at least $K = N_{cand} = 1024$ for the non-center-shifting SD-aided iterative receiver. However, thanks to the SIC-MMSE-aided center-shifting scheme, we can achieve the same goal by setting $K = N_{cand} = 16$, while imposing a factor of 11 lower compuational complexity that that associated with the list-generation part and imposing a factor of 64 lower computational efforts by the soft-bit information calculation of the SD receiver using no center-shifting. A further additional performance gain of 0.8 dB can be obtained by setting $K = 32$, at the cost of a modestly increased computational complexity. Furthermore, our extensive simulation results indicate that in a heavily rank-deficient system, setting K to a value higher than 32 can hardly improve the achievable performance gain further, if our target BER is below 10^{-2}, since a near-MAP performance has already been achieved.

Performance Gain & Computational Complexity Reduction Achieved by the SIC-MMSE Scheme in an (8×4)-element 4-QAM SDM/OFDM Rank-Deficient System

BER	Center-Shifting	$N_{cand}(K)$	Iterations	SNR	Memories	SD Compl.	MAP Compl.
10^{-5}	NONE	1024	3	10.5	8196	13652	49152
		128	3	11.2	1024	2388	6144
		64	2	12	512	1364	2048
		32	2	12.8	256	724	1024
		16	2	15	128	404	512
	SIC-MMSE	64	3	10.2	512	4092	3072
		32	3	10.2	256	2172	1536
		16	3	11	128	1212	768

Table 3.7: Performance comparison of the conventional non-center-shifting K-best SD and the SIC-MMSE-aided center-shifting K-best SD iterative detection in the scenario of an (8×4) rank-deficient SDMA/OFDM system: Note that the computational complexity of the SD, i.e. the list generation by the SD, is calculated in terms of the total number of PED evaluations, while that of the soft information generation by the SD/MAP detector is computed on the basis of Eq.(3.16) in terms of the total number of OF evaluations corresponding to the two terms in Eq.(3.14).

3.3 *Apriori*-LLR-Threshold-Assisted Low-Complexity SD

It transpires from Section 2.2.3 that having an insufficiently large candidate list, $N_{cand} = K$, does not guarantee for the K-best SD of Section 2.2.3 that its candidate list includes the ML point, while its depth-first counterpart of Section 2.2.2 does. When the value of K is kept low for the sake of maintaining a low computational complexity, this resulted in a considerable performance degradation in Figure 2.8. In order to circumvent this problem, in this section another novel complexity-reduction scheme, referred to as the *Apriori*-LLR-Threshold (ALT) aided technique is designed for the K-best SD. Similarly to the center-shifting scheme, its philosophy is also based on the exploitation of the *a priori* LLRs provided by the outer channel decoder, albeit this is achieved in a rather different way. First of all, in Section 3.3.1, the operating principle of this novel complexity-reduction technique is highlighted. The analysis of this technique in terms of its achievable perfromance and the computational complexity imposed is carried out with the aid of our simulation results in Section 3.3.2.

3.3.1 Principle of the *Apriori*-LLR-Threshold Aided Detector

First of all, let us review the definition of the *a priori* LLRs, which is the logarithm of the ratio of the bit probabilities associated with $+1$ and -1 [104], which can be expressed as follows:

$$L_A(x_j) = \ln \frac{P[x_j = +1]}{P[x_j = -1]}. \tag{3.34}$$

Therefore, the sign of the resultant LLRs indicates whether the current bit is more likely to be $+1$ or -1, whereas the magnitude reflects how reliable the decision concerning the current bit is. For example, given a large positive *a priori* LLR delivered by the outer channel decoder of Fig-

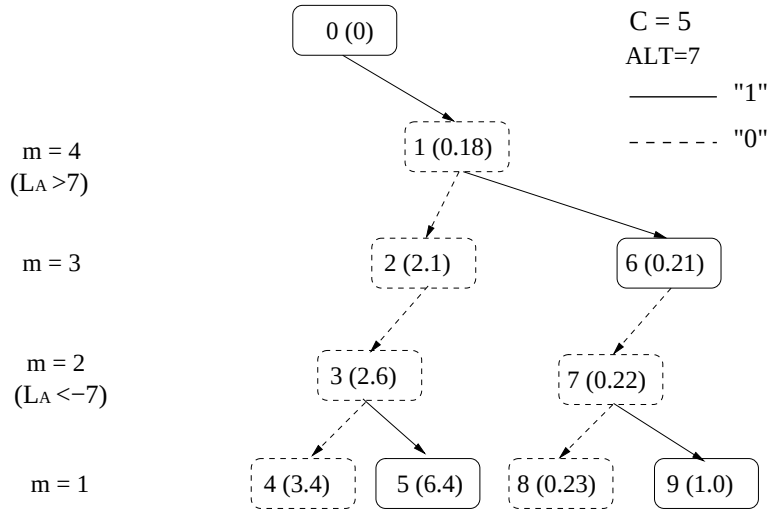

Figure 3.22: Illustration of the depth-first SD algorithm with the aid of ALT scheme where ALT=7: The figure in ( ) indicates the PED of a specific node for the trial point in the modulated constellation; while the number outside represents the order in which the points are visited.

ure 3.1, it is implied that the corresponding transmitted bit is likely to have been $+1$. In light of this, the search tree of the depth-first SD of Section 2.2.2 may be significantly simplified by invoking an ALT. To be specific, first we consider BPSK modulation as an example. If the *a priori* LLR of the mth user's BPSK symbol is sufficiently high (higher than the ALT), there is no need to carry out the detection for that particular user during the SD process. In other words, at the $(m+1)$th search tree level, all the resultant tree nodes are expanded by a single branch instead of retaining both legitimate detection options. Therefore, for the depth-first SD of Section 2.2.2, the computational complexity is expected to be significantly reduced as we can observe from the search tree portrayed in Figure 3.22 in the scenario of a BPSK SDMA system where 4 users are supported. The application of the ALT scheme in the context of the example shown in Figure 2.4 of Section 2.2.2 generates a more simple tree structure, which imposes a reduced detection complexity. Since ALT=7, which is lower than the absolute values of both the $(m=4)$th user's and $(m=2)$nd user's LLRs arriving from the outer decoder of Figure 3.1 after a certain number of iterations, the SD will discard all the branches corresponding to $s_4 = 0$ at the $(m=4)$th level and $s_2 = 1$ at the $(m=2)$nd level. Consequently, the final ML solution is attained after visiting only 9 tree nodes and leaves in Figure 3.22. Hence, as long as the ALT is not too low, the computational complexity imposed can be substantially reduced by invoking the ALT scheme without any BER performance degradation, which becomes explicit by comparing the search trees as shown in Figures 2.4 and 3.22.

The depth-first SD of Section 2.2.2 was briefly revisited in the previous section, when invoking the ALT technique, which is also applicable in the context of the breadth-first-style K-best SD. More explicitly, the main benefit of employing the ALT scheme, for the breadth-first SD, such as the K-best SD of Section 2.2.3, is not the achievable complexity reduction, but rather the potential performance improvement attained, since although there still only K candidates are expected to be retained at the mth search tree level of Figure 3.23, the affordable search-complexity is assigned to the candidates having a specific bit value at the mth position, which is determined by the specific LLR-based decision. In other words, the LLR-based search-tree pruning portrayed in Figure 3.23(b) decreases the probability of discarding a potentially correct path at an early search stage,

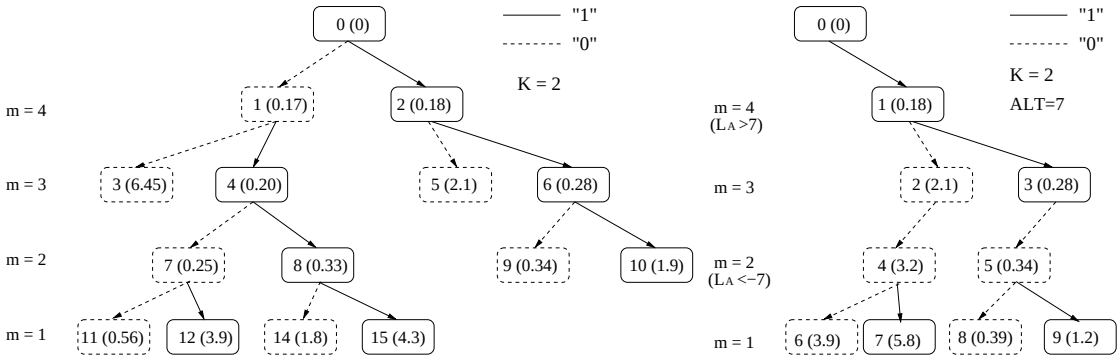

(a) The Search Tree of the Non-ALT-Assisted K-Best SD in the Scenario of a 4-User BPSK SDMA System, where $K = 2$ and the ALT=7

(b) The Search Tree of the ALT-Assisted K-Best SD in the Scenario of a 4-User BPSK SDMA System, where $K = 2$ and the ALT=7

Figure 3.23: Illustration of the K-Best SD Algorithm with the Aid of ALT Scheme where ALT=7: The figure in ( ) indicates the PED of a specific node for the trial point in the modulated constellation; while the number outside represents the order in which the points are visited.

especially when the value of K is set relatively small. When applying the ALT-assisted K-best SD to a 4-user BPSK modulated SDMA system, the resultant search tree is portrayed in Figure 3.23. As seen in Figure 3.23(a), when dispensing with the ALT scheme, after 15 PED evaluations the SD opts for the specific tree leaf having Euclidean distance of 0.56. Then the search portrayed in Figure 3.23(a) backtracks to the $(m = 4)$th level, yielding the hypothesized ML solution. However, as the ALT scheme is invoked, a better pruning search tree is obtained for the K-best SD, which is shown in Figure 3.23(b), if we assume the absolute values of the *a priori* LLRs of both the $(m = 4)$th and the $(m = 2)$nd users exceed the preset ALT value. Only 9 PED evaluations have been carried out for this particular example, indicating a considerable reduction of the computational complexity imposed. However, even more importantly, the fact that the SD successfully identifies the true ML solution, which is different from the one generated by the SD characterized in Figure 3.23(a), which dispenses with the ALT technique. This is achieved by backtracking during the search from a different tree leaf having a smaller Euclidean distance of 0.39 to the $(m = 4)$th level. Hence the incorrect search branch corresponding to $s_4 = 0$ is truncated as early as at the $(m = 4)$th level, hence reducing the computational complexity imposed, while simultaneously avoiding the situation of discarding a potential path leading to the true ML solution, which may be the case for the non-ALT-assisted K-best SD at the $(m = 2)$nd level due to the fact that the true ML path may have a temporarily larger PED.

3.3.2 Features of the ALT-Assisted K-Best SD Receiver

3.3.2.1 BER Performance Gain

In this section, we concentrate our investigations on the novel ALT scheme in the context of the K-best SD, which is based on our simulation results. Figure 3.24 depicts the BER perfor-

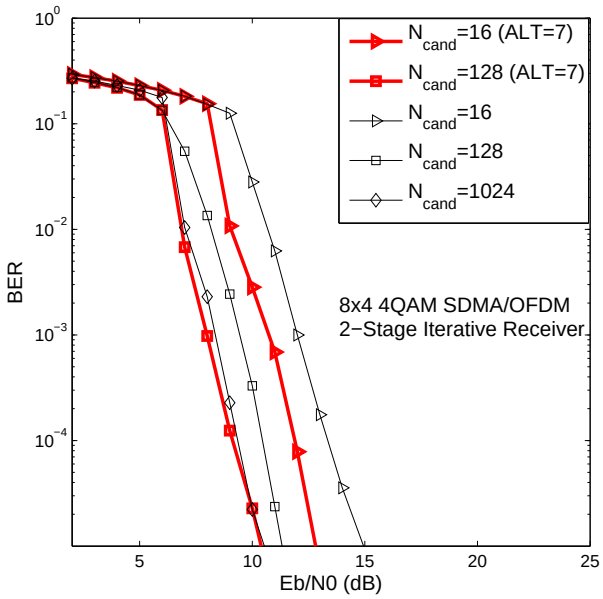

Figure 3.24: BER performance of the two-stage LLR-threshold-aided K-best SD iterative receiver in an (8×4)-element 4QAM SDMA/OFDM System

mance of the ALT-assited K-best SD in the scenario of the (8×4)-element rank-deficient 4-QAM SDMA/OFDM system in comparison to the system dispensing with the ALT technique. Given a target BER of 10^{-5} and a fixed list-length $\mathcal{N}_{cand} = K = 16$, a performance gain of 2.5 dB can be achieved by setting the *a priori*-LLR-threshold to 7, whereas a performance gain of about 1 dB can be obtained for the system using $K = 128$. Actually, the ALT-aided receiver associated with $K = 128$ has already attained the MAP performance, which required at least $K = 1024$ for the equivalent system dispensing with the ALT technique. The ratio of these system complexities is as high as eight.

3.3.2.2 Computational Complexity

Under the assumption that the conventional K-best SD iterative receiver dispensing with the ALT technique generates the candidate list only once at the first iteration, which is stored in the memory for the *extrinsic* LLR calculation of the forthcoming iterations, the performance gains attained by both the center-shifting scheme introduced in Section 3.2.3 and the ALT scheme are achieved at the cost of an acceptable computational complexity investment, since the candidate list has to be regenerated at each iteration. However, the memory requirement imposed is expected to be reduced, since there is no need to store the resultant candidate list. The complexity imposed by invoking the ALT scheme can be viewed in Figure 3.25(a), where the overall computational complexity quantified in terms of the number of PED-evaluations per channel use imposed by the system operating both with and without the aid of the ALT scheme (ALT=7) are plotted for (8×4)-element rank-deficient 4QAM SDMA/OFDM system scenario. Specifically, since SD has to be carried out only once per channel use, regardless of how many iterations have been carried out, the receiver not benefitting from the ALT technique exhibits the same computational complexity of

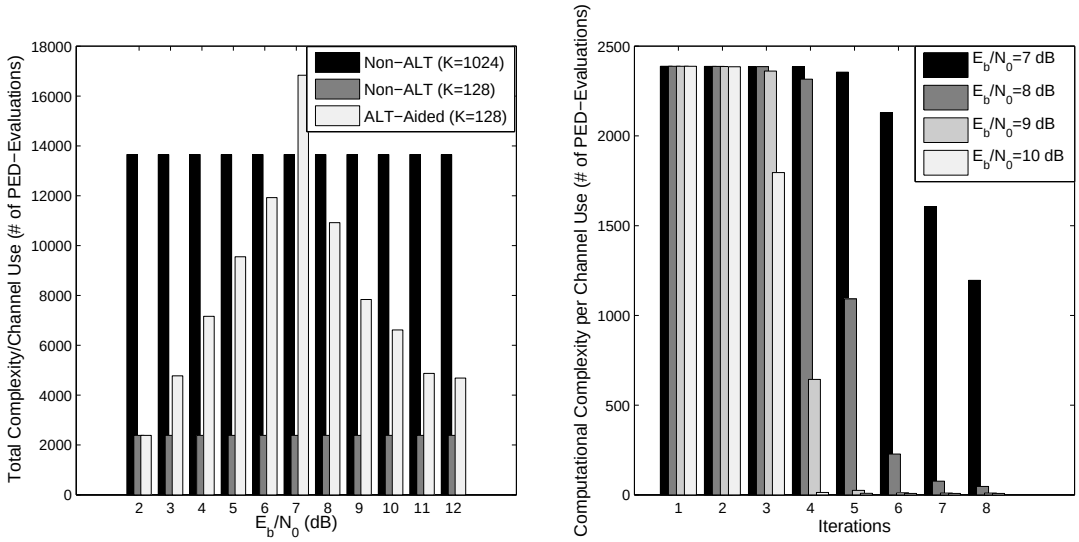

(a) (b)

Figure 3.25: Histogram of the candidate list generation related computational complexity imposed by the ALT-aided K-best SD in the (8×4)-element rank-deficient 4QAM SDMA/OFDM system scenario: (a) the overall computational complexity per channel use for different E_b/N_0 values (ALT=7); (b) computational complexity per channel use of each iteration (K=128, ALT=7). Note: the maximum number of iterations for all different E_b/N_0 value was fixed to 8 and the iterative detection was terminated as soon as there is no more iteration gain can be achieved, i.e. the resultant EXIT trajectory line reached the convergence point of $[I_A, I_E] = [1, 1]$.

2,388 PED-evaluations per channel use for $K = 128$, regardless of the channel SNR. By contrast, the number of PED-evaluations required by the ALT-assisted receiver differs for different SNRs. To be specific, observe in Figure 3.25(a) that the complexity increases steadily as the SNR increases from 2 dB to 7 dB, peaking at about 17,000 PED-evaluations per channel use. Beyond 7 dB, the complexity decays steadily as the SNR increases further, but levels out around 5,000 PED-evaluations at an SNR of 12 dB. Upon inspecting both Figure 3.24 and Figure 3.25(a), we observe that no performance gain is achieved by the ALT-aided receiver when the SNR is lower than 6 dB, despite the additional computational efforts of regenerating the candidate list at each iteration. This is not unexpected, since it is unlikely that the *a priori* LLRs gleaned by the outer channel decoder become higher than the threshold of the ALT scheme, because the intersection of the inner and outer EXIT curve occures at a low I_A value in Figure3.42(a). Hence, it is unwise to activate the ALT scheme, when the SNR is low, since it may impose an increased complexity without any performance improvements.

On the other hand, as seen in Figure 3.24, with the advent of the ALT scheme the K-best SD becomes capable of achieving a near-MAP performance by setting $K = N_{cand} = 128$ instead of 1024. Recall our arguments on the complexity of the *extrinsic* LLR calculation for the list SD outlined in Section 3.2.1.2 that the corresponding complexity is linearly proportional to N_{cand}, as explicitly expressed in Eq.(3.16). From this perspective, given a fixed target BER performance, the

computational complexity imposed by the *extrinsic* LLR calculation of the K-best SD can be considerably reduced by employing the ALT scheme. Furthermore, with reference to Figure 3.25(a), the candidate list generation complexity of the ALT-aided receiver is well below that of its 'non-ALT-aided' counterpart for the SNR range spanning from 2 dB to 12 dB except for SNRs in the immediate vicinity of 7 dB, if our aim is to achieve the near-MAP BER performance quantified in Figure 3.24, which can be attained by having $K = N_{cand} = 1024$ for the system operating without the ALT technique or by setting $K = N_{cand} = 128$ in the presence of the ALT scheme. More specifically, the number of PED-evaluations per channel use carried out by the non-ALT-aided system using $N_{cand} = 1024$ remains as high as 13,652, regardless of the SNR and the number of iterations. On the other hand, in the presence of the ALT scheme, the candidate list has to be regenerated at each iteration, but nontheless, the total complexity imposed is substantially reduced, except for SNRs in the immediate vicinity of 7 dB. There are two reasons for this phenomenon. 1) When the SNR is low, the number of iterations providing a useful gain is low, because there is no open tunnel between the EXIT curves of the inner and the outer decoder, unless the SNR is sufficiently high. 2) By contrast, when the SNR is high, the resultant stair-case shaped decoding trajectory can readily pass through the widely open EXIT tunnel and reaches the point of perfect convergence at $[I_A, I_E] = [1, 1]$ after a low number of iterations. Furthermore, when the SNR is high, the number of PED-evaluations carried out at each iteration is expected to decrease, as the iterations continues, as oberved in Figure 3.25(b). This is due to the fact that the *a priori* LLRs fed back from the outer decoder of Figure 3.1 to the SD are likely to become higher than the LLR threshold after the first few iterations, and this allows the ALT-assisted SD to directly truncate the low-probability branches, hence leading to a reduced constellation size, which in turn results in a reduced complexity. More specifically, the complexity histogram of Figure 3.25(b) indicates that the higher the SNR, the more sharply the complexity drops as the iterations continue. Actually, when the SNR is relatively high, the complexity imposed becomes more modest after a few iterations, since the majority of the *a priori* LLRs fed back from the outer decoder to the SD of Figure 3.1 becomes higher than the LLR threshold. From a different perspective, this observation also explains the reason why we experience a complexity peak at the moderate SNR of 7 dB, where the ALT-related complexity does not decrease sufficiently substantially as the iterations continue and hence a high number of iterations are required to attain the maximum achievable iteration gain, since only a rather narrow EXIT tunnel was created between the EXIT curves of the inner and the outer decoder.

3.3.2.3 Choice of the LLR Threshold

In the previous ALT-related simulations of Sections 3.3.2.1 and 3.3.2.2, we have maintained an LLR threshold of ALT=7, which ensured that the proposed ALT scheme performed well. However, it is intuitively that the LLR threshold cannot be set arbitrarily, since it plays a vital role in determining the system's performance. To be more specific, if the threshold is set too high, the ALT scheme can hardly affect the system's operation, since the *a priori* LLRs provided by the outer decoder are unlikely to be higher than the threshold, even after several iterations. By contrast, if the threshold is set to an excessively low value, though the computational complexity can be substantially reduced, but naturally, a BER performance degradation is imposed. The above conjectures are verified by

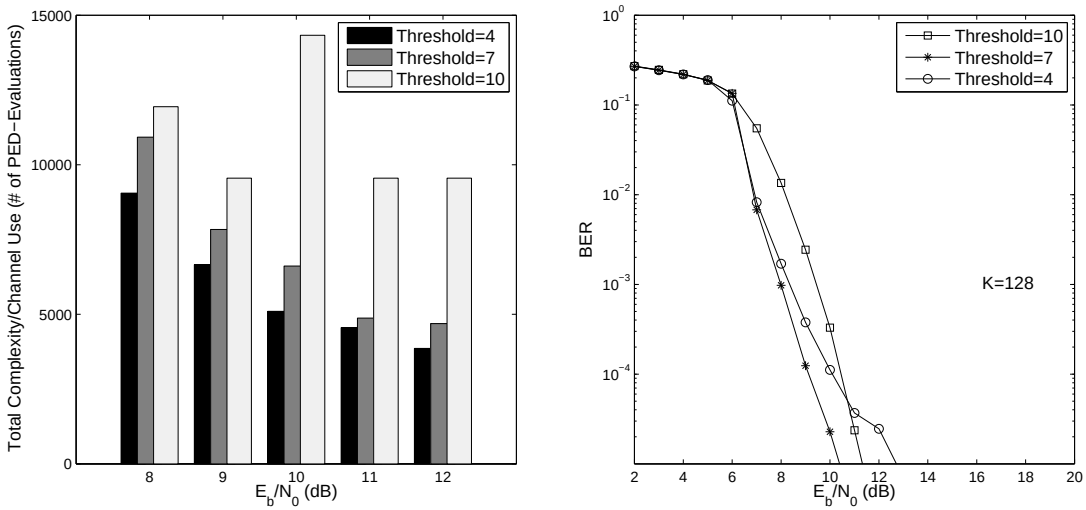

(a) Effects on Computational Complexity

(b) Effects on BER Performance

Figure 3.26: Effects of the LLR-threshold on both the BER performance and the computational compleixty of the K-best SD iterative receiver in an (8×4)-element 4QAM SDMA/OFDM System. Note: the maximum number of iterations for all different E_b/N_0 values was 8 and the iterative detection was terminated as soon as no more iteration gain was achieved, i.e. the resultant decoding trajectory either reached the convergence point, or became trapped.

our simulation results shown in Figure 3.26, where the bars in the histogram of Figure 3.26(a) represent the computational complexity imposed, which was quantified in terms of the number of the PED-evaluations per channel use. The LLR-thresholds employed by the ALT-assisted K-Best SD iterative receiver were set to values of ALT=4, 7 and 10. Observe Figure 3.26(a) that the lower the LLR-threshold, the higher the complexity reduction attained. The corresponding BER curves plotted in Figure 3.26(b), however, demonstrate that when the threshold is set to an excessively low value, this may be expected to impose a performance degradation, as the SNR increases. This is not unexpected because when the SNR becomes high, the *a priori* LLRs fed back by the outer decoder to the SD are becoming predominantly higher than the LLR-threshold set at the very beginning of the iterative detection process. This may trigger an aggressive search-tree-truncation, which in turn results in discarding the true ML branch. In other words, in this scenario the truncation introduced by the ALT technique was activated too early, before the receiver attained a sufficiently high iterative gain. For example, given a target BER of 10^{-5}, a performance gain of about 1.5 dB was observed in Figure 3.26(b) over that of the receiver operating without the ALT technique, with the aid of a threshold of ALT=7, while a performance degradation of about 1.5 dB was imposed by setting the threshold to ALT=4. Note in Figure 3.26(b) that the BER curve corresponding to the threshold of ALT=10 is actually coincident with that of the 'non-ALT-assisted' system, as shown in Figure 3.24, implying that the ALT scheme does not have any beneficial effect with the aid of such a high threshold value. In conclusion, the threshold has to be carefully adjusted for the sake of achieving the target performance as a function of the SNR encountered.

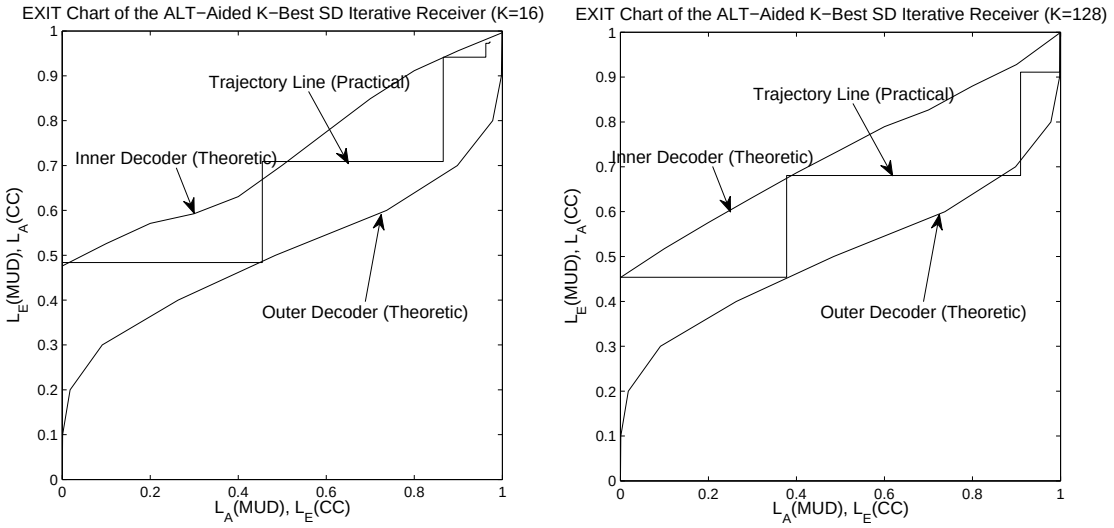

(a) K=16 (Number of Iterations:6) (b) $K = 128$ (Number of Iterations:4)

Figure 3.27: EXIT Chart of the ALT-Aided K-Best SD Iterative Receiver in the Scenario of an (8×4)-element 4-QAM SDMA/OFDM System at SNR=10 dB.

3.3.2.4 Non-Gaussian Distributed LLRs Caused by the ALT Scheme

Although the proposed ALT scheme is capable of provding useful performance improvements, a vital problem, which limits its capacity, can be observed from Figure 3.27, where the EXIT charts of the ALT-assisted receiver are plotted for four and six iterations. The decoding trajectories seen in both Figure 3.27(a) and Figure 3.27(b), which indicate the practically achievable mutual information improvements at the outputs of the inner and the outer decoders during the iterative process as a benefit of exploiting the *a priori* information available, do not match the corresponding theoretical EXIT curves very well, leading to an achievable maximum iteration gain, which is significantly lower than that implied by the theoretical EXIT curves. In comparison to the EXIT chart depicted in Figure 3.27(b), where we have $K = N_{cand} = 128$, this EXIT chart mismatch becomes even worse when K and N_{cand} are as low as 16, as shown in Figure 3.27(a). More specifically, even though a widely open EXIT tunnel was created between the EXIT curves of the inner and the outer decoders in Figure 3.27(a) with the aid of the ALT scheme, the decoding trajectory fails to reach the point of perfect convergence at $(1, 1)$, since it becomes trapped at the point $(0.96, 0.96)$, regardless of the number of iterations. This results in a significantly worse performance in comparison to the situation when we use $K = N_{cand} = 128$, as observed in Figure 3.24. Actually, the ALT-aided receiver remains unable to achieve a near-error-free performance at SNR=10 dB even for $K = 128$, regardless of the number of iterations, and despite having an open tunnel between the EXIT curves of the inner and outer decoder.

Recall that the EXIT chart analysis of an iterative receiver is sufficiently accurate only on condition, when the *a priori* LLRs at the input and the *a posteriori* LLRs at the output of a constituent module of the iterative scheme exhibit a Gaussian distribution. That is the reason why the length of the interleaver between the inner and outer decoders has to be sufficiently high, in order to maintain

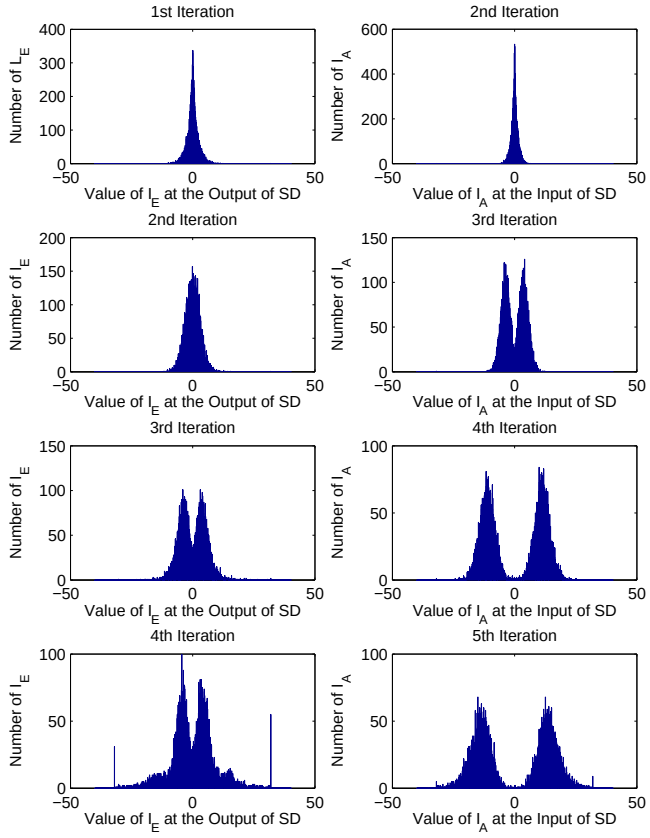

Figure 3.28: Histogram of the LLRs at Both the Input and the Output of the K-Best SD During the Iterative Process in the Scenario of an (8×4)-element 4-QAM SDM/OFDM System for $K = N_{cand} = 1024$, SNR=10 dB.

an approximate Gaussian distribution. Otherwise, a mismatch may occur between the predicted and the practically achievable gains, yielding a smaller iterative gain and difficulties in system performance prediction. However, we found from previous discussion and simulation results presented in Figure 3.27 for LSDs, that apart from the interleaver length, the maximum iteration gain is also substantially affected by the value of K and N_{cand}, as evidenced by the EXIT chart of Figure 3.2 presented in Section 3.2.1.3. Again, a non-Gaussian distribution exhibited by the resultant LLRs at the input and output of the SD is the cause of this phenomenon, as indicated by the simulation-based histogram of both the *a priori* LLRs and of the *extrinsic* LLRs of the SD module after each iteration in Figure 3.28 and Figure 3.29. When K and N_{cand} are sufficiently high, such as 1024, as shown in Figure 3.28, an approximate Gaussian distribution is recorded for the LLRs upon increasing the number of iterations, while also exhibiting an increasingly higher variance. However, when K and N_{cand} are set to an excessively low value, such as 32 as shown in Figure 3.29, after two iterations the majority of the resultant LLRs at both the input and the output of the SD have values, which are close to the LLR truncation value of 32 used in our case, leading to a distinctively non-Gaussian distribution. Hence, we cannot expect the EXIT chart analysis, which is based on the premise of experiencing a Gaussian LLR distribution, to produce an accurate performance prediction.

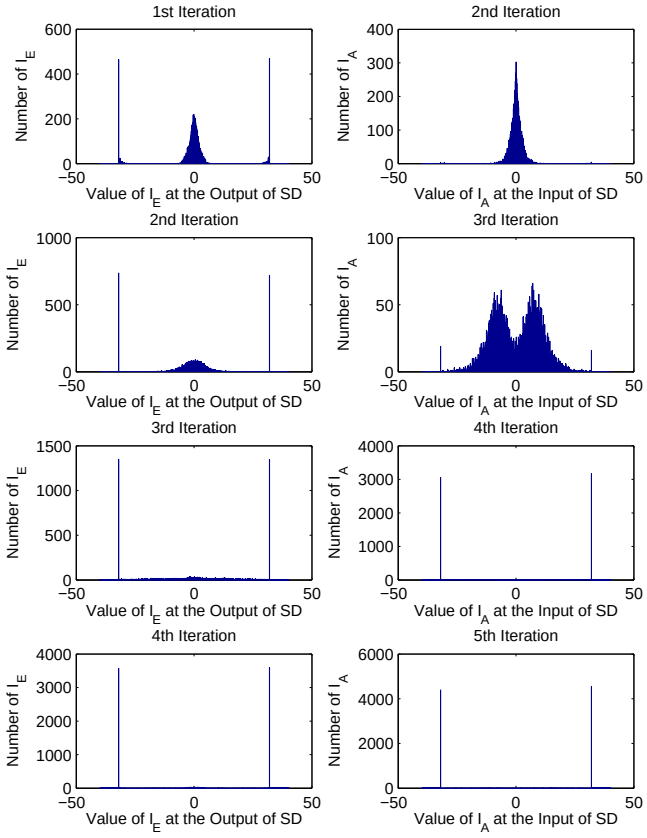

Figure 3.29: Histogram of the LLRs at both the input and the output of the K-best SD during the iterative process in the scenario of an (8×4)-element 4-QAM SDM/OFDM system for $K = N_{cand} = 32$, SNR=10 dB.

In order to further investigate the reason behind the EXIT chart mismatch seen in Figure 3.27, we compare the histograms of both the *a priori* and the *extrinsic* LLRs of the SD with and without the ALT scheme in Figure 3.30 and Figure 3.31. Consequently, we found that the application of the ALT scheme actually degrades the accuracy of the approximate Gaussian distribution exhibited by the LLRs at an earlier stage of the iterations, resulting in a more severe EXIT chart mismatch problem. To be specific, in the absence of the ALT scheme, we observe in Figure 3.30 at the fifth iteration the Gaussian-like distribution is eliminated. However, in the presence of the ALT scheme, a non-Gaussian distribution appears even earlier after the fourth iteration, as seen in Figure 3.31. Hence, although the theoretical EXIT curve of the ALT-aided receiver obtained under the assumption of having a near-Gaussian distributed LLRs all the time, as previously shown in Figure 3.27, can indeed reach the (1, 1) point, the problem of EXIT chart mismatch imposed by the non-Gaussian distribution of the LLRs at both the input and output of the SD is aggravated by the application of the ALT scheme. This leads to a more limited iterative gain than that expected from the theoretical EXIT curves of Figure 3.27.

On the other hand, although the employment of the ALT scheme results in an unreliable EXIT chart analysis owing to the EXIT chart mismatch, the BER performance of the system is still

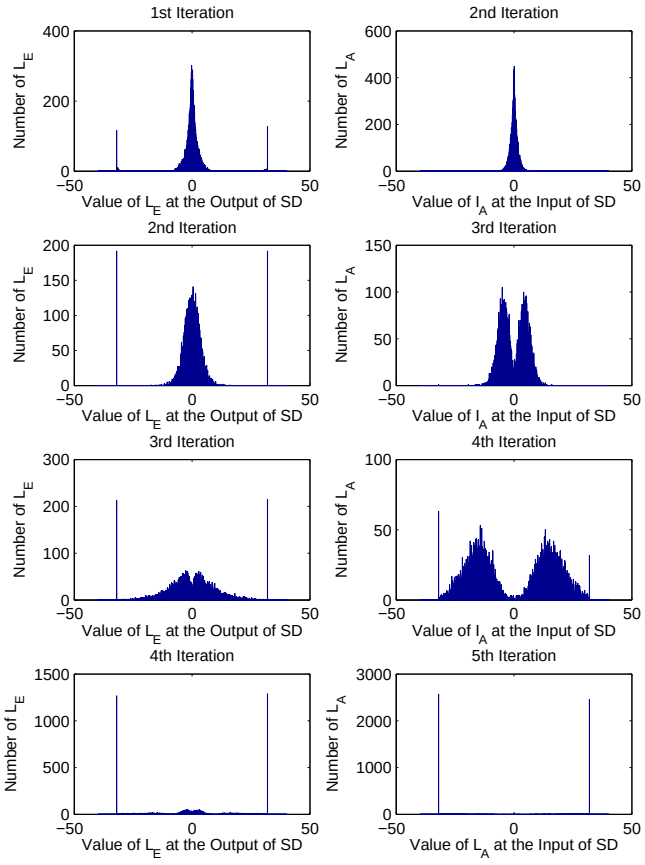

Figure 3.30: Histogram of the LLRs at both the input and the output of the K-best SD during the iterative process in the scenario of an (8×4)-element 4-QAM SDMA/OFDM system for $K = N_{cand} = 128$, SNR=10 dB.

significantly improved as it was previously shown in Figure 3.24. This performance enhancement can also be observed by comparing Figures 3.32 and 3.33, where not only the distribution of the LLRs, but also the achievable error-correction capability of the iterative system is observed. More explicitly, the horizontal axis characterizes the deviation of the LLRs from their legitimate value, where encountering a positive sign indicate that the LLR indeed reflects the correct polarity, while a negative value implies having the wrong polarity. By contrast, the total area associated with the histogram peaks indicates the relative frequency approximating the probability of correct and erroneous SD decisions. Observe in Figure 3.32 that for the first a few iterations, the variance of the near-Gaussian distributed LLRs increases, indicating that the *a priori* information improves upon iterating. As expected, the Gaussian-like distribution is then gradually destroyed since a large portion of the LLRs are assigned a value, which is close to the truncated LLR value as the iterations proceed, especially for the ALT-assisted system. However, observed in Figure 3.33 that after the fifth iteration, the ALT-assisted system becomes capable of generating a higher proportion of correct large-valued LLRs, implying a more significant performance gain.

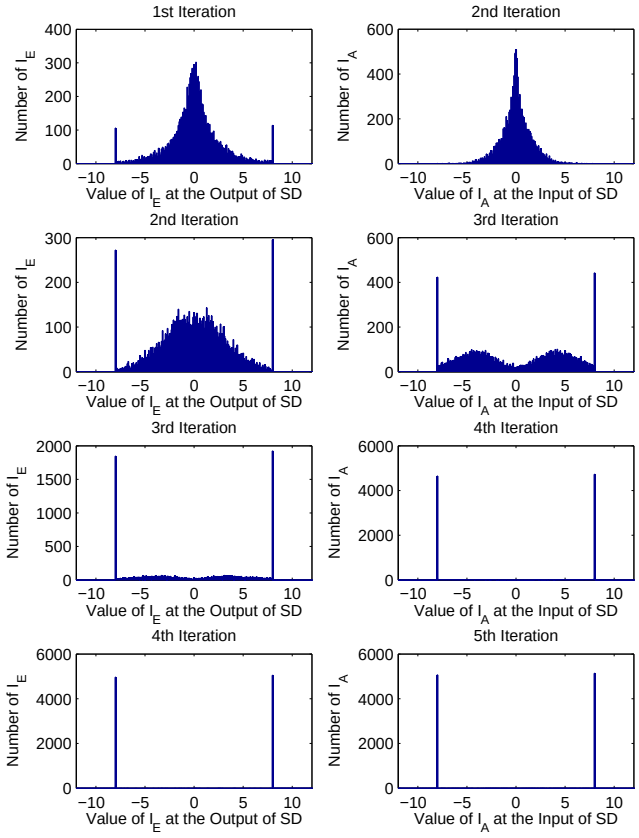

Figure 3.31: Histogram of the LLRs at both the input and the output of the ALT-assisted K-best SD during the iterative process in the scenario of an (8×4)-element 4-QAM SDMA/OFDM system for $K = N_{cand} = 128$, ALT-aided, SNR=10 dB.

3.3.3 The ALT-Assisted Center-Shifting Hybrid Sphere Detection

3.3.3.1 Comparison of the Center-Shifting and the ALT Schemes

Both the propsed center-shifting and ALT schemes require the repeated generation of candidate lists throughout the iterative detection process. In this section, we first compare the ALT scheme to the SIC-MMSE-aided center-shifting scheme, which was formed to be the most efficient of all the three center-shifting schemes proposed in Section 3.2.3.

From the BER curves depicted in Figures 3.21 and 3.24, we observe that in order to achieve the near-MAP performance exhibited by the SIC-MMSE-aided center-shifting K-best SD iterative receiver using K=32, we have to set K=128 for the ALT-assisted receiver. In other words, given a target BER, the SIC-MMSE-aided center-shifting scheme imposes a significantly lower complexity than the ALT scheme, as quantified in Figure 3.34(a), where their corresponding computational complexity is characterized versus the SNR quantified in terms of the total number of PED-evaluations per channel use. Specifically, although a fairly sharp drop can be seen in the complexity imposed by the ALT-assisted receiver as the SNR increased from a moderate level to a relatively high value, the ALT-assisted receiver still requires a considerably higher computational

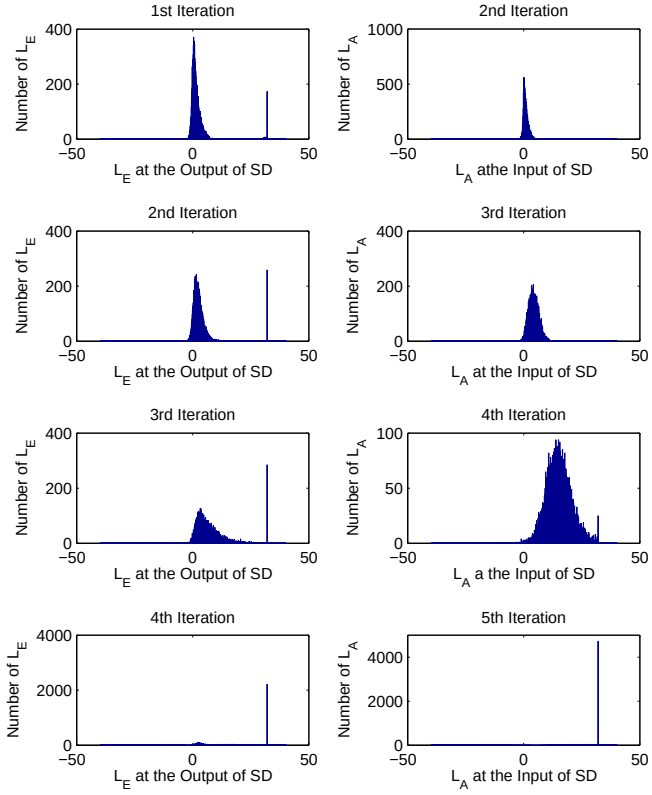

Figure 3.32: ($K = N_{cand} = 128$, SNR=10 dB) LLR histograms at both the input and the output of the K-best SD dispensing with ALT scheme during the iterative process in the scenario of an (8×4)-element 4-QAM SDMA/OFDM system: The horizontal axis represents the value of the LLRs, where the positive sign indicate the LLR has the correct polarity, while the negative implies the wrong polarity. Therefore, the vertical axis indicates the relative frequency of correct or wrong LLRs.

effort for matching the BER performance of its center-shifting-aided counterpart. On the other hand, the above-mentioned sharp drop in the complexity imposed by the ALT-aided K-best SD when the SNR is increased relatively high is caused by the fact that the complexity imposed per iteration decreases as the iterative detection proceeds as can be observed in Figure 3.34(b), where we have a relatively high of SNR=8dB.

3.3.3.2 ALT-Assisted Center-Shifting Hybrid Sphere Detection

Since the computational complexity imposed by the ALT scheme per iteration is expected to decrease as the iterations proceed as observed in Figure 3.34(b), in this section we propose a hybrid SD-aided iterative receiver, which combines the benefits of the ALT scheme and the SIC-MMSE center-shifting scheme, for the sake of attempting to reduce the associated complexity further. In comparison to the center-shifting SD receiver dispensing with the ALT technique, a small performance degradation is imposed if the ALT scheme is employed, as seen in Figure 3.35. This is not

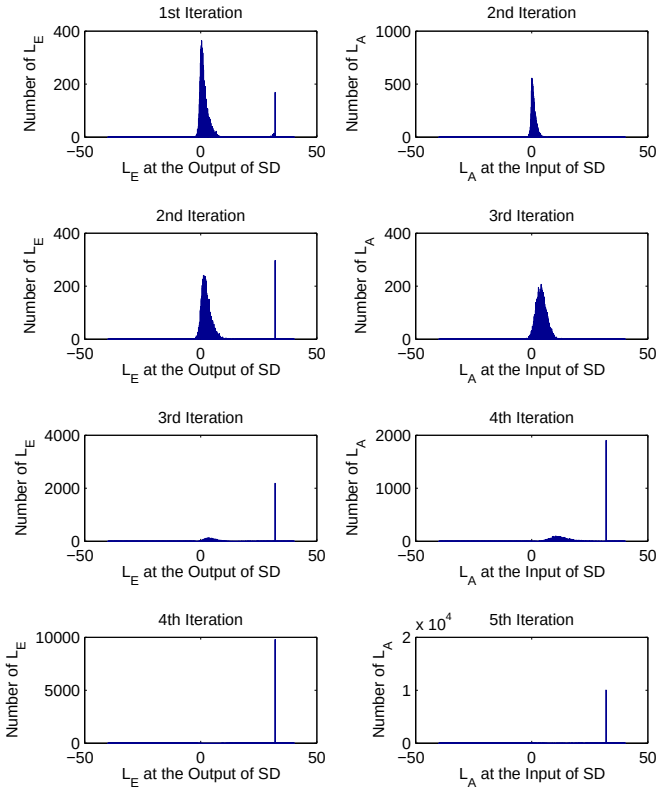

Figure 3.33: ($K = N_{cand} = 128$, SNR=10 dB) LLR histograms at both the input and the output of the K-best SD using ALT scheme during the iterative process in the scenario of an (8×4)-element 4-QAM SDMA/OFDM system: The horizontal axis represents the value of the LLRs, where the positive sign indicate the LLR has the correct polarity, while the negative implies the wrong polarity. Therefore, the vertical axis indicates the relative frequency of correct or wrong LLRs.

unexpected, since a non-Gaussian distribution was exhibited by the soft bit information, i.e. by the LLRs, which are exchanged between the inner and outer decoders, leading to a limited iterative gain. On the other hand, the computational complexity imposed by the candidate list generation phase of the SD is significantly reduced, as seen in Figure 3.36. More specifically, Figure 3.36(a) depicts the overall computational complexity of the hybrid receiver per channel use for different SNRs in contrast to that of the pure SIC-MMSE-assisted center-shifting SD receiver. By contrast, Figure 3.36(b) shows the computational complexity per channel use at each iteration, i.e. as a function of the iteration index. Both of the two receivers we compared here have to carry out the candidate list regeneration at each iteration. As shown in Figure 3.36(b), when invoking the ALT scheme, the hybrid system exhibits a gradually reduced complexity, as the iterations proceed, while the pure center-shifting-aided receiver imposes a constant complexity at each iteration. Hence, the resultant overall computational complexity of the hybrid receiver is significantly reduced. To be specific, for the candidate list generation phase, only about half the computational efforts are required by the hybrid receiver at high SNRs, as seen in Figure 3.36(a).

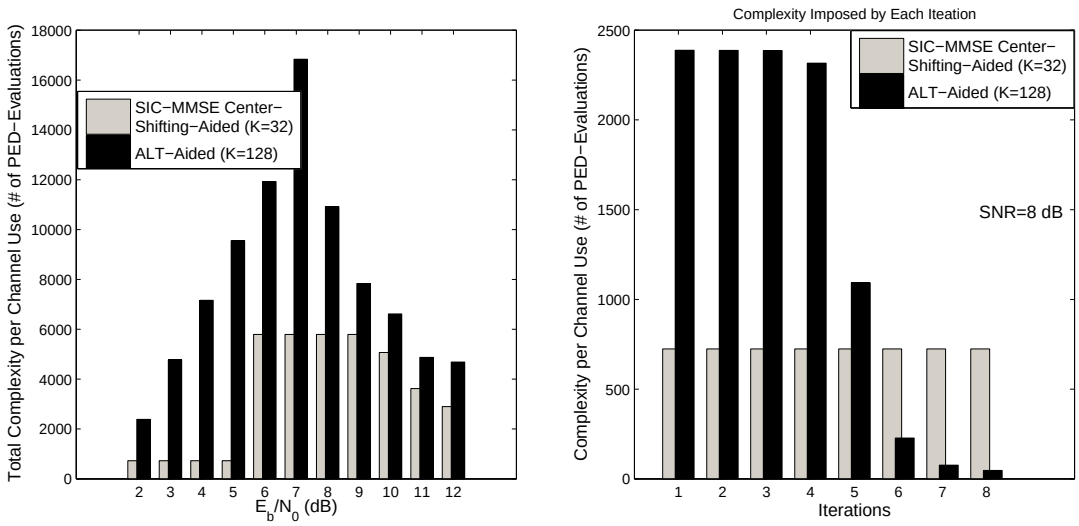

(a) (b)

Figure 3.34: The candidate list generation related computational complexity comparison of the SIC-MMSE center-shifting-aided and the ALT-aided K-best SD iterative receiver in (8×4)-element SDMA/OFDM system: (a) the overall computational complexity per channel use for different E_b/N_0s; (b) computational complexity per channel use of each iteration. Note: the maximum number of iterations for all different E_b/N_0s is 8 and the iterative detection will be terminated as soon as there is no more iteration gain can be achieved, i.e. the resultant trajectory line reaches the convergence point.

3.4 Unity-Rate-Code-Aided Three-Stage Iterative Receiver Employing SD

Recently, a unity-rate-code-aided (URC) 3-stage serially concatenated system was proposed [111] in the context of single-input single-output MMSE Turbo Equlization. A rate-1 encoder and its corresponding decoder are amalgamated with the transmitter and the receiver, respectively. Therefore, the *extrinsic* LLRs are exchanged between three blocks, i.e. the MMSE equalizer, the URC decoder and the convolutional decoder at the receiver, resulting in a significant performance gain which was explicitly indicated by the resultant EXIT charts shown in [111] [112]. In this section, we transplant the URC-aided three-stage concept into our SD-aided MIMO system. Investigation of the resultant system's performance has been carried out using both EXIT chart analysis and Monte Carlo simulations. Finally, the performance of the center-shifting scheme in this scenario will also be studied.

3.4.1 Unity-Rate-Code-Aided Three-Stage Iterative Receiver

Figure 3.37 depicts the system model of the SD-aided 3-stage serially concatenated transceiver in the context of an Uplink (UL) SDMA/OFDM system, where each user has a single transmit

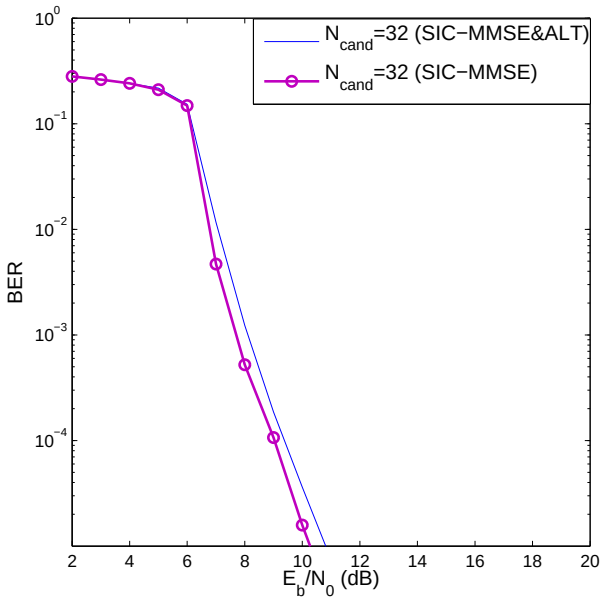

Figure 3.35: BER performance of the two-stage K-best SD iterative receiver using the combined SIC-MMSE center-shifting and the ALT schemes in an (8×4)-element 4QAM SDM/OFDM System. All other system parameters are listed in Table 3.1.

antenna, as we have always assumed so far. At the transmitter, a block of L information bits u_1 is first encoded by the convolutional channel encoder I in order to generate the coded bits c_1, which are interleaved by the interleaver Π_1 of Figure 3.37. Then the resultant permuted bits u_2 are successively fed through the URC encoder II and the interleaverΠ_2, yielding the interleaved double-encoded bits u_3, which are delivered to the bit-to-symbol modulator/mapper. Note that the labels u and c represent the uncoded and coded bits, respectively, corresponding to a specific module as indicated by the subscript. For example, u_2 and c_2 denote the uncoded bits and the coded bits at the input and the output of the URC encoder II of Figure 3.37, respectively. At the receiver of Figure 3.37 which is constituted by three modules, namely the SD, the URC decoder II and the convolutional channel decoder II, the extrinsic information is exchanged amongst the blocks in a number of consecutive iterations. Specifically, as shown in Figure 3.37, $A(\cdot)$ represents the *a priori* information expressed in terms of the LLRs, while $E(\cdot)$ denotes the corresponding *extrinsic* information. Hence, the URC decoder generates two *extrinsic* outputs by processing two *a priori* inputs delivered from both the SD and the convolutional decoder II. After completing the last iteration, the estimates $\hat{u}_1$ of the original transmitted information bit u_1 are produced by the convolutional channel decoder I.

We denote the MI between the *a priori* value $A(s)$ and the symbol s as $I_{A(s)}$, while the MI between the *extrinsic* value $E(s)$ and the symbol s by $I_{E(s)}$. Hence, the MI of the two outputs of the URC decoder, namely, $I_{E(u_2)}$ and $I_{E(c_2)}$, are functions of the two *a priori* MI input, namely, $I_{A(u_2)}$ and $I_{A(c_2)}$. Explicitly, we have [111]:

$$I_{E(u_2)} = T_{u_2}(I_{A(u_2)}, I_{A(c_2)}), \tag{3.35}$$

$$I_{E(c_2)} = T_{c_2}(I_{A(u_2)}, I_{A(c_2)}). \tag{3.36}$$

Therefore, two 3D EXIT charts corresponding to the above two equations are needed in order to

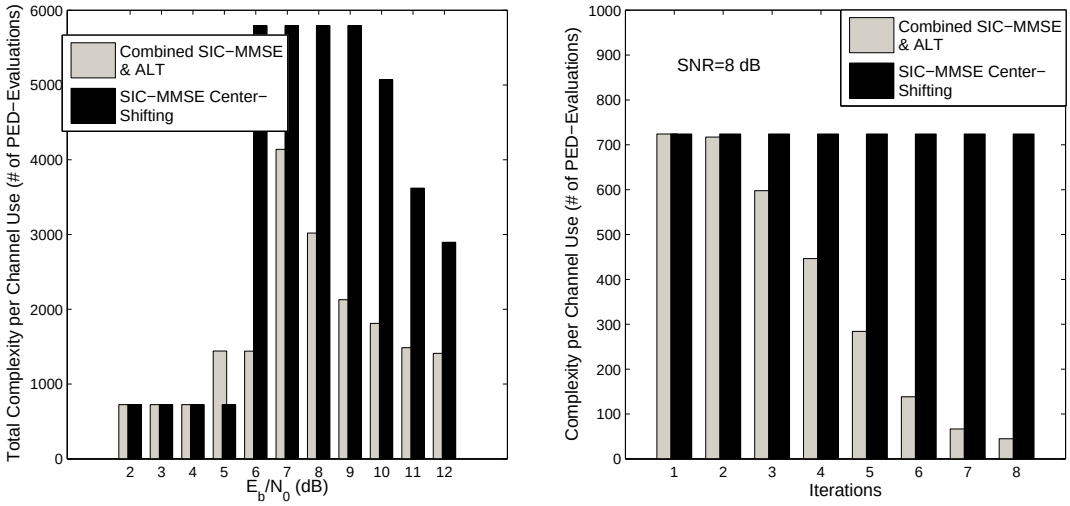

(a) (b)

Figure 3.36: The candidate list generation related computational complexity comparison of the hybrid K-best SD iterative receiver which combines the SIC-MMSE center-shifting scheme and the ALT technique: (a) the overall computational complexity per channel use for different E_b/N_0s; (b) computational complexity per channel use for each iteration. Note: the maximum number of iterations for all different E_b/N_0s is 8 and the iterative detection will be terminated as soon as there is no more iteration gain can be achieved, i.e. the resultant trajectory line reaches the convergence point.

fully describe the EXIT characteristics of the URC decoder. In contrast to the double-input-double-output URC module of Figure 3.37, both the SD and the convolutional decoder can be viewed as single-input-single-output modules, for a given received signal vector. Thus, a single 2D EXIT chart is sufficient for characterizing each of them. Similarly, we have the corresponding EXIT functions expressed as [111]:

$$I_{E(u_3)} = T_{u_3}(I_{A(u_3)}, E_b/N_0) \tag{3.37}$$

for the SD and

$$I_{E(c_1)} = T_{c_1}(I_{A(c_1)}) \tag{3.38}$$

for the convolutional channel decoder. We note that since the MI $I_{E(u_3)}$ of the SD's output, is independent of $I_{A(u_2)}$, the traditional EXIT curve of the SD portrayed in the 2D space of Figure 3.2 can be extende to the 3D space by sliding the EXIT curve along the $I_{A(u_2)}$ axis. That is to say the EXIT characteristics of the SD can be portrayed as an EXIT surface in one of the two 3D EXIT charts of the URC decoder, namely Figure 3.38(a). Similarly, the EXIT surface of the outer convolutional decoder can be generated as depicted in Figure 3.38(b) together with the other 3D EXIT chart of the URC decoder, since $I_{E(c1)}$ of Eq.(3.38) is independent of $I_{A(c2)}$. Consequently, totally two 3D EXIT charts are required for plotting all the EXIT functions. To be specific, Figure 3.38(a) for Eq.(3.36) and Eq.(3.37), while Figure 3.38(b) for Eq.(3.35) and Eq.(3.38).

The intersection of the surfaces of the SD and the URC decoder characterizes the best possi-

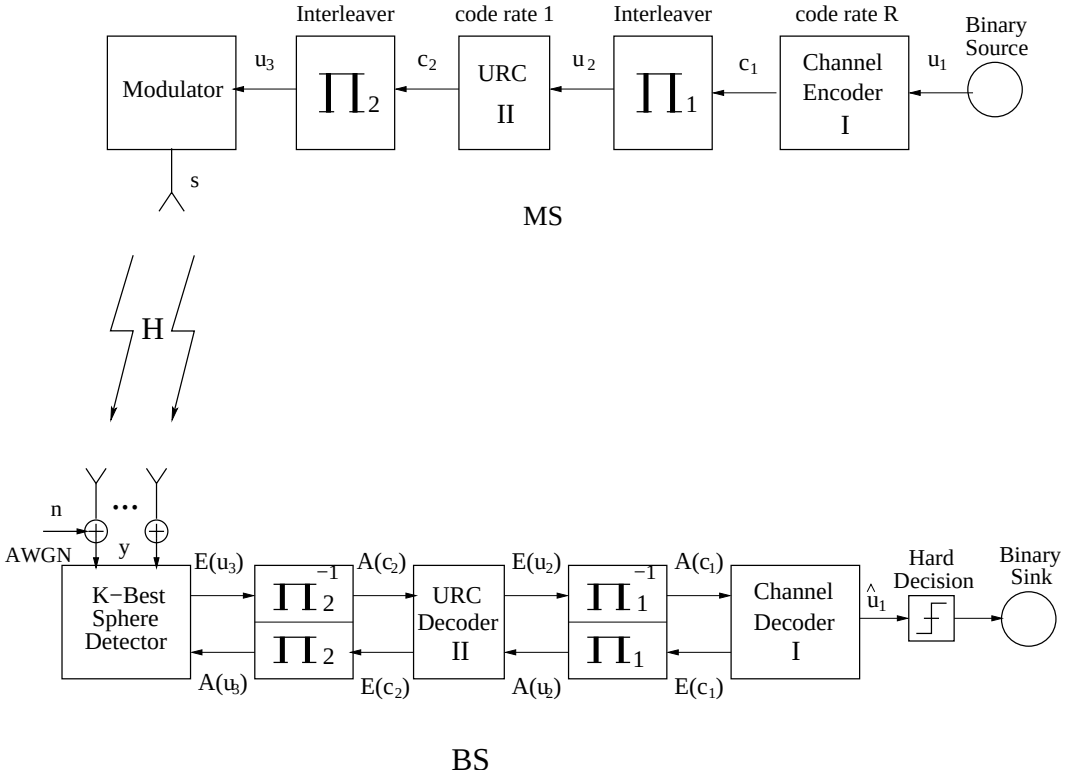

Figure 3.37: Unity-rate-code-aided 3-Stage iterative detection scheme

ble achieveable performance for different fixed values of $I_{A(u_2)}$ as the iterations between the SD and the URC decoder are carried out, during which the soft bit information is exchanged. More importantly, according to Eq.(3.35), for each point $(I_{A(u_2)}, I_{A(c_2)}, I_{E(c_2)})$ of the intersection line as seen in Figure 3.38(a), there is a specific point $(I_{A(u_2)}, I_{A(c_2)}, I_{E(u_2)})$ determined by the two *a priori* inputs of the URC decoder on the surface of the URC decoder in Figure 3.38(b). Hence, there must be a line (not plotted) on the surface of the URC decoder in Figure 3.38(b) corresponding to the intersection line in Figure 3.38(a). In order to simplify the complicated 3D EXIT chart representation, we view the SD and the URC decoder as a joint module with single input $I_{E(u_2)}$ and single output $I_{A(u_2)}$. As a result, a classical 2D EXIT chart can be plotted, which can be also obtained by projecting the aforementioned line on the surface of the URC decoder in Figure 3.38(b) on the $I_{E(u_2)}$-$I_{A(u_2)}$ plane, as seen in Figure 3.39(a).

Figure 3.39(a) shows the 2D EXIT chart of decoder I and the combined module of the decoder II and the SD, in comparison with that of the conventional two-stage iterative receiver. As observed in Figure 3.2, due to the insufficient length of the candidate list, the maximum achievable iterative gain becomes rather limited, since the EXIT curve of the SD intersects with that of the channel decoder at an earlier stage, if we have K or N_{cand} values of 16 or 32. In other words, when the resultant decoding trajectory gets trapped at the intersection point of the EXIT chart, where the decoding convergence point, after a certain number of iterations, typically a residual error floor persists. However, with the aid of the URC decoder II seen in Figure 3.37, the point of the EXIT curve intersection of the joint decoder II and SD module and that of decoder I moves close to the $(1, 1)$ point, resulting in a near-error-free performance, as long as there is an open tunnel between the two EXIT curves. More specifically, as observed in Figure 3.39(a), for the SD-aided iterative receiver

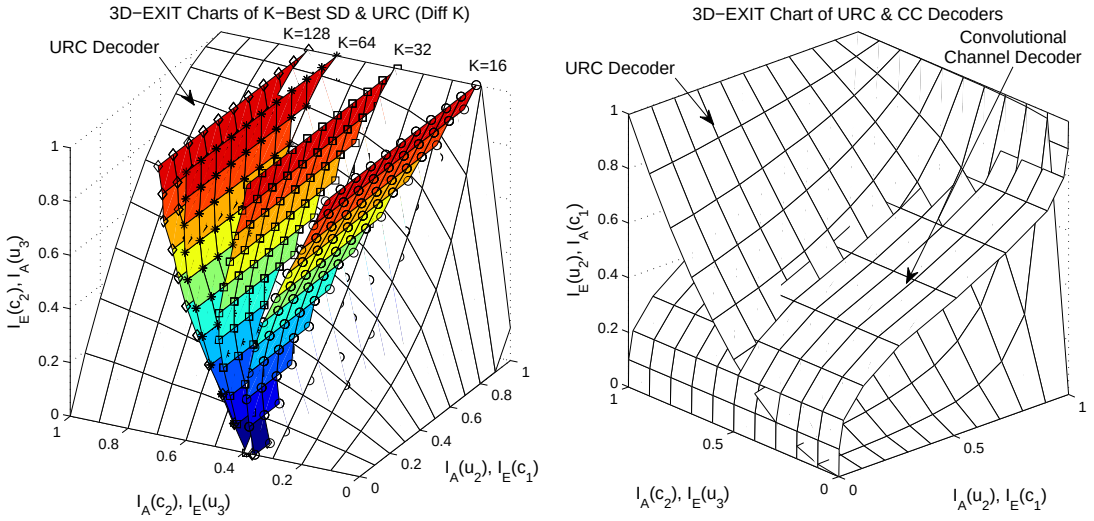

(a) (b)

Figure 3.38: (SNR=8 dB) 3D-EXIT charts of K-best SD-aided 3-stage iterative receiver in the scenario of (8×4) rank-deficient 4-QAM SDMA/OFDM system.

using $K = 16$, an open tunnel is created between the EXIT curve of the joint of SD and decoder II module and that of decoder I at an SNR of 10.2 dB. Thus, the corresponding BER curve plotted in Figure 3.39(b) confirmed the predictions of the EXIT chart analysis seen in Figure 3.39(a), indicating that the BER decreases sharply, once the SNR is in excess of about 10.2 dB. Similarly, when we have $K = 32$, a lower convergence threshold of 9.7 dB associated with an even earlier decrease of the BER curve, as shown in Figure 3.39(b). Consequently, given a target BER of 10^{-5}, nearly 4 dB and 2 dB performance gain can be attained over the conventional 2-stage iterative receiver, when employing the URC decoder II in conjunction with $K = 16$ and $K = 32$, respectively. However, as a price, the BER of the three-stage scheme is expected to be higher than that of the 2-stage receiver at low SNRs. The reason behind this phenomenon becomes clearer, if we refer to the EXIT chart comparison of the 2-stage and the 3-stage iterative receivers characterized in Figure 3.39(a), where we observe that the EXIT curve of the inner decoder of the conventional 2-stage receiver has a significantly higher starting point than that of its 3-stage counterpart, resulting in a lower convergence threshold, which in turn leads to a potential higher iterative gain at relatively low SNRs. Although the employment of the URC encoder/decoder pair at the transmitter/receiver is capable of moving the EXIT curve intercept point closer to $(1, 1)$, an open tunnel can only be formed, if the value of K or N_{cand} as well as that of the SNR is sufficiently high. This explains, why the BER curve of the SD using $(K = 32)$ drops sharply at a lower SNR than that of the SD employing $(K = 16)$, as seen in Figure 3.39(b).

The reason why a URC will make the slope of the EXIT chart curve steeper hence resulting in a lower error floor and a higher BER waterfall threshold, can be interpreted as follows. Since the URC has an Infinite-Impulse-Response (IIR) due to its recursive coding structure, the corresponding EXIT chart curve is capable of reaching the highest point of perfect convergence to an infinitesimally low BER $(1, 1)$, provided that the interleaver length is sufficiently large [113]. On

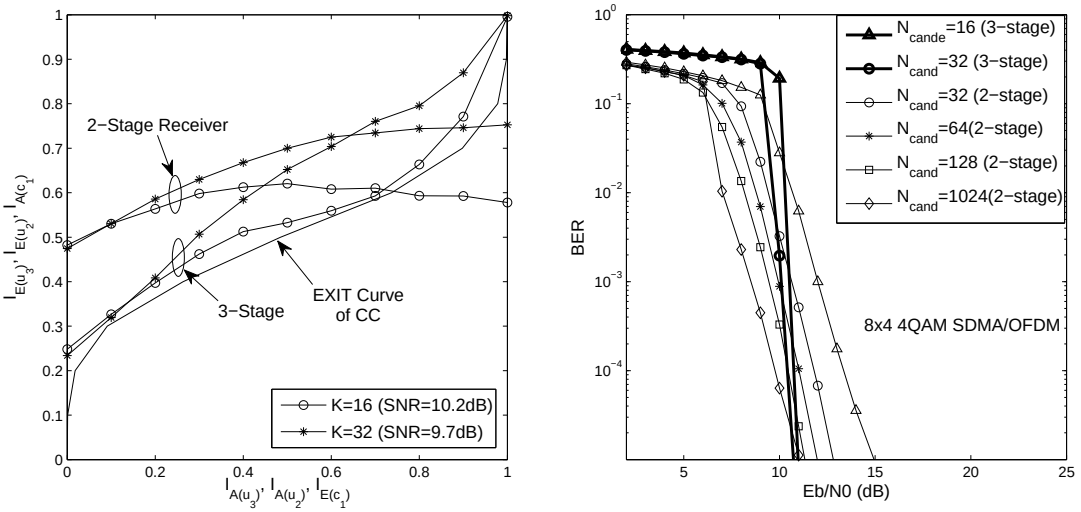

(a) 2D EXIT Chart

(b) BER Performance

Figure 3.39: EXIT analysis and BER performance of the three-stage iterative receiver using the K-best SD.

the other hand, since the URC decoder employs the MAP decoding scheme, the extrinsic probability computed at the output of the URC decoder contains the same amount of information as the sequence at the input of the URC decoder. In other words, the area under the inner EXIT curve remains unchanged regardless of the employment of the URC [114, 115]. Hence, a higher ending point of the EXIT curve leads to having a lower starting point, implying a steeper slope of the EXIT curve.

3.4.2 Performance of the Three-Stage Receiver Employing the Center-Shifting SD

The decay observed in Figure 3.2 for the combined SD and URC decoder II module's EXIT curve observed when K and N_{cand} are set to an insufficiently high value is caused by the corresponding EXIT surface of the SD as plotted in Figure 3.38(a). Our previous investigations for the center-shifting scheme indicated that the SIC-MMSE-aided scheme is capable of ensuring that the EXIT curve of the inner decoder, namely, that of the SD monotonically increases upon increasing I_A, as seen in Figure 3.20(a). Hence, we apply the SIC-MMSE center-shifting scheme in the context of the URC-aided three-stage iterative receiver, in order to improve the shape of the EXIT curve seen in Figure 3.39(a), which may result in a relatively high convergence threshold. The three-stage SIC-MMSE-aided center-shifting K-best SD assisted iterative receiver is portrayed in Figure 3.40, where the SIC-MMSE-aided center-calculation is applied. Thus, re-detection using an updated search center has to be carried out during each iteration that invokes the SD.

Figure 3.41 shows the resultant 3D EXIT chart of the three-stage scheme, where we observe that the EXIT surfaces do not suffer from a severe bending as those of the non-center-shifting-aided receiver characterized in Figure 3.38(a), even when K or N_{cand} is relatively small. The resultant

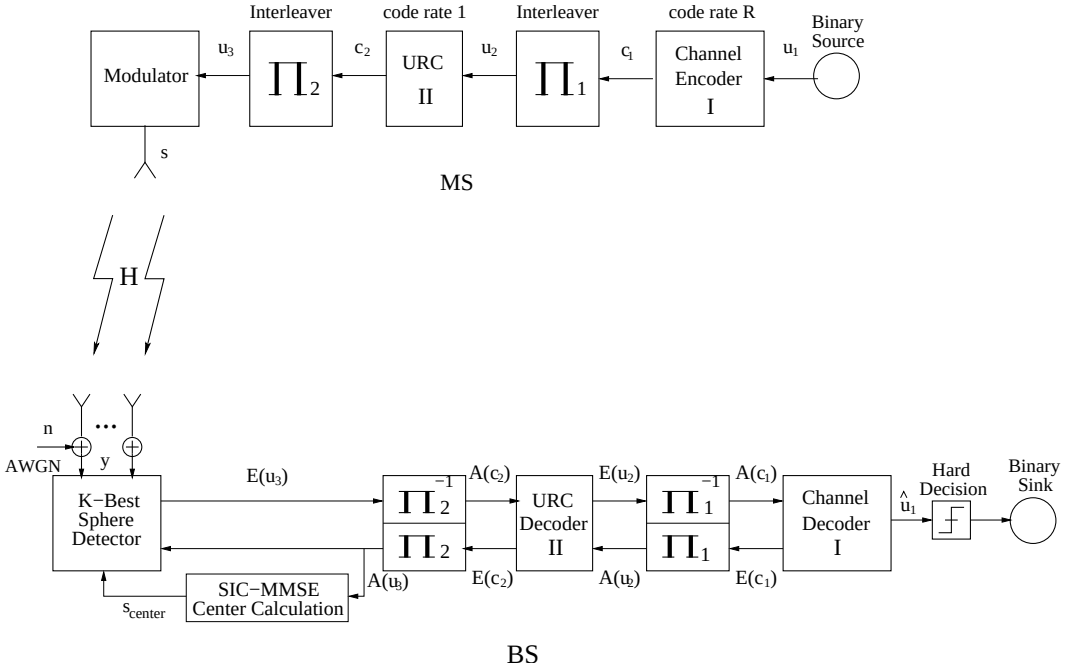

Figure 3.40: SIC-MMSE-aided center-shifting *K*-best SD-aided three-stage iterative detection scheme

EXIT curve of the combined SD and URC decoder II module is plotted in Figure 3.42(a), for $K = N_{cand} = 16$, which does not touch the EXIT curve of decoder I. To be specific, the original convergence threshold of the three-stage receiver using no center-shifting is about 10.2 dB, since an open tunnel is just formed for SNRs in excess of this level. For SNRs below this level, the EXIT curve of the combined module would fall below that of decoder I, leading to a consistently closed EXIT tunnel, as exemplified by the situation characterized by SNR=9.6 dB, as also portrayed in Figure 3.42(a). However, thanks to the employment of the SIC-MMSE-aided center-shifting scheme, a wide open tunnel has been created between the EXIT curves. The convergence threshold of the SIC-MMSE center-shifting aided three-stage scheme was reduced to about 9.6 dB and the resultant BER curve is plotted in Figure 3.42(b) in comparison to that of the three-stage receiver dispensing with center-shifting. Indeed, with the aid of the center-shifting scheme, the BER curve starts to drop more sharply at a slightly lower SNR, which is similar to the convergence threshold observed in Figure 3.42(a), yielding a performance gain of 0.5 dB for the target BER of 10^{-5}. It is not unexpected that the attainable performance improvement is insignificant, since the SIC-MMSE center-shifting scheme fails to increase the relatively low starting point of the EXIT curve, which is brought about by the employment of the URC decoder II.

3.4.3 Irregular Convolutional Codes for Three-Stage Iterative Receivers

The so-called Irregular Convolutional Codes (IrCCs) [116, 117] proposed by Tüchler and Hagenauer, encode appropriately chosen 'fractions' of the input stream using punctured constituent convolutional codes having different code rates. The appropriate 'fractions' are specifically designed with the aid of EXIT charts, for the sake of improving the convergence behavior of iteratively decoded systems. Thus, with the aid of IrCCs, we are able to solve the mismatch between the EXIT

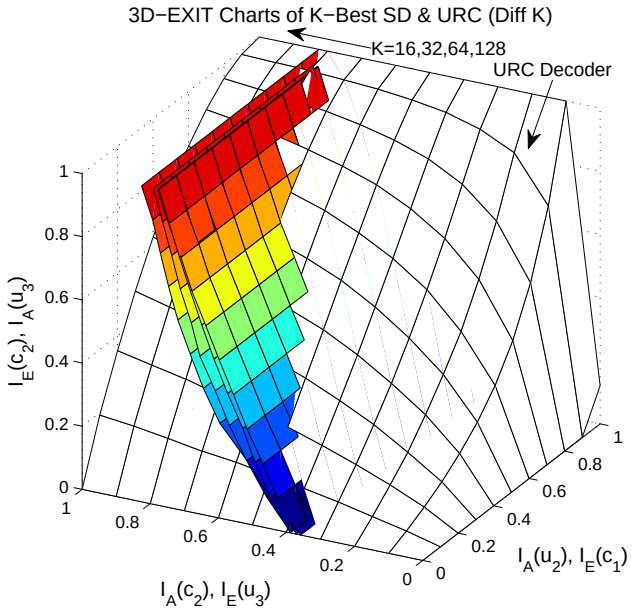

Figure 3.41: 3D EXIT chart of the three-stage SIC-MMSE-aided center-shifting K-best SD assisted iterative receiver

curve of the inner decoder in the three-stage receiver and the EXIT curve of the RSC $(2,1,3)$ code marked by crosses in Fig. 3.43. Our goal is to achieve an improved convergence behavior for the three-stage concantenated system by minimizing the area between the EXIT curve of the amalgamated two-compound inner code and that of the outer code. The resultant EXIT curve of the optimized IrCC having a code rate of 0.5 is represented by the dotted line in Fig. 3.43. Hence, a narrow but still open EXIT-chart tunnel is created, which implies having a near-capacity performance attained at the cost of a potentially high number of decoding iterations, although the 'per-iteration' complexity may be low.

Monte Carlo simulations were performed for characterizing the decoding convergence prediction of the IrCC design in the high-throughput overloaded (8×4) SDMA/OFDM system. As our benchmarker system, the half-rate RSC(2,1,3) code's EXIT curve marked by crosses in Fig. 3.43 is employed as the outer code of the traditional two-stage receiver. As our proposed scheme, the half-rate IrCC corresponding to the EXIT curve represented by the dotted line in Fig. 3.43 is used as the outer code in the URC-assisted three-stage receiver. Fig. 3.44 compares the BER performance of both systems, where we can see that at relatively high SNRs, both three-stage concatenated receivers - namely that using the SD employing the classic RSC code as well as the one employing the optimized IrCC code - are capable of outperforming the traditional two-stage receiver equipped with the SD. Specifically, given a target BER of 10^{-5}, a performance gain of 2.5 dB can be attained by the three-stage receiver over its two-stage counterpart, when both of them employ the SD ($N_{cand} = 32$) and the regular RSC. Remarkably, when amalgamated with the URC encoder/decoder, the three-stage receiver using the SD and $N_{cand} = 32$ becomes capable of outperforming the two-stage receiver using the high-complexity near-MAP SD having $N_{cand} = 1024$, provided that the SNR is in excess of about 11 dB. Furthermore, an addiational performance gain of 1 dB can be attained by employing the optimized IrCC in comparison to the classic RSC aided three-stage system. Moreover, in order to further enhance the achievable performance, when the

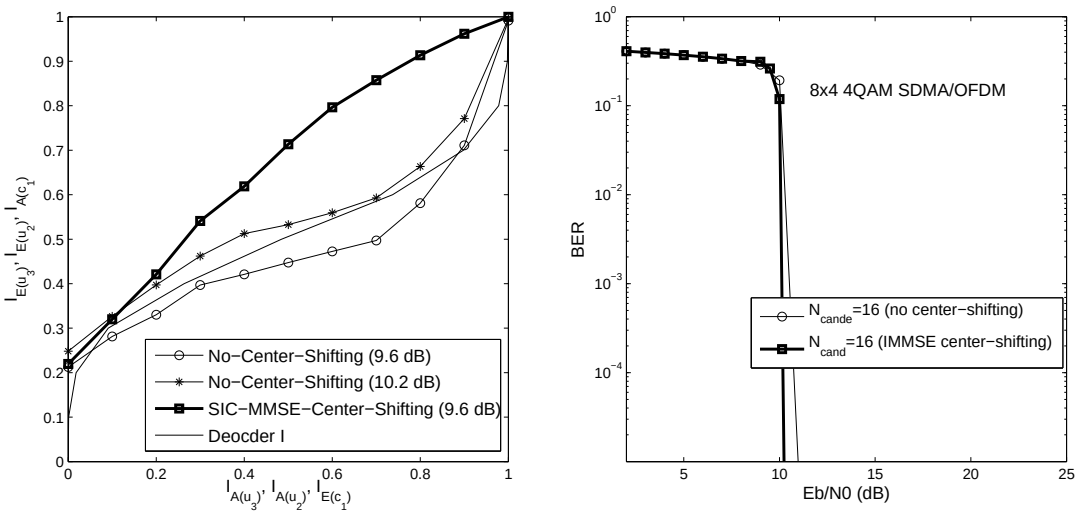

(a) 2D EXIT Chart $(K = 16)$ (b) BER Performance

Figure 3.42: EXIT Analysis and BER Performance of SIC-MMSE-Aided Center-Shifting K-Best SD 3-Stage Iterative Receiver.

SIC-MMSE-aided iterative center-shifting SD is invoked, another approximately 1 dB additional performance gain is attained. Consequently, as observed in Fig. 3.44, given a target BER of 10^{-5}, overall performance gains of 4.5 dB and 2 dB are attained by our proposed system in comparison to its SD ($N_{cand} = 32$) aided and SD ($N_{cand} = 1024$) assisted two-stage counterparts, respectively.

In line with the EXIT chart based predictions of Fig. 3.43, a sharp BER improvement is achieved by the three-stage receiver, as seen in Fig. 3.44, since the EXIT curve of the inner code will rise above that of the outer code for SNRs in excess of a certain level, resulting in a consistently open EXIT tunnel leading to the point of convergence at $(1,1)$, which is exemplified in Fig. 3.45 by the curve recorded at SNR$=$ 9.5 dB when using the half-rate IrCC as the outer code. Also shown in Fig. 3.45 is the stair-case shaped decoding trajectory evolving through the open tunnel to the point of convergence at $(1,1)$, as recorded during our Monte Carlo simulations. The activation order of the three SISO modules used is $[3\ 2\ 1\ 2\ 1\ 2]$, where the integers represent the Index (I) of the three SISO modules. Specifically, $I = 3$ denotes the SD, $I = 2$ represents the URC decoder II and $I = 1$ denotes the channel decoder I of Fig. 3.40. Hence, the vertical coordinates of the points A_1, A_3 and A_5 in Fig. 3.45 quantify the $I_{E(u_2)}$ value measured at the output of the URC decoder II corresponding to its three successive activations during the first iteration, respectively, while the segments between A_1 and A_2 as well as between A_3 and A_4 represent two successive activations of the channel decoder I during the first iteration, respectively. The segment between A_5 and A_6 in Fig. 3.45 denotes the beginning of a new iteration associated with similar decoding activations.

Figure 3.46 depicts the computational complexity - which is quantified in terms of the number of PED evaluations corresponding to the term ϕ of Eq.(2.24) - imposed by the SD versus E_b/N_0 for the above-mentioned receivers. Note that the computational complexity imposed by the K-best SD dispensing with the center-shifting scheme remains constant for both two-stage and three-stage

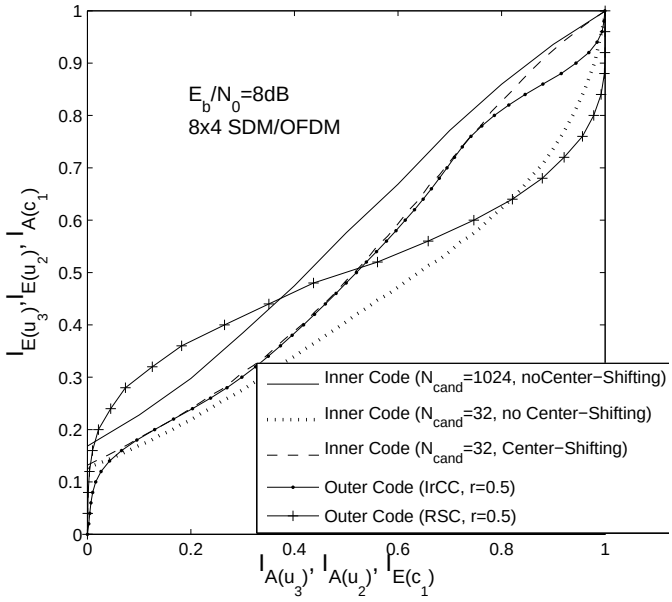

Figure 3.43: EXIT charts of the URC-aided three-stage receiver in the scenario of an (8×4)-element SDMA/OFDM system at $E_b/N_0 = 8$ dB.

receivers regardless of the SNR and the number of iterations, under the assumption that the buffer size is sufficiently large to store the resultant candidate list $\mathcal{L}$, which is generated by the SD just once during the first iteration between the SD and the channel decoder. On the other hand, every time the search center $\mathbf{x}_c$ in the transmit domain is updated, the SD is required to regenerate the candidate list. However, as observed in Figure 3.46 the candidate list size N_{cand} can be substantially reduced with the aid of the center-shifting scheme, hence the resultant overall complexity imposed by the SD becomes significantly lower than that of the receiver using no center-shifting. Explicitly, the candidate list generation complexity of the SIC-MMSE center-shifting-aided two-stage receiver is well below that of the receiver using no center-shifting right across the SNR range spanning from 2 dB to 12 dB. This statement is valid, if our aim is to achieve the near-MAP BER performance quantified in Figure 3.44, which can be attained by having $K = N_{cand} = 1024$ for the system operating without the center-shifting scheme or by setting $K = N_{cand} = 32$ in the presence of the center-shifting scheme. Actually, the number of PED evaluations carried out per channel use by the system dispensing with the center-shifting scheme remains as high as 13,652, regardless of the SNR and the number of iterations. On the other hand, in the presence of the center-shifting scheme, the candidate list has to be regenerated at each iteration, but nonetheless, the total complexity imposed is substantially reduced. We can also observe from Figure 3.46 that the center-shifting K-best SD employed by the URC-aided three-stage system imposes a computational complexity, which is even below that of its center-shifting-aided two-stage counterpart, while achieving a performance gain of 2 dB for target BER of 10^{-5}, as seen in Figure 3.44. Hence, the significant complexity reduction facilitated by the proposed SD scheme in the context of the three-stage receiver outweighs the relatively small additional complexity cost imposed by the URC, which only employs a two-state trellis, leading to an overall reduced complexity. Furthermore, in addition to the complexity reduction achieved by the proposed scheme, another benefit is the attainable memory reduction,

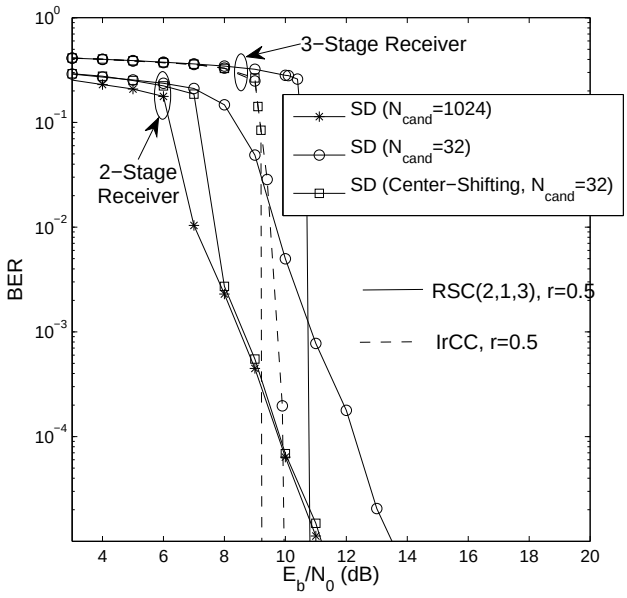

Figure 3.44: BER performance of the three-stage iterative receiver using the K-best SD in the scenario of an (8×4)-element SDMA/OFDM system.

since there is no need to store the resultant candidate list for the forthcoming iterations. As a result, the memory size required can be substantially reduced by having a significantly reduced value of K.

3.5 Chapter Conclusions

In this chapter, our main objective was to reduce the complexity encountered by the conventional LSD in the channel coded iterative receiver and to contrive a near-capacity design for the SD-aided MIMO system. To be specific, although the conventional LSD was capable of achieving a significant complexity reduction in comparison to the exact MAP detector, it may still impose a potentially excessive complexity, since the LSD has to generate soft information for every transmitted bit, which requires the observation of a high number of hypotheses about the transmitted MIMO symbol, thus generating a large candidate list to represent the entire lattice. This complexity problem may be aggravated by supporting an increased number of users and/or using a high-order modulation scheme, especially in high-dimensional rank-deficient MIMO systems. Therefore, in order to maintain a near-MAP performance, while relying on a small set of symbol hypotheses, we proposed two complexity-reduction techniques, namely the iterative center-shifting based SD scheme of Section 3.2 and the ALT-assisted SD scheme of Section 3.3, both of which rely on the exploitation of the soft-bit-information delivered by the outer channel decoder in the iterative receiver.

More specifically, in Section 3.2.3 three different algorithms were proposed for the iterative center-shifting SD, namely, the DHDC, the DSDC and the SIC-MMSE assisted search-center calculation schemes. It was shown in Figure 3.21(b) that the SIC-MMSE-aided scheme outperforms the other two. This is not unexpected, since although the SIC-MMSE-aided SD scheme imposes a

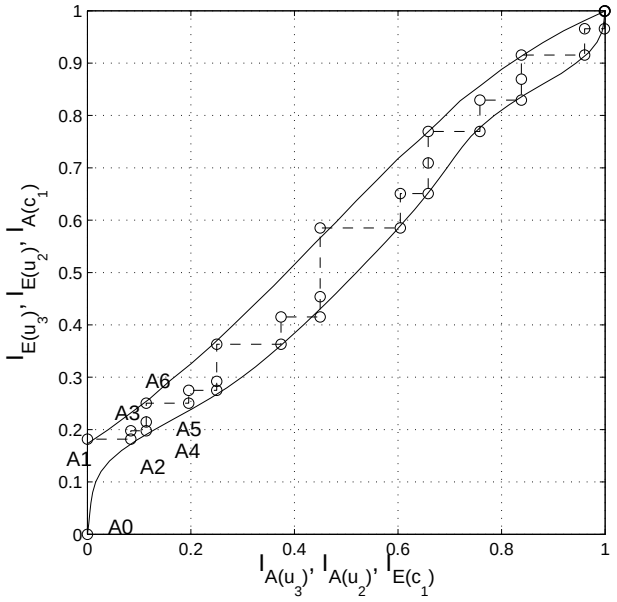

Figure 3.45: EXIT charts and recorded decoding trajectory for the three-stage receiver using IrCC at $E_b/N_0 = 9.5$ dB in the scenario of an (8×4)-element SDMA/OFDM system

.

slightly higher complexity in order to attain a more accurate search center, a significant complexity reduction may be achieved, which is associated with the list generation and soft-bit-information calculation carried out by the SD. Our proposition in Section 3.2.2 was that the search center may be generated by a more sophisticated detector than the LS or MMSE detector of conventional SDs. This generic proposition turned the SD into a high-flexibility detector, which may be beneficially combined with highly sophisticated or low-complexity linear or nonlinear detectors. In other words, the total affordable computational complexity may be flexibly split between the SD's search-center calculation phase and the search phase.

Based on the exploitation of the soft-bit-information, namely, the *a priori* LLRs gleaned from the outer channel decoder, in Section 3.3 we proposed another reduced-complex technique termed as the ALT-aided SD scheme. Given the definition of the *a priori* LLRs, the sign of the LLR indicates whether the current bit is more likely to be $+1$ or -1, whereas the magnitude reflects how reliable the decision concerning the current bit is. Hence, the basic idea behind the ALT-aided SD scheme of Section 3.3 is as follows: when the absolute value of the *a priori* LLR of a specific bit is larger than the preset ALT threhold, we assume that we have reliable knowledge of this bit being 0 or 1. As a result, the tree search of the SD may be significantly simplified, since the number of the tentative candidates for the corresponding tree search level may be reduced. As evidenced by Figure 3.26(b), the threshold has to be carefully adjusted for the sake of achieving the target performance as a function of the SNR encountered. As seen in Figure 3.24, the proposed ALT scheme is capable of providing useful performance improvements, although these are slightly less significantly than those achieved by the SIC-MMSE based center-shifting-assisted SD scheme in Figure 3.21(a). This is because the non-Gaussian distribution of the LLRs recorded at the output of the ALT-aided SD in Figure 3.29 during the iterative detection process limits the efficiency

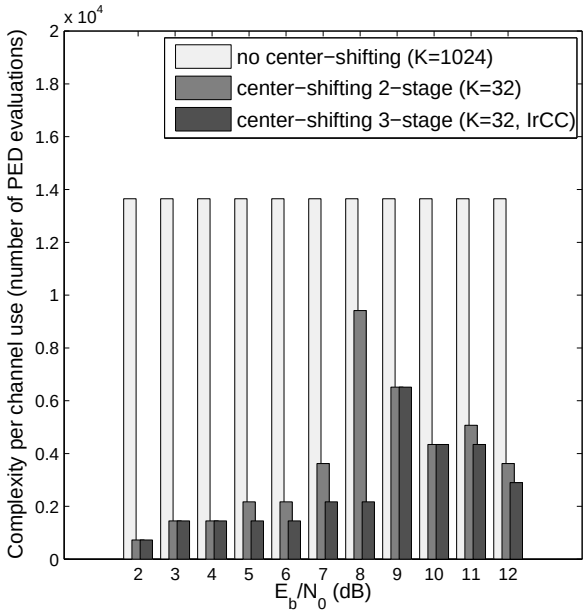

Figure 3.46: Complexity reduction achieved by the three-stage iterative receiver using the K-best SD in the scenario of an (8×4)-element SDMA/OFDM system.

of the iterative detection process and imposes difficulties in the EXIT chart assisted performance prediction.

Finally, motivated by the URC-aided three-stage SISO turbo equalizer of [111], in Section 3.4 we significantly improved the performance of the conventional two-stage SD-aided turbo receiver of Figure 3.1. We achieved this improvement by intrinsically amalgamating the SD with the decoder of a URC having an IIR, both of which were embedded in a channel-coded SDMA/OFDM transceiver, thereby creating the powerful three-stage serially concatenated scheme of Figure 3.40. For the sake of achieving a near-capacity performance, observed in Figure 3.40 that IrCCs were used as the outer code for the proposed iterative center-shifting SD aided three-stage system. Consequently, we demonstrated in Figure 3.44 that at a target BER of 10^{-5}, an E_b/N_0 performance gain as high as 4.5 dB was attained by the system of Figure 3.40 using the MMSE-based center-shifting SD relying on a low-complexity candidate list size of $N_{cand} = 32$, in comparison to its two-stage counterpart of Figure 3.18 in the challenging scenario of an (8×4)-element rank-deficient 4-QAM SDMA/OFDM uplink system.

In Table 3.8 we quantitatively summarize and compare the different SD-aided receiver's performance as well as complexity in the context of an $(\mathbf{8} \times \mathbf{4})$-element 4-QAM SDM/OFDM Rank-Deficient System. As observed in Table 3.8 the combination of the SIC-MMSE-aided center-shifting and the ALT schemes is capable of achieving a near-MAP performance at the lowest complexity for the conventional 2-stage receiver. A further performance gain of 1.6 dB may be attained by our near-capacity design using the URC-aided 3-stage receiver.

Performance & Computational Complexity of Various SD-Aided Receiver in an (8×4)-element 4-QAM SDM/OFDM Rank-Deficient System (Targe BER: 10^{-5})							
SD-Aided Receiver		$N_{cand}(K)$	**Iterations**	**SNR**	**Memories**	**SD Compl.**	**MAP Compl.**
2-stage receiver (RSC)	conventional SD (no center-shifting, no ALT)	1024	3	10.5	8196	13652	49152
		128	3	11.2	1024	2388	6144
		64	2	12	512	1364	2048
		32	2	12.8	256	724	1024
		16	2	15	128	404	512
	SIC-MMSE aided center-shifting SD (no ALT)	64	3	10.2	512	4092	3072
		32	3	10.2	256	2172	1536
		16	3	11	128	1212	768
	ALT-aided SD (no center-shifting)	128	4	10.2	1024	5070	8192
		16	6	12.8	128	N/A	1536
	SIC-MMSE aided center-shifting SD using ALT	32	4	10.8	256	1490	2048
3-stage receiver (IrCC)	SIC-MMSE aided center-shifting SD IrCC, r=0.5	32	9	9.2	256	6520	4608

Table 3.8: Summary of the SD-aided receiver investigations of Chapter 3. Note that the computational complexity of the SD, i.e. the list generation by the SD, is calculated in terms of the total number of PED evaluations, while that of the soft information generation by the SD/MAP detector is computed on the basis of Eq.(3.16) in terms of the total number of OF evaluations corresponding to the two terms in Eq.(3.14).

Chapter 4

Sphere Packing Modulated MIMO-OFDM Employing Multi-Dimensional Tree Search Assisted Sphere Detection

4.1 Introduction

4.1.1 System Model

In previous chapters, the SDMA/OFDM system supporting U single-antenna-assisted MSs was considered, where the multiuser data streams sharing the same time/frequency channel can be distinguished at the BS with the aid of their unique user-specific spatial signature constituted by their CIRs, resulting in a potentially significant increase in spectral efficiency. The separability of the individual MIMO links relies on the presence of rich multipath propagation, which requires a sufficiently high antenna spacing, in order to ensure that the individual channels between pairs of the transmit and receive antennas exhibit an independent Rayleigh distribution and the absence of a strong Line-Of-Sight (LOS) path. In the light of this interpretation, SDMA transmissions can be viewed as MIMO schemes maximizing the system's overall throughput.

On the other hand, instead of maximizing the system's overall throughput, another powerful family of MIMO schemes was designed for achieving spatial diversity, which is usually quantified in terms of the number of decorrelated spatial branches available at the transmitter or receiver, which is referred to as the *diversity order*. An effective and practical way of achieving MIMO-aided diversity is to employ space-time coding (STC), which is a specific coding technique designed for MIMO systems equipped with multiple spatially separated transmit antennas. When the signals of a specific user are launched from different transmit antennas during different time slots, the independently fading channels are less likely to simultaneously encounter deep fades. Hence, the

MIMO system is capable of exploiting the independently fading paths of multipath propagation environments.

Hence, the family of MIMO transmission schemes may be subdivided into two main categories, i.e. those designed for achieving spatial multiplexing and spatial diversity, which aim to maximize the data rate and to minimize the transmission error rate, respectively. It is worth noting, however that there have been proposals in the literature, which are capable of striking a more flexible compromise between the achievable rate and reliability [22]. Therefore, in this chapter we consider a UL Multi-User MIMO (MU-MIMO) system, where the SDMA technique used as a spatial multiple access scheme significantly increases the system's overall throughput without requiring extra spectrum. Meanwhile, in order to attain the spatial diversity gains, multiple antennas are assumed to be employed by each user. Thus, the multiple-transmit-antenna-assisted STC scheme may be employed by each user providing the diversity gains on top of the spatial multiplexing gain, which renders the system more robust to the hostile wireless fading channels.

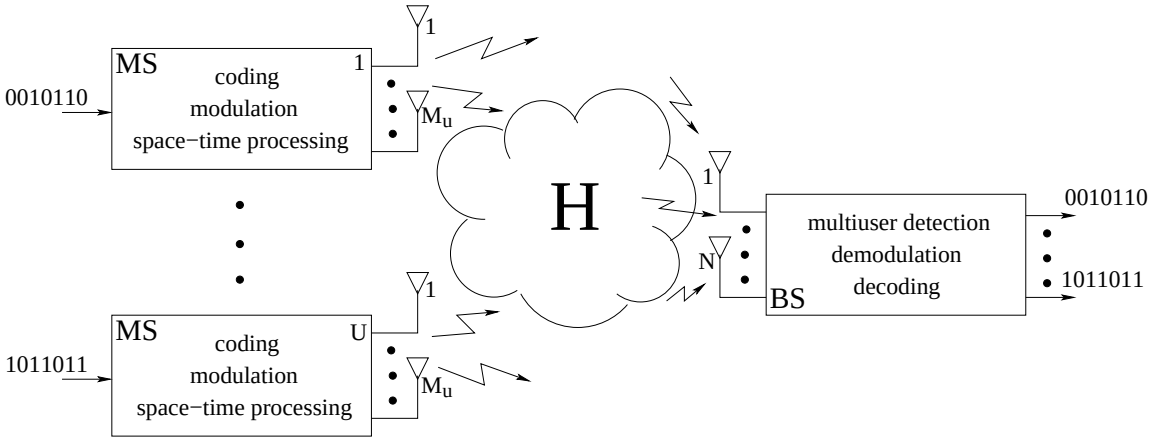

Figure 4.1: Schemtic of a generalized SDMA/OFDM wireless uplink transmission system.

More specifically, the generalized SDMA/OFDM UL transmission scenario is now depicted in Figure 4.1, where each of the U synchronous co-channel users/mobile stations (MS) is equipped with M_u transmit antennas and employs a specific STC scheme, while the BS has N receive antenna elements. Hence, under the assumption that each MS is equipped with the same number of transmit antenna elements, the total number of transmit antennas is $M = M_1 + M_2 +, ..., +M_U = U \cdot M_u$. The space-time modulator of the uth MS maps a *sequence* of bits $b(k)_{k=0}^{B-1}$ to a *sequence* of $M_u \times 1$ symbol vectors $\mathbf{s}(t)_{t=0}^{J-1}$, which are transmitted with the aid of its own M_u number of transmit antenna elements during J successive symbol periods of duration T. Generally, each space-time signal of the uth MS can be expressed as a $(M_u \times J)$-element matrix given by

$$\mathbf{S} = \left[\mathbf{s}^{(u)}(T), \mathbf{s}^{(u)}(2T), ..., \mathbf{s}^{(u)}(JT)\right], \tag{4.1}$$

$$= \begin{bmatrix} s_1^{(u)}(T) & s_1^{(u)}(2T) & \cdots & s_1^{(u)}(JT) \\ s_2^{(u)}(T) & s_2^{(u)}(2T) & \cdots & s_2^{(u)}(JT) \\ \vdots & \vdots & \ddots & \vdots \\ s_{M_u}^{(u)}(T) & s_{M_u}^{(u)}(2T) & \cdots & s_{M_u}^{(u)}(JT), \end{bmatrix}_{M_u \times J}, \tag{4.2}$$

where $s_m^{(u)}(jT)$ denotes the symbol transmitted by the transmit antenna element m $(m = 1, 2, ..., M_u)$

of user u $(u = 1, 2, ..., U)$ during the jth symbol period $(j = 1, 2, ..., J)$. Hence, the resultant average rate, or throughput, of a specific space-time code is B/J bits/sec/Hz. Note that for a pure spatial multiplexing system, we have $J = 1$, since there is no spatial or temporal correlation introduced among the transmitted signals.

The multiple transmit antennas of each MS are assumed to be positioned as far apart as possible to ensure that signals launched from the different transmit antennas experience independent or spatially uncorrelated fading channels. Hence, at an arbitrary time, the link between each pair of transmit and receiver antennas may be characterized with the aid of a unique transmit-antenna-specific FDCTF, which is denoted as $h_{nm}^{(u)}$. The superscript and subscript of h represent the user and the antenna element index, respectively. For example, the FDCTF or the spatial signature of transmit antenna element m of the uth user can be expressed as a column vector:

$$\mathbf{h}_m^{(u)} = \left[h_{1m}^{(u)}, h_{2m}^{(u)}, ..., h_{Nm}^{(u)}\right]^T, \tag{4.3}$$

with $m \in 1, ..., M_u$ and $u \in 1, ..., U$. If the mth transmit antenna element's signal is denoted by $s_m^{(u)}$, and the received signal plus the additive white Gaussian noise (AWGN) at receive antenna element n is represented by y_n and w_n, respectively, the entire SDMA system can be described by a matrix equation written as:

$$\mathbf{y} = \mathbf{H}\mathbf{s} + \mathbf{w}, \tag{4.4}$$

where the received signal vector is $\mathbf{y} \in \mathbb{C}^{N\times 1}$, the transmitted signal vector is $\mathbf{s} \in \mathbb{C}^{M\times 1}$, and the noise vector is $\mathbf{w} \in \mathbb{C}^{N\times 1}$, which are given by the following equations, respectively:

$$\begin{aligned}
\mathbf{y} &= [y_1, y_2, ..., y_N]^T, && (4.5)\\
\mathbf{s} &= \left[s_1^{(1)}, s_2^{(1)}, ..., s_{M_1}^{(1)}, ..., s_1^{(U)}, s_2^{(U)}, ..., s_{M_U}^{(U)}\right]^T, && (4.6)\\
&= [s_1, s_2, ..., s_M]^T, && (4.7)\\
\mathbf{w} &= [w_1, w_2, ..., w_N]^T. && (4.8)
\end{aligned}$$

The system's overall FDCTF matrix $\mathbf{H} \in \mathbb{C}^{N\times M}$ is constituted by M FDCTF column vectors $\mathbf{h}_m^{(u)} \in \mathbb{C}^{N\times 1}$, which correspond to the spatial signature of the mth transmit antenna element of the uth user, as defined by Eq.(4.3). Hence, the FDCTF matrix $\mathbf{H}$ can be expressed as:

$$\mathbf{H} = [\underbrace{\mathbf{h}_1^{(1)}, \mathbf{h}_2^{(1)}, ..., \mathbf{h}_{M_1}^{(1)}, ..., \mathbf{h}_1^{(U)}, \mathbf{h}_2^{(U)}, ..., \mathbf{h}_{M_U}^{(U)}}_{M\ columns}], \tag{4.9}$$

where each column represents a certain transmit antenna's unique spatial signature of a specific user. Here, we assume that the FDCTF $h_{nm}^{(u)}$ between the uth user's tranmsit antenna element $m \in 1, 2, ..., M_u$ and receive antenna element $n \in 1, 2, ..., N$ are independent, stationary, complex valued Gaussian distributed processes with a zero-mean and a unit variance [3]. Furthermore, both the mth transmit antenna element's signal $s_m^{(u)}$ of user u, and the AWGN noise, w_n, at the nth antenna element exhibit a zero-mean and a variance of σ_s^2 and $2\sigma_w^2$, respectively. Note that the elements of the matrix $\mathbf{H}$ represent the FDCTF, since our SDMA systems are considered to be combined with OFDM systems [3] as discourse in Section 1.3.

Finally, although the above-mentioned system model describes a generalized MU-MIMO transmission scheme, it is also applicable to a Single-User MIMO (SU-MIMO) scenario, when setting $U = 1$.

4.1.2 Chapter Contributions and Outline

The concept of combining orthogonal transmit diversity designs with the principle of Sphere Packing (SP) [118] was introduced by Su *et al.* in [119] for the sake of maximizing the achievable coding advantage, demonstrating that the proposed SP-aided STBC (STBC-SP) scheme was capable of outperforming the conventional orthogonal design based STBC schemes of [18, 20, 120] in the SU-MIMO DL scenario. Against this background, our main contribution in this chapter is the challenging design of the K-best SD for SP-modulated systems, which extends the employment of STBC-SP schemes to MU-MIMO scenarios, while approaching the MAP performance at a moderate complexity. More specifically, the novel contributions of this chapter are listed as follows:

- *We improve the STBC performance by jointly designing the space-time signals of the two time slots of an SDMA UL scheme using SP modulation, while existing orthogonal designs make no attempt to do so owing to its potentially complex detection.*
- *We solve this potential complexity problem by further developing the K-best SD for the detection of SP modulation, because SP offers a substantial SNR reduction at the cost of an increased complexity, which is reduced by the new SD.*

The remainder of this chapter is organized as follows. The fundamentals of othogonal STBC schemes are briefly reviewed in Section 4.2.1, followed by a discourse on the orthogonal design of STBC schemes using SP modulation in Section 4.2.2. Then, in Section 4.3 our SD design contrived for the STBC-SP assisted MU-MIMO system is detailed. More specifically, based on the bit-by-bit MAP detection scheme designed for the STBC-SP aided MU-MIMO system derived in Section 4.3.1, a multi-layer tree search referred to as the user-based tree search is proposed in Section 4.3.2 in order to render the conventional SD applicable to the above-mentioned SP modulated scenario. Finally, we provide our concluding remarks in Section 4.4

4.2 Orthogonal Transmit Diversity Design with Sphere Packing Modulation

4.2.1 Space-Time Block Codes

4.2.1.1 STBC Encoding

Space-Time Block Codes (STBC) describe the relationship between the original symbol stream stored in the column vector $\mathbf{x}$ and the redundant signal replicas artificially constructed at the transmitter for transmission from the different antennas during different time slots or symbol periods. Generally, a STBC can be described by a $(M_u \times J)$-dimensional transmission matrix as defined earlier in Eq.(4.2) of Section 4.1.1.

A simple but elegant Orthogonal STBC (OSTBC) scheme employing two transmit antennas was discovered by Alamouti [18] and was later generalised by Tarokh *et al.* in [120] to an arbitrary number of antennas. This remarkable scheme enables the receiver to perform ML detection based

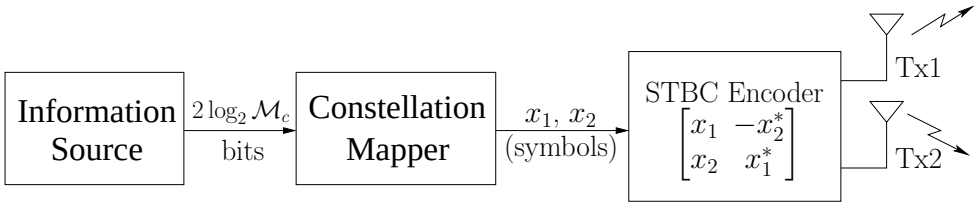

Figure 4.2: Transmit diversity using Alamouti G2 STBC code

on low-complexity linear processing, yet achieving the maximum attainable transmit diversity by imposing a low extra encoding complexity at the transmitter. The corresponding block diagram of Alamouti's STBC aided transmitter employing a constellation size of M_c symbols is shown in Figure 4.2, where $2\log_2 M_c$ number of bits of the information source are fed into the constellation mapper in order to generate the modulated symbols x_1 and x_2. Instead of using spatial multiplexing to double the throughput in comparison to its single antenna based counterpart, the two-transmit-antenna-aided MS launches the signals x_1 and x_2 as well as their conjugates simultaneously from the two antennas during two successive symbol periods or time slots. To be more specific, during the first symbol period, x_1 and x_2 are transmitted from antenna Tx1 and Tx2, respectively. Then, in the forthcoming symbol period $-x_2^*$ is assigned to antenna Tx1 and x_1^* is assigned to antenna Tx2, so that correlation is introduced in both time and spatial domain. Hence, according to the generalized STBC transmission matrix defined in Eq.(4.2), during the two consecutive symbol periods of jT and $(j+1)T$ the uth MS associated with the transmitted codeword of Alamouti's scheme - also known as $\mathbf{G}_2$ STBC scheme - can be represented with the aid of the following matrix:

$$\begin{aligned} \mathbf{G2} &= \begin{bmatrix} s_1^{(u)}(jT) & s_1^{(u)}((j+1)T) \\ s_2^{(u)}(jT) & s_2^{(u)}((j+1)T) \end{bmatrix} \\ &= \begin{bmatrix} x_1^{(u)} & -x_2^{(u)*} \\ x_2^{(u)} & x_1^{(u)*} \end{bmatrix}, \end{aligned} \tag{4.10}$$

where the column index of the matrix denotes the symbol period index, while the row index represents the transmit antenna index.

4.2.1.2 Equivalent STBC Channel Matrix

A key assumption when employing the above $\mathbf{G}_2$ scheme is that the channel magnitude and phase are quasi-static, as defined for $h_{nm}^{(u)}(t)$ in Section 4.1.1, implying that the FDCTF observed for the path between the uth MS's mth transmit antenna and the nth receive antenna of the BS at time instant t remains constant during two consecutive symbol periods. Explicitly, in the context of the $\mathbf{G}_2$ scheme we arrive at:

$$h_{nm}^{(u)}(jT) = h_{nm}^{(u)}[(j+1)T], \tag{4.11}$$

where $m = 1,2$, $n = 1,2,...,N$ and $u = 1,2,...,U$ denote the indices of the transmit antennas of a specific MS, of the receive antenna and of the MS, respectively. Furthermore, it is also assumed throughout this chapter that the FDCTF $h_{nm}^{(u)}(t)$ is perfectly known at the receiver. Therefore the

noise-contaminated signals of the uth MS received by the nth antenna at the BS during the jth symbol period can be expressed as:

$$y_n^{(u)}(jT) = \sum_{m=1}^{M_u} h_{nm}^{(u)}(jT)s_m^{(u)}(jT) + w_n(jT), \tag{4.12}$$

where M_u is the number of transmit antennas employed by the uth MS. Furthermore, with the aid of Eq.(4.10) and Eq.(4.11), we can expand Eq.(4.12) to obtain an expression for the signal of the uth MS received by the nth antenna in two consecutive symbol periods, respectively, as follows:

$$y_n^{(u)}(jT) = h_{n1}^{(u)}(jT)x_1^{(u)} + h_{n2}^{(u)}(jT)x_2^{(u)} + w_n(jT), \tag{4.13}$$

$$y_n^{(u)}((j+1)T) = -h_{n1}^{(u)}(jT)x_2^{(u)*} + h_{n2}^{(u)}(jT)x_1^{(u)*} + w_n((j+1)T). \tag{4.14}$$

For notational simplicity, the time index can be omitted. Consequently, we arrive at:

$$y_{1,n}^{(u)} = h_{n1}^{(u)}x_1^{(u)} + h_{n2}^{(u)}x_2^{(u)} + w_{1,n}, \tag{4.15}$$

$$y_{2,n}^{(u)} = -h_{n1}^{(u)}x_2^{(u)*} + h_{n2}^{(u)}x_1^{(u)*} + w_{2,n}. \tag{4.16}$$

According to [104, 121], Eq.(4.15) and Eq.(4.16) together can be rewritten in a more compact matrix form as:

$$\tilde{\mathbf{y}}_n^{(u)} = \tilde{\mathbf{H}}_n^{(u)} \cdot \mathbf{x}^{(u)} + \tilde{\mathbf{w}}_n, \tag{4.17}$$

where

$$\mathbf{x}^{(u)} = [x_1^{(u)} \quad x_2^{(u)}]^T \tag{4.18}$$

represents the transmitted symbols of the uth MS during two consecutive symbol periods, and $\tilde{\mathbf{H}}_n^{(u)}$ is defined as the *equivalent STBC channel matrix* between the M_u number of transmit antennas of the uth MS and the nth receive antenna at the BS, which can be expressed for the $\mathbf{G}_2$ scheme as [104, 121]:

$$\tilde{\mathbf{H}}_n^{(u)} = \begin{bmatrix} h_{n1}^{(u)} & h_{n2}^{(u)} \\ h_{n2}^{(u)*} & -h_{n1}^{(u)*} \end{bmatrix}. \tag{4.19}$$

Moreover, $\tilde{\mathbf{y}}$ of Eq.(4.17) is defined as the *equivalent received signal vector*, which is given by:

$$\tilde{\mathbf{y}}_n^{(u)} = [y_{1,n}^{(u)} \quad y_{2,n}^{(u)*}]^T, \tag{4.20}$$

where the first element $y_{1,n}$ corresponds to the signal received by the nth antenna during the first symbol period and the second element $y_{2,n}^*$ is the conjugate of the signal received at the same antenna during the second symbol period, while $\tilde{\mathbf{w}}$ of Eq.(4.17) is referred to as the *equivalent noise vector*, which is written as:

$$\tilde{\mathbf{w}}_n = [w_{1,n} \;\; w_{2,n}^*]^T, \tag{4.21}$$

where again, $w_{1,n}$ denotes the AWGN imposed on the nth receive antenna during the first symbol period and $w_{2,n}^*$ is the conjugate of the AWGN inflicted during the second symbol period. The AWGN encountered during each symbol period has a zero mean and a variance of $2\sigma_w^2$.

4.2.1.3 STBC Diversity Combining and Maximum-Likelihood Detection

Without loss of generality, let us now consider a $\mathbf{G}_2$-assisted SU-MIMO system supporting only the uth MS with the aid of a single receive antenna at the BS, whose equivalent system model may be expressed as:

$$\tilde{\mathbf{y}} = \tilde{\mathbf{H}} \cdot \mathbf{x} + \tilde{\mathbf{w}} \tag{4.22}$$

$$= \begin{bmatrix} h_{11}^{(u)} & h_{12}^{(u)} \\ h_{12}^{(u)*} & -h_{11}^{(u)*} \end{bmatrix} \begin{bmatrix} x_1^{(u)} \\ x_2^{(u)} \end{bmatrix} + \begin{bmatrix} w_{1,1} \\ w_{2,1}^* \end{bmatrix}. \tag{4.23}$$

For notational simplicity, both the receive antenna index and the user index are omitted, resulting in:

$$\tilde{\mathbf{y}} = \begin{bmatrix} h_1 & h_2 \\ h_2^* & -h_1^* \end{bmatrix} \begin{bmatrix} x_1 \\ x_2 \end{bmatrix} + \begin{bmatrix} w_1 \\ w_2^* \end{bmatrix}. \tag{4.24}$$

In the light of the orthogonality of $\tilde{\mathbf{H}}_n^{(u)}$ of Eq. (4.19), we multiply both sides of Eq.(4.24) with the conjugate transpose of $\tilde{\mathbf{H}}$, yielding:

$$\check{\mathbf{y}} = \tilde{\mathbf{H}}^H \cdot \tilde{\mathbf{y}}, \tag{4.25}$$

$$= \begin{bmatrix} |h_1|^2 + |h_2|^2 & 0 \\ 0 & |h_1|^2 + |h_2|^2 \end{bmatrix} \begin{bmatrix} x_1 \\ x_2 \end{bmatrix} + \check{\mathbf{w}}, \tag{4.26}$$

$$= \begin{bmatrix} (|h_1|^2 + |h_2|^2)x_1 + h_1^* w_1 + h_2 w_2^* \\ (|h_1|^2 + |h_2|^2)x_2 + h_2^* w_1 - h_1 w_2^* \end{bmatrix}, \tag{4.27}$$

where $\check{\mathbf{w}} = \tilde{\mathbf{H}}^* \cdot \tilde{\mathbf{w}}$ has a zero mean and a covariance of $(|h_1|^2 + |h_2|^2) \cdot \mathbf{I}_2$, while the elements of $\check{\mathbf{w}}$ are i.i.d. [121]. The process of obtaining the estimates of the transmitted symbol vector as outlined in Eq.(4.25) is also referred to as *STBC-aided diversity combining*. Then the estimate vector $\check{\mathbf{y}}$ is forwarded to the ML detector, which uses the detection rule outlined in [121]:

$$\hat{\mathbf{x}} = \arg \min_{\check{\mathbf{x}} \in \mathcal{M}_c^M} ||\check{\mathbf{y}} - (|h_1|^2 + |h_2|^2) \cdot \check{\mathbf{x}})||^2, \tag{4.28}$$

where $\mathcal{M}_c$ is the constellation set of the modulation scheme. Therefore, $\mathcal{M}_c^M$ denotes the M-dimensional legitimate constellation set.

According to Eq.(4.27), the x_1 and x_2 transmitted from the two transmit antennas during the two successive symbol periods do not interfere with each other's estimate, which correspond to the first and second elements of $\check{\mathbf{y}}$. As a result, the observation enables us to 'decompose' the ML detection rule into two independent low-complexity detection operations for x_1 and x_2, as follows [18]:

$$\hat{x}_1 = \arg \min_{\check{x}_1 \in \mathcal{M}_c} (|h_1|^2 + |h_2|^2 - 1)|\check{x}_1|^2 + d^2(\check{y}_1, \check{x}_1), \tag{4.29}$$

$$\hat{x}_2 = \arg \min_{\check{x}_2 \in \mathcal{M}_c} (|h_1|^2 + |h_2|^2 - 1)|\check{x}_2|^2 + d^2(\check{y}_2, \check{x}_2), \tag{4.30}$$

where $d^2(\mathbf{x}, \mathbf{y})$ is the *squared Euclidean distance* between the signal vector $\mathbf{x}$ and $\mathbf{y}$. Typically, for constant-modulus modulation schemes, such as BPSK or QPSK, the detection criteria described by Eq.(4.29) and Eq.(4.30) can be further simplified as [18]:

$$\hat{x}_1 = \arg \min_{\check{x}_1 \in \mathcal{M}_c} d^2(\check{y}_1, \check{x}_1), \tag{4.31}$$

$$\hat{x}_2 = \arg \min_{\check{x}_2 \in \mathcal{M}_c} d^2(\check{y}_2, \check{x}_2). \tag{4.32}$$

Consequently, the original ML detector's search space is substantially reduced from $\mathcal{M}_c^M$ to $(M \cdot \mathcal{M}_c)$, resulting in a reduced detection complexity, while maintaining the ML performance as well as the maximum achievable transmit diversity gain.

For multiple receive antenna-aided scenarios, i.e. for $N \geq 2$, the same STBC decoding process, namely that of Eq.(4.25) can be invoked for each receive antenna and then the outputs of the antennas are combined, before passing them through the ML detector. Assuming that there are N number of receive antennas, the STBC decoding process is represented as:

$$\begin{aligned} \check{\mathbf{y}} &= \tilde{\mathbf{H}}^H \cdot \tilde{\mathbf{y}} && (4.33)\\ &= (|h_{11}|^2 + |h_{12}|^2 + \cdots + |h_{N1}|^2 + |h_{N2}|^2) \cdot \mathbf{I}_2 \cdot \begin{bmatrix} x_1 \\ x_2 \end{bmatrix} + \check{\mathbf{w}}, && (4.34)\\ &= \begin{bmatrix} \sum_{n=1}^{N}(|h_{n1}|^2 + |h_{n2}|^2)x_1 + \check{w}_1 \\ \sum_{n=1}^{N}(|h_{n1}|^2 + |h_{n2}|^2)x_2 + \check{w}_2 \end{bmatrix}, && (4.35) \end{aligned}$$

where

$$\tilde{\mathbf{H}} = \begin{bmatrix} \tilde{\mathbf{H}}_1^{(1)} \\ \tilde{\mathbf{H}}_2^{(1)} \\ \vdots \\ \tilde{\mathbf{H}}_N^{(1)} \end{bmatrix} = \begin{bmatrix} h_{11} & h_{12} \\ h_{12}^* & -h_{11}^* \\ \vdots & \\ h_{N1} & h_{N2} \\ h_{N2}^* & -h_{N1}^* \end{bmatrix} \tag{4.36}$$

and $\check{w}_1$ and $\check{w}_2$ are the noise terms corresponding to the first and second components of $\check{\mathbf{w}} = \tilde{\mathbf{H}}^H \cdot \tilde{\mathbf{w}}$. Then the estimated vector $\check{\mathbf{y}}$ is fed into the ML detector, which invokes the detection rules described by Eq.(4.31) and Eq.(4.32) in order to recover the transmitted symbol, if a constant-modulus constellation is employed. Otherwise, we have the generalized detection criterion for our $\mathbf{G}_2$-aided system having N number of receive antennas, which are given by:

$$\hat{x}_1 = \arg \min_{\check{x}_1 \in \mathcal{M}_c} \Big(\sum_{n=1}^{N} (|h_{n1}|^2 + |h_{n2}|^2) - N)|\check{x}_1|^2 + d^2(\check{y}_1, \check{x}_1), \tag{4.37}$$

$$\hat{x}_2 = \arg \min_{\check{x}_2 \in \mathcal{M}_c} \Big(\sum_{n=1}^{N} |(h_{n1}|^2 + |h_{n2}|^2) - N)|\check{x}_2|^2 + d^2(\check{y}_2, \check{x}_2). \tag{4.38}$$

Hence, according to Eq.(4.35), when employing N number of receive antennas, a total transmit and receive diversity associated with the diversity order of $M \cdot N = 2N$ can be achieved by the $\mathbf{G}_2$-aided system without having a less than unity transmission rate in comparion to the single-antenna-aided multiuser system, since the coding rate of the STBC $\mathbf{G}_2$ is unity. Additionally, as observed from Eq.(4.35) for a single-user system, after the STBC decoding operation of Eq.(4.33), there is no Multi-Stream-Interference (MSI), as a benefit of the orthogonality of the equivalent channel matrix $\tilde{\mathbf{H}}_n^{(u)}$ of Eq. (4.19).

4.2.1.4 Other STBCs and Orthogonal Designs

Again, orthogonal STBC designs have recently attracted considerable interests in multiple-antenna-aided wireless systems, as motivated by the STBC scheme proposed by Alamouti in [18] for a two-transmit-antenna scenario, which was further generalized for an arbitrary number of transmit

antennas by Tarokh *et al.* in [120]. In [120], Tarokh also showed that the maximum achievable rate of OSTBC schemes designed for complex-valued constellations cannot exceed 1, i.e. we have $R \leq 1$. Later it was shown in [19] by Liang and Xia that this rate is in fact always smaller than unity, namely, we have $R < 1$, when the number of transmit antennas exceeds two. Recently, Su and Xia in [20] proved that the rate cannot exceed $3/4$ for more than two transmit antennas.

According to [20], the process of square-shaped orthogonal encoder-matrix design can be carried out by commencing from $\mathbf{G}_1(x_1) = x_1\mathbf{I}_1$, and then recursively invoking the OSTBC construction equation as follows:

$$\mathbf{G}_{2^k}(x_1, \cdots, x_{k+1}) = \begin{bmatrix} \mathbf{G}_{2^{k-1}}(x_1, \cdots, x_k) & -x_{k+1}^* \mathbf{I}_{2^{k-1}} \\ x_{k+1}\mathbf{I}_{2^{k-1}} & \mathbf{G}_{2^{k-1}}^H(x_1, \cdots, x_k) \end{bmatrix} \tag{4.39}$$

for $k = 1, 2, 3, \cdots$, where $(\cdot)^*$ represents the conjugate of a complex symbol, $(\cdot)^H$ denotes the Hermitian of a complex matrix, and $\mathbf{I}_n$ is a $(n \times n)$-element identity matrix. Again, the rows and columns respectively represent the spatial and temporal dimensions. Therefore, $\mathbf{G}_{2^k}$ is an orthogonal design of $(2^k \times 2^k)$-element, which determines how to transmit $(k+1)$ number of complex modulated symbols, i.e. $x_1, x_2, \cdots, x_{k+1}$, from 2^k transmit antennas during 2^k consecutive symbol periods. Hence, the resultant symbol rate of $\mathbf{G}_{2^k}$ is equal to $(k+1)/2^k$. Considering the OSTBC design contrived for four transmit antennas for example where we have $k = 2$, we arrive at:

$$\mathbf{G}_4(x_1, x_2, x_3, x_4) = \begin{bmatrix} x_1 & -x_2^* & -x_3^* & 0 \\ x_2 & x_1^* & 0 & -x_3^* \\ x_3 & 0 & x_1^* & x_2^* \\ 0 & x_3 & -x_2 & x_1 \end{bmatrix}. \tag{4.40}$$

4.2.2 Orthogonal Design of STBC Using Sphere Packing Modulation

4.2.2.1 Joint Orthogonal Space-Time Signal Design Using Sphere Packing

Conventionally, the orthogonal design of STBCs [18, 20, 120] discussed in Section 4.2.1 is based on conventional PSK/QAM modulated symbols. In other words, the inputs $(x_1, x_2, \cdots, x_{k+1})$ of the STBC encoder are chosen independently from the constellation corresponding to a specific modulation scheme, then mapped to 2^k number of transmit antennas using for example Eq.(4.39), which are then transmitted during 2^k concecutive symbol periods. Therefore, no efforts was made by the Aloumti's scheme to jointly design the input symbols $(x_1, x_2, \cdots, x_{k+1})$. However, it was shown by Su *et al.* in [119] that combining the orthogonal design with Sphere Packing (SP) [118] is capable of attaining extra coding gains by maximizing the diversity product[1] of the STBC signals in the presence of temporally correlated fading channels. The diversity product expression for the square-shaped OSTBC matrix $\mathbf{G}_{2^k}$ expressed in the context of time-correlated fading channels is given by [119]:

$$\zeta_{\mathbf{G}_{2^k}} = \frac{1}{2\sqrt{k+1}} \min_{(x_1,\cdots,x_{k+1}) \neq (\tilde{x}_1,\cdots,\tilde{x}_{k+1})} \left(\sum_{i=1}^{k+1} |x_i - \tilde{x}_i|^2\right)^{1/2}, \tag{4.41}$$

[1] which is defined as the estimated SNR gain over an uncoded system having the same diversity order as the coded system [120]

where x_i and $\tilde{x}_i$ are the elements of two distinct space-time signaling matrices C and $\tilde{C}$, respectively. From Eq.(4.41) we can observe that the diversity product is actually determined by the Minimum Euclidean Distance (MED) among all the possible ST signal vectors $(x_1, x_2, \cdots, x_{k+1})$. Thus, the idea of combining the individual antenna signals into a joint ST design using SP is both straighforward and desirable, since the SP modulated symbols have the best known MED in the $2(k+1)$-dimensional real-valued Euclidean space $\mathbb{R}^{2(k+1)}$ [118]. Hence the system becomes capable of maximizing the achievable diversity product of STBC codes, which in turn minimizes the transmission error probability.

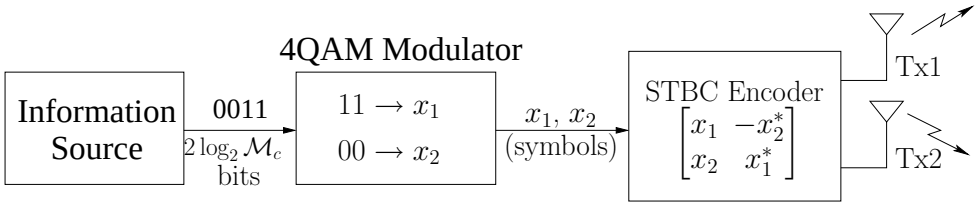

Figure 4.3: Alamouti G2 STBC scheme using 4QAM modulation

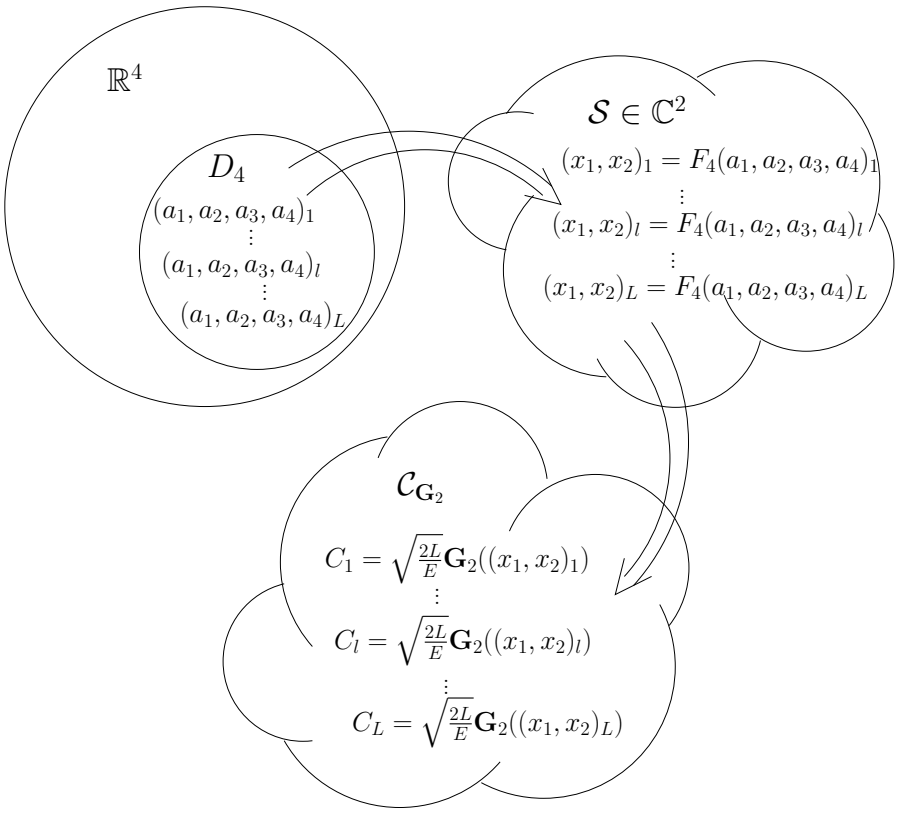

Figure 4.4: Procedure of joint ST signal design using sphere packing for $\mathbf{G}_2$ STBC scheme

Without loss of generality, we consider the $\mathbf{G}_2$ scheme again as a simple example, where the corresponding space-time signaling matrix of Eq.(4.10) is rewritten here for convenience:

$$\mathbf{G}_2(x_1, x_2) = \begin{bmatrix} x_1 & -x_2^* \\ x_2 & x_1^* \end{bmatrix}, \tag{4.42}$$

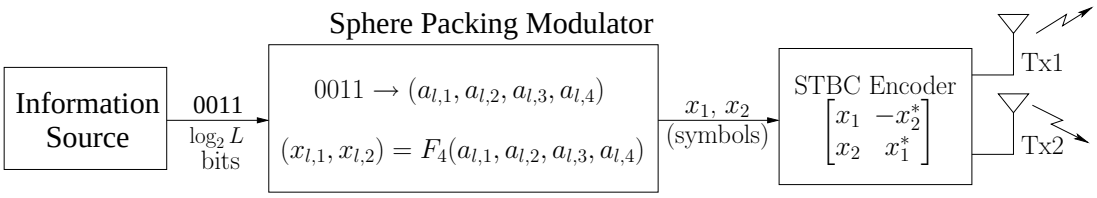

Figure 4.5: Alamouti G2 STBC scheme using sphere packing modulation

where the elements of the input vector (x_1, x_2) of STBC encoder are chosen independently from PSK/QAM modulation constellations conventionally, e.g. BSPK or 4QAM, as shown in Figure 4.3. Let us now define the lattice D_4 as a SP having the best MED from all other $(L-1)$ legitimate phasor points in four-dimensional real-valued Euclidean space $\mathbb{R}^4$ [118], which may be also defined as a lattice that consists of all legitimate SP constellation points having integer coordinates $[a_1, a_2, a_3, a_4]$. These coordinates uniquely and unambiguously describe the legitimate combinations of the two time-slots' modulated symbols in the $\mathbf{G}_2$ scheme, while obeying the SP constraint of:

$$a_1 + a_2 + a_3 + a_4 = p, \tag{4.43}$$

where p is an even integer [122]. Furthermore, each two-dimensional complex-valued input vector of the $\mathbf{G}_2$ scheme, i.e. (x_1, x_2), can be represented in the following way:

$$(x_1, x_2) = (\Re\{x_1\} + j\Im\{x_1\}, \Re\{x_2\} + j\Im\{x_2\}), \tag{4.44}$$

where $\Re\{\cdot\}$ and $\Im\{\cdot\}$ denote the real and imaginary components of a complex number. In other words, any two-dimensional complex-valued vector, i.e. (x_1, x_2), in the two-dimensional complex-valued space $\mathbb{C}^2$, can be represented by four real numbers, which as a whole corresponds to the coordinates of a four-dimensional real-valued phasor in the $\mathbb{R}^4$ space represented in the following way:

$$(x_1, x_2) \Longleftrightarrow (\Re\{x_1\}, \Im\{x_1\}, \Re\{x_2\}, \Im\{x_2\}). \tag{4.45}$$

Hence, the joint design of (x_1, x_2) in the two-dimensional complex-valued space $\mathbb{C}^2$ is readily transformed into the four-dimensional real-valued Euclidean space $\mathbb{R}^4$. Explicitly, the procedure of joint signal design over two individual transmit antennas is portrayed in Figure 4.4, from which we can see that with the aid of the above-mentioned SP scheme, the joint ST signal design of the individual transmit antennas can be achieved by maximizing the coding advantage of $\mathbf{G}_2$ by maximizing the Euclidean distance of the four-tuples [122]

$$\begin{aligned} (x_{l,1}, x_{l,2}) &= F_4(a_{l,1}, a_{l,2}, a_{l,3}, a_{l,4}), \\ &= (a_{l,1} + ja_{l,2}, a_{l,3} + ja_{l,4}), \end{aligned} \tag{4.46}$$

Upon choosing L legitimate constellation points from the lattice D_4 to construct a set denoted by $\mathcal{A} = \{\boldsymbol{a}_l = [a_{l,1}, a_{l,2}, a_{l,3}, a_{l,4}]^T \in \mathbb{R}^4 : 0 \leq l \leq L-1\}$, the L resultant energy-normalised codewords given by:

$$\mathbf{C}_l = \sqrt{\frac{2L}{E_{total}}}\mathbf{G}_2(F_4(\boldsymbol{a}_l)), \quad l = 0, 1, \cdots, L-1, \tag{4.47}$$

Layer	Constellation Points				Norm	Number of Combinations
0	0	0	0	0	0	1
1	±1	±1	0	0	2	24
2	±2	0	0	0	4	8
	±1	±1	±1	±1	4	16
3	±2	±1	±1	0	6	96
4	±2	±2	0	0	8	24
5	±2	±2	±1	±1	10	96
	±3	±1	0	0	10	48
6	±3	±1	±1	±1	12	64
	±2	±2	±2	0	12	32
7	±3	±2	±1	0	14	192
8	±2	±2	±2	±2	16	16
	±4	0	0	0	16	8
9	±4	±1	±1	0	18	96
	±3	±2	±2	±1	18	192
	±3	±3	0	0	18	24
10	±4	±2	0	0	20	48
	±3	±3	±1	±1	20	96

Table 4.1: The First 10 Layers of the Lattice D_4 © [7].

where $E_{total} \triangleq \sum_{l=1}^{L}(|a_{l,1}|^2 + |a_{l,2}|^2 + |a_{l,3}|^2 + |a_{l,4}|^2)$, constitutes the ST signal space $\mathcal{C}_{\mathbf{G}_2}$, whose diversity product $\zeta_{\mathbf{G}_2}$ is determined by the MED of the set $\mathcal{A}$ formulated in Eq.(4.41).

Consequently, we arrive at the SP-aided $\mathbf{G}_2$ scheme portrayed in Figure 4.5, where a SP symbol represented by the two-dimensinal complex-valued phasor points of $(x_{l,1}, x_{l,2})$ is transmitted over two symbol periods, resulting in a coding rate of $R = 0.5$ in comparion to the conventially-modulated system, where the coding rate of $\mathbf{G}_2$ is unity. For example, if we assume that a $L = 16$-point SP (16-SP) scheme is employed, the effective throughput per channel use can be calculated as:

$$T_{eff} = (\log_2 L) \cdot R = 2 \ \ bits/sec, \tag{4.48}$$

which is equal to that of the 4-QAM modulated system depicted in Figure 4.3.

4.2.2.2 Sphere Packing Constellation Construction [7, 118]

According to Eq.(4.47) describing the $\mathbf{G}_2$ codeword construction based on the SP scheme, a power normalisation factor of $\sqrt{\frac{2L}{E_{total}}}$ is used. Thus, it is desirable to choose a specific subset of L number of SP constellation points from the entire set of legitimate SP constellation points hosted by D_4

based on the criterion of maintaining the minimum total energy E_{total}, while having a certain MED among the selected SP symbols. However, a potential excessive computer search has to be carried out for attaining the best subset of the L SP symbols out of all possible choices, when searching for the SP-symbols having the best MED, hence maximizing the coding advantage of the resultant STBC scheme, if there are more than L number of SP symbols satisfying the above-mentioned minimum total energy condition.

Furthermore, the lattice D_4 can be divided into layers or shells which classify all the legitimate constellation points into a layer according to their Euclidean distances from the origin, i.e. their norms or energy. As an example, the first 10 SP layers in the D_4 SP-constellation are provided in Table 4.1, where we view the four-integer-element phasor of a specific layer as the basis vector of a SP constellation and any choice of signs and any ordering of the coordinates is legitimate [118]. To be more explicit, all legitimate permutations and signs for the corresponding constellation points listed in Table 4.1 have to be applied in order to generate the full list of SP constellation points for a specific layer.

4.2.3 System Model for STBC-SP-Aided MU-MIMO Systems

Let us now construct the generalized system equations for an STBC-aided UL MU-MIMO scenario, where the SDMA/OFDM system supports a total of U UL users and employs N number of receive antennas at the BS. For the sake of simplicity, the $\mathbf{G}_2$ scheme using two transmit antennas is employed by each user. The overall equivalent MU-MIMO system equation can be derived in complete analogy to the case of STBC-assisted SU-MIMO systems as discussed in Section 4.2.1.2 with the aid of the so-called equivalent channel matrix. After straightforward manipulations, under the assumption that the CIR taps between each of the two transmit antennas of a specific user and the nth receive antenna at the BS remain constant during two consecutive symbol periods, we have:

$$\tilde{\mathbf{y}} = \begin{bmatrix} \tilde{\mathbf{y}}_1 \\ \tilde{\mathbf{y}}_2 \\ \vdots \\ \tilde{\mathbf{y}}_N \end{bmatrix}_{2N\times 1} = \begin{bmatrix} \sum_{u=1}^{U} \tilde{\mathbf{H}}_1^{(u)} \cdot \mathbf{x}^{(u)} \\ \sum_{u=1}^{U} \tilde{\mathbf{H}}_2^{(u)} \cdot \mathbf{x}^{(u)} \\ \vdots \\ \sum_{u=1}^{U} \tilde{\mathbf{H}}_N^{(u)} \cdot \mathbf{x}^{(u)} \end{bmatrix}_{2N\times 1} + \begin{bmatrix} \tilde{\mathbf{w}}_1 \\ \tilde{\mathbf{w}}_2 \\ \vdots \\ \tilde{\mathbf{w}}_N \end{bmatrix}_{2N\times 1}, \tag{4.49}$$

$$= \tilde{\mathbf{H}} \cdot \mathbf{x} + \tilde{\mathbf{w}}, \tag{4.50}$$

where the overall equivalent channel matrix $\tilde{\mathbf{H}}$ can be expressed as:

$$\tilde{\mathbf{H}} = \begin{bmatrix} \tilde{\mathbf{H}}_1^{(1)} & \tilde{\mathbf{H}}_1^{(2)} & \cdots & \tilde{\mathbf{H}}_1^{(U)} \\ \tilde{\mathbf{H}}_2^{(1)} & \tilde{\mathbf{H}}_2^{(2)} & \cdots & \tilde{\mathbf{H}}_2^{(U)} \\ \vdots & \vdots & \ddots & \vdots \\ \tilde{\mathbf{H}}_N^{(1)} & \tilde{\mathbf{H}}_N^{(2)} & \cdots & \tilde{\mathbf{H}}_N^{(U)} \end{bmatrix}, \tag{4.51}$$

with each submatrix $\tilde{\mathbf{H}}_n^{(u)}$ being defined as Eq.(4.19). Additionally, the transmitted symbol vector $\mathbf{x}$ of the entire MU-MIMO system is a column vector created by concatenating each user's transmitted symbol vector $\mathbf{x}^{(u)}$ which is given by:

$$\mathbf{x}^{(u)} = F_4(\boldsymbol{a}^{(u)}) = [x_1^{(u)}\ x_2^{(u)}]^T. \tag{4.52}$$

Thus the transmitted symbol vector $\mathbf{x}$ may be expressed as:

$$\begin{aligned}\mathbf{x} &= [F_4((\boldsymbol{a}^{(1)})^T) \quad F_4((\boldsymbol{a}^{(2)})^T) \quad \cdots \quad F_4((\boldsymbol{a}^{(U)})^T)]^T && (4.53)\\ &= [F_4((\boldsymbol{a}^{(1)})^T \quad (\boldsymbol{a}^{(2)})^T \quad \cdots \quad (\boldsymbol{a}^{(U)})^T)]^T && (4.54)\\ &= [(\mathbf{x}^{(1)})^T \quad (\mathbf{x}^{(2)})^T \quad \cdots \quad (\mathbf{x}^{(U)})^T]^T. && (4.55)\end{aligned}$$

Thus, by defining $\mathbf{a} = [(\boldsymbol{a}^{(1)})^T \ (\boldsymbol{a}^{(2)})^T \ \cdots \ (\boldsymbol{a}^{(u)})^T]^T$, we have:

$$\mathbf{x} = F_4(\mathbf{a}). \tag{4.56}$$

Moreover, as observed in Eq.(4.49), the *equivalent received noise-contaminated signal vector* $\tilde{\mathbf{y}}$ and the *equivalent noise vector* $\tilde{\mathbf{w}}$ is formed by concatenating the N number of two-elements sub-vector $\tilde{\mathbf{y}}_n$ and $\tilde{\mathbf{w}}_n$, respectively, which can be written as:

$$\tilde{\mathbf{y}}_n = [y_{1,n} \ \ y_{2,n}^*]^T, \tag{4.57}$$

where the first element $y_{1,n}$ corresponds to the signal received by the nth antenna during the first symbol period and the second element $y_{2,n}^*$ is the conjugate of the signal received at the same antenna during the second symbol period, while

$$\tilde{\mathbf{w}}_n = [w_{1,n} \ \ w_{2,n}^*]^T, \tag{4.58}$$

where again $w_{1,n}$ denotes the AWGN imposed on the nth receive antenna during the first symbol period and $w_{2,n}^*$ is the conjugate of the AWGN inflicted during the second symbol period. The AWGN encountered during each symbol period has a zero mean and a variance of $2\sigma_w^2$.

4.3 Sphere Detection Design for Sphere Packing Modulation

According to our discussions in Section 4.2.1.3, an OSTBC scheme eliminates the MSI among the MIMO elements of a specific user, owing to the orthogonality of the equivalent channel matrix $\tilde{\mathbf{H}}_n^{(u)}$ formulated in Eq.(4.19). Therefore, the receiver is capable of performing ML detection based on low-complexity linear processing in order to achieve full transmit diversity by imposing a negligible extra encoding complexity at the MS in the STBC-SP-assisted SU-MIMO UL scenario considered in Section 4.2.1.3. However, in the context of a MU-MIMO system, the resultant overall equivalent channel matrix $\tilde{\mathbf{H}}$ of Eq.(4.51) is no longer orthogonal, since we have:

$$\begin{aligned}\tilde{\mathbf{H}}^H\tilde{\mathbf{H}} &= \begin{bmatrix} (\tilde{\mathbf{H}}_1^{(1)})^* & (\tilde{\mathbf{H}}_2^{(1)})^* & \cdots & (\tilde{\mathbf{H}}_N^{(1)})^* \\ (\tilde{\mathbf{H}}_1^{(2)})^* & (\tilde{\mathbf{H}}_2^{(2)})^* & \cdots & (\tilde{\mathbf{H}}_N^{(2)})^* \\ \vdots & \vdots & \ddots & \vdots \\ (\tilde{\mathbf{H}}_1^{(U)})^* & (\tilde{\mathbf{H}}_2^{(U)})^* & \cdots & (\tilde{\mathbf{H}}_N^{(U)})^* \end{bmatrix} \begin{bmatrix} \tilde{\mathbf{H}}_1^{(1)} & \tilde{\mathbf{H}}_1^{(2)} & \cdots & \tilde{\mathbf{H}}_1^{(U)} \\ \tilde{\mathbf{H}}_2^{(1)} & \tilde{\mathbf{H}}_2^{(2)} & \cdots & \tilde{\mathbf{H}}_2^{(U)} \\ \vdots & \vdots & \ddots & \vdots \\ \tilde{\mathbf{H}}_N^{(1)} & \tilde{\mathbf{H}}_N^{(2)} & \cdots & \tilde{\mathbf{H}}_N^{(U)} \end{bmatrix}, \\ &= \begin{bmatrix} \sum_{n=1}^{N}(|h_{n1}^{(1)}|^2 + |h_{n2}^{(1)}|^2)\mathbf{I}_2 & \mathbf{MUI} & \cdots & \mathbf{MUI} \\ \mathbf{MUI} & \sum_{n=1}^{N}(|h_{n1}^{(2)}|^2 + |h_{n2}^{(2)}|^2)\mathbf{I}_2 & \cdots & \mathbf{MUI} \\ \vdots & \vdots & \ddots & \vdots \\ \mathbf{MUI} & \mathbf{MUI} & \cdots & \sum_{n=1}^{N}(|h_{n1}^{(U)}|^2 + |h_{n2}^{(U)}|^2)\mathbf{I}_2 \end{bmatrix}, \end{aligned} \tag{4.59}$$

where $\mathbf{I}_2$ denotes a (2×2)-element identity matrix and the term **MUI** refers to the (2×2)-element Multiple-Access-Interference (MUI) sub-matrix, which contains non-zero elements imposed by the co-channel users. Hence, although as a benefit of having a diagonal sub-matrix $\sum_{n=1}^{N}(|h_{n1}^{(u)}|^2 + |h_{n2}^{(u)}|^2)\mathbf{I}_2$ in Eq.(4.59), there is no MSI between the two transmit antennas of a specific MS, a significant performance loss will be caused by the MUI in the context of a multiuser system in comparison to that of the single user scenario considered in Section 4.2.1.3, provided that we still simply apply the detection criterion formulated in Eq.(4.37) and Eq.(4.38) of Section 4.2.1.3, namely:

$$\hat{x}_1 = \arg\min_{\check{x}_1 \in \mathcal{M}_c} (\sum_{n=1}^{N}(|h_{n1}|^2 + |h_{n2}|^2) - N)|\check{x}_1|^2 + d^2(\check{y}_1, \check{x}_1), \tag{4.60}$$

$$\hat{x}_2 = \arg\min_{\check{x}_2 \in \mathcal{M}_c} (\sum_{n=1}^{N}|(h_{n1}|^2 + |h_{n2}|^2) - N)|\check{x}_2|^2 + d^2(\check{y}_2, \check{x}_2), \tag{4.61}$$

in order to separately carry out signal detection for each user without considering the effects of MUI produced by the co-channel users. In order to mitigate the effects of MUI imposed in the multi-user scenario considered, a successive interference cancellation (SIC) scheme was proposed in [121], which significantly improves the achievable BER performance of the STBC aided multi-user system. On the other hand, powerful near-ML SD techniques of Chapter 2 designed for classic modulation schemes are also readily applicable to STBC-aided multi-user systems, at a potentially reduced complexity. Hence, in order to avoid using the traditional brute-force ML detector, we intend to further develop the *K*-best SD of Section 2.2.3 to be used at the BS in the STBC-SP-assisted SDMA/OFDM UL scenario, in order to achieve a near-MAP performance at a moderate complexity.

4.3.1 Bit-Based MAP Detection for SP Modulated MU-MIMO Systems

According to Eq.(4.50) and Eq.(4.56), the conditional PDF $p(\tilde{\mathbf{y}}|\mathbf{a})$ for MU-MIMO systems using $N_D = 4$-dimensional real-valued SP modulation is given by:

$$p(\tilde{\mathbf{y}}|\mathbf{a}) = \frac{1}{(2\pi\sigma_w^2)^{\frac{N_D}{2}}} e^{-\frac{1}{2\sigma_w^2}||\tilde{\mathbf{y}} - \tilde{\mathbf{H}} \cdot F_4(\mathbf{a})||^2}. \tag{4.62}$$

Then, using Bayes' theorem, and exploiting the independence of the bits in the vector $\mathbf{b} = [b_1, b_2, \cdots b_{B \cdot U}]$ carried by the received symbol vector $\tilde{\mathbf{y}}$ we can factorize the joint bit-probabilities into their products [51], hence the LLR of bit k for $k = 1, \cdots, B \cdot U$ can be written as:

$$L_D(\mathbf{b}_k|\tilde{\mathbf{y}}) = L_A(\mathbf{b}_k) + \underbrace{\ln \frac{\sum_{\mathbf{a} \in \mathcal{A}_{k=1}^{U}} p(\tilde{\mathbf{y}}|\mathbf{a}) \cdot e^{\sum_{j=1, j\neq k}^{B \cdot U} \mathbf{b}_j L_A(\mathbf{b}_j)}}{\sum_{\mathbf{a} \in \mathcal{A}_{k=0}^{U}} p(\tilde{\mathbf{y}}|\mathbf{a}) \cdot e^{\sum_{j=1, j\neq k}^{B \cdot U} \mathbf{b}_j L_A(\mathbf{b}_j)}}}_{L_E(\mathbf{b}_k|\tilde{\mathbf{y}})}, \tag{4.63}$$

where $\mathcal{A}_{k=1}^{U}$ and $\mathcal{A}_{k=0}^{U}$ are subsets of the multi-user SP symbol constellation $\mathcal{A}^U$ where we have $\mathcal{A}_{k=1}^{U} \triangleq \{\mathbf{a} \in \mathcal{A}^U : b_k = 1\}$, and in a similar fashion, $\mathcal{A}_{k=0}^{U} \triangleq \{\mathbf{a} \in \mathcal{A}^U : b_k = 0\}$. Using

Eq.(4.62), we arrive at:

$$L_D(\mathbf{b}_k|\tilde{\mathbf{y}}) = L_A(\mathbf{b}_k) + \underbrace{\ln \frac{\sum_{\mathbf{a}\in\mathcal{A}_{k=1}^{U}} e^{[-\frac{1}{2\sigma_w^2}||\tilde{\mathbf{y}}-\tilde{\mathbf{H}}\cdot F_4(\mathbf{a})||^2+\sum_{j=1,j\neq k}^{B\cdot U}\mathbf{b}_j L_A(\mathbf{b}_j)]}}{\sum_{\mathbf{a}\in\mathcal{A}_{k=0}^{U}} e^{[-\frac{1}{2\sigma_w^2}||\tilde{\mathbf{y}}-\tilde{\mathbf{H}}\cdot F_4(\mathbf{a})||^2+\sum_{j=1,j\neq k}^{B\cdot U}\mathbf{b}_j L_A(\mathbf{b}_j)]}}}_{L_E(\mathbf{b}_k|\tilde{\mathbf{y}})}. \tag{4.64}$$

4.3.2 Sphere Detection Design for Sphere Packing Modulation

4.3.2.1 Transformation of the ML Metric

Although the basic idea behind the ML detector is to maximize the *a posteriori* probability of the received signal vector $\tilde{\mathbf{y}}$, this problem can be readily transformed into an issue of maximizing the *a priori* probability of Eq.(4.62) with the aid of Bayes' theorem [3]. Consequently, maximizing the *a priori* probability of Eq.(4.62) is equivalent to minimizing the Euclidean distance $||\tilde{\mathbf{y}} - \tilde{\mathbf{H}}F_4(\mathbf{a})||^2$. Therefore, the ML solution can be written as:

$$\hat{\mathbf{a}}_{ML} = arg \min_{\check{\mathbf{a}}\in\mathcal{A}^U} ||\tilde{\mathbf{y}} - \tilde{\mathbf{H}} \cdot F_4(\check{\mathbf{a}})||_2^2, \tag{4.65}$$

where $F_4(\cdot)$ is defined in Eq.(4.56) in the context of our multi-user system. Observe from Eq.(4.65) that a potentially excessive-complexity search may be encountered, depending on the size of the set $\mathcal{A}^U$, which prevents the application of the full-search-based ML detectors in high-throughput scenarios. By comparing the unconstrained LS solution of $\hat{\mathbf{a}}_{ls} = F_4^{-1}(\hat{\mathbf{x}}_{ls}) = F_4^{-1}((\tilde{\mathbf{H}}^H\tilde{\mathbf{H}})\tilde{\mathbf{H}}^H\tilde{\mathbf{y}})$ to all legitimate constrained/sliced solution, namely $\check{\mathbf{a}} \in \mathcal{A}^U$, the ML solution of Eq.(4.65) can be transformed into:

$$\hat{\mathbf{a}}_{ML} = arg \min_{\check{\mathbf{a}}\in\mathcal{A}^U} F_4(\check{\mathbf{a}} - \hat{\mathbf{a}}_{ls})^H(\tilde{\mathbf{H}}^H\tilde{\mathbf{H}})F_4(\check{\mathbf{a}} - \hat{\mathbf{a}}_{ls}). \tag{4.66}$$

4.3.2.2 Channel Matrix Triangularization

Let us now generate the $(2U \times 2U)$-dimensional upper-triangular matrix $\mathbf{U}$, which satisfies $\mathbf{U}^H\mathbf{U} = \tilde{\mathbf{H}}^H\tilde{\mathbf{H}}$ with the aid of Cholesky factorization [47]. Then, upon defining a matrix $\mathbf{Q}$ with elements $q_{i,i} \triangleq u_{i,i}^2$ and $q_{i,j} \triangleq u_{i,j}/u_{i,i}$ we can rewrite Eq.(4.66) as:

$$\begin{aligned}
& \hat{\mathbf{a}}_{ML} \\
= \;& arg \min_{\check{\mathbf{a}}\in\mathcal{A}^U} F_4(\check{\mathbf{a}} - \hat{\mathbf{a}}_{ls})^H\mathbf{U}^H\mathbf{U}F_4(\check{\mathbf{a}} - \hat{\mathbf{a}}_{ls}), \\
= \;& arg \min_{\check{\mathbf{a}}\in\mathcal{A}^U} \{\sum_{u=1}^{U} q_{2u-1,2u-1}[\mathbf{e}_1^{(u)} + \sum_{v=u+1}^{U} q_{2u-1,2v-1}\mathbf{e}_1^{(v)} \\
+ \;& \sum_{v=u}^{U} q_{2u-1,2v}\mathbf{e}_2^{(v)}]^2 + \sum_{u=1}^{U} q_{2u,2u}[\mathbf{e}_2^{(u)} \\
+ \;& \sum_{v=u+1}^{U} q_{2u,2v-1}\mathbf{e}_1^{(v)} + \sum_{v=u+1}^{U} q_{2u,2v}\mathbf{e}_2^{(v)}]^2\},
\end{aligned} \tag{4.67}$$

where $\mathbf{e}^{(u)}$ is the uth two-element sub-vector of the multi-user vector $\mathbf{e} = [(\mathbf{e}^{(1)})^T \cdots (\mathbf{e}^{(u)})^T \cdots (\mathbf{e}^{(U)})^T]^T$, corresponding to the uth user, and is given by:

$$\mathbf{e}^{(u)} = \check{\mathbf{x}}^{(u)} - \hat{\mathbf{x}}_{ls}^{(u)}, \tag{4.68}$$

where $\check{\mathbf{x}}^{(u)} = [\check{\mathbf{x}}_1^{(u)}, \check{\mathbf{x}}_2^{(u)}]^T = F_4(\boldsymbol{a}^{(u)})$, $\boldsymbol{a}^{(u)} \in \mathcal{A}$ and $\hat{\mathbf{x}}_{ls}^{(u)} = [\hat{\mathbf{x}}_{ls\,1}^{(u)}, \hat{\mathbf{x}}_{ls\,2}^{(u)}]^T = F_4(\hat{\mathbf{a}}_{ls}^{(u)})$. Hence, the sum in $\{\cdot\}$ of Eq. (4.67) is the *user-based* accumulated PED between the tentative symbol vector $\check{\mathbf{x}} = [(\check{\mathbf{x}}^{(1)})^T, (\check{\mathbf{x}}^{(2)})^T, \cdots, (\check{\mathbf{x}}^{(U)})^T]^T$ and the search center $\hat{\mathbf{x}}_{ls} = [(\hat{\mathbf{x}}_{ls}^{(1)})^T, (\hat{\mathbf{x}}_{ls}^{(2)})^T, \cdots, (\hat{\mathbf{x}}_{ls}^{(U)})^T]^T$.

4.3.2.3 User-Based Tree Search

Let us now recall the tree search carried out by the K-best SD of Section 2.2.3 for conventional modulation schemes, such as BPSK, where each tree level represents an independent data stream corresponding to a certain transmit antenna of a specific user. Each tree node corresponds to a legitimate BPSK symbol[2] in the constellation of domain $\mathbb{C}^1$. Consequently, in the absence of joint ST signal design for the $M_u = 2$ transmit antennas, the BPSK constellations of the two adjacent tree levels corresponding to a specific user are independent and identical. Figure 4.6

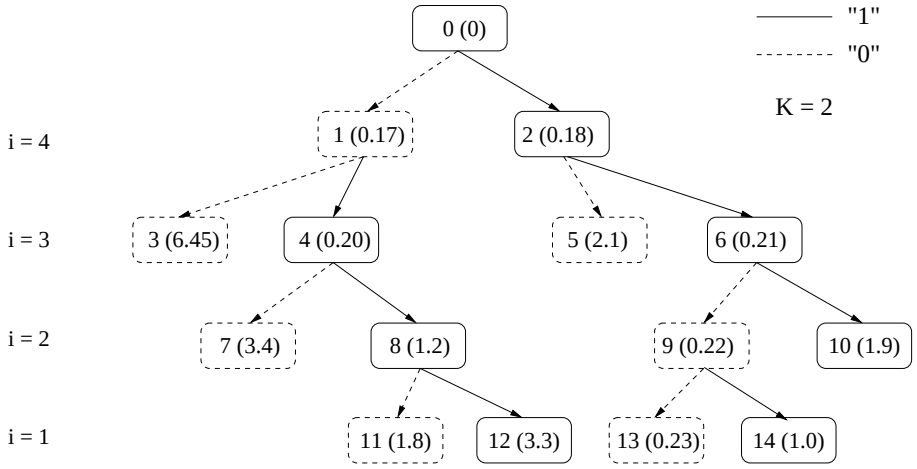

Figure 4.6: The search tree of K-best SD in the scenario of a four-transmit-antenna BPSK SDMA system, where $K = 2$.

shows the search tree of the K-best SD when it is applied to a four-transmit-antenna scenario, where K is set to two, which means that the maximum number of two candidates are retained at each level. Consequently, the search is carried out in the downward direction only along the search tree. The number in the bracket indicates the corresponding PED of the current tree node accumulated from the top level of the tree down to the current tree node, while the number outside the bracket represents the order in which the tree nodes are visited. At the (m=4) level, both the candidates are retained, which result in four candidates at the (m=3) level. Then we choose two candidates having the lowest two accumulated PEDs from the search center $\hat{\mathbf{x}}_c$, i.e. 0.2 and 0.21, out of four, which again generate four candidates at the (m=2) level. The search goes on in a similar way, until it reaches the tree leaf point having the lowest Euclidean distance of 0.23 from $\hat{\mathbf{x}}_c$. Then the estimated signal vector can be obtained by doing the backtracing, which is assumed to be the ML solution. However, the K-best SD does not necessarily find the ML solution, unless the value of K is large enough. An extreme example is when $K = 1$, the resultant K-best SD degenerates into the linear LS detector.

[2]In this treatise, we consider complex-valued BPSK symbols having zero imaginary parts.

On the other hand, when the joint ST signals are transmitted from the $M_u = 2$ transmit antennas of the uth user, they are combined into a joint ST design with the aid of the SP scheme as discussed in Section 4.2.2. The corresponding SP-symbol based search tree structure is depicted in Fig. 4.7, where the search tree of the modified K-best SD is exemplified in the context of an UL SDMA system supporting $U = 2$ $\mathbf{G}_2$-SP-aided users, where $K = 2$ and a 4-point-SP constellation is employed. Explicitly, the two adjacent tree levels corresponding to the SP-symbols of the jointly designed STBC-SP data streams of a specific user should be considered together in the tree search process, resulting in multi-dimensional/multi-layer tree nodes in the $\mathbb{C}^2$ SP-symbol domain, which we refer to as a *user-wise* tree search. The resultant 2-D complex-valued tree node is constituted of two complex-valued BPSK symbols, which are the constituent components of a transformed SP symbol $F_4(\boldsymbol{a})$. On the other hand, due to the joint consideration of the two adjacent BPSK tree levels, the number of effective search tree levels is reduced by a factor of two, whilst each symbols becomes quaternary, instead of being binary.

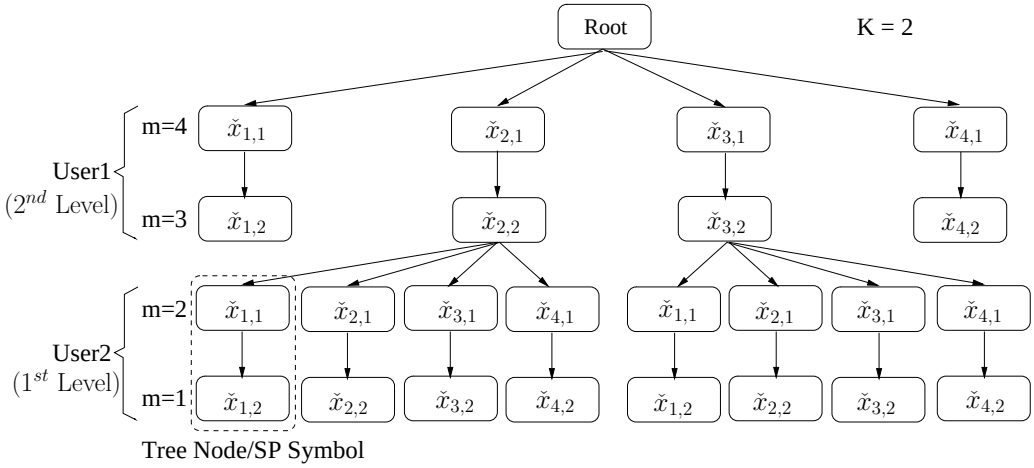

Figure 4.7: The search tree of K-best SD in the scenario of an STBC-SP aided uplink SDMA system: the number of users is $U = 2$, the number of transmit antennas per user is $M_u = 2$ and the number of candidates retained at each search tree level is $K = 2$.

As observed in Fig. 4.7, since a 4-SP scheme is employed and the number of candidate tree nodes retained at each tree level is $K = 2$, each of the two selected tree nodes having the smallest two accumulated PED values at the previous search-tree level of the survivor path has to be expanded into four child nodes at the current level. Consequently, in analogy to the conventional K-best algorithm [61], both the calculation of the user-based accumulated PEDs as well as the tree pruning process continues in the downward direction of Fig. 4.7 all the way along the tree, until it reaches the tree-leaf level, producing a candidate list of $\mathcal{L}_{cand} \in \mathcal{A}^U$. This list contains $N_{cand} = K$ number of SP symbol candidate solutions, which are then used for the *extrinsic* bit LLR calculation using Eq.(4.64). Having a reduced candidate list size assists us in achieving a substantial

complexity reduction. Explicitly, after the max-log-approximation, we arrive at:

$$L_E(\mathbf{b}_k|\tilde{\mathbf{y}}) = \max_{\mathbf{a}\in\mathcal{L}_{cand}\cap\mathcal{A}_{k=1}^{U}} [-\frac{1}{2\sigma_w^2}||\tilde{\mathbf{y}} - \tilde{\mathbf{H}}\cdot F_4(\mathbf{a})||^2 + \sum_{j=1,j\neq k}^{B\cdot U} \mathbf{b}_j L_A(\mathbf{b}_j)]$$
$$- \max_{\mathbf{a}\in\mathcal{L}_{cand}\cap\mathcal{A}_{k=0}^{U}} [-\frac{1}{2\sigma_w^2}||\tilde{\mathbf{y}} - \tilde{\mathbf{H}}\cdot F_4(\mathbf{a})||^2 + \sum_{j=1,j\neq k}^{B\cdot U} \mathbf{b}_j L_A(\mathbf{b}_j)]. \quad (4.69)$$

Fianlly, the K-best SD algorithm designed for $N_D = 4$-dimensional SP modulation scheme is summarized as follows:

The preprocessing phase:

1) Obtain the upper-triangular matrix $\mathbf{U}$ via Cholesky factorization on the Grammiam matrix $\mathbf{G} = \tilde{\mathbf{H}}^H\tilde{\mathbf{H}}$, namely, we have $\mathbf{U} = Chol(\mathbf{G})$.

2) Calculate the search center $\hat{\mathbf{x}}_{ls}$ by:

$$\hat{\mathbf{x}}_{ls} = \mathbf{G}^{-1}\tilde{\mathbf{H}}^H\mathbf{y}. \quad (4.70)$$

The tree search phase:

The first stage:

1) $m = M$, $d_M = \hat{x}_{lsM}$, where M is the total number of transmit antennas supported by the system.

2) Calculate the corresponding PED for each SP symbol $(\check{x}_{l,1},\ \check{x}_{l,2})$, $l = 1, 2, \cdots, L$ in the constellation of $\mathbb{C}^2$ domain as follows:

$$e_M = \hat{x}_{lsM} - \check{x}_{l,1}, \quad (4.71)$$
$$d_{M-1} = \hat{x}_{lsM-1} + \frac{u_{M-1,M}}{u_{M-1,M-1}} e_M, \quad (4.72)$$
$$PED = u_{M-1,M-1}^2(d_{M-1} - \check{x}_{l,2}). \quad (4.73)$$

3) Choose K number of SP symbols $(\check{x}_{k,1},\ \check{x}_{k,2})$, $k = 1, 2, \cdots, K$ that have the K smallest PEDs.

4) For each chosen SP symbol, compute

$$e_{M-1} = \hat{x}_{lsM-1} - \check{x}_{k,2}, \quad (4.74)$$
$$d_{M-2} = \hat{x}_{lsM-1} + \frac{u_{M-2,M-1}}{u_{M-2,M-2}} e_{M-1} + \frac{u_{M-1,M}}{u_{M-1,M-1}} e_M. \quad (4.75)$$

The mth stage:

1) $m = m - 2$.

2) For each survived search tree path from the previous tree level, calculate the corresponding PED for each SP symbol $(\check{x}_{l,1},\ \check{x}_{l,2})$ in the constellation of $\mathbb{C}^2$ domain:

$$e_m = \hat{x}_{ls\ m} - \check{x}_{l,1}, \quad (4.76)$$
$$d_{m-1} = \hat{x}_{ls\ m-1} + \sum_{j=m}^{M} \frac{u_{m-1,j}}{u_{m-1,m-1}} e_j, \quad (4.77)$$
$$PED = u_{m-1,m-1}^2(d_{m-1} - \check{x}_{l,2}). \quad (4.78)$$

3) Choose K number of SP symbols $(\check{x}_{k,1},\ \check{x}_{k,2})$, $k = 1,2,\cdots,K$ that have the K smallest PEDs.

4) For each chosen SP symbol, compute

$$e_{m-1} = \hat{x}_{ls\ m-1} - \check{x}_{k,2}, \tag{4.79}$$

$$d_{m-2} = \hat{x}_{ls\ m-1} + \frac{u_{m-2,m-1}}{u_{m-2,m-2}} e_{m-1} + \frac{u_{m-1,m}}{u_{m-1,m-1}} e_m. \tag{4.80}$$

5) If $m-1 = 1$, obtain the solution by backtracing from the tree leaf having the largest accumulated PED to the tree root. Otherwise, go to step 1 of the mth stage.

4.3.3 Simulation Results and Discussion

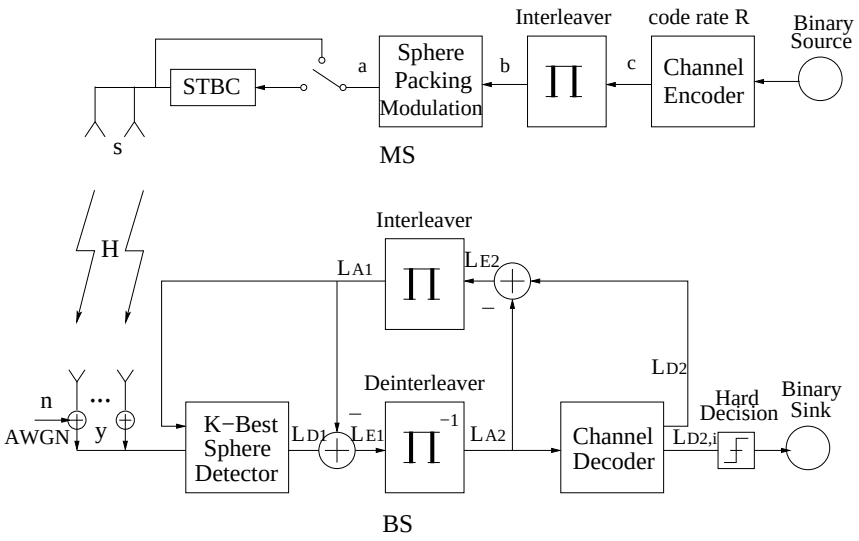

Figure 4.8: Schematic of the uplink SP modulated multi-user MIMO system using K-best SD.

The schematic of the system is depicted in Fig.4.8, where the transmitted source bits of the uth user are channel encoded and then interleaved by a random bit-interleaver. The B interleaved bits $\mathbf{b}^{(u)} = b^{(u)}_{0,\cdots,B-1} \in \{0,1\}$ are mapped to an SP modulated symbol $\mathbf{a}^{(u)} \in \mathcal{A}$ by the SP modulator/mapper of Fig. 4.8, where $B = \log_2 L$. The $\mathbf{G}_2$ encoder then maps the SP modulated symbol $\mathbf{a}^{(u)}$ to a space-time signal $\mathbf{C}^{(u)} = \sqrt{\frac{2L}{E_{total}}}\mathbf{G}_2(F_4(\mathbf{a}^{(u)})) \in \mathcal{C}_{\mathbf{G}_2}$ by invoking Eq.(4.42) and Eq.(4.46). Finally, the space-time signal $\mathbf{C}^{(u)}$ is transmitted from the two tranmsit antennas of the uth MS during consecutive two time slots.

In Fig.4.8 the interleaver and deinterleaver pair seen at the BS divides the receiver into two parts, namely the SD (*inner decoder*) and the channel decoder (*outer decoder*). Note that in Fig.4.8 L_A, L_E and L_D denote the *a priori*, the *extrinsic* and the *a posteriori* LLRs, while the subscript '1' and '2' represent the bit LLRs associated with the inner decoder and the outer decoder, respectively. It was detailed throughout [104] and [105] that the iterative exchange of extrinsic information between these serially concatenated receiver blocks results in substantial performance improvements. In this treatise we assume familiarity with the classic turbo detection principles [104, 105].

	Scenario I	*Scenario II*
Modulation	4-QAM/16-SP	16-QAM/256-SP
Users Supported	4	2
Normalized Doppler Freq.	0.1	
System	SDMA/OFDM	
Sub-Carriers	1024	
STBC	$\mathbf{G}_2$	
Rx at BS	4	
CIR Model	$P(\tau_k) = [0.5\ 0.3\ 0.2]$	
Detector/MAP	K-Best List-SD	
List Length	$\mathcal{N}_{cand} = K$	
Channel Code	Half-Rate RSC(2,1,3) $(5/7)$	
BW Efficiency	4 bits/sec/Hz	

Table 4.2: Summary of System Parameters

For the sake of investigating the performance of the STBC-SP-assisted multi-user SDMA/OFDM UL system, we compare the SP-modulated system with its conventionally-modulated counterpart in the two scenarios using the system parameters summarised in Table 4.2. Fig. 4.9(a) and 4.9(b) depict, respectively, the corresponding EXIT charts [123] used as a convenient visualization technique for analyzing the convergence characteristics of turbo receivers. This technique computes the MI of the output *extrinsic* and input *a priori* components, which are denoted by I_E and I_A respectively, corresponding to the associated bits for each of the iterative SISO blocks of Fig. 4.8, namely, to the SD and the RSC(2,1,3) channel decoder. As observed in Fig. 4.9, the maximum achievable iterative gains of traditional QAM-modulated systems employing the conventional K-best SD using $N_{cand} = K = 128$ are rather limited in comparison to our SP-aided K-best SD specifically designed for SP signals having the same list size of $N_{cand} = 128$. This is because the EXIT curve of the SD used the conventional 4- and 16-QAM-based system has a relatively low I_E value at $I_A = 1$, in contrast to the corresponding EXIT curve of its SP-modulated counterpart. Nonetheless, we also observe from Fig. 4.9 that the SD's EXIT curve in the QAM-modulated system emerges from a higher starting point at $I_A = 0$ than that of its SP-modulated counterpart. This leads to a potentially higher BER at relatively low SNRs, where I_A is also low, although the exact detection-convergence behavior is determined by the SD's complexity as well as by the SNR. Observe in Fig. 4.9 that in principle the employment of SP modulation is capable of eliminating the EXIT curve intercept point at a lower SNR, hence leading to an infinitesimally low BER. However, an open EXIT tunnel can only be formed, if the value of $K = N_{cand}$ as well as that of the SNR is sufficiently high.

Monte Carlo simulations were performed for characterizing the above-mentioned decoding convergence prediction in both *Scenario I* and *Scenario II* of Table 4.2. Figs. 4.10(a) and 4.10(b) suggest that the SP-modulated system exhibits a relatively higher BER at low SNRs in both scenarios, which matches the predictions of the EXIT charts seen in Fig. 4.9. On the other hand, as a benefit of employing the SP modulation, performance gains of 1.5 dB and 3.5 dB can be achieved by 16-SP and 256-SP modulated systems in *Scenario I* and *Scenario II* of Table 4.2, respectively, in comparison to their identical-throughput QAM-based counterparts, given a target BER of 10^{-4} and

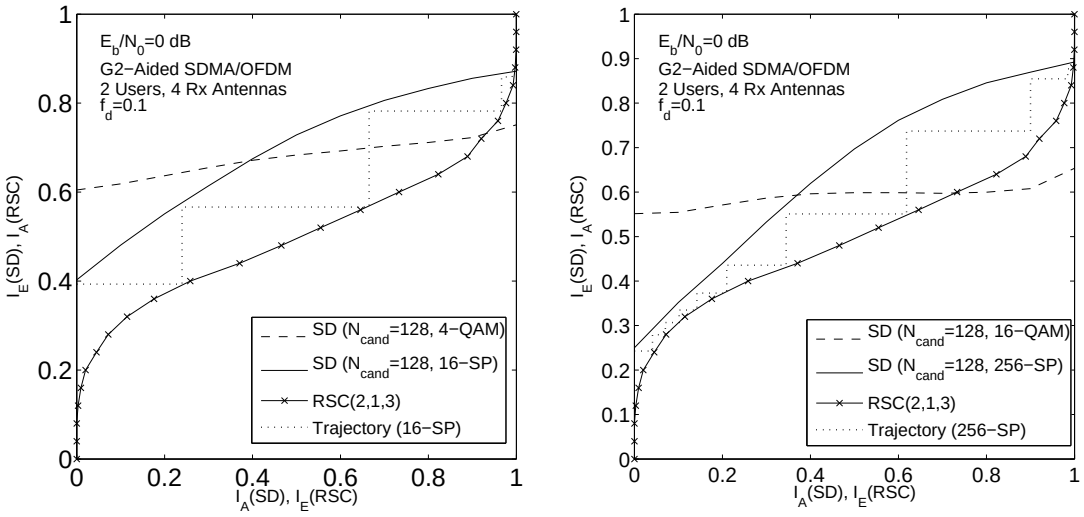

(a) Scenario I (b) Scenario II

Figure 4.9: EXIT charts of STBC-SP-aided iterative receiver of Fig. 4.8 employing the modified *K*-best SD and the parameters of Table 4.2. The overall system throughput is 8 bits/symbol.

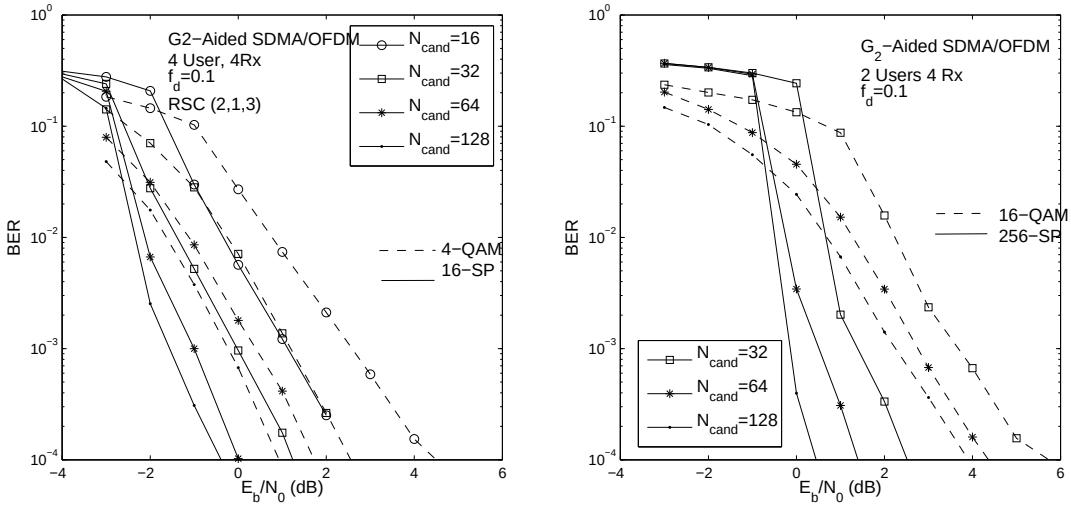

(a) Scenario I (b) Scenario II

Figure 4.10: BER performance of the system of Fig. 4.8 in *Scenario I* and *Scenario II* of Table 4.2. The overall system throughput is 8 bits/symbol.

$N_{cand} = 128$. Furthermore, as observed from Figs. 4.10(a) and 4.10(b), an attractive compromise can be achieved between the achievable performance and the complexity imposed by adjusting the list size N_{cand} employed by the K-best SD.

4.4 Chapter Conclusions

In comparison to the SDMA/OFDM system models employed in previous chapters, where only a single transmit antenna is employed by each MS, in this chapter a looser constraint is assumed for the sake of allowing the employment of multiple antennas at each MS, in order to enhance the system's robustness to the hostile wireless fading channel wth the aid of transmit diversity gains. Therefore, the simple but elegant OSTBC scheme, which was initially devised by Alamouti [18] for two-transmit-antenna aided transmission may be employed in the MU-MIMO scenario. As discussed in Section 4.2.1, the OSTBC scheme is capable of enabling the receiver to perform ML detection based on low-complexity linear processing, yet achieving the maximum attainable transmit diversity by imposing a low encoding complexity at the transmitter. Furthermore, in comparison to the conventional orthogonal design of STBCs based on PSK/QAM modulated symbols, in Section 4.2.2 we proposed an orthogonal transmit diversity design using SP modulation, which is capable of attaining extra coding gains by maximizing the diversity product of the STBC signals in the presence of temporally correlated fading channels.

On the other hand, although the resultant STBC-SP scheme has recently been investigated by researchers in the context of SU-MIMO systems, existing designs make no attempt to employ it in MU-MIMO systems owing to its relatively complex detection scheme. More specifically, despite having no MSI between the transmit antennas of a specific user, a significant performance loss will be inflicted by the MUI imposed by the co-channel users, if we insist on using low-complexity linear detection schemes, as in the SU-MIMO scenario. Although SIC based non-linear detection schemes [124] are capable of enhancing the achievable performance, these improvements erode, if the number of users increases, especially when the system becomes rank-deficient, potentially resulting in an inadequate performance. Based on this background, we proposed the so-called multi-layer tree search mechanism in order to render the powerful low-complexity near-ML SD scheme applicable to the STBC-SP-assisted MU-MIMO system. Consequently, with the aid of our K-best SD, a significant performance gain can be attained by the SP-modulated system over its conventionally-modulated identical-throughput counterpart in MU-MIMO scenarios. For example, a performance gain of 3.5 dB was achieved in Figure 4.10 over a 16-QAM benchmarker by the 256-SP scheme in the scenario of a four-receive-antenna SDMA UL system supporting $U = 2$ $\mathbf{G}_2$-assisted users, given a target BER of 10^{-4}.

Chapter 5

Multiple-Symbol Differential Sphere Detection for Differentially Modulated Cooperative OFDM Systems

5.1 Introduction

Multiple antenna aided transmit diversity arrangements [9] constitute powerful techniques of mitigating the deleterious effects of fading, hence improving the end-to-end system performance, which is usually achieved by multiple co-located antenna elements at the transmitter and/or receiver, as discussed in Chapter 4. However, in cellular communication systems, it is often impractical for the mobile to employ several antennas for the sake of achieving a diversity gain due to its limited size. Furthermore, owing to the limited separation of the antenna elements, they rarely experience independent fading, which limits the achievable diversity gain and may be further compromised by the detrimental effects of the shadow fading, imposing further signal correlation amongst the antennas in each others vicinity. Fortunately, as depicted in Figure 5.1, in multi-user wireless systems mobiles may cooperatively share their antennas in order to achieve uplink transmit diversity by forming a Virtual Antenna Array (VAA) in a distributed fashion. Thus, so-called cooperative diversity relying on the cooperation among multiple terminals may be achieved [7, 125].

On the other hand, in order to carry out classic coherent detection, channel estimation is required at the receiver, which relies on using training pilot signals or tones and exploits the fact that in general the consecutive CIR taps are correlated in both the time and frequency-domain of the OFDM subchannels. However, channel estimation for an M-transmitter, N-receiver MIMO system requires the estimation of $(M \times N)$ CIRs, which imposes both an excessive complexity and a high pilot overhead, especially in mobile environments associated with relatively rapidly fluctuating channel conditions. Therefore, in such situations, differential encoded transmissions combined with non-coherent detection and hence requiring no CSI at the receiver becomes an attractive design alternative, leading to differential modulation assisted cooperative communications [7]. Three

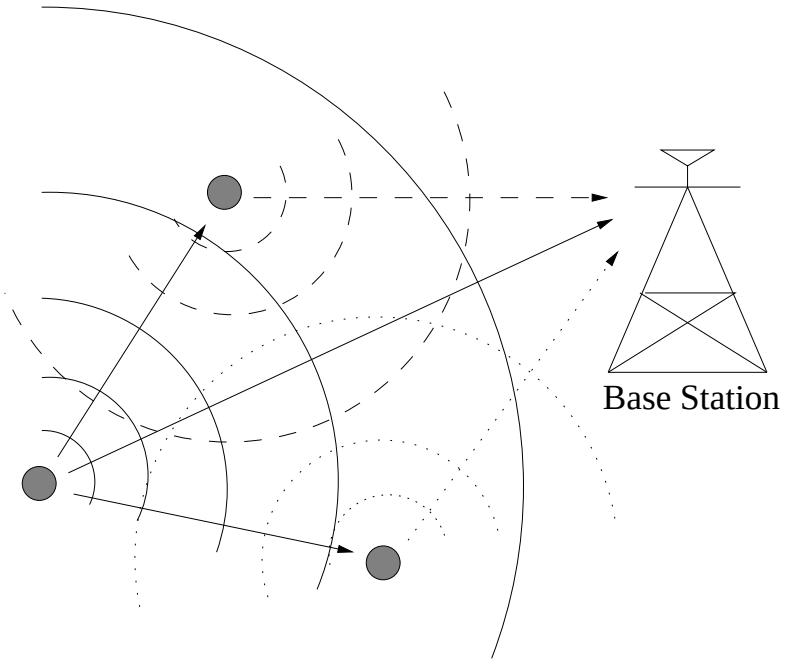

Figure 5.1: Cooperative diversity exploiting cooperation among multiple termianls

different channel models corresponding to three distinct communication environments will be considered in this chapter, namely, the Typical Urban (TH), the Rural Area (RA) and the Hilly Terrain (HT) scenarios summarized in Table 5.1.

5.1.1 Differential-Phase-Shift-Keying and Conventional Differential Detection

5.1.1.1 Conventional Differential Signalling and Detection

In this section, we briefly review the conventional differential encoding and detection process. Let $\mathcal{M}_c$ denote an M_c-ary PSK constellation which is defined as the set $\{2\pi m/M_c; m = 0, 1, \cdots, M_c - 1\}$, where $v[n] \in \mathcal{M}_c$ represent the data to be transmitted over a slow-fading frequency-flat channel. The differential signaling process commences by transmitting a single reference symbol $s[0]$, which is normally set to unity, followed by a differential encoding process, which can be expressed as:

$$s[n] = s[n-1]v[n], \tag{5.1}$$

where $s[n-1]$ and $s[n]$ represent the symbols transmitted during the $(n-1)$st and nth time slots, respectively.

By representing the signals arriving at the receiver corresponding to the $(n-1)$st and nth transmitted symbols as:

$$y[n-1] = h[n-1]s[n-1] + w[n-1], \tag{5.2}$$

$$y[n] = h[n]s[n] + w[n], \tag{5.3}$$

CHANNEL MODELS	
TYPICAL URBAN	**Parameter**
No. of Taps	$N_{taps} = 6$
Power Profile	$\sigma = [-7.21904 - 4.21904 - 6.21904 - 10.219 - 12.219 - 14.219]$
Delay Profile	$\tau = [0\ 2\ 6\ 16\ 24\ 50]$
RURAL AREA	**Parameter**
No. of Taps	$N_{taps} = 4$
Power Profile	$\sigma = [-2.40788 - 4.40788 - 12.4079 - 22.4079]$
Delay Profile	$\tau = [0\ 2\ 4\ 6]$
HILLY TERRAIN	**Parameter**
No. of Taps	$N_{taps} = 6$
Power Profile	$\sigma = [-4.05325 - 6.05325 - 8.05325 - 11.0533 - 10.0533 - 16.0533]$
Delay Profile	$\tau = [0\ 2\ 4\ 6\ 150\ 172]$

Table 5.1: Channel models considered: sampling frequency $f_s = 10$ MHz and the unit of the power profile is dB.

System Parameters	Choice
System	OFDM
Subcarrier BW	$\triangle f = 10$ kHz
Number of Sub-Carriers	$D = 1024$
Modulation	DPSK in time domain
Normalised Doppler Freq.	$f_d = 0.001$
Channel Model	typical urban, refer to Table 5.1

Table 5.2: Summary of system parameters for differential modulation aided OFDM system.

respectively, and assuming a slow fading channel, i.e. $h[n-1] = h[n]$, we arrive at:

$$y[n] = h[n-1]s[n-1]v[n] + w[n], \tag{5.4}$$

$$= y[n-1]v[n] + \underbrace{w[n] - w[n-1]v[n]}_{w'[n]}, \tag{5.5}$$

where $w[n-1]$ and $w[n]$ denote the AWGN with a variance of $2\sigma_w^2$ added at the receiver during the consecutive two time slots. Consequently, the differentially encoded data $v[n]$ can be recovered in the same manner as in the conventional coherent detection scheme in a single-input-singlel-output context by using $y[n-1]$ as the reference signal of the differential detector. This is achieved without any CSI at the expense of a 3 dB performance loss in comparison to its coherent counterpart caused by the doubled noise $w'[n]$ at the decision device, which has a variance of $4\sigma_w^2$. This can be verified by the BER curves of the single-antenna-aided OFDM system characterized in Figure 5.2 for two different throughputs, namely, for 1 bits/symbol and for 2 bits/symbol, respectively. The other system parameters are summarised in Table 5.2.

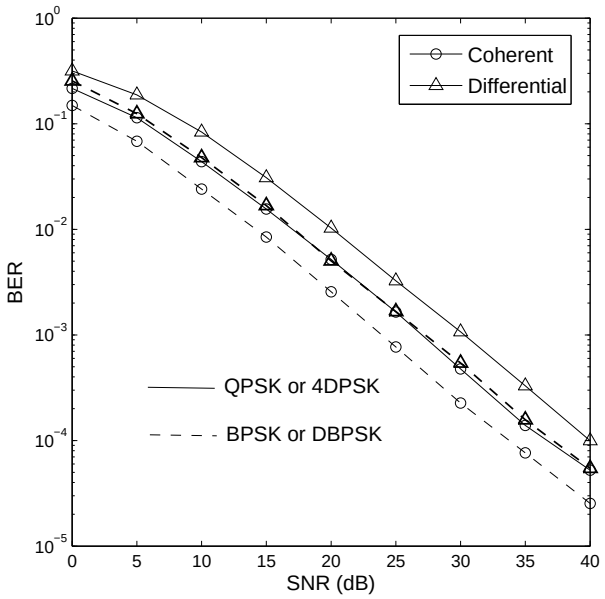

Figure 5.2: BER performance comparison between conventional coherent and differential detection in an SISO system.

5.1.1.2 Effects of Time-Selective Channels on Differential Detection

Apart from the 3 dB performance loss suffered by Conventional Differential Detection (CDD) in slow-fading scenarios as discussed in Section 5.1.1, an error floor may be encountered by the CDD in fast-fading channels, if DPSK modulation is carried out in the time direction, i.e. for the same subcarrier of consecutive OFDM symbols, since the fading channel is deemed to be more correlated between the same subcarrier of consecutive OFDM symbols than between adjacent subcarriers of a given OFDM symbol. In other words, the assumption that $h[n-1] = h[n]$ does not hold any more, leading to unrecoverable phase information between consecutive transmitted DPSK symbols even in the absence of noise. Furthermore, all the channel models considered in Table 5.1 exhibit temporally Rayleigh-distributed fading for each of the D subcarriers employed by the OFDM system with the autocorrelation function expressed as:

$$\varphi_{hh}^{t}[\kappa] \triangleq \mathcal{E}\{h[n+\kappa]h^{*}[n]\} \tag{5.6}$$

$$= J_0(2\pi f_d \kappa), \tag{5.7}$$

where $J_0(\cdot)$ denotes the zeroth-order Bessel function of the first kind and f_d is the normalized Doppler frequency.

Figure 5.3(a) depicts the magnitude of temporal correlation function for various normalized Doppler frequencies f_d, while Figure 5.3(b) plots the corresponding BER curves of the DQPSK modulated CDD-aided OFDM system with the system parameter summarised in Figure 5.2. Given a Doppler frequency of $f_d = 0.001$, the BER curves decrease continuously, as the SNR increases. However, the BER curve tends to create an error floor, when f_d becomes high, which is caused by the relative mobility between the transmitter and the receiver. For example, with a relatively high Doppler frequency of $f_d = 0.03$, the magnitude of the temporal correlation function of the typical

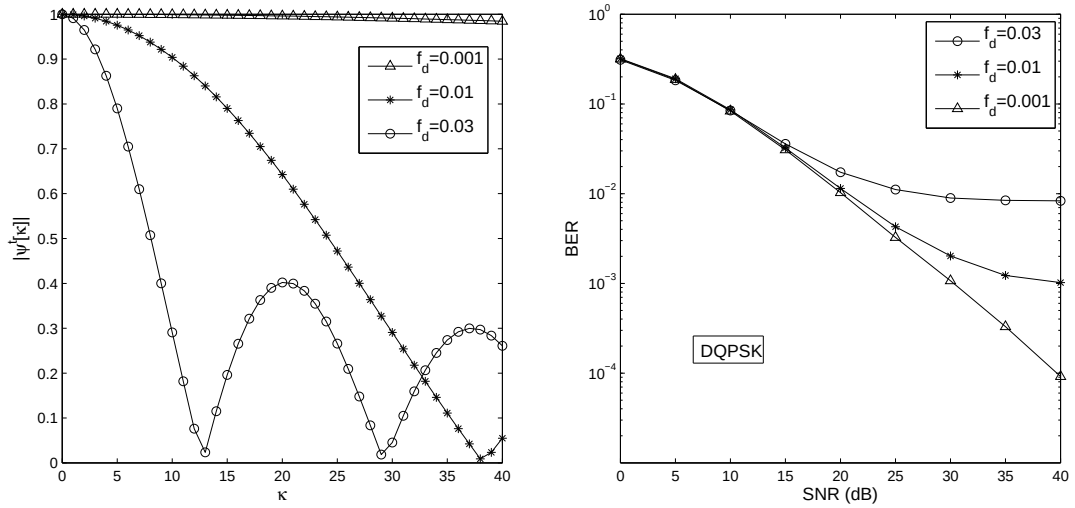

(a) Magnitude of temporal correlation function of Rayleigh fading channels

(b) Effects of dopper frequency on performance of CDD

Figure 5.3: Impact of mobility on the performance of CDD.

urban channel model of Table 5.1 decreases rapidly, as κ increases. Therefore, the CDD, which is capable of achieving a desirable performance in slow fading channels, suffers from a considerable performance loss, when the transmit terminal is moving at a high speed relative to the receiver.

5.1.1.3 Effects of Frequency-Selective Channels on Differential Detection

Our discussions in Section 5.1.1.2 were focused on the CDD employing differentially encoded modulation along the Time-Domain (TD) - which is referred to here as T-DPSK modulation - for each of the D subcarriers of an OFDM system. In general, the time- and frequency-domain differentially encoding have their own merits. Specifically, the T-DPSK modulated OFDM system is advantageous for employment in continuous transmissions, because the effective throughput remains high, since the overhead constituted by the reference symbol $s[0]$ tends to zero in conjunction with a relatively large transmission block/frame size, namely with an increasing transmission frame duration. However, T-DPSK aided OFDM is less suitable for burst transmission, when the consecutive OFDM symbols may experience fairly uncorrelated fading. Hence, employment of Frequency-Domain (FD) differentially encoded modulation - which is referred to here as F-DPSK - is preferable for above-mentioned scenario. Before investigating the impact of the channel's frequency-selectivity for the channel models summarized in Table 5.1 on performance of CDD, we review the frequency-domain (FD) autocorrelation function of OFDM having D active subcarriers and a subcarrier frequency spacing of $\triangle f$, which can be expressed as:

$$\varphi_{hh}^{f}[\mu] \triangleq \mathcal{E}\{h[k+\mu]h^{*}[k]\}, \tag{5.8}$$

$$= \sum_{l-1}^{N_{taps}} \sigma_l^2 e^{-j2\pi\mu\triangle f\tau_l}, \tag{5.9}$$

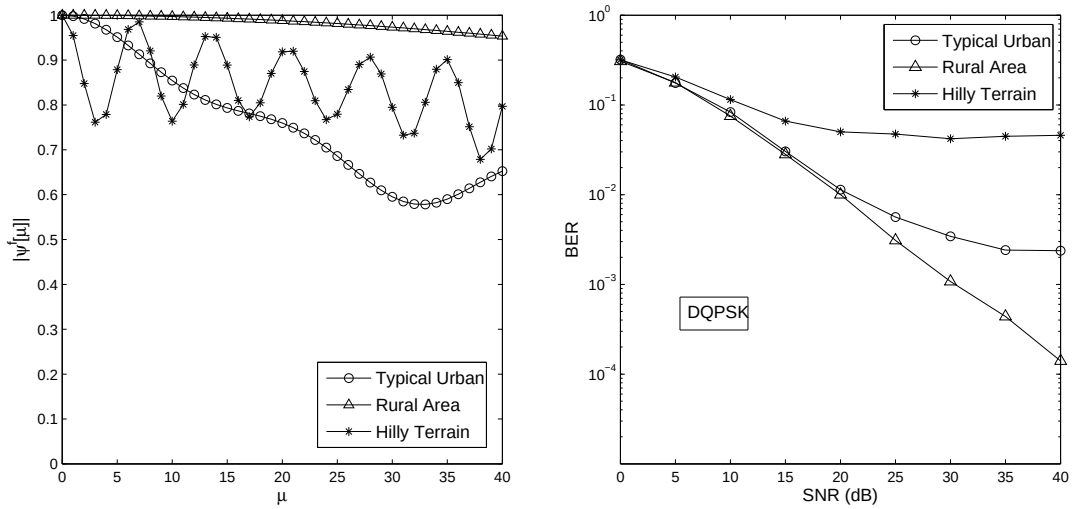

(a) Magnitude of frequency correlation function of Rayleigh fading channels

(b) Effects of frequency-selective channel on performance of CDD

Figure 5.4: Impact of frequency-selective channels on the performance of CDD.

where N_{taps}, σ_l and τ_l represent the number of paths, the elements of the power profile $\boldsymbol{\sigma}$ and the delay profile $\boldsymbol{\tau}$ of the channel models given by Table 5.1, respectively.

Accordingly, Figure 5.4(a) depicts the magnitude of the FD autocorrelation function for the three different channel models of Table 5.1, namely, of the TU, of the RA and of the HT channel models, assuming that we have $D = 1024$ and $\triangle f = 10$ kHz. Note that the OFDM symbol duration is:

$$T_f = DT_s + T_g, \tag{5.10}$$

where $T_s = 1/(\triangle f D)$ is the OFDM symbol duration, and T_g denotes the guard interval. We observe that the magnitude of the spectral correlation of the RA channel model decreases slowly as μ increases, since the maximum path delay τ_{max} is as small as $6T_s$. Thus, a moderately frequency-selective channel is expected, resulting in a gracefully decreasing BER curve, as observed in Figure 5.4(b), where the BER curves corresponding to the TU and HT channel models were also plotted. The latter two BER curves exhibit an error floor as the SNR increases, especially the one corresponding to the HT scenario. This is not unexpected, since we observe a sharp decay in $|\varphi^f_{hh}[\mu]|$ during the interval $(\mu = 0, 1 \cdots 4)$ and a "strong nonconcave" behaviour for $|\varphi^f_{hh}[\mu]|$, as seen in Figure 5.4(a). This is caused by the large maximum path delay of $\tau_{max} = 172T_s$.

5.1.2 Chapter Contributions and Outline

As observed in Sections 5.1.1.2 and 5.1.1.3, significant channel-induced performance degradations suffered by the CDD-aided direct-transmission based OFDM system simply imply that the cooperative diversity gains achieved by the cooperative system may erode, as the relative mobile velocities of the cooperating users with respect to both each other and to the BS increase. The detrimental effects of highly time-selective channels imposed on the T-DPSK modulated scenario were char-

acterized in Figure 5.3(b), while those of heavily frequency-selective channels on the F-DPSK modulated system were quantified in Figure 5.4(b). In order to eliminate this performance erosion and still achieve full cooperative diversity in conjunction with differential detection in wide-band OFDM based cooperative systems, in Section 5.2 we will invoke the Multiple-Symbol Differential Sphere Detection (MSDSD) technique, which was proposed by Lutz *et al.* in [53] in order to cope with fast-fading channels in single-input-single-output narrow-band scenarios. We will demonstrate in Section 5.3 that although a simple MSDSD scheme may be implemented at the relay, more powerful detection schemes are required at the BS of both the DAF- and DDF-aided cooperative systems in order to achieve a desirable end-to-end performance. Hence, the novel contributions of this chapter are as follows:

- *A generalized equivalent multiple-symbol based system model is constructed for the differentially encoded cooperative system using either the Differential Amplify-and-Forward (DAF) or Differential Decode-and-Forward (DDF) scheme.*
- *With the aid of the multi-layer search tree mechanism proposed for the SD in Chapter 4 in the context of the SP-modulated MIMO system, the MSDSD is specifically designed for both the DAF- and DDF-aided cooperative systems based on the above-mentioned generalized equivalent multiple-symbol system model. Our design objective is to retain the maximum achievable diversity gains at high mobile velocities, for example, when T-DPSK is employed, while imposing a low complexity.*

The remainder of this chapter is organized as follows. The principle of the single-path MSDSD, which was proposed for the employment in single-input single-output systems, is reviewed in Section 5.2, where we will demonstrate that the MSDSD is capable of significantly mitigating the channel-induced error-floor for both T-DPSK and F-DPSK modulated OFDM systems, provided that the second-order statistics of the fading and noise are known at the receiver. Given the duality of the time- and frequency-dimensions, we will only consider the T-DPSK modulated system in Section 5.3, where we focus our attention on the multi-path MSDSD design, which is detailed for both the DAF- and DDF-aided cooperative cellular UL. The construction of the generalized equivalent multiple-symbol cooperative system model is detailed in Section 5.3.3.1. Finally, we provide our concluding remarks in Section 5.4 based on the simulation results of Section 5.3.4.

5.2 The Principle of Single-Path Multiple-Symbol Differential Sphere Detection [53]

Differential detection schemes may be broadly divided into two categories, namely CDD and Multiple-Symbol Differential Detection (MSDD) as seen in Figure 5.5. Since a data symbol is mapped to the phase difference between the successive transmitted PSK symbols, CDD estimates the data symbol by directly calculating the phase difference of the two successive received symbols. In contrast to CDD having an observation window size of $N_{wind} = 2$, the MSDD collects $N_{wind} > 2$ consecutively received symbols for joint detection of the $(N_{wind} - 1)$ data symbols. This family may be further divided into two subgroups, namely the optimum maximum-likelihood

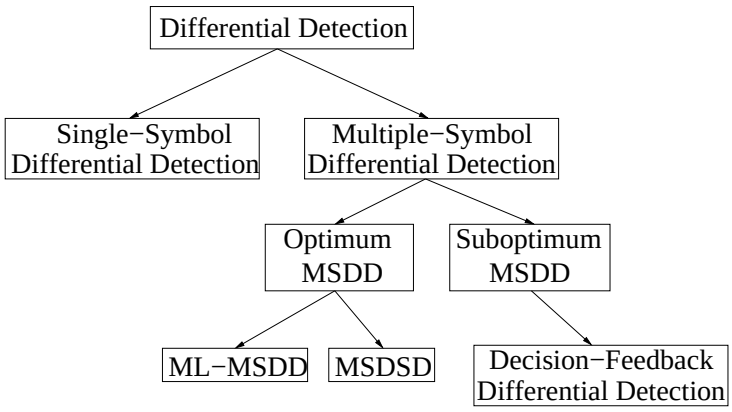

Figure 5.5: Differential Detection classification.

(ML)-MSDD and sub-optimum MSDD schemes, as seen in Figure 5.5. The ML-MSDD is the optimum scheme in terms of performance, but exhibits a potentially excessive computational complexity in conjunction with a large observation window size N_{wind}. One of the sub-optimum approaches that may be employed to achieve a low-complexity near-ML-MSDD is the linear-prediction-based Decision-Feedback Differential Detection (DFDD). Recently, the SD algorithm [41] was also used to resolve the complexity problem imposed by the ML-MSDD without sacrificing the achievable performance [25, 53, 54, 57], leading to the so-called Multiple-Symbol Differential Sphere Detection (MSDSD) arrangement, which will be introduced in the forthcoming sections.

5.2.1 Maximum-Likelihood Metric for Multiple-Symbol Differential Detection

The basic idea behind ML-MSDD is the exploitation of the correlation between the phase distortions experienced by the consecutive N_{wind} transmitted DPSK symbols [126]. In other words, the receiver makes a decision about a block of $(N_{wind}-1)$ consecutive symbols based on N_{wind} received symbols, enabling the detector to exploit the statistics of the fading channels. Ideally, the error floor encountered when performing CDD as observed in Figure 5.3 and Figure 5.4 can be essentially eliminated, provided that the value of N_{wind} is sufficiently high.

More explicitly, the MSDD at the receiver jointly processes the ith received symbol vector constituted of N_{wind} consecutively received symbols

$$\mathbf{y}[i_{N_{wind}}] \triangleq [y\left[(N_{wind}-1)i-(N_{wind}-1)\right], \cdots, y[(N_{wind}-1)i]]^T, \tag{5.11}$$

where $i_{N_{wind}}$ is the symbol vector index, in order to generate the ML estimate vector $\hat{\mathbf{s}}[i_{N_{wind}}]$ of the corresponding N_{wind} transmitted symbols

$$\mathbf{s}[i_{N_{wind}}] \triangleq [s[(N_{wind}-1)i-(N_{wind}-1)], \cdots, s[(N_{wind}-1)i]]^T. \tag{5.12}$$

Then, when using differential decoding by carrying out the inverse of the differential encoding process of Eq.(5.1), the estimate vector $\hat{\mathbf{v}}[i_{N_{wind}}]$ of the corresponding $(N_{wind}-1)$ differentially encoded data symbols

$$\mathbf{v}[i_{N_{wind}}] \triangleq [v[(N_{wind}-1)i-(N_{wind}-2)], \cdots, v[(N_{wind}-1)i]]^T \tag{5.13}$$

can be attained. Note that due to differential encoding, consecutive block $\mathbf{y}[i_{N_{wind}}]$ overlap by one scalar received symbol [56]. For the sake of representation simplicity, we omit the symbol block index $i_{N_{wind}}$ without any loss of generality.

Under the assumption that the fading is a complex-valued zero-mean Gaussian process with a variance of σ_h^2 and that the channel noise has a variance of $2\sigma_w^2$, the PDF of the received symbol vector $\mathbf{y} = [y_0, y_1, \cdots y_{N_{wind}-1}]^T$ conditioned on the transmitted symbol vector $\mathbf{s} = [s_0, s_1, \cdots s_{N_{wind}-1}]^T$ spanning over N_{wind} symbol periods is expressed as [53]:

$$p(\mathbf{y}|\mathbf{s}) = \frac{\exp\left(-Tr\left\{\mathbf{y}^H \Psi^{-1} \mathbf{y}\right\}\right)}{(\pi^{N_{wind}} det \Psi)}, \tag{5.14}$$

where

$$\Psi = \mathcal{E}\left\{\mathbf{y}\mathbf{y}^H | \mathbf{s}\right\} \tag{5.15}$$

denotes the conditional autocorrelation matrix of the Rayleigh fading channel. Then, the ML solution, which maximizes the probability of Eq.(5.14) can be obtained by exhaustively searching the entire transmitted symbol vector space. Thus, the ML metric of the MSDD can be expressed as [56]:

$$\hat{\mathbf{s}}_{ML} = \arg \max_{\check{\mathbf{s}} \in \mathcal{M}_c^{N_{wind}}} p(\mathbf{y}|\check{\mathbf{s}}), \tag{5.16}$$

$$= \arg \min_{\check{\mathbf{s}} \in \mathcal{M}_c^{N_{wind}}} Tr\left\{\mathbf{y}^H \Psi^{-1} \mathbf{y}\right\}. \tag{5.17}$$

5.2.2 Metric Transformation

In order to further elaborate on the ML metric of Eq.(5.16), we extended the conditional autocorrelation matrix Ψ as [53]:

$$\Psi = \mathcal{E}\left\{\mathbf{y}\mathbf{y}^H | \mathbf{s}\right\}, \tag{5.18}$$

$$= \text{diag}(\mathbf{s})\, \mathcal{E}\left\{\mathbf{h}\mathbf{h}^H\right\} \text{diag}\left(\mathbf{s}^H\right) + \mathcal{E}\left\{\mathbf{n}\mathbf{n}^H\right\}, \tag{5.19}$$

$$= \text{diag}(\mathbf{s}) \left(\mathcal{E}\left\{\mathbf{h}\mathbf{h}^H\right\} + 2\sigma_w^2 \mathbf{I}_{N_{wind}}\right) \text{diag}\left(\mathbf{s}^H\right), \tag{5.20}$$

$$= \text{diag}(\mathbf{s})\ \mathbf{C}\ \text{diag}\left(\mathbf{s}^H\right), \tag{5.21}$$

where $\mathcal{E}\left\{\mathbf{h}\mathbf{h}^H\right\}$ is the channel's covariance matrix in either the time- or the frequency-domain, which is determined by the specific domain of the differential encoding. More explicitly, the elements of the covariance matrix $\mathcal{E}\left\{\mathbf{h}\mathbf{h}^H\right\}$ can be computed by Eq.(5.7), when differential encoding at the transmitter is carried out along the TD. Otherwise, we employ Eq.(5.9) to obtain the covariance matrix, when differential encoding is employed in the FD. Furthermore, in the context of Eq.(5.21) we define

$$\mathbf{C} \triangleq \left(\mathcal{E}\left\{\mathbf{h}\mathbf{h}^H\right\} + 2\sigma_w^2 \mathbf{I}_{N_{wind}}\right) \tag{5.22}$$

in order to simplify Eq.(5.20).

Since we have $\text{diag}(\mathbf{s})^{-1} = \text{diag}(\mathbf{s})^H = \text{diag}(\mathbf{s}^*)$, the ML decision rule of Eq.(5.17) can

be reformulated as:

$$\hat{\mathbf{s}}_{ML} = \arg \min_{\mathbf{s} \in \mathcal{M}_c^{N_{wind}}} \left\{ \mathbf{y}^H \Psi^{-1} \mathbf{y} \right\}, \tag{5.23}$$

$$= \arg \min_{\mathbf{s} \in \mathcal{M}_c^{N_{wind}}} \left\{ \mathbf{y}^H \text{diag}\left(\mathbf{s}\right) \ \mathbf{C}^{-1} \ \text{diag}\left(\mathbf{s}\right)^H \mathbf{y} \right\}, \tag{5.24}$$

$$= \arg \min_{\mathbf{s} \in \mathcal{M}_c^{N_{wind}}} \left\{ \mathbf{s} \ \text{diag}\left(\mathbf{y}\right)^H \mathbf{C}^{-1} \text{diag}\left(\mathbf{y}\right) \mathbf{s}^* \right\}, \tag{5.25}$$

$$= \arg \min_{\mathbf{s} \in \mathcal{M}_c^{N_{wind}}} \left\{ \mathbf{s} \ \text{diag}\left(\mathbf{y}\right)^H \mathbf{F}^H \mathbf{F} \ \text{diag}\left(\mathbf{y}\right) \mathbf{s}^* \right\}, \tag{5.26}$$

where $\mathbf{F}$ is an upper-triangular matrix obtained using the Cholesky factorization of the inverse matrix $\mathbf{C}^{-1}$, namely, we have:

$$\mathbf{C}^{-1} = \mathbf{F}^H \mathbf{F}. \tag{5.27}$$

Then, by further defining an upper-triangular matrix as:

$$\mathbf{U} \triangleq \left(\mathbf{F} \ \text{diag}\left(\mathbf{y}\right)\right)^*, \tag{5.28}$$

we finally arrive at [53]:

$$\hat{\mathbf{s}}_{ML} = \arg \min_{\mathbf{s} \in \mathcal{M}_c^{N_{wind}}} \left\{ ||\mathbf{U}\mathbf{s}||^2 \right\}, \tag{5.29}$$

which completes the process of transforming the ML-MSDD metric of Eq.(5.17) to a *shortest-vector* problem [53].

5.2.3 Complexity Reduction Using Sphere Detection

While the performance of the MSDD improves steadily as N_{wind} is increased, the drawback is its potentially excessive computational complexity, which increases exponentially with N_{wind}. On the other hand, SD algorithms [41, 99, 127] are well-known for their efficiency, when solving the so-called shortest-vector problem in the context of multi-user/multi-stream detection in MIMO systems. Thus, due to the upper-triangular structure of the $\mathbf{U}$ matrix, the traditional SD algorithm can be employed to solve the shortest-vector problem as indicated by Eq.(5.29). Consequently, the ML solution of the ML-MSDD metric of Eq.(5.17) can be obtained a component-by-component basis at a significantly lower complexity. Note that all the SD algorithms discussed in Chapter 2 can be employed to solve the shortest-vector problem of Eq.(5.29).

5.2.4 Simulation Results

Monte Carlo simulations are provided in this section in order to characterize the achievable performance and the complexity imposed by the MSDSD for both TD and FD differentially encoded OFDM system. The simulation parameters are summarised in Table 5.3.

5.2.4.1 Time-Differential Encoded OFDM System

Let us now consider the application of the MSDSD in the TD-differentially encoded OFDM system for three different normalized Doppler frequencies in the presence of the typical urban channel

System Parameters	Choice
System	OFDM
Subcarrier BW	$\triangle f = 10$ kHz
Number of Sub-Carriers	$D = 1024$
Modulation	T-DQPSK/F-DQPSK
Frame Length	101 OFDM symbols
Normalised Doppler Freq.	$f_d = 0.001, 0.01, 0.03$
Channel Model	typical urban if not specified

Table 5.3: Simulation parameters for time-differential modulation aided OFDM system.

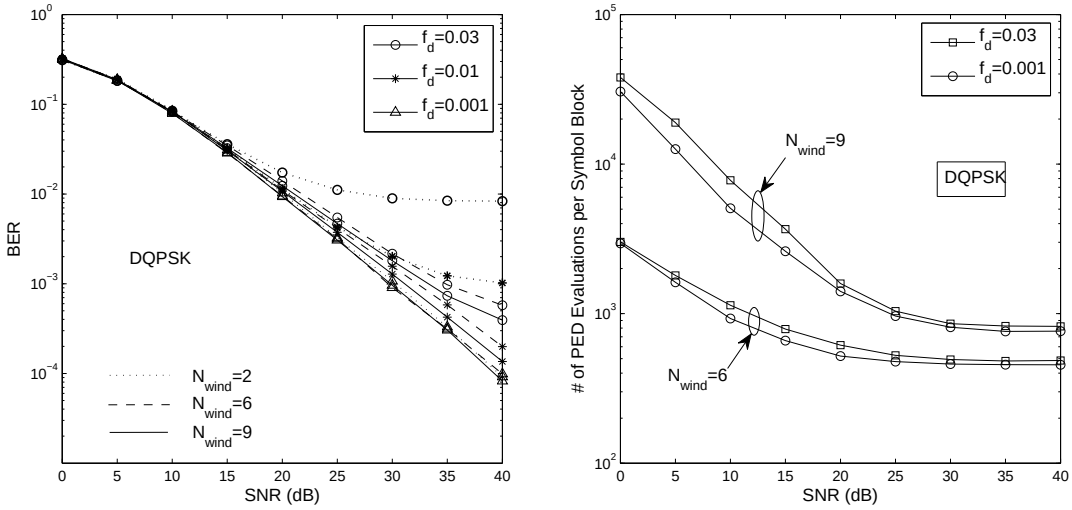

(a) BER performance of T-DQPSK-modulated OFDM system using MSDSD in Rayleigh fading channels with different normalised doppler frequency.

(b) Complexity imposed by the MSDSD versus the SNR.

Figure 5.6: The Application of MSDSD in the time-differential modulated OFDM system.

given by Table 5.1. The T-DQPSK modulation scheme is employed at the transmitter, while the MSDSD employing three different observation window sizes N_{wind} is used at the receiver, namely, $N_{wind} = 2,\ 6,\ 9$. Note that as mentioned in Section 5.1.1, when we have $N_{wind} = 2$, the MSDSD actually degenerates to the CDD. Additionally, since T-DQPSK is employed, a relatively short transmission frame length of 101 OFDM symbols is utilized in order to reduce the detection delay imposed by the MSDSD. Figure 5.6(a) depicts the BER performance of the MSDSD for normalized Doppler frequencies $f_d = 0.03,\ 0.01,\ 0.001$, where we observe that for the slow-fading channel associated with $f_d = 0.001$, there is no need to employ an observation window size of more than $N_{wind} = 2$, since CDD does not suffer from an error floor. In other words, the MSDSD is unable to further improve the CDD's performance by increasing N_{wind}. However, when the channel becomes more uncorrelated, i.e. when we have $f_d = 0.03$ or 0.01, the BER curve is shifted downwards by employing an N_{wind} value larger than 2, approaching that observed for $f_d = 0.001$, at the expense of imposing a higher computational complexity. The complexity imposed by the MSDSD versus the SNR is plotted in Figure 5.6(b), where the complexity curves corresponding to $N_{wind} = 9$ are

evidently above than those corresponding to $N_{wind} = 6$. Moreover, the complexity imposed by the MSDSD decreases steadily as the SNR increases and finally levels out in the high-SNR range. This is not unexpected, since under the assumption of having a reduced noise contamination, it is more likely that the ML solution point $\hat{\mathbf{s}}_{ML}$ is located near the search center (the origin in this case) of the SD used for finding the MSDD solution. As a result, the SD's search process may converge much more rapidly, imposing a reduced complexity. Again, for more details about the characteristics of SDs, please refer to Chapter 2. Furthermore, we can also observe from Figure 5.6(b) that the Doppler frequency has a crucial effect not only on the performance achieved by the MSDSD, but also on its complexity.

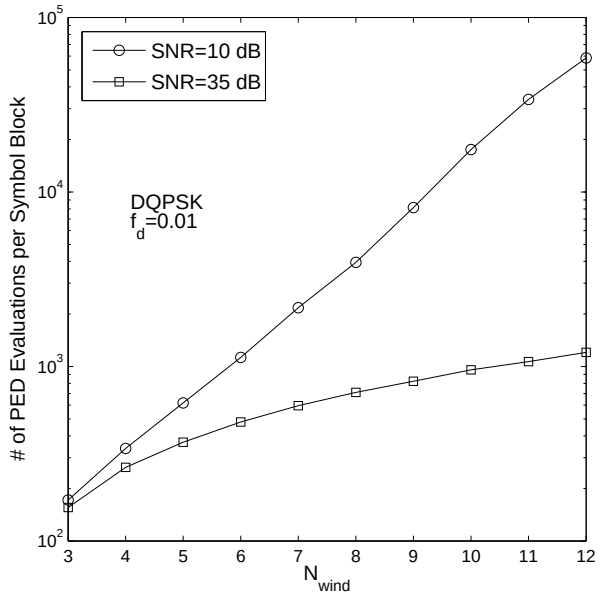

Figure 5.7: Complexity imposed by the MSDSD versus the observation window size N_{wind}.

Given a Doppler frequency of $f_d = 0.01$, let us now investigate the complexity of the MSDSD from a different angle by plotting the complexity versus N_{wind} in Figure 5.7, where complexity curves are drawn for two different SNRs. Although both of the two complexity curves exhibit an increase upon increasing the value of N_{wind}, the one corresponding to the relatively low SNR of 10 dB, rises more sharply than the other one recorded for an SNR of 35 dB.

5.2.4.2 Frequency-Differential Encoded OFDM System

As discussed in Section 5.1.1.3 in the scenario of burst transmissions or detection-delay-sensitive communications, F-DPSK is preferable to its TD counterpart. However, the channels experienced by the OFDM modem may exhibit a moderate time but a significant frequency-selectivity, as exemplified by the TU and HT channel models given in Table 5.1. Therefore, the BER curves corresponding to the TU and HT channel models exhibit an error floor, when using the CDD associated with $N_{wind} = 2$, as observed in Figure 5.8, due to the channel's frequency-selectivity. Other simulation parameters are summarized in Table 5.3. Similar to the results obtained in the T-DPSK scenario, the error floor can be eliminated with the aid of the MSDSD, where the observation win-

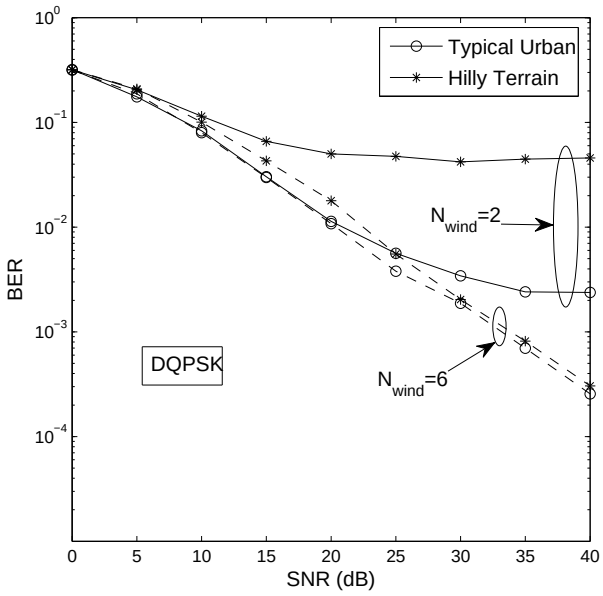

Figure 5.8: BER performance of F-DQPSK modulated OFDM system using MSDSD for the different channel models of Table 5.1.

dow size was $N_{wind} = 6$. Remarkably, a signficant performance improvement is achieved by the MSDSD for the severely frequency-selective HT environment as seen in Figure 5.8. The BER curve associated with the CDD levels out as soon as the SNR increases beyond than 20dB, while the MSDSD using $N_{wind} = 6$ completely removes the error floor, hence resulting in a steadily decreasing BER curve as the SNR increases.

5.3 Multi-Path MSDSD Design for Cooperative Communication

5.3.1 System Model

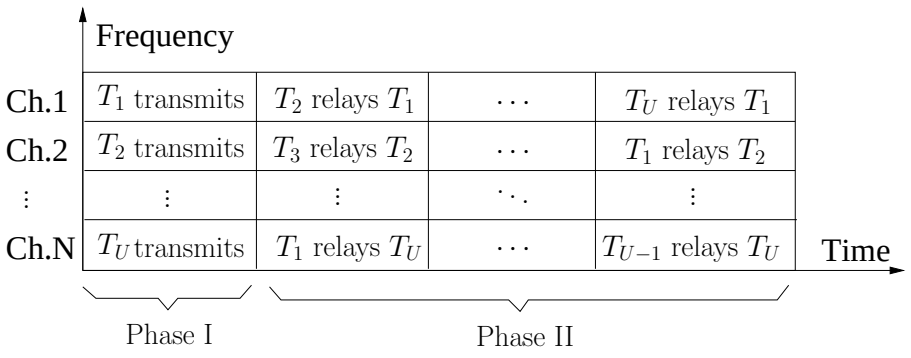

Figure 5.9: Repetion-based channel allocation scheme.

After the brief review of the principle of the MSDSD designed for single-path channels in Section 5.2, we continue by specifically designing a MSDSD scheme for the cooperative system

discussed in Section 5.1. As depicted in Figure 5.9, we consider a U-user cooperation-aided system, where signal transmission involves two transmission phases, namely, the broadcast phase and the relay phase, which are also referred to as phase I and II. A user who directly sends his/her own information to the destination are regarded as a *source* node, while the other users who assist in forwarding the information received from the source node is considered as *relay* nodes. In both phases, any of the well-established multiple access schemes can be employed by the users to guarantee an orthogonal transmission among them, such as Time Division Multiple Access (TDMA), Frequency Division Multiple Access (FDMA), or Code Division Multiple Access (CDMA). In this report, TDMA is considered for the sake of simplicity. Furthermore, due to the symmetry of channel allocation among users, as indicated in Figure 5.9, we focus our attention on the information transmission of source terminal T_S seen in Figure 5.10, which potentially employs $(U-1)$ relay terminals $T_{R_1}, T_{R_2}, \cdots, T_{R_{U-1}}$ in order to achieve cooperative diversity by forming a VAA. Without loss of generality, we simply assume the employment of a single antenna for each of the collaborating MSs and that of N receive antennas for the BS. Additionally, a unity total power P shared by the collaborating MSs for transmitting a symbol is assumed.

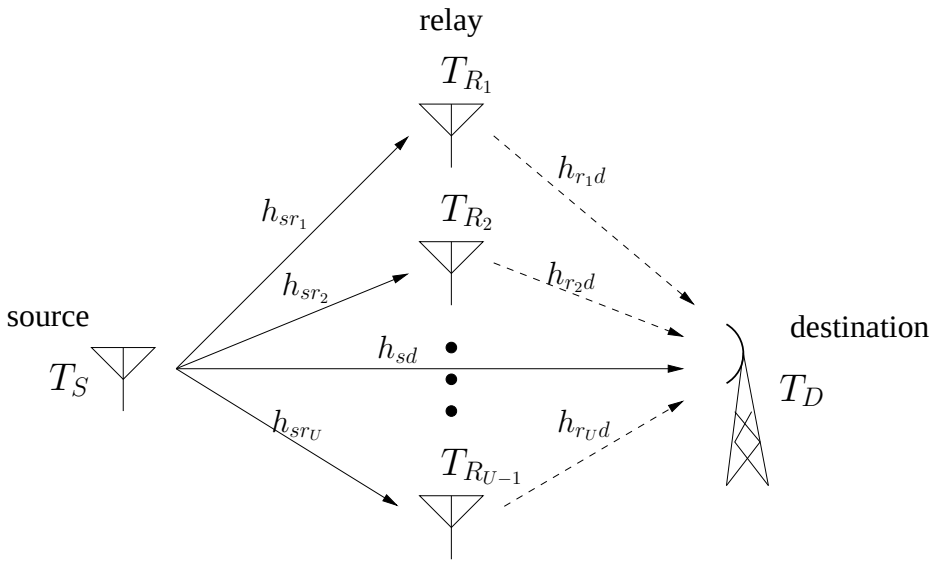

Figure 5.10: Multiple-relay-node-aided cooperative communication schematics.

Owing to the potential transmission inefficiency and implementational difficulty imposed by the channel estimation in cooperation-aided systems, differential encoding and detection without the acquisition of the CSI is preferable to the employment of substantially more complex coherent transmission techniques, as we have discussed in Section 5.1. Hence, we assume that in phase-I, the source broadcasts its differentially encoded signals, while the destination as well as the relay terminals are also capable of receiving the signal transmitted by the source. In the forthcoming phase-II, we consider two possible cooperation protocols, which can be employed by the relay nodes: the relay node may either directly forward the received signal to the destination after signal amplification (Amplify-and-Forward (AF) scheme) or differentially decode and re-encode the received signal before its re-transmission (Decode-and-Forward (DF) scheme).

Recall from Section 5.1.1.1, that the information is conveyed in the difference of the phases of

two consecutive PSK symbols for differentially encoded transmission. In the context of the user cooperation-aided system of Figure 5.10, the source termianl T_S broadcasts the lth differentially encoded frame $\mathbf{s}^l$ during phase-I, which is constituted of L_f number of DMPSK symbols $s[n]$ $(n = 1, 2, \cdots, L_f)$ given by Eq.(5.1). According to Eq.(5.1), the differential encoding process of the source node may be expressed as:

$$s_s[n] = s_s[n-1]v_s[n], \tag{5.30}$$

where $v_{sd}[n] \in \mathcal{M}_c = \{e^{j2\pi m/M_c}; m = 0, 1, \cdots, M_c - 1\}$ is the information symbol obtained after bit-to-symbol mapping, and $s_{sd}[n] \in \mathcal{M}_c = \{e^{j2\pi m/M_c}; m = 0, 1, \cdots, M_c - 1\}$ represents the differentially encoded symbols during the nth time slot. We assume a total power of unity, i.e. $P = 1$ for transmitting a DMPSK symbol of the source over the entire user cooperation period and introducing the broadcast transmit power ratio η which is equal to the transmit power P_s employed by the source. Hence, during the forthcoming phase-II, the total power consumed by all the $(U-1)$ number of relay nodes used for transmitting the signal received from the source is $\sum_{u=1}^{U-1} P_{r_u} = 1 - \eta$, where P_{r_u} is the power consumed by the relay terminal T_{R_u} for conveying the signal of the source node. For the sake of mitigating the impairments imposed by the time-selective channels on the T-DPSK modulated transmission, frame-based rather than symbol-based user-cooperation is carried out, which is achieved at the expense of both a higher detection delay and increased memory requirements.

Furthermore, according to the cooperative strategy of Figure 5.9, where each of the $(U-1)$ spatially dispersed relay nodes helps forward the signal from the source node to the destination node in $(U-1)$ successive time slots, we construct the a *single-symbol system model* for the source node's nth transmit symbol in the context of the TDMA-based user-cooperation aided system of Figure 5.10 as:

$$\mathbf{Y}_n = \mathbf{P}\mathbf{S}_n\mathbf{H}_n + \mathbf{W}_n, \tag{5.31}$$

where the diagonal matrix $\mathbf{P}$ is introduced to describe the transmit power allocation amongst the collaborating MSs, which is defined as:

$$\mathbf{P} \triangleq \text{diag}\left(\left[\sqrt{P_s}\ \sqrt{P_{r_1}}\ \cdots\ \sqrt{P_{r_{U-1}}}\right]\right). \tag{5.32}$$

Additionally, in Eq. (5.31) $\mathbf{S}_n$ and $\mathbf{Y}_n$ represent the *transmitted user-cooperation based signal matrix* and the received signal matrix at the destination, respectively, during both phase-I and phase-II. Additionally, $\mathbf{H}_n$ and $\mathbf{W}_n$ denote the channel matrix and the AWGN matrix, respectively. Upon

further elaborating on Eq.(5.31), we arrive at:

$$\begin{aligned}
&\begin{bmatrix} y_{sd_1}[n] & \cdots & y_{sd_N}[n] \\ y_{r_1d_1}[n+1\cdot L_f] & \cdots & y_{r_1d_N}[n+1\cdot L_f] \\ \vdots & \cdots & \vdots \\ y_{r_{U-1}d_1}[n+(U-1)L_f] & \cdots & y_{r_{U-1}d_N}[n+(U-1)L_f] \end{bmatrix}_{U\times N} \\
=&\mathbf{P}\begin{bmatrix} s_s[n] & 0 & \cdots & 0 \\ 0 & s_{r_1}[n+1\cdot L_f] & \cdots & 0 \\ \vdots & \vdots & \ddots & \vdots \\ 0 & 0 & \cdots & s_{r_{U-1}}[n+(U-1)L_f] \end{bmatrix}_{U\times U} \\
\times&\begin{bmatrix} h_{sd_1}[n] & \cdots & h_{sd_N}[n] \\ h_{r_1d_1}[n+1\cdot L_f] & \cdots & h_{r_1d_N}[n+1\cdot L_f] \\ \vdots & \cdots & \vdots \\ h_{r_{U-1}d_1}[n+(U-1)L_f] & \cdots & h_{r_{U-1}d_N}[n+(U-1)L_f] \end{bmatrix}_{U\times N} \\
+&\begin{bmatrix} w_{sd_1}[n] & \cdots & w_{sd_N}[n] \\ w_{r_1d_1}[n+1\cdot L_f] & \cdots & w_{r_1d_N}[n+1\cdot L_f] \\ \vdots & \cdots & \vdots \\ w_{r_{U-1}d_1}[n+(U-1)L_f] & \cdots & w_{r_{U-1}d_N}[n+(U-1)L_f] \end{bmatrix}_{U\times N},
\end{aligned} \tag{5.33}$$

where the rows and columns of the transmitted user-cooperation based signal matrix $\mathbf{S}_n$ denote the spatial and temporal dimensions, respectively. Moreover, since the source and multiple relay terminals are assumed to be far apart, the elements of the channel matrix $\mathbf{H}_n$, corresponding to the CIRs between the source and the destination nodes as well as those between the relay node and the destination node are mutually uncorrelated, but each of them may be correlated along the TD according to the time-selective characteristics of the channel. Additionally, the elements of the AWGN matrix are modeled as independent complex-valued Gaussian random variables with zero means and a variance of $N_0 = 2\sigma_w^2$.

More specifically, since we have the transmitted symbol $s_s[n] \in \mathcal{M}_c = \{e^{j2\pi m/M_c}; m_s = 0, 1, \cdots, M_c - 1\}$ at the source node, the $(U \times U)$-element transmitted signal matrix $\mathbf{PS}_n$ in the general system model of Eq.(5.33) can be reformatted for the DAF-aided cooperative system as:

$$\mathbf{PS}_n = \begin{bmatrix} \sqrt{P_s}\cdot e^{j2\pi m_s/M_c} & 0 & \cdots & 0 \\ 0 & f_{AM_{r_1}} y_{sr_1}[n] & \cdots & 0 \\ \vdots & \vdots & \ddots & \vdots \\ 0 & 0 & \cdots & f_{AM_{r_{U-1}}} y_{sr_{U-1}}[n] \end{bmatrix}, \tag{5.34}$$

where $f_{AM_{r_u}}$ is the signal gain employed by the uth relay node to make sure that the average tranmsitted power of the uth relay is P_{r_u} and

$$\begin{aligned}
&y_{sr_u}[n] \\
=&\sqrt{P_s}\cdot s_s[n]h_{sr_u}[n] + w_{sr_u}[n], &(5.35)\\
=&\sqrt{P_s}\cdot e^{j2\pi m_s/M_c}h_{sr_u}[n] + w_{sr_u}[n], \quad (m_s = 0, 1, \cdots, M_c - 1) &(5.36)
\end{aligned}$$

represents the signal received at the uth relay node during the broadcast phase-I.

As for the DDF-aided user-cooperation system, where the relay node differentially detects and re-encodes the signal received from the source node before forwarding it to the destination, the $(U \times U)$-element transmitted signal matrix $\mathbf{PS}_n$ in the general system model of Eq.(5.33) can be rewritten as follows under the assumption that the output of the differentially detected relay is error-free:

$$\mathbf{PS}_n = \begin{bmatrix} \sqrt{P_s} \cdot e^{j2\pi m_s/M_c} & 0 & \cdots & 0 \\ 0 & \sqrt{P_{r_1}} \cdot e^{j2\pi m_s/M_c} & \cdots & 0 \\ \vdots & \vdots & \ddots & \vdots \\ 0 & 0 & \cdots & \sqrt{P_{r_{U-1}}} \cdot e^{j2\pi m_s/M_c} \end{bmatrix}. \tag{5.37}$$

5.3.2 Differentially Encoded Cooperative Communication Using CDD

In this section, for the sake of simplicity, we consider two differential modulation based two-user cooperative schemes, namely, the Differential Amplify-and-Forward (DAF) and Differential Decode-and-Forward (DDF). Both the DAF and DDF schemes are amenable to the CDD in fading channels after a linear signal combination process, which will be discussed in our forthcoming discourse.

5.3.2.1 Signal Combining at the Destination for Differential Amplify-and-Forward Relaying

For the DAF scheme, the $(U-1)$ relay nodes of Figure 5.10 amplify the signal received from the source node and forward it to the destination node in a preset order over $(U-1)$ successive time slots during phase-II. In order to ensure that the average transmit power of the uth relay node remains P_{r_u}, the corresponding amplification factor $f_{AM_{r_u}}$ in Eq. (5.34) employed by the uth relay node can be specified as [128]:

$$f_{AM_{r_u}} = \sqrt{\frac{P_{r_u}}{P_s \sigma_{sr_u}^2 + N_0}}, \tag{5.38}$$

where $\sigma_{sr_u}^2$ is the variance of the channel's envelope spanning between the source and the uth relay node, which can be obtained by long-term averaging of the received signals. Therefore, the signal received at the destination from the uth relay node $y_{r_u d}[n + uL_f]$ in Eq.(5.33) can be represented as follows [128]:

$$y_{r_u d}[n + uL_f] = f_{AM_{r_u}} y_{sr_u}[n] h_{r_u d}[n + uL_f] + w_{r_u d}[n + uL_f], \tag{5.39}$$

where $y_{sr_u}[n]$ is the signal received from the source node at the uth relay node during the broadcast phase-I, which was given by Eq. (5.35).

The destination BS linearly combines the signal at each of the N receive antennas received from the source through the direct link during the broadcast, namely phase-I and those at each receive antenna received from all the relay nodes during phase-II, followed by the CDD process operating without acquiring any CSI. Based on the multichannel differential detection principle of [6], we combine the multi-path signal of the U-user cooperation aided system of Figure 5.10 prior to the CDD process as:

$$y = \sum_{i=1}^{N} \left[a_0 (y_{sd_i}[n-1])^* y_{sd_i}[n] + \sum_{u=1}^{U-1} a_u (y_{r_u d_i}[n + uL_f - 1])^* y_{r_u d_i}[n + uL_f] \right], \tag{5.40}$$

where L_f is the length of the frame, while the coefficients a_0 and $a_u, (u = 1, 2, \cdots)$ are respectively given by:

$$a_0 = \frac{1}{N_0}, \tag{5.41}$$

$$a_u = \frac{P_s\sigma^2_{sr_u} + N_0}{N_0(P_s\sigma^2_{sr_u} + P_{r_u}\sigma^2_{r_ud} + N_0)}, \tag{5.42}$$

where $\sigma^2_{sr_u}$ and $\sigma^2_{r_ud}$ are the variances of the link between the source and relay nodes as well as of the link between the relay node and the BS, respectively. By assuming that the CIRs h_{sr_u} as well as h_{r_ud} are almost constant over two successive symbol periods, the destination node carries out CDD based on the combined signal y of Eq.(5.40) as:

$$e^{j2\pi\hat{m}/M_c} = \arg \max_{\check{m}=0,1,\cdots,M_c-1} \Re\{e^{-j2\pi\check{m}/M_c} y\}, \tag{5.43}$$

where $\Re\{\cdot\}$ denotes the real component of a complex number.

5.3.2.2 Signal Combining at Destination for Differential Decode-and-Forward Relaying

For the DDF-aided U-user cooperation assisted system of Figure 5.10, each relay node differetially decodes and re-encodes the signal received from the source node, before forwarding it to the BS. Similarly, based on the multichannel differential detection techniques of [6, 129], the combined signal prior to differential detection by the DDF scheme can be expressed in exactly the same form as that of Eq.(5.40) for the DAF scheme, which is repeated here for convenience:

$$y = \sum_{i=1}^{N} \left[a_0 (y_{sd_i}[n-1])^* y_{sd_i}[n] + \sum_{u=1}^{U-1} a_u (y_{r_ud_i}[n+uL_f-1])^* y_{r_ud_i}[n+uL_f] \right], \tag{5.44}$$

noting that different diversity combining weights of a_0 and $a_u, (u = 1, 2, \cdots, U-1)$ are used. Note that the choice of diversity combining weights may affect the achievable system performance. For example, when the normalized total power of $P = 1$ used for transmitting a symbol during the entire user cooperation aided process is equally divided among the source and relay nodes, namely, when we have $P_s = P_{r_u} = 1/U, (u = 1, 2, \cdots, U-1)$, the SNR of the combiner output is maximized by opting for [129]:

$$a_0 = a_u = \frac{1}{N_0}, \tag{5.45}$$

provided that the corresponding channel variances are identical. Although the choice of the diversity combining weights is not optimum in general, it is optimum for the case when the SNR of the source-destination link and those of the multiple relay-destination links are the same. Again, by assuming that the CIRs taps h_{sr_u} as well as h_{r_ud} are constant during two successive symbol periods, the CDD process of Eq.(5.43) can be carried out by the destination after combining the multi-path signals.

5.3.2.3 Simulation Results

Figure 5.11 depicts the BER performance versus P/N_0 for both the single-user non-cooperative system and the two-user DAF-aided cooperative system, using the simulation parameters summa-

System Parameters	Choice
System	Two-User Cooperative OFDM
Number of Relay Nodes	1
Subcarrier BW	$\triangle f = 10$ kHz
Number of Sub-Carriers	$D = 1024$
Modulation	T-DQPSK
Frame Length L_f	101
CRC	CCITT-6
Normalised Doppler Freq.	$f_d = 0.03, 0.01, 0.001$
Channel Model	typical urban, refer to Table 5.1
Channel Variances	$\sigma_{sd}^2 = \sigma_{sr}^2 = \sigma_{rd}^2 = 1$
Power Allocation	$P_s = P_{r_1} = 0.5P = 0.5$
SNR at Relay and Destination	$P_s/N_0 = P_{r_1}/N_0$

Table 5.4: Summary of system parameters for a T-DPSK modulated two-user cooperation aided OFDM system.

rized in Table 5.4. Note that we consider a scenario, where the total power P used for transmitting a differentially encoded symbol during an entire user cooperation process is equally shared between the source as well as relay nodes, and the SNRs at both the receiver of the relay and destination nodes are identical. Additionally, in order to carry out a fair comparison between the non-cooperative and cooperative systems, we assume that the power consumed by the single-user non-cooperative system when transmitting a single T-DPSK symbol is also equal to $P = 1$, which is identical to that consumed by its user-cooperation aided counterpart. As observed from Figure 5.11, in the presence of the slowly-fading TU channel of Table 5.1 associated with $f_d = 0.001$, the DDF-aided two-user cooperation assisted system is capable of achieving the maximum attainable spatial diversity order of two, resulting in a significant performance gain of 10 dB, given a target BER of 10^{-4}. This high gain is not unexpected, since it is unlikely that both the direct and relay links suffer from a deep fade. However, since the T-DQPSK modulation scheme is employed, the performance achieved by CDD at the destination node degrades signficantly, as the normalized Doppler frequency f_d becomes higher. This is due to, for example, the relative mobility of the source and relay nodes with respect to the BS. For the sake of simplicity, here we assume the same normalized Doppler frequency exhibited by all the three links of the two-user cooperation aided system, namely, the source-relay, relay-destination as well as the source-destination links. As shown in Figure 5.11, an error floor is formed by the BER curves corresponding to the more time-selective scenarios associated with an increased normalized Doppler frequency f_d ranging from 0.001 to 0.03, which is an undesirable situation encountered also by the classic single-user non-cooperative benchmark system. However, the lowest achievable end-to-end BER of 10^{-3} exhibited by the CDD operating with the aid of the DAF-aided cooperation scheme, is still lower than the BER of 10^{-2} achieved by the non-cooperative system under the assumption of $f_d = 0.03$.

In comparison to the DAF-aided cooperation assisted system, where the relay node directly forwards the amplified signal to the destination, the differential decoding and re-encoding of the DDF-aided system are carried out by the relay node before forwarding, as discussed in Section 5.3.2.2. The simulation parameters are summarized in Table 5.4, where we can see that a Cyclic Redun-

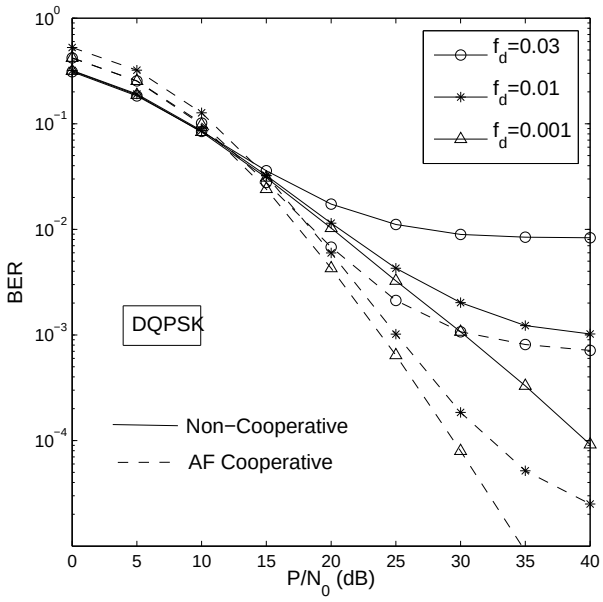

Figure 5.11: BER performance of the DAF-aided DQPSK-modulated two-user cooperation aided OFDM system in Rayleigh fading channels at different normalised Doppler frequencies. The system parameters were summarized in Table 5.4.

dancy Check (CRC) code is employed by the relay node in order to determine whether the current decoded signal is correct or not and only the error-freely decoded signal is forwarded to the destination. Otherwise, the relay remains silent during phase-II. Figure 5.12 plots the BER curves of the DDF-aided two-user cooperation assisted system using the CDD at both the relay and destination nodes in contrast to those of its non-cooperative counterpart. Again, the DDF-aided cooperation assisted scheme is capable of achieving the maximum attainable diversity order of two, leading to a significant performance gain for transmission over a slow-fading channel associated with $f_d = 0.001$. Furthermore, observe by comparing Figure 5.12 that a similarly negative impact is imposed on the end-to-end BER performance by the relative mobility of the source, relay and destination nodes for the DDF scheme as that imposed for the DAF scheme. Moreover, also note in Figure 5.12 that although the DDF-aided cooperative system outperforms its non-cooperative counterpart at the three different values of the normalized Doppler frequency considered, the achievable performance gain becomes more negligible, as f_d increases. Specifically, only a slightly lower error floor is exhibited in Figure 5.12 by the DDF-aided system associated with $f_d = 0.03$ than that presented by the classic single-user non-cooperative arrangement. In addition, as observed from both Figure 5.11 and Figure 5.12, both the DAF and DDF aided cooperative systems exhibit a worse BER performance than the classic non-cooperative one in the relatively low SNR range spanning from 0 to 15 dB, which can also be observed for the colocated-multiple-transmit-antenna-assisted system. This trend is not unexpected, since the effective SNR experienced at the receiver is halved for the two-transmit-antenna-aided system, and the benefit of diversity is overwhelmed by the deleterious effects of the noise, when the SNR is low.

Let us now investigate the benefit of the CRC-based error detection capability of the relay node on the end-to-end BER performance of a DDF-aided two-user cooperative system in Figure 5.13,

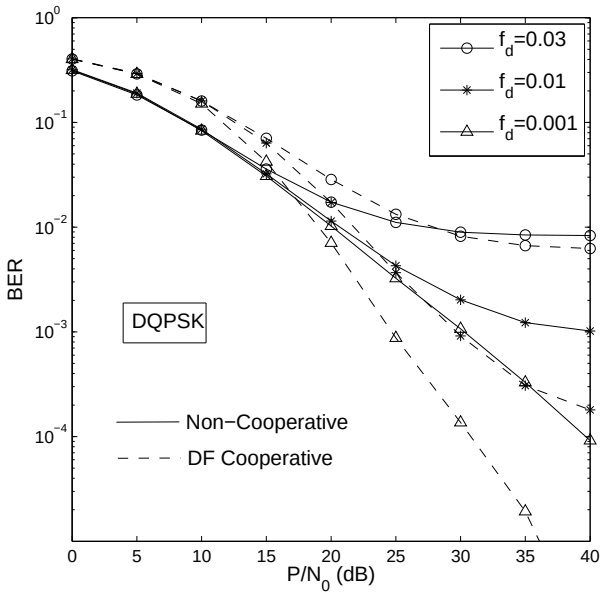

Figure 5.12: BER performance of the DDF-aided DQPSK-modulated cooperative system in Rayleigh fading channels at different normalised Doppler frequencies. The system parameters were summarized in Table 5.4.

where the BER curves corresponding to different CRC codes are plotted in contrast to those of the so-called fixed-relay based cooperative system as well as to that of the single-user non-cooperative one. Note that as summarized in Table 5.4, the frame length L_f employed is 101 DQPSK symbols, whereas CCITT-6 was used by the relay node similarly to the previously simulated DDF-aided cooperative systems of Figure 5.12, which exhibits a desirable error detection capability for this relatively short frame length, since a full diversity order of 2 can be achieved. For the sake of improving the achievable transmission efficiency, a CRC code using as few parity bits as possible is preferable, such as CCITT-4. However, as observed in Figure 5.13, the achievable BER performance of the DDF-aided cooperative system gradually degrades as the SNR increases, leading to an approximately 4 dB performance gain reduction at a target BER of 10^{-5} in comparison to the system employing the CCITT-6. Another extreme example worth considering is a fixed-relay based cooperation aided system, where the relay forwards the re-encoded differential signal to the destination without checking, whether the differentially decoded bits are correct or not. Hence, the achievable transmission efficiency is improved by sacrificing the maximum achievable diversity gain. Specifically, without the aid of the CRC, no spatial diversity gain can be achieved, although an additional transmit antenna provided by the relay node further assists the source by forwarding the signal to the BS. The reason for this trend is that without CRC checking the original diversity gain is eroded by the flawed information delivered by the relay node, which is further combined with the signal received via the direct link at the destination. Hence, a flexible compromise between maintaining a high transmission efficiency and the maximum achievable diversity gain can be struck by employing an appropriate CRC code.

In comparison to the classic colocated-multiple-transmit-antenna-assisted system, the performance of the user-cooperation aided system is affected by both the channel quality of the source-

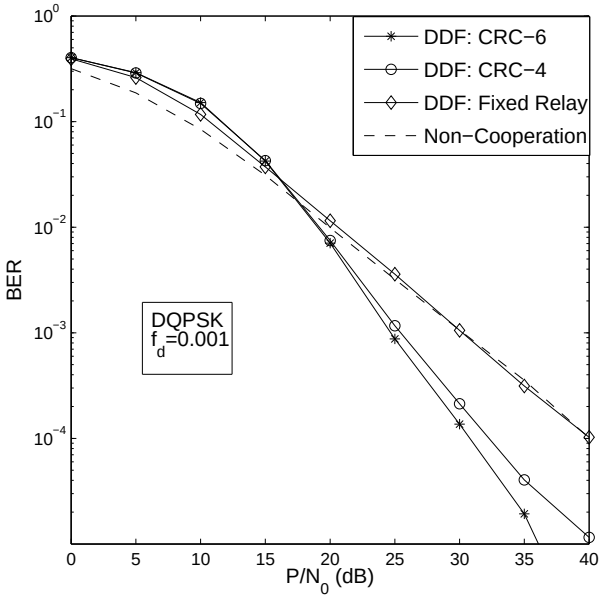

Figure 5.13: Benefits of the CRC-based error detection capability at the relay node on the end-to-end BER performance of a DDF-aided DQPSK-modulated cooperative system. The system parameters were summarized in Table 5.4.

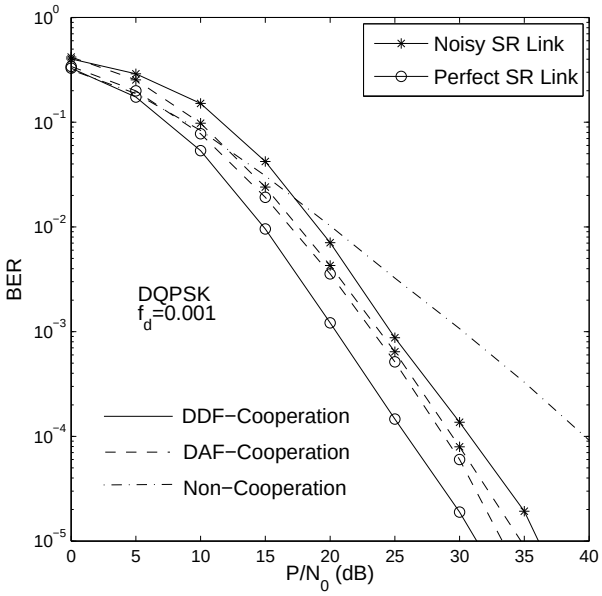

Figure 5.14: Impact of the source-relay link's quality on the end-to-end BER performance of a T-DQPSK modulated two-user cooperation system. The system parameters were summarized in Table 5.4.

destination and relay-destination links, as well as by that of the source-relay link. This statement is true for both the DAF-aided and DDF-aided cooperative systems as evidenced by our forthcoming discussions. Figure 5.14 compares the BER performance achieved by the two-user cooperation aided system employing either the DAF or the DDF scheme in two different scenarios, namely for a noisy source-relay link, as assumed in the scenarios characterized in Figure 5.12 and 5.13 and for a perfect noise-free source-relay link. In other words, the relay is assumed to have perfect knowledge of the source node's transmitted signal in the latter scenario, which can also be regarded as the conventional collocated-multiple-transmit-antenna-aided system, if the DDF scheme is employed. Additionally, recall from Figure 5.11 and 5.12 the maximum diversity order of two can indeed be achieved by the T-DPSK modulated two-user cooperation aided system using the CDD when a quasi-static scenario of a normalized Doppler frequency $f_d = 0.001$ is assumed. Although the maximum achievable diversity gain cannot be increased by having a perfect source-relay link, observe in Figure 5.14 that the system's BER performance was indeed improved. To be more specific, a performance gain as high as 5 dB was attained in Figure 5.14 for the system using the DDF scheme by having a perfect source-relay link, whereas only a negligible performance gain was attained in Figure 5.14 by its DAF-aided counterpart. Furthermore, by comparing the performance achieved by the DAF and DDF schemes in Figure 5.14, we can observe that the performance achieved by the latter is slightly outperformed by the former, if the transmissions between the source and relay nodes are carried out over a noisy link having an SNR at the relay node, which is equal to that measured at the destination node. However, it is expected that the latter will outperform the former as a benefit of having a better-quality source-relay link, as indicated by the extreme example of having a noise-free source-relay link, which was characterized in Figure 5.14. Therefore, when the source-relay link is of poor quality, it is preferable to employ the DAF scheme, which outperforms the DDF scheme despite its lower complexity, since there is no need to carry out any differential decoding and re-encoding.

5.3.3 Multi-Path MSDSD Design for Cooperative Communication

In order to mitigate the potential negative impact induced by strongly time-selective or frequency-selective channels on the conventional T-DPSK or F-DPSK scenarios of Section 5.1.1, the single-path MSDSD introduced in Section 5.2 constitutes an attractive scheme for employment by the relay nodes, when differential decoding is carried out at relay nodes using the DF protocol. Figure 5.15 characterizes the achievable performance improvements of the DDF-aided two-user cooperation assisted system attained by the single-path MSDSD scheme at the relay node in time-selective Rayleigh fading channels at different normalized Doppler frequencies. When employing the MSDSD scheme using $N_{wind} = 6$ at the relay node, observe in Figure 5.15 that the error floors encountered in time-selective channels corresponding to $f_d = 0.01$ and $f_d = 0.03$ are significantly mitigated, resulting in a substantial performance gain. For example, given a target BER of 10^{-4}, a performance gain in excess of 5 dB can be achieved for $f_d = 0.01$ as seen in Figure 5.15. However, since the end-to-end performance of the user cooperation aided system of Figure 5.10 is determined by the robustness of the differential detection schemes employed at both the relay and destination nodes, the single-path MSDSD aided relay terminals alone are unable to guarantee a desirable end-to-end performance. Hence, although a significant performance gain can be attained by improving

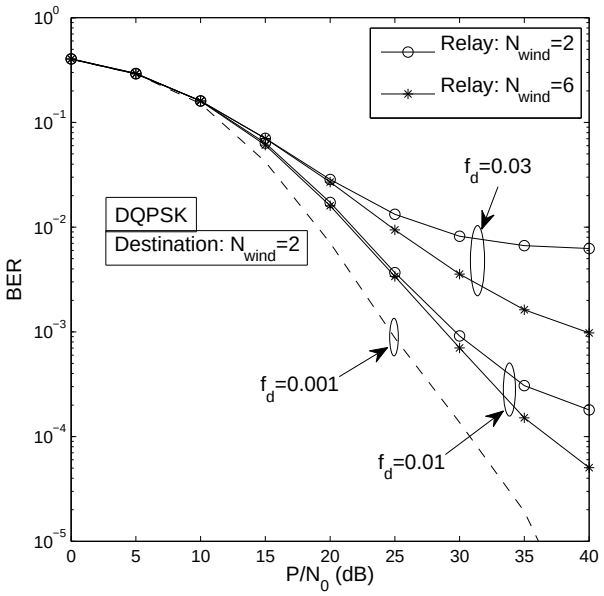

Figure 5.15: BER performance of DDF-aided DQPSK-modulated cooperative system using MSDSD-aided relays in Rayleigh fading channels.

the detection capability at the relay node, there is still a substantial performance gap between the BER curve obtained at $f_d = 0.01$ or $f_d = 0.03$ and that corresponding to $f_d = 0.001$. The maximum diversity order of two is not achieved at $f_d = 0.03$ or $f_d = 0.01$, as indicated by the slope of the BER curve seen in Figure 5.15. Hence, for the sake of further improving the performance of the DDF-aided cooperative system or that of the DAF-aided one, a powerful differential detector has to be applied at the destination node, which is robust to the impairments imposed by time-selective channels. Unfortunately, the single-path MSDSD scheme cannot be directly employed by the destination node in order to jointly differentially decode the multi-path signals received from the source and relay nodes. Thus, a potential channel-induced performance degradation may still occur when carrying out conventional differential detection of signals received over multi-path channel, which is discussed in Section 5.3.2. In the forthcoming sections, based on the principle of the single-path MSDSD, we will propose a MSDSD scheme specifically designed for user-cooperation aided communication systems, which is capable of jointly differentially detecting the multi-path signals delivered by the source and relay nodes.

5.3.3.1 Derivation of the Metric for Optimum Detection

5.3.3.1.1 Equivalent System Model for DDF-Aided Cooperative Systems

Following on from the principle of the single-path MSDSD discussed in Section 5.2, the receiver operating without the knowledge of CSI at the destination node collects N_{wind} number of consecutive user-cooperation based space-time symbols $\mathbf{S}_n, (n = 0, 1, \cdots, N_{wind} - 1)$. These samples are then used to jointly detect a block of $(N_{wind} - 1)$ consecutive symbols $v_s[n], (n = 0, 1, \cdots, N_{wind} - 2)$, which were differentially encoded by the source during phase-I by exploiting the correlation between the phase distortions experienced by the adjacent samples $\mathbf{S}_n, (n =$

$0, 1, \cdots, N_{wind}-1$). The nth user-cooperation based space-time symbol $\mathbf{S}_n$ was defined specifically for the DDF-aided cooperation system in Eq.(5.37), which is rewritten here as:

$$\mathbf{S}_n = \begin{bmatrix} e^{j2\pi m_s/M_c} & 0 & \cdots & 0 \\ 0 & e^{j2\pi m_s/M_c} & \cdots & 0 \\ \vdots & \vdots & \ddots & \vdots \\ 0 & 0 & \cdots & e^{j2\pi m_s/M_c} \end{bmatrix}, \tag{5.46}$$

where we have $m_s = 0, 1, \cdots, M_c-1$. Since the total power used for transmitting a single symbol $\mathbf{S}_n$ during the entire user-cooperation process is normalized, we have:

$$P_s + \sum_{u=1}^{U-1} P_{r_u} = 1, \tag{5.47}$$

where U is the number of users in the user-cooperation aided system of Figure 5.10. Moreover, with the aid of Eqs. (5.33) and (5.37), we can rewrite the generalized single-symbol-based cooperative system model of Eq.(5.31) for the DDF-aided cooperative transmission, resulting in the *equivalent single-symbol based system model* as follows:

$$\mathbf{Y}_n = \mathbf{P}\mathbf{S}_n\mathbf{H}_n + \mathbf{W}_n, \tag{5.48}$$

$$= \mathbf{S}_n\mathbf{P}\mathbf{H}_n + \mathbf{W}_n, \tag{5.49}$$

$$= \tilde{\mathbf{S}}_n\tilde{\mathbf{H}}_n + \tilde{\mathbf{W}}_n, \tag{5.50}$$

where the equivalent user-cooperation transmitted signal's unitary matrix $\tilde{\mathbf{S}}_n$ is represented by:

$$\tilde{\mathbf{S}}_n = \mathbf{S}_n = \begin{bmatrix} e^{j2\pi m_s/M_c} & 0 & \cdots & 0 \\ 0 & e^{j2\pi m_s/M_c} & \cdots & 0 \\ \vdots & \vdots & \ddots & \vdots \\ 0 & 0 & \cdots & e^{j2\pi m_s/M_c} \end{bmatrix}, \quad m_s = 0, 1, \cdots, M_c-1, \tag{5.51}$$

and the equivalent channel matrix $\tilde{\mathbf{H}}_n$ can be expressed as:

$$\tilde{\mathbf{H}}_n = \mathbf{P}\mathbf{H}_n, \tag{5.52}$$

$$= \begin{bmatrix} \sqrt{P_s}\cdot h_{sd_1}[n] & \cdots & \sqrt{P_s}\cdot h_{sd_N}[n] \\ \sqrt{P_{r_1}}\cdot h_{r_1d_1}[n+1\cdot L_f] & \cdots & \sqrt{P_{r_1}}\cdot h_{r_1d_N}[n+1\cdot L_f] \\ \vdots & \cdots & \vdots \\ \sqrt{P_{r_{U-1}d}}\cdot h_{r_{U-1}d_1}[n+(U-1)L_f] & \cdots & \sqrt{P_{r_{U-1}d}}\cdot h_{r_{U-1}d_N}[n+(U-1)L_f] \end{bmatrix}. \tag{5.53}$$

In addition, according to Eq. (5.33) the received signal matrix $\mathbf{Y}_n$ and the equivalent noise matrix $\tilde{\mathbf{W}}_n$ may be written as:

$$\mathbf{Y}_n = \begin{bmatrix} y_{sd_1}[n] & \cdots & y_{sd_N}[n] \\ y_{r_1d_1}[n+1\cdot L_f] & \cdots & y_{r_1d_N}[n+1\cdot L_f] \\ \vdots & \cdots & \vdots \\ y_{r_{U-1}d_1}[n+(U-1)L_f] & \cdots & y_{r_{U-1}d_N}[n+(U-1)L_f] \end{bmatrix} \tag{5.54}$$

and

$$\tilde{\mathbf{W}}_n = \mathbf{W}_n = \begin{bmatrix} w_{sd_1}[n] & \cdots & w_{sd_N}[n] \\ w_{r_1d_1}[n+1\cdot L_f] & \cdots & w_{r_1d_N}[n+1\cdot L_f] \\ \vdots & \cdots & \vdots \\ w_{r_{U-1}d_1}[n+(U-1)L_f] & \cdots & w_{r_{U-1}d_N}[n+(U-1)L_f] \end{bmatrix}, \tag{5.55}$$

respectively.

5.3.3.1.2 Equivalent System Model for the DAF-Aided Cooperative System

Similarly, with the aid of Eqs. (5.33), (5.34) as well as (5.35) and following a number of straightforward manipulations left out here for compactness, we arrive at the *equivalent single-symbol system model* for the DAF-aided cooperation system based on the generalized single-symbol based cooperative system model of Eq. (5.31) as follows:

$$\mathbf{Y}_n = \tilde{\mathbf{S}}_n \tilde{\mathbf{H}}_n + \tilde{\mathbf{W}}_n, \tag{5.56}$$

where the received signal matrix $\mathbf{Y}_n$ at the BS is expressed identically to that of the DDF-aided system as:

$$\mathbf{Y}_n = \begin{bmatrix} y_{sd_1}[n] & \cdots & y_{sd_N}[n] \\ y_{r_1d_1}[n+1\cdot L_f] & \cdots & y_{r_1d_N}[n+1\cdot L_f] \\ \vdots & \cdots & \vdots \\ y_{r_{U-1}d_1}[n+(U-1)L_f] & \cdots & y_{r_{U-1}d_N}[n+(U-1)L_f] \end{bmatrix}, \tag{5.57}$$

and the equivalent user-cooperation transmitted signal matrix $\tilde{\mathbf{S}}_n$ can be written as:

$$\tilde{\mathbf{S}}_n = \begin{bmatrix} e^{j2\pi m_s/M_c} & 0 & \cdots & 0 \\ 0 & e^{j2\pi m_s/M_c} & \cdots & 0 \\ \vdots & \vdots & \ddots & \vdots \\ 0 & 0 & \cdots & e^{j2\pi m_s/M_c} \end{bmatrix}, \quad m_s = 0, 1, \cdots, M_c - 1, \tag{5.58}$$

which is identical to the transmitted signal matrix given in Eq.(5.51) for the DDF-aided system. However, the resultant equivalent channel matrix $\tilde{\mathbf{H}}_n$ of the DAF-aided system is different from that obtained for its DDF-aided counterpart of Eq.(5.52), which is expressed as:

$$\tilde{\mathbf{H}}_n = [\tilde{\mathbf{h}}_1\ \tilde{\mathbf{h}}_2\ \cdots\ \tilde{\mathbf{h}}_N], \tag{5.59}$$

where the ith column vector $\tilde{\mathbf{h}}_i$ may be written as:

$$\mathbf{h}_i = \begin{bmatrix} \sqrt{P_s}\cdot h_{sd_i}[n] \\ \sqrt{\frac{P_{r_1}}{\sigma^2_{sr_1}+\frac{N_0}{P_s}}} h_{sr_1}[n] h_{r_1d_i}[n+1\cdot L_f] \\ \vdots \\ \sqrt{\frac{P_{r_{U-1}}}{\sigma^2_{sr_{U-1}}+\frac{N_0}{P_s}}} h_{sr_{U-1}}[n] h_{r_{U-1}d_i}[n+(U-1)\cdot L_f] \end{bmatrix}. \tag{5.60}$$

Moreover, the resultant equivalent noise term $\tilde{\mathbf{W}}_n$ can be represented as:

$$\tilde{\mathbf{W}}_n = [\tilde{\mathbf{w}}_1\ \tilde{\mathbf{w}}_2\ \cdots\ \tilde{\mathbf{w}}_N], \tag{5.61}$$

where the ith column vector $\tilde{\mathbf{w}}_i$ may be expressed as:

$$\tilde{\mathbf{w}}_i = \begin{bmatrix} w_{sd}[n] \\ \sqrt{\frac{P_{r_1}}{P_s\sigma^2_{sr_1}+N_0}} w_{sr_1}[n] h_{r_1d_i}[n+1\cdot L_f] + w_{r_1d_i}[n+1\cdot L_f] \\ \vdots \\ \sqrt{\frac{P_{r_{U-1}}}{P_s\sigma^2_{sr_{U-1}}+N_0}} w_{sr_{U-1}}[n] h_{r_{U-1}d_i}[n+(U-1)\cdot L_f] + w_{r_{U-1}d_i}[n+(U-1)\cdot L_f] \end{bmatrix}. \tag{5.62}$$

5.3.3.1.3 Optimum Detection Metric

Then, based on Eq.(5.50) and Eq.(5.56), we can construct the general input-output relation of the channel for multiple differential symbol transmissions for both DAF-aided and DDF-aided user-cooperation assisted systems, where we have the *equivalent multiple-symbol based system model* as:

$$\underline{\mathbf{Y}} = \underline{\tilde{\mathbf{S}}_d}\underline{\tilde{\mathbf{H}}} + \underline{\tilde{\mathbf{W}}}. \tag{5.63}$$

Note that if $\mathbf{A}$ represents a matrix, then $\underline{\mathbf{A}}$ is a block matrix, $\mathbf{A}_d$ denotes a diagonal matrix, and $\underline{\mathbf{A}}_d$ represents a block diagonal matrix. The block matrix $\underline{\mathbf{Y}}$ hosting the received signal, which contains signals received during N_{wind} successive user-cooperation based symbol durations corresponding to N_{wind} consecutively transmitted differential symbols $s_s[n], (n = 0, 1, \cdots, N_{wind} - 1)$ of the source node, is defined as:

$$\underline{\mathbf{Y}} = [\mathbf{Y}_n^T \ \mathbf{Y}_{n+1}^T \ \cdots \ \mathbf{Y}_{n+N_{wind}-1}^T]^T, \tag{5.64}$$

and the block matrix $\underline{\tilde{\mathbf{H}}}$ representing the channel as well as the block matrix $\underline{\tilde{\mathbf{W}}}$ of the AWGN are defined likewise by vertically concatenating N_{wind} matrices $\tilde{\mathbf{H}}_n, (n = 0, 1, \cdots, N_{wind} - 1)$ and $\tilde{\mathbf{W}}_n, (n = 0, 1, \cdots, N_{wind} - 1)$, respectively. Therefore, we can represent $\underline{\tilde{\mathbf{H}}}$ as:

$$\underline{\tilde{\mathbf{H}}} = [\tilde{\mathbf{H}}_n^T \ \tilde{\mathbf{H}}_{n+1}^T \ \cdots \ \tilde{\mathbf{H}}_{n+N_{wind}-1}^T]^T, \tag{5.65}$$

and express $\underline{\tilde{\mathbf{W}}}$ as:

$$\underline{\tilde{\mathbf{W}}} = [\tilde{\mathbf{W}}_n^T \ \tilde{\mathbf{W}}_{n+1}^T \ \cdots \ \tilde{\mathbf{W}}_{n+N_{wind}-1}^T]^T. \tag{5.66}$$

Furthermore, the diagonal block matrix of the transmitted signal is constructed as:

$$\underline{\tilde{\mathbf{S}}_d} = \text{diag}\left(\tilde{\mathbf{S}}_n, \ \tilde{\mathbf{S}}_{n+1}, \ \cdots, \ \tilde{\mathbf{S}}_{n+N_{wind}-1}\right) \tag{5.67}$$

$$= \begin{bmatrix} \tilde{\mathbf{S}}_n & 0 & \cdots & 0 \\ 0 & \tilde{\mathbf{S}}_{n+1} & \cdots & 0 \\ \vdots & \vdots & \ddots & \vdots \\ 0 & 0 & \cdots & \tilde{\mathbf{S}}_{n+N_{wind}-1} \end{bmatrix}, \tag{5.68}$$

where $\tilde{\mathbf{S}}_n \ (n = 0, 1, \cdots, N_{wind} - 1)$ was given by Eq. (5.51) or Eq. (5.58).

We note that all the elements in $\tilde{\mathbf{H}}_n$ and $\tilde{\mathbf{W}}_n$ of (5.52) and (5.55) possess a standard Gaussian distribution for the DDF-aided cooperative system, whereas most terms in $\tilde{\mathbf{H}}_n$ and $\tilde{\mathbf{W}}_n$ of (5.59) and (5.61) do not for its DAF-aided counterpart. However, our informal simulation-based investigations suggest that the resultant noise processes are near-Gaussian distributed in the DAF-aided scenario. As a result, the PDF of the corresponding received signal in (5.63) is also near-Gaussian especially for low SNRs, as seen in Fig. (5.16). Hence, under the simplifying assumption that the *equivalent* fading and noise are zero-mean complex Gaussian processes in the DAF-aided cooperative system, the PDF of the non-coherent receiver's output $\underline{\mathbf{Y}}$ at the BS for both the DAF- and DDF-aided cooperative systems can be obtained based on its counterpart of Eq. (5.14) derived for the single-transmit-antenna scenario in Section 5.2 as:

$$Pr(\underline{\mathbf{Y}}|\underline{\tilde{\mathbf{S}}_d}) = \frac{\exp(-Tr\{\underline{\mathbf{Y}}^H \underline{\Psi}^{-1} \underline{\mathbf{Y}}\})}{(\pi^{UN_{wind}} \det(\underline{\Psi}))^N}, \tag{5.69}$$

where the conditional autocorrelation matrix is given by:

$$\underline{\Psi} = \mathcal{E}\{\underline{\mathbf{Y}}\underline{\mathbf{Y}}^H|\underline{\tilde{\mathbf{S}}_d}\}, \tag{5.70}$$

$$= \underline{\tilde{\mathbf{S}}_d}\mathcal{E}\{\underline{\tilde{\mathbf{H}}}\underline{\tilde{\mathbf{H}}}^H\}\underline{\tilde{\mathbf{S}}_d}^H + \mathcal{E}\{\underline{\tilde{\mathbf{W}}}\underline{\tilde{\mathbf{W}}}^H\}. \tag{5.71}$$

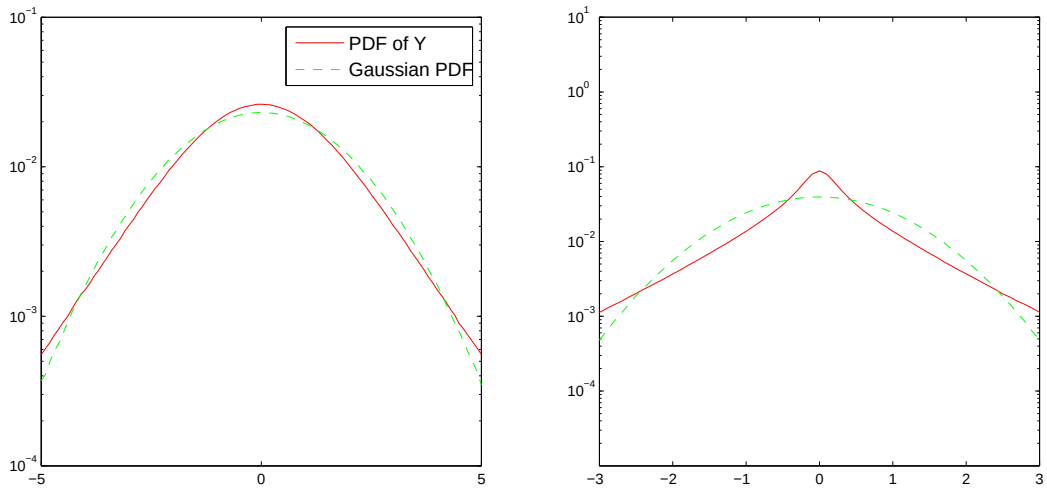

(a) SNR=0 dB (b) SNR=20 dB

Figure 5.16: PDF of the received signal $\underline{\mathbf{Y}}$ of Eq. (5.64) in the DAF-aided cooperative system.

Specifically, for the DDF-aided cooperative system having an equivalent channel matrix $\tilde{\mathbf{H}}_n$ given by Eq.(5.52) and a noise matrix given by Eq.(5.55), the channel's autocorrelation matrix $\mathcal{E}\{\underline{\tilde{\mathbf{H}}}\underline{\tilde{\mathbf{H}}}^H\}$ formulated in Eq.(5.71) can be further extended as:

$$\mathcal{E}\{\underline{\tilde{\mathbf{H}}}\underline{\tilde{\mathbf{H}}}^H\} = \mathcal{E}\left\{\begin{bmatrix}\tilde{\mathbf{H}}_n \\ \vdots \\ \tilde{\mathbf{H}}_{n+N_{wind}-1}\end{bmatrix}\begin{bmatrix}\tilde{\mathbf{H}}_n^* & \cdots & \tilde{\mathbf{H}}_{n+N_{wind}-1}^*\end{bmatrix}\right\}, \tag{5.72}$$

$$= N\begin{bmatrix}\Gamma_{DF}(0) & \Gamma_{DF}(1) & \cdots & \Gamma_{DF}(N_{wind}-1) \\ \Gamma_{DF}(-1) & \Gamma_{DF}(0) & \cdots & \Gamma_{DF}(N_{wind}-2) \\ \vdots & \vdots & \ddots & \vdots \\ \Gamma_{DF}(1-N_{wind}) & \Gamma_{DF}(2-N_{wind}) & \cdots & \Gamma_{DF}(0)\end{bmatrix}, \tag{5.73}$$

by defining

$$\Gamma_{DF}(\kappa) \triangleq \begin{bmatrix}\varphi_{sd}^t[\kappa] & 0 & \cdots & 0 \\ 0 & \varphi_{r_1d}^t[\kappa] & \cdots & 0 \\ \vdots & \vdots & \ddots & \vdots \\ 0 & 0 & \cdots & \varphi_{r_{U-1}d}^t[\kappa]\end{bmatrix}\mathbf{P}^2, \tag{5.74}$$

$$= \begin{bmatrix}P_s\varphi_{sd}^t[\kappa] & 0 & \cdots & 0 \\ 0 & P_{r_1}\varphi_{r_1d}^t[\kappa] & \cdots & 0 \\ \vdots & \vdots & \ddots & \vdots \\ 0 & 0 & \cdots & P_{r_{U-1}}\varphi_{r_{U-1}d}^t[\kappa]\end{bmatrix}, \tag{5.75}$$

where $\mathbf{P}$ is the transmit power allocation matrix given by Eq.(5.32), while $\varphi_{sd}^t[\kappa]$ and $\varphi_{r_ud}^t[\kappa]$ respectively represent the channel's autocorrelation function for the direct link and relay-destination link between the uth relay node and the destination BS. Under the assumption of Rayleigh fading

channels, the channel's autocorrelation function can be expressed as:

$$\varphi^t[\kappa] \triangleq \mathcal{E}\{h[n+\kappa]h^*[n]\} \tag{5.76}$$

$$= J_0(2\pi f_d \kappa), \tag{5.77}$$

with $J_0(\cdot)$ denoting the zeroth-order Bessel function of the first kind and as usual f_d representing the normalized Doppler frequency. Furthermore, under the assumption of an identical noise variance observed at each terminal, $\mathcal{E}\{\underline{\tilde{\mathbf{W}}}\underline{\tilde{\mathbf{W}}}^H\}$ of the DDF-aided system can be expressed with the aid of the equivalent noise matrix given by Eq.(5.55) as:

$$\mathcal{E}\{\underline{\tilde{\mathbf{W}}}\underline{\tilde{\mathbf{W}}}^H\} = N_0 N \mathbf{I}_{UN_{wind}}, \tag{5.78}$$

where N and N_0 respectively denote the number of receive antennas employed at the BS and the Gaussian noise variance, while $I_{UN_{wind}}$ is a $(UN_{wind} \times UN_{wind})$-element identity matrix.

On the other hand, when considering the DAF-aided user-cooperation assisted system having an equivalent channel matrix $\tilde{\mathbf{H}}_n$ given by Eq.(5.59) and a noise matrix given by Eq.(5.61), the channel's autocorrelation matrix $\mathcal{E}\{\underline{\tilde{\mathbf{H}}}\underline{\tilde{\mathbf{H}}}^H\}$ can be expressed as:

$$\mathcal{E}\{\underline{\tilde{\mathbf{H}}}\underline{\tilde{\mathbf{H}}}^H\} = \mathcal{E}\left\{\begin{bmatrix}\tilde{\mathbf{H}}_n \\ \vdots \\ \tilde{\mathbf{H}}_{n+N_{wind}-1}\end{bmatrix}\begin{bmatrix}\tilde{\mathbf{H}}_n^* & \cdots & \tilde{\mathbf{H}}_{n+N_{wind}-1}^*\end{bmatrix}\right\}, \tag{5.79}$$

$$= N\begin{bmatrix}\Gamma_{AF}(0) & \Gamma_{AF}(1) & \cdots & \Gamma_{AF}(N_{wind}-1) \\ \Gamma_{AF}(-1) & \Gamma_{AF}(0) & \cdots & \Gamma_{AF}(N_{wind}-2) \\ \vdots & \vdots & \ddots & \vdots \\ \Gamma_{AF}(1-N_{wind}) & \Gamma_{AF}(2-N_{wind}) & \cdots & \Gamma_{AF}(0)\end{bmatrix}, \tag{5.80}$$

where

$$\Gamma_{AF}(\kappa) \triangleq \begin{bmatrix}\varphi_{sd}^t[\kappa] & 0 & \cdots & 0 \\ 0 & \varphi_{sr_1}^t[\kappa]\varphi_{r_1d}^t[\kappa] & \cdots & 0 \\ \vdots & \vdots & \ddots & \vdots \\ 0 & 0 & \cdots & \varphi_{sr_{U-1}}^t[\kappa]\varphi_{r_{U-1}d}^t[\kappa]\end{bmatrix}\mathbf{P}^2\mathbf{F}_{AM}^2 \tag{5.81}$$

$$= \begin{bmatrix}P_s\varphi_{sd}^t[\kappa] & 0 & \cdots & 0 \\ 0 & \frac{P_{r_1}\varphi_{sr_1}^t[\kappa]\varphi_{r_1d}^t[\kappa]}{\sigma_{sr_1}^2+\frac{N_0}{P_s}} & \cdots & 0 \\ \vdots & \vdots & \ddots & \vdots \\ 0 & 0 & \cdots & \frac{P_{r_{U-1}}\varphi_{sr_{U-1}}^t[\kappa]\varphi_{r_{U-1}d}^t[\kappa]}{\sigma_{sr_{U-1}}^2+\frac{N_0}{P_s}}\end{bmatrix} \tag{5.82}$$

with the diagonal matrix $\mathbf{F}_{AM}$ is defined as:

$$\mathbf{F}_{AM} = \begin{bmatrix}1 & 0 & \cdots & 0 \\ 0 & f_{AM_{r_1}} & \cdots & 0 \\ \vdots & \vdots & \ddots & \vdots \\ 0 & 0 & \cdots & f_{AM_{r_{U-1}}}\end{bmatrix}, \tag{5.83}$$

which contains all the signal gain factors $f_{AM_{r_u}}(u = 1, 2, \cdots, N_{wind}-1)$ of Eq.(5.38) employed by the $(U-1)$ relay nodes, respectively, in the U-user cooperation aided communication system

of Figure 5.10. Moreover, with the aid of the equivalent noise matrix given by Eq.(5.61) for the DAF-aided system, we can express $\mathcal{E}\{\underline{\tilde{\mathbf{W}}\tilde{\mathbf{W}}}^H\}$ as:

$$\mathcal{E}\{\underline{\tilde{\mathbf{W}}\tilde{\mathbf{W}}}^H\} = N\mathbf{I}_{N_{wind}} \otimes \begin{bmatrix} N_0 & 0 & \cdots & 0 \\ 0 & (\frac{P_{r_1}\sigma^2_{r_1 d}}{P_s\sigma^2_{sr_1}+N_0}+1)N_0 & \cdots & 0 \\ \vdots & \vdots & \ddots & \vdots \\ 0 & 0 & \cdots & (\frac{P_{r_{U-1}}\sigma^2_{r_{U-1}d}}{P_s\sigma^2_{sr_{U-1}}+N_0}+1)N_0 \end{bmatrix}, \quad (5.84)$$

where N represents the number of receive antennas employed at the BS, while $\mathbf{I}_{N_{wind}}$ denotes a $(N_{wind} \times N_{wind})$-element identity matrix. Note that $\otimes$ denotes the Kronecker product. Hence, the noise autocorrelation matrices $\mathcal{E}\{\underline{\tilde{\mathbf{W}}\tilde{\mathbf{W}}}^H\}$, which were given by Eqs. (5.78) and (5.84) for the DDF-aided and DAF-aided systems, respectively, are diagonal due to the temporally and spatially uncorrelated nature of the AWGN.

Although the basic idea behind the ML detector is that of maximizing the *aposteriori* probability of the received signal block matrix $\underline{\mathbf{Y}}$, this problem can be readily shown to be equivalent to maximizing the *a priori* probability of Eq.(5.69) with the aid of Bayes' theorem [3]. Thus, based on the ML detection rule, an exaustive search has to be carried out over the entire transmitted signal vector space in order to find the specific solution, which maximizes the *a priori* probability of Eq.(5.69). Thus, the ML metric of the multi-path MSDD can be expressed as:

$$\underline{\hat{\mathbf{S}}}_{ML} = \arg \max_{\underline{\tilde{\mathbf{S}}}_d \to \tilde{\mathbf{s}} \in \mathcal{M}_c^{N_{wind}}} Pr(\underline{\mathbf{Y}}|\underline{\tilde{\mathbf{S}}}_d), \quad (5.85)$$

$$= \arg \min_{\underline{\tilde{\mathbf{S}}}_d \to \tilde{\mathbf{s}} \in \mathcal{M}_c^{N_{wind}}} Tr\{\underline{\mathbf{Y}}^H \underline{\Psi}^{-1} \underline{\mathbf{Y}}\}, \quad (5.86)$$

where $\mathbf{s}$ is a column vector hosting all the diagonal elements of the diagonal matrix $\underline{\tilde{\mathbf{S}}}_d$. Note that although $\mathbf{s}$ has UN_{wind} elements, each of which is chosen from an identical constellation set of $\mathcal{M}_c$, we have $\mathbf{s} \in \mathcal{M}_c^{N_{wind}}$ instead of $\mathbf{s} \in \mathcal{M}_c^{UN_{wind}}$, since all the U diagonal elements of our derived equivalent U-user-cooperation transmitted signal $\tilde{\mathbf{S}}_n$ of Eq. (5.51) or Eq. (5.58) have the same symbol value as that of of the nth signal transmitted from the source in the broadcast phase-I. More specifically, $\tilde{\mathbf{s}}$ may be expressed as:

$$\tilde{\mathbf{s}} = [\underbrace{\tilde{s}_1\ \tilde{s}_2\ \cdots\ \tilde{s}_U}_{\tilde{\mathbf{s}}_1}\ \cdots\ \underbrace{\tilde{s}_{(n-1)U+1}\ \cdots\ \tilde{s}_{nU}}_{\tilde{\mathbf{s}}_n}\ \cdots\ \underbrace{\tilde{s}_{N_{wind}U+1}\ \cdots\ \tilde{s}_{N_{wind}U}}_{\tilde{\mathbf{s}}_{N_{wind}}}]^T, \quad (5.87)$$

where the sub-vector $\tilde{\mathbf{s}}_n$ is a column vector containing all the diagonal elements of the matrix $\tilde{\mathbf{S}}_n$.

5.3.3.2 Transformation of the ML Metric

Again, in a user-cooperation aided system, the noise contributions imposed at the relay and destination nodes are both temporally and spatially uncorrelated, thus we have diagonal noise autocorrelation matrices for both the DDF-aided and DAF-aided systems, as observed in Eq.(5.78) and Eq.(5.84), respectively. Additionally, the equivalent transmitted signal matrix $\underline{\tilde{\mathbf{S}}}_d$ of the user-cooperation aided system as constructed in either Eq.(5.51) or Eq.(5.58) for the above-mentioned two systems is a unitary matrix, hence we have:

$$\underline{\tilde{\mathbf{S}}}_d^{-1} = \underline{\tilde{\mathbf{S}}}_d^H. \quad (5.88)$$

Then, we can further extend Eq.(5.71) as:

$$\underline{\Psi} = \underline{\tilde{\mathbf{S}}_d}\mathcal{E}\{\underline{\tilde{\mathbf{H}}\tilde{\mathbf{H}}}^H\}\underline{\tilde{\mathbf{S}}_d}^H + \mathcal{E}\{\underline{\tilde{\mathbf{W}}\tilde{\mathbf{W}}}^H\}, \tag{5.89}$$

$$= \underline{\tilde{\mathbf{S}}_d}(\mathcal{E}\{\underline{\tilde{\mathbf{H}}\tilde{\mathbf{H}}}^H\} + \mathcal{E}\{\underline{\tilde{\mathbf{W}}\tilde{\mathbf{W}}}^H\})\underline{\tilde{\mathbf{S}}_d}^H, \tag{5.90}$$

$$= \underline{\tilde{\mathbf{S}}_d}\mathbf{C}\underline{\tilde{\mathbf{S}}_d}^H, \tag{5.91}$$

where we have

$$\mathbf{C} \triangleq \mathcal{E}\{\underline{\tilde{\mathbf{H}}\tilde{\mathbf{H}}}^H\} + \mathcal{E}\{\underline{\tilde{\mathbf{W}}\tilde{\mathbf{W}}}^H\}, \tag{5.92}$$

which is defined as the $(UN_{wind} \times UN_{wind})$-element *channel-noise autocorrelation* matrix. Now, the ML metric of Eq. (5.86) generated for the multi-path MSDD can be re-formulated by substituting Eq.(5.91) characterizing Ψ into Eq.(5.86) as:

$$\underline{\hat{\mathbf{S}}_{ML}} = \arg \min_{\underline{\tilde{\mathbf{S}}_d} \to \tilde{\mathbf{s}} \in \mathcal{M}_c^{N_{wind}}} Tr\{\underline{\mathbf{Y}}^H \underline{\Psi}^{-1} \underline{\mathbf{Y}}\}, \tag{5.93}$$

$$= \arg \min_{\underline{\tilde{\mathbf{S}}_d} \to \tilde{\mathbf{s}} \in \mathcal{M}_c^{N_{wind}}} Tr\{\underline{\mathbf{Y}}^H (\underline{\tilde{\mathbf{S}}_d}\mathbf{C}\underline{\tilde{\mathbf{S}}_d}^H)^{-1} \underline{\mathbf{Y}}\}. \tag{5.94}$$

Furthermore, since the $\underline{\tilde{\mathbf{S}}_d}$ is unitary, we arrive at:

$$\underline{\hat{\mathbf{S}}_{ML}} = \arg \min_{\underline{\tilde{\mathbf{S}}_d} \to \tilde{\mathbf{s}} \in \mathcal{M}_c^{N_{wind}}} Tr\{\underline{\mathbf{Y}}^H \underline{\tilde{\mathbf{S}}_d} \mathbf{C}^{-1} \underline{\tilde{\mathbf{S}}_d}^H \underline{\mathbf{Y}}\}. \tag{5.95}$$

Now we define two matrix transformation operators, namely, $\mathcal{F}_y(\cdot)$ and $\mathcal{F}_s(\cdot)$, for the received signal matrix $\underline{\mathbf{Y}}$ of Eq. (5.54) or Eq. (5.57) and the transmitted signal matrix $\underline{\tilde{\mathbf{S}}_d}$ of Eq. (5.51) or Eq. (5.58), respectively, in the scenario of a differentially modulated U-user cooperative system employing N receive antennas at the BS and jointly differentially detecting N_{wind} received symbols. Specifically, the operator $\mathcal{F}_y(\cdot)$ is defined as follows:

$$\mathcal{F}_y(\underline{\mathbf{Y}}) \triangleq \begin{bmatrix} \overrightarrow{\mathbf{y}}_1 & \mathbf{0} & \cdots & \mathbf{0} \\ \mathbf{0} & \overrightarrow{\mathbf{y}}_2 & \cdots & \mathbf{0} \\ \vdots & \vdots & \ddots & \vdots \\ \mathbf{0} & \mathbf{0} & \cdots & \overrightarrow{\mathbf{y}}_{UN_{wind}} \end{bmatrix}, \tag{5.96}$$

where $\overrightarrow{\mathbf{y}}_i$ is the ith row of the matrix $\underline{\mathbf{Y}}$ and the resultant matrix is a $(UN_{wind} \times UNN_{wind})$-element matrix. On the other hand, the operator $\mathcal{F}_s(\cdot)$, which is applied to the diagonal transmitted signal matrix $\underline{\mathbf{S}_d}$, is defined as:

$$\mathcal{F}_s(\underline{\tilde{\mathbf{S}}_d}) \triangleq \begin{bmatrix} \tilde{s}_1\mathbf{I}_N \\ \tilde{s}_2\mathbf{I}_N \\ \vdots \\ \tilde{s}_{UN_{wind}}\mathbf{I}_N \end{bmatrix}, \tag{5.97}$$

where $\tilde{s}_i$ is the ith element of the column vector $\tilde{\mathbf{s}}$ of Eq. (5.87) hosting all the UN_{wind} diagonal elements of the diagonal matrix $\underline{\tilde{\mathbf{S}}_d}$. Thus, the resultant matrix is of $(UNN_{wind} \times N)$-dimension.

Consequently, we exploit the transformation operators $\mathcal{F}_y(\cdot)$ defined in Eq.(5.96) and $\mathcal{F}_s(\cdot)$ defined in Eq.(5.97), which allow us to further reformulate the ML solution expression of Eq.(5.95)

as:

$$\underline{\hat{\mathbf{S}}_{ML}} = \arg \min_{\underline{\tilde{\mathbf{S}}_d} \to \tilde{\mathbf{s}} \in \mathcal{M}_c^{N_{wind}}} Tr\{\underline{\mathbf{Y}}^H \underline{\tilde{\mathbf{S}}_d} \mathbf{C}^{-1} \underline{\tilde{\mathbf{S}}_d}^H \underline{\mathbf{Y}}\}, \tag{5.98}$$

$$= \arg \min_{\underline{\mathbf{S}_\mathcal{F}} \to \tilde{\mathbf{s}} \in \mathcal{M}_c^{N_{wind}}} Tr\{\underline{\mathbf{S}}_\mathcal{F}^T \underline{\mathbf{Y}}_\mathcal{F}^H \mathbf{C}^{-1} \underline{\mathbf{Y}}_\mathcal{F} \underline{\mathbf{S}}_\mathcal{F}^*\}, \tag{5.99}$$

where we have:

$$\underline{\mathbf{Y}_\mathcal{F}} = \mathcal{F}_y(\underline{\mathbf{Y}}) \tag{5.100}$$

and

$$\underline{\mathbf{S}_\mathcal{F}} = \mathcal{F}_s(\underline{\tilde{\mathbf{S}}_d}) = \begin{bmatrix} \tilde{s}_1 \mathbf{I}_N \\ \tilde{s}_2 \mathbf{I}_N \\ \vdots \\ \tilde{s}_{UN_{wind}} \mathbf{I}_N \end{bmatrix} = \begin{bmatrix} \underline{\mathbf{S}_{\mathcal{F}_1}} \\ \underline{\mathbf{S}_{\mathcal{F}_2}} \\ \vdots \\ \underline{\mathbf{S}_{\mathcal{F}_{N_{wind}}}} \end{bmatrix}, \tag{5.101}$$

where the $(UN \times N)$-dimension matrix $\underline{\mathbf{S}_{\mathcal{F}_i}}$ represents the ith sub-matrix of the block matrix $\underline{\mathbf{S}_\mathcal{F}}$, which may be expressed as:

$$\underline{\mathbf{S}_{\mathcal{F}_i}} = \begin{bmatrix} \tilde{s}_{U(i-1)+1} \mathbf{I}_N \\ \tilde{s}_{U(i-1)+2} \mathbf{I}_N \\ \vdots \\ \tilde{s}_{Ui} \mathbf{I}_N \end{bmatrix}_{UN \times N}, \tag{5.102}$$

where all the non-zero elements having an identical symbol value, whichs corresponds to the ith symbol transmitted from the source during the broadcast phase-I.

5.3.3.3 Channel-Noise Autocorrelation Matrix Triangularization

Let us now generate the $(UN_{wind} \times UN_{wind})$-element upper-triangular matrix $\mathbf{F}$, which satisfies $\mathbf{F}^H \mathbf{F} = \mathbf{C}^{-1}$ with the aid of Cholesky factorization. Then we arrive at:

$$\underline{\hat{\mathbf{S}}_{ML}} = \arg \min_{\underline{\mathbf{S}_\mathcal{F}} \to \tilde{\mathbf{s}} \in \mathcal{M}_c^{N_{wind}}} Tr\{\underline{\mathbf{S}_\mathcal{F}}^T \underline{\mathbf{Y}_\mathcal{F}}^H \mathbf{F}^H \mathbf{F} \underline{\mathbf{Y}_\mathcal{F} \mathbf{S}_\mathcal{F}}^*\}. \tag{5.103}$$

Then, by further defining a $(UN_{wind} \times UNN_{wind})$-element matrix $\mathbf{U}$ as:

$$\mathbf{U} \triangleq (\mathbf{F} \underline{\mathbf{Y}_\mathcal{F}})^*, \tag{5.104}$$

$$= \begin{bmatrix} \mathbf{U}_{1,1} & \mathbf{U}_{1,2} & \cdots & \mathbf{U}_{1,N_{wind}} \\ \mathbf{0} & \mathbf{U}_{2,2} & \cdots & \mathbf{U}_{2,N_{wind}} \\ \vdots & \vdots & \ddots & \vdots \\ \mathbf{0} & \mathbf{0} & \cdots & \mathbf{U}_{N_{wind},N_{wind}} \end{bmatrix}, \tag{5.105}$$

where we have

$$\mathbf{U}_{i,j} \triangleq \begin{bmatrix} u_{U(i-1)+1,UN(j-1)+1} & u_{U(i-1)+1,UN(j-1)+2} & \cdots & u_{U(i-1)+1,UNj} \\ u_{U(i-1)+2,UN(j-1)+1} & u_{U(i-1)+2,UN(j-1)+2} & \cdots & u_{U(i-1)+2,UNj} \\ \vdots & \vdots & \ddots & \vdots \\ u_{Ui,UN(j-1)+1} & u_{Ui,UN(j-1)+2} & \cdots & u_{Ui,UNj} \end{bmatrix}_{U \times UN}, \tag{5.106}$$

we finally arrive at:

$$\underline{\hat{\mathbf{S}}_{ML}} = \arg \min_{\underline{\mathbf{S}_{\mathcal{F}}} \to \tilde{\mathbf{s}} \in \mathcal{M}_c^{N_{wind}}} ||\mathbf{U}\underline{\mathbf{S}_{\mathcal{F}}}||^2, \tag{5.107}$$

which completes the process of transforming the multi-path ML-MSDD metric of Eq.(5.86) to a *shortest-vector* problem.

5.3.3.4 Multi-Dimensional Tree Search Aided MSDSD Algorithm

Although the problem of finding an optimum solution for the ML-MSDD has been transformed into the so-called *shortest-vector* problem of Eq.(5.107), the multi-path ML-MSDD designed for user-cooperation aided systems may impose a potentially excessive computational complexity, when aiming for finding the solution, which minimizes Eq.(5.107), especially, when a high-order differential modulation scheme and/or a high observation window size N_{wind} is employed. Fortunately, in the light of the SD algorithms discussed in Chapter 2, the computational complexity imposed may be significantly reduced by carrying out a tree search within a reduced-size hypersphere confined by either the search radius C for the depth-first SD or the maximum number of candidates K retained at each search tree level for the breadth-first SD. In our following discourse, we consider the depth-first SD algorithm as an example and demonstrate how to reduce the complexity imposed by the ML-MSSD.

In order to search for the ML solution of Eq.(5.107) in a confined hypersphere, an initial search radius C is introduced. Thus, we obtain the metric relevant for the multi-path Multiple-Symbol Differential Sphere Detection (MSDSD) scheme as:

$$\underline{\hat{\mathbf{S}}_{ML}} = \arg \min_{\underline{\mathbf{S}_{\mathcal{F}}} \to \tilde{\mathbf{s}} \in \mathcal{M}_c^{N_{wind}}} ||\mathbf{U}\tilde{\mathbf{s}}||^2 \leq C^2, \tag{5.108}$$

$$= \arg \min_{\underline{\mathbf{S}_{\mathcal{F}}} \to \tilde{\mathbf{s}} \in \mathcal{M}_c^{N_{wind}}} \left|\left| \begin{bmatrix} \mathbf{U}_{1,1} & \mathbf{U}_{1,2} & \cdots & \mathbf{U}_{1,N_{wind}} \\ \mathbf{0} & \mathbf{U}_{2,2} & \cdots & \mathbf{U}_{2,N_{wind}} \\ \vdots & \vdots & \ddots & \vdots \\ \mathbf{0} & \mathbf{0} & \cdots & \mathbf{U}_{N_{wind},N_{wind}} \end{bmatrix} \begin{bmatrix} \underline{\mathbf{S}_{\mathcal{F}_1}} \\ \underline{\mathbf{S}_{\mathcal{F}_2}} \\ \vdots \\ \underline{\mathbf{S}_{\mathcal{F}_{N_{wind}}}} \end{bmatrix} \right|\right|^2 \leq C^2, \tag{5.109}$$

$$= \arg \min_{\underline{\mathbf{S}_{\mathcal{F}}} \to \tilde{\mathbf{s}} \in \mathcal{M}_c^{N_{wind}}} \left|\left| \sum_{n=1}^{N_{wind}} \left(\sum_{m=n}^{N_{wind}} \mathbf{U}_{n,m} \underline{\mathbf{S}_{\mathcal{F}_m}} \right) \right|\right|^2 \leq C^2. \tag{5.110}$$

Since the tree search is carried out commencing from $n = N_{wind}$ to $n = 1$, the accumulated PED between the candidate $\underline{\mathbf{S}_{\mathcal{F}}}$ and the origin can be expressed:

$$\mathcal{D}_n = \underbrace{\left|\left| \mathbf{U}_{n,n} \underline{\mathbf{S}_{\mathcal{F}_n}} + \sum_{m=n+1}^{N_{wind}} \mathbf{U}_{n,m} \underline{\mathbf{S}_{\mathcal{F}_m}} \right|\right|^2}_{\delta_n} + \underbrace{\left|\left| \sum_{l=n+1}^{N_{wind}} \left(\sum_{m=l}^{N_{wind}} \mathbf{U}_{l,m} \underline{\mathbf{S}_{\mathcal{F}_m}} \right) \right|\right|^2}_{\mathcal{D}_{n+1}} \leq C^2. \tag{5.111}$$

Furthermore, due to the employment of a differential modulation scheme, the information is encoded as the phase difference between the consecutively transmitted symbols. Hence, in the light of the multi-layer tree search proposed for the SD in Section 4.3.2.3, the MSDSD scheme can start the search from $n = (N_{wind} - 1)$ by choosing a trial sub-matrix for $\underline{\mathbf{S}_{\mathcal{F}_{N_{wind}-1}}}$ satisfying

$$\mathcal{D}_{N_{wind}-1} \leq C^2 \tag{5.112}$$

from the legitimate candidate pool, after simply assuming that the N_{wind}th symbol transmitted by the source is $s_s = 1$, namely, according to Eq. (5.102) we have:

$$\underline{\mathbf{S}}_{\mathcal{F}_{N_{wind}}} = \underbrace{[\mathbf{I}_N\ \mathbf{I}_N\ \cdots\ \mathbf{I}_N]^T}_{U \text{ identity sub-matrices}} . \tag{5.113}$$

Given the trial sub-matrix $\underline{\mathbf{S}}_{\mathcal{F}_{N_{wind}-1}}$ satisfying Eq.(5.112), the search continues and a candidate matrix is selected for $\underline{\mathbf{S}}_{\mathcal{F}_{N_{wind}-2}}$ based on the criterion that the value of the resultant PED computed using Eq.(5.111) does not exceed the squared radius, namely:

$$\mathcal{D}_{N_{wind}-2} \leq C^2. \tag{5.114}$$

This recursive process will continue, until n reaches 1, namely when we choose a trial value for $\tilde{\mathbf{s}}_1$ within the computed range. Then the search radius C is updated by calculating the Euclidean distance between the newly obtained signal point $\underline{\mathbf{S}}_{\mathcal{F}}$ and the origin and a new search is carried out within a reduced compound confined by the newly obtained search radius. The search then proceeds in the same way, until no more legitimate signal points can be found in the increasingly reduced search area. Consequently, the last legitimate signal point $\underline{\mathbf{S}}_{\mathcal{F}}$ found this way is regarded as the ML solution of Eq.(5.107). Therefore, in comparison to the multi-path ML-MSDD algorithm of Eq.(5.107), the MSDSD algorithm may achieve a significant computational complexity reduction, as its single-path counterpart does, as observed in Section 5.2. For more details on the principle of SD algorithm please refer to Chapter 2 and on the idea of multi-layer tree search please refer to Chapter 4.

5.3.4 Simulation Results

5.3.4.1 Performance of the MSDSD-Aided DAF-User-Cooperation System

System Parameters	Choice
System	Two-User Cooperative OFDM
Number of Relay Nodes	1
Subcarrier BW	$\triangle f = 10$ kHz
Number of Sub-Carriers	$D = 1024$
Modulation	T-DPSK
Frame Length L_f	101
CRC	CCITT-6
Normalised Doppler Frequency	If it is not specified, $f_{d,sd} = f_{d,sr} = f_{d,rd} = f_d$
Channel Model	typical urban, refer to Table 5.1
Channel Variances	$\sigma_{sd}^2 = \sigma_{sr}^2 = \sigma_{rd}^2 = 1$
Power Allocation	$P_s = P_{r_1} = 0.5P = 0.5$
SNR at Relay and Destination	$P_s/N_0 = P_{r_1}/N_0$

Table 5.5: Summary of system parameters used for the T-DPSK modulated two-user cooperation aided OFDM system.

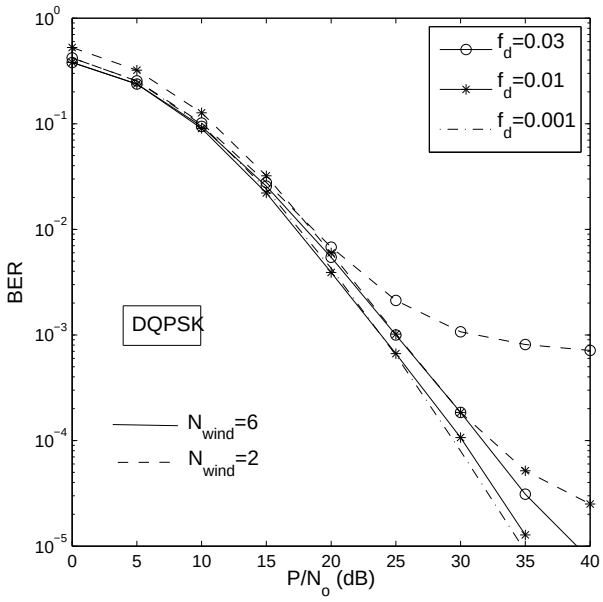

Figure 5.17: BER performance improvement achieved by the MSDSD employing $N_{wind} = 6$ for the DAF-aided T-DQPSK-modulated cooperative system in time-selective Rayleigh fading channels. All other system parameters are summarized in Table 5.5.

As discussed in Section 5.3.2.3, the relative mobility among users imposes a performance degradation on the user-cooperation aided sysem. Thus, the multi-path MSDSD scheme proposed in Section 5.3.3, which relies on the exploitation of the correlation between the phase distortions experienced by the N_{wind} consecutive transmitted DPSK symbols, is employed in order to mitigate the channel-induced error floor encountered by the CDD characterized in Figure 5.17. The system parameters used in our simulations are summarized in Table 5.5.

Figure 5.17 depicts the BER performance improvement achieved by the MSDSD employed at the destination node for the DAF-aided two-user cooperative system in the presence of three different normalized Doppler frequencies, namely $f_d = 0.03$, $f_d = 0.01$ and $f_d = 0.001$. With the aid of the MSDSD employing $N_{wind} = 6$ at the destination node, both the error floors experienced in Rayleigh channels having normalized frequencies of $f_d = 0.03$ and 0.01 are significantly mitigated. Specifically, the BER curve corresponding to the normalized Doppler frequency $f_d = 0.01$ almost coincides with that associated with $f_d = 0.001$, indicating a performance gain of about 10 dB over the system dispensing with the MSDSD. Remarkably, in the scenario of a fast fading channel having $f_d = 0.03$, the BER curve obtained when the CDD is employed at the destination node levels out just below 10^{-3}, as the SNR increases. By contrast, with the aid of the MSDSD the resultant BER curve decreases steadily, suffering a modest performance loss of only about 4 dB at target BER of 10^{-5} in comparison to the curve associated with $f_d = 0.001$. Hence, the more time-selective the channel, the more significant the performance improvement achieved by the proposed MSDSD scheme.

For the sake of further reducing the detrimental impact induced by the time-selective channel on the DAF-aided user-cooperation assisted system, an observation window size of $N_{cand} = 11$ is

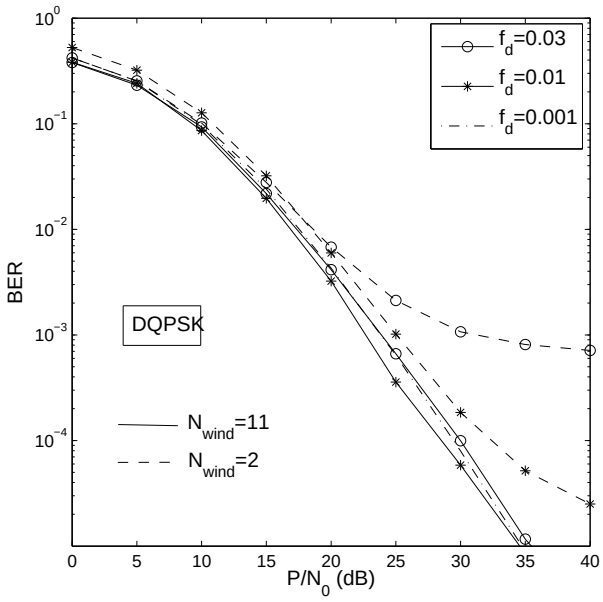

Figure 5.18: BER performance improvement achieved by the MSDSD scheme employing $N_{wind} = 11$ for the DAF-aided T-DQPSK-modulated cooperative system in time-selective Rayleigh fading channels. All other system parameters are summarized in Table 5.5.

employed by the MSDSD arrangement at the destination node at the expense of a higher detection complexity. As seen in Figure 5.18, the MSDSD using $N_{wind} = 11$ is capable of eliminating the error floor encountered by the system employing the CDD, even when the channel is severely time-selective, namely, for $f_d = 0.03$. In other words, the BER curve corresponding to the MSDSD-aided system in Figure 5.18 and obtained for $f_d = 0.03$ coincides with that of its CDD-aided counterpart recorded for $f_d = 0.001$. Furthermore, the MSDSD-aided system with $N_{wind} = 11$ in a fast-fading channel associated with $f_d = 0.01$ is able to outperform the system employing $N_{wind} = 2$, even if the latter is operating in a slow-fading channel having $f_d = 0.001$. Therefore, even in the presence of a severely time-selective channel, the DAF-aided user-cooperation assisted system employing the MSDSD is capable of achieving an attractive performance by jointly differentially detecting a sufficiently high number of consecutively received user-cooperation based joint symbols $\mathbf{S}_n$ $(n = 0, 1, \cdots, N_{wind} - 1)$ of Eq.(5.58) by exploiting the knowledge of the equivalent channel autocorrelation matrix $\mathcal{E}\{\underline{\underline{\tilde{\mathbf{H}}}}\underline{\underline{\tilde{\mathbf{H}}}}^H\}$ of Eq.(5.79), which characterizes the CIR statistics of both the direct and relay links.

	$f_{d,sd}$	$f_{d,sr}$	$f_{d,rd}$
Scenario I (S moves, R&D relatively immobile)	0.03	0.03	0.001
Scenario II (R moves, S&D relatively immobile)	0.001	0.03	0.03
Scenario III (D moves, S&R relatively immobile)	0.03	0.001	0.03

Table 5.6: Normalized Doppler frequency of three different scenarios.

All the previously described simulations were carried out under the assumption that an identical normalized Doppler frequency is exhibited by each link of the user-cooperation system, namely that we have $f_{d,sd} = f_{d,sr} = f_{d,rd} = f_d$. However, a more realistic scenario is the one where the relative

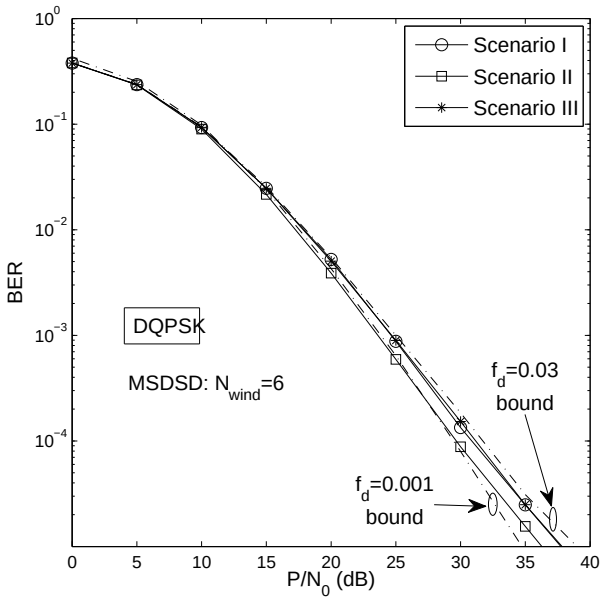

Figure 5.19: The impact of the relative mobility among the source, relay and destination nodes on the BER performance of the DAF-aided T-DQPSK-modulated cooperative system employing MSDSD at the destination node in Rayleigh fading channels. All other system parameters are summarized in Tables 5.5 and 5.6.

speeds of all the cooperative users as well as of the destination terminal are different from each other, leading to a different Doppler frequency for each link. Thus, in order to investigate the impact of different relative speeds among all the nodes on the attainable end-to-end performance of the DAF-aided system, Monte Carlo simulations were carried out for the three different scenarios summarized in Table 5.6. In all the three situations, only one of the three nodes in the two-user cooperation-aided system is supposed to move relative to the other two nodes at a speed resulting in a normalized Doppler frequency of 0.03, while the latter two remain stationary relative to each other, yielding a normalized Doppler frequency of 0.001.

In Figure 5.19 the BER curves corresponding to the three different scenarios of Table 5.6 are bounded by the two dashed-dotted BER curves having no legends, which were obtained by assuming an identical normalized Doppler frequency of $f_d = 0.03$ and $f_d = 0.001$ for each link in the user-cooperation aided system, respectively. This is not unexpected, since the two above-mentioned BER bounds correspond to the least and most desirable time-selective channel conditions considered in this chapter, respectively. The channel quality of the direct link characterized in terms of its grade of time-selectivity predetermines the achievable performance of the DAF-aided user-cooperation assisted system employing the MSDSD. Hence, it is observed in Figure 5.19 that the system is capable of attaining a better BER performance in Scenario II ($f_{d,sd} = 0.001$) than in the other two scenarios ($f_{d,sd} = 0.03$). However, as seen in Figure 5.19, due to the high speed of the relay node observed in Scenario II relative to the source and destination nodes, the MSDSD employing $N_{wind} = 6$ remains unable to completely eliminate the impairments induced by the time-selective channel, unless a higher N_{wind} value is employed. Therefore, a modest performance degradation occurs in comparison to the $f_d = 0.001$ scenario. On the other hand, the MSDSD-

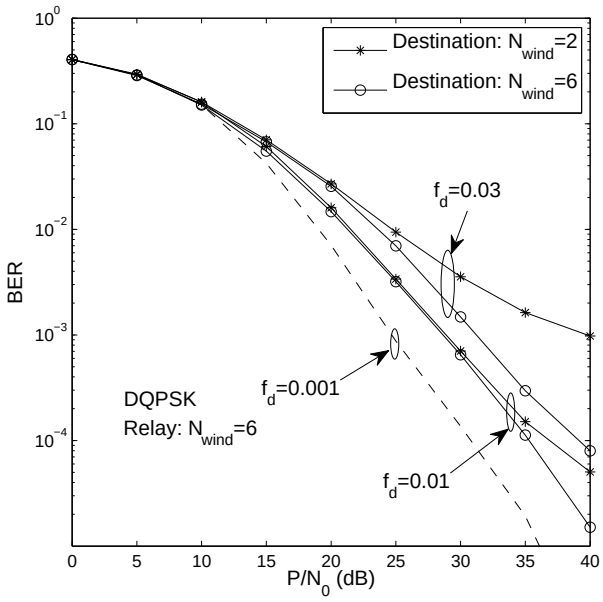

Figure 5.20: BER performance improvement achieved by the multi-path based MSDSD scheme employing $N_{wind} = 6$ at the destination node of the DDF-aided T-DQPSK-modulated cooperative system in Rayleigh fading channels. All other system parameters are summarized in Table 5.5.

aided system exhibits a similar performance in Scenario I and Scenario III, since the source-relay and relay-destination links are symmetric and thus they are exchangable in the context of the DAF scheme, as observed in Eq.(5.81).

5.3.4.2 Performance of the MSDSD-Aided DDF-User-Cooperation System

Despite the fact that the performance degradation experienced by the conventional DDF-aided user-cooperation assisted system employing the CDD in severely time-selective channels can be mitigated by utilizing the single-path MSDSD at the relay node, a significant performance loss remains unavoidable due to the absence of a detection technqiue at the destination node, which is robust to the time-selective channel, as previously seen in Figure 5.15. Fortunately, the multi-path based MSDSD designed for the user-cooperation aided system devised in Section 5.3.3 can be employed at the destination node in order to further mitigate the channel-induced performance degradation of the DDF-aided system.

Figure 5.20 demonstrates a significant performance improvement attained by the multi-path based MSDSD design employing $N_{wind} = 6$ at the destination node of the DDF-aided two-user cooperative system over its counterpart dispensing with MSDSD at the destination at both $f_d = 0.03$ and $f_d = 0.001$ for each links, respectively. The more severely time-selective the channel, the higher the end-to-end performance gain that can be achieved by the MSDSD assisted DDF-aided system. Specifically, for a given target BER of 10^{-3}, a performance gain as high as 9 dB is achieved at $f_d = 0.03$, whereas only negligible performance improvement is attained at $f_d = 0.01$. On the other hand, by comparing the simulation results of Figure 5.17 and Figure 5.20, we observe

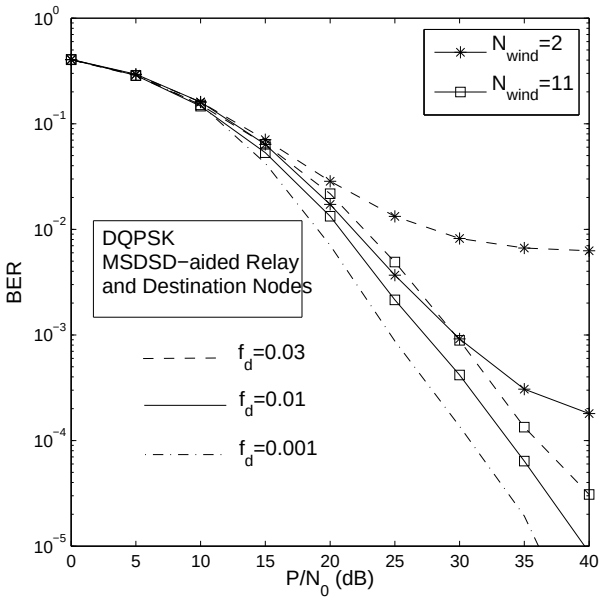

Figure 5.21: BER performance improvement achieved by the multi-path MSDSD employing $N_{wind} = 11$ at the destination node of the DDF-aided T-DQPSK-modulated cooperative system in Rayleigh fading channels. All other system parameters are summarized in Table 5.5.

that the performance gains achieved by the MSDSD employed at the destination node of the DDF-aided system is significantly lower than those recorded for its DAF-aided counterpart. Even though $N_{wind} = 11$ is employed, there is still a conspicuous gap between the BER curves corresponding to high values of f_d and the one obtained at $f_d = 0.001$ in the context of the DDF-aided system, as shown in Figure 5.21. This trend is not unexpected due to the fact that the design of the multi-path MSDSD used in the DDF-aided user-cooperation assisted system is carried out under the assumption of an idealized perfect reception-and-forward process at the relay node, while actually the relay will keep silent when it fails to correctly detect the received signal, as detected by the CRC check. In other words, the MSDSD employed at the destination simply assumes that the relay node, has the knowledge of the signal transmitted by the source node as implied by the system model of Eq.(5.37) describing the DDF-aided system, operating without realizing that sometimes only noise is presented to the receive antenna during the relay phase-II.

In comparison to its DAF-aided counterpart, the end-to-end performance of the DDF-aided system is jointly determined by the robustness of the differential detection technique to time-selective channels at the destination node, as well as by that at the relay node. Previously, we employed the same observation window size N_{wind} for the MSDSDs used at both relay and destination nodes. However, in reality there exists situations where the affordable overall system complexity is limited and hence a low value of N_{wind} has to be used at both the relay and destination nodes. Thus, it is beneficial to characterize the importance of the detection technique employed at the relay and destination nodes for the sake of determining the system's required complexity. Figure 5.22 plots the BER curve of the DDF-aided two-user cooperative system for $N_{wind} = 6$ at the relay node and for $N_{wind} = 2$ at the destination node against that generated by reversing the N_{wind} allocation, namely by having $N_{wind} = 2$ and $N_{wind} = 6$ at the relay and destination nodes, respectively. Observe

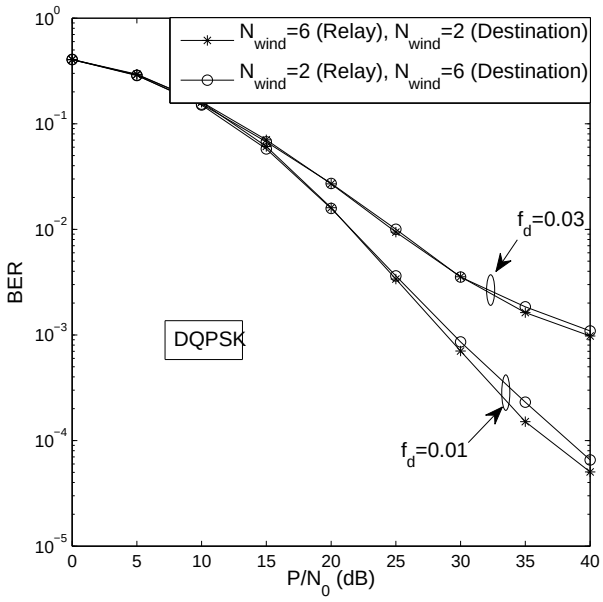

Figure 5.22: BER performance of the DDF-aided T-DQPSK-modulated cooperative system employing MSDSD in conjunction with different detection-complexity allocations in Rayleigh fading channels. All other system parameters are summarized in Table 5.5.

in Figure 5.22 that the system having a more robust differential detector at the relay node slightly outperforms the other in the high SNR range at both $f_d = 0.03$ and $f_d = 0.01$. This is because a less robust detection scheme employed at the relay node may erode the benefits of relaying in the DDF-aided user-cooperation assisted system. Naturally, this degrades the achievable performance of the MSDSD at the destination, which carries out the detection based on the assumption of a reliable relayed signal. Hence, in the context of the DDF-aided user-cooperation assisted system employing the MSDSD, a higher complexity should be invested at the relay node in the interest of achieving an enhanced end-to-end performance.

Let us now investigate the effect of the relative mobility of the source, relay and destination nodes on the achievable BER performance of the DDF-aided two-user cooperation assisted system by considering the BER curves corresponding to the three scenarios of Table 5.6, in Figure 5.23. Based on our previous discussions, we understand that the performances of the detection schemes employed at both the relay and destination nodes are equally important factors in determining the achievable end-to-end system performance, which are mainly affected by the Doppler frequency characteristics of both the source-relay link and the source-destination link in the DDF-aided user-cooperation assisted system. In Scenario I of Table 5.6 the system exhibits the worst BER performance, which is roughly the same as the $f_d = 0.03$ performance bound, since the benefits brought about by a high-quality, near-stationary relay-destination link may be eroded by a low-quality, high-Doppler source-relay link dominating the achievable performance of the MSDSD scheme at the relay node, which in turn substantially degrades the achievable end-to-end system performance. In Scenario II of Table 5.6, we assumed that the source and destination nodes experience a low Doppler frequency in the direct link ($f_{d,sd} = 0.001$), which is one of the two above-mentioned dominant links in the DDF-aided system. Thus, for a given target BER of 10^{-4}, the system achieves

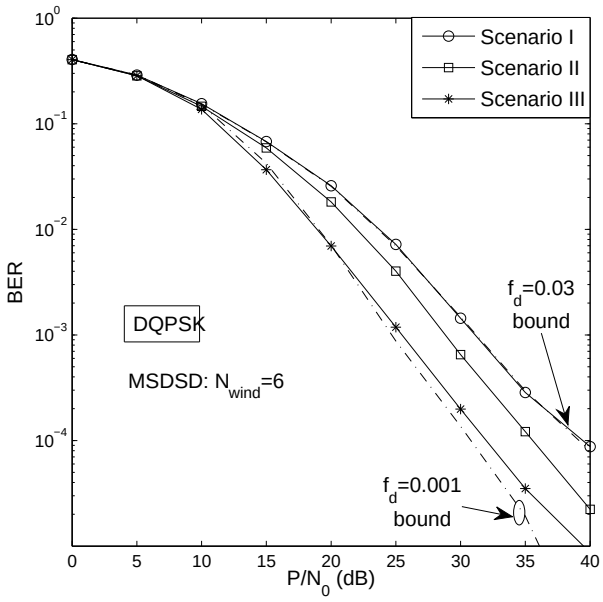

Figure 5.23: The impact of the relative mobility among the source, relay and destination nodes on the BER performance of the DDF-aided T-DQPSK-modulated cooperative system employing MSDSD at both the relay and destination nodes in Rayleigh fading channels. All other system parameters are summarized in Tables 5.5 and 5.6.

a performance gain as high as 5 dB in Scenario II over that attained in the benchmark scenario having an identical Doppler frequency of $f_d = 0.03$ for each link, as observed in Figure 5.23. Moreover, the achievable performance gain can be almost doubled, if the system is operating in Scenario III, where in turn the other important link, namely, the source-relay link, becomes a slow-fading channel associated with $f_d = 0.001$. Remarkably, the performance achieved in Scenario III is comparable to that attained by the same system in the benchmark scenario, where we have $f_d = 0.001$ for each of the three links. More specifically, the system operating in Scenario III only suffers a performance loss of about 1 dB at a target BER of 10^{-4} in comparison to that associated with the slow-fading benchmark scenario.

5.4 Chapter Conclusions

Cooperative diversity, emerging as an attractive diversity-aided technique to circumvent the cost and size constraints of implementing multiple antennas on a pocket-sized mobile device with the aid of antenna-sharing amongst multiple cooperating single-antenna-aided users, is capable of effectively combating the effects of channel fading and hence improving the attainable performance of the network. However, the user-cooperation mechanism may result in a complex system when using coherent detection, where not only the BS but also the cooperating MSs would require channel estimation. Channel estimation would impose both an excessive complexity and a high pilot overhead. This situation may be further aggravated in mobile environments associated with relatively rapidly fluctuating channel conditions. Therefore, the consideration of cooperative system design

without assuming the knowledge of the CSI at transceivers becomes more realistic, which inspires the employment of the differentially encoded modulation at the transmitter and that of non-coherent detection dispensing with both the pilots and channel estimation at the receiver. However, as discussed in Section 5.1.1, the performance of the low-complexity CDD aided direct-transmission based OFDM system may substantially degrade in highly time-selective or frequency-selective channels, depending on the domain in which the differential encoding is carried out. Fortunately, as argued in Section 5.2, the single-path MSDSD, which has been contrived to mitigate the channel-induced error floor encountered by differentially encoded single-input single-output transmission, jointly differentially detects multiple consecutively received signals by exploiting the correlation amongst their phase distortions. Hence, inspired by the proposal of the single-path MSDSD, our main objective in this chapter is to specifically design a multi-path MSDSD, which is applicable to the differentially encoded cooperative systems in order to make the overall system robust to the effects of the hostile wireless channel. To this end, in Section 5.3.3.1 we constructed a generalized equivalent multiple-symbol system model for the cooperative system employing either the DAF or DDF scheme, which facilitated the process of transforming the optimum detection metric to a shortest-vector problem, as detailed in Section 5.3.3.2. Then, it was shown in Section 5.3.3.4 that the resultant shortest-vector problem may be efficiently solved by a multi-layer tree search scheme, which is similar to that proposed in Section 4.3.2.3. This procedure relies on the channel-noise autocorrelation matrix triangularization procedure of Section 5.3.3.3.

Our Monte Carlo simulation results provided in Section 5.3.4.1 have demonstrated that the resultant multi-path MSDSD employed at the BS is capable of completely eliminating the performance loss encountered by the DAF-aided cooperative system, provided that a sufficiently high value of N_{wind} is used. For example, observe in Figure 5.18 that given a target BER of 10^{-3}, a performance gain of about 10 dB can be attained by the proposed MSDSD employing $N_{wind} = 11$ for a DQPSK modulated two-user cooperative system in a relatively fast-fading channel associated with a normalized Doppler frequency of 0.03. In contrast to the DAF-aided cooperative system, it was shown in Figure 5.21 of Secton 5.3.4.2 that although a significant performance improvement can be also achieved by the multi-path MSDSD at the BS in highly time-selective channels for the DDF-aided system, the channel-induced performance loss was not completely eliminated, even when $N_{wind} = 11$ was employed. This was because the MSDSD employed at the BS simply assumed a guaranteed perfect decoding at the relay, operating without taking into account that sometimes only noise is presented to the receive antenna during the relay's phase-II, namely when the relay keeps silent owing to the failure of recovering the source's signal. Furthermore, our investigation of the proposed MSDSD in the practical Rayleigh fading scenario, where a different Doppler frequency is assumed for each link, demonstrated that the channel quality of the direct source-destination link characterized in terms of its grade of time-selectivity predetermines the achievable performance of the DAF-aided cooperative system. By contrast, the source-relay and relay-destination links are symmetric and thus they may be interchanged without affecting the end-to-end performance. By contrast, observe in Figure 5.23 that the achievable performance of the DDF-aided system employing the MSDSD is dominated by the source-relay link. This is not unexpected, since a high-quality, near-stationary source-relay link enhances the performance of the MSDSD at the BS, making its assumption of a perfect decoding at the relay more realistic. Finally, based on the simulation results obtained in this chapter, we quantitatively summarize the performance gains achieved by the

MSDSD for the direct-transmission based non-cooperative system as well as for both the DAF- and DDF-aided cooperative systems in Table 5.7.

Performance of the Single-Relay-Aided Cooperative System						
	f_d	N_{wind}	P/N_0 (dB)		Gain (dB)	
			BER			
			10^{-3}	10^{-4}	10^{-3}	10^{-4}
Non-Cooperative System	$f_{d,sd} = f_{d,sr} = f_{d,rd} = 0.001$	2	30	40	-	-
		6	30	40	0.0	0.0
	$f_{d,sd} = f_{d,sr} = f_{d,rd} = 0.01$	2	40	N/C	-	-
		6	32	N/A	8	N/A
	$f_{d,sd} = f_{d,sr} = f_{d,rd} = 0.03$	2	N/C	N/C	-	-
		6	35	N/A	∞	N/A
DAF Cooperative System	$f_{d,sd} = f_{d,sr} = f_{d,rd} = 0.001$	2	23.5	29	-	-
		6	23.5	29	0.0	0.0
	$f_{d,sd} = f_{d,sr} = f_{d,rd} = 0.01$	2	25	33	-	-
		6	23.5	30	1.5	3
	$f_{d,sd} = f_{d,sr} = f_{d,rd} = 0.03$	2	32.5	N/C	-	-
		6	25	32	7.5	∞
	$f_{d,sd} = f_{d,sr} = 0.03$, $f_{d,rd} = 0.001$	6	24	31	-	-
	$f_{d,sr} = f_{d,rd} = 0.03$, $f_{d,sd} = 0.001$	6	23	30	1	1
	$f_{d,sd} = f_{d,rd} = 0.03$, $f_{d,sr} = 0.001$	6	24	31	0.0	0.0
DDF Cooperative System	$f_{d,sd} = f_{d,sr} = f_{d,rd} = 0.001$	R: 2, D: 2	24.5	31	-	-
		R: 6, D: 2	24.5	31	0.0	0.0
		R: 2, D: 6	24.5	31	0.0	0.0
		R: 6, D: 6	24.5	31	0.0	0.0
	$f_{d,sd} = f_{d,sr} = f_{d,rd} = 0.01$	R: 2, D: 2	30	58	-	-
		R: 6, D: 2	29	37	1	21
		R: 2, D: 6	30	38	0	20
		R: 6, D: 6	29	35.5	1	22.5
	$f_{d,sd} = f_{d,sr} = f_{d,rd} = 0.03$	R: 2, D: 2	N/C	N/C	-	-
		R: 6, D: 2	40	N/C	∞	0
		R: 2, D: 6	41	N/C	∞	0
		R: 6, D: 6	31.3	41	∞	∞
	$f_{d,sd} = f_{d,sr} = 0.03$, $f_{d,rd} = 0.001$	R, D: 6	31	40	-	-
	$f_{d,sr} = f_{d,rd} = 0.03$, $f_{d,sd} = 0.001$	R, D: 6	29	36	2	4
	$f_{d,sd} = f_{d,rd} = 0.03$, $f_{d,sr} = 0.001$	R, D: 6	25.5	32	5.5	8

Table 5.7: Performance summary of the MSDSD investigated in Chapter 5. The system parameters were given by Table 5.5. Note that "N/C" means the target BER is not achievable, regardless of the SNR, while "N/A" means the data is not available.

Chapter 6

Resource Allocation for the Differentially Modulated Cooperation-Aided Cellular Uplink in Fast Rayleigh Fading Channels

6.1 Introduction

6.1.1 Chapter Contributions and Outline

It was observed in Chapter 5 that the differentially modulated user-cooperative uplink systems employing either the DAF scheme of Section 5.3.2.1 or the DDF scheme of Section 5.3.2.2 was capable of achieving cooperative diversity gain, while circumventing the cost and size constraints of implementing multiple antennas in a pocket device. Additionally, by avoiding the challenging task of estimating all the $(N_t \times N_r)$ CIRs of multi-antenna-aided systems, the differentially encoded cooperative system may exhibit a better performance than its coherently detected, but non-cooperative counterpart, since the CIRs cannot be perfectly estimated by the terminals. The CIR estimation becomes even more challenging, when the MS travels at a relatively high speed, resulting in a rapidly fading environment. On the other hand, although it was shown in Chapter 5 that a full spatial diversity can be usually achieved by the differentially modulated user-cooperative uplink system, the achievable end-to-end BER performance may significantly depend on the specific choice of the cooperative protocol employed and/or on the quality of the relay channel. Therefore, in the scenario of differentially modulated cooperative uplink systems, where multiple cooperating MSs are roaming in the area between a specific MS and the BS seen in Figure 6.1, an appropriate Cooperative-Protocol-Selection (CPS) as well as a matching Cooperating-User-Selection (CUS) becomes necessary in order to maintain a desirable end-to-end performance. Motivated by the above-mentioned observations, the novel contributions of this chapter are as follows:

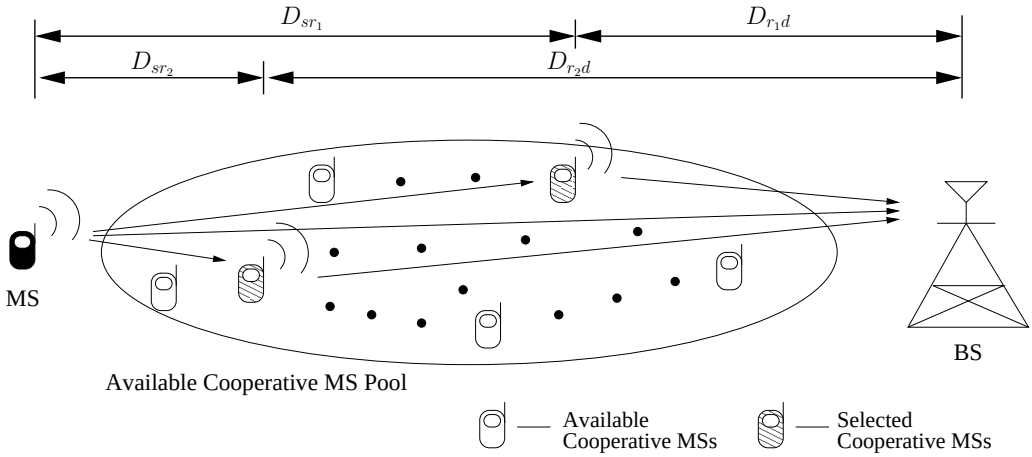

Figure 6.1: Cooperation-aided uplink systems using relay selection.

- *The achievable end-to-end performance is theoretically analyzed for both the DAF- and DDF-aided cooperative systems.*
- *Based on the above-mentioned analytical results, both CUS schemes and Adaptive Power Control (APC) schemes are proposed for above two types of cooperative system in the interest of achieving the best possible performance.*
- *Intensive comparative studies of the most appropriate resource allocation in the context of both DAF- and DDF-assisted cooperative systems are carried out.*
- *In order to make the most of the complementarity of the DAF- and DDF-aided cooperative systems, a more flexible resource-optimized apdative hybrid cooperation-aided system is proposed, yielding a further improved performance.*

The remainder of this chapter is organized as follows. In Section 6.2 we first theoretically analyze the achievable end-to-end performance of both the DAF- and DDF-assisted cooperative systems. Then, based on the BER performance analysis of Section 6.2, in Sections 6.3.1 and 6.3.2 we will propose appropriate CUS schemes for both the above-mentioned two types of cooperative systems, along with an optimized power control arrangement. Additionally, in order to further improve the achievable end-to-end performance of the cooperation-aided UL of Figure 6.1 and to create a flexible cooperative mechanism, in Section 6.4 we will also investigate the CPS of the UL in conjunction with the CUS as well as the power control, leading to a resource-optimized adaptive cooperation-aided system. Finally, our concluding remarks will be provided in Section 6.5.

6.1.2 System Model

To be consistent with the system model employed in Chapter 5, the U-user TDMA uplink is considered for the sake of simplicity. Again, due to the symmetry of channel allocation among users, as indicated in Figure 5.9, we focus our attention on the information transmission of a specific source MS seen in Figure 6.1, which potentially employs M_r out of the $\mathcal{P}_{cand} = (U-1)$ available Relay Station (RS) in order to achieve cooperation-aided diversity by forming a VAA. Without loss of

generality, we simply assume the employment of a single antenna for each terminal. For the sake of simple analytical tractability, we assume that the sum of the distances D_{sr_u} between the source MS and the uth RS, and that between the uth RS and the destination BS, which is represented by $D_{r_u d}$, is equal to the distance D_{sd} between the source MS and the BS. Equivalently, as indicated by Figure 6.1 we have:

$$D_{sr_u} + D_{r_u d} = D_{sd}, \quad u = 1, 2, \cdots, U-1. \tag{6.1}$$

Furthermore, by considering a path-loss exponent of v [2], the average power $\sigma_{i,j}^2$ at the output of the channel can be computed according to the inter-node distance $D_{i,j}$ as follows:

$$\sigma_{i,j}^2 = C \cdot D_{i,j}^{-v}, \quad i, j \in \{s, r_u, d\}, \tag{6.2}$$

where C is a constant, which can be normalized to unity without loss of generality and the subscripts s, r_u and d represent the source, the uth relay and the destination, respectively. Thus, Eq. (6.2) can be expressed as:

$$\sigma_{i,j}^2 = D_{i,j}^{-v}, \quad i, j \in \{s, r_u, d\}. \tag{6.3}$$

Additionally, under the assumption of having a total transmit power of P and assuming that M_r cooperating MSs are activated out of a total of $\mathcal{P}_{cand}$, we can express the associated power contraint as:

$$P = P_s + \sum_{m=1}^{M_r} P_{r_m}, \tag{6.4}$$

where P_s and P_{r_m} $(m = 1, 2, \cdots, M_r)$ are the transmit power employed by the source MS and the mth RS, respectively.

6.2 Performance Analysis of the Cooperation-Aided Uplink

In this section, we commence analyzing the error probability performance of both the DAF-aided and DDF-aided systems, where the MSDSD devised in Chapter 5 is employed in order to combat the effects of fast fadings caused by the relative mobility of the MSs and BS in the cell. Recall from Chapter 5 that the Doppler-frequency-induced error floor encountered by the CDD (or equivalently by the MSDSD using $N_{wind} = 2$) is expected to be significantly eliminated by jointly detecting $N_{wind} > 2$ number of consecutive received symbols with the aid of the MSDSD, provided that N_{wind} is sufficiently high. Therefore, under the assumption that the associated performance degradation can be mitigated by the MSDSD in both the DAF-aided and DDF-aided cooperative system, it is reasonable to expect that the BER performance exhibited by the cooperation-assisted system employing the MSDSD in a relatively rapidly fading environment can be closely approximated by that achieved by the CDD in slow fading channels. Hence, in the ensuing two sections our performance analysis is carried out without considering the detrimental effects imposed by the mobility of the MSs, since these effects are expected to be mitigated by the employment of the MSDSD of Section 5.3. Consequently, our task may be interpreted as the performance analysis of a CDD-assisted differentially modulated cooperative system operating in slow-fading channels.

6.2.1 Theoretical Analysis of Differential Amplify-and-Forward Systems

6.2.1.1 Performance Analysis

First of all, without loss of accuracy, we drop the time index n and rewrite the signal of Eq. (5.35) received at the mth cooperating MS and that of Eq. (5.39) from the mth RS at the BS as follows:

$$y_{sr_m} = \sqrt{P_s} s_s h_{sr_m} + w_{sr_m}, \tag{6.5}$$

$$y_{r_m d} = f_{AM_{r_m}} y_{sr_m} h_{r_m d} + w_{r_m d}, \tag{6.6}$$

where the amplification factor $f_{AM_{r_m}}$ employed by the mth relay node can be specified as [128]:

$$f_{AM_{r_m}} = \sqrt{\frac{P_{r_m}}{P_s \sigma^2_{sr_m} + N_0}}, \tag{6.7}$$

with N_0 being the variance of the AWGN imposed at all cooperating MSs as well as at the BS. Then, we can further reformat Eq. (6.6) with the aid of Eq. (6.5) in order to express the signal received at the destination BS from the RS as:

$$y_{r_m d} = f_{AM_{r_m}} h_{r_m d} (\sqrt{P_s} h_{sr_m s_s} + w_{sr_m}) + w_{r_m d}, \tag{6.8}$$

$$= f_{AM_{r_m}} \sqrt{P_s} h_{r_m d} h_{sr_m} s_s + f_{AM_{r_m}} h_{r_m d} w_{sr_m} + w_{r_m d}. \tag{6.9}$$

Hence, we can calculate the received signal-to-noise ratio (SNR) per symbol at the BS for both the direct and the relaying links, respectively, as:

$$\gamma^s_{sd} = \frac{P_s |h_{sd}|^2}{N_0}, \tag{6.10}$$

$$\gamma^s_{r_m d} = \frac{P_s P_{r_m} |h_{sr_m}|^2 |h_{r_m d}|^2}{N_0 (P_s \sigma^2_{sr_m} + P_{r_m} |h_{r_m d}|^2 + N_0)}. \tag{6.11}$$

Furthermore, MRC is assumed to be employed at the BS prior to the CDD scheme for the system using the DAF arrangement characterized in Eq. (5.40) of Section 5.3.2.1, which is rewritten here for convenience as:

$$y = a_0 (y_{sd}[n-1])^* y_{sd}[n] + \sum_{m=1}^{M_r} a_m (y_{r_m d}[n + mL_f - 1])^* y_{r_m d}[n + mL_f], \tag{6.12}$$

where L_f is the length of the transmission packet, while the coefficients a_0 and $a_m, (m = 1, 2, \cdots, M_r)$ are given by:

$$a_0 = \frac{1}{N_0}, \tag{6.13}$$

$$a_m = \frac{P_s \sigma^2_{sr_m} + N_0}{N_0 (P_s \sigma^2_{sr_m} + P_{r_m} |h_{r_m d}|^2 + N_0)}. \tag{6.14}$$

According to the basic property of the MRC scheme, the SNR at the MRC's output can be expressed as:

$$\gamma^s = \gamma^s_{sd} + \sum_{m=1}^{M_r} \gamma^s_{r_m d}. \tag{6.15}$$

Equivalently, we can express the SNR per bit at the output of the MRC as:

$$\begin{aligned}\gamma^b &= \frac{\gamma^s_{sd}}{\log_2 M_c} + \sum_{m=1}^{M_r} \frac{\gamma^s_{r_m d}}{\log_2 M_c}, \\ &= \gamma^b_{sd} + \sum_{m=1}^{M_r} \gamma^b_{r_m d},\end{aligned} \tag{6.16}$$

where M_c is the constellation size of a specific modulation scheme.

On the other hand, the end-to-end BER expression conditioned on the SNR per bit at the combiner's output, namely γ^b of Eq. (6.16) for the DAF-aided system activating M_r RSs for a specific source MS can be expressed as [130]:

$$P^{DAF}_{BER|\gamma^b}(a,b,M_r) = \frac{1}{2^{2(M_r+1)}\pi} \int_{-\pi}^{\pi} f(a,b,M_r+1,\theta) e^{-\alpha(\theta)\gamma^b} d\theta, \tag{6.17}$$

where we have [130]:

$$\begin{aligned}f(a,b,L,\theta) = \frac{b^2}{2\alpha(\theta)} \sum_{l=1}^{L} \binom{2L-1}{L-l} [(\beta^{-l+1} - \beta^{l+1}) \cos((l-1)(\phi+\pi/2)) \\ - (\beta^{-l+2} - \beta^{l}) \cos(l(\phi+\pi/2))],\end{aligned} \tag{6.18}$$

$$\alpha(\theta) = \frac{b^2(1+2\beta\sin\theta+\beta^2)}{2}, \tag{6.19}$$

and

$$\beta = a/b. \tag{6.20}$$

In Eq. (6.17) the parameters a and b are the modulation-dependent factors defined in [6]. Specifically, $a = 10^{-3}$ and $b = \sqrt{2}$ for DBPSK modulation, while $a = \sqrt{2-\sqrt{2}}$ and $b = \sqrt{2+\sqrt{2}}$ for DQPSK modulation using Gray coding. Additionally, the parameter β, which is defined as Eq. (6.20), can be calculated according to the specific modulation scheme employed [6]. Moreover, the parameter L of Eq. (6.18) denotes the number of diversiy paths. For example, when M_r cooperating MSs are activated, we have $L = M_r + 1$, assuming that the BS combines the signals received from all the M_r RSs as well as that from the direct link.

On the other hand, since a non-dispersive Rayleigh fading channel is considered here, the PDF of the channel's fading amplitude r can be expressed as [2]:

$$p_r(r) = \begin{cases} \frac{2r}{\Omega}\exp(\frac{-r^2}{\Omega}), & 0 \le r \le \infty \\ 0, & r < 0, \end{cases} \tag{6.21}$$

where $\Omega = \overline{r^2}$ represents the mean square value of the fading amplitude. Hence, the PDF of the instantaneous received SNR per bit at the output of the Rayleigh fading channel is given by the so-called Γ distribution [2]:

$$p_{\gamma^b}(\gamma) = \begin{cases} \frac{1}{\gamma^b}\exp(-\frac{\gamma}{\gamma^b}), & \gamma \ge 0 \\ 0, & \gamma < 0 \end{cases}, \tag{6.22}$$

where $\overline{\gamma^b}$ denotes the average received SNR per bit, which can be expressed as:

$$\overline{\gamma^b} = \frac{P_{t,bit} \cdot \Omega}{N_0}, \tag{6.23}$$

$$= \frac{P_{t,symbol} \cdot \Omega}{N_0 \cdot \log_2 \mathcal{M}_c}, \tag{6.24}$$

with $P_{t,bit}$ and $P_{t,symbol}$ representing the transmit power per bit and per symbol, respectively.

Now, the unconditional end-to-end BER of the DAF-aided cooperative system can be calculated by averaging the conditional BER expression of Eq. (6.17) over the entire range of received SNR per bit values by weighting it according to its probability of occurrence represented with the aid of its PDF in Eq. (6.22) as follows [130, 131]:

$$P_{BER}^{DAF}(a,b,M_r) = \int_{-\infty}^{+\infty} P_{BER|\gamma^b}^{DAF} \cdot p_{\gamma^b}(\gamma) d\gamma, \tag{6.25}$$

$$= \frac{1}{2^{2(M_r+1)}\pi} \int_{-\pi}^{\pi} f(a,b,M_r+1,\theta) \int_{-\infty}^{+\infty} e^{-\alpha(\theta)\gamma} p_{\gamma^b}(\gamma) d\gamma d\theta, \tag{6.26}$$

$$= \frac{1}{2^{2(M_r+1)}\pi} \int_{-\pi}^{\pi} f(a,b,M_r+1,\theta) \mathcal{M}_{\gamma^b}(\theta) d\theta, \tag{6.27}$$

where the Joint Moment Generating Function (MGF) [131] of the received SNR per bit γ^b given by Eq. (6.16) is defined as:

$$\mathcal{M}_{\gamma^b}(\theta) = \int_{-\infty}^{+\infty} e^{-\alpha(\theta)\gamma} p_{\gamma^b}(\gamma) d\gamma, \tag{6.28}$$

$$= \underbrace{\int_{-\infty}^{+\infty} \cdots \int_{-\infty}^{+\infty}}_{(M_r+1)-fold} e^{-\alpha(\theta)(\gamma_{sd}+\sum_{m=1}^{M_r}\gamma_{r_m d})} p_{\gamma_{sd}^b}(\gamma_{sd}) \prod_{m=1}^{M_r} p_{\gamma_{r_m d}^b}(\gamma_{r_m d}) d\gamma_{sd} d\gamma_{r_1 d} \cdots d\gamma_{r_{M_r} d}, \tag{6.29}$$

$$= \mathcal{M}_{\gamma_{sd}^b}(\theta) \prod_{m=1}^{M_r} \mathcal{M}_{\gamma_{r_m d}^b}(\theta), \tag{6.30}$$

with $\mathcal{M}_{\gamma_{sd}^b}(\theta)$ and $\mathcal{M}_{\gamma_{r_m d}^b}(\theta)$ representing the MGF of the received SNR per bit γ_{sd}^b of the direct link and that of the received SNR per bit $\gamma_{r_m d}^b$ of the mth relay link. Specifically, with the aid of Eq. (6.22) we have [128, 131]:

$$\mathcal{M}_{\gamma_{sd}^b}(\theta) = \frac{1}{1+k_{sd}(\theta)}, \tag{6.31}$$

$$\mathcal{M}_{\gamma_{r_m d}^b}(\theta) = \frac{1}{1+k_{sr_m}(\theta)} \left(1 + \frac{k_{sr_m}(\theta)}{1+k_{sr_m}(\theta)} \frac{P_s \sigma_{sr_m}^2 + N_0}{P_{r_m}} \frac{1}{\sigma_{r_m d}^2} Z_{r_m}(\theta)\right), \tag{6.32}$$

where

$$k_{sd}(\theta) \triangleq \frac{\alpha(\theta) P_s \sigma_{sd}^2}{N_0}, \tag{6.33}$$

$$k_{sr_m}(\theta) \triangleq \frac{\alpha(\theta) P_s \sigma_{sr_m}^2}{N_0}, \tag{6.34}$$

and

$$Z_{r_m}(\theta) \triangleq \int_0^{\infty} \frac{e^{-\frac{u}{\sigma_{r_m d}^2}}}{u + R_{r_m}(\theta)} du, \tag{6.35}$$

with

$$R_{r_m}(\theta) \triangleq \frac{P_s\sigma_{sr_m}^2 + N_0}{P_{r_m}[1 + k_{sr_m}(\theta)]}. \tag{6.36}$$

According to Eq. (3.352.2) and Eq. (8.212.1) of [132], Eq. (6.35) can be further extended as:

$$Z_{r_m}(\theta) = -e^{R_{r_m}(\theta)/\sigma_{r_md}^2}\left(\zeta + \ln\frac{R_{r_m}(\theta)}{\sigma_{r_md}^2} + \int_0^{R_{r_m}(\theta)/\sigma_{r_md}^2}\frac{e^{-t}-1}{t}dt\right), \tag{6.37}$$

where $\zeta \triangleq 0.57721566490...$ denotes the Euler constant. In order to circumvent the integration, Eq. (6.37) can be expressed with aid of the Taylor series as:

$$Z_{r_m}(\theta) = -e^{R_{r_m}(\theta)/\sigma_{r_md}^2}\left(\zeta + \ln\frac{R_{r_m}(\theta)}{\sigma_{r_md}^2} + \sum_{n=1}^{\infty}\frac{\left(-\frac{R_{r_m}(\theta)}{\sigma_{r_md}^2}\right)^n}{n\cdot n!}\right), \tag{6.38}$$

$$\approx -e^{R_{r_m}(\theta)/\sigma_{r_md}^2}\left(\zeta + \ln\frac{R_{r_m}(\theta)}{\sigma_{r_md}^2} + \sum_{n=1}^{N_n}\frac{\left(-\frac{R_{r_m}(\theta)}{\sigma_{r_md}^2}\right)^n}{n\cdot n!}\right), \tag{6.39}$$

where the parameter N_n is introduced to control the accuracy of Eq. (6.39). Since the Taylor series in Eq. (6.38) converges fast, the integration in Eq. (6.37) can be approximated by the sum of the first N_n elements in Eq. 6.39. Consequently, the average BER of the DAF-aided cooperative system where the desired source MS relies on M_r cooperating MSs activated in order to form a VAA can be expressed as:

$$P_{BER}^{DAF}(a,b,M_r) = \frac{1}{2^{2(M_r+1)}\pi}\int_{-\pi}^{\pi}\frac{f(a,b,M_r+1,\theta)}{1+k_{sd}(\theta)}\prod_{m=1}^{M_r}\frac{1}{1+k_{sr_m}(\theta)} \times\left(1+\frac{k_{sr_m}(\theta)Z_{r_m}(\theta)}{1+k_{sr_m}(\theta)}\frac{P_s\sigma_{sr_m}^2+N_0}{P_{r_m}\sigma_{r_md}^2}\right)d\theta. \tag{6.40}$$

Using the same technique as in [128], the BER expression of Eq. (6.40) can be upper-bounded by bounding $Z_{r_m}(\theta)$ of Eq. (6.35), for the sake of simplifying the exact BER expression of Eq. (6.40). Specifically, $R_{r_m}(\theta)$ of Eq. (6.36) reaches its minimum value when $\alpha(\theta)$ of Eq. (6.19) is maximized at $\theta = \pi/2$, which in turn maximizes $Z_{r_m}(\theta)$ of Eq. (6.35). Thus, the error probability of Eq. (6.40) may be upper-bounded as:

$$P_{BER}^{DAF}(a,b,M_r) \lessapprox \frac{1}{2^{2(M_r+1)}\pi}\int_{-\pi}^{\pi}\frac{f(a,b,M_r+1,\theta)}{1+k_{sd}(\theta)}\prod_{m=1}^{M_r}\frac{1}{1+k_{sr_m}(\theta)} \times\left(1+\frac{k_{sr_m}(\theta)Z_{r_m,max}}{1+k_{sr_m}(\theta)}\frac{P_s\sigma_{sr_m}^2+N_0}{P_{r_m}\sigma_{r_md}^2}\right)d\theta, \tag{6.41}$$

where

$$Z_{r_m,max} \triangleq -e^{R_{r_m,min}/\sigma_{r_md}^2}\left(\zeta + \ln\frac{R_{r_m,min}}{\sigma_{r_md}^2} + \sum_{n=1}^{N_n}\frac{\left(-\frac{R_{r_m,min}}{\sigma_{r_md}^2}\right)^n}{n\cdot n!}\right), \tag{6.42}$$

in which

$$R_{r_m,min} \triangleq \frac{P_s\sigma_{sr_m}^2 + N_0}{P_{r_m}[1 + P_s\sigma_{sr_m}^2 b^2(1+\beta)^2/2N_0]}. \tag{6.43}$$

Similarly, the average BER of Eq. (6.40) can be lower bounded by minimizing $Z_{r_m}(\theta)$ of Eq. (6.35) at $\theta = -\pi/2$. Specifically, from Eq. (6.40) we arrive at the error probability expression of:

$$P_{BER}^{DAF}(a,b,M_r) \gtrapprox \frac{1}{2^{2(M_r+1)}\pi}\int_{-\pi}^{\pi}\frac{f(a,b,M_r+1,\theta)}{1+k_{sd}(\theta)}\prod_{m=1}^{M_r}\frac{1}{1+k_{sr_m}(\theta)} \times\left(1+\frac{k_{sr_m}(\theta)Z_{r_m,min}}{1+k_{sr_m}(\theta)}\frac{P_s\sigma_{sr_m}^2+N_0}{P_{r_m}\sigma_{r_md}^2}\right)d\theta, \tag{6.44}$$

where

$$Z_{r_m,min} \triangleq -e^{R_{r_m,max}/\sigma_{r_md}^2}\left(\zeta+\ln\frac{R_{r_m,max}}{\sigma_{r_md}^2}+\sum_{n=1}^{N_n}\frac{\left(-\frac{R_{r_m,max}}{\sigma_{r_md}^2}\right)^n}{n\cdot n!}\right), \tag{6.45}$$

in which

$$R_{r_m,max} \triangleq \frac{P_s\sigma_{sr_m}^2+N_0}{P_{r_m}[1+P_s\sigma_{sr_m}^2 b^2(1-\beta)^2/2N_0]}. \tag{6.46}$$

For the sake of further simplifying the BER expressions of Eq. (6.41) and Eq. (6.44), we can neglect all the additive terms of '1' in the denominators of both of the above-mentioned BER expressions by considering the relatively high-SNR region. Consequently, after some further manipulations, the approximated high-SNR BER upper-bound and its lower-bound counterpart respectively can be expressed as follows:

$$P_{BER,high-snr}^{DAF}(a,b,M_r) \lessapprox \frac{F(a,b,M_r+1)N_0^{M_r+1}}{P_s\sigma_{sd}^2}\prod_{m=1}^{M_r}\frac{P_{r_m}\sigma_{r_m,d}^2+P_s\sigma_{sr_m}^2 Z_{r_m,max}}{P_sP_{r_m}\sigma_{sr_m}^2\sigma_{r_md}^2} \tag{6.47}$$

$$P_{BER,high-snr}^{DAF}(a,b,M_r) \gtrapprox \frac{F(a,b,M_r+1)N_0^{M_r+1}}{P_s\sigma_{sd}^2}\prod_{m=1}^{M_r}\frac{P_{r_m}\sigma_{r_m,d}^2+P_s\sigma_{sr_m}^2 Z_{r_m,min}}{P_sP_{r_m}\sigma_{sr_m}^2\sigma_{r_md}^2}, \tag{6.48}$$

where we have

$$F(a,b,L) = \frac{1}{2^{2L}\pi}\int_{-\pi}^{\pi}\frac{f(a,b,L,\theta)}{\alpha^L(\theta)}d\theta, \tag{6.49}$$

Then $R_{r_m,min}$ of Eq. (6.43) and $R_{r_m,max}$ of Eq. (6.46) can be approximated as:

$$R_{r_m,min} \approx \frac{2N_0}{b^2(1+\beta)^2P_{r_m}}, \tag{6.50}$$

$$R_{r_m,max} \approx \frac{2N_0}{b^2(1-\beta)^2P_{r_m}}, \tag{6.51}$$

respectively. Importantly, both the BER upper- and lower-bounds of Eq. (6.47) and (6.48) imply that a DAF-aided cooperative system having M_r selected cooperating users is capable of achieving a diversity order of $L = (M_r+1)$, as indicated by the exponent L of the noise variance N_0.

6.2.1.2 Simulation Results and Discussion

Let us now consider a DAF-aided cooperative cellular uplink system using M_r relaying MSs in an urban area having a path loss exponent of $v = 3$. Without loss of generality, all the activated relaying MSs are assumed to be located about half-way between the source MS and the BS, while the total power used for transmitting a single modulated symbol is equally shared among the source

System Parameters	Choice
System	User-Cooperative Cellular Uplink
Cooperative Protocol	DAF
Number of Relay Nodes	M_r
Number of Sub-Carriers	$D = 1024$
Modulation	DPSK
Packet Length	$L_f = 128$
Normalised Doppler Freq.	$f_d = 0.008$
Path Loss Exponent	Typical urban area, $v = 3$ [2]
Channel Model	typical urban, refer to Table 5.1
Relay Location	$D_{sr_m} = D_{sd}/2,\ m = 1, 2, \cdots, M_r$
Power Control	$P_s = P_{r_m} = \frac{P}{(M_r+1)},\ m = 1, 2, \cdots, M_r$
Noise Variance at MS and BS	N_0

Table 6.1: Summary of system parameters

MS and the M_r RSs. To be more specific, we have $D_{sr_m} = D_{sd}/2,\ P_s = P_{r_m} = P/(M_r + 1),\ m = 1, 2, \cdots, M_r$. Moreover, the normalized Doppler freqeuncy is set to $f_d = 0.01$ under the assumption that multiple MSs are randomly moving around in the same cell. The system parameters considered in this section are summarized in Table 6.1.

The theoretical BER curves of Eq. (6.40) versus the SNR received for slow-fading channels are depicted in Figure 6.2 in comparison to the results obtained by our Monte Carlo simulations, where the MSDSD of Section 5.3 using $N_{wind} = 8$ is employed at the BS to eliminate the performance loss imposed by the relative mobility of the cooperating MSs, which is again modelled by a normalized Doppler frequency of $f_d = 0.01$. As suggested previously in Section 6.2.1.1 that the Taylor series in Eq. (6.38) converges rapidly and hence we employ $N_n = 5$ in Eq. (6.39) for the sake of reducing the computational complexity, while maintaining the required accuracy. Observe Figure 6.2 that all theoretical BER curves, corresponding to different number of activated cooperating MSs and to DBPSK and DQPSK modulation schemes, match well with the BER curves obtained by our Monte-Carlo simulations. Therefore, with the aid of the MSDSD of Section 5.3 employed at the BS, a full diversity order of $L = (M_r + 1)$ can be achieved by the DAF-aided cooperative system in rapidly fading channels, where the achievable BER performance can be accurately predicted using Eq. (6.40).

Additionally, the BER upper and lower bounds of Eqs.(6.41) and (6.44) derived for both DBPSK and DQPSK modulated DAF-aided cooperative systems are plotted in Figures 6.3(a) and 6.3(b), respectively, against the theoretical BER curve of Eq.(6.40). Both the lower and upper bounds are tight in comparison to the exact BER curve of Eq.(6.40) when the DBPSK modulation scheme is used, as observed in Figure 6.3(a). On the other hand, a relatively loose upper bound is obtained by invoking Eq.(6.41) for the DQPSK modulated system, while the lower bound associated with Eq. (6.44) still remains very tight. Therefore, it is sufficiently accurate to approximate the BER perforamnce of the DAF-aided cooperative system using the lower bound of Eq. (6.44).

Futhermore, in order to simplify the lower bound expression of Eq. (6.41), the integration term of Eq. (6.37) is omitted completely, assuming that we have $N_n = 0$ in Eq. (6.45). The

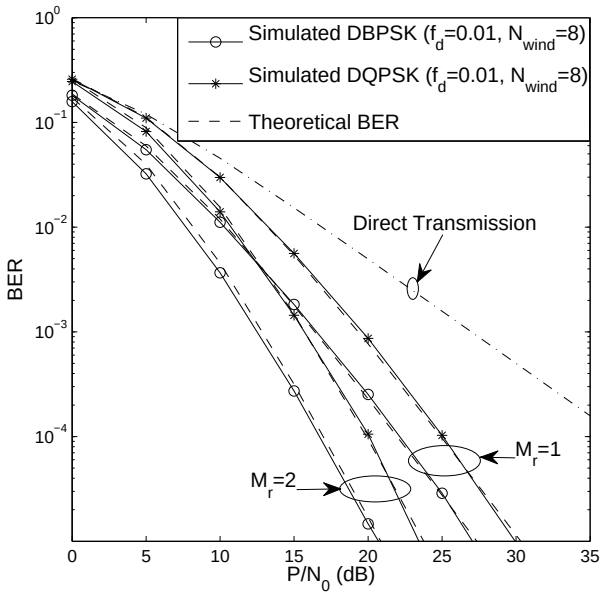

Figure 6.2: BER performance versus SNR for DAF-aided cooperative cellular systems, where there are M_r activated cooperating MSs, each having fixed transmit power and location. The MSDSD using $N_{wind} = 8$ is employed at the BS. All other system parameters are summarized in Table 6.1.

corresponding BER curves are depicted in Figure 6.4 against those obtained, when having $N_n = 5$. It is observed that the lower bound obtained after discarding the integration term in Eq. (6.37) still remains accurate and tight in the relatively high SNR region. More specifically, the resultant BER lower bound remains tight over a wide span of SNRs and only becomes inaccurate, when the SNR of P/N_0 dips below 5 dB and 10 dB for the DBPSK and DQPSK modulated cooperative systems, respectively.

When the SNR is sufficiently high and hence the employment of the high-SNR-based lower bound of Eq. (6.48) can be justified, its validity is verified by the BER curves of Figures 6.5(a) and 6.5(b) for the DBPSK and DQPSK modulated systems, respectively. Specifically, the simplified high-SNR-based BER lower-bound of Eq. (6.48) having $N_n = 0$ in Eq. (6.45) is capable of accurately predicting the BER performance achieved by the DAF-aided cooperative cellular uplink, provided that the transmitted SNR expressed in terms of P/N_0 is in excess of 15 dB for both the DBPSK and DQPSK modulation schemes considered.

6.2.2 Theoretical Analysis of Differential-Decode-and-Forward Systems

6.2.2.1 Performance Analysis

In the following discourse, the analytical BER performance expressions will be derived for a DDF-aided cooperative cellular system in order to facilitate our resource allocation to be outlined in Section 6.3.2. In contrast to its DAF-aided counterpart of Section 6.2.1, the M_r cooperating MSs selected will make sure that the information contained in the frame or packet received from the

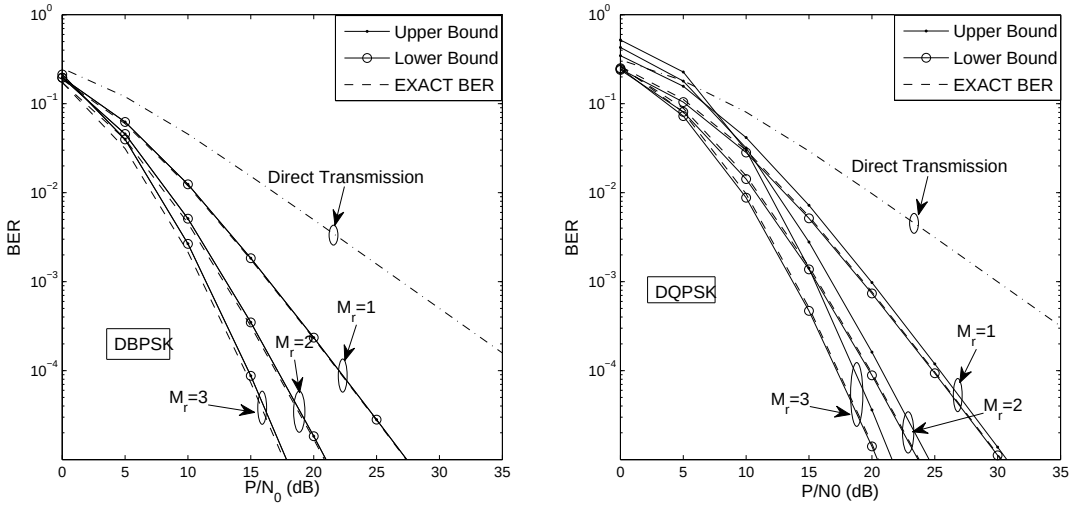

(a) DBPSK (b) DQPSK

Figure 6.3: BER lower and upper bounds versus SNR for DAF-aided cooperative cellular systems where there are M_r activated cooperating MSs, each having fixed transmit power and location. All other system parameters are summarized in Table 6.1.

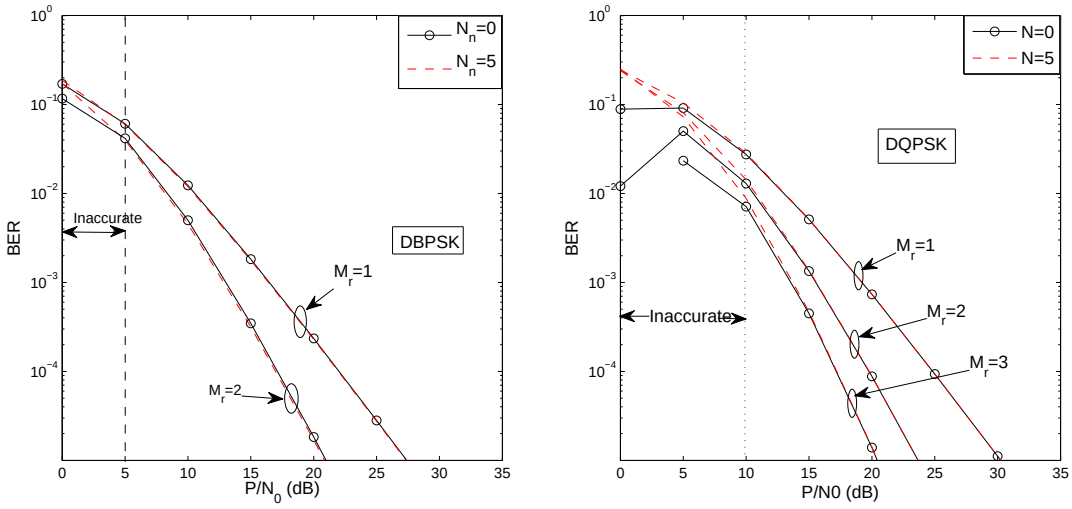

(a) DBPSK (b) DQPSK

Figure 6.4: Impact of N_n of Eq. (6.45) on the BER lower bounds versus SNR for DAF-aided cooperative cellular systems, where there are M_r activated cooperating MSs, each having fixed transmit power and location. All other system parameters are summarized in Table 6.1.

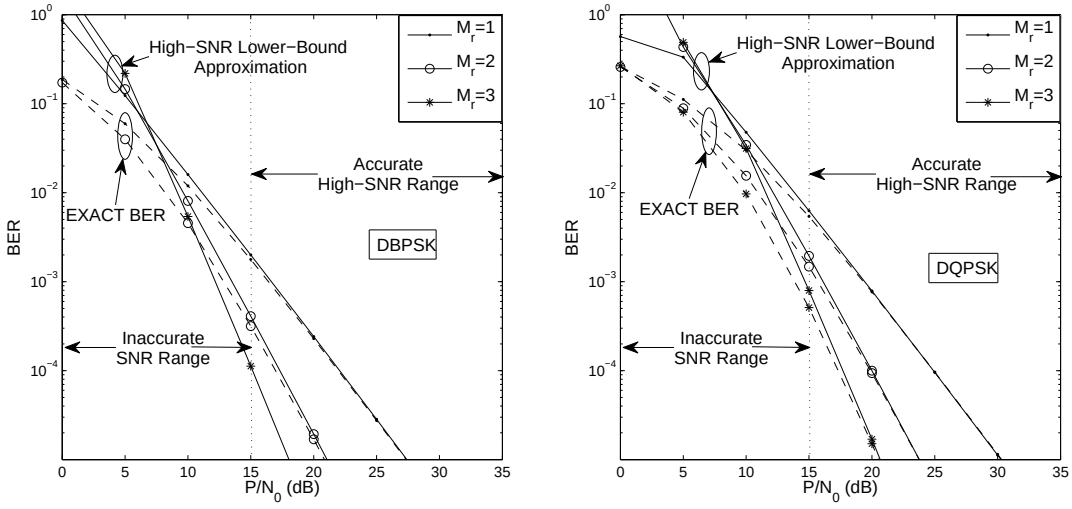

(a) DBPSK (b) DQPSK

Figure 6.5: High-SNR-based BER lower bounds versus SNR for DAF-aided cooperative cellular systems, where there are M_r activated cooperating MSs, each having transmit power and location. All other system parameters are summarized in Table 6.1.

source MS can be correctly recovered by differentially decoding the received signal with the aid of CRC checking, prior to forwarding it to the BS. In other words, some of the M_r cooperating MSs selected may not participate during the relaying phase, for the sake of avoiding potential error propagation due to the imperfect signal recovery. By simply assuming that the packet length is sufficiently high with respect to the channel's coherent time, the worst-case Packet Loss Ratio (PLR) at the mth cooperating MS can be expressed as:

$$P_{PLR_m,upper} = 1 - (1 - P_{SER_m})^{L_f}, \tag{6.52}$$

for a given packet length L_f, where P_{SER_m} represents the symbol error rate at the mth cooperating MS, which can be calculated as [133]:

$$P_{SER_m} = \frac{M_c - 1}{M_c} + \frac{|\rho_m| \tan(\frac{\pi}{M_c})}{\xi(\rho_m)} \left[\frac{1}{\pi} \arctan\left(\frac{\xi(\rho_m)}{|\rho_m|} \right) - 1 \right], \tag{6.53}$$

where ρ_m and the function $\xi(x)$, respectively, can be written as follows:

$$\rho_m = \frac{\frac{P_s \sigma_{sr_m}^2}{N_0}}{1 + \frac{P_s \sigma_{sr_m}^2}{N_0}}, \tag{6.54}$$

$$\xi(x) = \sqrt{1 - |x|^2 + \tan^2(\pi / M_c)}. \tag{6.55}$$

Then, based on the $P_{PLR_m,upper}$ expression of Eq.(6.52), the average end-to-end BER upper bound of a DDF-aided cooperative system can be obtained. Explicitly, in the context of a system, where only $M_r = 1$ cooperating user is selected to parcipate in relaying the signal from the source MS to the BS, the average end-to-end BER upper bound, $P_{BER,upper}^{DDF}$ is obtained by the summation of the

average BERs of two scenarios as:

$$P_{BER,upper}^{DDF} = (1 - P_{PLR_1,upper})P_{BER}^{\Phi_1} + P_{PLR_1,upper}P_{BER}^{\Phi_2}, \tag{6.56}$$

where Φ_1 is defined as the first scenario when the cooperating MS perfectly recovers the information received from the source MS and thus transmits the differentially remodulated signal to the BS. By contrast, Φ_2 is defined as the second scenario, when the cooperating MS fails to correctly decode the signal received from the source MS and hence remains silent during the relaying phase. Therefore, the scenarios Φ_1 and Φ_2 can be simply represented as follows, depending on whether the transmit power P_{r1} of the cooperating MS is zero or not during the relaying phase. Thus, we can represent Φ_1 and Φ_2 as:

$$\Phi_1 \triangleq \{P_{r_1} \neq 0\}, \tag{6.57}$$

$$\Phi_2 \triangleq \{P_{r_1} = 0\}, \tag{6.58}$$

respectively. Recall our BER analysis carried out for the DAF-aided system in Section 6.2.1.1, where the end-to-end BER expression of a cooperative system conditioned on the received SNR per bit γ^b can be written as:

$$P_{BER|\gamma^b}(a,b,L) = \frac{1}{2^{2L}\pi}\int_{-\pi}^{\pi} f(a,b,L,\theta)e^{-\alpha(\theta)\gamma^b}d\theta, \tag{6.59}$$

where $f(a,b,L,\theta)$ given by Eq.(6.18) is a function of the number of multi-path components L and is independent of the received SNR per bit γ^b. The parameter a and b are modulation-dependent, as defined in [6]. Consequently, the unconditional end-to-end BER, $P_{BER}^{\Phi_i}$, corresponding to the scenario Φ_i can be expressed as:

$$P_{BER}^{\Phi_i} = \int_{-\infty}^{\infty} P_{BER|\gamma_{\Phi_i}^b} \cdot p_{\gamma_{\Phi_i}^b}(\gamma)d\gamma, \tag{6.60}$$

where $p_{\gamma_{\Phi_i}^b}(\gamma)$ represents the PDF of the received SNR per bit after diversity combining at the BS in the scenario Φ_i of Eqs. (6.57) and (6.58).

On the other hand, since the MRC scheme is employed at the BS to combine the signals potentially forwarded by multiple cooperating MSs and the signal transmitted from the source MS as characterized by Eq.(5.44) using the combining weights of Eq.(5.45), the received SNR per bit after MRC combining is simply the sum of that of each combined path, which is expressed as:

$$\gamma_{\Phi_1}^b = \gamma_{sd}^b + \gamma_{r_1d}^b, \tag{6.61}$$

$$\gamma_{\Phi_2}^b = \gamma_{sd}^b. \tag{6.62}$$

Therefore, the unconditional BER of the scenario Φ_1 can be computed as:

$$P_{BER}^{\Phi_1} = \frac{1}{2^{2L}\pi}\int_{-\pi}^{\pi} f(a,b,L=2,\theta)\int_{-\infty}^{\infty} e^{-\alpha(\theta)\gamma_{\Phi_1}^b} p_{\gamma_{\Phi_1}^b}(\gamma)d\gamma d\theta, \tag{6.63}$$

$$= \frac{1}{2^{2L}\pi}\int_{-\pi}^{\pi} f(a,b,L=2,\theta)\mathcal{M}_{\gamma_{\Phi_1}^b}(\theta)d\theta, \tag{6.64}$$

where the joint MGF of the received SNR per bit recorded at the BS for the scenario Φ_1 is expressed

as:

$$\mathcal{M}_{\gamma^b_{\Phi_1}}(\theta) = \int_{-\infty}^{\infty} e^{-\alpha(\theta)\gamma^b_{\Phi_1}} p_{\gamma^b_{\Phi_1}}(\gamma) d\gamma, \tag{6.65}$$

$$= \int_{-\infty}^{\infty}\int_{-\infty}^{\infty} e^{-\alpha(\theta)(\gamma^b_{sd}+\gamma^b_{r_1d})} p_{\gamma^b_{sd}}(\gamma_{sd}) p_{\gamma^b_{r_1d}}(\gamma_{r_1d}) d\gamma_{sd} d\gamma_{r_1d}, \tag{6.66}$$

$$= \mathcal{M}_{\gamma^b_{sd}}(\theta)\mathcal{M}_{\gamma^b_{r_1d}}(\theta), \tag{6.67}$$

$$= \frac{N_0^2}{(N_0+\alpha(\theta)P_s\sigma^2_{sd})(N_0+\alpha(\theta)P_{r_1}\sigma^2_{r_1d})}, \tag{6.68}$$

with $p_{\gamma^b_{sd}}(\gamma_{sd})$ and $p_{\gamma^b_{r_1d}}(\gamma_{r_1d})$, respectively, denoting the PDF of the received SNR per bit for the direct link and for the RD relay link. Both of these expressions were given by Eq.(6.22). In parallel, the unconditional BER corresponding to the scenario Φ_2 can be obtained as:

$$P^{\Phi_2}_{BER} = \frac{1}{2^{2L}\pi}\int_{-\pi}^{\pi} f(a,b,L=1,\theta)\int_{-\infty}^{\infty} e^{-\alpha(\theta)\gamma^b_{\Phi_2}} p_{\gamma^b_{\Phi_2}}(\gamma) d\gamma d\theta, \tag{6.69}$$

$$= \frac{1}{2^{2L}\pi}\int_{-\pi}^{\pi} f(a,b,L=1,\theta)\mathcal{M}_{\gamma^b_{\Phi_2}}(\theta) d\theta, \tag{6.70}$$

where the MGF of the received SNR per bit recorded at the BS for the scenario Φ_2 is written as:

$$\mathcal{M}_{\gamma^b_{\Phi_2}}(\theta) = \int_{-\infty}^{\infty} e^{-\alpha(\theta)\gamma^b_{\Phi_2}} p_{\gamma^b_{\Phi_2}}(\gamma) d\gamma, \tag{6.71}$$

$$= \int_{-\infty}^{\infty} e^{-\alpha(\theta)\gamma^b_{sd}} p_{\gamma^b_{sd}}(\gamma_{sd}) d\gamma_{sd}, \tag{6.72}$$

$$= \frac{N_0}{N_0+\alpha(\theta)P_s\sigma^2_{sd}}. \tag{6.73}$$

Similarly, the BER upper bound can also be attained for cooperative systems relying on $M_r > 1$ cooperating users. For example, when $M_r = 2$, the average end-to-end BER upper bound $P^{DDF}_{BER,upper}$ becomes the sum of the average BERs of four scenarios expressed as:

$$\begin{aligned} & P^{DDF}_{BER,upper} \\ =&(1-P_{PLR_1,upper})(1-P_{PLR_2,upper})P^{\Phi_1}_{BER} + P_{PLR_1,upper}(1-P_{PLR_2,upper})P^{\Phi_2}_{BER}, \\ &+(1-P_{PLR_1,upper})P_{PLR_2,upper}P^{\Phi_3}_{BER} + P_{PLR_1,upper}P_{PLR_2,upper}P^{\Phi_4}_{BER}, \end{aligned} \tag{6.74}$$

where the four scenarios are defined as follows:

$$\Phi_1 = \{P_{r_1}\neq 0,\ P_{r_2}\neq 0\}, \tag{6.75}$$

$$\Phi_2 = \{P_{r_1}= 0,\ P_{r_2}\neq 0\}, \tag{6.76}$$

$$\Phi_3 = \{P_{r_1}\neq 0,\ P_{r_2}= 0\}, \tag{6.77}$$

$$\Phi_4 = \{P_{r_1}= 0,\ P_{r_2}= 0\}. \tag{6.78}$$

6.2.2.2 Simulation Results and Discussion

Under the assumption of a relatively rapidly Rayleigh fading channel associated with a normalized Doppler frequency of $f_d = 0.008$ and a packet length of $L_f = 16$ DQPSK modulated symbols, the BER curves corresponding to DDF-aided cooperative systems with $M_r = 1$ and $M_r = 2$

System Parameters	Choice
System	User-Cooperative Cellular Uplink
Cooperative Protocol	DDF
Number of Relay Nodes	M_r
Number of Sub-Carriers	$D = 1024$
Modulation	DQPSK
Packet Length	L_f
CRC	CCITT-4
Normalised Doppler Freq.	$f_d = 0.008$
Path Loss Exponent	Typical urban area, $v = 3$ [2]
Channel Model	typical urban, refer to Table 5.1
Relay Location	$D_{sr_m} = D_{sd}/2,\ m = 1, 2, \cdots, M_r$
Power Control	$P_s = P_{r_m} = \frac{P}{(M_r+1)},\ m = 1, 2, \cdots, M_r$
Noise Variance at MS and BS	N_0

Table 6.2: Summary of system parameters

cooperating MSs are plotted in comparison to the worst-case theorectical BERs of Eq.(6.56) and Eq.(6.74) in Figure 6.6(a). Since the worst-case BER expression derived in Section 6.2.2.1 for the DDF-aided system does not take the negative impact of the time-selective channel into account, the resultant asymptotic line may not be capable of accurately approximating the true achievable BER performance of a DDF-aided system employing the CDD in the context of a rapidly fading environment. However, with the aid of the MSDSD of Section 5.3 using $N_{wind} > 2$, the performance loss induced by the relative mobility of the cooperating terminals and the BS can be significantly eliminated. Thus, as revealed by Figure 6.6(a), the worst-case BER bound closely captures the dependency of the system's BER on the P/N_0 ratio. On the other hand, the BER curves of DDF-aided cooperative systems employing the MSDSD using different packet lengths L_f are plotted together with the corresponding worst-case theoretical BER bound in Figure 6.6(b). Likewise, the theoretical BER bound based on Eq.(6.56) closely captures the dependency of the MSDSD-aided system's BER on the packet length L_f employed in the scenario of a rapidly fading channel associated with a normalized Doppler frequency of $f_d = 0.008$.

6.3 Cooperating-User-Selection for the Uplink

User-cooperation aided cellular systems are capable of achieving substantial diversity gains by forming VAAs constituted by the concerted action of distributed mobile users, while eliminating the space- and cost- limitations of the shirt-pocket-sized mobile phones. Hence, the cost of implementing user-cooperation in cellular systems is significantly reduced, since there is no need to specifically set up additional relay stations. On the other hand, it is challenging to realize user-cooperation in a typical coherently detected cellular system, since $(N_t \times N_r)$ CIRs have to be estimated. For the sake of eliminating the implementationally complex channel estimation, in particular at the RSs, it is desirable to employ differentially detected modulation schemes in conjunction with the MSDSD scheme of Section 5.3. Furthermore, even if the Doppler-frequency-induced

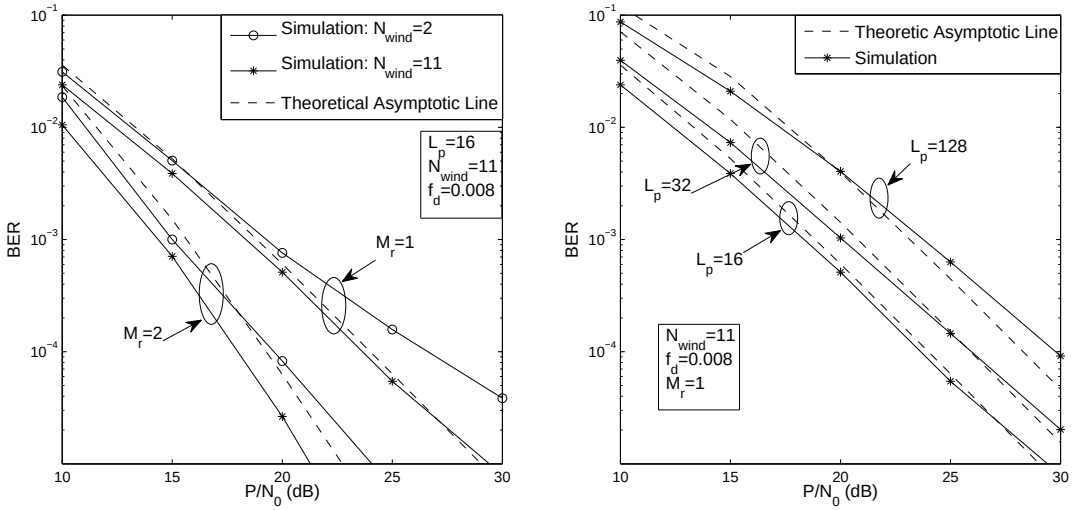

(a) Different numbers of cooperating MSs M_r.

(b) Different Frame lengths L_f.

Figure 6.6: BER performance versus SNR for DDF-aided cooperative cellular systems, where there are M_r activated cooperating MSs, each having fixed transmit power and location. The MSDSD using $N_{wind} = 11$ is employed at the BS. All other system parameters are summarized in Table 6.2.

degradations are eliminated by the employment of the MSDSD, another major problem is how to choose the required number of cooperating users from the pool of P_{cand} available candidates, which may significantly affect the end-to-end performance of the cooperative system. These effects have been observed in our previous simulation results shown in Figure 5.14 in Section 5.3.2.3, where we indicated that the quality of the source-relay link quantified in terms of the SNR, which is dominated by the specific location of the cooperating users, plays a vital role in determining the achievable end-to-end performance of a cooperative system. Moreover, the employment of Adaptive Power Control (APC) among the cooperating users is also important in order to maximize the achievable transmission efficiency. Hence, we will commence our discourse on the above-mentioned two schemes, namely, the Cooperating-User-Selection (CUS) and the APC schemes, in the context of the cooperative uplink, which will be based on the end-to-end performance analysis carried out in Section 6.2. More specifically, we will propose a CUS scheme combined with APC for the DAF-aided cooperative system employing the MSDSD of Section 5.3 and its DDF-aided counterpart in Sections 6.3.1 and 6.3.2, respectively.

6.3.1 Cooperating-User-Selection Scheme for Differential Amplify-and-Forward Systems with Adaptive Power Control

6.3.1.1 Adaptive Power Control for DAF-aided Systems [131]

As discussed in Section 6.1.2, for the sake of simplicity and analytical tractability, we assume that the source MS is sufficiently far away from the BS and the available cooperating MSs can be considered to be moving along the direct line-of-sight (LOS) path between them, as specified by Eq. (6.1) of Section 6.1.2. Explicitly, Eq. (6.1) can be rewritten by normalizing D_{sd} to 1, as follows:

$$D_{sr_u} + D_{r_u d} = D_{sd} = 1, \quad u = 1,\ 2,\ \cdots,\ \mathcal{P}_{cand}, \tag{6.79}$$

where $\mathcal{P}_{cand}$ is the RS pool size. This simplified model is readily generalized to a more realistic geography by taking into account the angle between the direct link and the relaying links. Furthermore, given a path-loss exponent of v, the average power $\sigma_{i,j}^2$ of the channel fading coefficient can be computed according to Eq. (6.3), which is repeated here for convenience:

$$\sigma_{i,j}^2 = D_{i,j}^{-v}, \quad i,\ j \in \{s,\ r_u,\ d\}. \tag{6.80}$$

Then, by defining

$$d_m \triangleq \frac{D_{sr_u}}{D_{sd}}, \tag{6.81}$$

we can represent $\sigma_{sr_u}^2$ and $\sigma_{r_u d}^2$ respectively as:

$$\sigma_{sr_u}^2 = \sigma_{sd}^2 \cdot d_m^v = d_m^v, \tag{6.82}$$

$$\sigma_{r_u d}^2 = \sigma_{sd}^2 \cdot (1-d_m)^v = (1-d_m)^v. \tag{6.83}$$

It was found in Section 6.2.1.2 that the simpler high-SNR-based BER lower bound expression of Eq. (6.48) associated with $N_n = 0$ in Eq. (6.45) is tight in a wide range of SNRs of interest, for example, for SNRs in excess of 15 dB for both the uncoded DBPSK and DQPSK modulated DAF-aided cooperative systems, as observed in Figure 6.5. Therefore, a power control scheme taking into account the location of the selected cooperating mobile users can be formulated, in order to minimize the BER of Eq. (6.48) under the total transmit power constraint of Eq. (6.4), i.e. when we have $P = P_s + \sum_{m=1}^{M_r} P_{r_m}$[1]. Thus, we arrive at:

$$\left[\hat{P}_s, \{\hat{P}_{r_m}\}_{m=1}^{M_r} \mid \{d_m\}_{m=1}^{M_r}\right]$$

$$= \arg \min_{\check{P}_s, \{\check{P}_{r_m}\}_{m=1}^{M_r}} \left\{ \frac{F(a,b,M_r+1) N_0^{Mr+1}}{\check{P}_s \sigma_{sd}^2} \prod_{m=1}^{M_r} \frac{\check{P}_{r_m} \sigma_{r_m,d}^2 + \check{P}_s \sigma_{sr_m}^2 Z_{r_m,min}}{\check{P}_s \check{P}_{r_m} \sigma_{sr_m}^2 \sigma_{r_m d}^2} \right\}, \tag{6.84}$$

$$= \arg \min_{\check{P}_s, \{\check{P}_{r_m}\}_{m=1}^{M_r}} \left\{ \frac{F(a,b,M_r+1) N_0^{Mr+1}}{\check{P}_s \sigma_{sd}^2} \prod_{m=1}^{M_r} \frac{\check{P}_{r_m} \sigma_{sd}^2 (1-d_m)^v + \check{P}_s \sigma_{sd}^2 d_m^v Z_{r_m,min}}{\check{P}_s \check{P}_{r_m} \sigma_{sd}^4 d_m^v (1-d_m)^v} \right\}, \tag{6.85}$$

$$= \arg \min_{\check{P}_s, \{\check{P}_{r_m}\}_{m=1}^{M_r}} \left\{ \frac{1}{\check{P}_s^{M_r+1}} \prod_{m=1}^{M_r} \frac{\check{P}_{r_m} (1-d_m)^v + \check{P}_s d_m^v \tilde{Z}_{r_m,min}}{\check{P}_{r_m}} \right\}, \tag{6.86}$$

[1] In this context we note that here we effectively assume that perfect power-control is used both when a specific mobile is transmitting its own data as well when it is acting as a RS. Naturally, the associated transmit power may be rather different in these two modes.

which is subjected to the power contraint of $P = P_s + \sum_{m=1}^{M_r} P_{r_m}$ and $P_{r_m} > 0$, $(m = 1, 2, \cdots, M_r)$. The variable $\tilde{Z}_{r_m,min}$ in Eq. (6.86) is defined as:

$$\tilde{Z}_{r_m,min} \triangleq -e^{\tilde{R}_{c_m}} \left(\zeta + \ln \tilde{R}_{c_m}\right), \tag{6.87}$$

where we have

$$\tilde{R}_{c_m} \triangleq \frac{R_{rm,max}}{(1-d_m)^v}, \tag{6.88}$$

$$= \frac{2N_0}{(1-d_m)^v b^2 (1-\beta)^2 P_s c_m}. \tag{6.89}$$

In order to find the solution of the minimization problem formulated in Eq. (6.86) with the aid of the Lagrangian method, we first define the function $f(Ps, c_m)$ by taking the logarithm of the right hand side of Eq. (6.86) as:

$$f(P_s, c_m) \triangleq \ln \left(\frac{1}{P_s^{M_r+1}} \prod_{m=1}^{M_r} \frac{c_m(1-d_m)^v + d_m^v \tilde{Z}_{r_m,min}}{c_m} \right), \tag{6.90}$$

$$= -(M_r+1)\ln P_s - \sum_{m=1}^{M_r} \ln c_m + \sum_{m=1}^{M_r} \ln \left(c_m(1-d_m)^v - d_m^v \tilde{Z}_{r_m,min} \right), \tag{6.91}$$

where we have

$$c_m \triangleq \frac{P_{r_m}}{P_s}. \tag{6.92}$$

Furthermore, we define the function $g(Ps, c_m)$ based on the transmit power constraint of Eq. (6.4) as follows:

$$g(P_s, c_m) \triangleq \mathbf{c}^T \mathbf{1} - \frac{P}{P_s}, \tag{6.93}$$

where

$$\mathbf{c} \triangleq [1,\ c_1,\ \cdots,\ c_{M_r}]^T, \tag{6.94}$$

and $\mathbf{1}$ represents an $(M_r \times 1)$-element column vector containing all ones. Then, the Lagrangian function Λ can be defined as:

$$\Lambda(P_s, c_m, \lambda) \triangleq f(P_s, c_m) + \lambda g(P_s, c_m), \tag{6.95}$$

$$= -(M_r+1)\ln P_s - \sum_{m=1}^{M_r} \ln c_m + \sum_{m=1}^{M_r} \ln \left(c_m(1-d_m)^v - d_m^v \tilde{Z}_{r_m,min} \right) + \lambda \left(\mathbf{c}^T \mathbf{1} - \frac{P}{P_s} \right), \tag{6.96}$$

where λ is the Lagrangian multiplier. Hence, the first order conditions for the optimum solution can be found by setting the partial derivatives of Eq. (6.96) with respect to both P_s and c_m to zero:

$$\frac{\partial \Lambda(P_s, c_m, \lambda)}{\partial P_s} = -\frac{M_r+1}{P_s} + \lambda \frac{P}{P_s^2} + \sum_{m=1}^{M_r} \frac{d_m^v \frac{e^{\tilde{R}_{c_m}}}{P_s} \left[\tilde{R}_{c_m}(\zeta + \ln \tilde{R}_{c_m}) + 1 \right]}{c_m(1-d_m)^v - d_m^v e^{\tilde{R}_{c_m}} (\zeta + \ln \tilde{R}_{c_m})} = 0, \tag{6.97}$$

$$\frac{\partial \Lambda(P_s, c_m, \lambda)}{\partial c_m} = \lambda - \frac{1}{c_m} + \frac{(1-d_m)^v + d_m^v \left[\frac{\tilde{R}_{c_m} e^{\tilde{R}_{c_m}}}{c_m} (\zeta + \ln \tilde{R}_{c_m}) + \frac{e^{\tilde{R}_{c_m}}}{c_m} \right]}{c_m(1-d_m)^v - d_m^v e^{\tilde{R}_{c_m}} (\zeta + \ln \tilde{R}_{c_m})} = 0, \tag{6.98}$$

$$\frac{\partial \Lambda(P_s, c_m, \lambda)}{\partial \lambda} = \mathbf{c}^T \mathbf{1} - \frac{P}{P_s} = 0. \tag{6.99}$$

Consequently, by combining Eqs. (6.97) as well as (6.98) and following a few further manipulations, we arrive at:

$$\frac{(M_r+1)P_s}{P}-\frac{1}{c_m}+\frac{(1-d_m)^v+d_m^v\left[\frac{2N_0}{b^2(1-\beta^2)(1-d_m)^vP_sc_m^2}e^{\tilde{R}_{c_m}(\zeta+\ln\tilde{R}_{c_m})+\frac{e^{\tilde{R}_{c_m}}}{c_m}}\right]}{c_m(1-d_m)^v-d_m^ve^{\tilde{R}_{c_m}}(\zeta+\ln\tilde{R}_{c_m})} - \frac{1}{P}\sum_{m=1}^{M_r}\frac{\frac{2N_0d_m^ve^{\tilde{R}_{c_m}}}{b^2(1-\beta)^2(1-d_m)^v}\left(\zeta+\ln\tilde{R}_{c_m}+\frac{1}{\tilde{R}_{c_m}}\right)}{c_m\left[c_m(1-d_m)^v-d_m^ve^{\tilde{R}_{c_m}}(\zeta+\ln\tilde{R}_{c_m})\right]}=0. \tag{6.100}$$

Therefore, the optimum power control can be obtained by finding the specific values of c_m $(m=1,2,\cdots,M_r)$ that satisfy both Eq. (6.99) and (6.100), which involves an $L=(M_r+1)$-dimensional search as specified in the summation of Eq. (6.100) containing power control of each of the M_r cooperating users. Hence, a potentially excessive computational complexity may be imposed by the search for the optimum power control solution. For the sake of significantly reducing the search space, the summation in the last term of Eq. (6.100) may be removed, leading to

$$\frac{(M_r+1)P_s}{P}-\frac{1}{c_m}+\frac{(1-d_m)^v+d_m^v\left[\frac{2N_0}{b^2(1-\beta^2)(1-d_m)^vP_sc_m^2}e^{\tilde{R}_{c_m}(\zeta+\ln\tilde{R}_{c_m})+\frac{e^{\tilde{R}_{c_m}}}{c_m}}\right]}{c_m(1-d_m)^v-d_m^ve^{\tilde{R}_{c_m}}(\zeta+\ln\tilde{R}_{c_m})} - \frac{1}{P}\frac{\frac{2N_0d_m^ve^{\tilde{R}_{c_m}}}{b^2(1-\beta)^2(1-d_m)^v}\left(\zeta+\ln\tilde{R}_{c_m}+\frac{1}{\tilde{R}_{c_m}}\right)}{c_m\left[c_m(1-d_m)^v-d_m^ve^{\tilde{R}_{c_m}}(\zeta+\ln\tilde{R}_{c_m})\right]}=0, \tag{6.101}$$

so that the resultant Eq. (6.101) depends only on the specific c_m value of interest. In other words, the original (M_r+1)-dimensional search is reduced to a single-dimensional search, resulting in a substantially reduced power control complexity, while the resultant power control is close to that corresponding to Eq. (6.100).

6.3.1.2 Cooperating-User-Selection Scheme for DAF-aided Systems

Since the quality of the relay-related channels, namely, of the source-to-relay and the relay-to-destination links dominates the achievable end-to-end performance of a DAF-aided cooperative system, the appropriate choice of cooperating users from the candidate pool of MSs roaming between the source MS and the BS as depicted in Figure 6.1 appears to be important in the scenario of cellular systems. In parallel to the APC scheme designed for the DAF-aided cooperative system discussed in Section 6.3.1.1, the CUS scheme is devised based on the minimization problem of Eq. (6.84), which can be further simplified as:

$$\left[\{\hat{d}_m\}_{m=1}^{M_r}\mid P_s,\{P_{r_m}\}_{m=1}^{M_r}\right]$$

$$=\arg\min_{\{\check{d}_m\}_{m=1}^{M_r}}\left\{\prod_{m=1}^{M_r}\frac{P_{r_m}\sigma_{sd}^2(1-\check{d}_m)^v+P_s\sigma_{sd}^2\check{d}_m^vZ_{rm,min}}{\sigma_{sd}^4\check{d}_m^v(1-\check{d}_m)^v}\right\}, \tag{6.102}$$

$$=\arg\min_{\{\check{d}_m\}_{m=1}^{M_r}}\left\{\prod_{m=1}^{M_r}\frac{P_{r_m}(1-\check{d}_m)^v+P_s\check{d}_m^v\tilde{Z}_{rm,min}}{\check{d}_m^v(1-\check{d}_m)^v}\right\}, \tag{6.103}$$

which is subjected to the physical constraint of having a normalized relay location of $0<d_m<1$, $(m=1,2,\cdots,M_r)$ measured from the source.

Although Eq. (6.103) can be directly solved numerically, it is difficult to get physically tangible insights from a numerical solution. To further simplify the minimization problem of Eq. (6.103), we define the function $f(d_m)$ by taking the logarithm of the right hand side of Eq. (6.103), leading to:

$$f(d_m) \triangleq \ln\left(\prod_{m=1}^{M_r} \frac{P_{r_m}(1-d_m)^v + P_s d_m^v \tilde{Z}_{rm,min}}{d_m^v (1-d_m)^v}\right), \tag{6.104}$$

$$= -v\sum_{m=1}^{M_r} \ln\left(d_m(1-d_m)\right) + \sum_{m=1}^{M_r} \ln\left(P_{r_m}(1-d_m)^v + P_s d_m^v \tilde{Z}_{rm,min}\right). \tag{6.105}$$

Then, by differentiating Eq. (6.105) with respect to the normalized relay locations $d_m, (m = 1, 2, \cdots, M_r)$ and equating the results to zero, we arrive at:

$$\frac{\partial f_{d_m}}{\partial d_m} = \frac{v(2d_m-1)}{d_m(1-d_m)} + \frac{-P_{r_m} v(1-d_m)^{v-1} + P_s v d_m^{v-1}\tilde{Z}_{r_m,min} + P_s d_m^v \frac{v(e^{\tilde{R}_{cm}} - \tilde{Z}_{r_m,min}\tilde{R}_{c_m})}{1-d_m}}{P_{r_m}(1-d_m)^v + P_s d_m^v \tilde{Z}_{r_m,min}} = 0. \tag{6.106}$$

Hence, the optimum normalized relay distance of d_m for a specific power control can be obtained by finding the specific d_m values which satisfy Eq. (6.106). Consequently, the original M_r-dimensional search of Eq. (6.103) is broken down into M_r single-dimensional search processes.

Although the optimized location of the cooperating users can be calculated for a given power control, the resultant location may not be the global optimum in terms of the best achievable BER performance. In other words, for the sake of attaining the globally optimum location and then activating the available cooperating candidates that happen to be closest to the optimum location, an iterative power-versus-RS-location optimization process has to be performed. To be more specific, the resultant global optimization steps are as follows:

Step 1: Initialize the starting point $(\{c_m\}_{m=1}^{M_r}, \{d_m\}_{m=1}^{M_r})$ for the search in the $2M_r$-dimensional space, hosting the M_r powers and RS locations.

Step 2: Calculate the locally optimum location $\{d_{m,local}\}_{m=1}^{M_r}$ of the cooperating users for the current power control, $\{c_m\}_{m=1}^{M_r}$.

Step 3: If we have $\{d_{m,local}\}_{m=1}^{M_r} \neq \{d_m\}_{m=1}^{M_r}$, then let $\{d_m\}_{m=1}^{M_r} = \{d_{m,local}\}_{m=1}^{M_r}$. Otherwise, stop the search, since the globally optimum solution has been found: $\{d_{m,globle}\}_{m=1}^{M_r} = \{d_{m,local}\}_{m=1}^{M_r}$ and $\{c_{m,globle}\}_{m=1}^{M_r} = \{c_m\}_{m=1}^{M_r}$.

Step 4: Calculate the locally optimum power control $\{c_{m,local}\}_{m=1}^{M_r}$ of the cooperating RSs for the current location, $\{d_m\}_{m=1}^{M_r}$.

Step5: If we have $\{c_{m,local}\}_{m=1}^{M_r} \neq \{c_m\}_{m=1}^{M_r}$, then let $\{c_m\}_{m=1}^{M_r} = \{c_{m,local}\}_{m=1}^{M_r}$ and continue to **Step1**. Otherwise, stop the search, since the globally optimum solution has been found: $\{d_{m,globle}\}_{m=1}^{M_r} = \{d_{m,local}\}_{m=1}^{M_r}$ and $\{c_{m,globle}\}_{m=1}^{M_r} = \{c_m\}_{m=1}^{M_r}$.

Furthermore, it is worth emphasizing that the above optimization process requires an "off-line" operation. Hence, its complexity does not contribute to the complexity of the real-time CUS scheme.

As mentioned previously in this section, since it is likely that no available cooperating MS candidate is situated in the exact optimum location found by the off-line optimization, the proposed CUS scheme simply chooses the available MS that roams closest to the optimum location and then adaptively adjusts the power control. The rationale of the CUS scheme is based on the observation that the achievable BER is proportional to the distance between the cooperating MS and the optimum location, as will be seen in Section 6.3.1.3.

6.3.1.3 Simulation Results and Discussion

System Parameters	Choice
System	User-Cooperative Cellular Uplink
Cooperative Protocol	DAF
Number of Relay Nodes	M_r
Number of Sub-Carriers	$D = 1024$
Modulation	DQPSK
Detection	MSDSD ($N_{wind} = 11$)
Packet Length	$L_f = 128$
Normalised Doppler Freq.	$f_d = 0.008$
Path Loss Exponent	Typical urban area, $v = 3$ [2]
Channel Model	typical urban, refer to Table 5.1
Noise Variance at MS and BS	N_0

Table 6.3: Summary of system parameters

Both the APC and CUS schemes designed for the DAF-aided cooperative system, which were devised in Sections 6.3.1.1 and 6.3.1.2, respectively, are based on the high-SNR-related BER lower bound of Eq. (6.48), which was shown to be a tight bound for a wide range of SNRs in Figure 6.5. In order to further characterize the proposed APC and CUS schemes and to gain insights into the impact of power control as well as that of the cooperating user's location on the end-to-end BER performance of the DAF-aided uplink supporting different number of cooperating users, the BER lower bounds are plotted versus P_s/P and d_m in Figures 6.7(a) and 6.7(b), respectively, in comparison to the exact BER of Eq. (6.40) and to its upper bound of Eq. (6.47). DQPSK modulation is assumed to be used here. Furthermore, in order to cope with the effects of the rapidly fluctuating fading channel, the MSDSD scheme of Section 5.3 is employed at the BS. For the sake of simplicity, we assume that an equal power is allocated to all activated cooperating MSs, which are also assumed to be located at the same distance from the source MS. All the other system parameters are summarized in Table 6.3. Observe from both Figure 6.7(a) and 6.7(b) that at a moderate SNR of 15 dB the lower bounds remain tight across the entire horizontal axes, i.e. regardless of the specific values of P_s/P and d_m. By contrast, the upper bound of Eq. (6.47) fails to accurately predict the associated BER trends, especially when the number of the activated cooperating MSs, M_r, is high. Therefore, despite using the much simpler optimization metrics of Eqs. (6.86) and (6.103), which are based on the high-SNR-related BER lower bound of Eq. (6.48), the APC and CUS schemes of Sections 6.3.1.1 and 6.3.1.2 are expected to remain accurate for quite a wide range of SNRs.

Furthermore, both the power control strategy and the specific location of the cooperating MSs

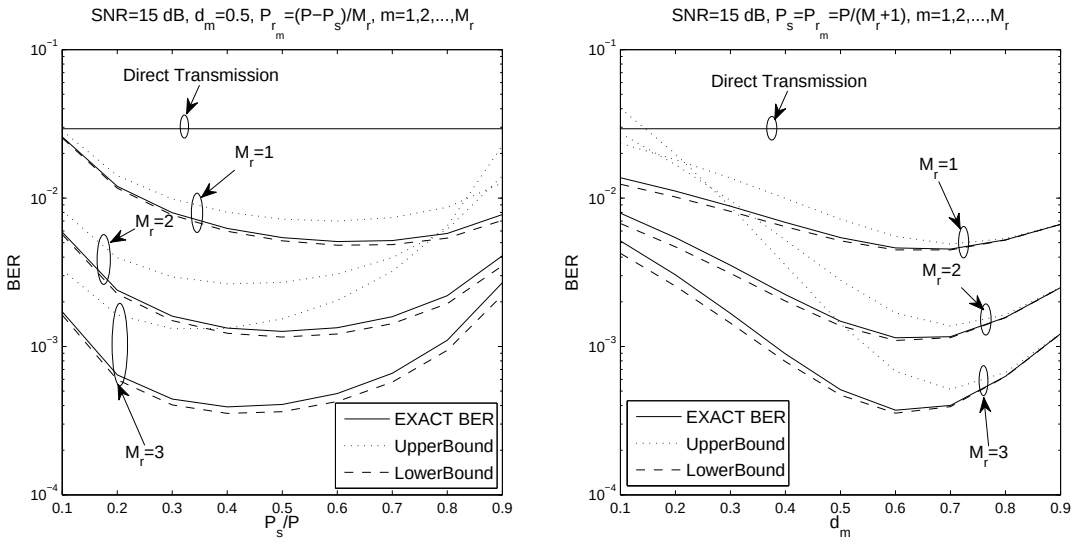

(a) Effects of the power control

(b) Effects of the cooperating MS' locations.

Figure 6.7: Effects of the power control and of the cooperating MS's location on the BER performance of DQPSK modulated DAF-aided cooperative cellular systems having M_r activated cooperating MSs. All other system parameters are summarized in Table 6.3.

play a vital role in determining the achievable BER performance of the DAF-aided cooperative system. Specifically, as shown in Figure 6.7(a), under the assumption that all the activated cooperating users are located about half-way between the source MS and the BS, i.e. for $d_m = 0.5$, $(m = 1, 2, \cdots, M_r)$ and for an equal-power-allocation among the cooperating users, i.e. for $P_{r_m} = (P - P_s)/M_r$, $(m = 1, 2, \cdots, M_r)$, the minimum of the BER curve is shifted to the left, when an increased number of cooperating MSs participate in signal relaying. This indicates that the transmit power employed by the source MS should be decreased in order to attain the best achievable end-to-end BER performance. On the other hand, under the assumption of an equal power allocation among the source MS and all the cooperating MSs, i.e. where we have $P_s = P_{r_m} = P/M_r$, $(m = 1, 2, \cdots, M_r)$, we observe from Figure 6.7(b) that the shape of the BER curves indicates a stronger sensitivity of the system's performance to the location of the cooperating users. This trend becomes even more dominant as the number of cooperating MSs, M_r, increases. However, in contrast to the phonomenon observed in Figure 6.7(a), the position of the BER minimum remains nearly unchanged as observed in Figure 6.7(b), indicating that the optimum location of the cooperating users remains unaffected for this specific system arrangement, regardless of M_r.

Importantly, the horizontal coordinate of the BER minimum represents the optimum MS location for the equal power allocation arrangement employed. Therefore, the achievable BER seen in Figure 6.7(b) is proportional to the distance between the RS and the optimum location, which provides the rationale for our distance-based CUS scheme.

In order to examine the tightness of the high-SNR-based BER lower bound of Eq. (6.48) for the DAF-aided cooperative system at different transmit SNRs of P/N_0, the BER lower bounds

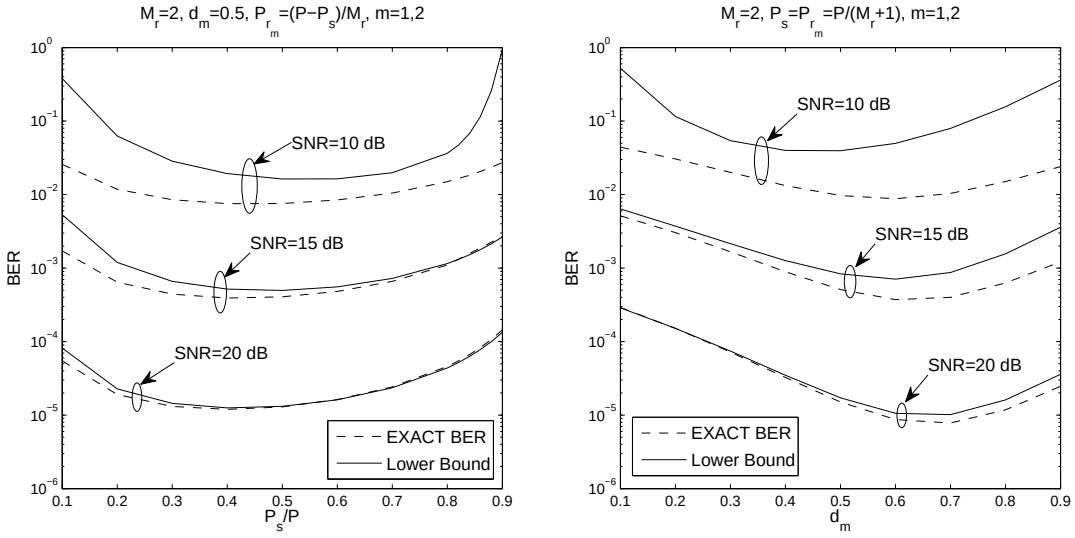

(a) BER versus P_s/P

(b) BER versus d_m

Figure 6.8: Effects of the SNR on the tightness of the high-SNR-based BER lower bound for the DQPSK modulated DAF-aided cooperative cellular uplink having two activated cooperating MSs. All other system parameters are summarized in Table 6.3.

corresponding to three distinct values of P/N_0 versus different power controls and relay locations are depicted in Figures 6.8(a) and 6.8(b), respectively. Let us assume that $M_r = 2$ cooperating MSs are activated. When having an SNR as high as 20dB, the lower bound is tight, as seen in both Figure 6.8(a) and 6.8(b). As the SNR decreases, the lower bound becomes increasingly loose, but remains capable of accurately predicting the BER trends and the best achievable performance in the vicinity of a moderate SNR level of 15 dB. However, when the SNR falls to as low a value as 10 dB, the lower bound remains no longer tight to accurately approximate the exact BER, thus the APC and the CUS scheme devised under the assumption of having a high SNR may not hold the promise of an accurate solution. Nevertheless, since the low SNR range corresponding to high BER levels, such as for example 10^{-2}, is not within our range of interest, the proposed APC and CUS schemes of Sections 6.3.1.1 and 6.3.1.2 are expected to work appropriately for a wide range of SNRs.

Let us now continue by investigating the performance improvements achieved by the optimization of the power control and the cooperating user's location. In Figure 6.9(a) the BER performance of the DAF-aided cooperative system employing the APC scheme of Section 6.3.1.1 is depicted versus the cooperating user's location, d_m, in comparison to that of the system dispensing with the APC scheme. Again, we simply assume that multiple activated cooperating users are located at the same distance from the source user. Observe in Figure 6.9 that significant performance improvements can be achieved by the APC scheme, when the cooperating user is situated closer to the BS than to the source MS. Hence the attainable BER is expected to be improved as the cooperating user moves increasingly closer to the BS. For example, the single-cooperating-user-assisted ($M_r = 1$) DAF-aided cooperative system using the APC scheme is capable of attaining its lowest possible BER at SNR=15 dB, when we have $d_1 = D_{sr_1}/D_{sd} = 0.8$. Therefore, the performance improvement

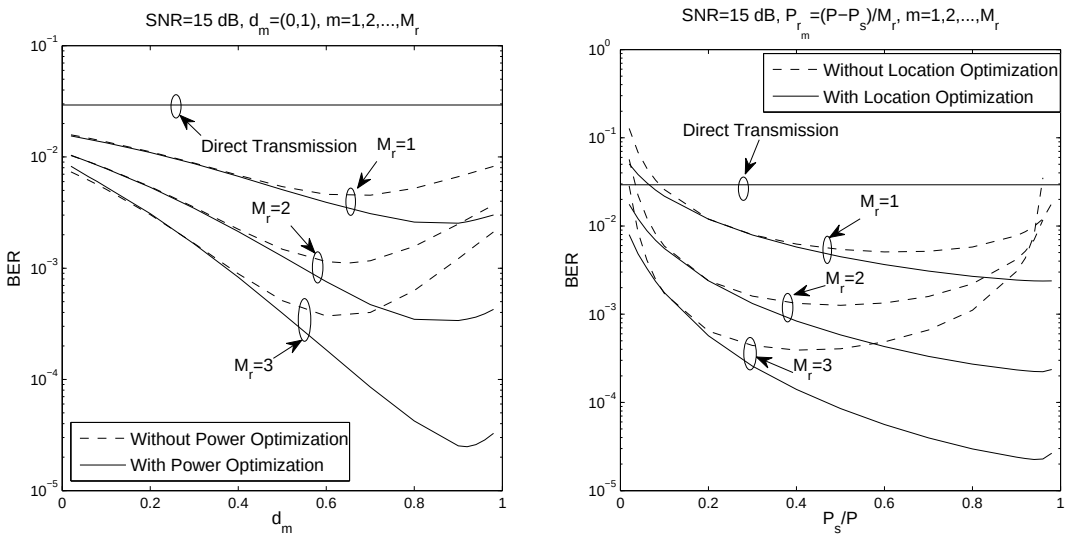

(a) Adaptive power control

(b) Relay location optimization

Figure 6.9: Power and relay location optimization for DQPSK modulated DAF-aided cooperative cellular systems having M_r activated cooperating MSs. All other system parameters are summarized in Table 6.3.

achieved by the APC scheme largely depends on the specific location of the cooperating users. Furthermore, the performance gains attained by the APC scheme for a specific arrangement of d_m is also dependent on the number of activated cooperating MSs, M_r. More specifically, when we have $M_r = 3$, a substantially larger gap is created between the BER curve of the system dispensing with the APC scheme and that of its APC-aided counterpart than that observed for $M_r = 1$, as seen in Figure 6.9(a).

At the same time, the BER performance of the DAF-aided system using relay location optimization is plotted in Figure 6.9(b) in comparison to that of the cooperative system, where the multiple activated cooperating users roam midway between the source MS and the BS. Similarly, a potentially substantial performance gain can be achieved by optimizing the location of the cooperating users, although naturally, this gain depends on the specific power control regime employed as well as on the number of activated cooperating users. To be specific, observe in Figure 6.9(b) that it is desirable to assign the majority of the total transmit power to the source MS in favour of maximizing the achievable performance gain by the location optimization. Moreover, the more cooperating users are activated, the higher the performance enhancement attained. Importantly, in the presence of a deficient power control regime, for example, when less than 10% of the overall transmit power is assigned to the source MS, the DAF-aided system may suffer from a severe performance loss, regardless of the location of the cooperating users. This scenario results in an even worse performance than that of the non-cooperative system. Therefore, by observing Figures 6.9(a) and 6.9(b) we infer that for the DAF-aided cooperative uplink, it is beneficial to assign the majority of the total transmit power to the source MS and choose the specific cooperating users roaming in the vicinity of the BS in order to enhance the achievable end-to-end BER performance.

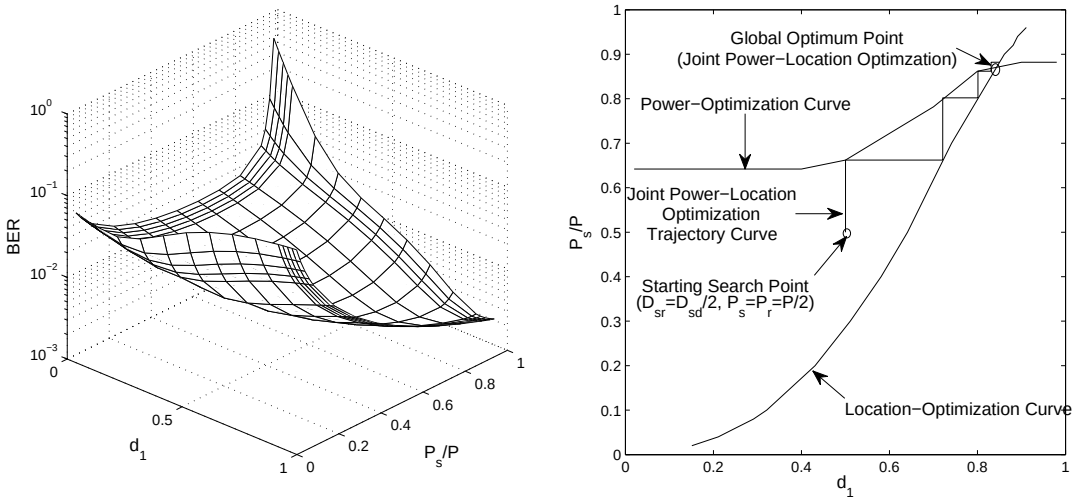

(a) BER surface

(b) Search Trajectory

Figure 6.10: Optimum cooperative resource allocation for DQPSK modulated DAF-aided cooperative cellular systems having a single activated cooperating MS at SNR=15 dB. All other system parameters are summarized in Table 6.3.

The above observations concerning the cooperative resource allocation of the DAF-aided system can also be inferred by depicting the three-dimensional BER surface versus both the power control and the cooperating MS's location in Figure 6.10(a) for a single-RS-aided cooperative system ($M_r = 1$). Indeed, the optimum solution is located in the area where both P_s/P and d_1 have high values. In order to reach the optimum operating point, the iterative optimization process discussed in Section 6.3.1.2 has to be invoked. The resultant optimization trajectory is depicted in Figure 6.10(b) together with the individual power-optimization and location-optimization based curves. The intersection point of the latter two lines represents the globally optimum joint power-location solution. As seen in Figure 6.10(b), by commencing the search from the center of the two-dimensional power-location plane, the optimization process converges after four iterations between the power and location optimization phases, as the corresponding trajectory converges on the above-mentioned point of intersection.

Let us now consider a DAF-aided DQPSK-modulated cooperative cellular system employing both the CUS and the APC schemes of Sections 6.3.1.1 and 6.3.1.2, where $M_r = 3$ cooperating MSs are activated in order to amplify and forward the signal received from the source MS to the BS, which are selected from $\mathcal{P}_{cand} = 9$ candidates roaming between the latter two. Without loss of generality, we simply assume that the locations of all the cooperating candidates are independent and uniformly distributed along the direct LOS link connecting the source MS and the BS, which are expected to change from time to time. Figure 6.11 depicts the performance of the DAF-aided cooperative system employing the CUS and the APC schemes of Sections 6.3.1.1 and 6.3.1.2 in comparison to both that exhibited by its counterpart dispensing with the above-mentioned techniques and that of the direct transmission based system operating without user cooperation in Rayleigh fading channels associated with different normalized Doppler frequencies. Figure 6.11 demonstrates that

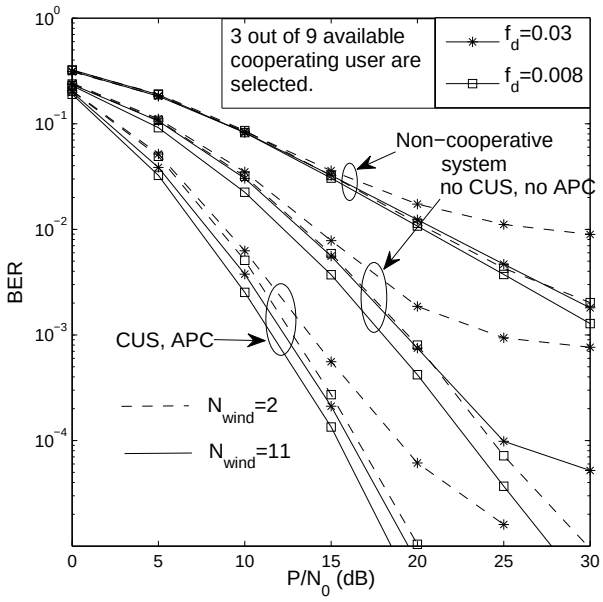

Figure 6.11: Performance improvements achieved by the CUS and APC schemes for a DAF-aided DQPSK modulated user-cooperative cellular system employing the MSDSD of Section 5.3, where 3 out of 9 cooperating user candidates are activated. All other system parameters are summarized in Table 6.3.

the DAF-aided cooperative system is capable of achieving a significantly better performance than the non-cooperative system. Observe in Figure 6.11 that a further significant performance gain of 10 dB can be attained by invoking the CUS and APC schemes for a cooperative system employing the CDD of Section 5.1.1 ($N_{wind} = 2$), at a BER target of 10^{-5} and a normalized Doppler frequency of $f_d = 0.008$. Furthermore, the employment of the CUS combined with the APC makes the cooperative cellular system more robust to the deleterious effects of time-selective channels. Indeed, observe in Figure 6.11 that an error floor as induced by a normalized Doppler frequency of $f_d = 0.03$ at BER of 10^{-3} for the cooperative system dispensing with the CUS and the APC arrangements, while the BER curve corresponding to the system carrying out cooperative resource allocation only starts to level out at a BER of 10^{-5}. For the sake of further eliminating the BER degradation caused by severely time-selective channels, the MSDSD employing $N_{wind} > 2$ can be utilized at the BS. As observed in Figure 6.11, for a target BER level of 10^{-5}, an P/N_0 degradation of about 7 dB was induced by increasing f_d from 0.008 to 0.03 for the CDD-aided system, while it was reduced to 1 dB by activating the MSDSD scheme of Section 5.3 using $N_{wind} = 11$.

Let us now consider the BER performance of DAF-aided cooperative systems dispensing with at least one of the two above-mentioned schemes, which is plotted in Figure 6.12(a). To be more specific, given a target BER of 10^{-5}, performance gains of 6 dB and 2.5 dB can be achieved respectively by the employment of the CUS and the APC over the benchmark system, where three cooperating users are randomly selected from the available 9 RS candidates and the total transmit power is equally divided between the source and the relaying MSs. Hence, the distance-based CUS scheme of Section 6.3.1.2 performs well as a benefit of activating the RS candidiates closest to the predetermined optimum locations, even in conjunction with a relatively small cooperating RS

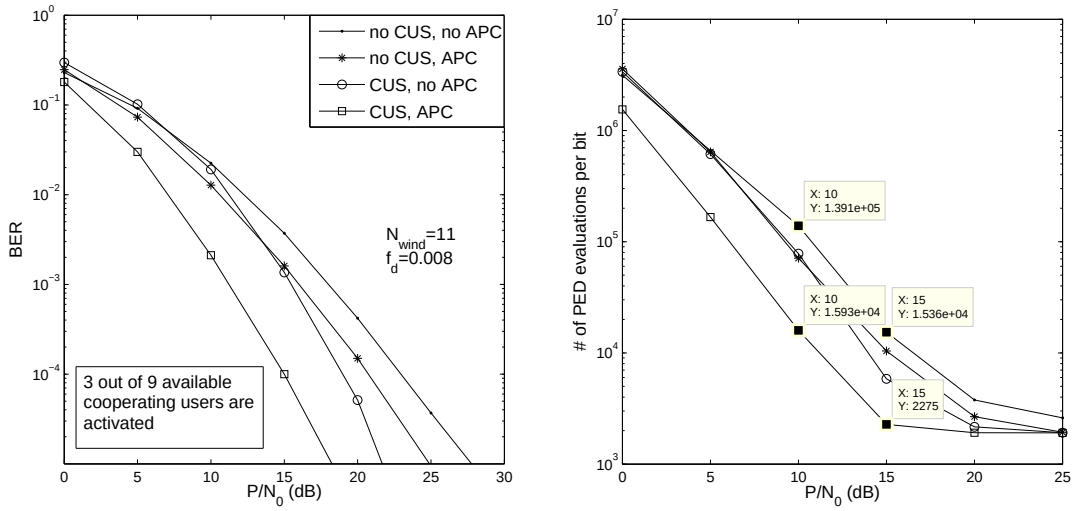

(a) BER performance

(b) Complexity imposed by the MSDSD

Figure 6.12: BER performance and the MSDSD complexity reductions achieved by the CUS and APC schemes for DAF-aided DQPSK modulated user-cooperative cellular uplink, where 3 out of 9 cooperating RS candidates are activated. All other system parameters are summarized in Table 6.3.

candidate pool, where it is more likely that none of the available RS candidates is situated in the optimum locations. In order to further enhance the achievable end-to-end performance, APC is carried out based on the cooperating users' location as activated by the CUS and results in a performance gain as high as about 9.5 dB over the benchmark system, as demonstrated in Figure 6.12(a). Moreover, besides providing performance gains, the CUS and APC schemes are also capable of achieving a significant complexity reduction in the context of the MSDSD employed by the BS, as seen in Figure 6.12(b), where the complexity imposed by the MSDSD using $N_{wind} = 11$ expressed in terms of the number of the PED evaluations versus P/N_0 is portrayed correspondingly to the four BER curves of Figure 6.12(a). Although the complexity imposed by the MSDSD in all of the four scenarios considered decreases steadily, as the transmit SNR increases and then levels out at a certain SNR value around 20 dB. Observe in Figure 6.12(b) that a reduced complexity is imposed, when either the CUS or the APC scheme is employed. Remarkably, the complexity imposed by the MSDSD at the BS can be reduced by a factor of about 10 for a wide range of transmit SNRs, when the CUS and the APC are amalgamated. By carefully comparing the simulation results of Figures 6.12(a) and 6.12(b), it may be readily observed that the transmit SNR level, which guarantees BER of 10^{-5} is roughly the SNR level at which the complexity imposed by the MSDSD starts to level out. Therefore, it is inferred from the above observations that an appropriate cooperative resouce allocation expressed in terms of the transmit power control and the appropriate cooperating user selection may significantly enhance the achievable end-to-end BER performance of the DAF-aided cooperative cellular uplink, while substantially reducing the computing power required by the MSDSD at the BS.

In a typical cellular system, the number of users roaming in a cell may also be referred to as the

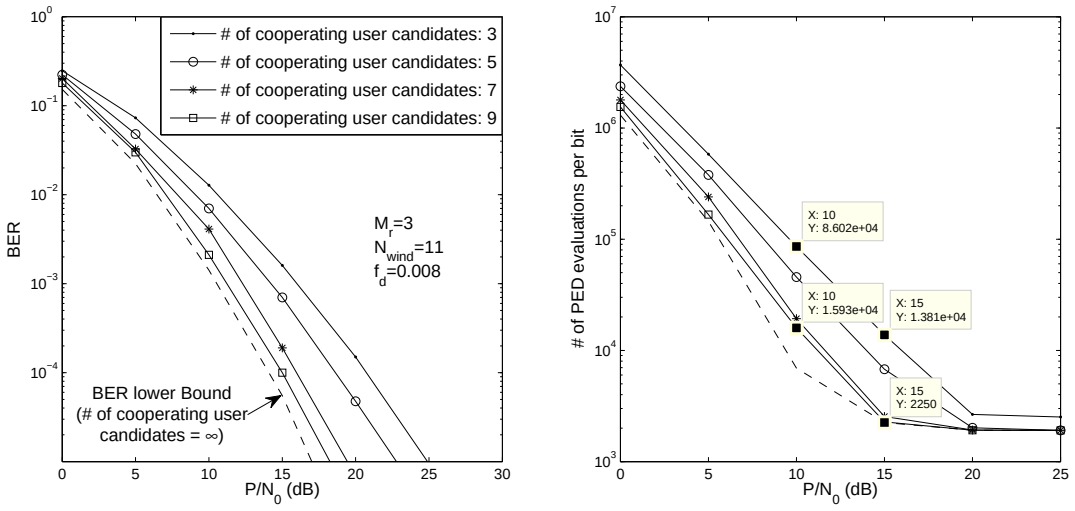

(a) BER performance

(b) Complexity imposed by the MSDSD

Figure 6.13: The effects of the size of the cooperating RS pool on the DAF-aided DQPSK modulated user-cooperative cellular uplink employing the CUS and APC schemes, where $M_r = 3$ cooperating users are activated. All other system parameters are summarized in Table 6.3.

size of the cooperating user candidate pool denoted by $\mathcal{P}_{cand}$ in the scenario of the user-cooperative uplink. In order to investigate its impacts on the end-to-end BER performance of the DAF-aided cooperative system employing the CUS and the APC schemes, the BER curves corresponding to different values of $\mathcal{P}_{cand}$ are plotted versus the transmit SNR, P/N_0, against that of the idealized scenario used as a benchmark, where the activated RSs are situated exactly in the optimum locations and have the optimum power control. Again, we assume that $M_r = 3$ RSs are activated, which are selected from the $\mathcal{P}_{cand}$ MSs roaming in the same cell. Interestingly, despite having a fixed number of activated cooperating MSs, the end-to-end BER performance of the DAF-aided system steadily improves and approaches that of the idealized benchmark system upon increasing the value of $\mathcal{P}_{cand}$, as observed in Figure 6.13(a). On the other hand, it can be seen in Figure 6.13(b) that the higher the number of cooperating candidates, the lower the computational complexity imposed by the MSDSD at the BS. Specifically, by increasing the size of the candidate pool from $\mathcal{P}_{cand} = 3$ to 9, a performance gain of about 7 dB can be attained, while simultaneously achieving a detection complexity reduction factor of 6.5 at the target BER of 10^{-5}. In comparison to the idealized scenario, where an inifinite number of cooperating candidates are assumed to be independently and uniformly distributed between the source MS and the BS, the DAF-aided cooperative system using both the CUS and APC schemes only suffers a negligible performance loss, when having $\mathcal{P}_{cand} = 9$ cooperating candidates. Therefore, the benefits brought about by the employment of the CUS and APC schemes may be deemed substantial in a typical cellular uplink.

6.3.2 Cooperating-User-Selection Scheme for Differential-Decode-and-Forward Systems with Adaptive Power Control

In contrast to the process of obtaining the optimum power and location allocation arrangements discussed in Section 6.3.1 for DAF-aided cooperative systems, the first order conditions obtained by differentiating the BER bound of a DDF-aided cooperative system formulated in Eq.(6.56) and (6.74) for $M_r = 1$ and $M_r = 2$ scenarios have complicated forms, which are impervious to an analytical solutions. However, their numerical solution is feasible, instead of resorting to Monte Carlo simulations. Explicitly, by taking $M_r = 1$ as an example, the optimum power control can be obtained for a given RS location arrangement by minimizing the worst-case BER of Eq. (6.56), yielding:

$$\begin{aligned}&\left[\hat{P}_s, \{\hat{P}_{r_m}\}_{m=1}^{M_r} \mid \{d_m\}_{m=1}^{M_r}\right] \\ &= \arg \min_{\check{P}_s, \{\check{P}_{r_m}\}_{m=1}^{M_r}} \left\{(1 - P_{PLR_1,upper}) P_{BER}^{\Phi_1} + P_{PLR_1,upper} P_{BER}^{\Phi_2}\right\},\end{aligned} \tag{6.107}$$

where $P_{PLR_1,upper}$ is the worst case packet loss ratio at the cooperating MS, which is given by Eq. (6.52), while $P_{BER}^{\Phi_1}$ and $P_{BER}^{\Phi_2}$ are given by Eq. (6.64) and Eq. (6.70), respectively, corresponding to the average BER measured at the BS both with and without the signal forwarded by the RS. In parallel, the optimum location allocation can be obtained for a specific power control arrangement as:

$$\begin{aligned}&\left[\{\hat{d}_m\}_{m=1}^{M_r} \mid P_s, \{P_{r_m}\}_{m=1}^{M_r}\right] \\ &= \arg \min_{\{\hat{d}_m\}_{m=1}^{M_r}} \left\{(1 - P_{PLR_1,upper}) P_{BER}^{\Phi_1} + P_{PLR_1,upper} P_{BER}^{\Phi_2}\right\}.\end{aligned} \tag{6.108}$$

Then, for the sake of attaining the globally optimum location and then activating the available cooperating candidates that happen to be closest to the optimum location, an iterative power-versus-RS-location optimization process identical to that discussed in Section 6.3.1.2 in the context of an AF scheme has to be performed. Again, the rationale of the proposed CUS scheme for the DDF-aided system is based on the observation that the achievable BER is proportional to the distance between the cooperating MS and the optimum location, as will be demonstrated in Section 6.3.2.1.

6.3.2.1 Simulation Results and Discussion

The beneficial effects of cooperative resource allocation, in terms of the transmit power and the cooperating user's location on the achievable BER performance of the DDF-aided cooperative system are investigated in Figure 6.14. Under the assumption that the channel fluctuates extremely slowly, e.g. for $f_d = 0.0001$, the worst-case BER performance corresponding to Eq.(6.56) for $M_r = 1$ and to Eq.(6.74) for $M_r = 2$, for the DQPSK-modulated DDF-aided cooperative systems employing either equal-power allocation or the optimized power control are plotted versus the different cooperating users' locations in Figure 6.14(a). The information bit stream is CCITT-4 coded by the source MS in order to carry out the CRC checking at the cooperating MS with the aid of a 32-bit CRC sequence. Hence, for the sake of maintaining a relatively high effective throughput, two different transmission packet lengths are used, namely, $L_f = 128$ and $L_f = 64$ DQPSK symbols. All

System Parameters	Choice
System	User-Cooperative Cellular Uplink
Cooperative Protocol	DDF
Number of Relay Nodes	M_r
Number of Sub-Carriers	$D = 1024$
Modulation	DQPSK
CRC Code	CCITT-4
Detection	MSDSD ($N_{wind} = 11$)
Packet Length	L_f
Normalised Doppler Freq.	f_d
Path Loss Exponent	Typical urban area, $v = 3$ [2]
Channel Model	typical urban, refer to Table 5.1
Noise Variance at MS and BS	N_0

Table 6.4: Summary of system parameters

other system parameters are summarized in Table 6.3. Observe in Figure 6.14(a) that the end-to-end BER performance can be substantially enhanced by employing the optimized power control, if the cooperating MS is not roaming in the neighborhood of the source MS. Similarly to the observation obtained for its DAF-aided counterparts characterized in Figure 6.9(a) of Section 6.3.1.3, the higher the number of active cooperating MSs, M_r, the more significant the performance gain attained by optimizing the power control for the DDF-aided system. However, due to the difference between the relaying mechanisms employed by the two above-mentioned cooperative systems, it is interesting to observe that the trends seen in Figure 6.14(a) are quite different from those emerging from Figure 6.9(a). Specifically, recall from the results depicted in Figure 6.9(a) that it is desirable to choose multiple cooperating users closer to the BS than to the source MS in a DAF-aided cooperative system, espcially when employing the optimized power control for sharing the power among the cooperating users. By contrast, Figure 6.14(a) demonstrates that the cooperating MSs roaming in the vicinity of the source MS are prefered for a DDF-aided system in the interest of maintaining a better BER performance. Furthermore, the performance gap between the DAF-aided systems employing both the equal- and optimized power allocations becomes wider, as the cooperating MS moves closer to the optimum location corresponding to the horizontal coordinate of the lowest-BER point in Figure 6.9(a). By contrast, only a negligible performance improvement can be achieved by optimizing the power control, if the cooperating MS is close to the optimum location corresponding also to the horizontal coordinate of the lowest-BER point in Figure 6.14(a). In other words, the DDF-aided system suffers a relatively modest performance loss by employing the simple equal power allocation, if the multiple cooperating MSs are closer to their desired locations. Additionally, recall from Figure 6.9(a) recorded for the DAF-aided system that the worst-case BER performance was encountered owing to having no cooperating user closer to the optimum locations, regardless whether the optimum power control is used or not, but the performance of this RS-aided DAF system was still slightly better than that of the conventional direct transmission system. By contrast, the DDF-aided system employing equal-power allocation may unfortunately be outperformed by the direct transmission based non-cooperative system, if the cooperating MSs are located nearer to the BS than to the source MS. Finally, in contrast to the DAF-assisted system, the

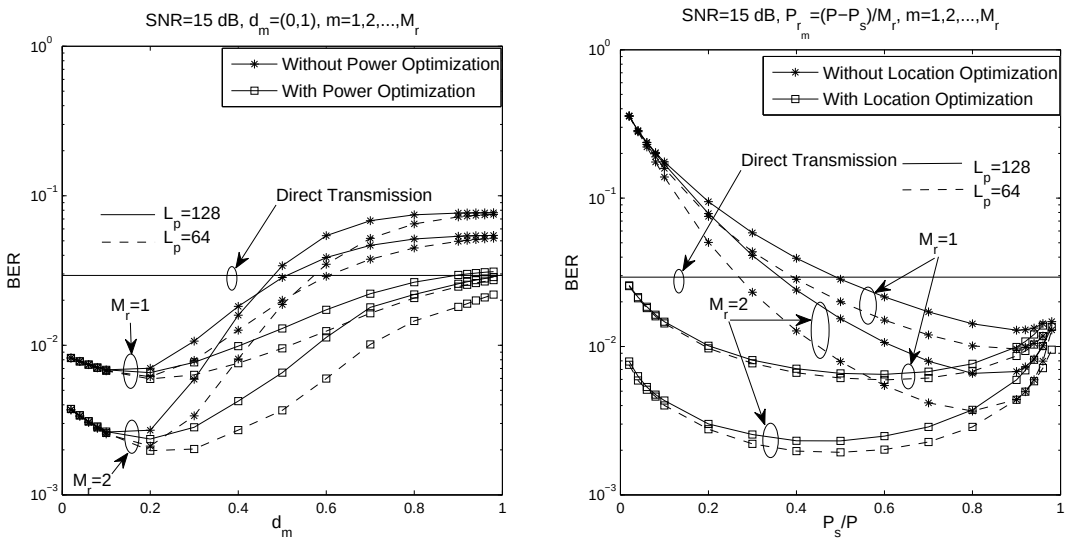

(a) Adaptive power control

(b) Relay location optimization

Figure 6.14: Power and relay location optimization for the DQPSK modulated DDF-aided cooperative cellular systems having M_r activated cooperating MSs. All other system parameters are summarized in Table 6.4.

performance achieved by the DDF-aided system is dependent on the specific packet length, L_f, due to the potential relaying deactivation controlled by the CRC check carried out at the cooperating MS. To be specific, the shorter the packet length, L_f, the lower the resultant BER.

In parallel, the BER performance of the above-mentioned DDF-aided systems is depicted against P_s/P in Figure 6.14(b). Here, the transmit power of $(P - P_s)$ is assumed to be equally shared across multiple cooperating users. Again, similar to the results recorded for the DAF-aided system in Figure 6.9(b), a significant performance gain can be attained by locating the cooperating MS at the optimum position rather than in the middle of the source MS and BS path. This performance gain is expected to become even higher, as the number of actively cooperating MSs, M_r, increases as seen in Figure 6.14(b). By contrast, for optimum cooperating user location, instead of allocating the majority of the total transmit power to the source MS - as it was suggested by Figure 6.9(b) as for the DAF-aided system in the interest of achieving an improved BER performance - the results of Figure 6.14(b) suggest that only about half of the total power has to be assigned to the source MS, if the DDF scheme is used. Furthermore, the mild sensitivity of the BER performance observed in Figure 6.14(b) for the DDF-aided system benefiting from the optimum cooperating user location as far as the power control is concerned coincides with the trends seen in Figure 6.14(a), namely that a desirable BER performance can still be achieved without optimizing the power control, provided that all the coopearting MSs roam in the vicinity of their optimum locations. Interestingly, in contrast to the conclusions inferred from Figure 6.14(a) for the DAF-aided system, the originally significant performance differences caused by the different packet lengths of $L_f = 128$ and $L_f = 64$, can be substantially reduced for the DDF-aided system, provided that the cooperating user is situated at the optimum location. Finally, as observed in Figure 6.14(b), when no active RS can be found in the vicinity of the optimum cooperating user locations, the DDF-aided

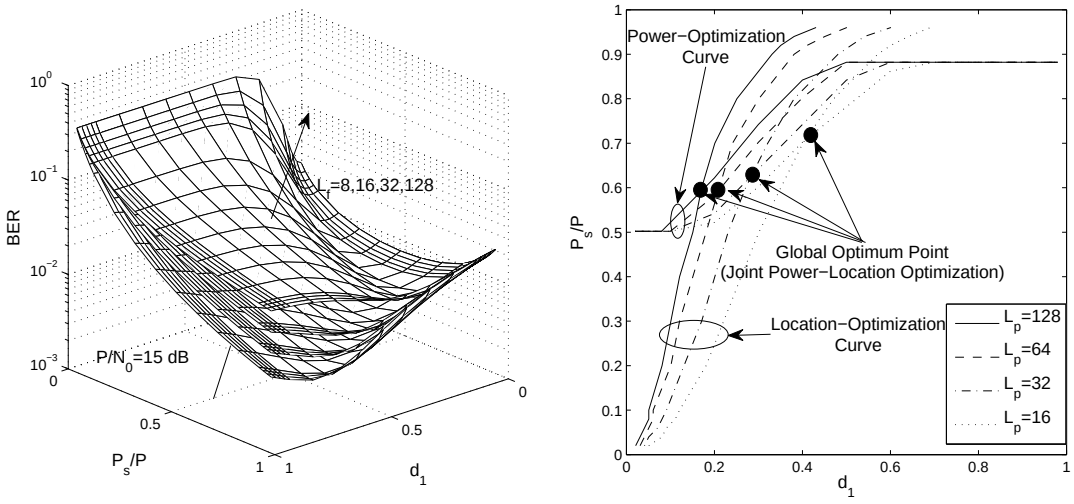

(a) BER surface

(b) Globally Optimum Point

Figure 6.15: Optimum cooperative resource allocation for the DQPSK modulated DDF-aided cooperative cellular systems having a single activated cooperating MS at SNR=15 dB. All other system parameters are summarized in Table 6.4.

system might be outperformed by its more simple direct transmission counterpart in the presence of deficient power control imposed by high power-control errors.

Observe for the $M_r = 1$ scenario by merging Figure 6.14(a) and 6.14(b) that the globally optimum cooperative resource allocation characterized in terms of the transmit power control and RS selection regime can be visualized as the horizontal coordinates of the lowest point of the resultant 3D BER surface portrayed in Figure 6.15(a), where the 3D BER surface corresponding to different L_f values is plotted against P_s/P and $d_1 = D_{sr_1}/D_{sd}$ for the DDF-aided cooperative system. The smaller the packet length, L_f, the lower the BER. This is because the likelihood that the activated cooperating MS improves the signal relaying is inversely proportional to the packet length L_f. However, observe in Figure 6.15(a) that the gap between the different BER curves of 3D surface becomes relatively small in the vicinity of the globally optimum BER point, as predicted by Figure 6.14(a) and 6.14(b). On the other hand, similarly to the results of Figure 6.10(b) recorded for the DAF-aided cooperative system, we plot the power-optimized curve against d_1, while drawing the location-optimized curve versus P_s/P for the DDF-aided system associated with $M_r = 1$ in Figure 6.15(b), where the intersection of the two curves is the globally optimum solution corresponding to the projection of the lowest BER point onto the horizontal plane in Figure 6.15(a). The globally optimum solution can be found by the joint power-location iterative optimization process discussed in Section 6.3.1.2. Furthermore, the globally optimum resource allocation, denoted by the black dot in Figure 6.15(b), changes as the packet length L_f varies. To be more specific, by increasing the packet length L_f, the optimum cooperating user location moves increasingly closer to the source MS, while the percentage of the total transmit power assigned to the source MS gradually decreases. This is not unexpected, since the propability of perfectly recovering all the symbols of the source MS by the cooperating MS is reduced upon employing a higher packet length L_f,

which has to be increased by choosing a cooperating MS closer to the source MS in the interest of increasing the received SNR at the cooperating MS.

Let us now continue by examining the BER performance improvement achieved by optimizing the resource allocation for the DDF-aided cooperative system in Figure 6.16, where the four subfigures depict the BER performance of the systems both with and without optimized cooperative resource allocation in terms of the transmit power and relay locations, while varying the packet length L_f. As seen in Figure 6.16, significant performance gains can be attained by using an optimum power control among the M_r cooperating users and the source user as well as by assuming that all the M_r actively cooperating users are situated in their optimum locations, especially when we have a relatively large packet length L_f. Although a better PLR performance is attained when using short packets, the achievable performance gain is reduced, as indicated by the increasingly narrower gap between the BER curves obtained with and without the optimized resource allocation. Consider the $M_r = 2$ scenario as an example, the originally achievable performance gain of 5 dB recorded for $L_f = 128$ is reduced to about 0.5 dB for $L_f = 16$ at a BER of 10^{-5}. In fact, this phenomenon coincides with the observation inferred from our previous simulation results, such as for example the 3D BER surface shown in Figure 6.15(a), which can be explained by the fact that the BER and PLR performance loss induced by a high packet length L_f may be significantly reduced by optimizing the cooperative resouce allocation. Again for the scenario of $M_r = 2$, a performance loss of 5 dB is endued , when employing $L_f = 64$ instead of $L_f = 16$ in the absence of resource allocation optimization, whereas the performance loss is reduced to 1.5 dB, when the cooperative resource allocation is optimized. Furthermore, we also found that interestingly the asymptotic theoretical curves based on the worst-case BER expressions of Eq.(6.56) and Eq.(6.74) for $M_r = 1$ and $M_r = 2$, respectively, become tighter for the DDF-aided system using optimized resource allocation.

Figure 6.17 separately investigates the impact of the CUS and that of the APC on the end-to-end BER performance of a DDF-aided cooperative system employing the MSDSD in a relatively rapidly Rayleigh fading channel associated with $f_d = 0.008$, where $N_{wind} = 8$ is employed to combat the performance degradation induced by the time-selective fading channel. Similarly to the results of Figure 6.12(a) recorded for the DAF-aided system, a more significant performance improvement can be attained by invoking CUS than APC. However, in contrast to its DAF-aided counterpart, the joint employment of the CUS and APC schemes for the DDF-aided system only leads to a negligible additional performance gain over the scenario, where only the CUS is carried out. This is not unexpected, if we recall the observations inferred from Figure 6.14(a), namely, that the additional performance improvement achieved by optimizing the power control gradually erodes, as the activated cooperating MS approaches the optimum location. Furthermore, unlike the CUS scheme, which simply selects the cooperating MS that is closest to the optimum location calculated in an offline manner, the APC scheme, which conducts a real-time search for the optimum power control based on the actual location of the activated cooperating MS, may impose an excessive complexity. Hence, for the sake of reducing the complexity, the DDF-aided cooperative system may simply employ equal-power allocation, while being still capable of achieving a desirable performance with the aid of the CUS scheme.

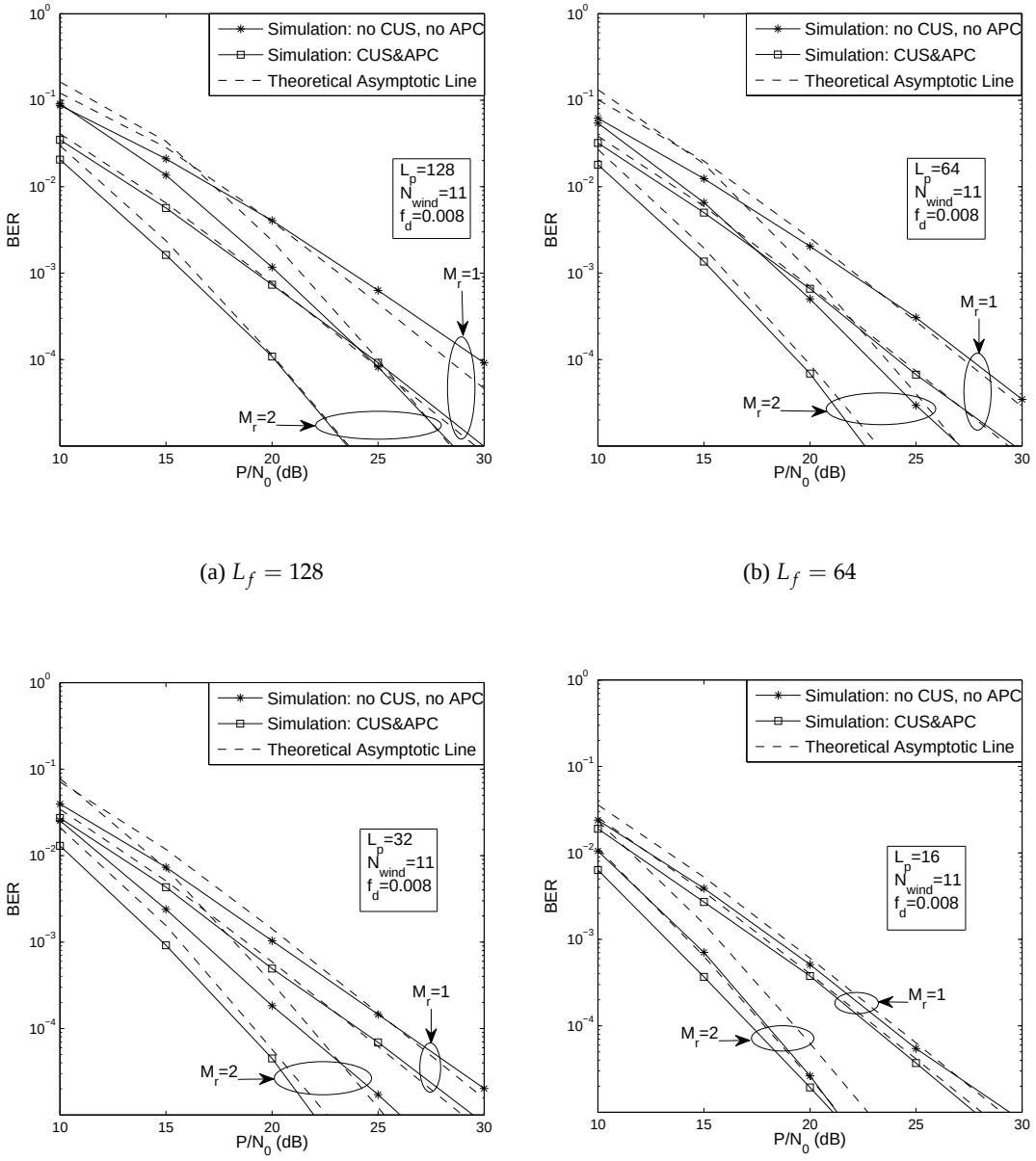

(a) $L_f = 128$

(b) $L_f = 64$

(c) $L_f = 32$

(d) $L_f = 16$

Figure 6.16: Performance improvement achieved by optimizing the cooperative resources for the DQPSK modulated DDF-aided cooperative cellular systems employing the MSDSD in relatively fast Rayleigh fading channel, where the M_r activated cooperating users are assumed to be situated in their optimum location. All other system parameters are summarized in Table 6.4.

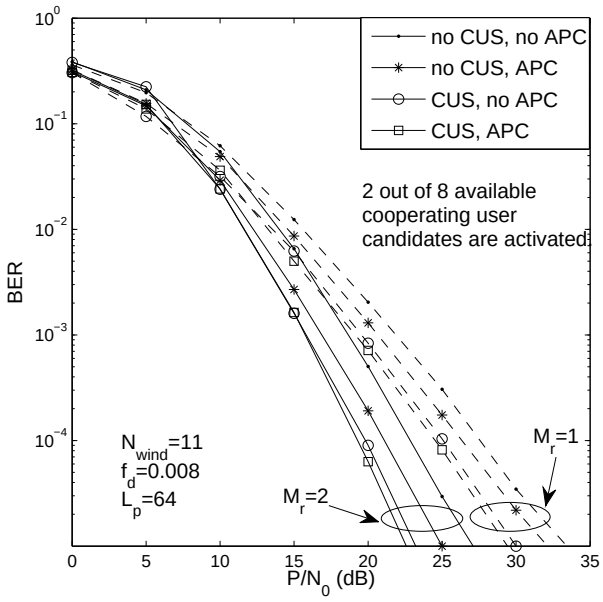

Figure 6.17: Performance improvements achieved by the CUS and APC schemes for the DDF-aided DQPSK modulated user-cooperative cellular system employing the MSDSD in a relatively fast Rayleigh fading channel, where 2 out of 8 cooperating users are activated. All other system parameters are summarized in Table 6.4.

6.4 Joint CPS and CUS Scheme for the Differentially Modulated Cooperative Cellular Uplink Using APC

From our discussions on the performance of the DAF- and DDF-aided cooperative cellular uplink in Sections 6.3.1.3 and 6.3.2.1, respectively, we may conclude that the above-mentioned two scenarios exhibit numerous distinct characteristics due to the employment of different relaying mechanisms. Therefore, the comparison of these two cooperative schemes will be further detailed in Section 6.4.1. Based on the initial comparison of the DAF and DDF schemes, a novel hybrid CPS scheme will be proposed in Section 6.4.2. In conjunction with the CUS and the APC arrangements, we will then create a more flexible cooperative system, where the multiple cooperating MSs roaming in different areas might employ different relaying mechanisms to assist in forwarding the source MS's message to the BS for the sake of achieving the best possible BER performance. This system may be viewed as a sophisticated hybrid of a BS-aided ad hoc network or - alternatively - as an ad hoc network assisted cellular network.

6.4.1 Comparison Between the DAF- and DDF-Aided Cooperative Cellular Uplink

Sensitivity to the Source-Relay Link Quality

The fundamental difference between the DAF and the DDF schemes is whether decoding and re-encoding operations are required at the RS or not. Thus, generally speaking, the overall complexity imposed by the DDF-aided cooperative system is expected to be higher than that of its DAF-aided

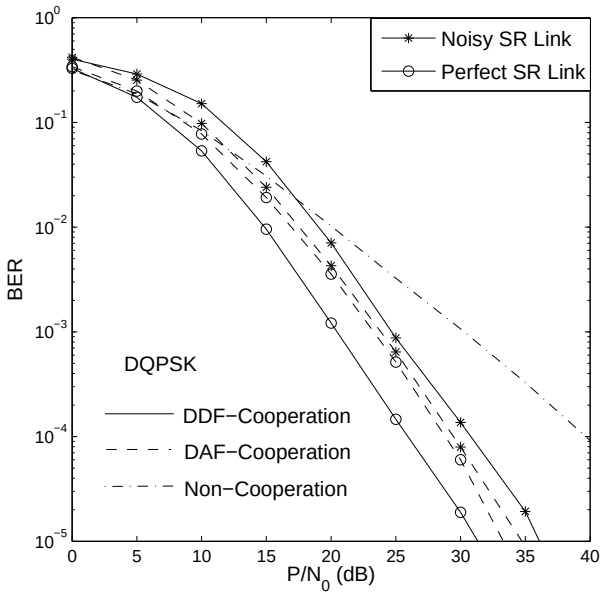

Figure 6.18: Impact of the source-relay link's quality on the end-to-end BER performance of a DQPSK modulated cooperative system employing $M_r = 1$ cooperating RS roaming about halfway between the source MS and the BS. The CDD is employed by both the RS and the BS in a Rayleigh fading channel having a Doppler frequency of $f_d = 0.001$.

counterpart. However, as a benefit of preventing error propagation by the RS, the DDF-aided system is expected to outperform the DAF-aided one, provided that a sufficiently high source-relay link quality guarantees a near-error-free transmission between the source MS and the RS, as previously indicated by Figure 5.14 of Section 5.3.2.3. For convenience, we repeat these results here in Figure 6.18, where we observe that the sensitivity of the DDF-aided system to the source-relay link quality is significantly higher than that of the DAF-aided system. This is because the CRC employed may suggest to the RS to refrain from participating in forwarding the signal to the BS with a high probability, when the source-relay link is of low quality, which in turn leads to a rapid performance degradation. In practice, a high performance can be achieved for the DDF-aided system by activating the cooperating MSs roaming in the vicinity of the source MS and/or by invoking channel encoding.

Effect of the Packet Length

In contrast to its DAF-aided counterpart, where the achievable performance is independent of the packet length L_f employed in absence of the channel encoding, the DDF-aided system's performance is sensitive to the packet length L_f, as it was previously demonstrated for example by Figure 6.16 of Section 6.3.2.1. This trend is not unexpected, since in the absence of the channel coding the PLR increases proportional to the value of L_f. This in turn may result in error-precipitation in the context of a DDF-aided system. However, this performance degradation can be substantially reduced by invoking the CUS of Section 6.3.2, as evidenced by Figure 6.14.

Cooperative Resource Allocation

As demonstrated by the simulation results of Sections 6.3.1.3 and 6.3.2.1, significant performance

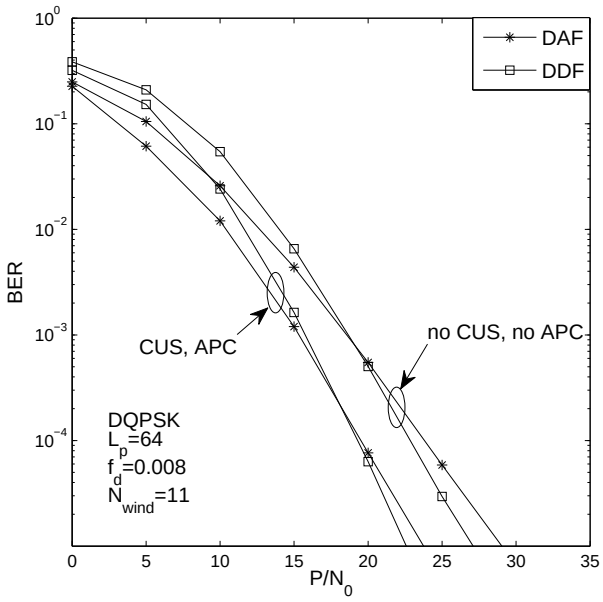

Figure 6.19: Performance comparison between the DAF-aided and DDF-aided DQPSK modulated user-cooperative cellular systems employing the MSDSD, where 2 out of 8 cooperating user candidates are activated. All other system parameters are summarized in Table 6.3.

gains can be attained for both the DAF- and the DDF-aided cellular uplink by optimizing the associated cooperative resource allocation with the aid of the CUS and APC schemes of Section 6.3. More explicitly, the BER performance of both the above-mentioned systems operating with and without the CUS and APC schemes is constrasted in Figure 6.19, where it is assumed that the $M_r = 2$ out of the $\mathcal{P}_{cand} = 8$ available cooperating MS candidates are activated and the MSDSD of Section 5.3 using $N_{wind} = 11$ is employed in order to eliminate the detrimental effects of the fading having a Doppler frequency of $f_d = 0.008$. Moreover, the variance of the noise added at each terminal of the cooperative system is assumed to be identical, namely N_0. Indeed, as seen in Figure 6.19, the performance of both the DAF and DDF systems is significantly enhanced by the employment of the CUS and APC schemes. We also note that the DAF-assisted system exhibits a better performance than the DDF-aided one, when the SNR of P/N_0 is relatively low, while the former is expected to be outperformed by the latter, as the SNR of P/N_0 is in excess of 20 dB. Again, this trend is not unexpected, since the sensitivity of the BER performance to the source-relay link's quality leads to a more rapid BER decrease upon increasing the SNR of P/N_0.

On the other hand, we also observed in Table 6.5 that due to their distinct relaying mechanisms, which leads to different levels of sensitivity to the quality of the source-relay link, the desirable cooperative resource allocation arrangement for the DAF-aided system may be quite different from that of its DDF-aided counterpart. As indicated by the RS's location arrangement of $[d_1, d_2, \cdots, d_{M_r}]$ seen in Table 6.5, the cooperating MSs roaming in the area near the BS are expected to be activated for the DAF-aided cooperative uplink, while those roaming in the neighborhood of the source MS should be selected for its DDF-aided counterpart in the interest of achieving the best possible BER performance. It is also indicated in Table 6.5 that the increase of the SNR, P/N_0, or the number of activated cooperating MSs, M_r, will move the desirable RS's location

Optimized Cooperative Resource Allocation for the DAF- and DDF-Aided Uplink					
M_r	P/N_0 (dB)	DAF-Aided Uplink		DDF-Aided Uplink ($L_f = 64$)	
		$[P_s,\ P_{r_1},\cdots P_{r_{M_r}}]$	$[d_1,\ d_2\cdots d_{M_r}]$	$[P_s,\ P_{r_1},\ \cdots P_{r_{M_r}}]$	$[d_1,\ d_2\cdots d_{M_r}]$
1	10	[0.882, 0.118]	[0.811]	[0.582, 0.418]	[0.192]
	20	[0.882, 0.118]	[0.871]	[0.622, 0.378]	[0.231]
	30	[0.882, 0.118]	[0.891]	[0.622, 0.378]	[0.231]
2	10	[0.76, 0.2, 0.04]	[0.74, 0.88]	[0.602, 0.202, 0.196]	[0.26, 0.26]
	20	[0.76, 0.2, 0.04]	[0.82, 0.91]	[0.602, 0.202, 0.196]	[0.31, 0.31]
	30	[0.78, 0.2, 0.02]	[0.85, 0.94]	[0.602, 0.202, 0.196]	[0.31, 0.31]
3	10	[0.88, 0.04, 0.04, 0.04]	[0.89, 0.89, 0.89]	[0.502, 0.102, 0.202, 0.194]	[0.31, 0.21, 0.26]
	20	[0.88, 0.04, 0.04, 0.04]	[0.92, 0.92, 0.92]	[0.502, 0.102, 0.202, 0.194]	[0.36, 0.26, 0.26]
	30	[0.88, 0.04, 0.04, 0.04]	[0.93, 0.93, 0.93]	[0.702, 0.102, 0.102, 0.094]	[0.41, 0.41, 0.41]

Table 6.5: Cooperative Resource Allocation for DAF- and DDF-Aided Uplinks

slightly further away from the source MS towards to the BS for both the DAF- and DDF-aided scenarios. As to the optimized power control, the majority of the total transmit power P, namely about 88%, should be allocated to the source MS for the DAF-aided systems, as revealed by the optimized power control arrangement of $[P_s,\ P_{r_1},\cdots,\ P_{r_{M_r}}]$ seen in Table 6.5. By contrast, only about 60% of the power should be assigned to the source MS for the DDF-aided system. It is noteworthy that the optimized transmit power assigned to the M_r RSs as well as their optimum locations are not expected to be identical in both the DAF- and DDF-aided scenarios, as revealed in Table 6.5.

Furthermore, by comparing Figure 6.12(a) of Section 6.3.1.3 and Figure 6.17 of Section 6.3.2.1, we observe that a significant performance degradation may occur if the DAF-aided system dispenses with either the CUS or the APC scheme. By contrast, only a negligible performance loss is imposed, when the DDF-aided system dispenses with the APC schemes rather than with the CUS scheme. Additionally, the CUS scheme of Section 6.3.2 is carried out by selecting the cooperating MSs roaming in the area closest to the optimum locations which may be determined offline, i.e. before initiating a voice call or data session. By contrast, the APC scheme of Section 6.3.2 may impose a relatively high real-time complexity, when calculating the optimum power control arrangement based on the current location of the activated RS. Hence, for the sake of minimizing the complexity imposed by the cooperative resource allocation process, the DDF-aided system employing the CUS scheme may dispense with APC, simply opting for the equal-power allocation arrangement at the expense of a moderate performance loss. In contrast to the DDF scheme, the DAF-aided system has to tolerate a high BER performance degradation, if it dispenses with the APC scheme. It is also noteworthy that in contrast to the DAF-aided cooperative system, the DDF-assisted scheme employing neither the CUS nor the APC may be outperformed by the classic non-cooperative system, as observed in Figure 6.14, which is a consequence of its sensitivity to the quality of the source-relay link.

6.4.2 Joint CPS and CUS Scheme for the Cellular Uplink Using APC

Each cooperative cellular uplink considered in this report up to now employs either the DAF or the DDF. As argued in the context of Figure 6.20, they both have their desirable RS area, when the

CUS is employed. Generally speaking, the neighbourhood of the BS and that of the source MS are the specific areas, where the RS should be activated for the DAF- and DDF-aided scenarios, respectively, again as dicussed in Sections 6.3.1 and 6.3.2. Thus, often no available cooperating MS is roaming in the desirable RS location area, and hence a performance loss may be imposed by selecting a cooperating MS roaming far away from the optimum RS location. Furthermore, although the DDF-aided system exhibits a better performance than its DAF-aided counterpart in the presence of a high source-relay link quality, the former may be outperformed by the latter, as the quality of the source-relay link degrades despite imposing a higher overall system complexity. On the other hand, from our comparison of the DAF- and DDF-aided cooperative systems in Section 6.4.1, we realized that the two above-mentioned relaying mechanisms have complementary characteristics, reflected for example, by their distinct optimum cooperative resource allocations. In the light of the complementarity of the two relaying schemes, a more flexible cooperative scenario can be created, where either the DAF or DDF schemes are activated in the interest of enhancing the achievable performance of the cooperative system, while maintaining a moderate complexity. In contrast to the conventional cooperative system employing a single cooperative mechanism, the cooperating MSs roaming in different areas between the source MS and the BS may be activated and the relay schemes employed by each activated RSs may be adaptively selected, for the sake of achieving the best possible performance.

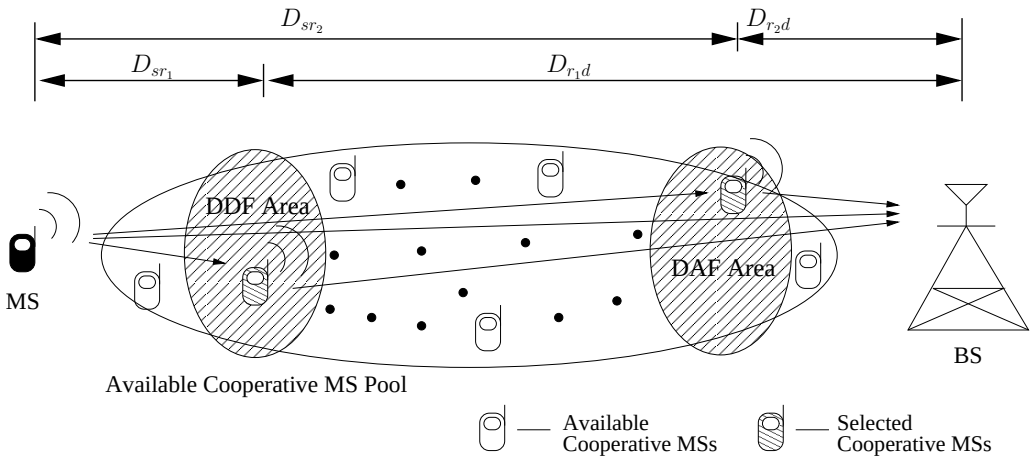

Figure 6.20: Cooperation-aided uplink systems using the joint CPS and CUS scheme.

For the sake of simplicity, let us now consider the hybrid cooperative cellular uplink employing the joint CPS and CUS scheme, as portrayed in Figure 6.20, where $M_r = 2$ cooperating MSs roaming in the preferred DDF- and the DAF-RS-area are activated, in order to forward the source MS's information to the BS. The particular cooperative protocol employed by the activated RSs is determined according to the specific area which they happen to be situated in. In order to make the most of the complementarity of the DAF and DDF schemes, it may be assumed that one of the cooperating MSs is activated in the preferred area of the DAF-RS, while the other from the 'DDF-area', although naturally, there may be more than one cooperating MSs roaming within a specific desirable area. Finally, under the assumption that the first selected cooperating MS is roaming in the 'DDF-area', while the second one is roaming in the 'DAF-area', the MRC scheme employed by the BS, which combines the signals received from the source MS and the cooperating MSs, can

be expressed as:

$$y = a_0(y_{sd}[n-1])^* y_{sd}[n] + \sum_{m=1}^{2} a_m(y_{r_m d}[n+mL_f-1])^* y_{r_m d}[n+mL_f], \tag{6.109}$$

where L_f is the length of the transmission packet, while the coefficients a_0 and $a_m, (m=1,2)$ are given by:

$$a_0 = a_1 = \frac{1}{N_0}, \tag{6.110}$$

and

$$a_2 = \frac{P_s\sigma_{sr_2}^2 + N_0}{N_0(P_s\sigma_{sr_2}^2 + P_{r_2}\sigma_{r_2 d}^2 + N_0)}. \tag{6.111}$$

In order to determine the optimum RS areas for the hybrid cooperative system employing $M_r = 2$ cooperating users, the worst case BER expression will be first derived in a similar manner to that derived for the DDF-aided system of Section 6.2.1 in our following discourse.

First of all, let us define the scenario Φ_1 as the situation, when the cooperating MS employing the DDF scheme perfectly recovers the information from the source MS and then transmits the differentially remodulated signal to the BS, which is formulated as:

$$\Phi_1 \triangleq \{P_{r_1} \neq 0\}. \tag{6.112}$$

By contrast, the senario Φ_2 is defined as the situation, when the cooperating MS using the DDF scheme fails to correctly decode the signal received from the source MS and keeps silent during the relay phase, which can be formulated as:

$$\Phi_2 \triangleq \{P_{r_1} = 0\}. \tag{6.113}$$

Then, based on the differentially encoded conditional BER of Eq. (6.59) invoked in Section 6.2.2, the unconditional BER observed at the BS is the scenario of Φ_1 can be expressed as:

$$P_{BER}^{\Phi_1} = \frac{1}{2^{2L}\pi}\int_{-\pi}^{\pi} f(a,b,L=3,\theta)\int_{-\infty}^{\infty} e^{-\alpha(\theta)\gamma_{\Phi_1}^b} p_{\gamma_{\Phi_1}^b}(\gamma)d\gamma d\theta, \tag{6.114}$$

$$= \frac{1}{2^{2L}\pi}\int_{-\pi}^{\pi} f(a,b,L=3,\theta)\mathcal{M}_{\gamma_{\Phi_1}^b}(\theta)d\theta, \tag{6.115}$$

where $\gamma_{\Phi_1}^b$ denotes the received SNR per bit after MRC combining, which can be written as:

$$\gamma_{\Phi_1}^b = \gamma_{sd}^b + \gamma_{r_1 d}^b + \gamma_{r_2 d}^d. \tag{6.116}$$

Then, the joint MGF, $\mathcal{M}_{\gamma_{\Phi_1}^b}(\theta)$, of the received SNR per bit experienced at the BS in the scenario Φ_1 is expressed as:

$$\mathcal{M}_{\gamma_{\Phi_1}^b}(\theta) = \int_{-\infty}^{\infty} e^{-\alpha(\theta)\gamma_{\Phi_1}^b} p_{\gamma_{\Phi_1}^b}(\gamma)d\gamma, \tag{6.117}$$

$$= \int_{-\infty}^{\infty}\int_{-\infty}^{\infty}\int_{-\infty}^{\infty} e^{-\alpha(\theta)(\gamma_{sd}^b+\gamma_{r_1 d}^b+\gamma_{r_2 d}^b)} \times$$

$$p_{\gamma_{sd}^b}(\gamma_{sd}) p_{\gamma_{r_1 d}^b}(\gamma_{r_1 d}) p_{\gamma_{r_2 d}^b}(\gamma_{r_2 d}) d\gamma_{sd} d\gamma_{r_1 d} d\gamma_{r_2 d}, \tag{6.118}$$

$$= \mathcal{M}_{\gamma_{sd}^b}(\theta)\mathcal{M}_{\gamma_{r_1 d}^b}(\theta)\mathcal{M}_{\gamma_{r_2 d}^b}(\theta), \tag{6.119}$$

where we have:

$$\mathcal{M}_{\gamma^b_{sd}}(\theta) = \frac{N_0}{N_0+\alpha(\theta)P_s\sigma^2_{sd}}, \tag{6.120}$$

$$\mathcal{M}_{\gamma^b_{r_1d}}(\theta) = \frac{N_0}{N_0+\alpha(\theta)P_{r_1}\sigma^2_{r_1d}}, \tag{6.121}$$

$$\mathcal{M}_{\gamma^b_{r_2d}}(\theta) = \frac{1}{1+k_{sr_2}(\theta)}\left(1+\frac{k_{sr_2}(\theta)}{1+k_{sr_2}(\theta)}\frac{P_s\sigma^2_{sr_2}+N_0}{P_{r_2}}\frac{1}{\sigma^2_{r_2d}}Z_{r_2}(\theta)\right), \tag{6.122}$$

and $k_{r_2d}(\theta)$ and $Z_{r_2}(\theta)$ are given by Eqs. (6.34) and (6.35), respectively.

In parallel, the unconditional BER corresponding to the scenario Φ_2 can be formulated as:

$$P^{\Phi_2}_{BER} = \frac{1}{2^{2L}\pi}\int_{-\pi}^{\pi} f(a,b,L=2,\theta)\int_{-\infty}^{\infty} e^{-\alpha(\theta)\gamma^b_{\Phi_2}} p_{\gamma^b_{\Phi_2}}(\gamma)d\gamma d\theta, \tag{6.123}$$

$$= \frac{1}{2^{2L}\pi}\int_{-\pi}^{\pi} f(a,b,L=2,\theta)\mathcal{M}_{\gamma^b_{\Phi_2}}(\theta)d\theta, \tag{6.124}$$

where $\gamma^b_{\Phi_2}$ denotes the received SNR per bit after MRC combining, which can be expressed as:

$$\gamma^b_{\Phi_2} = \gamma^b_{sd} + \gamma^d_{r_2d}, \tag{6.125}$$

and hence the MGF of the received SNR per bit recorded at the BS for the scenario Φ_2 is written as:

$$\mathcal{M}_{\gamma^b_{\Phi_2}}(\theta) = \int_{-\infty}^{\infty} e^{-\alpha(\theta)\gamma^b_{\Phi_2}} p_{\gamma^b_{\Phi_2}}(\gamma)d\gamma, \tag{6.126}$$

$$= \int_{-\infty}^{\infty}\int_{-\infty}^{\infty} e^{-\alpha(\theta)(\gamma^b_{sd}+\gamma^b_{r_2d})} p_{\gamma^b_{sd}}(\gamma_{sd}) p_{\gamma^b_{r_2d}}(\gamma_{r_2d})d\gamma_{sd}d\gamma_{r_2d}, \tag{6.127}$$

$$= \mathcal{M}_{\gamma^b_{sd}}(\theta)\mathcal{M}_{\gamma^b_{r_2d}}(\theta), \tag{6.128}$$

where $\mathcal{M}_{\gamma^b_{sd}}(\theta)$ and $\mathcal{M}_{\gamma^b_{r_2d}}(\theta)$ are given by Eqs. (6.120) and (6.122), respectively.

Finally, based on the worst-case packet loss ratio of $P_{PLR_1,upper}$ given by Eq. (6.52), the average end-to-end BER upper bound, $P^{CPS}_{BER,upper}$, is obtained by the summation of the average BERs of two scenarios as:

$$P^{CPS}_{BER,upper} = (1-P_{PLR_1,upper})P^{\Phi_1}_{BER} + P_{PLR_1,upper}P^{\Phi_2}_{BER}. \tag{6.129}$$

Hence, when using the minimum BER criterion, the desirable RS area can be located by finding the globally optimum RS locations using the iterative power-versus-RS-location optimization process of Sections 6.3.2 or 6.3.2. Considering the $M_r = 2$ scenario as an example, the globally optimum power and distance allocation arrangements are summarized in Table 6.6 under the assumption that the first cooperating MS is activated in the DDF mode. As expected, the figures shown in Table 6.6 reveal that the 'DDF-area' and the 'DAF-area' are still located in the vicinity of the source MS and the BS, respectively. Additionally, the majority of the total transmit power, i.e. about 70%, should be allocated to the source MS, while $\frac{2}{3}$ of the remaining power should be assigned to the cooperating MS roaming in the 'DDF-area'.

The BER performance of the hybrid cooperative cellular uplink, where $M_r = 2$ out of $\mathcal{P}_{cand} = 8$ cooperating MSs are activated, is portrayed in comparison to that of its DAF- and DDF-aided counterparts in Figure 6.21. Remarkably, as demonstrated by Figure 6.21, the hybrid cooperative

Optimized Cooperative Resource Allocation for the Hybrid Cooperative Uplink			
M_r	P/N_0 (dB)	$[P_s,\ P_{r_1},\cdots\ P_{r_{M_r}}]$	$[d_1,\ d_2\cdots\ d_{M_r}]$
2	10	[0.702, 0.202, 0.096]	[0.26, 0.86]
	20	[0.702, 0.202, 0.096]	[0.31, 0.86]
	30	[0.702, 0.202, 0.096]	[0.31, 0.91]

Table 6.6: Cooperative Resource Allocation for the Hybrid Cooperative Uplink

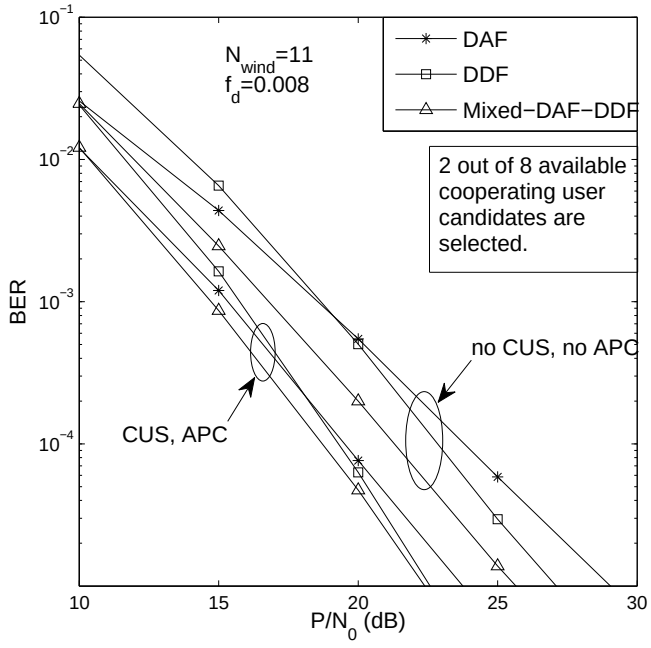

Figure 6.21: Performance improvement by the joint CPS and CUS for the DQPSK modulated user-cooperative cellular uplink employing the MSDSD, where 2 out of 8 cooperating user candidates are activated. All other system parameters are summarized in Table 6.3.

system outperforms both the DAF- and DDF-aided systems, regardless of whether the joint-CPS-CUS-APC scheme is employed. These conclusions remain valid across a wide SNR range of our interest, although the performance advantage of the hybrid scheme over the latter two systems decreases in the context of the joint-CPS-CUS-APC scheme. Furthermore, as the SNR increases, the DDF-aided system is expected to become superior to the other two systems, since the DDF-aided system performs best, when error-free transmissions can be assumed between the source MS and the RS. By contrast, if the SNR is low, the DAF-aided system performs best amongst the three. In addition to the performance advantage of the joint-CPS-CUS-APC-aided hybrid cooperative system, the overall system complexity becomes moderate in comparison to that of DDF-aided system, since only half of the activated MSs have to decode and re-encode the received signal prior to forwarding it. Therefore, the proposed hybrid cooperative system employing the joint-CPS-CUS-APC scheme is capable of achieving an attractive performance, despite maintaining a moderate overall system complexity.

Comparison between DAF- and DDF-Aided Uplinks			
	DAF-Aided Uplink	**DDF-Aided Uplink**	**References**
Overall Performance	Better when SR link quality is poor	Better when SR link quality is good	Fig. 6.19
Overall Complexity	Relatively low, no decoding at RSs	Relatively high, decoding and re-encoding at RSs	
Performance's Sensitivity to Source-Relay Link Quality	Relatively moderate	Strong	Figs. 5.19 5.23 , 6.19
Performance's Sensitivity to Packet Length L_f	Insensitive	Strong without CUS, minor with CUS	Figs. 6.14, 6.16
Desirable RS Locations	Near the BS	Near the source MS	Table 6.5
Desirable Transmit Power for the Source MS	About 88% of the total power	About 60% of the total power	Table 6.5
Worst Case Performance (Inappropriate Resource Allocation)	Slightly better than the non-cooperative system	Significantly worse than the non-cooperative system	Figs. 6.9, 6.14
Importance of CUS and APC	Equally important	CUS is significantly more important	Figs. 6.12(a), 6.17

Table 6.7: Comparison between the DAF- and DDF-aided cooperative cellular uplinks

6.5 Chapter Conclusions

In this chapter, CUS schemes and APC schemes designed for both the DAF- and DDF-aided cooperative systems were investigated based on our theoretical performance analysis. Significant performance gains can be achieved with the aid of the optimized resouce allocation arrangements for both the DAF- and DDF-aided systems. Due to the different levels of sensitivity to the quality of the source-relay link, the optimum resouce allocation arrangements corresponding to the two above-mentioned systems were shown to be quite different. Specifically, it is desirable that the activated cooperating MSs are roaming in the vicinity of the source MS for the DDF-aided system, while the cooperating MS roaming in the neighborhood of the BS are prefered for its DAF-aided counterpart. In comparison to the former system, a larger portion of the total transmit power should be allocated to the source MS in the context of a DAF-aided system. Apart from achieving an enhanced BER performance, the complexity imposed by the MSDSD of Chapter 5 may also be significantly reduced by employing the CUS and APC schemes, even in the context of rapid fading channels. Based on the simulation results throughout this chapter, the natures of the DAF- and DDF-aided systems are summarized and compared in Table 6.7. Furthermore, in order to make the most of the complementarity of the two above-mentioned cooperative systems, a more flexible resouce-optimized adaptive hybrid cooperation-aided system was proposed in this chapter, where the cooperative protocol employed by a specific cooperating MS may also be adaptively selected in the interest of achieving the best possible BER performance.

Finally, we quantitatively summarize and compare the performance gains achieved by the DAF-aided, the DDF-aided as well as the hybrid cooperative systems over the direct-transmission based system in Table 6.8, based on the simulation results obtained throughout the chapter. Observe in Table 6.8 that given a target BER of 10^{-3}, the DAF-aided cooperative system is capable of achiev-

Performance Gains Achieved by Various Two-Relay-Aided Differential Cooperative Systems With and Without Cooperative Resource Optimization					
Target BER	**System Type**	**Power Control** $[P_s, P_{r_1}, P_{r_2}]$	**Relay Selection** $[d_{r_1}, d_{r_2}]$	**SNR (dB)**	**Gain (dB)**
10^{-3}	direct transmission	N/A	N/A	27.3	-
	DAF-Aided	[0.33, 0.33, 0.33]	[0.5,0.5]	18.8	8.5
	Cooperative System	[0.76, 0.2, 0.04]	[0.81, 0.9]	15.4	11.9
	DDF-Aided	[0.33, 0.33, 0.33]	[0.5,0.5]	18.9	8.4
	Cooperative system	[0.602, 0.202, 0.196]	[0.29, 0.29]	15.8	11.5
	Hybrid DAF/DDF	[0.33, 0.33, 0.33]	[0.5,0.5]	16.9	10.4
	Cooperative System	[0.702, 0.202, 0.096]	[0.28, 0.86]	14.9	12.4
10^{-5}	direct transmission	N/A	N/A	50	-
	DAF-Aided	[0.33, 0.33, 0.33]	[0.5,0.5]	29	21
	Cooperative System	[0.76, 0.2, 0.04]	[0.82, 0.91]	23.7	26.3
	DDF-Aided	[0.33, 0.33, 0.33]	[0.5,0.5]	27	23
	Cooperative system	[0.602, 0.202, 0.196]	[0.31, 0.31]	22.5	27.5
	Hybrid DAF/DDF	[0.33, 0.33, 0.33]	[0.5,0.5]	25.7	24.3
	Cooperative System	[0.702, 0.202, 0.096]	[0.31, 0.86]	22.3	27.7

Table 6.8: Summary of the resource-optimized cooperative systems investigated in Chapter 5.

ing a slightly higher performance gain than that attained by its DDF-aided counterpart, regardless of the employment of the optimized resource allocation. However, given a target BER of 10^{-5}, the latter becomes capable of achieving performance gains of 2 dB and 1.2 dB over the former for the non-optimized and optimized resource allocation arrangements, respectively, as seen in Table 6.8. Furthermore, amongst the three types of cooperative systems investigated in this chapter, the adaptive hybrid DAF/DDF cooperative system performs the best for a wide range of SNRs. Remarkably, as observed in Table 6.8, the hybrid cooperative system is capable of achieving performance gains over its direct-transmission based counterpart, which are as high as 12.4 dB and 27.7 dB for the BER targets of 10^{-3} and 10^{-5}, respectively, when the optimized resource allocation is employed.

Chapter 7

The Near-Capacity Differentially Modulated Cooperative Cellular Uplink

7.1 Introduction

In point-to-point communication systems using a single-antenna or co-located multiple antennas, it is feasible to achieve a high spectral efficiency by approaching Shannon's capacity limit with the aid of channel coding, as argued in Chapter 3. However, in contrast to the well-understood limitations of point-to-point single-user transmissions, researchers are only beginning to understand the fundamental performance limits of wireless multiuser networks, such as, for example the cooperative cellular uplink considered in Chapters 5 and 6. To be more specific, in the scenarios of the uncoded DAF as well as DDF cooperative cellular uplinks, the best achievable BER performance can be approached by optimizing both the power control and the cooperating user selection, as discussed in Chapters 6. Naturally, the resultant cooperative system's performance is expected to be better than that of non-cooperative transmission. The attainable transmit diveristy gains as well as path loss reduction achieved by the cooperative relay-aided system were considered in Chapter 6, which translate into substantially enhanced robustness against fading for a given transmit power, or into a significantly reduced transmit power requirement for the same BER performance. However, the transmit diversity gains or cooperative diversity gains promised by the cooperative system considered are actually achieved at the cost of suffering a significant multiplexing loss compared to direct transmissions, which is imposed by the half-duplex communications of practical transceivers. More explicitly, realistic transceivers cannot transmit and receive simultaneously, because at a typical transmit power of say 0dB and receiver-sensitivity of -100dBm the transmit-power leakage imposed by the slightest power-amplifer non-linearity would leak into the receiver's Automatic Gain Control (AGC) circuit and would saturate it. Hence, the saturated AGC would become desensitized against low-power received signals. Furthermore, the cooperative diversity gains achieved by the relay-aided system over its direct-transmission based counterpart may become modest in practical channel coded scenarios, where the interleaving and channel coding gains dominate. Therefore, when a cooperative wireless communication system is designed to ap-

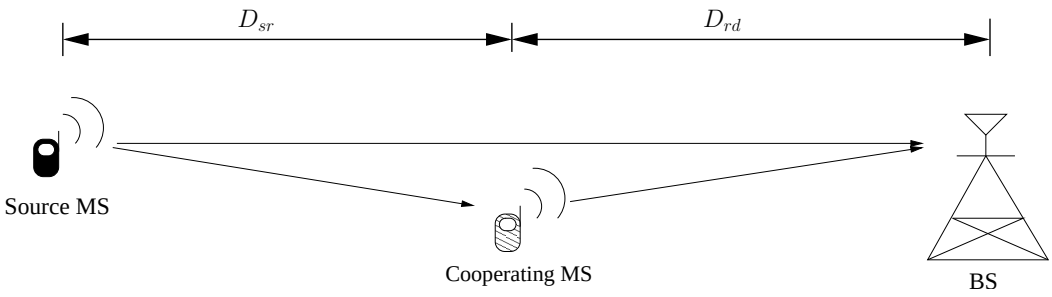

Figure 7.1: Single-relay-aided cooperative cellular uplink.

proach the maximum achievable spectral efficiency by taking the cooperation-induced multiplexing loss into account, it is not obvious whether or not the repetition-based relay-aided system becomes superior to its direct-transmission based counterpart, especially when advanced channel coding techniques are employed. In other words, in the interest of achieving a high spectral efficiency, we have to answer the grave fundamental question: is it worth introducing cooperative mechanisms into the development of wireless networks, such as the cellular voice and data networks?

7.1.1 System Architecture and Channel Model

7.1.1.1 System Model

Since the realistic condition of having an imperfect source-to-relay communication link is taken into account, the predominant DF as well as AF protocols employed, may suffer from potential error propagation and noise-enhancement, respectively, as observed in Chapters 5 and 6 where no channel coding was used. Fortunately, thanks to the advances of channel coding, well-designed channel coded DF schemes are capable of guaranteeing near-error-free SR transmissions without noise-enhancement, which in turn typically results in a superior performance in contrast to their AF-aided counterparts. In this context, only the differentially encoded and non-coherently detected DF-aided cooperative system dispensing with channel estimation will be investigated in the context of channel coding in this chapter. Naturally, in this scenario a more advanced channel-coded RS is required. Examples of channel coded cooperative system designs may be found in [134, 135], although these contributions used coherent detection. To be consistent with the system model employed in Chapters 5 and 6, the differentially modulated TDMA cellular uplink is considered without any loss of generality, where no ICR estimation is required. For the sake of simplicity, we consider a single-relay-assisted scenario, where only one cooperating MS is activated in order to decode and re-encode the signal received from the source MS prior to forwarding the signal to the BS. Again, we simply assume the employment of a single antenna for each terminal, owing to the cost- and size-constraints of portable transceivers. Although we revealed in Chapter 6 that an optimized transmit power control and RS selection scheme may result in an enhanced end-to-end BER performance for the uncoded DDF-aided system, we simply assume here that the total transmit power is equally divided between the source MS and the single cooperating RS, which is assumed to be located half-way between the source MS and the BS, as depicted in Figure 7.1. This is because the emphasis in this chapter is on investigating the achievable network capacity

of a general repetition-coded cooperative scenario and on techniques of approaching it. More specifically, for the sake of analytical tractability, we simply assume that the sum of the normalized distances D_{sr} between the source MS and the RS, and that between the RS and the destination BS, which is represented by D_{rd}, is equal to the normalized distance D_{sd} between the source MS and the BS. Naturally, the normalized SD-distance is equal to unity. As a result, observe in Figure 7.1 that we have:

$$D_{sr} = D_{rd} = \frac{1}{2} D_{sd} = 1. \tag{7.1}$$

Furthermore, as seen in Eq. (6.3), the normalized average power $\sigma_{i,j}^2$ at the output of the channel is inversely proportional to the inter-node distance $D_{i,j}$, which is rewritten as follows:

$$\sigma_{i,j}^2 = D_{i,j}^{-v}, \quad i, j \in \{s, r, d\}, \tag{7.2}$$

where v denotes the path-loss exponent [2] and the subscripts s, r and d represent the source, relay and destination, respectively. Additionally, under the assumption of having a total transmit power of P and an equal-power-allocation amongst the source and cooperating MSs, we may express the associated power contraint as:

$$P_s = P_r = \frac{1}{2} P, \tag{7.3}$$

where P_s and P_r are the transmit power of the source and cooperating MSs, respectively.

7.1.1.2 Channel Model

Throughout this chapter we assume that the complex-valued basedband signals undergo Rayleigh fading, which is modelled by multiplying the transmitted signal by a complex-valued Gaussian random variable. In order to provide a good approximation for TDMA-based cooperative systems and to facilitate the study of the non-coherent detection-based channel capacity, we consider a block-fading Rayleigh channel, where the fading coefficients are assumed to change in an i.i.d. manner from block to block. This assumption allows us to focus our attention on a single fading block [136,137]. On the other hand, instead of employing the *standard block-fading channel*, where the fading coefficient remains constant over the duration of several consecutive symbol periods, we consider here a *time-selective block-fading model* [138], which includes the former as a special case. In the time-selective block-fading channel model considered, the channel's envelope exhibits correlation within a transmission block according to the Doppler frequency induced by the relative movement of the tranceivers.

Consider a single-antenna-assisted point-to-point transmission scheme communicating over a block-fading channel, which exhibits a correlated envelope for the duration of T_b consecutive symbols. Then, the received signal may be formulated as:

$$\mathbf{y} = \mathbf{S}_d \mathbf{h} + \mathbf{w}, \tag{7.4}$$

where we have

$$\mathbf{y} = \left[y_1, y_2, \cdots, y_{T_b}\right]^T, \tag{7.5}$$

$$\mathbf{h} = \left[h_1, h_2, \cdots, h_{T_b}\right]^T, \tag{7.6}$$

and

$$\mathbf{w} = \left[w_1,\ w_2, \cdots, w_{T_b}\right]^T \tag{7.7}$$

representing the received signal column vector, the fading coefficient column vector obeying a complex-valued Gaussian distribution $\mathcal{CN}(0, \sigma_h^2)$ and the Gaussian noise column vector having a distribution of $\mathcal{CN}(0, 2\sigma_w^2)$, respectively. The diagonal elements of the matrix $\mathbf{S}_d$ in Eq.(7.4) may be expressed as:

$$\mathbf{S}_d = \text{diag}\{\mathbf{s}\} = \begin{bmatrix} s_1 & 0 & \cdots & 0 \\ 0 & s_2 & \cdots & 0 \\ \vdots & \vdots & \ddots & \vdots \\ 0 & 0 & \cdots & s_{T_b} \end{bmatrix}, \tag{7.8}$$

where we have

$$\mathbf{s} = \left[s_1,\ s_2, \cdots, s_{T_b}\right]^T, \tag{7.9}$$

which represents the T_b consecutively transmitted signals within a fading block. Furthermore, in the cooperative communication scenario of Figure 7.1, the normalized channel fading variance σ_h^2 of each link was formulated in Eq.(7.2) by taking the path-loss into account. Given the assumption of Rayleigh fading, $\mathbf{h}$ is a zero-mean complex-valued Gaussian vector with a $(T_b \times T_b)$-element covariance matrix Σ_h, which may be written as:

$$\begin{aligned} \Sigma_h =& \mathcal{E}\{\mathbf{h}\mathbf{h}^H\} \\ =& \sigma_h^2 \cdot \begin{bmatrix} \varphi^t[0] & \varphi^t[1] & \cdots & \varphi^t[T_b-1] \\ \varphi^t[-1] & \varphi^t[0] & \cdots & \varphi^t[T_b-2] \\ \vdots & \vdots & \ddots & \vdots \\ \varphi^t[1-T_b] & \varphi^t[2-T_b] & \cdots & \varphi^t[0] \end{bmatrix}, \end{aligned} \tag{7.10}$$

where $\varphi^t[\kappa]$ represents the channel's autocorrelation function, which can be expressed as:

$$\varphi^t[\kappa] \triangleq \mathcal{E}\{h[n+\kappa]h^*[n]\} \tag{7.11}$$

$$= J_0(2\pi f_d \kappa), \tag{7.12}$$

with $J_0(\cdot)$ denoting the zeroth-order Bessel function of the first kind and as usual, f_d represents the normalized Doppler frequency.

7.1.2 Chapter Contributions and Outline

Against the afore-mentioned background, the main objectives of this chapter are to investigate the necessity of introducing the cooperative mechanisms of Figure 7.1 into wireless networks, such as cellular voice and data networks. This design dilemma may be approached both from a pure capacity perspective and from the practical perspective of approaching the Discrete-input Continuous-output Memoryless Channel (DCMC) capacity of the cooperative network. More specifically, the novel contributions of this chapter are as follows:

- *From a pure capacity perspective, we answer the grave fundamental dilemma, whether it is worth incorporating cooperative mechanisms into wireless networks.*

- *A novel Irregular Distributed Hybrid Concatenated Differential (Ir-DHCD) coding scheme is proposed for the DDF cooperative system, in order to maximize the system's spectral efficiency.*
- *Based on our low-complexity near-capacity design criterion, we propose a practical framework of designing an Ir-DHCD-assisted cooperative system, which is capable of performing close to the network's corresponding non-coherent DCMC capacity.*
- *In order to further reduce the complexity imposed, while approaching the cooperative network's DCMC capacity, the so-called adaptive-window-duration based SISO iterative MSDSD scheme is proposed.*

The remainder of this chapter is organized as follows. The fundamemtal performance limits of the non-coherent detection aided direct-transmission based system will be first studied in Section 7.2, followed by the review of the MAP-based SISO MSDSD in Section 7.3, which is capable of achieving a near-capacity performance at a low complexity. In order to answer the previously-mentioned question related to the ultimate spectral efficiency of the repetition-based cooperative relay-aided system, the fundamental performance limits of the DDF-aided cooperative system will be investigated in Section 7.4.1 in comparison to those of its direct-transmission based counterpart. Then, based on the novel Ir-DHCD coding scheme of Section 7.4.2 contrived for the DDF-aided cooperative system, a practical framework designed for approaching the DCMC capacity of the cooperative network will be proposed in Section 7.4.3, which is - naturally - different from that of point-to-point links. Hence, Section 7.4.4 will demonstrate that the cooperative scheme designed is capable of performing close to the corresponding network's DCMC capacity. Finally, our concluding remarks will be provided in Section 7.5.

7.2 Channel Capacity of Non-coherent Detectors

Since one of our goals in this chapter is to compare the maximum achievable spectral efficiency of the DDF-aided cooperative system and that of its differentially modulated direct-transmission based counterpart as discussed in Section 7.1, the corresponding fundamental performance limits have to be investigated in the first place. Hence, in this section we first focus our attention on the non-coherent DCMC capacity of the classic single-antenna-assisted point-to-point communication scenario, based on which the non-coherent DCMC network capacity of the DDF-aided cooperative system will be studied in Section 7.4.1.

Recall the conditional PDF of the received signal vector from Eq. (5.14), which was used for the derivation of the ML metric of the multiple-symbol differential detection (MSDD) scheme discussed in Section 5.2.1. The PDF of the received signal vector $\mathbf{y}$ in Eq. (7.5) was conditioned on the transmitted signal vector $\mathbf{s}$ of Eq. (7.9), which may be readily expressed as:

$$p(\mathbf{y}|\mathbf{s}) = \frac{\exp(-\mathbf{y}^H \Psi^{-1} \mathbf{y})}{\det(\pi\Psi)}, \tag{7.13}$$

where we have

$$\Psi = \mathcal{E}\{\mathbf{y}\mathbf{y}^H|\mathbf{s}\} \tag{7.14}$$

$$= \mathbf{S}_d \Sigma_h \mathbf{S}_d^H + 2\sigma_w^2 \mathbf{I}_{T_b} \tag{7.15}$$

with $\mathbf{I}_{T_b}$ denoting the $(T_b \times T_b)$-element identity matrix.

Since differentially encoded modulation schemes, such as DQPSK, are assumed to be employed at MSs, and each element s_i of the transmitted signal vector $\mathbf{s}$ is chosen independently from a finite constellation set $\mathcal{M}_c$ with equal probabilities, the non-coherent DCMC capacity can be expressed as a function of the SNR as follows:

$$C(\text{SNR}) = H(\mathbf{y}) - H(\mathbf{y}|\mathbf{s}), \tag{7.16}$$

where H represents the differential entropy [139] of a random variable $\mathbf{x}$ defined as $H(\mathbf{x}) = -\int p(\mathbf{x}) \log_2 p(\mathbf{x}) d\mathbf{x}$, with $p(\cdot)$ denoting the corresponding PDF. According to [139], the differential entropy $H(\mathbf{y}|\mathbf{s})$ may be readily calculated as follows:

$$H(\mathbf{y}|\mathbf{s}) = -\int p(\mathbf{y}|\mathbf{s}) \ln p(\mathbf{y}|\mathbf{s}) d\mathbf{y} \tag{7.17}$$

$$= -\int p(\mathbf{y}|\mathbf{s}) \Big[-\mathbf{y}^H \Psi^{-1} \mathbf{y} - \ln \det(\pi\Psi) \Big] d\mathbf{y} \tag{7.18}$$

$$= \mathcal{E}\left\{ \sum_{i,j} \mathbf{y}_i^* (\Psi^{-1})_{i,j} \mathbf{y}_j \right\} + \ln \det(\pi\Psi) \tag{7.19}$$

$$= \mathcal{E}\left\{ \sum_{i,j} \mathbf{y}_i^* \mathbf{y}_j (\Psi^{-1})_{i,j} \right\} + \ln \det(\pi\Psi) \tag{7.20}$$

$$= \sum_{i,j} \mathcal{E}\left\{ \mathbf{y}_j \mathbf{y}_i^* \right\} (\Psi^{-1})_{i,j} + \ln \det(\pi\Psi) \tag{7.21}$$

$$= \sum_{j} \sum_{i} \Psi_{j,i} (\Psi^{-1})_{i,j} + \ln \det(\pi\Psi) \tag{7.22}$$

$$= \sum_{j} (\Psi\Psi^{-1})_{jj} + \ln \det(\pi\Psi) \tag{7.23}$$

$$= T_b + \ln \det(\pi\Psi) \tag{7.24}$$

$$= \ln \det(\pi \mathrm{e} \Psi) \qquad \textit{nats} \tag{7.25}$$

$$= \log \det(\pi \mathrm{e} \Psi) \qquad \textit{bits}. \tag{7.26}$$

On the other hand, the entropy $H(\mathbf{y})$ of the continuous-valued faded and noise-contaminated received signal vector $\mathbf{y}$ cannot be evaluated in a closed form. When the fading block size T_b over which the fading envelope is assumed to be correlated is limited, a practical approach to the numerical evaluation of $H(\mathbf{y})$ is to carry out Monte-Carlo integration as follows [140]:

$$H(\mathbf{y}) = -\int p(\mathbf{y}) \log p(\mathbf{y}) d\mathbf{y} \tag{7.27}$$

$$= -\mathcal{E}\left\{ \log_2 \left(\frac{1}{M_c^{T_b} \det(\pi\Psi)} \sum_{\check{\mathbf{s}} \in \chi} \exp\left(-\mathbf{y}^H \Psi^{-1} \mathbf{y} \right) \right) \right\}, \tag{7.28}$$

where χ is the set of all $M_c^{T_b}$ hypothetically transmitted symbol vectors $\check{\mathbf{s}}$. The expectation value in Eq. (7.28) is taken with both respect to different CIR realizations and to the noise.

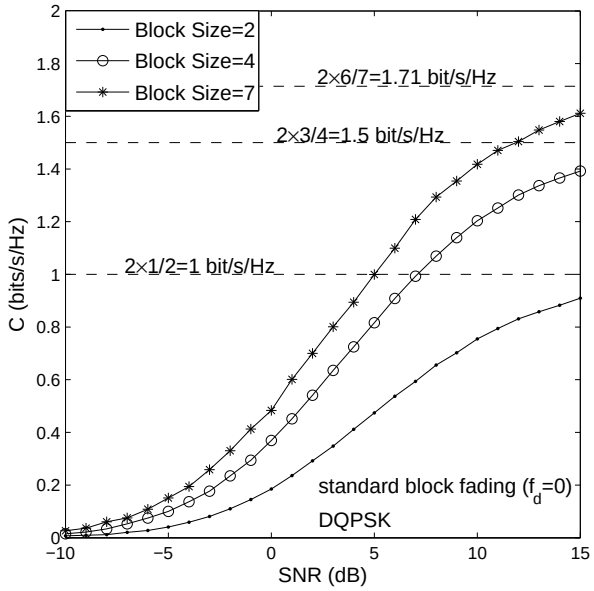

Figure 7.2: Non-coherent DCMC capacity of the single-input single-output standard block-fading channel ($f_d = 0$) for different block sizes of $T_b = 2,\ 4$ and 7.

The non-coherent DCMC capacity of the standard block-fading channel computed using the DQPSK modulation scheme is plotted in Figure 7.2 for various fading block sizes of $T_b = 2,\ 4$ and 7. As observed in Figure 7.2, all the three DCMC capacity curves associated with different values of T_b rise as the SNR increases and they are expected to saturate, when the SNR reaches a certain value, although this is not explicitly shown in the figure. Moreover, a larger fading block size T_b results in a higher DCMC capacity over a wide range of SNRs, while the capacity difference between the scenarios of $T_b = 2,\ 4$ and 7 becomes increasingly wider, as the SNR increases. Nonetheless, their capacity difference above the saturation-SNR remains constant. In other words, although an identical differential modulation scheme (DQPK) is employed, the maximum achievable spectral efficiency associated with a sufficiently high SNR is dependent on the fading block size T_b. This is not unexpected, since the differential signaling process commences by transmitting a reference symbol for each fading block, as argued earlier in Section 5.1.1.1, which does not contain any information. This reference symbol constitutes unexploited transmission overhead, i.e. redundancy, which hence imposes a diminishing capacity erosion, as T_b is increased. Thus, given a sufficiently high SNR, the maximum achievable bandwidth efficiency η_{max}, which can be calculated as:

$$\eta_{max} = \log_2 M_c \times (T_b - 1)/T_b, \quad \text{bits/s/Hz} \tag{7.29}$$

approaches that of the coherent detection aided transmission scheme, as the fading block size T_b increases towards infinity.

On the other hand, according to [138], the predictability of the channel is characterized by the rank Q of the channel's covariance matrix Σ_h formulated in Eq. (7.10). For example, the block-fading channel, where the fading envelope remains constant over the entire fading block is associated with the most predictable fading envelope, when the channel's covariance matrix has a rank of $Q = 1$. By contrast, the fading process has a finite differential entropy and becomes less

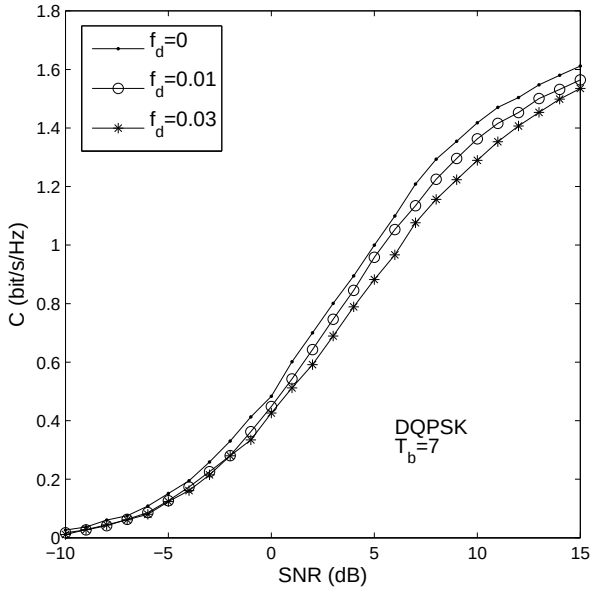

Figure 7.3: Non-coherent DCMC capacity of the single-input single-output time-selective block-fading channel for various normalized Doppler frequencies $(f_d = 0,\ 0.01,\ 0.03)$ and for $T_b = 7$. The fading envelope was correlated over each fading block, but changed in a random independent manner between fading blocks.

predictable, when we have $Q = T_b$. Figure 7.3 compares the non-coherent DCMC capacity of the time-selective block-fading channel computed from Eq. 7.16 for the DQPSK modulation scheme and for various normalized Doppler frequencies characterizing the correlation of the fading envelope exhibited over each fading block period. When we have an increased channel unpredictability owing to increased Doppler frequency, a capacity loss is observed in Figure 7.3. In addition, it is also shown in [138] that for a fixed value of Q, the non-coherent capacity approaches the coherent capacity, as T_b increases towards infinity. Hence, the observation of Figure 7.2 and 7.3 suggests that the non-coherent DCMC capacity of a time-seletive block-fading channel is dependent on both the fading block size T_b and the fading correlation over blocks characterized by the corresponding covariance matrix Σ_h.

7.3 Soft-Input Soft-Output MSDSD

For the sake of creating a near-capacity system design, the hard-input hard-output multiple-symbol differential sphere detector (MSDSD) of Chapter 5 is invoked here. The MSDSD is capable of approaching the optimum ML performance in a channel-uncoded scenario at a significantly lower complexity than the brute-force full-search based maximum-likelihood multiple-symbol differential detector (ML-MSDD). The MSDSD will be employed in the context of the well-known bit-interleaved coded modulation scheme using iterative detection (BICM-ID) [104], as portrayed in Figure 7.4. Hence, the MSDSD of Chapter 5 has to be modified in order to be able to process as well as to generate soft bit information at the its input and output, respectively, enabling the

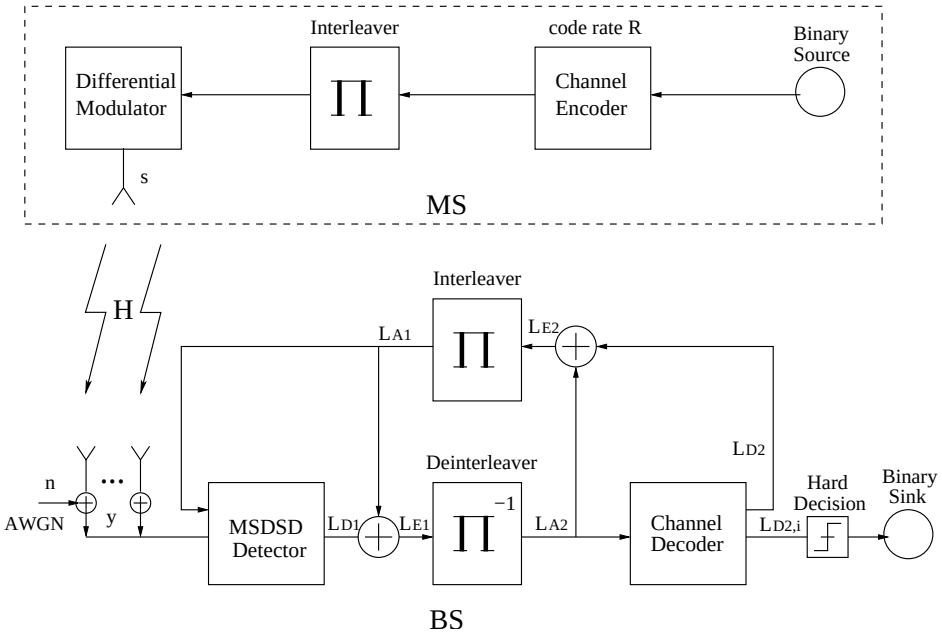

Figure 7.4: Schematic diagram of iterative MSDSD detection.

exchange of soft-information between the outer channel decoder and itself.

7.3.1 Soft-Input Processing [54]

Recall from Section 5.2 that the principle of the ML-MSDD or the MSDSD is to maximize the *a posteriori* probability $Pr(\mathbf{s}|\mathbf{y})$, which can be expressed as:

$$\hat{\mathbf{s}}_{ML} = \max_{\check{\mathbf{s}}\in\chi} Pr(\check{\mathbf{s}}|\mathbf{y}) \tag{7.30}$$

$$= \max_{\check{\mathbf{s}}\in\chi} \frac{p(\mathbf{y}|\check{\mathbf{s}})Pr(\check{\mathbf{s}})}{p(\mathbf{y})} \tag{7.31}$$

using Bayes' theorem [3, 6]. Due to the equiprobable nature of the transmitted symbol vectors $\mathbf{s}$ and the independence of $p(\mathbf{y})$ from $\mathbf{s}$, Eq. (7.31) may be further simplified, yielding the ML metric as:

$$\hat{\mathbf{s}}_{ML} = \max_{\check{\mathbf{s}}\in\chi} p(\mathbf{y}|\check{\mathbf{s}}). \tag{7.32}$$

When coupled with the outer channel decoder of Figure 7.4 in order to construct the iterative detection aided receiver, the inner detector is provided with soft-bit-information, i.e. with the LLRs, output by the outer decoder, which is regarded as the *a priori* knowledge of the transmitted symbol vector $\mathbf{s}$. For convenience, the above-mentioned *a priori* LLR $L_{A1}(x_k)$ of the kth bit of the bit vector $\mathbf{x}$, which was defined in Eq. (3.8) of Section 3.1.1.2 is rewritten here as:

$$L_{A1}(x_k) = \ln \frac{Pr(x_k = +1)}{Pr(x_k = -1)}. \tag{7.33}$$

Thus, the transmitted symbol vectors $\mathbf{s} \in \chi$ can no longer be considered as equiprobable by the inner MSDD detector of Figure 7.4. Consequently, bearing in mind the aim of maximizing the

a posteriori probability $Pr(\mathbf{s}|\mathbf{y})$ of the transmitted symbol vector $\mathbf{s}$, we refer to the proposed detector as the MAP-MSDD scheme, which can be implemented by incorporating the *a priori* soft information delivered by the channel decoder of Figure 7.4, based on the MAP metric expressed as follows:

$$\hat{\mathbf{s}}_{MAP} = \max_{\check{\mathbf{s}}\in\chi} Pr(\check{\mathbf{s}}|\mathbf{y}) \tag{7.34}$$

$$= \max_{\check{\mathbf{s}}\in\chi} p(\mathbf{y}|\check{\mathbf{s}})Pr(\check{\mathbf{s}}). \tag{7.35}$$

The *a priori* probability $Pr(\mathbf{s})$ of the transmitted symbol vector may be readily computed from the *a priori* LLRs of Eq. (7.33) by taking into account the binary-to-M_c-ary bit-to-symbol mapping scheme characterized as $\mathbf{s} = \text{map}(\mathbf{x})$, under the assumption that due to interleaving the coded symbols may indeed be considered to be independent.

Furthermore, the MAP metric of Eq. (7.35) may be reformulated by taking the logarithm of the right-hand-side as:

$$\hat{\mathbf{s}}_{MAP} = \max_{\check{\mathbf{s}}\in\chi} \{\ln\left(p(\mathbf{y}|\check{\mathbf{s}})Pr(\check{\mathbf{s}})\right)\} \tag{7.36}$$

$$= \max_{\check{\mathbf{s}}\in\chi} \{\ln\left(p(\mathbf{y}|\check{\mathbf{s}})\right) + \ln\left(Pr(\check{\mathbf{s}})\right)\}. \tag{7.37}$$

Then, based on the conditional PDF $p(\mathbf{y}|\mathbf{s})$ of Eq. (7.13), the transformation of the MAP metric of Eq. (7.35) to the so-called *shortest-vector* problem can be completed by further reformatting Eq. (7.37) as:

$$\hat{\mathbf{s}}_{MAP} = \max_{\check{\mathbf{s}}\in\chi} \left\{-\mathbf{y}^H\Psi^{-1}\mathbf{y} + \ln\left(Pr(\check{\mathbf{s}})\right)\right\} \tag{7.38}$$

$$= \min_{\check{\mathbf{s}}\in\chi} \left\{||\mathbf{U}\check{\mathbf{s}}||^2 - \ln\left(Pr(\check{\mathbf{s}})\right)\right\}, \tag{7.39}$$

where $\mathbf{U}$ is an upper-triangular matrix defined in Eq. (5.28) of Section 5.2.2. Additionally, according to the principles of differentially encoded modulation discussed in Section 5.1.1.1, a phase-shift common to all components of the transmitted symbol vector $\mathbf{s}$ does not alter the MAP metric of Eq. (7.39), which in turn yields the same data symbol vector $\mathbf{v}$. This is not unexpected, since the nth data symbol v_n of the symbol vector $\mathbf{v}$ to be transmitted is differentially encoded as the phase difference between the two consecutive transmitted symbols of s_{n-1} and s_n. Hence, for the sake of convenience, we may assume that the phase of the last element of the transmitted symbol vector $\mathbf{s}$ is fixed and set to zero. In the sequel, the other elements of the vector $\mathbf{s}$ may be obtained cumulatively as:

$$s_n = \begin{cases} \prod_{m=n}^{N_{wind}-1} v_m^*, & 1 \le n \le N_{wind}-1 \\ 1, & n = N_{wind}, \end{cases} \tag{7.40}$$

where N_{wind} is the observation window size employed by the MSDSD. Due to the unique relation amongst the data bit vector $\mathbf{x}$, the data symbol vector $\mathbf{v}$ and the differentially encoded signaling symbol vector $\mathbf{s}$, they are treated interchangeably in our forthcoming discourse. Moreover, owing to the independence of the $(N_{wind}-1)$ symbols v_n, $(n = 1, 2, \cdots, N_{wind}-1)$ from each other, we have:

$$\ln\left[Pr(\mathbf{s})\right] = \ln\left[Pr(\mathbf{x})\right] = \ln\left[Pr(\mathbf{v})\right] = \sum_{n=1}^{N_{wind}-1} \ln\left[Pr(v_n)\right]. \tag{7.41}$$

Then, by exploiting the upper-triangular structure of $\mathbf{U}$, Eq. (7.39) can be rewritten as:

$$\hat{\mathbf{v}}_{MAP} = \min_{\check{\mathbf{v}}\to\check{\mathbf{s}}\in\chi} \left\{ ||\mathbf{U}\check{\mathbf{s}}||^2 - \ln\left(Pr(\check{\mathbf{v}})\right) \right\}, \tag{7.42}$$

$$= \min_{\check{\mathbf{v}}\to\check{\mathbf{s}}\in\chi} \left\{ \sum_{n=1}^{N_{wind}} \left(\left| \sum_{m=n}^{N_{wind}} u_{n,m}\check{s}_m \right|^2 \right) - \sum_{n=1}^{N_{wind}-1} \ln\left(Pr(\check{v}_n)\right) \right\} \tag{7.43}$$

$$= \min_{\check{\mathbf{v}}\to\check{\mathbf{s}}\in\chi} \left\{ \sum_{n=1}^{N_{wind}-1} \left(\left| \sum_{m=n}^{N_{wind}} u_{n,m}\check{s}_m \right|^2 - \ln\left(Pr(\check{v}_n)\right) \right) + |u_{N_{wind},N_{wind}}|^2 \right\}, \tag{7.44}$$

where $u_{n,m}$ represents the specific element of the upper-triangular matrix $\mathbf{U}$ in row n and column m, while "$\to$" beneath the min sign denotes the generation of $\check{\mathbf{s}}$ from a trial vector $\check{\mathbf{v}}$ using Eq. (7.40). In order to efficiently solve the minimization problem of Eq. (7.44), the MAP-MSDSD algorithm introduces a search radius R in order to reduce the search space, yielding:

$$\hat{\mathbf{v}}_{MAP}$$

$$= \min_{\check{\mathbf{v}}\to\check{\mathbf{s}}\in\chi} \left\{ \sum_{n=1}^{N_{wind}-1} \left(\left| \sum_{m=n}^{N_{wind}} u_{n,m}\check{s}_m \right|^2 - \ln\left(Pr(\check{v}_n)\right) \right) + |u_{N_{wind},N_{wind}}|^2 \le R^2 \right\} \tag{7.45}$$

$$= \min_{\check{\mathbf{v}}\to\check{\mathbf{s}}\in\chi} \left\{ \sum_{n=1}^{N_{wind}-1} \left(\left| \sum_{m=n}^{N_{wind}} u_{n,m}\check{s}_m \right|^2 - \ln\left(Pr(\check{v}_n)\right) \right) \le R^2 - |u_{N_{wind},N_{wind}}|^2 \right\} \tag{7.46}$$

$$= \min_{\check{\mathbf{v}}\to\check{\mathbf{s}}\in\chi} \left\{ \sum_{n=1}^{N_{wind}-1} \left(\left| \sum_{m=n}^{N_{wind}} u_{n,m}\check{s}_m \right|^2 - \ln\left(Pr(\check{v}_n)\right) \right) \le \tilde{R}^2 \right\}, \tag{7.47}$$

where we have

$$\tilde{R}^2 \triangleq R^2 - |u_{N_{wind},N_{wind}}|^2. \tag{7.48}$$

Equivalently, the search space for each component symbol v_n, $n = 1, 2, \cdots, (N_{wind}-1)$ is also confined in a manner described as:

$$\mathcal{D}_n \triangleq \underbrace{\left| u_{n,n}\check{\mathbf{s}}_{n+1}\check{\mathbf{v}}_n^* + \sum_{m=n+1}^{N_{wind}} \mathbf{U}_{nm}\check{\mathbf{s}}_m \right|^2 - \ln\left(Pr(\check{\mathbf{v}}_n)\right)}_{\triangleq \delta_n^2}$$

$$+ \underbrace{\sum_{l=n+1}^{N_{wind}-1} \left(\left| \sum_{m=l}^{N_{wind}} \mathbf{U}_{lm}\check{\mathbf{s}}_m \right|^2 - \ln\left(Pr(\check{\mathbf{v}}_l)\right) \right)}_{\mathcal{D}_{n+1}} \le \tilde{R}^2, \tag{7.49}$$

where $\mathcal{D}_n$ denotes the accumulated PED between the subvector candidate $[\check{v}_n, \check{v}_{n+1}, \cdots, \check{v}_{N_{wind}-1}]^T$ and the origin. Hence, the MAP-MSDSD scheme starts the search from the $(N_{wind}-1)$st element of the symbol vector $\mathbf{v}$ by choosing a legitimate symbol candidate $\check{v}_{N_{wind}-1}$ from the constellation set of $\mathcal{M}_c$, which satisfies Eq. (7.49), and then proceeds to search for the $(N_{wind}-2)$nd element, and so forth, until it reaches the $n = 1$st element. In other words, a trial vector $\check{\mathbf{v}} = [\check{v}_1, \check{v}_2, \cdots, \check{v}_{N_{wind}-1}]^T$ and the vector $\check{\mathbf{s}} = [\check{s}_1, \check{s}_2, \cdots, \check{s}_{N_{wind}}]$ generated using Eq. (7.40) are found. Then, the search radius is updated to

$$R^2 = \mathcal{D}_1 = \|\mathbf{U}\check{\mathbf{s}}\|^2 - \ln\left[Pr(\check{\mathbf{v}})\right], \tag{7.50}$$

based on which the search is repeated by starting with the $n = 2$nd component of the symbol vector $\mathbf{v}$. Therefore, the tree search employed by the MSDSD is carried out in a depth-first manner, which was the subject of a comprehensive discussion in Section 2.2.2. Finally, if the MSDSD of Figure 7.4 cannot find any legitimate symbol vector within the increasingly shrinking hypersphere based search space, the previously obtained vector $\check{\mathbf{v}}$ is deemed to be the MAP solution of Eq. (7.44).

7.3.2 Soft-Output Generation

Besides incorporating the *a priori* soft bit information $L_{A1}(x_k)$ of Eq. (7.33) delivered by the outer channel decoder of Figure 7.4, the iterative detection scheme requires the MAP-MSDSD to provide the *a posteriori* soft bit information $L_{D1}(x_k)$ that will be used as *a priori* information by to the decoder component, which can be calculated as follows:

$$L_{D1}(x_k) = \ln \frac{Pr(x_k = +1|\mathbf{y})}{Pr(x_k = -1|\mathbf{y})} \tag{7.51}$$

$$= \ln \frac{p(\mathbf{y}|x_k = +1)Pr(x_k = +1)/p(\mathbf{y})}{p(\mathbf{y}|x_k = -1)Pr(x_k = -1)/p(\mathbf{y})} \tag{7.52}$$

$$= \ln \frac{\sum_{\mathbf{x}\in\mathbb{X}_{k,+1}} p(\mathbf{y}|\mathbf{x})Pr(\mathbf{x})}{\sum_{\mathbf{x}\in\mathbb{X}_{k,-1}} p(\mathbf{y}|\mathbf{x})Pr(\mathbf{x})} \tag{7.53}$$

$$= \ln \frac{\sum_{\mathbf{x}\in\mathbb{X}_{k,+1}} \exp\left[-\mathbf{y}^H\Psi\mathbf{y} + \ln\left(Pr(\mathbf{x})\right)\right]}{\sum_{\mathbf{x}\in\mathbb{X}_{k,-1}} \exp\left[-\mathbf{y}^H\Psi\mathbf{y} + \ln\left(Pr(\mathbf{x})\right)\right]} \tag{7.54}$$

$$= \ln \frac{\sum_{\mathbf{x}\in\mathbb{X}_{k,+1}} \exp\left(-\|\mathbf{U}\mathbf{s}\|^2 + \ln\left[Pr(\mathbf{x})\right]\right)}{\sum_{\mathbf{x}\in\mathbb{X}_{k,-1}} \exp\left(-\|\mathbf{U}\mathbf{s}\|^2 + \ln\left[Pr(\mathbf{x})\right]\right)}, \tag{7.55}$$

where $\mathbb{X}_{k,+1}$ represents the set of $\frac{M_c^{N_{wind}}}{2}$ number of legitimate transmitted bit vectors $\mathbf{x}$ associated with $x_k = +1$, and similarly, $\mathbb{X}_{k,-1}$ is defined as the set corresponding to $x_k = -1$.

For the sake of reducing the computation complexity imposed by the calculation of Eq. (7.55), the *Jacobian logarithm* [51] may be employed to approximate the *a posteriori* LLRs, which can be expressed as:

$$Jac\left[\ln(a_1, a_2)\right] = \ln(e^{a_1} + e^{a_2}) \tag{7.56}$$

$$= \max(a_1, a_2) + \ln(1 + e^{-|a_1 - a_2|}), \tag{7.57}$$

where the second term may be omitted in order to further approximate the original logarithmic function, since $\ln(1 + e^{-|a_1-a_2|})$ can be regarded as a refinement or correction term of the coarse "sum-max" approximation provided by the maximum, i.e. the first term of Eq. (7.57). Explicitly, we have:

$$max\_sum\left[\ln(a_1, a_2)\right] = \max(a_1, a_2). \tag{7.58}$$

Therefore, the so-called "sum-max" approximation of the exact *a posteriori* LLR of Eq. (7.55) can

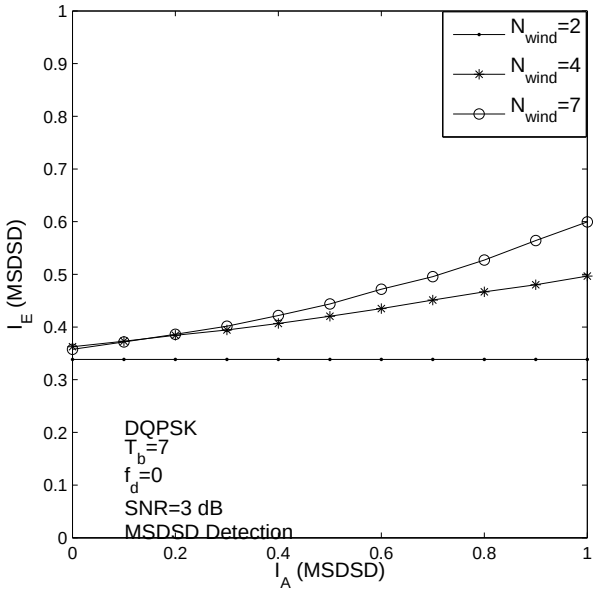

Figure 7.5: EXIT curves of the MSDSD for various observation window sizes N_{wind}. The Rayleigh fading envelope was constant for $T_b = 7$ symbols and it was then randomly and independently faded for the next block.

be reformulated with the aid of Eq. (7.39) as:

$$L_{D1}(x_k) = \ln \frac{\max_{\mathbf{x}\in\mathbb{X}_{k,+1}} \left\{ \exp\left(-\|\mathbf{Us}\|^2 + \ln\left[Pr(\mathbf{x})\right] \right) \right\}}{\max_{\mathbf{x}\in\mathbb{X}_{k,-1}} \left\{ \exp\left(-\|\mathbf{Us}\|^2 + \ln\left[Pr(\mathbf{x})\right] \right) \right\}} \tag{7.59}$$

$$= -\left\| \mathbf{U}\hat{\mathbf{s}}_{MAP}^{x_k=+1} \right\|^2 + \ln\left[Pr(\hat{\mathbf{x}}_{MAP}^{x_k=+1}) \right] + \left\| \mathbf{U}\hat{\mathbf{s}}_{MAP}^{x_k=-1} \right\|^2 - \ln\left[Pr(\hat{\mathbf{x}}_{MAP}^{x_k=-1}) \right], \tag{7.60}$$

where $\hat{\mathbf{s}}_{MAP}^{x_k=b}$ and $\hat{\mathbf{x}}_{MAP}^{x_k=b}$ represent the MAP algorithm based symbol vector estimation and MAP bit vector estimation, respectively, obtained by the MSDSD by fixing the kth bit value to $b, (b = -1 \text{ or } +1)$. In the sequel, the extrinsic LLR, $L_{E1}(x_k)$ seen in Figure 7.4 can be obtained by excluding the corresponding *a priori* LLR, $L_{A1}(x_k)$, from the *a posteriori* LLR, $L_{D1}(x_k)$, as:

$$L_{E1}(x_k) = L_{D1}(x_k) - L_{A1}(x_k), \tag{7.61}$$

which is exploited by the outer decoder after passing it through the interleaver.

7.3.3 Maximum Achievable Rate Versus the Capacity: An EXIT Chart Perspective

In order to visualize the extrinsic information transfer charateristics of the iterative MSDSD scheme, we plot the EXIT curves associated with different observation window sizes of N_{wind} in Figure 7.5 by measuring the *extrinsic* mutual information, I_E, at the output of the MSDSD for a given input stream of bit LLRs along with the *a priori* mutual information I_A at SNR of 3 dB. A Rayleigh block-fading channel associated with a block-length of $T_b = 7$ was assumed. Thus, the maximum

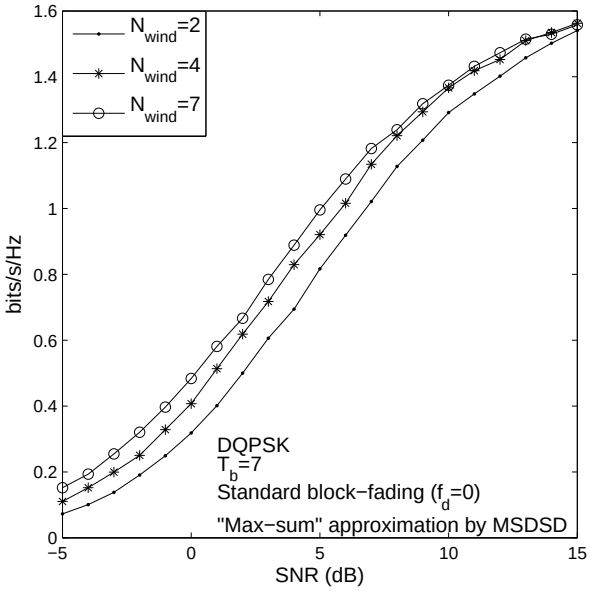

Figure 7.6: Maximum achievable rate of the single-input single-output differentially encoded QPSK modulated system using the MSDSD for various observation window sizes N_{wind}. The Rayleigh fading envelope was constant for $T_b = 7$ symbols and it was then randomly and independently faded for the next block.

value of N_{wind} that may be employed by the MSDSD is seven. As observed in Figure 7.5, the slope of the EXIT curve becomes increasingly steeper, as the value of N_{wind} increases. More specifically, the EXIT curve associated with conventional differential detection (CDD) or $N_{wind} = 2$ is horizontal when Gray mapping is employed, indicating that no performance gains can be produced by the iterative detection mechanism. However, apart from having a higher starting point in the EXIT curve, a steeper slope is expected, when jointly and differentially detecting $(N_{wind} - 1) > 1$ data symbols using the MSDSD, leading to significantly increased iterative gains. In addition, according to the area properties of EXIT charts [115, 141], the area $\mathcal{A}$ under the bit-based EXIT curve of a soft-detector/soft-demapper is equal to the maximum possible code rate $R_{outer,max}$ of the outer channel code that can be employed to achieve near error-free transmissions. Hence, the maximum achievable near-error-free transmission rate $R_{overall,max}$ of a differentially encoded system is computed as:

$$R_{overall,max} = \left(\frac{T_b - 1}{T_b}\log_2 M_c\right) \cdot R_{outer,max}, \tag{7.62}$$

$$= \left(\frac{T_b - 1}{T_b}\log_2 M_c\right) \cdot \mathcal{A} \quad \text{bits/s/Hz}, \tag{7.63}$$

which may be improved with the aid of the MSDSD.

In the sequel, the maximum achievable rate of a differentially encoded system employing the MSDSD may be plotted against the SNR, as shown in Figure 7.6, by evaluating the area under the corresponding EXIT curve of the MSDSD. Observe in Figure 7.6 that a performance gain of about 2 dB may be attained by using the MSDSD associated with $N_{wind} = 7$ over the system employing the CDD of Section 5.1.1.1 for a wide range of SNRs, although naturally this is achieved at an

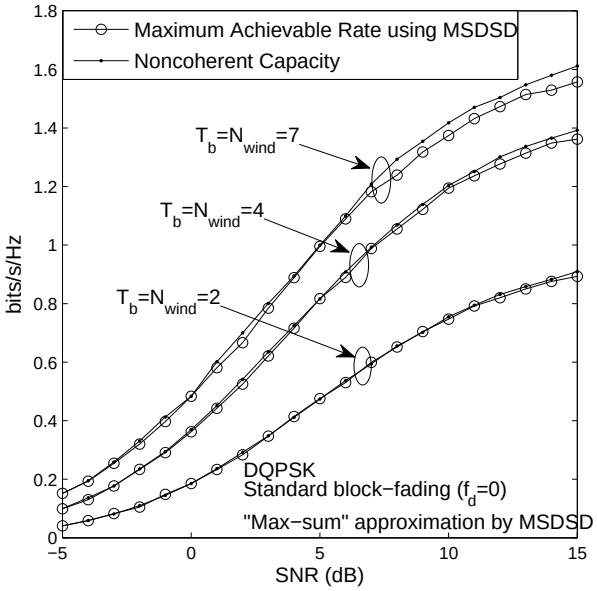

Figure 7.7: Maximum achievable rate of the single-input single-output differentially encoded QPSK modulated system using the MSDSD and the non-coherent DCMC capacity for various fading block lengths T_b. The Rayleigh fading envelope was constant for $T_b = 7$ symbols and it was then randomly and independently faded for the next block.

increased complexity owing to the higher observation window size N_{wind} as well as due to the potential increased number of iterations between the MSDSD and the outer channel decoder.

On the other hand, according to area properties of the EXIT chart [115], the area under the EXIT curve of a MAP detector/demapper is equal to the maximum possible code rate of the outer channel code, which can be employed in order to approach the DCMC capacity. In other words, the MAP-based MSDSD employing the highest possible observation window size N_{wind} can be regarded as the optimum differential detector in the interest of approaching the theoretically maximum transmission rate for a given differentially encoded modulation scheme. Figure 7.7 depicts the maximum achievable transmission rate curve of the system employing the MSDSD in comparison to the non-coherent DCMC capacity of Section 7.2 for various fading block lengths T_b, when aiming for a vanishingly low BER. Indeed, the former almost coincides with the latter for the Rayleigh block-fading channels associated with the three different T_b values considered. The slight gap between them is not unexpected, since the "max-sum" approximation algorithm of Eq. (7.60) is employed by the MSDSD in order to reduce the complexity imposed by the computation of the *a posteriori* LLRs. Consequently, based on Eq. (7.63), we have:

$$C_{DCMC} = R_{overall,max}, \tag{7.64}$$

$$= \left(\frac{T_b - 1}{T_b} \log_2 M_c\right) \cdot \mathcal{A}, \tag{7.65}$$

$$= \left(\frac{T_b - 1}{T_b} \log_2 M_c\right) \cdot R_{outer,max}, \tag{7.66}$$

when the MSDSD is employed with an observation window size of $N_{wind} = T_b$.

7.4 Approaching the Capacity of the Differentially Modulated Cooperative Cellular Uplink

7.4.1 Relay-Aided Cooperative Network Capacity

7.4.1.1 Perfect SR-Link-Based DCMC Capacity

In Sections 7.2 and 7.3 we discussed the non-coherent DCMC capacity of the single-input single-output direct-transmission based system and the corresponding near-capacity MAP-based MSDSD detection scheme, respectively. Let us now continue by investigating the proposed near-capacity system design for the differentially modulated single-relay-aided cooperative system of Figure 7.1 by studying the corresponding network's DCMC capacity. We first define the two-hop single-relay-aided network's capacity as the maximum achievable rate attained during the transmission of the source MS in the broadcast phase, namely, Phase I, which consists of L_s symbol periods, and an independent transmission by the RS during the relaying phase, namely, Phase II, when L_r symbols are transmitted. Initially a perfect SR link is assumed in order to guarantee "error-free" relaying. Thus the above-mentioned network capacity is termed as the cooperative system's DCMC capacity, which is not affected or constrained by the quality of the SR link. Hence we refer to it in parlance as the 'perfect-SR-link' based capacity. By contrast, in Section 7.4.1.2 its 'imperfect-SR-link' based counterpart will be investigated by considering the specific performance limitations imposed by the potentially error-prone SR link. According to the above definition, the corresponding network's 'perfect-SR-link' based DCMC capacity may be formulated as:

$$C^{coop}_{DCMC}(\alpha, \mathrm{SNR}^{overall}_t) = \alpha C^{sd}_{DCMC}(\mathrm{SNR}^s_e) + (1-\alpha) C^{rd}_{DCMC}(\mathrm{SNR}^r_e), \tag{7.67}$$

$$= \alpha C_{DCMC}(\mathrm{SNR}^s_e) + (1-\alpha) C_{DCMC}\left[\mathrm{SNR}^r_e + 10\log_{10}(\sigma^2_{rd})\right], \tag{7.68}$$

where

$$\alpha \triangleq \frac{L_s}{L_s + L_r}. \tag{7.69}$$

In Eq. (7.68) σ^2_{rd} characterizes the reduced-path-loss related power-gain, which was given by Eq. (7.2) and $C_{DCMC}(\cdot)$ represents the single-input single-output non-coherent DCMC capacity formula of Eq. (7.16). Furthermore, SNR^s_e and SNR^r_e in Eq. (7.68) represent the equivalent SNRs at the source and relay transmitters, respectively, which have the following relationship with the network's overall equivalent SNR, $\mathrm{SNR}^{overall}_e$, as:

$$\mathrm{SNR}^{overall}_e = \mathrm{SNR}^s_e + \mathrm{SNR}^r_e. \tag{7.70}$$

According to the simple cooperative resource allocation scheme mentioned in Section 7.1.1.1, namely, the equal-power-allocation and the mid-point relay location, Eq. (7.68) can be written as:

$$C^{coop}_{DCMC}(\alpha, \mathrm{SNR}^{overall}_e) = \alpha C_{DCMC}\left(\frac{\mathrm{SNR}^{overall}_e}{2}\right) + (1-\alpha) C_{DCMC}\left(\frac{\mathrm{SNR}^{overall}_e}{2} + 10\log_{10}(0.5^{-v})\right), \tag{7.71}$$

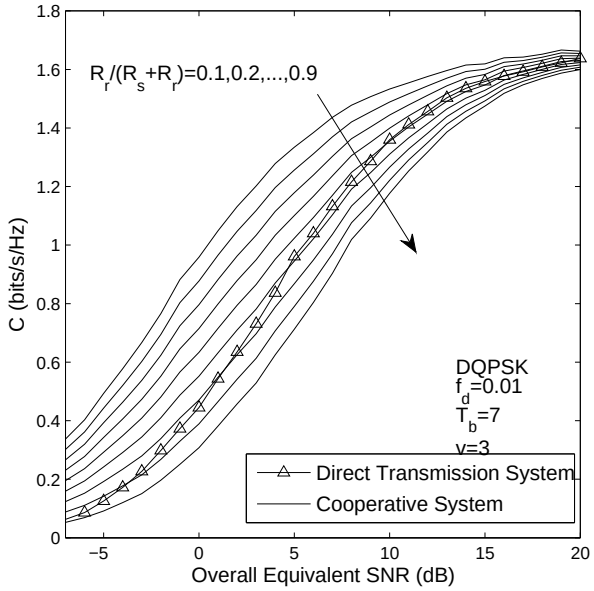

Figure 7.8: The single-relay-assisted cooperative system's constant code-rate-ratio based DCMC capacity curves for the 'perfect-SR-link' based scenario.

where v is the path-loss exponent. Furthermore, since the ratio of the differential-encoding frame lengths used by the source and relay is inversely proportional to the ratio of the channel code rate employed by the two, we have:

$$\frac{L_s}{L_s + L_r} = \frac{R_r}{R_s + R_r} = \alpha. \tag{7.72}$$

Hence, Eq. (7.71) may be reformulated as:

$$\begin{aligned} C_{DCMC}^{coop}(\alpha, \mathrm{SNR}_e^{overall}) &= \frac{R_r}{R_s + R_r} C_{DCMC}\left(\frac{\mathrm{SNR}_e^{overall}}{2}\right) \\ &\quad + \frac{R_s}{R_s + R_r} C_{DCMC}\left(\frac{\mathrm{SNR}_e^{overall}}{2} + 10\log_{10}(0.5^{-v})\right), \qquad (7.73) \\ &= \alpha C_{DCMC}\left(\frac{\mathrm{SNR}_e^{overall}}{2}\right) \\ &\quad + (1-\alpha)\, C_{DCMC}\left(\frac{\mathrm{SNR}_e^{overall}}{2} + 10\log_{10}(0.5^{-v})\right). \qquad (7.74) \end{aligned}$$

Therefore, in contrast to the independence of the DCMC capacity of the channel code rate employed in the scenario of the conventional direct transmission system, the DCMC capacity of the relay-aided cooperative system is dependent on the ratio $\frac{R_s}{R_r}$ of the channel code rates employed by the source and relay or, equivalently, dependent on α. In Figure 7.8 the cooperative system's DCMC capacity curves associated with different values of α are depicted based on Eq. (7.74) for the 'perfect-SR-link' scenario at a *constant code-rate-ratio* in comparison to the DCMC capacity curve of the direct-transmission based system. As observed in Figure 7.8, the cooperative system's DCMC capacity is gradually decreased as α is increased. This is not unexpected, since the

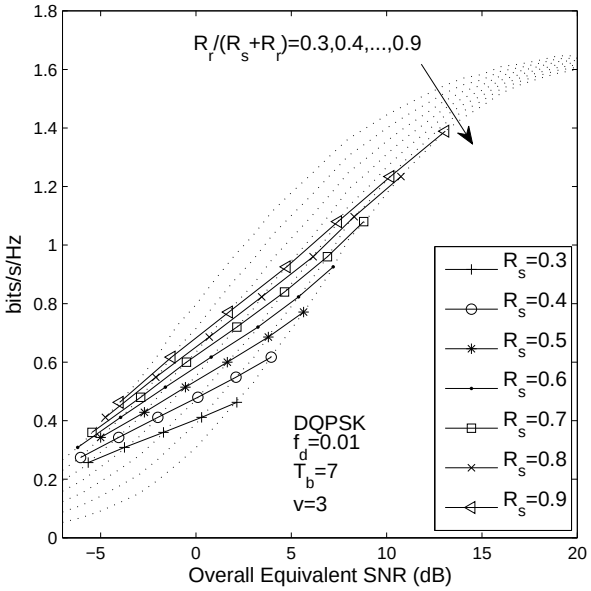

Figure 7.9: The single-relay-assisted cooperative system's constant-R_s based DCMC capacity curves.

weight of the second term in Eq. (7.74) decreases as that of the first term increases, while the second term is typically larger than the first term owing to the reduced-path-loss related power gain. Furthermore, since the source has to remain silent, when the relay is transmitting during Phase II, the system's constant code-rate-ratio based 'perfect-SR-link' associated DCMC capacity may become even lower than that of the direct-transmission based system, as seen in Figure 7.8, if both the overall equivalent SNR and α is sufficiently high. Natually, the half-duplex constraint imposes a potentially substantial multiplexing loss. In other words, despite the reduced-path-loss related power gain, the single-relay-assisted cooperative system considered does not necessarily outperform its direct-transmission based counterpart in terms of the maximum achievable transmission rate. In order to prevent this potential performance-loss, a careful system design is required.

On the other hand, given the channel code rates (R_s, R_r) employed by the source and relay, the resultant bandwidth efficiency, η, may be expressed as:

$$\eta = \frac{L_s}{L_s + L_r} R_s \frac{T_b - 1}{T_b} \log_2 M_c \tag{7.75}$$

$$= \frac{R_s R_r}{R_s + R_r} \frac{T_b - 1}{T_b} \log_2 M_c \tag{7.76}$$

$$= \alpha R_s \frac{T_b - 1}{T_b} \log_2 M_c. \tag{7.77}$$

Hence, by fixing the value of R_s and varying that of α, the resultant bandwidth efficiency η can be calculated using Eq. (7.77). Based on Eq. (7.77) the corresponding minimum overall equivalent SNR required by near-error-free transmissions may be found with the aid of the constant code-rate-ratio based 'perfect-SR-link' associated DCMC capacity curves seen in Figure 7.8.

Consequently, the cooperative system's constant-R_s 'perfect-SR-link' based DCMC capacity curves were plotted from Eq. (7.77) based on Figure 7.8 for various values of R_s in Figure 7.9,

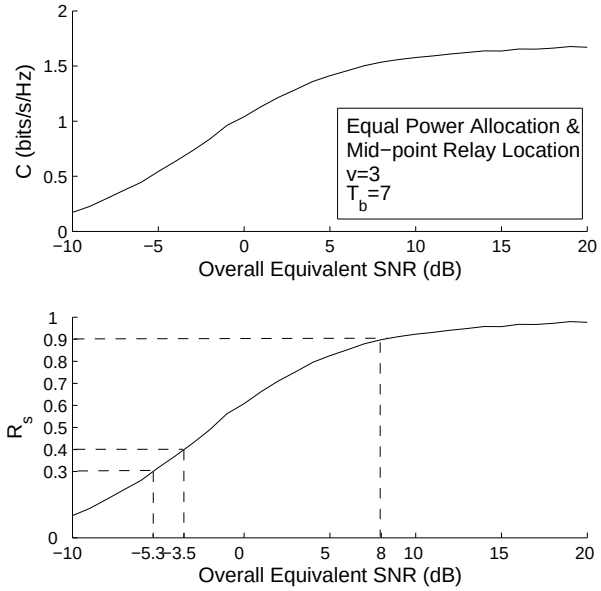

Figure 7.10: Non-coherent DCMC capacity of the SR link and its corresponding capacity-achieving channel code rate R_s employed by the source MS.

where we observe that the capacity increases as R_s increases. However, all the constant-R_s-related capacity curves depicted in Figure 7.9 would intersect the capacity curve of the direct-transmission based system plotted in Figure 7.8, if the overall equivalent SNR becomes sufficiently high. This results in a reduced maximum achievable transmission rate compared to its direct-transmission based counterpart. Therefore, based on the observation of Figures 7.8 and 7.9, we may state that although the cooperative system's capacity increases steadily as the overall equivalent SNR increases, it might remain lower than that of its direct-transmission based counterpart, even under the assumption of an idealized error-free SR link, if both R_s and α are of relatively high values. In other words, under the assumption of a perfect SR link, the single-relay-assisted DDF cooperative system is capable of exhibiting a higher capacity than its point-to-point transmission system, provided that the target throughput is low.

7.4.1.2 Imperfect-SR-Link Based DCMC Capacity

Until now the single-relay-assisted DDF cooperative system's capacity has been investigated under the assumption of an idealized error-free SR link. However, in practice the wireless channel connecting the source and relay MSs is typically far from perfect and its quality plays an important role in determining the overall cooperative network's achievable performance, as disusssed in Chapter 6 in the context of uncoded scenarios. Furthermore, in order to create a near-capacity design for the overall cooperative system, near-capacity transmission over the potentially error-infested SR link during the broadcast Phase I is a natural prerequisite, which in turn leads to the investigation of the performance limitations imposed by the SR link on the overall cooperative system.

Under the assumption of equal-power-allocation and a mid-point relay location, the non-coherent

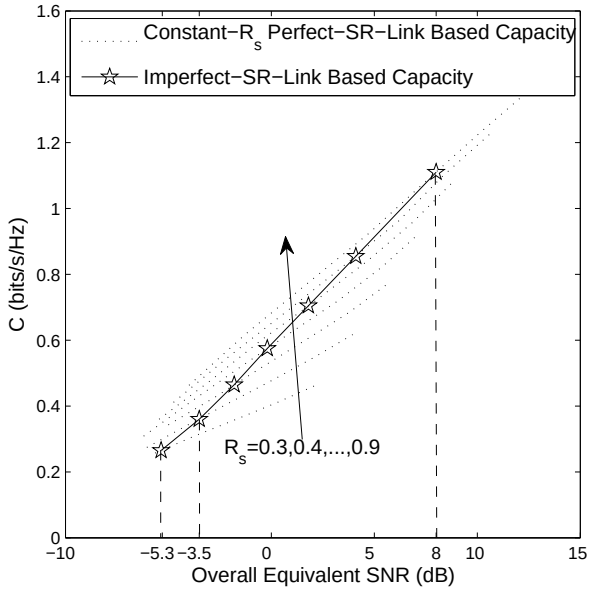

Figure 7.11: Imperfect-SR-link based DCMC capacity.

DCMC capacity of the SR link may be expressed as:

$$C_{DCMC}^{sr}\left(\mathrm{SNR}_e^{overall}\right) = C_{DCMC}\left(\frac{\mathrm{SNR}_e^{overall}}{2} + 10\log_{10}(0.5^{-v})\right), \tag{7.78}$$

where $C_{DCMC}(\cdot)$ was formulated in Eq. (7.16). Hence, the non-coherent DCMC capacity of the SR link may be plotted versus the overall equivalent SNR, as shown in Figure 7.10. Then, according to Eq. (7.66), we can calculate the capacity-achieving channel code rate employed by the source as:

$$R_{s,capacity}(\mathrm{SNR}_e^{overall}) = \frac{T_b \cdot C_{DCMC}^{sr}\left(\mathrm{SNR}_e^{overall}\right)}{(T_b - 1)\cdot \log_2 M_c}, \tag{7.79}$$

which is also depicted versus the overall equivalent SNR in Figure 7.10. Therefore, the minimum overall equivalent SNR corresponding to a certain value of R_s, which faciliates near-error-free information delivery from the source to the relay, may be observed in Figure 7.10. These minimum overall equivalent SNRs characterize the performance limits imposed by the practical imperfect SR link on the entire cooperative system, when the corresponding rate R_s is employed by the source. Given these minimum overall equivalent SNRs associated with different values of R_s, we can now draw the cooperative system's 'imperfect-SR-link' related DCMC capacity based on the constant-R_s 'perfect-SR-link' based DCMC capacity curves of Figure 7.9. More specifically, observe in Figure 7.11 that in order to find, for example, the cooperative system's 'imperfect-SR-link' based DCMC capacity for $R_s = 0.3$, we locate the particular point on the constant-R_s 'perfect-SR-link' based DCMC capacity curve associated with $R_s = 0.3$, whose horizontal coordinate is equal to the corresponding minimum overall equivalent SNR of -5.3 dB found previously in the context of Figure 7.10. Then, the vertical coordinate of the point is the 'imperfect-SR-link' based DCMC capacity of the cooperative system for $R_s = 0.3$ or when we have $\mathrm{SNR}_e^{overall} = -5.3$dB.

In order to gain an insight into the benefits of the single-relay-assisted DDF cooperative system over its conventional point-to-point direct-transmission based counterpart from a pure capacity

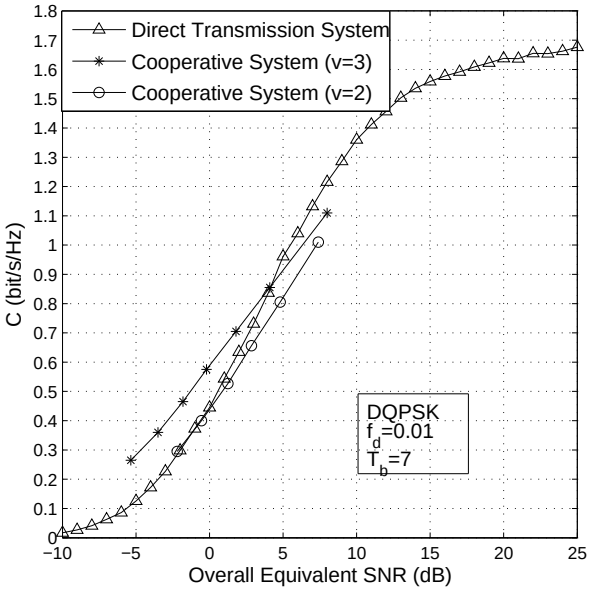

Figure 7.12: Capacity comparison of the single-relay-aided cooperative system and its direct-transmission based counterpart.

perspective, the 'imperfect-SR-link' based DCMC capacity of the cooperative system associated with both $v = 2$ and $v = 3$ is depicted in comparison to that of the direct-transmission based one in Figure 7.12. It may be observed in the figure that when the overall equivalent SNR is relatively low, the single-relay-assisted cooperative system exhibits a significantly higher capacity than its direct-transmission based counterpart in typical urban cellular radio scenarios, e.g. when having a path-loss exponent of $v = 3$. However, the achievable capacity gain may be substantially reduced if we encounter a free-space propagation scenario, i.e. $v = 2$, since the reduced-path-loss-related power-gain achieved is insufficiently high to compensate for the significant multiplexing loss inherent in the single-relay-aided half-duplex cooperative system. Moreover, as the overall equivalent SNR increases to a relatively high value, there is no benefit in invoking a single-relay-aided cooperative system, since its capacity becomes lower than that of the conventional point-to-point system.

7.4.2 Irregular Distributed Hybrid Concatenated Differential Encoding/Decoding for the Cooperative Cellular Uplink

In conventional relay-aided decode-and-forward cooperative systems, the relay decodes the signal received from the source and re-encodes it using an identical channel encoder. Then the destination receives two versions of the same code word, namely those from the source and relay, respectively, which may be viewed as a repetition code. Finally, the two replicas of the signal may be combined using maximal ratio combining (MRC) prior to the decoding. In order to enhance the coding gain achieved by the repetition code constituted by the relay-aided system, while maintaining the cooperative diversity gain, the classic turbo coding mechanism was introduced into the DF aided cooperative system of [142], resulting in the so-called distributed turbo coding scheme. Specifically, according to the principle of parallel concatenated convolutional code based turbo coding,

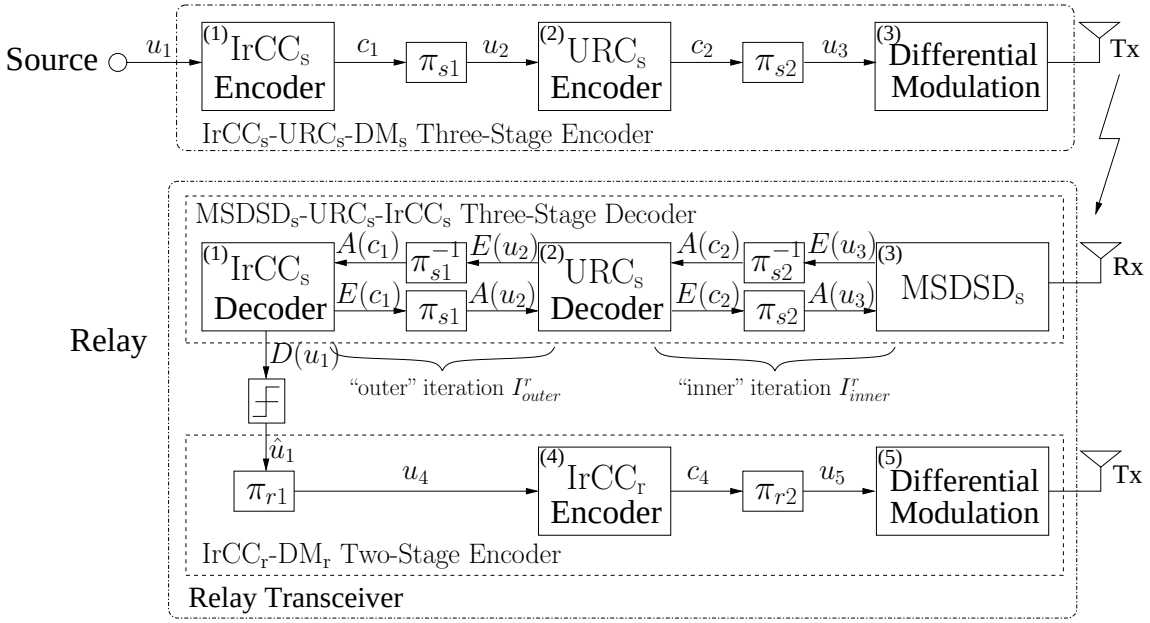

Figure 7.13: Schematic of the irregular distributed hybrid concatenated differential coding encoder.

the data and its interleaved version are encoded in parallel, using two distinct recursive systematic convolutional (RSC) codes, respectively. Therefore, a distributed turbo code may be readily constructed at the relay by interleaving its received estimated source data prior to re-encoding. Owing to this interleaving at the RS, its encoded stream may be expected to be different from that of the source. Consequently, the direct encoding of the original bit-stream takes place at the source, while the encoding of the interleaved sequence ensues at the RS in a distributed manner. A standard turbo decoder may be implemented at the destination. It was revealed in [142] that a significantly enhanced coding gain can be achieved by a distributed turbo code in comparison to that attained by a single convolutional code for transmission over two independently fading channels.

In order to improve the iterative decoder's achievable performance and hence achieve near-error-free transmissions between the source and relay, a unity-rate-coded (URC) three-stage serially concatenated transceiver employing the irregular convolutional codes (IrCCs) of Section 3.4.3, may be employed in the single-relay-aided DDF cooperative system. More specifically, since the URC has an infinite impulse response due to its recursive encoder architecture, the resultant EXIT curve of the URC-aided inner decoder is capable of reaching the point $(1,\ 1)$ of the EXIT chart, provided that the interleaver length is sufficiently high [141]. Furthermore, since the URC decoder employs the MAP decoding scheme, the extrinsic probability generated at the output of the URC decoder contains the same amount of information as the sequence at the input of the URC decoder [113, 143]. In other words, the area under the inner EXIT curve remains the same, regardless of the URC's employment. Hence, a higher ending point of the EXIT curve leads to a lower starting point, implying a steeper slope for the EXIT curve, which in turn yields a reduced error floor and a higher SNR threshold, above which decoding convergence to a vanishingly low BER becomes possible, as we will demonstrate in the forthcoming sections.

Based on the above-mentioned arguments, the transmitter's architecture proposed for the source

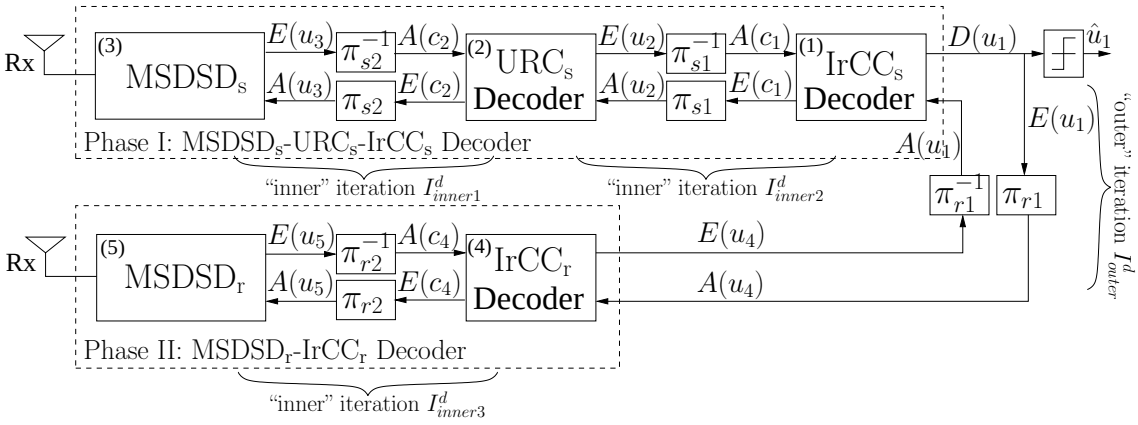

Figure 7.14: Iterative receiver at the destination BS.

is depicted in Figure 7.13, where we use a conventional differential modulation scheme, such as DQPSK, which is amalgamated with the URC encoder in order to create a two-stage inner code, whereas an IrCC associated with an average code rate of R_s, namely IrCC$_s$, is employed as the outer code for the sake of achieving a performance that is close to the capacity of the SR link. Specifically, at the transmitter of the source in Figure 7.13, a block of L information bits u_1 is first encoded by the IrCC$_s$ encoder, in order to generate the coded bits c_1, which are interleaved by the interleaver π_{s1}. Then the resultant permuted bits u_2 are successively fed through the URC$_s$ encoder and the interleaver π_{s2}, yielding the interleaved double-encoded bits u_3, which are delivered to the bit-to-symbol differential modulator of Figure 7.13. Note that the labels u and c represent the uncoded and coded bits, respectively, corresponding to a specific module as indicated by the subscript. The corresponding URC decoder assisted three-stage receiver proposed for the relay is also portrayed in Figure 7.13 together with its two-stage transmitter schematic. Specifically, at the receiver of the relay, which is constituted by three modules, namely the MSDSD$_s$, the URC$_s$ decoder and the IrCC$_s$ decoder, the extrinsic information is exchanged amongst the modules in a number of consecutive iterations. As shown in Figure 7.13, $A(\cdot)$ represents the *a priori* information expressed in terms of the LLRs, while $E(\cdot)$ denotes the corresponding *extrinsic* information. At the transmitter of the relay, the estimated data bit stream is fed through the interleaver π_{r1} prior to the IrCC$_r$ encoder having an average code rate of R_r, as observed in Figure 7.13, in order to construct a distributed turbo code together with the source. Consequently, the proposed relay-aided cooperative system may be referred to here as an Irregular Distributed Hybrid Concatenated Differential (Ir-DHCD) coding scheme, under the assumption of an error-free decoding at the relay.

At the destination BS, according to the principles of the distributed turbo decoding mechanism proposed in [142], the novel iterative receiver of Figure 7.14 is used for decoding the Ir-DHCD coding scheme of Figure 7.13. To be specific, the first part of the iterative receiver is an amalgamated "MSDSD$_s$-URC$_s$-IrCC$_s$" iterative decoder, which is used to iteratively decode the signal received directly from the source during Phase I, while the second part is constituted of the MSDSD$_r$ differential detector and the IrCC$_r$ decoder, which is employed to iteratively decode the signal forwarded by the relay during Phase II. Since the "MSDSD$_s$-URC$_s$-IrCC$_s$" decoder and the "MSDSD$_r$-IrCC$_r$" decoder may be regarded as the two-component decoders of a turbo receiver, the extrinsic information exchange between them, which is referred to as 'the 'outer iteration", is

expected to significantly enhance the achievable coding gain. In comparison to the conventional relay-aided cooperative system, where a simple repetition code is constructed, the extra coding gain achieved by the proposed Ir-DHCD coding scheme may be interpreted as the interleaving gain of the turbo code and the turbo processing gain of the outer iterations.

7.4.3 Approaching the Cooperative System's Capacity

Single-Relay-Aided Cooperative Cellular Uplink		
	Scenario I	***Scenario II***
Path Loss Exponent	$v = 2$	$v = 3$
Doppler Frequency	$f_d = 0.01$	
Fading Block Size	$T = 7$	
Tx at Source or Relay MS	1	
Rx at Relay MS or BS	1	
Modulation	DQPSK	
Detector/MAP	MSDSD	
Channel Code	IrCC (17 subcodes)	
Code Rate at Source MS	$R_s = 0.5$	
Power Allocation	$P_s = P_r = \frac{1}{2}P = 0.5$	
Relay Location	$D_{sr} = D_{rd} = \frac{1}{2}D_{sd} = 0.5$	

Table 7.1: Summary of system parameters

In this section, we propose a practical framework, which is capable of approaching the cooperative system's capacity. We propose a reduced-complexity near-capacity system design for the DQPSK-modulated single-relay-assisted DDF cooperative cellular uplink. We will consider two different propagation scenarios associated with a path loss exponent of $v = 2$ and $v = 3$, respectively. Based on the proposed cooperative system design, we will verify in Section 7.4.4 that a single-relay-aided DDF cooperative system is not always superior to its conventional direct-transmission based counterpart in terms of the maximum achievable bandwidth efficiency. The time-selective block fading channel model of Section 7.1.1.2 is employed in conjunction with a normalized Doppler frequency of $f_d = 0.01$. For the sake of simplicity, the equal-power-allocation and the mid-point relay location scenarios are assumed for the single-relay-aided cooperative system, where each terminal is equipped with a single Tx/Rx antenna. All other system parameters are summarized in Table 7.1.

7.4.3.1 Reduced-Complexity Near-Capacity Design at Relay Mobile Station

Without loss of generality, the average code rate R_s of the IrCC$_s$ at the source is chosen to be 0.5. Based on Eq. (7.79) of Section 7.4.1.2, the maximum possible code rate R_s that may be employed by the source to facilitate near-error-free transmissions between the source and relay is plotted in

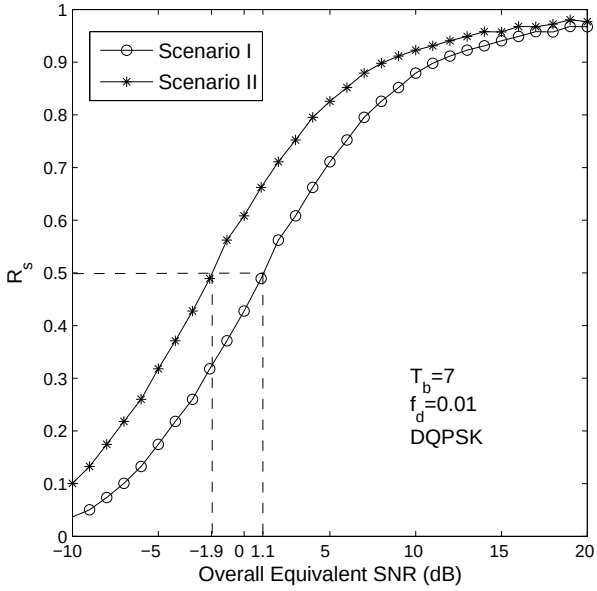

Figure 7.15: SR-link-capacity-achieving channel code rate R_s employed by the source versus the corresponding overall equivalent SNR required.

Figure 7.15 versus the corresponding overall equivalent SNR required for both Scenarios I and II of Table 7.1. According to Figure 7.15, the minimum overall equivalent SNRs required to support a SR-link transmission at an infinitesimally low BER are 1.1 dB and -1.9 dB for Scenarios I and II, respectively, when we have $R_s = 0.5$. The 3 dB SNR gain attained in Scenario II in comparison to Scenario I is due to the difference of the path-loss-related power gains/losses achieved in the two scenarios of Table 7.1, namely:

$$10\log_{10}(0.5^{-3}) - 10\log_{10}(0.5^{-2}) = 3 \text{ dB}. \tag{7.80}$$

Theoretically, the SR-link's non-coherent DCMC capacity can be achieved, with the aid of an infinite number of iterations between the inner combined "MSDSD$_s$-URC$_s$" decoder and an ideally designed outer IrCC$_s$ decoder at the relay's receiver of Figure 7.13, although naturally this would impose an excessive computational complexity. However, in practice, for the sake of avoiding a potentially excessive complexity at the relay, while approaching the capacity, a 'higher-than-necessary' EXIT curve may be ensured for the inner "MSDSD$_s$-URC$_s$" decoder by having a slightly higher overall equivalent SNR of 2.3 dB for Scenario I or -0.7 dB for Scenario II, as depicted in Figure 7.16 for different number of iterations between the MSDSD$_s$ and URC$_s$ blocks. The observation window size of the MSDSD was set to its maximum value of $N_{wind} = 7$ in the time-selective block fading channel having a fading block size of $T_b = 7$. It may be observed from Figure 7.16 that the iterative information exchange between the MSDSD$_s$ and URC$_s$ blocks approaches convergence as early as at their second iteration. Hence, the number of iterations between the MSDSD$_s$ and URC$_s$ blocks was set to $I^r_{inner} = 2$ in our future simulations, in order to avoid any unnecessarily imposed complexity, while maintaining a near-capacity performance. Then, using the EXIT curve of the inner amalgamated "MSDSD$_s$-URC$_s$" decoder, the optimized weighting coefficients of the half-code-rate IrCC$_s$ can be obtained with the aid of the EXIT curve

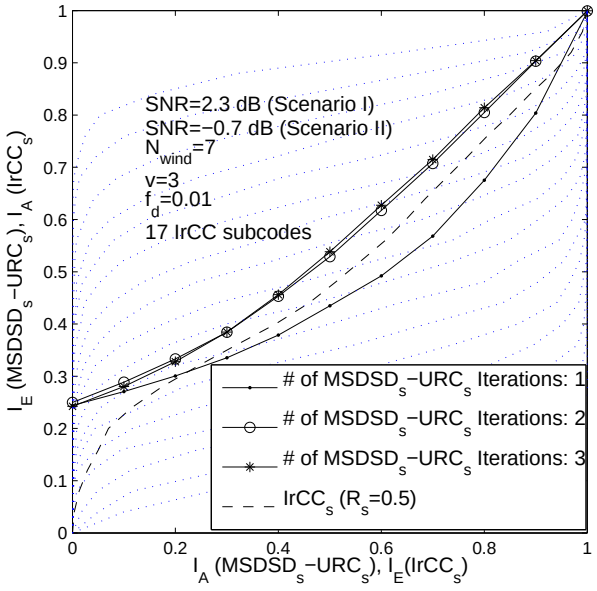

Figure 7.16: EXIT chart at the relay (Design of the IrCC$_s$).

matching algorithm of [117], resulting in a narrow but marginally open tunnel between the EXIT curves of the inner amalgamated "MSDSD$_s$-URC$_s$" decoder and the outer IrCC$_s$ decoder, as seen in Figure 7.16.

On the other hand, in order to further reduce the complexity imposed by the "MSDSD$_s$-URC$_s$" decoder during the iterative decoding process at the relay, an adaptive-window based scheme is proposed for the MSDSD$_s$, where the observation window size was initially set to the smallest value of $N_{wind} = 2$, which will be slightly increased as soon as the iterative decoding between the "MSDSD$_s$-URC$_s$" decoder and the IrCC$_s$ decoder converges. The proposed adaptive-window based scheme is characterized by Figure 7.17(a), where it is observed that the resultant bit-by-bit Monte-Carlo simulation based iterative decoding trajectory fails to reach the $(1,\ 1)$ point associated with $N_{wind} = 2$ and $N_{wind} = 4$. By contrast, it does indeed reach the $(1,\ 1)$ point of the EXIT chart for $N_{wind} = 7$. Thus, the original maximum achievable iteration gain corresponding to $N_{wind} = 7$ can be maintained by the adaptive-window based scheme, despite having a reduced overall complexity imposed by the MSDSD$_s$. This is not unexpected, since although an increased number of iterations may be needed between the "MSDSD$_s$-URC$_s$" decoder and the IrCC$_s$ decoder to achieve the same amount of iteration gain when the adaptive-window based scheme is employed, the complexity per iteration imposed by the MSDSD$_s$ using a reduced N_{wind} value is expected to be exponentially reduced, yielding a potentially reduced overall complexity. Indeed, the complexity imposed is significantly reduced by the adaptive-window based scheme, as observed in Figure 7.17(b), where the complexity imposed by the MSDSD$_s$ in terms of the number of the PED evaluations per bit is plotted versus the overall equivalent SNR for both systems operating with and without the adaptive-window based scheme. To be specific, regardless of the employment of the adaptive-window aided scheme, the complexity imposed by the MSDSD$_s$ arrangement during the iterative decoding process gradually decreases in Figure 7.17(b) as the SNR increases from about 2 dB for Scenario I, where a narrow-but-open tunnel is created by using $N_{wind} = 7$. This is because a

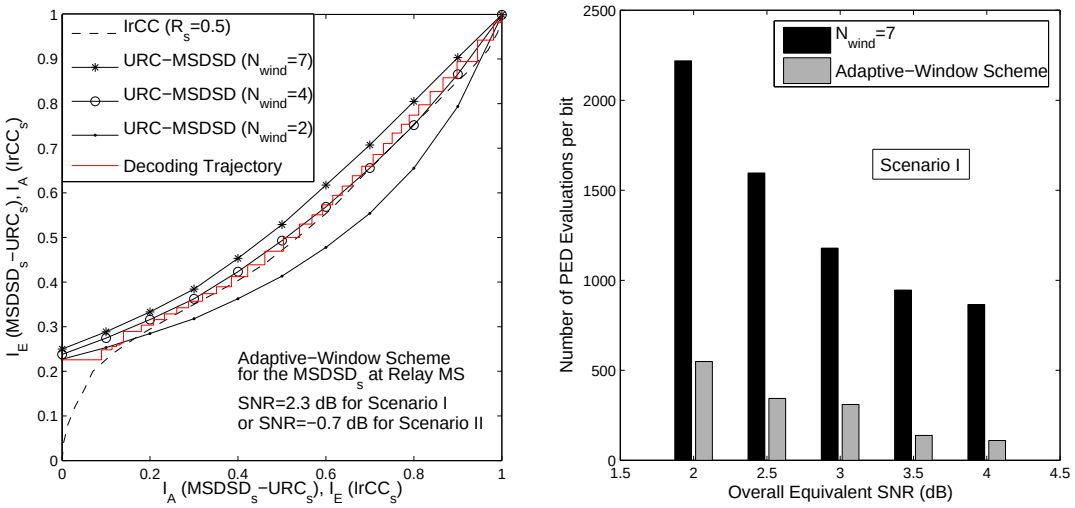

(a) EXIT trajectory at relay MS.

(b) Complexity reduction achieved.

Figure 7.17: Characterization of the adaptive-window aided scheme for the MSDSD$_s$ at the relay.

reduced number of iterations is required in Figure 7.17(a) in the presence of an increasingly wider open EXIT tunnel. Remarkably, the complexity imposed by the MSDSD$_s$ in Scenario I is substantially reduced in Figure 7.17(b) with the aid of the adaptive-window assisted scheme by as much as 75% at $SNR_t^{overall} = 2$ dB, when the open EXIT tunnel created by having $N_{wind} = 7$ becomes rather narrow. The attainable complexity reduction increases even further to about 83%, when the open EXIT tunnel becomes wider at $SNR_t^{overall} = 4$ dB, as seen in Figure 7.17(b).

7.4.3.2 Reduced-Complexity Near-Capacity Design at Destination Base Station

In Section 7.4.3.1 the IrCC$_s$ decoder of Figure 7.13 was specifically designed to allow a near-capacity operation over the SR link with the aid of the EXIT curve matching algorithm of [117] carried out at the relay. Let us now consider the destination BS and optimize the weighting coefficients of the other irregular convolutional code employed by the RS's transmitter in Figure 7.13. In other words, we consider the IrCC$_r$ design now, in order to approach the overall cooperative system's capacity quantified in Section 7.4.1.2, whilst maintaining at a relatively low complexity. First of all, the EXIT curves of the amalgamated "MSDSD$_s$-URC$_s$-IrCC$_s$" decoder employed by the BS are depicted in Figure 7.18 for various values of N_{wind} for both Scenarios I and II associated with an overall equivalent SNR of 2.3 dB and -0.7 dB, respectively. The number of iterations between the MSDSD$_s$ and the URC$_s$ of Figure 7.14 as well as that between the combined "MSDSD$_s$-URC$_s$" decoder and the IrCC$_s$ scheme are set to $I_{inner1}^d = 1$ and $I_{inner2}^d = 5$, respectively. It may be observed from Figure 7.18 that the desirable choice of the observation window size employed by the MSDSD$_s$ at the BS for Scenario I is $N_{wind} = 4$, while we have $N_{wind} = 2$ for Scenario II, under our low-complexity near-capacity design criterion.

Then, based on the above-mentioned desirable choices of N_{wind}, we continue by determining

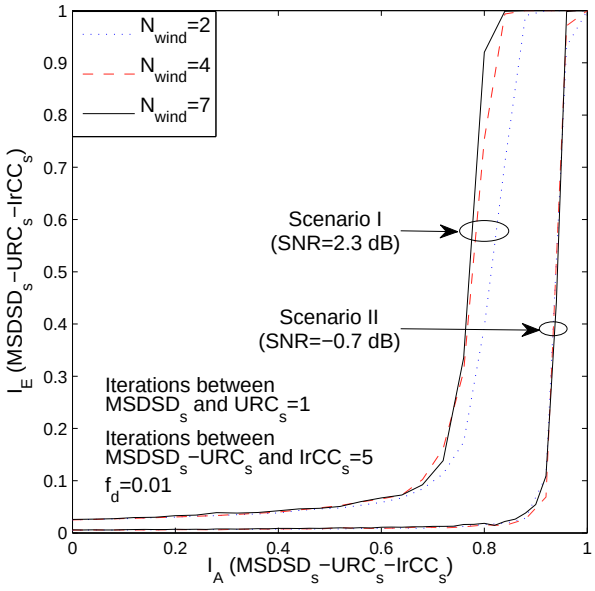

Figure 7.18: EXIT curves of the amalgamated "MSDSD$_s$-URC$_s$-IrCC$_s$" decoder employed by the destination BS for various observation window sizes N_{wind}.

the desirable number of iterations between the MSDSD$_s$ and the URC$_s$ arrangements as well as that required between the combined "MSDSD$_s$-URC$_s$" decoder and the IrCC$_s$, by plotting the EXIT curves of the amalgamated "MSDSD$_s$-URC$_s$-IrCC$_s$" decoder associated with various numbers of iterations in Figure 7.19. Specifically, as observed in Figure 7.19(a) for Scenario I, only a modest iteration gain may be attained by having more than a single iteration (i.e. $I^d_{inner1} = 1$) between the MSDSD$_s$ and the URC$_s$ blocks of Figure 7.14. By contrast, we need about $I^d_{inner2} = 5$ iterations between the combined "MSDSD$_s$-URC$_s$" decoder and the IrCC$_s$, while beyond $I^d_{inner2} = 5$ the increase of the area under the EXIT curve of the "MSDSD$_s$-URC$_s$-IrCC$_s$" decoder becmes marginal. Similarly, observe in Figure 7.19(b) that a sharply-rising EXIT curve can be created for Scenario II when using our the low-complexity near-capacity design criterion, since only a single iteration ($I^d_{inner1} = 1$) is required between the MSDSD$_s$ and the URC$_s$, while $I^d_{inner2} = 6$ iterations may be necessitated between the combined "MSDSD$_s$-URC$_s$" decoder and the IrCC$_s$.

For the sake of determining the 17 optimized weighting coefficients of the IrCC$_r$ employed by the transmitter of the relay seen in Figure 7.13, we commence by investigating the EXIT funtion of the amalgamated "MSDSD$_r$-IrCC$_r$" decoder associated with the 17 IrCC subcodes, which constitutes the second component decoder of the iterative receiver of Figure 7.14 employed at the BS. Since the previously considered equal-power-allocation and mid-point relay location based scenario is assumed, an identical EXIT chart will be created for the combined "MSDSD$_r$-IrCC$_r$" decoder at the BS for Scenarios I and II associated with an overall equivalent SNR of 2.3 dB and -0.7 dB, respectively, as shown in Figure 7.20. The EXIT curves of the combined "MSDSD$_r$-IrCC$_r$" decoder associated with each of the 17 IrCC subcodes are plotted in Figure 7.20(a) for the various values of N_{wind} employed by the MSDSD$_r$. It may be observed that the EXIT curves are shifted to the left upon increasing the value of N_{wind}, which result in an increased *extrinsic* mutual information I_E evaluated at the output of the combined "MSDSD$_r$-IrCC$_r$" decoder of Figure 7.14 for

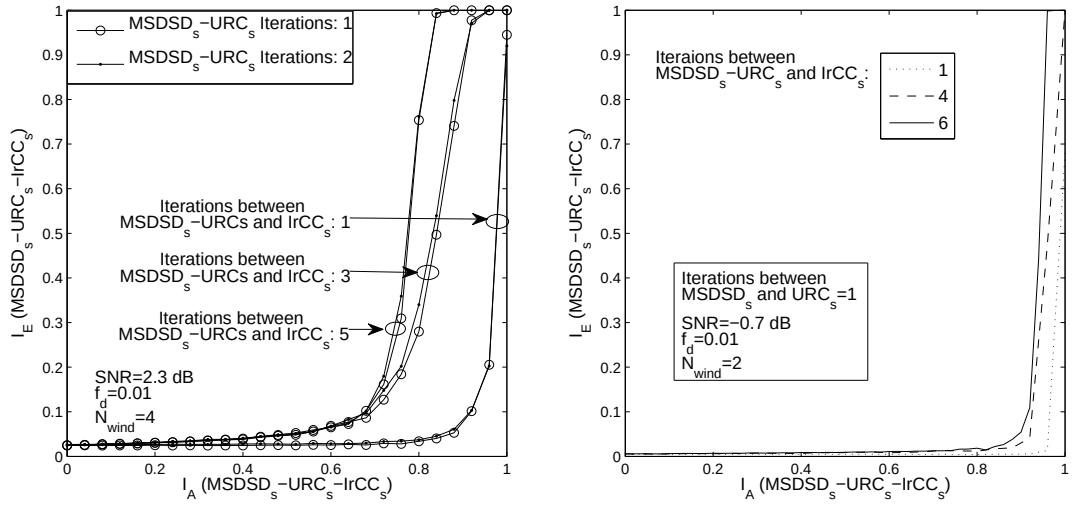

(a) Scenario I

(b) Scenario II

Figure 7.19: EXIT curves of the amalgamated "MSDSD$_s$-URC$_s$-IrCC$_s$" decoder of Figure 7.14 employed by the destination BS for different numbers of sub-iterations between the MSDSD$_s$ and the URC$_s$ and between the combined "MSDSD$_s$-URC$_s$" decoder and the IrCC$_s$.

a given input *a priori* mutual information I_A. However, for the sake of achieving a near-capacity performance at a relatively low complexity, $N_{wind} = 4$ is considered to be a reasonable choice, which strikes a compromise between the achievable performance and the complexity imposed. On the other hand, the EXIT curves of the combined "MSDSD$_r$-IrCC$_r$" decoder associated with 3 selected IrCC subcodes are also depicted in Figure 7.20(b) for different numbers of iterations between the MSDSD$_r$ and the IrCC$_r$. As observed in Figure 7.20(b), although the EXIT curve can be shifted to the left by increasing the number of iterations between the MSDSD$_r$ and the IrCC$_r$, any further shifting of the EXIT curve starts to become rather difficult when the number of iterations exceeds $I^d_{inner3} = 2$. Hence, based on the low-complexity near-capacity design criterion, the number of iterations between the MSDSD$_r$ and the IrCC$_r$ blocks of Figure 7.14 is chosen to be $I^d_{inner3} = 2$. In the sequel, a group of EXIT curves corresponding to the "MSDSD$_r$-IrCC$_r$" subcodes associated with $N_{wind} = 4$ and $I^d_{inner3} = 2$ iterations can be seen in Figures 7.21.

Finally, we use the EXIT curve matching algorithm of [117] in order to match the SNR-dependent EXIT curve of the combined "MSDSD$_r$-IrCC$_r$" decoder of Figure 7.14 to the target EXIT curves of the amalgamated "MSDSD$_s$-URC$_s$-IrCC$_s$" decoder of the BS portrayed in Figures 7.19(a) and 7.19(b) for Scenarios I and II of Table 7.1, respectively, as shown in Figure 7.21. As a result, for the sake of achieving a near-capacity performance while maintaining a moderate computational complexity, a 'wider-than-necessary' EXIT tunnel is created between the EXIT curve of the amalgamated "MSDSD$_s$-URC$_s$-IrCC$_s$" decoder and that of the combined "MSDSD$_r$-IrCC$_r$" decoder at the BS. Thus, the resultant average coding rates, R_r, of the IrCC$_r$ scheme designed for Scenario I and II of Table 7.1 are equal to 0.6 and 0.5, respectively, which cannot be achieved by simply using one of 17 IrCC$_r$ subcodes having the same code rate, as observed in Figure 7.21, owing to the absence of an open EXIT tunnel. The corresponding Monte-Carlo simulation based

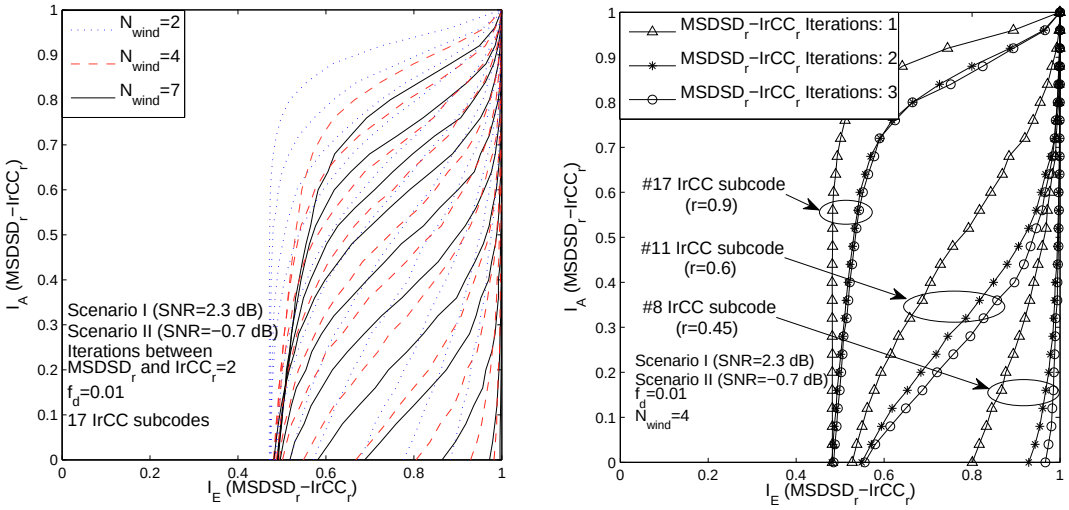

(a) For various N_{wind}.

(b) For different number of sub-iterations between the MSDSD$_r$ and the IrCC$_r$

Figure 7.20: EXIT curves of the amalgamated "MSDSD$_r$-IrCC$_r$" decoder employed by the destination BS.

decoding trajectory is also plotted in Figure 7.21 for both Scenarios I and II of Table 7.1, which reaches the $(1.0,\ 1.0)$ point of the EXIT chart, indicating the achievement of decoding convergence to an infinitesimally low BER at near-capacity SNRs for the Ir-DHCD coding scheme proposed in Section 7.4.2.

We have now completed the low-complexity near-capacity system design for the single-relay-aided cooperative system contrived for both Scenarios I and II of Table 7.1. Since the average code rate is fixed to $R_s = 0.5$ for the $IrCC_s$ at the transmitter of the source and the resultant capacity-achieving code rates R_r of the IrCC$_r$ employed at the relay are 0.6 and 0.5 for Scenario I and II, respectively, we can calculate the corresponding bandwidth efficiency using Eq. (7.77) as follows:

$$\eta^{coop}_{\text{Scenario I}} = \frac{R_s R_r}{R_s + R_r} \frac{T_b - 1}{T_b} \log_2 M_c \tag{7.81}$$

$$= 0.4664 \ \text{bits/s/Hz}, \tag{7.82}$$

and

$$\eta^{coop}_{\text{Scenario II}} = 0.4286 \ \text{bits/s/Hz}. \tag{7.83}$$

7.4.4 Simulation Results and Discussion

In order to carry out a fair comparison between the cooperative system and its conventional direct-transmission based counterpart, we also carry out a near-capacity system design for the latter in this section, which has exactly the same bandwidth efficiency as the former. To be more specific, according to Eq. (7.62), we can obtain the required code rate of the outer IrCC decoder employed

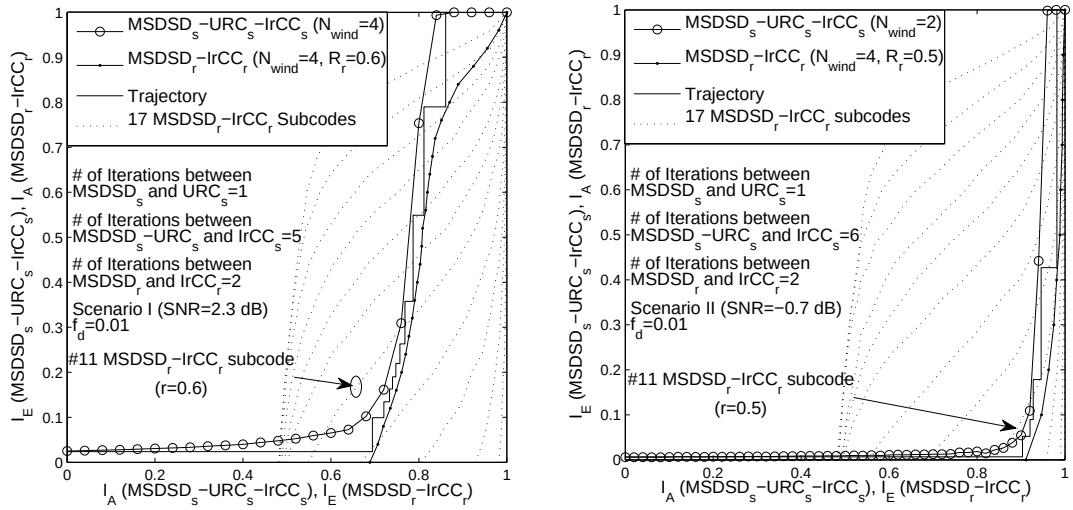

(a) Scenario I (b) Scenario II

Figure 7.21: Iterative decoding trajectory at the BS.

by the direct-transmission based system in Scenario I as follows:

$$R_{outer,\text{ScenarioI}} = \frac{T_b \cdot R_{overall}}{(T_b - 1) \cdot \log_2 M_c}, \tag{7.84}$$

$$= \frac{T_b \cdot \eta^{coop}_{\text{Scenario I}}}{(T_b - 1) \cdot \log_2 M_c}, \tag{7.85}$$

$$= 0.27, \tag{7.86}$$

and similarly for Scenario II, we have

$$R_{outer,\text{ScenarioII}} = \frac{T_b \cdot \eta^{coop}_{\text{Scenario II}}}{(T_b - 1) \cdot \log_2 M_c}, \tag{7.87}$$

$$= 0.25. \tag{7.88}$$

Hence, the near-capacity design for the URC-aided three-stage direct-transmission based system can be carried out for the target bandwidth efficiency, and the corresponding EXIT charts and Monte-Carlo simulation based iterative decoding trajectories are plotted in Figure 7.22 for both Scenarios I and II of Table 7.1.

Let us now depict the BER versus the overall equivalent SNR curves for both the point-to-point transmission based system and the single-relay-assisted cooperative system in Figure 7.23, which were previously designed to approach their corresponding capacity at a relatively low complexity. It is clearly shown in Figure 7.23 that upon using the near-capacity system design of Section 7.4.3 the proposed Ir-DHCD coding scheme becomes capable of performing within about 2 dB and 1.8 dB from the corresponding single-relay-aided DDF cooperative system's DCMC capacity in Scenarios I and II, respectively. Similarly, an infinitesimally low BER can be achieved by the point-to-point transmission based system at a SNR of 1.6 dB and 1.9 dB from the corresponding single-input single-output non-coherent DCMC capacity in Scenarios I and II of Table 7.1, respectively.

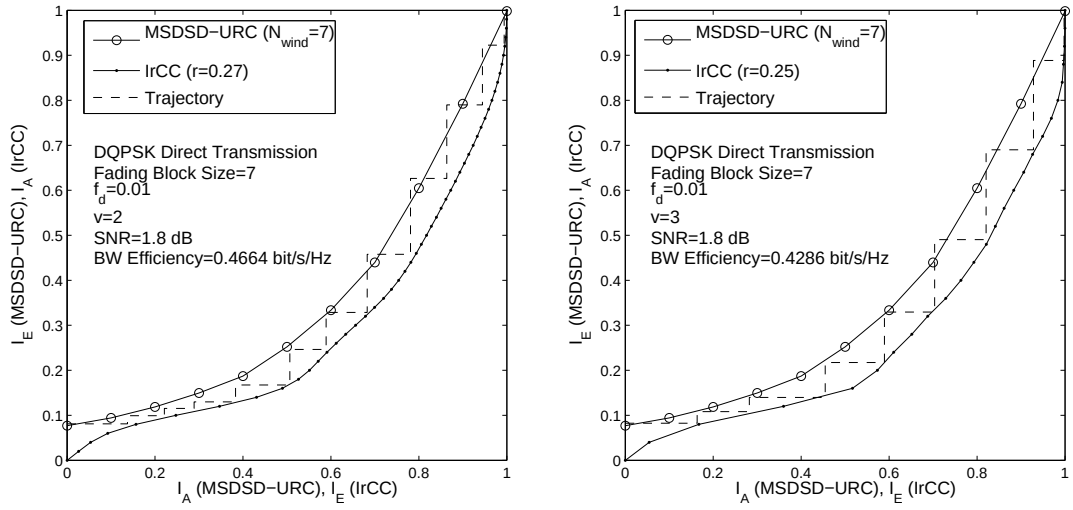

(a) Scenario I (b) Scenario II

Figure 7.22: Near-capacity design of the direct transmission system for both Scenarios I and II.

Furthermore, in line with our predictions made in Section 7.4.1.2, it is observed from Figure 7.23 that for a given target bandwidth efficiency, the single-relay-aided cooperative system does not necessarily guarantee a performance superior to that of the conventional direct-transmission based system. More specifically, in Scenario I, where the path loss exponent was set to $v = 2$ to simulate a free-space propagation environment, an SNR gain of 0.65 dB can be achieved by the direct-transmission based system over its single-relay-aided coopeartive counterpart, given a bandwidth efficiency of 0.4664 bits/s/Hz, as shown in Figure 7.23(a). However, when we have $v = 3$, in order to model the typical urban area cellular radio environment of Scneario II, the single-relay-aided cooperative system becomes capable of outperforming significantly the direct-transmission based system, requiring an overall transmit power which is about 2.5 dB lower than that needed by the latter to achieve an infinitesimally low BER, while maintaining a bandwidth efficiency of 0.4286 bits/s/Hz.

7.5 Chapter Conclusions

In Section 7.1, we commenced by reviewing the single-input single-output non-coherent DCMC capacity. More specifically, in Section 7.4.1 the single-relay-assisted DDF cooperative system's DCMC capacity was investigated and compared to that of the conventional direct-transmission based system. For the sake of convenience, we repeat the non-coherent DCMC capacity curves of both the direct transmission based and of the cooperative systems in Figure 7.24. In order to create a near-capacity design for the cooperative system, in Sections 7.4.2 and 7.4.3 the so-called Ir-DHCD encoding/decoding schemes were proposed together with the adaptive-window-aided MSDSD scheme, respectively, which are capable of approaching the capacity at a relatively low complexity. In contrast to the conventional point-to-point system, the proposed near-capacity

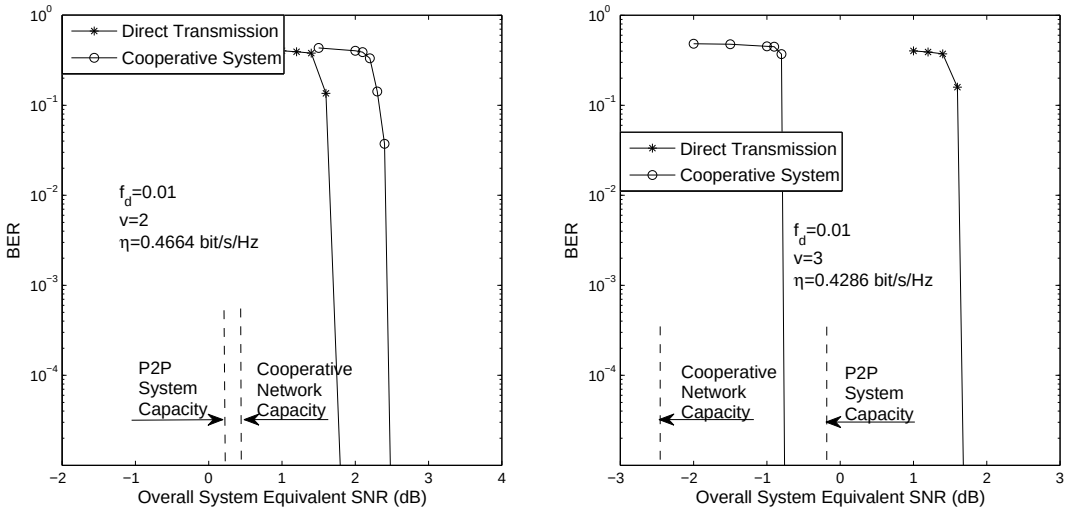

(a) Scenario I

(b) Scenario II

Figure 7.23: Achievable BER performance of the near-capacity designed single-relay-assisted cooperative system.

design of the single-relay-aided DDF cooperative system may be regarded as a joint source-and-relay mode design procedure, which was simplified in Section 7.4.3 to two EXIT curve matching problems in order to optimize the weighting coefficients of the IrCC decoders employed by both the source and the relay. A near-capacity performance can indeed be achieved by the proposed Ir-DHCD encoding/decoding schemes obeying our joint source-and-relay mode design, as demonstrated in Figure 7.24. More importantly, based on the capacity and on the practically achievable performance of classic direct transmission and single-relay-aided cooperative systems, we found in Figure 7.23(a) that the latter might be outperformed by the former, owing to the significant multiplexing loss inherent in the half-duplex single-relay-aided cooperative system. To be specific, in Figure 7.24 the single-relay-aided cooperative system was shown to be superior in comparison to its direct-transmission based counterpart only in the specific scenario when the reduced-path-loss related power gain was sufficiently high in order to compensate for the multiplexing loss. In our future research we will consider successive relaying aided arrangements [144] in order to mitigate the above-mentioned multiplexing loss.

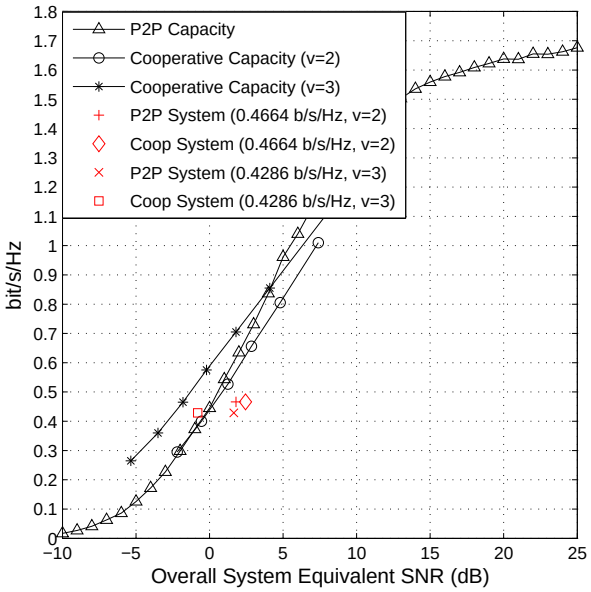

Figure 7.24: EXIT curves of the amalgamated "MSDSD$_s$-URC$_s$-IrCC$_s$" decoder employed by the destination BS for various observation window sizes N_{wind}.

Chapter 8

Conclusions and Future Research Ideas

In this treatise, we designed and investigated the low-complexity near-optimum SD assisted MIMO schemes contrived for transmission over fading wireless channels operating in multi-user scenarios, where multiple users may transmit simultaneously relying purely on their own transmit antenna(s) or may cooperatively share their transmit antenna(s) in order to form a VAA. Hence, this treatise is constituted of two major parts focusing on the above-mentioned two distinct types of MIMO systems, respectively, namely, on the non-cooperative systems of Chapter 2-4 and on the user-cooperation based systems of Chapter 5-7. The philosophy of the latter family was proposed quite recently in order to circumvent the cost- and size-limitations of pocket-sized mobiles in the pursuit of attaining spatial transmit diversity gain in the single-antenna aided multi-user cellular systems. For the sake of achieving a near-optimum performance at a low complexity, the coherent SD was invoked for non-cooperative MIMO systems, where $(N_t \times N_r)$ CIRs have to be estimated. By contrast, its non-coherent counterpart, namely, the MSDSD, may be employed in user-cooperation based systems, where no channel estimation is needed at the RS or at the destination BS. This allows us to avoid the potentially excessive channel-estimation-related complexity as well as the high pilot overheads, especially in mobile environments associated with relatively rapidly fluctuating channel conditions.

The concluding remarks provided in this chapter are based on an amalgam of our chapter conclusions provided at the end of Chapter 2-7. Our current remarks allow us to establish their logical connection. To this end, the contributions of this treatise belong to three categories:

1). SD algorithm optimization: The SD algorithm of Section 3.2.1 was optimized for MIMO systems employing channel coding and iterative detection, in order to further reduce its imposed complexity while maintaining a near-optimum performance. The generic center-shifting based SD of Section 3.2.3 and the ALT-assisted SD scheme of Section 3.3 were proposed for non-cooperative MIMO systems. By contrast, the adaptive-window-duration based MSDSD of Section 7.4.3.1 was designed for cooperative MIMO systems.

2.) SD applications: With the aid of the proposed multi-layer tree search mechanism, the SD of Section 2.2 was then further developed for employment in the SP-modulated non-cooperative MU-MIMO system of Chapter 4 as well as for the DAF- and DDF-aided cooperative systems of

Chapter 5. Our main design goal was that of maximizing the achievable transmit diversity gains.

3). SD-aided MIMO system design: The issues of power allocation amongst the source and relays as well as cooperating user selection techniques were discussed in Chapter 6, in the context of user-cooperation based systems. Furthermore, near-capacity system designs were contrived for SD-assisted cooperative and non-cooperative MIMO systems in Chapters 7 and 3, respectively, for the sake of maximizing the achievable spetral efficiency. In the following sections, our novel contributions falling into categories are highlighted, along with our suggestions for future research.

8.1 SD Algorithm Optimization in Pursuit of Reduced Complexity

8.1.1 Exploitation of the LLRs Delivered by the Channel Decoder

Although the conventional LSD is capable of achieving a near-MAP performance, while imposing a significantly reduced complexity in comparison to the exact-MAP detector, the complexity of the LSD may still become excessive in the channel-coded iterative detection aided MIMO system supporting a high number of users/transmit antennas and/or employing high-order modulation schemes, such as 16-QAM. This is because the size of the transmitted MIMO symbol candidate list generated by the LSD has to remain sufficiently large in the above-mentioned scenarios, in order to deliver sufficiently accurate soft bit information, i.e. LLRs, to the channel decoder during the iterative detection process, hence achieving a high iteration gain. Otherwise, the LSD's EXIT curve may even decay upon increasing the *a priori* information fed back by the channel decoder, as observed in Figure 3.2 of Section 3.2.1.3 as a consequence of having an insufficiently large candidate list size. This results in a significantly reduced iteration gain. This is because the inner SD and outer channel decoder of Figure 3.1 exchange flawed information owing to a shortage of candidate solutions, more particularly, owing to the absence of the ML solution in the candidate list, as revealed in Section 3.2.1.3. Thus, in order to further reduce the computational complexity imposed by the conventional LSD, we optimized the LSD algorithm based on the exploitation of the LLRs gleaned from the channel decoder during the iterative detection process by devising two enhanced SD schemes, namely, the center-shifting-based SD of Section 3.2 and the ALT-based SD of Section 3.3.

More specifically, the SD procedure may be divided into two successive phases, namely, the search center calculation phase followed by the confined tree search phase, as shown in Figure 8.1. The operations in both of these phases may be optimized independently by exploiting the LLRs provided by the channel decoder during the iterative detection process. For the center calculation phase, conventional SDs employ either the LS or the MMSE algorithm for the computation of the search center $\hat{\mathbf{c}}$, as discussed in Section 3.2.2, which is carried out only once during the first iteration. However, during our investigations in Section 3.2.2, we realized that it would be desirable to set the SD's search center to a multiuser signal constellation point, which may be obtained using more sophisticated algorithms rather than the LS or MMSE scheme and thus is expected to be closer to the real MAP solution than both the LS and MMSE solutions, because this would allow us to reduce the SD's search space and hence its complexity.

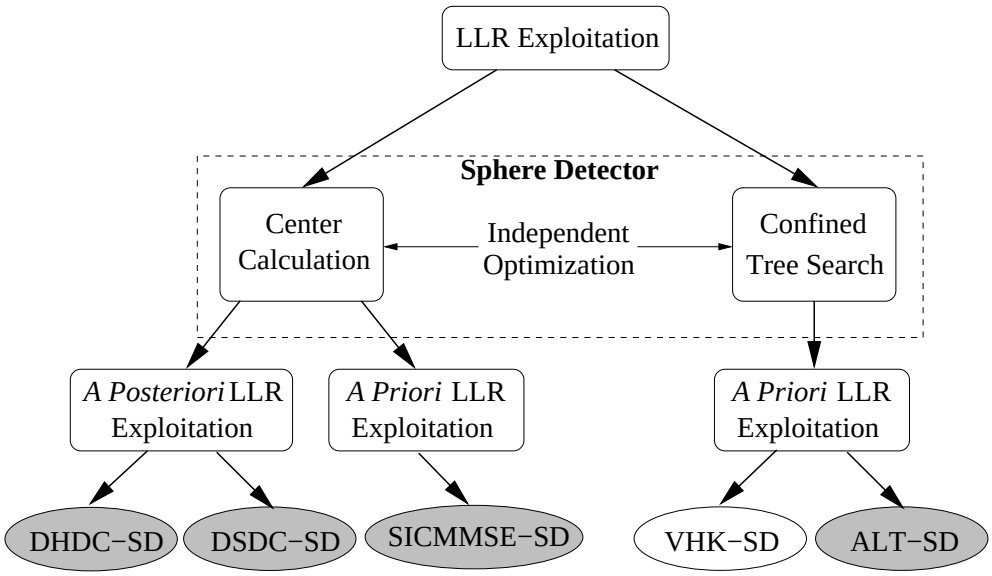

Figure 8.1: Independent search center calculation and search phase operations that may be used by the SD. Note that the shaded ellipses represent the novel schemes contrived in this treatise.

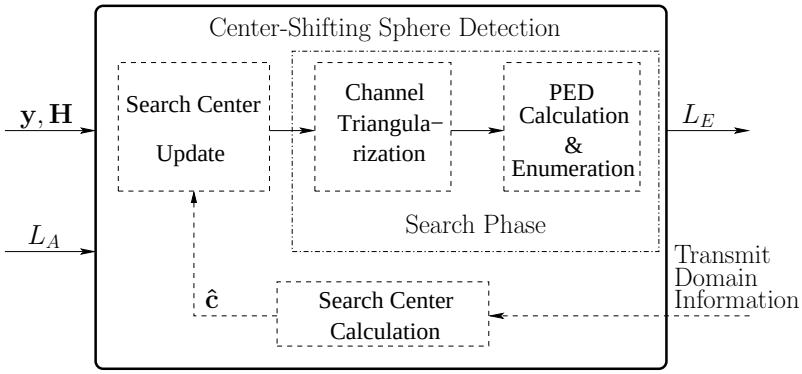

Figure 8.2: The structure of the generic iterative center-shifting based SD scheme.

Then, based on the center-shifting theory, we proposed a generic center-shifting-aided SD scheme in Section 3.2.2, as portrayed in Figure 8.2, which may be expected to become significantly more powerful, if it is employed in an iterative detection aided channel coded system, since the process of generating a more accurate search center is further aided by the channel decoder, which substantially contributes towards the total error-correction capability of the iterative receiver. Hence, in this treatise, three particular center-shifting based SD schemes were devised, as shown in Figure 8.1, which are the DHDC-aided center-shifting SD of Section 3.2.3.1, the DSDC-aided center-shifting SD of Section 3.2.3.2 and the SIC-MMSE-aided center-shifting SD of Section 3.2.3.3. The former two simply update the search center of the SD by the hard- and soft-decisions of the corresponding transmitted MIMO symbols, respectively, which are obtained based on the *a posteriori* LLRs at the output of the channel decoder, while the latter one exploits the slightly more sophisticated SIC-MMSE algorithm in order to update the search center based on the *a priori* LLRs provided by the channel decoder. The operations of the proposed center-shifting schemes are summarized in Table 8.1 in contrast to those of the conventional SD using no center-shifting. Note that in contrast to the LSD dispensing with center-shifting scheme, which may

Operations of Various Iterative Center-Shifting-Based SD Schemes				
	Conventional SD	**DHDC-SD**	**DSDC-SD**	**SICMMSE-SD**
Center-Update Algorithm	no center-update	direct-hard-decision	direct-soft-decision	SIC-MMSE
Type of Exploited LLR in Center-Update Phase	no LLR-exploitation	*a posteriori* LLR fed by outer decoder	*a posteriori* LLR fed by outer decoder	*a priori* LLR fed by outer decoder
When to Update Center	compute center only once at the first iteration	center-update is activated when iteration converges	identical to DHDC	center-update activated at the beginning for each iteration
When to Regenerate Candidate List	no need to regenerate during iterations	regenerate every time the center is updated	identical to DHDC	identical to DHDC
When to Recalculate the Output LLRs	recalculate for each iteration	identical to conventional SD	identical to conventional SD	identical to conventional SD

Table 8.1: Operations of various iterative center-shifting-based SD schemes in comparison to that of the conventional SD.

generate the candidate-list only once at the very beginning of the entire iterative detection process, our proposed iterative center-shifting based SDs have to regenerate the candidate-list for the following soft-bit-information calculation, as long as the search center is updated during the iterative detection process. However, the computational complexity imposed by each candidate-list generation of the center-shifting based SD may be exponentially reduced, since the increasingly accurate search centers generated during the iterative detection process allow us to rely on a significantly reduced candidate-list size, while maintaining a near-MAP performance. Hence, the overall complexity imposed by the iterative center-shifting based SD is expected to be significantly reduced in comparison to the conventional SD dispensing with the center-shifting scheme, despite having an increased number of list generations during the entire iterative detection process.

According to the iterative center-shifting based SD receiver design of Sections 3.2.3.1-3.2.3.3, the center-shifting SD aided receiver design principles can be summarized as follows:

1) *The search center calculation is based on the soft bit information provided by the channel decoder.*

2) *The search center update can be carried out in a more flexible manner by activating the proposed center-shifting scheme, whenever the system requires its employment during the iterative detection process in order to maximize the achievable iterative gain.*

3) *The search center update is flexible, since it may be carried out by any of the well-known linear or non-linear detection techniques.*

The key simulation results obtained in Section 3.2 as to the BER performance and complexity of the three proposed iterative-center-shifting based SDs are summarized and quantified in Table 3.7, in comparison to the conventional SD-aided iterative receiver using no center-shifting scheme. Specifically, in the challenging (8×4)-element 4QAM SDMA/OFDM system, the DHDC-aided, the DSDC-assisted and the SIC-MMSE-aided center-shifitng SDs of Sections 3.2.3.1-3.2.3.3 using $K = N_{cand} = 32$ are capable of achieving a BER of 10^{-5} by requiring 0.1dB, 0.6dB and 2.6dB lower transmit power or SNR than that necessitated by the conventional SD dispensing with the center-shifting scheme and using the same values of K as well as N_{cand}. Remarkably, the SIC-MMSE center-shifting SD scheme of Section 3.2.3.3 using $K = N_{cand} = 32$ may en-

Performance Gain & Computational Complexity Reduction Achieved by Various Center-Shifting Schemes in an (8×4)-element 4-QAM SDM/OFDM Rank-Deficient System

BER	Center-Shifting	$N_{cand}(K)$	Iterations	SNR	Memories	SD Compl.	MAP Compl.
10^{-5}	NONE	1024	3	10.5	8196	13652	49152
		128	3	11.2	1024	2388	6144
		64	2	12	512	1364	2048
		32	2	12.8	256	724	1024
		16	2	15	128	404	512
	DHDC	64	2+2	11.3	512	4092	4096
		32	2+2	12.7	256	2172	2048
	DSDC	64	2+2	10.5	512	4092	4096
		32	2+2	12.2	256	2172	2048
	SIC-MMSE	64	3	10.2	512	4092	3072
		32	3	10.2	256	2172	1536
		16	3	11	128	1212	768

Table 8.2: Comparison of the conventional *K*-best SD and our proposed iterative center-shifting-based *K*-best SDs in the scenario of an (8×4)-element rank-deficient SDMA/OFDM system: Note that the computational complexity of the SD, i.e. the list generation complexity of the SD, is calculated in terms of the total number of PED evaluations, while that of the soft information generation by the SD/MAP detector is quantified on the basis of Eq.(3.16) in terms of the total number of OF evaluations corresponding to the two terms in Eq.(3.14).

able the iterative receiver to exhibit a near-MAP performance which is achieved by the conventional SD using no center-shifting in conjunction with a significantly larger candidate list size of $K = N_{cand} = 1024$. This near-MAP performance is achieved, despite imposing a reduced detection-candidate-list-generation-related complexity, which is about an order of magnitude lower than that exhibited by the list-SD dispensing with the proposed center-shifting scheme. As a further benefit, the computational complexity associated with the *extrinsic* LLR calculation was reduced by a factor of about 64. The associated memory requirements were also reduced by a factor of 64.

As shown in Figure 8.1, the soft-bit-information delivered by the channel decoder may be exploited for both the tree-search phase and the center calculation phase of the SD. The LSD proposed by the Vikalo, Hassibi and Kailath (VHK-SD) [52] was the first one to exploit the *a priori* LLRs provided by the channel decoder in the confined tree search process, which was arranged by including the effect of the *a priori* LLRs in the OF of the SD in a similar manner to that seen in Eq. (7.44) of Section 7.3.1, where the exploitation of the soft-bit-information by the MSDSD was highlighted. In Section 3.3, another reduced-complex technique termed as the ALT-aided SD scheme was devised by exploiting the reliability of the bit decision conveyed by the *a priori* LLRs. More specifically, the philosophy of the ALT-aided SD is to assume a perfect knowledge of a particular bit, i.e. 0 or 1, and then testing whether the absolute value of the corresponding *a priori* LLR is higher than the preset threshold (ALT), followed by pruning the branch associated with the opposite bit value, before the tree search continues. Thus, a better pruning search tree may be formed as seen for example in Figure 3.23 of Section 3.3.1, resulting in an improved performance and a reduced complexity, as observed in Figure 3.24 of Section 3.3.2.1 and Figure 3.25 of Sec-

Comparison of ALT and Center-Shifting Schemes for SDs		
	ALT	**Center-Shifting (CS)**
LLR-Exploitation Based	yes	yes
Type of Exploited LLR	*a priori* LLR	*a posteriori* or *a priori* LLR, depending on the employed center-calculation algorithm
Optimization Target	tree search phase	center calculation phase
Center Recalculation	no	yes
Candidate List Regeneration	yes, for each iteration	yes, when the center is updated
Achievable Benefits	1). significant overall reduced detection-complexity 2). significant reduced memory requirements	More pronounced achievements in detection-complexity and memroy requirements than ALT
Overheads (Side Effects)	1). Performance sensitive to threshold choice 2). non-Gaussian output LLRs	increased complexity in center-calculation phase for each iteration
CS-ALT Combination	significantly more detection-complexity-reductions can be achieved	
Applications	applicable to both coherent SDs and non-coherent MSDSDs of Chapter 5	only works for coherent SDs, no center-update is needed for MSDSDs (centered at the origin)

Table 8.3: Comparison of the center-shifting and the ALT aided SDs of Sections 3.3 and 3.2.

tion 3.3.2.2, respectively. As demonstrated in Section 3.3.2.3, the ALT threhold has to be carefully adjusted for the sake of achieving the target performance as a function of the SNR encountered. Furthermore, Section 3.3.2.4 demonstrated that the non-Gaussian distribution of the LLRs at the output of the ALT-aided SD during the iterative detection process limits its capacity and imposes difficulties in the EXIT chart assisted performance prediction. On the other hand, although the proposed ALT scheme is capable of providing useful performance improvements, which are slightly less significant than those achieved by the SIC-MMSE-assisted center-shifting based SD scheme of Section 3.2.3.3, an attractive performance-complexity trade-off may be achieved by the combination of the two, as seen in Section 3.3.3. More particularly, the detection-complexity imposed by the SIC-MMSE-assisted center-shifting SD can be halved with the aid of the ALT technique as observed in Figure 3.36, despite suffering a modest performance loss of about 0.5dB, as demonstrated in Figure 3.35 in the (8×4)-element 4QAM SDMA/OFDM scenario. The features of the proposed ALT technique are summarized in comparison to those of the center-shifting scheme in Table 8.3. Note that the ALT scheme is applicable to both the coherent SD and the non-coherent SDs (MSDSD), whereas the center-shifting scheme works only for the coherent SDs. This is because the equivalent search center of the MSDSD of Chapter 5 is the origin, which is independent of the transmitted signal, hence requiring no updates.

8.1.2 EXIT-Chart-Aided Adaptive SD Mechanism

As a further evolution of the LLR-exploitation-based complexity-reduction schemes contrived for coherent SD-aided iterative receivers in Sections 3.2 and 3.3, an EXIT-chart-aided adaptive mech-

Generic Adaptive SD Mechanism for Iterative Receivers	
Adaptive Parameter Choice	As the parameter increases: 1). the SD's complexity exhibits an exponential growth; 2). the corresponding EXIT curve is shifted increasingly higher.
Operations	1). set the parameter to the smallest value; 2). slightly increase it as soon as the iterative decoding converges; 3). candidate list regeneration is required if the value of the parameter is changed.
Achievable Benefits	significant complexity reduction, as seen in Figure 7.17(b)
Overheads	increased number of total detection iterations
Applications	applicable to both the coherent SD and the non-coherent SD

Table 8.4: Generic adaptive SD mechanism.

anism was proposed for the sake of reducing the complexity imposed by a SD-aided near-capacity system in the context of non-coherently detected SD aided cooperative systems. Specifically, an adaptive-window-duration based MSDSD scheme was devised in Section 7.4.3.1. The philosophy of the proposed adaptive-window based scheme, which is characterized by the EXIT chart of Figure 7.17(a) in Section 7.4.3.1, is based on the observation that the intersection point of the EXIT curves of the inner and outer decoders may be gradually pushed towards the $(1,\ 1)$ point by increasing the observation window size N_{wind} at the cost of imposing an exponentially increased computational complexity per iteration. Thus, in order to reduce the overall detection-complexity, while maintaining a near-capacity performance, the observation window size of the adaptive-window-duration based MSDSD was initially set to the smallest value of $N_{wind} = 2$, which would be slightly increased as soon as the iterative decoding between the inner and outer decoders converged. The significantly reduced overall complexity observed in Figure 7.17(b) of Section 7.4.3.1 is due to the exponentially reduced complexity imposed by the early-stage iterations using small values of N_{wind}, despite having an increased total number of iterations required by the decoding trajectory to reach the $(1,\ 1)$ point. Remarkably, the complexity imposed by the MSDSD$_s$ is substantially reduced, as seen in Figure 7.17(b) of Section 7.4.3.1, which is a benefit of the adaptive-window assisted scheme. Quantitatively, observe in Figure 7.17(b) that this complexity reduction may be as high as 75% at $SNR_t^{overall} = 2$ dB, when the open EXIT tunnel created by having $N_{wind} = 7$ becomes rather narrow. The attainable complexity reduction increases even further to about 83%, when the open EXIT tunnel becomes wider at $SNR_t^{overall} = 4$ dB, as also seen in Figure 7.17(b).

Importantly, we would like to point out here that the simple yet powerful adaptive SD mechanism proposed for the MSDSD in Section 7.4.3.1 may be also applied to the coherent SD-aided iterative receiver of Chapter 3 for the sake of reducing the overall iterative-detection-complexity. More specifically, the candidate-list size N_{cand} may be adaptively increased based on the same philosophy used by the adaptive-window-duration aided scheme during the iterative detection process, since the EXIT curve is shifted upward as the value of N_{cand} increases, as observed for example in Figure 3.2 of Section 3.2.1.3. The principles of the generic adaptive SD mechanism invoked in iterative receivers are summarized in Table 8.4 along with its major characteristics.

8.2 Transmit Diversity Schemes Employing SDs

A multi-layer tree search mechanism was proposed for SDs in Chapter 4 in order to facilitate its application in STBC-SP-assisted MU-MIMO systems in the interest of achieving a near-MAP performance at a low complexity. Based on the philosophy of the multi-layer tree search, we also adopted the SD algorithm at the BS for the differentially modulated user-cooperation based cellular uplink scenario of Chapter 5 for the sake of jointly and non-coherently detecting the multi-path signals transmitted by the source and relay nodes. In the ensuing Section 8.2.1 the idea of the multi-layer tree search aided SD will be briefly echoed, followed by the summary of its applications in the above-mentioned transmit-diversity-oriented systems in Section 8.2.2.

8.2.1 Generalized Multi-Layer Tree Search Mechanism

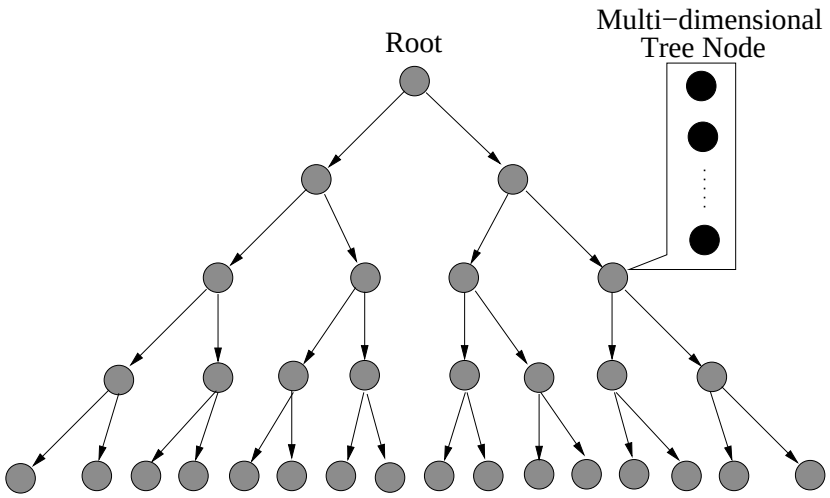

Figure 8.3: Generic multi-layer search tree.

In comparison to the tree search of Section 2.2 conducted by the conventional SD algorithm, where each tree node is a single dimension associated with the trial symbol point transmitted from a specific transmit antenna, the tree node of the generic multi-layer search tree depicted in Figure 8.3 may be constituted of a number of symbol candidates transmitted from multiple spatially seperated antennas of either a particular user or of different users, and thus may be of multi-dimensional nature. Actually, the generic multi-layer tree search mechanism of Section 4.3.2.3 includes the conventional single-layer tree search as a special case, when the signals transmitted from different antennas are uncorrelated with each other. In other words, when the signals transmitted from different antennas are jointly designed as, for example, experienced in the STBC-SP-aided MU-MIMO system of Section 4.2.2.1 or exhibit correlations as, for exmpale, encountered in the user-cooperation based systems of Section 5.3.1, the multi-layer tree search of Section 4.3.2.3 has to be invoked.

8.2.2 Spatial Diversity Schemes Using SDs

It was argued in Section 4.2.2.1 that combining orthogonal transmit diversity designs with the principle of SP is capable of maximizing the achievable coding advantage. The resultant STBC-SP

scheme was capable of outperforming the conventional orthogonal design based STBC schemes in the SU-MIMO scenario. Specifically, the STBC-SP scheme of Section 4.2.2.1 combines the signals transmitted from multiple antennas into a joint ST design using the SP scheme, as demonstrated in Figure 4.4. However, existing MU-MIMO designs make no attempt to do so, owing to the associated complex detection. We solved this complexity problem by further developing the SD for the detection of SP modulation using the proposed multi-layer tree search mechanism in Section 4.3, because SP may offer a substantial SNR reduction, although at a potentially excessive complexity, which can be reduced by the multi-dimensional tree search based SD of Section 4.3.2. Explicitly, the K-best SD algorithm designed for a 4-dimensional SP modulation scheme was summarized in Section 4.3.2.3. The enhanced coding advantage achieved by the STBC-SP is indicated by the increased area under the corresponding EXIT curve in contrast to that associated with the conventional STBC scheme, as observed in Figure 4.9 of Section 4.3.3. More particularly, as a benefit of employing the SP modulation, performance gains of 1.5 dB and 3.5 dB can be achieved by 16-SP and 256-SP modulated systems in *Scenario I* and *Scenario II* of Table 4.2, respectively, in comparison to their identical-throughput QAM-based counterparts, given a target BER of 10^{-4} and $N_{cand} = 128$, as observed from Figures 4.10(a) and 4.10(b) of Section 4.3.3.

Although co-located multiple transmit antenna aided diversity techniques are capable of mitigating the deleterious effects of fading, as noted in Chapter 4, it is often impractical for a pocket-size terminal to employ a number of antennas owing to its limited size and cost constraint. Fortunately, another type of transmit diversity, namely, the so-called cooperative diversity relying on the cooperation amongst multiple single-antenna-assisted terminals may be achieved in multi-user wireless systems. On the other hand, a more realistic user-cooperation mechanism requiring no CSI was advocated in Chapter 5, which was based on differentially encoded transmissions and on non-coherent detection techniques. Hence they circumvent the potentially excessive-complexity channel estimation as well as the high pilot overhead encountered by conventional coherent detection aided cooperative systems, especially in mobile environments associated with relatively rapidly fluctuating channel conditions. The ML-MSDD technique of Section 5.2.1 was introduced in support of user-cooperation in the context of the multi-layer tree search based SD algrithm of Section 5.3.3.4, for the sake of rendering the system robust to time-selective propagation environments at an affordable complexity, leading to a MSDSD-aided differential user-cooperation based system. The characteristics of the uncoded MSDSD-aided cooperative systems using both the DAF and DDF schemes of Sections 5.3.2.1 and 5.3.2.2 are compared and summarized in Table 8.5. Note that during the MSDSD design procedure adopted for differentially encoded cooperative systems in Section 5.3.3, we relied on the assumptions that both the signal and noise received at the BS in the DAF-aided system obey complex Gaussian distributions and that the source's signal can always be error-freely decoded prior to forwarding it to the BS in the DDF-aided system. This allowed us to significantly simplify the associated MSDSD design problems, while still being able to construct a powerful non-coherent detector, which is substantially more robust to the effects of mobile environments than the CDD. Finally, since the SD devised for both the STBC-SP-based non-cooperative MU-MIMO system of Chapter 4 and for the differentially encoded user-cooperation-based system of Chapter 5 employs the multi-layer tree search mechanism, the salient features concerning the multi-dimensional search tree are summarized in Table 8.6.

Characteristics Comparison of the Channel-Uncoded DAF- and DDF-Aided Cooperative Systems			
	DAF	**DDF**	**Remarks**
Sensitivity to SR Link	modest	strong	see Fig.5.14
Potential Drawbacks	noise amplification	error propagation	see Eq.(5.62) for DAF & Fig.5.13 for DDF
MSDSD Design Assumptions	Gaussican distributed received signal & noise	error-free decoding at RS	reasonable assumptions significantly simplify the MSDSD design problem
Complexity at Relay	low (amplify)	high (decode and re-encode)	E2E performance improves as more computational efforts put into RS, see Fig.5.15
SR Link vs RD Link	equally important	SR link is more important	exchangeability of SR & RD links for DAF system is seen in Eq.(5.60) & Fig.5.19, SR link's importance for DDF is seen Fig. 5.22
Performance Gain Achieved by MSDSD	error-floor completely eliminated	error-floor completely eliminated	see Fig.(5.18) for DAF, see Fig.(5.21) for DDF

Table 8.5: Characteristics of the DAF- and DDF-aided cooperative systems of Sections 5.3.2.1 and 5.3.2.2.

Generic Multi-Layer Tree Search Based SD in Two Particular Applications		
	STBC-SP-Based MU-MIMO System (Chapter 4)	**Differential User-Cooperation-Based System (Chapter 5)**
Tree Node Representation	the SP-aided joint ST designed signal transmitted by each user, see Eq. (4.52)	the equivalent user-cooperation based ST signal transmitted by the source and relays, see Eq. (5.46)
Tree Node Dimension	number of antennas per user (M_u)	number of cooperating users (U)
Tree Node Structure	column vector	diagonal signal matrix

Table 8.6: Generic multi-layer tree search based SD in two particular applications.

8.3 SD-Aided MIMO System Designs

8.3.1 Resource-Optimized Hybrid Cooperative System Design

Although it was shown in Chapter 5 that the maximum attainable spatial diversity gain can usually be achieved by the differentially modulated user-cooperative uplink system, the achievable end-to-end BER performance may significantly depend on the specific choice of the cooperative protocol employed and/or on the quality of the relay channel. Therefore, the resource allocation arrangements employed by the cooperative cellular uplink, namely the transmit power allocaton and the RS's geometric location, play a vital role in achieving the best possible performance. In order to achieve the best possible BER performance, a flexible resouce-optimized adaptive hybrid cooperation-aided system was designed in Chapter 6. The corresponding system design procedure based on the major findings of each section of Chapter 6 is summarized in Table 8.7. More specifically, the associated theoretical performance analysis was carried out for both the DAF- and DDF-aided cooperative systems in Sections 6.2.1 and 6.2.2, respectively. The derived exact end-to-end BER expression of Eq. (6.40) for the DAF-aided system was significantly simplified by assuming a high SNR and by using the same technique as in [128], resulting in the tight BER lower bound

Resource-Optimized Differentially Modulated Hybrid Cooperative System Design Procedure	
Theoretical BER Performance Analysis (Section 6.2)	**1)**. For DAF systems, the simplified high-SNR-based BER lower bound of Eq.(6.48) was found to be tight in Fig.6.5; **2)**. For DDF systems, based on the worst-case PLR of Eq.(6.52) at the RS, the BER upper bound of Eq.(6.56) closely captured the BER's dependency on the SNR in Fig.6.6.
↓ **Resource-Allocation Optimization** (Section 6.3)	**1). Criterion:** minimum-BER; **2). Optimized resources:** power allocation & RS location; **3). Benefits:** performance gain (see Figs.6.9 and 6.14) & detection-complexity reduction (see Fig.6.12(b)), which may be enhanced by iterative power-versus-RS-location optimization schemes (see Figs.6.11 and 6.17).
↓ **Comparative Studies of Resource-Optimized DAF and DDF Systems** (Section 6.4.1)	**1). Sensitivity to the SR link quality:** DDF system's performance degrades more rapidly for a poor SR link quality (see Fig. 6.18); **2). Effect of the packet length:** the DAF system's performance is independent of the employed packet length L_f, while its DDF counterpart's performance is sensitive to L_f (see Fig. 6.16); **3). Resource allocation:** DAF and DDF systems exhibit complementarity (see Fig.6.19, Tables 6.5 and 6.7).
↓ **Resource-Optimized Hybrid System Design** (Section 6.4.2)	**1). Goal:** exploit the complementarity of the DAF and DDF systems in order to design a more flexible resource-optimized hybrid cooperative system; **2). Mechanism:** cooperative protocol employed by the activated RS is adaptively chosen in the interest of achieving the best BER performance. **3). Benefits:** improved performance (see Fig.6.21)

Table 8.7: Resource-optimized differentially modulated hybrid cooperative system design procedure.

of Eq. (6.48), as characterized in Figure 6.5, which was valid for high SNRs. As to the DDF-aided system, the BER upper bound of Eq. (6.56) was derived for the single-relay-assisted system as an example based on the worst-case PLR of Eq.(6.52) at the RS, which was shown to be capable of closely capturing the dependency of the BER on the SNR, as seen in Figure 6.6.

The above-mentioned power allocation and RS location selection schemes were investigated for both the DAF- and DDF-aided systems in Section 6.3 With the aid of our theoretical BER results of Section 6.2. More particularly, based on the minimum-BER criterion, the APC schemes of the DAF- and DDF-aided system were devised in Sections 6.3.1.1 and 6.3.2 respectively, which were capable of achieving significant performance gains by finding the optimum power allocation for a given RS location arrangement, as depicted in Figures 6.9(a) and 6.14(a). On the other hand, based on the observation of Figures 6.9(b) and 6.14(b) we found that the achievable BER is proportional to the distance between the cooperating MS and the optimum RS location. Hence the CUS schemes, which were contrived for both the DAF- and DDF-aided systems in Sections 6.3.1.2 and 6.3.2, respectively, simply activate the RS closest to the optimum location from the available RS candidate pool, resulting in substantial performance improvements, as observed in Figures 6.11 and 6.17. For the sake of achieving the globally optimum resource allocation, iterative power-versus-RS-location optimization was also carried out in Sections 6.3.1.2 and 6.3.2, as illustrated in Figures 6.10 and 6.15. Remarkably, apart from having an enhanced BER performance, the complexity imposed

by the MSDSD of Chapter 5 can be also significantly reduced by employing the CUS and APC schemes in the context of rapidly fading channels, as observed in Figures 6.12(b) and 6.13(b).

Due to the different levels of sensitivity to the quality of the SR link as seen in Figure 6.18, the optimum resouce allocation arrangements corresponding to the two above-mentioned systems may be quite different, as revealed by our comparative studies in Section 6.4.1. Specifically, as indicated by Table 6.5, it is desirable that the activated cooperating MS are roaming in the vicinity of the source MS for the DDF-aided system, while the cooperating MS roaming in the neighbourhood of the BS are prefered for its DAF-aided counterpart. Additionally, in comparison to the former system, a larger portion of the total transmit power should be allocated to the source MS in the context of a DAF-aided system. Furthermore, in order to exploit the complementarity of the above-mentioned cooperative systems, a more flexible resouce-optimized adaptive hybrid cooperation-aided system was proposed in Section 6.4.2, where the protocol employed by a specific cooperating MS may also be adaptively selected in the interest of achieving the best possible BER performance. Thus, the DAF and DDF cooperative protocols may co-exist in the same cooperative network. As an example, the operations of the hybrid cooperative cellular uplink system are summarized as follows:

[**1**] *Determine the DAF and DDF areas between the source MS and the BS by calculating the globally optimum RS locations via the proposed iterative power-versus-RS-location optimization scheme.*

[**2**] *In order to exploit the complementarity of the DAF and DDF schemes, activate an RS in each above-defined areas, which is situated closest to the globally optimum location.*

[**3**] *Adaptively calculate the power allocation solution based on the actual locations of the activated RSs.*

8.3.2 Near-Capacity Cooperative and Non-cooperative System Designs

For the sake of achieving a performance, which is close to the system's capacity, we devised a low-complexity near-capacity system design with the aid of near-optimum SDs for both the non-cooperative and cooperative MIMO systems in Section 3.4 and Section 7.4, respectively. The near-capacity design of the former system, which is reduced to an EXIT curve matching problem, serves as the fundamental method of achieving the cooperative network's capacity for the latter system, since the joint source-and-relay mode design procedure of the single-relay-aided cooperative system can be decoupled into two separate EXIT curve matching problems.

For the non-cooperative MIMO system, the near-capacity system design procedure is summarized in Table 8.8 along with its corresponding URC-aided three-stage receiver structure. To be specific, in order to approach the channel capacity of the non-cooperative MIMO system, we demonstrated in Section 3.4.1 that the iterative decoding convergence of this two-stage system may be improved by incorporating a URC having an infinite impulse response, which improves the efficiency of extrinsic information exchange, as observed in Figure 3.39(a). More particularly, the URC-aided inner decoder's EXIT curve of Figure 3.39(a) is capable of reaching the $(1, 1)$ point by

Near-Capacity Design for Coherent-Detection-Aided Non-Cooperative MIMO Systems			
	MIMO Detector	Unity-Rate-Code	Channel Decoder
Three-Stage Receiver Structure	Low-complexity near-capacity center-shifting LSD of Section 3.2.3.3	Has an IIR, hence efficiently spreads the extrinsic information & improves the iteration gain	IrCCs [116], fixed average code rate, shaped EXIT curve
Key Method	EXIT curve matching algorithm of [117]		
Design Steps	**1).** Set the effective target throughput; **2).** Find the theorectical minimum SNR supporting the target transmission rate; **3).** In order to achieve a near-capacity performance at low complexity, generate the combined inner URC-SD decoder's EXIT curve at higher-than-necessary SNR; **4).** Design the IrCCs for the average target rate using EXIT curve matching.		

Table 8.8: Near-capacity design for non-cooperative coherent-detection-aided MIMO systems.

having a lower starting point, which in turn yields a reduced error floor and a higher SNR threshold, above which decoding convergence to a vanishingly low BER becomes possible. Furthermore, this slightly more complex three-stage system architecture allows us to use a low-complexity SD having a significantly reduced candidate list size N_{cand}. Alternatively, a reduced signal-to-noise ratio (SNR) is required. For example, as depicted in Figure 8.4(a), given a target BER of 10^{-5} and $N_{cand} = 32$ for the SD, the three-stage receiver is capable of achieving a performance gain of 2.5 dB over its two-stage counterpart in a rank-deficient SDMA/OFDM 4QAM system supporting $U = 8$ co-channel users and employing $N = 4$ receive antennas at the BS, namely, in an (8×4)-element system. For the sake of further enhancing the three-stage concatenated receiver, the proposed iterative center-shifting SD scheme of Section 3.2.3.3 and IrCCs of Section 3.4.3 are intrinsically amalgamated, leading to an additional performance gain of 2 dB, as also observed in Figure 8.4(a).

Figure 8.4(b) depicts the computational complexity - which is quantified in terms of the number of PED evaluations corresponding to the term ϕ of Eq.(2.24) - imposed by the SD versus the E_b/N_0 value for the above-mentioned receivers. The number of PED evaluations carried out per channel use by the system dispensing with the center-shifting scheme remains as high as 13,652, regardless of the SNR and the number of iterations, since we assume a sufficiently large buffer size to store the resultant candidate list in order to eliminate the need for list regeneration. On the other hand, in the presence of the center-shifting scheme, the candidate list has to be regenerated at each iteration, but nonetheless, the total complexity imposed by the center-shifting based SD of the two-stage receiver is substantially reduced, as seen in Figure 8.4(b). We can also observe from Figure 8.4(b) that the center-shifting K-best SD employed by the IrCC-aided three-stage system using the near-capacity design of Section 3.4.1 imposes a computational complexity, which is even below that of its center-shifting-aided two-stage counterpart, while achieving a performance gain of 2 dB at the target BER of 10^{-5}, as seen in Figure 8.4(a). Hence, the significant complexity reduction facilitated by the proposed SD scheme in the context of the three-stage receiver outweighs the relatively small additional complexity cost imposed by the URC, which only employs a two-state trellis, leading to an overall reduced complexity. Furthermore, in addition to the complexity reduction achieved by the proposed scheme, another benefit is the attainable memory reduction, since there is no need to store the resultant candidate list for the forthcoming iterations. As a result, the memory size

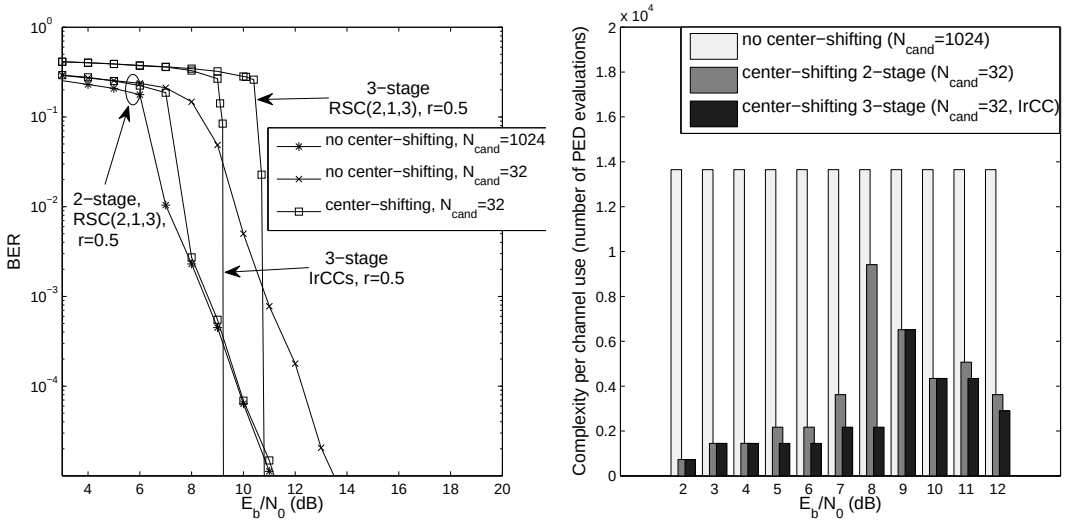

(a) BER performance

(b) Complexity

Figure 8.4: Near-capacity design for the coherent-detection-aided (8×4)-element SDMA systems. All the system parameters were given in Table 3.1.

required can be substantially reduced by having significantly reduced values of N_{cand} and K.

Prior to outlining the near-capacity design principles for the DDF-aided user-cooperation based system of Section 7.4.3, the corresponding DCMC capacity was quantified in Section 7.4.1 in comparison to that of its classic direct-transmission based counterpart in order to answer the grave fundamental question, whether it is worth introducing cooperative mechanisms into the development of wireless networks, such as the cellular voice and data networks. This is because when a cooperative wireless communication system is designed to approach the maximum achievable spectral efficiency by taking the cooperation-induced multiplexing loss into account, it is not obvious, whether or not the repetition-based relay-aided system becomes superior to its direct-transmission based counterpart, especially, when advanced channel coding techniques are employed. It was observed in Figure 7.12 of Section 7.4.1 that when the overall equivalent SNR is relatively low, the single-relay-assisted cooperative system exhibits a significantly higher capacity than its direct-transmission based counterpart in typical urban cellular radio scenarios, e.g. when having a path-loss exponent of $v = 3$. However, the achievable capacity gain may be substantially reduced, if we encounter a free-space propagation scenario [2], i.e. $v = 2$, since the reduced-path-loss-related power-gain achieved is insufficiently high to compensate for the significant multiplexing loss inherent in the single-relay-aided half-duplex cooperative system. Moreover, as the overall equivalent SNR increases to a relatively high value, there is no benefit in invoking a single-relay-aided cooperative system, since its capacity becomes lower than that of the conventional point-to-point system.

Then, based on the investigation of the single-relay-assisted DDF-based cooperative system's DCMC capacity detailed in Section 7.4.1, we proposed a practical framework of designing a cooperative system, which is capable of performing close to the network's corresponding non-coherent DCMC capacity. Specifically, based on our low-complexity near-capacity design criterion, a novel

Near-Capacity Design for Non-Coherent-Detection-Aided Cooperative MIMO Systems		
Transceiver Structure	**Ir-DHCD coding** (source+relay, Fig.7.13)	**Source's transmitter:** URC-aided three-stage transmitter employing IrCC$_s$ with code rate R_s, in order to achieve near-capacity SR transmission. **Relay's receiver:** URC-aided three-stage receiver employing the MSDSD. **Relay's transmitter:** two-stage receiver employing IrCC$_r$ having a code rate of R_r, an interleaver is added before the IrCC$_r$ to facilitate distributed turbo decoding at the BS.
	Ir-DHCD decoding (destination, Fig.7.14)	**Destination's receiver:** **1).** constituted of two parts: first part is a three-stage receiver identical to relay's receiver iterative decoding the signal received in broadcast phase; second part is a two-stage receiver corresponding to relay's transmitter, iterative decoding the signal received in relay phase. **2).** extrinsic information exchanges between the first and second parts.
Design Steps	**1).** Choose a specific network's effective throughput, based on which R_s and R_r are calculate; **2).** Find the theoretical minimum overall equivalent SNR supporting the target overall transmission rate according to the imperfect-SR-link based network's DCMC capacity of Fig.7.12; **3).** Carry out the near-capacity design for the SR link's transmission following the design steps for the P2P system of Table 8.8; **4).** Determine I^d_{inner1} and I^d_{inner2} of Fig.7.14 based on the low-complexity near-capacity criterion, as shown in Fig.7.19; **5).** Similarly, determine I^d_{inner3} of Fig.7.14 as shown in Fig.7.20. **6).** Design IrCC$_r$ for the average rate R_r, so that a narrow-but-open EXIT tunnel emerges between the EXIT curves associated with the first and second parts of the BS's receiver.	

Table 8.9: Near-capacity design for non-coherent-detection-aided cooperative MIMO systems.

Ir-DHDC coding scheme was contrived, which was depicted in Figure 7.13 in Section 7.4.2 for the DDF-aided cooperative system employing the low-complexity SISO iterative MSDSD scheme of Section 7.3. The SISO MSDSD was shown to be capacity-achieving for the direct transmission over time-selective block fading channels, as shown in Figure 7.7, provided that the observation window size N_{wind} employed was equal to the fading block length T_b. On the other hand, in order to enhance the coding gain achieved by the repetition code constituted by the relay-aided system, while maintaining a high cooperative diversity gain, the classic turbo coding mechanism was introduced into the DF aided cooperative system by interleaving the RS's estimated source data prior to re-encoding it, as seen in Figure 7.13 of Section 7.4.2, resulting in the so-called distributed turbo coding philosophy. Furthermore, in order to achieve near-capacity transmissions between the source and relay, a URC-aided three-stage serially concatenated transceiver employing the IrCCs of Section 3.4.3 may be employed in the single-relay-aided DDF cooperative system of in Figure 7.13 together with the corresponding three-stage receiver employed by the RS. According to the principles of the distributed turbo decoding mechanism proposed in [142], at the destination BS the novel iterative receiver of Figure 7.14 is used for decoding the Ir-DHCD coded signal received from the source and relay nodes. More explicitly, we have to iteratively decode the signal received during the broadcast phase and the relay phase, respectively, followed by the classic extrinsic information exchange between the two. The near-capacity single-relay-assisted cooperative system design procedure of Section 7.4.3 is summarized in Table 8.9 along with the proposed Ir-DHCD

coding scheme of Section 7.4.2.

It was clearly shown in Figure 7.23 that upon using the near-capacity system design of Section 7.4.3 the proposed Ir-DHCD coding scheme becomes capable of performing within about 2 dB and 1.8 dB from the corresponding single-relay-aided DDF cooperative system's DCMC capacity for the free space environment associated with $v = 2$ and for the typical urban scenario associated with $v = 3$, respectively. Furthermore, an SNR gain of 0.65 dB can be achieved in a free space scenario by the direct-transmission based system over its single-relay-aided cooperative counterpart, given a bandwidth efficiency of 0.47 bits/s/Hz, as shown in Figure 7.23(a). However, in a typical urban area cellular radio environment, the single-relay-aided cooperative system becomes capable of significantly outperforming the direct-transmission based system, requiring an overall transmit power which is about 2.5 dB lower than that necessitated by the latter in order to achieve an infinitesimally low BER, while maintaining a bandwidth efficiency of 0.43 bits/s/Hz, as depicted in Figure 7.23(b). Therefore, in line with our predictions made in Section 7.4.1.2, it was observed from Figures 7.23 and 7.24 that for a given target bandwidth efficiency, the single-relay-aided cooperative system does not necessarily guarantee a performance superior to that of the conventional direct-transmission based system.

8.4 Future Research Ideas

- **Apriori-LLR-Threshold-Assisted MSDSD in Channel-Coded Cooperative Systems:** In Chapter 3 the ALT scheme was proposed for the coherent SD-aided non-cooperative MIMO OFDM system in order to achieve the required complexity reduction. Similar ideas can be employed in the non-coherent SD-aided cooperative system for further reducing the complexity imposed.

- **DSTBC/DSFBC-SP Aided Cooperative Systems:** DSTBC/DSFBC scheme can be employed in the MSDSD-aided cooperative OFDM system in order to further improve the attainable transmission efficiency. Moreover, the sphere packing scheme of Chapter 4 can be also employed to jointly design the ST signals transmitted from distributed multiple antennas for the sake of further improving the achievable performance.

- **Resource Allocation for Channel-Coded Near-Capacity Differential Cooperative Systems:** Given the importance of resource allocation in the uncoded differential cooperative system of Chapter 6, it is worthwhile investigating cooperative resource allocation schemes designed for the channel-coded differentially encoded cooperative systems.

- **Successive-Relaying-Aided Differential Cooperative Systems:** As revealed in Chapter 7, the single-relay-assisted DDF cooperative system does not guarantee a superior performance in comparison to that achieved by the conventional direct-transmission based system, owing to the significant multiplexing loss inherent in the half-duplex relaying mechanism. In order to recover this multiplexing loss, a successive relaying cooperative protocol may be introduced in the differentially modulated cooperative system.

- **Interference-Limited Multi-User Differential Cooperative Systems:** In this treatise we

considered a single-source differentially encoded cooperative system in order to investigate the achievable diversity gains. However, it is worth investigating how to improve the fundamental tradeoffs between the achievable multi-path diversity gain and multiplexing gain in the context of interference-limited multi-user scenarios relying on half-duplex relay networks.

Bibliography

[1] E. Biglieri, J. Proakis, and S. Shamai, "Fading channels: information-theoretic and communications aspects," *IEEE Transactions on Information Theory*, vol. 44, pp. 2619–2692, Oct. 1998.

[2] T. S. Rappaport, *Wireless Communications Principles and Practise*. Pearson Education Asia Limited and Publishing House of Electronics Industry, second ed., 2002.

[3] L. Hanzo, M. Munster, B. J. Choi, and T. Keller, *OFDM and MC-CDMA for Broadband Multi-User Communications, WLANs and Broadcasting*. John Wiley and IEEE Press, 2003.

[4] C.Langton, *Orthogonal Frequency Division Multiplexing (OFDM) Tutorial*, 2004.

[5] A. V. Oppenheim, A. S. Willsky, and S. H. Nawab, *Signals and Systems*. second edition, Pearson Education, 2002.

[6] J. G. Proakis, *Digital Communications*. 4th edition, New York, NY: Mc-Graw-Hill, 2000.

[7] L. Hanzo, O. Alamri, M. El-Hajjar, and N. Wu, *Near-Capacity Multi-Functional MIMO Systems: sphere-packing, iterative detection, and cooperation*. First Edition, John Wiley & Sons Ltd and IEEE Press, 2009.

[8] G. J. Foschini, "Layered space-time architecture for wireless communication in fading environments when using multiple antennas," *Bell Labs Technical Journal*, vol. 2, pp. 41–59, 1996.

[9] G. J. Foschini and M. J. Gans, "On limits of wireless communications in a fading environment when using multiple antennas," *Wireless Personal Communications*, vol. 6, pp. 311–335, Mar. 1998.

[10] N. Chiurtu, B. Rimoldi, and E. Telatar, "On the capacity of multi-antenna Gaussian channels," in *Proceedings of the IEEE International Symposium on Information Theory*, (Washington, DC), June 2001.

[11] D. Gesbert, M. Shafi, D. shan Shiu, P. J. Smith, and A. Naguib, "From theory to practice: an overview of MIMO space-time coded wireless systems," *IEEE Journal on Selected Areas in Communications*, vol. 21, pp. 281–302, Apr. 2003.

[12] B. Friedlander and S. Scherzer, "Beamforming versus transmit diversity in the downlink of a cellular communications system," *IEEE Transactions on Vehicular Technology*, vol. 53, pp. 1023–1034, July 2004.

[13] A. El-Keyi and B. Champagne, "Collaborative uplink transmit beamforming with robustness against channel estimation errors," *IEEE Transactions on Vehicular Technology*, vol. 58, pp. 126–139, Jan. 2009.

[14] I. Koutsopoulos and L. Tassiulas, "The impact of space division multiplexing on resource allocation: a unified treatment of TDMA, OFDMA and CDMA," *IEEE Transactions on Communications*, vol. 56, pp. 260–269, Feb. 2008.

[15] U. Vornefeld, C. Walke, and B. Walke, "SDMA techniques for wireless ATM," *IEEE Communications Magazine*, vol. 37, pp. 52–57, Nov. 1999.

[16] G. D. Golden, C. J. Foschini, R. A. Valenzuela, and P. W. Wolniansky, "Detection algorithm and initial laboratory results using V-BLAST space-time communication architecture," *Electronics Letters*, vol. 35, pp. 14–16, Jan. 1999.

[17] B. Hochwald, T. L. Marzetta, and C. B. Papadias, "A transmitter diversity scheme for wideband CDMA systems based on space-time spreading," *IEEE Journal on Selected Areas in Communications*, vol. 19, pp. 48–60, Jan. 2001.

[18] S. M. Alamouti, "A simple transmit diversity technique for wireless communications," *IEEE Journal on Selected Areas in Communications*, vol. 16, pp. 1451–1458, Oct. 1998.

[19] X.-B. Liang and X.-G. Xia, "On the nonexistence of rate-one generalized complex orthogonal designs," *IEEE Transactions on Information Theory*, vol. 49, pp. 2984–2988, Nov. 2003.

[20] W. Su and X. G. Xia, "On space-time block codes from complex orthogonal designs," *Wireless Personal Communications*, vol. 25, pp. 1–26, April 2003.

[21] L. Z. Zheng and D. N. C. Tse, "Diversity and multiplexing: a fundamental tradeoff in multiple-antenna channels," *IEEE Transactions on Information Theory*, vol. 49, pp. 1073–1096, May 2003.

[22] R. W. Heath and A. J. Paulraj, "Switching between diversity and multiplexing in MIMO systems," *IEEE Transactions on Communications*, vol. 53, pp. 962–968, June 2005.

[23] P. Vandenameele, L. V. D. Perre, M. G. E. Engels, B. Gyselinckx, and H. J. D. Man, "A combined OFDM/SDMA approach," *IEEE Journal on Selected Areas in Communications*, vol. 18, pp. 2312–2321, Nov. 2000.

[24] A. van Zelst, R. van Nee, and G. A. Awater, "Space division multiplexing (SDM) for OFDM systems," in *IEEE 51st Vehicular Technology Conference Proceedings, VTC-Spring Tokyo.*, vol. 2, (Tokyo, Japan), pp. 1070–1074, 2000.

[25] V. Pauli, L. Lampe, and J. Huber, "Differential space-frequency modulation and fast 2-d multiple-symbol differential detection for MIMO-OFDM," *IEEE Transactions on Vehicular Technology*, vol. 57, pp. 297–310, Jan. 2008.

[26] A. Peled and A. Ruiz, "Frequency domain data transmission using reduced computational complexity algorithms," in *IEEE International Conference on Acoustics, Speech, and Signal Processing ICASSP '80.*, vol. 5, pp. 964–967, Apr. 1980.

[27] X. D. Wang and H. V. Poor, "Iterative (turbo) soft interference cancellation and decoding for coded CDMA," *IEEE Transactions on Communications*, vol. 47, pp. 1046–1061, July 1999.

[28] S. Chen, "Adaptive minimum bit-error-rate filtering," in *IEE Proceedings of Vision, Image and Signal Processing*, vol. 151, pp. 76–85, Feb. 2004.

[29] S. Chen, N. N. Ahmad, and L. Hanzo, "Adaptive minimum bit-error rate beamforming," *IEEE Transactions on Wireless Communications*, vol. 4, pp. 341–348, Mar. 2005.

[30] D. Gesbert, "Robust linear MIMO receivers: a minimum error-rate approach," *IEEE Transactions on Signal Processing*, vol. 51, pp. 2863–2871, Nov. 2003.

[31] S. Chen, B. Mulgrew, and L. Hanzo, "Least bit error rate adaptive nonlinear equalisers for binary signalling," in *Communications, IEE Proceedings-*, vol. 150, pp. 29–36, Feb. 2003.

[32] S. Chen, L. Hanzo, N. N. Ahmad, and A. Wolfgang, "Adaptive minimum bit error rate beamforming assisted QPSK receiver," in *Communications, 2004 IEEE International Conference on*, vol. 6, pp. 3389–3393, June 2004.

[33] C.-C. Yeh and J. R. Barry, "Adaptive minimum symbol-error rate equalization for quadrature-amplitude modulation," *IEEE Transactions on Signal Processing*, vol. 51, pp. 3263–3269, Dec. 2003.

[34] S. Chen, A. Livingstone, H. Q. Du, and L. Hanzo, "Adaptive minimum symbol error rate beamforming assisted detection for quadrature amplitude modulation," *IEEE Transactions on Wireless Communications*, vol. 7, pp. 1140–1145, Apr. 2008.

[35] P. A. Hoeher, S. Badri-Hoeher, W. Xu, and C. Krakowski, "Single-antenna co-channel interference cancellation for TDMA cellular radio systems," *IEEE Wireless Communications [see also IEEE Personal Communications]*, vol. 12, pp. 30–37, Apr. 2005.

[36] H. Lee, B. Lee, and I. Lee, "Iterative detection and decoding with an improved v-BLAST for MIMO-OFDM systems," *IEEE Journal on Selected Areas in Communications*, vol. 24, pp. 504–513, Mar. 2006.

[37] S. W. Kim and K. P. Kim, "Log-likelihood-ratio-based detection ordering in v-BLAST," *IEEE Transactions on Communications*, vol. 54, pp. 302–307, Feb. 2006.

[38] M. Ghotbi and M. R. Soleymani, "Multiuser detection of DS-CDMA signals using partial parallel interference cancellation in satellite communications," *IEEE Journal on Selected Areas in Communications*, vol. 22, pp. 584–593, Apr. 2004.

[39] A. Wolfgang, S. Chen, and L. Hanzo, "Parallel interference cancellation based turbo space-time equalization in the SDMA uplink," *IEEE Transactions on Wireless Communications*, vol. 6, pp. 609–616, Feb. 2007.

[40] A. Wolfgang, S. Chen, and L. Hanzo, "Decision feedback aided bayesian turbo space-time equalizer for parallel interference cancellation in SDMA systems," in *IEEE 62nd Vehicular Technology Conference, VTC 2005-Fall.*, vol. 4, pp. 2112–2116, Sept. 2005.

[41] M. O. Damen, K. Abed-Meraim, and J. C. Belfiore, "Generalised sphere decoder for asymmetrical space-time communication architecture," *Electronics Letters*, vol. 36, pp. 166–167, Jan. 2000.

[42] Z. Yang, C. Liu, and J. He, "A new approach for fast generalized sphere decoding in MIMO systems," *IEEE Signal Processing Letters*, vol. 12, pp. 41–44, Jan. 2005.

[43] T. Cui and C. Tellambura, "An efficient generalized sphere decoder for rank-deficient MIMO systems," *IEEE Communications Letters*, vol. 9, pp. 423–425, May 2005.

[44] J. Akhtman and L. Hanzo, "An optimized-hierarchy-aided maximum likelihood detector for MIMO-OFDM," *IEEE 63rd Vehicular Technology Conference, VTC 2006-Spring*, vol. 3, pp. 1526–1530, 2006.

[45] S. M. Kay, *Fundamentals of Statistical Signal Processing, Estimation Theory*. Prentice Hall New Jersey, 1993.

[46] U. Fincke and M. Pohst, "Improved methods for calculating vectors of short length in a lattice, including a complexity analysis," *Mathematics of Computation*, vol. Vol. 44, pp. 463–471, April 1985.

[47] E. Viterbo and J. Boutros, "A universal lattice code decoder for fading channels," *IEEE Transactions on Information Theory*, vol. 45, pp. 1639–1642, July 1999.

[48] L. Brunel and J. J. Boutros, "Lattice decoding for joint detection in direct-sequence CDMA systems," *IEEE Transactions on Information Theory*, vol. 49, pp. 1030–1037, Apr. 2003.

[49] B. Hassibi and H. Vikalo, "On the sphere-decoding algorithm i. expected complexity," *IEEE Transactions on Signal Processing*, vol. 53, pp. 2806–2818, Aug. 2005.

[50] T. Cui and C. Tellambura, "An efficient generalized sphere decoder for rank-deficient MIMO systems," *IEEE 60th Vehicular Technology Conference, VTC2004-Fall*, vol. 5, pp. 3689–3693, Sept. 2004.

[51] B. M. Hochwald and S. ten Brink, "Achieving near-capacity on a multiple-antenna channel," *IEEE Transactions on Communications*, vol. 51, pp. 389–399, Mar. 2003.

[52] H. Vikalo, B. Hassibi, and T. Kailath, "Iterative decoding for MIMO channels via modified sphere decoding," *IEEE Transactions on Wireless Communications*, vol. 3, pp. 2299–2311, Nov. 2004.

[53] L. Lampe, R. Schober, V. Pauli, and C. Windpassinger, "Multiple-symbol differential sphere decoding," *IEEE Transactions on Communications*, vol. 12, pp. 1981–1985, Dec. 2005.

[54] V. Pauli, L. Lampe, and R. Schober, ""Turbo DPSK" using soft multiple-symbol differential sphere decoding," *IEEE Transactions on Information Theory*, vol. 52, no. 4, pp. 1385–1398, 2006.

[55] D. Divsalar and M. K. Simon, "Multiple-symbol differential detection of MPSK," *IEEE Transactions on Communications*, vol. 38, pp. 300–308, Mar. 1990.

[56] D. Divsalar and M. K. Simon, "Maximum-likelihood differential detection of uncoded and trellis-coded amplitude phase modulation over awgn and fading channels–metrics and performance," *IEEE Transaction on Communications*, vol. 42, pp. 76–89, Jan. 1994.

[57] V. Pauli and L. Lampe, "Multiple-symbol differential sphere decoding for unitary space-time modulation," *IEEE Global Telecommunications Conference*, vol. 3, p. 6, Nov. 2005.

[58] V. Pauli and L. Lampe, "On the complexity of sphere decoding for differential detection," *IEEE Transactions on Information Theory*, vol. 53, pp. 1595–1603, Apr. 2007.

[59] J. Akhtman, A. Wolfgang, S. Chen, and L. Hanzo, "An optimized-hierarchy-aided approximate log-MAP detector for MIMO systems," *IEEE Transactions on Wireless Communications*, vol. 6, pp. 1900–1909, May 2007.

[60] Z. Guo and P. Nilsson, "Algorithm and implementation of the K-best sphere decoding for MIMO detection," *IEEE Journal on Selected Areas in Communications*, vol. 24, pp. 491–503, Mar. 2006.

[61] K. Wong, C. Tsui, R. S. K. Cheng, and W. Mow, "A VLSI architecture of a K-best lattice decoding algorithm for MIMO channels," vol. 3, pp. III–273 – III–276, May 2002.

[62] S. Thoen, L. Deneire, L. V. der Perre, M. Engels, and H. D. Man, "Constrained least squares detector for OFDM/SDMA-based wireless networks," *IEEE Transactions on Wireless Communications*, vol. 2, pp. 129–140, Jan. 2003.

[63] D. Gesbert, "Robust linear MIMO receivers: a minimum error-rate approach," *IEEE Transactions on Signal Processing*, vol. 51, pp. 2863–2871, Nov. 2003.

[64] H. Lee, B. Lee, and I. Lee, "Iterative detection and decoding with an improved v-BLAST for MIMO-OFDM systems," *IEEE Journal on Selected Areas in Communications*, vol. 24, pp. 504–513, Mar. 2006.

[65] R. Gallager, "Low-density parity-check codes," *IRE Transactions on Information Theory*, vol. 8, pp. 21–28, Jan. 1962.

[66] Z. Yang, C. Liu, and J. He, "A new approach for fast generalized sphere decoding in MIMO systems," *IEEE Signal Processing Letters*, vol. 12, pp. 41–44, Jan. 2005.

[67] R. Wang and G. B. Giannakis, "Approaching MIMO channel capacity with soft detection based on hard sphere decoding," *IEEE Transactions on Communications*, vol. 54, pp. 587–590, Apr. 2006.

[68] R. S. Mozos and M. J. F. G. Garcia, "Efficient complex sphere decoding for MC-CDMA systems," *IEEE Transactions on Wireless Communications*, vol. 5, pp. 2992–2996, Nov. 2006.

[69] H. Zhu, B. Farhang-Boroujeny, and R. R. Chen, "On performance of sphere decoding and markov chain monte carlo detection methods," *IEEE Signal Processing Letters*, vol. 12, pp. 669–672, Oct. 2005.

[70] B. Farhang-Boroujeny, H. Zhu, and Z. Shi, "Markov chain monte carlo algorithms for CDMA and MIMO communication systems," *IEEE Transactions on Signal Processing*, vol. 54, pp. 1896–1909, May 2006.

[71] P. Aggarwal and X. D. Wang, "Multilevel sequential monte carlo algorithms for MIMO demodulation," *IEEE Transactions on Wireless Communications*, vol. 6, pp. 750–758, Feb. 2007.

[72] H. Zhu, B. Farhang-Boroujeny, and R.-R. Chen, "On performance of sphere decoding and markov chain monte carlo detection methods," *IEEE Signal Processing Letters*, vol. 12, pp. 669–672, Oct. 2005.

[73] B. Farhang-Boroujeny, H. Zhu, and Z. Shi, "Markov chain monte carlo algorithms for CDMA and MIMO communication systems," *IEEE Transactions on Signal Processing*, vol. 54, pp. 1896–1909, May 2006.

[74] A. Doucet and X. D. Wang, "Monte carlo methods for signal processing: a review in the statistical signal processing context," *IEEE Signal Processing Magazine*, vol. 22, pp. 152–170, Nov. 2005.

[75] C. Ergun and K. Hacioglu, "Multiuser detection using a genetic algorithm in CDMA communications systems," *IEEE Transactions on Communications*, vol. 48, pp. 1374–1383, Aug. 2000.

[76] L. Wang, L. Xu, S. Chen, and L. Hanzo, "Channel coded iterative center-shifting k-best sphere detection for rank-deficient systems," in *Vehicular Technology Conference, 2008. VTC 2008-Fall. IEEE 68th*, (Calgary, BC), pp. 1–5, Sept. 2008.

[77] L. Wang, L. Xu, S. Chen, and L. Hanzo, "MMSE soft-interference-cancellation aided iterative center-shifting k-best sphere detection for MIMO channels," in *IEEE International Conference on Communications, 2008. ICC '08.*, (Beijing), pp. 3819–3823, May 2008.

[78] L. Wang, L. Xu, S. Chen, and L. Hanzo, "Generic iterative search-centre-shifting k-best sphere detection for rank-deficient SDM-OFDM systems," *Electronics Letters*, vol. 44, pp. 552–553, Apr. 2008.

[79] L. Wang, L. Xu, S. Chen, and L. Hanzo, "Apriori-LLR-threshold-assisted k-best sphere detection for MIMO channels," in *Vehicular Technology Conference, 2008. VTC Spring 2008. IEEE*, (Singapore), pp. 867–871, May 2008.

[80] L. Wang, O. Alamri, and L. Hanzo, "K-best sphere detection for the sphere packing modulation aided SDMA/OFDM uplink," in *IEEE Global Telecommunications Conference, 2008. IEEE GLOBECOM 2008.*, (New Orleans, LO), pp. 1–5, Nov./Dec. 2008.

[81] L. Wang, O. Alamri, and L. Hanzo, "Sphere packing modulation in the SDMA uplink using *k*-best sphere detection," *IEEE Signal Processing Letters*, vol. 16, pp. 291–294, Apr. 2009.

[82] L. Wang, L. Xu, S. Chen, and L. Hanzo, "Three-stage serially concatenated codes and iterative center-shifting k-best sphere detection for SDM-OFDM: An EXIT chart aided perspective," in *Wireless Communications and Networking Conference, 2008. WCNC 2008. IEEE*, (Las Vegas, NV), pp. 611–615, Mar./Apr. 2008.

[83] L. Wang, L. Xu, S. Chen, and L. Hanzo, "Three-stage irregular convolutional coded iterative center-shifting *k*-best sphere detection for soft-decision SDMAOFDM," *IEEE Transactions on Vehicular Technology*, vol. 58, pp. 2103–2109, May 2009.

[84] L. Wang and L. Hanzo, "Multiple-symbol differential sphere detection for the amplify-and-forward cooperative uplink," in *IEEE Vehicular Technology Conference, 2009. VTC Fall 2009.*, (Anchorage, USA), Sept. 2009.

[85] L. Wang and L. Hanzo, "The amplify-and-forward cooperative uplink using multiple-symbol differential sphere-detection," *IEEE Signal Processing Letters*, vol. 16, pp. 913–916, Oct. 2009.

[86] L. Wang and L. Hanzo, "The resource-optimized differentially modulated hybrid af/df cooperative cellular uplink," in *IEEE Global Telecommunications Conference, 2009. IEEE GLOBECOM 2009.*, (Hawaii, USA), Nov./Dec. 2009.

[87] L. Wang and L. Hanzo, "The resource-optimized differentially modulated hybrid AF/DF cooperative cellular uplink using multiple-symbol differential sphere detection," *IEEE Signal Processing Letters*, vol. 16, pp. 965–968, Nov. 2009.

[88] L. Wang, L. K. Kong, S. X. Ng, and L. Hanzo, "To cooperate or not: A capacity perspective," in *in IEEE Vehicular Technology Conference (VTC 2010 Spring), May 2010.*

[89] L. Wang, L. K. Kong, S. X. Ng, and L. Hanzo, "A near-capacity differentially encoded noncoherent adaptive multiple-symbol-detection aided three-stage coded scheme," in *in IEEE Vehicular Technology Conference (VTC 2010 Spring), May 2010.*

[90] A. M. Chan and I. Lee, "A new reduced-complexity sphere decoder for multiple antenna systems," vol. 1, pp. 460–464, Apr./May 2002.

[91] K. Su and I. J. Wassell, "A new ordering for efficient sphere decoding," in *IEEE International Conference on Communications, 2005. ICC 2005.*, vol. 3, pp. 1906–1910, May 2005.

[92] D. Pham, K. R. Pattipati, P. K. Willett, and J. Luo, "An improved complex sphere decoder for v-BLAST systems," *IEEE Signal Processing Letters*, vol. 11, pp. 748–751, Sept. 2004.

[93] Q. Liu and L. Yang, "A novel method for initial radius selection of sphere decoding," *IEEE 60th Vehicular Technology Conference 2004. VTC2004-Fall.*, vol. 2, pp. 1280–1283, Sept. 2004.

[94] J. Pons and P. Duvaut, "New approaches for lowering path expansion complexity of k-best MIMO detection algorithms," in *Communications, 2009. ICC '09. IEEE International Conference on*, (Dresden), pp. 1–6, June 2009.

[95] B. Kim, H. Kim, and K. Choi, "An adaptive k-best algorithm without SNR estimation for MIMO systems," in *Vehicular Technology Conference, 2008. VTC Spring 2008. IEEE*, (Singapore), pp. 817–821, May 2008.

[96] M. Pohst, "On the Computation of Lattice Vectors of Minimal Length, Successive Minima and Reduced Bases With Applications," *Proc. ACMSIGSAM*, pp. 37–44, 1981.

[97] M. O. Damen, K. Abed-Meraim, and M. S. Lemdani, "Further results on the sphere decoder," *Proceedings of the IEEE International Symposium on Information Theory*, p. 333, June 2001.

[98] J. Li and Y. Yang, "Ordered sphere detector for high rate spatial multiplexing architecture," *Proceedings of the IEEE 6th Circuits and Systems Symposium on Emerging Technologies: Frontiers of Mobile and Wireless Communication*, vol. 2, pp. 417–420, May/June 2004.

[99] O. Damen, A. Chkeif, and J. C. Belfiore, "Lattice code decoder for space-time codes," *IEEE Communications Letters*, vol. 4, pp. 161–163, May 2000.

[100] C. Berrou, A. Glavieux, and P. Thitimajshima, "Near shannon limit error-correcting coding and decoding: Turbo-codes. 1," in *in IEEE International Conference on Communications, 1993. ICC 93.*, vol. 2, (Geneva), pp. 1064–1070, May 1993.

[101] C. Berrou and A. Glavieux, "Near optimum error correcting coding and decoding: turbo-codes," *IEEE Transactions on Communications*, vol. 44, pp. 1261–1271, Oct. 1996.

[102] S. Benedetto, D. Divsalar, G. Montorsi, and F. Pollara, "Analysis, design, and iterative decoding of double serially concatenated codes with interleavers," *IEEE Journal on Selected Areas in Communications*, vol. 16, pp. 231–244, Feb. 1998.

[103] J. Li, K. B. Letaief, and Z. Cao, "Space-time turbo multiuser detection for coded MC-CDMA," *IEEE Transactions on Wireless Communications*, vol. 4, pp. 538–549, Mar. 2005.

[104] L. Hanzo, T. H. Liew, and B. L. Yeap, *Turbo Coding, Turbo Equalisation and Space-Time Coding for Transmission over Fading Channels*. John Wiley and IEEE Press, 2002.

[105] L. Hanzo, C. H. Wong, and M. S. Yee, *Adaptive Wireless Transceivers*. John Wiley and IEEE Press, 2002.

[106] S. Baro, J. Hagenauer, and M. Witzke, "Iterative detection of MIMO transmission using a list-sequential (LISS) detector," vol. 4, pp. 2653–2657, May 2003.

[107] M. S. Yee, "Max-log-MAP sphere decoder," *Proceedings of IEEE International Conference on Acoustics, Speech, and Signal Processing, 2005.*, vol. 3, Mar. 2005.

[108] M. Tuchler, A. C. Singer, and R. Koetter, "Minimum mean squared error equalization using a priori information," *IEEE Transactions on Signal Processing*, vol. 50, pp. 673–683, Mar. 2002.

[109] S. Tan, S. Chen, and L. Hanzo, "MBER turbo multiuser beamforming aided QPSK receiver design using EXIT chart analysis," in *IEEE 66th Vehicular Technology Conference, 2007. VTC-2007 Fall.*, (Baltimore, MD), pp. 561–565, Sept./Oct. 2007.

[110] L. Xu, S. Tan, S. Chen, and L. Hanzo, "Iterative minimum bit error rate multiuser detection in multiple antenna aided OFDM," *2006. WCNC 2006. IEEE Wireless Communications and Networking Conference*, vol. 3, pp. 1603–1607, Apr. 2006.

[111] J. Wang, S. X. Ng, L. L. Yang, and L. Hanzo, "Combined serially concatenated codes and MMSE equalization: An EXIT chart aided perspective," *IEEE 64th Vehicular Technology Conference, 2006. VTC-2006 Fall.*, pp. 1–5, Sept. 2006.

[112] J. Wang, S. X. Ng, A. Wolfgang, L. L. Yang, S.Chen, and L. Hanzo, "Near-Capacity Three-Stage MMSE Turbo Equalization Using Irregular Convolutional Codes," *in the 4th International Symposium on Turbo Codes in connection with 6th International ITG-Conference on Source and Channel Coding / ISTC'06, Munich, Germany*, April 2006.

[113] J. Kliewer, S. X. Ng, and L. Hanzo, "Efficient computation of exit functions for non-binary iterative decoding," *IEEE Transactions on Communications*, vol. 54, pp. 2133–2136, Dec. 2006.

[114] J. Kliewer, A. Huebner, and D. J. Costello, "On the achievable extrinsic information of inner decoders in serial concatenation," in *Proceedings of the IEEE International Symposium on Information Theory*, (Seattle, WA, USA), pp. 2680–2684, July 2006.

[115] S. X. Ng, J. Wang, and L. Hanzo, "Unveiling near-capacity code design: The realization of Shannon's communication theory for MIMO channels," *IEEE International Conference on Communications, 2008*, pp. 1415–1419, May 2008.

[116] M. Tüchler and J. Hagenauer, "Exit charts of irregular codes," *in Proceedings of Conference on the Information Science and Systems [CDROM], Princeton University*, pp. 20–22, 2002.

[117] M. Tüchler, "Design of serially concatenated systems depending on the block length," *IEEE Transactions on Communications*, vol. 52, pp. 209–218, Feb. 2004.

[118] J. H. Conway and N. J. A. Sloane, *Sphere Packings, Lattices and Groups*. third edition, Springer-Verlag, 1999.

[119] W. F. Su, Z. Safar, and K. J. R. Liu, "Space-time signal design for time-correlated Rayleigh fading channels," *IEEE International Conference on Communications 2003.*, vol. 5, pp. 3175–3179, May 2003.

[120] V. Tarokh, H. Jafarkhani, and A. R. Calderbank, "Space-time block codes from orthogonal designs," *IEEE Transactions on Information Theory*, vol. 45, pp. 1456–1467, July 1999.

[121] A. F. Naguib, N. Seshadri, and A. R. Calderbank, "Applications of space-time block codes and interference suppression for high capacity and high data rate wireless systems," *The Thirty-Second Asilomar Conference on Signals, Systems & Computers*, vol. 2, pp. 1803–1810, Nov. 1998.

[122] O. R. Alamri, B. L. Yeap, and L. Hanzo, "A turbo detection and sphere-packing-modulation-aided space-time coding scheme," *IEEE Transaction on Vehicular Technology*, vol. 56, pp. 575–582, Mar. 2007.

[123] S. ten Brink, "Convergence behavior of iteratively decoded parallel concatenated codes," *IEEE Transactions on Communications*, vol. 49, pp. 1727–1737, Oct. 2001.

[124] L. Hanzo, L.-L. Yang, E.-L. Kuan, and K. Yen, *Single and Multi-Carrier DS-CDMA: Multi-User Detection, Space-Time Spreading, Synchronisation, Networking and Standards*. Wiley-IEEE Press, 2003.

[125] J. N. Laneman, D. N. C. Tse, and G. W. Wornell, "Cooperative diversity in wireless networks: Efficient protocols and outage behavior," *IEEE Transaction on Information Theory*, vol. 50, pp. 3062–3080, Dec. 2004.

[126] D. Divsalar and M. K. Simon, "Multiple-symbol differential detection of mpsk," *IEEE Transaction on Communications*, vol. 38, no. 3, pp. 300–308, 1900.

[127] M. O. Damen, H. E. Gamal, and G. Caire, "On maximum-likelihood detection and the search for the closest lattice point," *IEEE Transactions on Information Theory*, vol. 49, pp. 2389–2402, Oct. 2003.

[128] T. Himsoon, W. Su, and K. J. R. Liu, "Differential transmission for amplify-and-forward cooperative communications," *IEEE Signal Processing Letters*, vol. 12, pp. 597–600, Sept. 2005.

[129] T. Himsoon, W. P. Siriwongpairat, W. Su, and K. J. R. Liu, "Differential modulation with threshold-based decision combining for cooperative communications," *IEEE Transaction on Signal Processing*, vol. 55, pp. 3905–3923, July 2007.

[130] M. K. Simon and M. S. Alouini, "A unified approach to the probability of error for noncoherent and differentially coherent modulations over generalized fading channels," *IEEE Transactions on Communications*, vol. 46, pp. 1625–1638, Dec. 1998.

[131] T. Himsoon, W. P. Siriwongpairat, W. Su, and K. J. R. Liu, "Differential modulations for multinode cooperative communications," *IEEE Transactions on Signal Processing*, vol. 56, pp. 2941–2956, July 2008.

[132] I. S. Gradshteyn and I. M. Ryzhik, *Table of Integrals, Series, and Products*. Seventh Edition, Springer-Verlag, 2007.

[133] Q. T. Zhang and X. W. Cui, "A closed-form expression for the symbol-error rate of M-ary DPSK in fast Rayleigh fading," vol. 53, pp. 1085–1087, 2005.

[134] S. X. Ng, Y. Li, and L. Hanzo, "Distributed turbo trellis coded modulation for cooperative communications," in *IEEE International Conference on Communications, 2009. ICC '09.*, (Dresden), pp. 1–5, June 2009.

[135] K. Lee and L. Hanzo, "Iterative detection and decoding for hard-decision forwarding aided cooperative spatial multiplexing," in *IEEE International Conference on Communications, 2009. ICC '09.*, (Dresden), pp. 1–5, June 2009.

[136] T. L. Marzetta and B. M. Hochwald, "Capacity of a mobile multiple-antenna communication link in rayleigh flat fading," *IEEE Transactions on Information Theory*, vol. 45, pp. 139–157, Jan. 1999.

[137] L. Z. Zheng and D. N. C. Tse, "Communication on the grassmann manifold: a geometric approach to the noncoherent multiple-antenna channel," *IEEE Transactions on Information Theory*, vol. 48, pp. 359–383, Feb. 2002.

[138] Y. Liang and V. V. Veeravalli, "Capacity of noncoherent time-selective rayleigh-fading channels," *IEEE Transactions on Information Theory*, vol. 50, pp. 3095–3110, Dec. 2004.

[139] T. M. Cover and J. A. Thomas, *Elements of Information Theory*. Second Edition, John Wiley & Sons, Inc., 2006.

[140] R. R. Chen, R. Koetter, U. Madhow, and D. Agrawal, "Joint noncoherent demodulation and decoding for the block fading channel: a practical framework for approaching shannon capacity," *IEEE Transactions on Communications*, vol. 51, pp. 1676–1689, Oct. 2003.

[141] A. Ashikhmin, G. Kramer, and S. ten Brink, "Extrinsic information transfer functions: model and erasure channel properties," *IEEE Transactions on Information Theory*, vol. 50, pp. 2657–2673, Nov. 2004.

[142] B. Zhao and M. C. Valenti, "Distributed turbo coded diversity for relay channel," *Electronics Letters*, vol. 39, pp. 786–787, May 2003.

[143] J. Kliewer, A. Huebner, and D. J. Costello, "On the achievable extrinsic information of inner decoders in serial concatenation," in *IEEE International Symposium on Information Theory, 2006.*, (Seattle, WA), pp. 2680–2684, July 2006.

[144] Y. Fan, C. Wang, J. Thompson, and H. V. Poor, "Recovering multiplexing loss through successive relaying using repetition coding," *IEEE Transactions on Wireless Communications*, vol. 6, pp. 4484–4493, Dec. 2007.

Glossary

3GPP-LTE	Third-Generation Partnership Projects Long Term Evolution
AF	Amplify-and-Forward
AGC	Automatic Gain Control
ALT	*Apriori*-LLR-Threshold
APC	Adaptive Power Control
APC	Adaptive-Power-Control
APP	*A Posteriori* Probability
AWGN	Additive White Gaussian Noise
BER	Bit Error Rate
BS	Base Station
CDD	Conventional Differential Detection
CDMA	Code Division Multiple Access
CIRs	Channel Impulse Responses
CP	Cyclic Prefix
CPS	Cooperative-Protocol-Selection
CRC	Cyclic Redundancy Check
CSCF	Cumulative Sub-Cost Function
CSI	Channel State Information
CUS	Cooperating-User-Selection
DAF	Differental-Amplify-and-Forward
DAF	Differential Amplify-and-Forward
DCMC	Discrete-input Continuous-output Memoryless Channel
DDF	Differential Decode-and-Forward
DDF	Differential-Decode-and-Forward
DF	Decode-and-Forward
DFDD	Decision-Feedback Differential Detection
DFT	Discrete Fourier Transform

DHDC	Direct-Hard-Decsion-Center-Shifting
DPSK	Differential Phase Shift Keying
DSDC	Direct-Soft-Decision-Center-Shifting
FD	Frequency-Domain
FDCTF	Frequency-Domain Channel Transfer Factor
FDM	Frequency Division Multiplexing
FDMA	Frequency Division Multiple Access
FFT	Fast Fourier Transform
GA	Genetic Algorithm
GSD	Generalized Sphere Detection
HIHO	Hard-Input Hard-Output
HT	Hilly Terrain
IDFT	Inverse Discrete Fourier Transform
IFFT	Inverse Fast Fourier Transform
IIR	Infinite-Impulse-Response
Ir-DHCD	Irregular Distributed Hybrid Concatenated Differential
IrCCs	Irregular Convolutional Codes
ISI	Inter-Symbol-Interference
ISR	Initial Search Radius
LDPC	Low-Density Parity-Check
LLR	Log-Likelihood Ratio
LOS	Line-Of-Sight
LS	Least Square
LSD	List Sphere Decoders
MAP	Maximum-a-Posteriori
MC	Multi-Carrier
MCMC	Markov Chain Monte Carlo
MED	Minimum Euclidean Distance
MGF	Joint Moment Generating Function
MI	Mutual Information
MIMO	Multiple-Input Multiple-Output
ML	Maximum-Likelihood
ML-MSDD	Maximum-Likelihood Multiple-Symbol Differential Detection
MMSE	Minimum Mean Squared Error
MS	Mobile Station
MSDD	Multiple-Symbol Differential Detection
MSDSD	Multiple-Symbol Differential Sphere Detection

MSE	Mean Squared Error
MSER	Minimum Symbol Error Rate
MSI	Multi-Stream-Interference
MU-MIMO	Multi-User MIMO
MUI	Multiple-Access-Interference
OF	Objective Function
OFDM	Orthogonal Frequency-Division Multiplexing
OHRSA	Optimized Hierarchy Reduced Search Algorithm
OHRSA	Optimized-Hierarchy-Reduced-Search-Algorithm
OSTBC	Orthogonal STBC
PED	Partial Euclidean Distance
PIC	Parallel Interference Cancellation
PLR	Packet Loss Ratio
QAM	Quadrature Amplitude Modulation
RA	Rural Area
RS	Relay Station
RSC	Recursive Systematic Convolutional
S/P	Serial-to-Parallel
SC	Single-Carrier
SCF	Sub-Cost Function
SD	Sphere Detection
SIC	Serial Interference Cancellation
SIC-MMSE	Soft Interference Cancellation aided MMSE
SISO	Soft-Input Soft-Output
SP	Sphere Packing
SSD	Sorted SD
SSD	Sorted Sphere Detection
SSD-TT	Termination-Threshold-Aided Sorted SD
SSD-UB	Updated-Bound-Aided Sorted SD
STBC	Space-Time Block Codes
STBC	Space-Time Block Coding
STC	Space-Time Coding
SU-MIMO	Single-User MIMO
TD	Time-Domain
TDMA	Time Division Multiple Access
TH	Typical Urban
TT	Termination Threshold

UL	Uplink
URC	Unity-Rate Code
URC	Unity-Rate-Code
V-BLAST	Vertical Bell LAbs Layered Space Time
VAA	Virtual Antenna Array

Subject Index

Author Index

V

W

X

Y

Z